

AMMRC MS 77-5

B

ADA 045877

CASE STUDIES IN FRACTURE MECHANICS

Edited by

THOMAS P. RICH and DAVID J. CARTWRIGHT
MECHANICS OF MATERIALS DIVISION

June 1977

AD No.
DDC FILE COPY

DDC
RECEIVED
NOV 3 1977
D

of

Approved for public release; distribution unlimited.

ARMY MATERIALS AND MECHANICS RESEARCH CENTER
Watertown, Massachusetts 02172

The findings in this report are not to be construed as an official Department of the Army position, unless so designated by other authorized documents.

Mention of any trade names or manufacturers in this report shall not be construed as advertising nor as an official indorsement or approval of such products or companies by the United States Government.

DISPOSITION INSTRUCTIONS

Destroy this report when it is no longer needed.
Do not return it to the originator.

UNCLASSIFIED

SECURITY CLASSIFICATION OF THIS PAGE (When Data Entered)

REPORT DOCUMENTATION PAGE		READ INSTRUCTIONS BEFORE COMPLETING FORM
1. REPORT NUMBER 14 AMMRC-MS-77-5	2. GOVT ACCESSION NO.	3. RECIPIENT'S CATALOG NUMBER
4. TITLE (and Subtitle) CASE STUDIES IN FRACTURE MECHANICS.		5. TYPE OF REPORT & PERIOD COVERED 9 Final Report.
7. Edited by 10 Thomas P. Rich David J. Cartwright		6. PERFORMING ORG. REPORT NUMBER
9. PERFORMING ORGANIZATION NAME AND ADDRESS Army Materials and Mechanics Research Center Watertown, Massachusetts 02172 DRXMR-TM		8. CONTRACT OR GRANT NUMBER(s)
11. CONTROLLING OFFICE NAME AND ADDRESS U. S. Army Materiel Development and Readiness Command, Alexandria, Virginia 22333		10. PROGRAM ELEMENT, PROJECT, TASK AREA & WORK UNIT NUMBERS D/A Project: 1T865803M75 AMCMS Code: 685803.7290012
14. MONITORING AGENCY NAME & ADDRESS (if different from Office)		12. REPORT DATE 11 June 1977
		13. NUMBER OF PAGES 496 125471
		15. SECURITY CLASS. (of this report) Unclassified
		15a. DECLASSIFICATION/DOWNGRADING SCHEDULE
16. DISTRIBUTION STATEMENT (of this Report) Approved for public release; distribution unlimited.		
17. DISTRIBUTION STATEMENT (of the abstract entered in Block 20, if different from Report)		
18. SUPPLEMENTARY NOTES *Department of Mechanical Engineering, The University of Southampton, England		
19. KEY WORDS (Continue on reverse side if necessary and identify by block number) (SEE REVERSE SIDE)		
20. ABSTRACT (Continue on reverse side if necessary and identify by block number) (SEE REVERSE SIDE)		

403105

UNCLASSIFIED

SECURITY CLASSIFICATION OF THIS PAGE(When Data Entered)

Block No. 19

KEY WORDS

Aerospace craft	Helicopter rotor	Reliability
Aircraft engines	Helicopters	Rocket engine cases
Airframes	Joints	Rotation
Cracking (fracturing)	Machines	Ships
Cracks	Materials	Spacecraft
Damage	Mechanics	Stress concentrations
Damage tolerance	Military bridges	Structural mechanics
Defects	Mounts	Structural response
Failure	Nondestructive testing	Structures
Fatigue (mechanics)	Pressure vessels	Turbines
Fracture (mechanics)	Propellers (Marine)	Vehicles
Fuselages	Railroads	Welds
Gun Barrels	Railroad tracks	Wings

Block No. 20

ABSTRACT

→ A collection of more than thirty case studies is presented covering a wide range of practical engineering applications of fracture mechanics to design, inspection, maintenance, and failure analysis. The case studies are written by individual specialists within industry, government, and academia from the United States and Great Britain. The collection is divided into five sections corresponding to (1) Aerospace, (2) Joints and Mountings, (3) Pressure Vessels and Rotating Machinery, (4) Surface Vehicles, and (5) Materials. Most of the case studies are between twelve and fifteen pages in length and written to a standard format. The interdisciplinary nature of fracture applications is reflected in the case studies, and the reader is brought through a sequential development and solution of actual engineering problems in an interesting and economical manner.

↑

ACCESSION for	
NTIS	White Section <input checked="" type="checkbox"/>
DDC	Buff Section <input type="checkbox"/>
UNANNOUNCED	<input type="checkbox"/>
JUSTIFICATION	
BY	
DISTRIBUTION/AVAILABILITY CODES	
Dist	AVAIL. and/or SPECIAL
A	

DDC
RECEIVED
NOV 3 1977
REGULATED
D

UNCLASSIFIED

SECURITY CLASSIFICATION OF THIS PAGE(When Data Entered)

PREFACE

The need to use materials which will be resistant to fracture and to design structures such that cracks/flaws will not cause catastrophic failure is well recognized. Research over the past two decades has provided a core of knowledge on the mechanics of fracture. This knowledge is now being used to solve important engineering problems in the safe design of structures which may contain flaws during their service life. The point has been reached at which the accumulated experience on the applications of fracture mechanics to design and failure makes possible the opportunity for a wide exchange of information. This will enable newcomers to the field of applied fracture mechanics to learn how it is actually utilized. It will also provide fracture specialists with a useful source of new ideas on fracture applications from areas outside their own specialization.

As part of its role as the U.S. Army Materiel Development and Readiness Command's (DARCOM) Lead Laboratory in Solid Mechanics, the Mechanics Research Laboratory of the Army Materials and Mechanics Research Center, Watertown, Massachusetts, conducted *A Survey of Fracture Mechanics Applications in the United States* (AMMRC MS 76-1, February 1976; also to be published in *Engineering Fracture Mechanics*). An analysis of the results of this survey indicated that the participants showed a high interest in developing a means for increased exchange of fracture mechanics data and design methodology. *Case Studies in Fracture Mechanics* is a step toward meeting this need. Contributions were collected from approximately fifty designers, engineers, and scientists across the United States and the United Kingdom of Great Britain who are directly involved with some aspect of the practical application of fracture mechanics. By this means, it has been possible to bring together in one volume a wide range of fracture applications written to a structured case study format. As the title indicates, *Case Studies in Fracture Mechanics* is a history of the experiences of engineers and scientists in the applications of fracture mechanics to engineering problems in design, maintenance, and failure analysis.

Many of the authors indicated a wish to discuss their contributions with each other and a small number of fracture specialists. With this in mind, a Forum on Case Studies in Fracture Mechanics was held at Massachusetts Institute of Technology on the 16th and 17th of June 1977. The sessions of the meeting followed the five section divisions of this volume: Aerospace, Joints and Mountings, Pressure Vessels and Rotating Machinery, Surface Vehicles, and Materials.

Case Studies in Fracture Mechanics will be of immediate use to all individuals concerned with hardware design and failure analysis. It will also provide a valuable supplement for fracture mechanics education in the academic community. In this way it is hoped to serve as a stimulation for continued documentation and transfer of experience on the actual uses of fracture mechanics. This could assist applications engineers in improving the fracture resistance of future designs as well as enabling the continued safe operation of existing equipment. It could also assist the research engineers and scientists in identifying new problem areas and directions for future investigations.

At this point we wish to recognize that without the considerable efforts of the authors of each individual case study, this publication would not have been possible. We also wish to acknowledge the support provided by both the Army Materials and Mechanics Research Center and the Technical Information Activities Program of DARCOM (E. J. Kolb) who jointly funded the publication and associated forum. Recognition is also due to Dr. Roy Reichenbach of the Army European Research Office for his additional support. We are indebted to Mr. Richard Shea, Chief, Mechanics Research Laboratory, AMMRC, for his support and confidence in this effort.

With regard to the forum, we would like to recognize the efforts of the following session chairmen:

Professor R. L. Bell, University of Southampton, England
Mr. J. I. Bluhm, Army Materials and Mechanics Research Center
Dr. Roland deWit, National Bureau of Standards
Dr. A. F. Grandt, Wright-Patterson Air Force Base
Professor F. A. McClintock, Massachusetts Institute of Technology
Professor J. Lyell Sanders, Jr., Harvard University

Thanks are also due to Dr. Oscar Orringer, Associate Director - Aeroelastic and Structures Research Laboratory, for his help in organizing the forum at MIT. One of us (David Cartwright) wishes to acknowledge the NATO Fellowship scheme of the Science Research Council in the United Kingdom which provided his support during this year at AMMRC.

Finally, we would like to thank our AMMRC colleagues who made valuable suggestions during the development of this case study project, and in particular to acknowledge the excellent support given by the Mechanics Research Laboratory's staff, the Technical Reports Office, and Mr. Frank DeAngelis of the Program Maintenance and Data Entry Branch.

TPR and DJC
21 June 1977

INTRODUCTION

The Journal of Fracture Mechanics provides a detailed documentation of accumulated experience in the application of fracture mechanics concepts and data. These applications include the design of new hardware against fracture, the inspection and maintenance of existing equipment for safe and durable performance, and the analysis of past failures to enlarge the understanding of fracture in actual engineering components and structures. Inasmuch as accumulated experience is widely accepted as having an important role in the new design of most types of engineering hardware, it is anticipated that this case study collection will provide a detailed, useful, and widely available record of current practical fracture mechanics usage. The enthusiastic support by segments of government, industry, and academia through the submission of over thirty comprehensive case studies to this collection confirms the importance assigned to the successful exchange of detailed design information on fracture. It is hoped that both a format and precedent are hereby established which will act as an inspiration to others to document the results of their fracture applications experience for the benefit and guidance of all. In this way the exchange of technical information on the incorporation of fracture mechanics into actual engineering problems can become more effective.

Traditionally, research into the fracture of solids has mainly followed lines of technical speciality, e.g., applied mathematics, materials science, nondestructive inspection, materials testing, etc. The results of this research have found ready outlets in the many technical journals associated with the appropriate specialities. However, applications in practical engineering problems of fracture most often require an interdisciplinary approach. Also, the practical problems are usually not as readily defined as are many research efforts in fracture mechanics. Thus, skills in engineering approximation, modelling and test design must often be called upon for the successful assessment of fracture control in an engineering component. During the practical application of fracture mechanics, areas of weakness and/or insufficient knowledge are often identified in the fracture theory itself. Unfortunately, these experiences have not had numerous outlets for publication as have the research findings. The requirement for "original research" has made much valuable case study material unacceptable for journal publication. The present case study collection is an attempt to alleviate this situation and provide an outlet for documented history of fracture mechanics applications, which are written by the people directly involved.

Because of the importance placed upon accurate and logical documentation of technical information on the application of fracture mechanics, a structured format for case study development (presented below) was provided to the authors to assist them in preparing their contributions. This format emphasizes a sequential flow of information that is designed to lead the reader through each stage of development of the particular fracture application. This is in contrast to a research paper, which endeavors to "tell the results" as soon as possible. A basic idea in the construction of this format was the ordering of information in a manner which allows a reader to break away at prescribed points and actively attempt to participate in the formulation, assessment, and concluding stages of the application. The italicized sentences indicate the potential areas of active involvement by a reader at the corresponding point in the case study.

CASE STUDIES FORMAT

Introduction

(i) *Historical Background* - Use any important dates, times, places, eyewitness accounts, photographs, sketches, etc., to set the scene for the study to be considered. The objectives of the investigation should be clearly stated, thus making evident the motivation for using fracture mechanics. Emphasize whether the case study involves the assessment of a new or existing design, the inspection and repair of components in service, a failure analysis, or some combination of these.

(ii) *Technical Background* - State the preliminary information from which the detailed tasks for the fracture analysis will subsequently be identified. Specific fracture mechanisms and accompanying lines of investigation should not be suggested at this stage. The only purpose of this section is to present the available evidence. The preliminary information should include a statement on the operating and loading conditions along with any special constraints: technical, legal, economic, etc.

* * * * *

At this stage a reader of the case study should be sufficiently familiar with the objectives and technical background to be able to formulate tasks for the investigation for himself. These tasks would involve the postulation of potential fracture mechanisms, the suggestion of corresponding lines of inquiry, and the identification of types of technical data required.

* * * * *

Formulation

(i) Definition of Tasks - Based upon the information provided in the Introduction, identify possible hypothetical mechanisms for fracture and, where possible, formulate theoretical and/or empirical expressions which can be used to examine the hypotheses. Justify the use of the expressions as far as possible and explain any underlying assumptions as they relate to the case study.

(ii) Technical Data - Present the actual data relevant to the case study. This data should include material properties, diagrams and tables characterizing material/mechanical response, e.g., S-N curves, and important component dimensions, e.g., notch radii. Give data which quantifies any special constraints that may be unique to a given case study, e.g., high costs of specialized materials.

* * * * *

At this stage a reader of the case study should be able to carry out calculations and assemble the arguments for himself. For a new or existing design or the repair of a component in service this assessment should enable him to identify the important design parameters which most influence safe performance and life. In the case of a failure analysis this assessment should enable the reader to explain the observed failure.

* * * * *

Assessment

Develop the theoretical and experimental details of the solution. Emphasize the engineering implications inherent in the analysis. Draw attention to gaps in current technology, areas of uncertainty in fracture mechanics theory, factors which keep the solution conservative, and any checks which were made on the solution. Summarize the results in a suitable form for subsequent interpretation.

For a design or in-service repair application, interpret the results and identify the important parameters which most influence the safe operation and life of the components. In the case of a failure analysis, use the results either to explain the observed failure or to eliminate specific fracture mechanisms as causes for the failure.

Conclusions

Indicate what steps were ultimately taken as a result of the analysis and the experience gained. Where possible, give drawings, specifications, and/or actual photographs which emphasize fracture-resistant aspects of the new design, modifications to enhance fracture resistance in the existing design, and action taken to preclude fracture of components in service.

It is important to note that this CASE STUDIES FORMAT was designed to focus on a single component or small system for a detailed design or failure analysis. Some of the case studies in this collection will be seen to address a more widely reaching philosophy and approach for fracture control in large engineering systems. In cases such as these, the suggested format has less applicability, and the active role of the reader is correspondingly reduced.

TPR and DJC
27 May 1977

CONTENTS

Section 1. AEROSPACE

PREFACE

INTRODUCTION

- 1.1 Investigation of Cracks in Nose Case of Aircraft Engine, A. WHITE
- 1.2 Damage Tolerance Design and Analysis of a Typical Aircraft Wing Structure (New or Existing), P. M. TOOR and B. M. PAYNE
- 1.3 A Post-Mortem Wing Strength Analysis, R. J. H. BOLLARD, E. H. DILL, A. S. KOBAYASHI, and R. TAGGART
- 1.4 Fracture Mechanics Correlation Study on Cracked Aircraft Structures, J. B. CHANG
- 1.5 The Application of Fracture Mechanics to Decisions on Structural Modifications of Existing Aircraft Fleets, J. F. McCARTHY, Jr., C. F. TIFFANY, and O. ORRINGER
- 1.6 Flaw Propagation Studies of the Minuteman III Third Stage Rocket Motor, W. L. HUFFERD and H. R. JACOBS
- 1.7 Metallurgical Evaluation of Proof Test Failure of a Second Stage Missile Motor Case, E. B. KULA and A. A. ANCTIL
- 1.8 Identification and Control of Fracture Critical Solid Rocket Booster (SRB) Structure, D. W. O'NEAL, D. A. DEAMER, R. M. FUJITA, and E. V. WYSOCKI
- 1.9 The Influence of Fracture Mechanics on Fail-Safe Design of a Large Space Structure, J. GORMAN, T. R. STAGLIANO, O. ORRINGER, and J. F. McCARTHY, Jr.

Section 2. JOINTS AND MOUNTINGS

- 2.1 Failure Analysis of Shrike Mounting Lugs, F. R. STONESIFER and H. L. SMITH
- 2.2 Analysis of Heavy Lift Helicopter (HLH) Rotor Hub Lower Lug, J. C. ZOLA
- 2.3 The Characterisation of Crack Growth and Fracture in a Military Bridge, N. J. ADAMS and D. WEBBER
- 2.4 Fracture Mechanics Analysis With Hybrid "Crack" Finite Elements, P. TONG, T. H. H. PIAN, and O. ORRINGER
- 2.5 Case Study in Utilization of Fracture Mechanics in the Failure Analysis of a Helicopter Float Cross Tube, D. W. HOEPPNER
- 2.6 Application of Finite-Element Analysis to Develop a Bi-Material Crack-Propagation Laboratory Test Specimen, O. ORRINGER, Ken-Yuan LIN, and J. W. MAR
- 2.7 Investigation of Cracks in Reinforced Concrete Building, A. WHITE

Section 3. PRESSURE VESSELS AND ROTATING MACHINERY

- 3.1 Application of Fracture Mechanics to Rotating Machinery Design, D. W. HOEPPNER
- 3.2 Fracture Mechanics Analysis of Ultrasonic Indications in CrMoV Alloy Steel Turbine Rotors, H. C. ARGO and B. B. SETH
- 3.3 Diesel Engine Crankshaft Failure, L. P. POOK
- 3.4 Fracture Mechanics Analysis of Steel Pipe Welds for Steam Turbines, L. K. L. TU and B. B. SETH
- 3.5 Explosion of an Ammonia Pressure Vessel, A. R. ROSENFELD and C. N. REID
- 3.6 Application of Fracture Mechanics to Welded Structures Design, D. A. BOLSTAD and L. W. LOECHEL
- 3.7 Stress Analysis of an Omega Seal Containing a Crack-Like Defect, G. R. SHARP
- 3.8 Fatigue and Fracture of Thick Walled Cylinders and Gun Barrels, B. D. GOLDTHORPE
- 3.9 Failure of a 175MM Cannon Tube and the Resolution of the Problem Using an Auto-frettage Design, T. E. DAVIDSON, J. F. THROOP, and J. H. UNDERWOOD

Section 4. SURFACE VEHICLES

- 4.1 A Fracture Mechanics Based Assessment of the Railway Rail Failure Problem in the U.K., D. F. CANNON
- 4.2 Development of Design and Test Criteria for the Structural Integrity of Rail Vehicle Mechanical Systems, O. ORRINGER, R. EHRENBECK, and P. TONG
- 4.3 Avoidance of Fatigue Crack Growth in Ships' Hydraulic Equipment, L. P. POOK
- 4.4 Failure and Safety Analysis of Controllable-Pitch Propellers, O. ORRINGER, J. E. KERWIN, and R. M. N. PELLOUX
- 4.5 Ultimate Strength Analysis of "Janek Chairlift," M. P. WNUK

Section 5. MATERIALS

- 5.1 Characterizations of Manufacturing Flaws in Graphite/Epoxy, G. A. HOFFMAN and D. Y. KONISHI
- 5.2 Catastrophic Cracking in Depleted Uranium Penetrators, S. G. FISHMAN and C. R. CROWE
- 5.3 The Design of Metal-Infiltrated Porous Ceramics for Maximum Fracture Resistance, R. A. QUEENEY

INVESTIGATION OF CRACKS IN NOSE CASE OF AIRCRAFT ENGINE

Dr. Ardis White
Department of Civil Engineering
University of Houston
Houston, Texas 77004

INTRODUCTION

Historical Background

Beginning about 1958, the Gulf Coast Dusting Company began converting Continental W-670-9A engines (used in WWII in tanks and barges) to aircraft engines by increasing the length of the crankshaft. The converted engines, designated W-670-240-Gulf Coast Dusting Company (See Fig. 1), are rated at 240 h.p. There is little difference between these engines and the 220 h.p. aircraft engines of the same type, and the increase in horsepower comes primarily from an increase in the compression ratio (5.4 to 6.1) and a slight increase in r.p.m.

Until 1963, no serious problems were encountered with the W-670-240 engines, which are used primarily in agricultural aircraft. A few crankcases did crack, but the number of such failures was not large enough to be a serious problem. (There were also a very few crankshaft failures.) However, during the season of 1963, front case cracking failures became numerous,



W-670-240 Aircraft Engine
Figure 1

compounded later in the summer by several crankshaft failures. Most of the cracked case failures occurred on the new Grumman AgCat, using a McCauley propeller. Most of the crankshaft failures occurred on the same airplane, but with a new Sensenich propeller, introduced during the latter part of 1962. Many of these engines have also been used on Stearman, Snow, and other aircraft.

Technical Background

At the time this investigation began, the engines under study were probably all more than twenty years old, and considerable difficulty was encountered in obtaining some initially desired technical information. Continental Motors Corporation personnel were most helpful in supplying information they could find regarding the W-670-9 engine, for which the nose case was of ALCOA 195 aluminum alloy, with a T63 heat treatment. This heat treatment consisted essentially of holding the metal at 960°F for twelve hours, followed by a water quench and ageing at 310°F at 12-20 hours. The ultimate tensile strength of the material varied from about 36,000 to 40,000 p.s.i. Much more specific material property data were obtained, but are not listed here, as the turn of events later in the investigation did not make much use of them.

For those not thoroughly familiar with the operation of agricultural application aircraft, a few comments may be in order. Usually, these planes are loaded to the point where they can barely stagger off the ground (usually, "ground" is the literally correct word--rarely do such planes have the advantage of taking off from a paved surface of any type). In many full days of work, a pilot may not obtain an altitude of more than two or three hundred feet. It is an exciting type of flying and insurance companies are usually reticent about writing insurance for pilots who engage in such activities. The base of supply for such operations is located as close as possible to the point where the material is to be applied from the air, for economy of time and fuel, time being more important, as sometimes a day or two can be critical in operations of this type. Once in the air, the plane flies initially with almost full power, and the pilot levels out in a straight line over the first point of application. At the appropriate instant, he releases the product, completes the first portion of the run, and then increases the throttle to its full position to gain speed and momentum for the dramatic rapid climbing turn at the end of the first run to begin the second run. After beginning the second run, the engine speed is decreased slightly until it is again necessary to use full throttle again as for the first turn. If the runs are fairly short, the engine will be running at full throttle almost all of the time; sometimes the shape of the field or the presence of more than one field being worked permits a less punishing usage of the aircraft and engine.

FORMULATION

Definition of Task

The definition of the task was a very simple one--namely, stop the engines from cracking. The problem had been quite specifically defined,

inasmuch as several of the engine nose cases had cracked, and were lying in a pile behind one of the aircraft hangers. The decision as to how to do this was not nearly so simple.

Technical Data

Fatigue was the primary suspect as a cause of the cracking, of course, because of the age and usage of the engines, but a number of unknown factors were involved. Neither the chronological age nor working time of any individual engine was known prior to use in some of the subject aircraft. Some of the engines had not been used prior to use in these planes. Previous attention has been drawn to the fact that although adequate material property data were available, they were not subsequently used very extensively.

ASSESSMENT

It was decided to use electric resistance strain gages as a primary device to obtain data to help solve the problem. The steps involved in this investigation were as follows:

- (1) Application of strain gages at each of the fillets at the base of each of the seven cylinders (See Fig. 2.).



Strain Gage Application on Nose Case

Figure 2

(2) Connection of the strain gages to a switching box, then to an Ellis BAM-1, and then to a Tektronix oscilloscope. The cockpit normally used for the product was steam cleaned and adapted for the equipment and space provided for the experimenter to stand and operate the equipment. The BAM-1 is self-powered, and the oscilloscope was powered by a converter powered by two 12-volt storage batteries connected in series. A polaroid camera was used with the oscilloscope.

(3) The next phase of the test work involved actual flight of the plane. Several flights were made, changing the pertinent variables and doing an adequate amount of work to add greater confidence that any one of the gages would provide as much information as any other. The conclusions from this work were that there was no significant difference between the strain signals obtained from the seven cylinders, so the switching box was disconnected, and a single gage connected to the BAM-1.

(4) A large number of flights were then made, using different settings of the pitch of the propellers (whose pitch could be changed on the ground, but not in the air), and at different operating speeds. The usual routine involved loading the polaroid camera on the ground (this could not be done in the air because of the slipstream in the open cockpit), taking off and reaching a safe altitude of a few hundred feet and then throttling the engine back until the airplane was almost ready to fall out of the sky. The sweep of the scope was then synchronized with the engine speed to obtain a photograph obtained such as that of Figure 3 providing the signals from the strain gage. A signal was then given the pilot to increase the engine speed by 100 r.p.m., and the scope again synchronized with engine speed and another photograph made. This was continued until the throttle had been advanced as far as it would go. The airplane would then be landed, a new supply of polaroid film loaded, a change in propeller or propeller pitch made, and the flight work repeated.

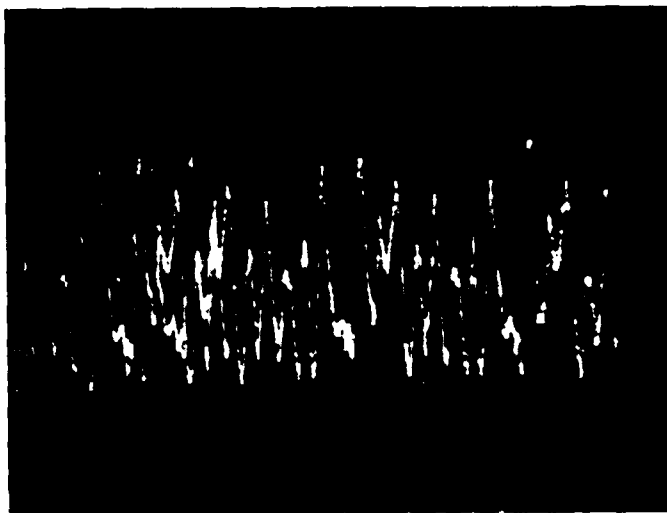


Figure 3. Strain Gage Signal

The data taken consisted of the photographs just mentioned, the propeller type, the propeller pitch, and the r.p.m. applicable to each photograph. The raw data were thus available for the solution of the problem, which was obtained as follows.

It was immediately apparent that one of the propellers produced strains greater than any of the others. Further intensive questioning of the personnel involved in use of the planes revealed that this particular propeller had been in use only a few months before the beginning of the severe crack problem. Such questioning had been done before, but had failed to cause anyone to remember this pertinent fact.

A crude, but effective, indication of the amount of punishment taken by the nose case at the point where cracking occurred is the height of the envelope of the peak strains indicated by the strain gages. Lines were thus drawn through the peaks at the top and bottom of the oscilloscope trace photographs (Fig. 3) and the heights of these envelopes expressed in microstrain. (The system was calibrated before each flight.) It was thus possible to plot a curve (Fig. 4) showing the height of the strain envelopes versus the engine speed. At the recommended speed of 2100 r.p.m., it apparently did not make very much difference whether the short or long shaft was used. It may be noted that the strain in the nose case actually drops off at full throttle, but the airframe itself was subject to considerable vibration at that speed, and the engine could not be operated at that throttle setting all the time.

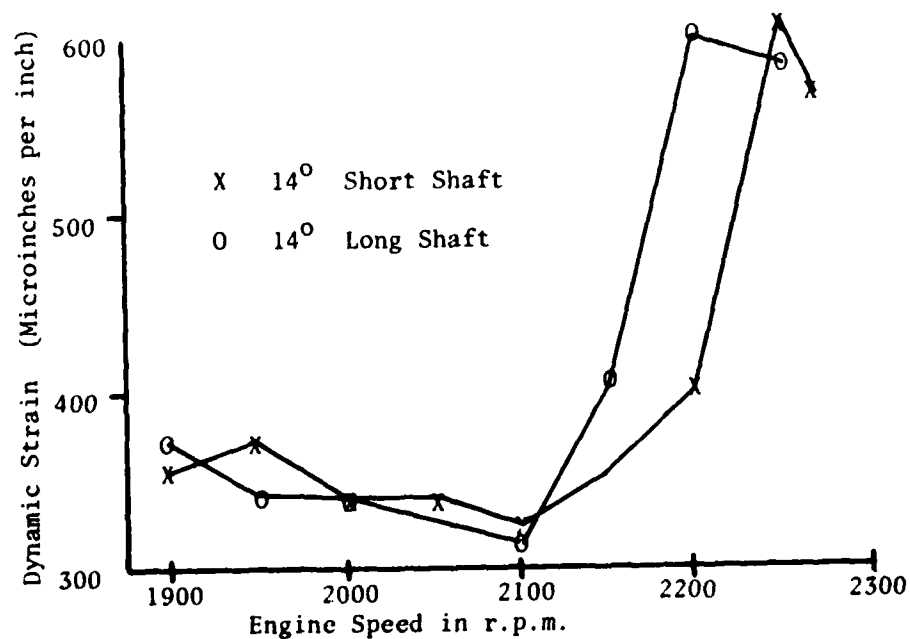


Figure 4 Dynamic Strain vs Engine r.p.m.

Figure 4 is the key to the solution of the problem of the cracking engines. The maximum strain envelope height (referred to as the "dynamic strain") was obtained at an r.p.m. of 2200 or 2250, which unfortunately happened to be the normal operating speed of the engine except when advanced to full throttle for turns. The obvious solution was to reduce the speed slightly, as the change in dynamic strain was dramatic with such a decrease. This was not considered a viable solution by the operators of the aircraft, but finally a compromise was reached whereby the reduction was accepted, together with an increase in the pitch of the propeller. This was not an ideal solution, of course, as the engine could not develop as much horsepower under these conditions. It did work, however, and the cracking began to decrease considerably. In some cases, a return was made to propellers used earlier, which also reduced the maximum strain.

ADDITIONAL COMMENTS

Preoccupation with nose cracks in this study has been evident, although there were some crankshaft failures. Furthermore, the problem was much more complex than is apparent from the presentation, involving, in addition to the information already mentioned, the following (a partial listing):

(1) The Continental W-670 engine was originally designed for aircraft use, and prior to and during WWII was used extensively as the power plant for primary trainer aircraft such as the Stearman biplane. For use in tanks and barges, a shorter crankshaft was used, which necessitated extension of the shaft for reconversion to aircraft use. There were two different lengths of shaft extensions involved (for different propellers), and considerable attention was given to the effect of this matter.

(2) The nose case cracking was a secondary phenomenon, the primary one being that of resonance of the crankshaft; this resonance being critically influenced by a large number of factors. The physical system consists essentially of the crankshaft, supported by the two main bearings and cantilevered outward of that point as necessary for a particular use. Such systems are extremely sensitive to balance of the propeller, the angular position of the propeller on the shaft in aircraft use, spark advance, and many other factors. Crankshaft failures of the original W-670 aircraft engine during WWII was common, and an investigation of this problem was carried out by Critchlow [1] and by Critchlow & Bean [2]. The existence of this previous work was learned in a chance conversation with Mr. Bean during the course of the investigation. His assistance and the two references were of great value during the course of the remainder of the work.

(3) "Make-up" or assembly strains and thermal strains and stresses were studied and the following summary of this work is given below: (These are approximate, as the strains from a single gage perpendicular to the potential cracks were used, assuming uniaxial stresses. The stresses parallel to the cracks were very low; this being established early in the work.)

Static assembly strains: 200 microinches per inch compression.

Static thermal strains (during operation): 1000 to 1200
microinches tension.

Dynamic strains (oscilloscope traces) during operation:
plus and minus 250 to 300 microinches per inch.

Thus at operating conditions, the static stress level was about 10,000 p.s.i., on which is imposed plus and minus stresses up to 3000 p.s.i. (Nothing was known, of course, regarding residual stresses due to casting, machining, or any other source prior to beginning of the investigation.)

(4) The highest peak strains from the oscilloscope traces were associated with firing of the cylinder near the gage at operating (flying) speeds. At low speeds (idling), cylinder-firing peak strains were not predominant.

(5) As the static stress level at operating conditions was rather high, the pattern and magnitude of the dynamic strains was very important in affecting the fatigue life of the nose case. A slight decrease in magnitude or change in pattern of dynamic strains could be very beneficial, and consideration was even given to stiffening and restraint of the front crankcase by various means.

(6) Extensive "detective" work revealed that the cracked case engines had two things in common:

(a) Some of the cases (perhaps most of them) had time from either barge or tank use before being put in use as "new" or rebuilt aircraft engines.

(b) They were apparently all put in use during the time a new man in the company was in charge of baking paint on the cases, and it was suspected that the baking was done at about 400°F. Metallurgists consulted could not agree on exact effect of use of this temperature as some thought annealing might occur, but the softer metal resulting might also be less susceptible to fatigue failure; others thought it might accelerate age hardening and increase the brittleness of the metal.

(7) Work was done with both "unbalanced" engines (as taken out of packing cases) and a "balanced" engine. The latter was an engine with which great care was taken to balance the crankshaft with a "bob" weight. This work was somewhat inconclusive, as other factors (such as shaft extension and propeller combinations) were also involved.

(8) Shot peening of the point of cracking was considered, but was not done. It was not absolutely certain that the initial cracking occurred on the outside of the case.

(9) Different engine mounts were tried, without much success.

CONCLUSIONS

One conclusion arising from this study is that a combination of technical detective work and either qualitative and/or quantitative work with a minimum of equipment may sometimes lead to the solution of a perplexing problem. Many factors necessary for a more sophisticated approach were unknown, and could not be determined.

Specifically, on the basis of Figure 4, which is representative of many curves of the same type obtained, it was recommended that the propeller pitch be set at 14° and the operating engine speed be limited to about 2100 r.p.m. Eventually, these recommendations were followed, with a gradual decrease in the frequency of nose cracking to a point considered acceptable.

Other recommendations included the use of lower nose case paint baking temperatures, and the use of engines without previous use in barges or tanks as long as they were available.

REFERENCES

1. Critchlow, B. E. F., "Measurement and Prediction of Aircraft Vibration," SAE Journal, v.2, no. 8, August, 1944.
2. Critchlow, B. E. F. and Bean, W. T., "Crankshaft Bending Vibrations," SAE Transactions, v. 1, no. 3, July, 1948, 330-388.

DAMAGE TOLERANCE DESIGN AND ANALYSIS OF A TYPICAL AIRCRAFT WING STRUCTURE (NEW OR EXISTING)

Pir M. Toor
Blanton M. Payne
Lockheed-Georgia Company
Marietta, Georgia

HISTORICAL BACKGROUND

Damage tolerance design has become a necessity in the design of modern aircraft although its importance was recognized as long as four centuries ago. Around the end of the fifteenth century the first technical notes were written on what must have been the first requirements for damage tolerant design. These were in notebooks of Leonardo da Vinci in which he discussed the physics of flight and the design of flying machines. He wrote:

"In constructing wings one should make one cord to bear the strain and a looser one in the same position so that if the one breaks under strain the other is in position to serve the same function."

About two decades ago (1954), after the disastrous failure [1] of Comet aircraft in the air near Italy, structural design engineers and research workers saw the need of applying damage tolerance concepts to the design of aircraft structure. The United States Civil Aeronautics Board has defined the damage tolerant structure as one in which:

"Catastrophic failure or excessive structural deformation, which could adversely affect the flight characteristics of the airplane, are not probable after damage or obvious partial damage of a single principal structural element."

In 1969, after the F-111 failures [2], the United States Air Force initiated the Air Force Structural Integrity Program with the coordination of the Aerospace Industry Association (AIA). Damage tolerance structure (structural safety and durability) is described in MIL-STD-1530A [3] and associated Military Specifications [4, 5]. The basic criterion is:

"The assurance that safety of flight structure of each aircraft will achieve and maintain a specified residual strength level throughout the anticipated service life. Further assurance that the fleet can operate effectively with a minimum of structural maintenance, inspection and downtime, etc."

However, the essence of damage tolerance design is to ensure that the structure will continue to sustain a high proportion of its design load even after damage has occurred. The basic philosophy of damage tolerant design is based on:

- 1 The acceptance that damage will occur for one reason or another despite all precautions taken.
- 2 An adequate system of inspection prescribed so that the damage (cracks) may be detected and repairs made at a proper time.
- 3 An adequate residual strength maintained in the damaged structure so that, during the period between inspections when the damage is undetected, ultimate failure of the structure is not possible.

In the early fifties, due to a lack of comprehensive damage tolerance methodology, large-scale component test results were used to develop empirical damage tolerance methods. Although in 1913 Inglis [6] attempted the elastic stress analysis of cracks in an infinite plate under various degrees of biaxial tension, it is only recently [7] that linear elastic fracture mechanics (LEFM) has been used to predict residual strength and crack growth rates in damaged structure.

The objective of this study case is a systematic investigation of the damage tolerance design capability (residual strength and crack growth) of a typical aircraft wing structure (new or existing) using linear elastic fracture mechanics. The assumptions made and the limitations applied are discussed in detail at each step of the development and analysis of the case study. A specific example in this case study is to establish inspection intervals for a typical aircraft wing structure lower surface rear span cap.

TECHNICAL BACKGROUND

A first approach toward minimizing the risk of catastrophic or rapid fracture in structures is to use materials with as high a fracture toughness as possible. This should be consistent with strength, environment, etc., involved in the specific application. In aircraft structures, weight-to-strength ratio is the most pertinent factor. Usually, weight considerations dictate relatively high stress levels so that the fracture toughness available is limited even on a very carefully selected material. Hence a trade-off is required and generally materials are used at lower than maximum strength. This results in a weight sacrifice.

Another way to ensure damage tolerant design is to employ ingenious design innovations rather than material specifications. In general, in a damage tolerant design concept the following points must be considered skillfully:

- a Material selection or control (material should be as flaw tolerant as possible).
- b Design concepts (multiple load paths).
- c Stress level selection and control (fatigue cracks should not propagate rapidly during the service life).

- d Inspection procedures - cracks must be detected prior to any impairment of the load carrying capacity of the structure.
- e Process control - control during manufacturing and processing to ensure that the initial flaws are small and the basic fracture properties are not impaired by manufacturing processing.
- f Environment effect - resistance to stress corrosion cracking must be evaluated and controlled.
- g Fracture toughness control - variation of fracture toughness and other associated parameters within the heat-treatment range must be thoroughly characterized.
- h Static and fatigue design allowables must be evaluated carefully.

STRESS INTENSITY FACTOR

The basic development of linear elastic fracture mechanics is well documented [8 - 14]. However, in order to systematically use fracture mechanics in the design and analysis of a structure, the stress intensity factor K and the influence of various parameters on it must be completely understood as the cracking rate is dependent upon it. The stress intensity factor K in the ideal case of an infinite plate containing a central straight crack of length $2a$ and subjected to plane stress σ acting uniformly and perpendicularly to the crack is expressed as:

$$K = \sigma \sqrt{\pi a} \quad (1)$$

where

K is the stress intensity factor (KSI $\sqrt{\text{IN}}$)

σ is the remote stress (KSI)

a is the half crack length (in)

THICKNESS EFFECT

The critical stress intensity factor is very much dependent on material thickness B . In real structure there is a large variation in thickness at various sections, therefore variation of K_c with thickness must be evaluated. Figure 1 displays the variation of K_c versus B for 7075-T6511. There are three distinct regions which exhibit three characteristic type of failure modes, namely, plane stress, mixed mode and plane strain. This curve is devel-

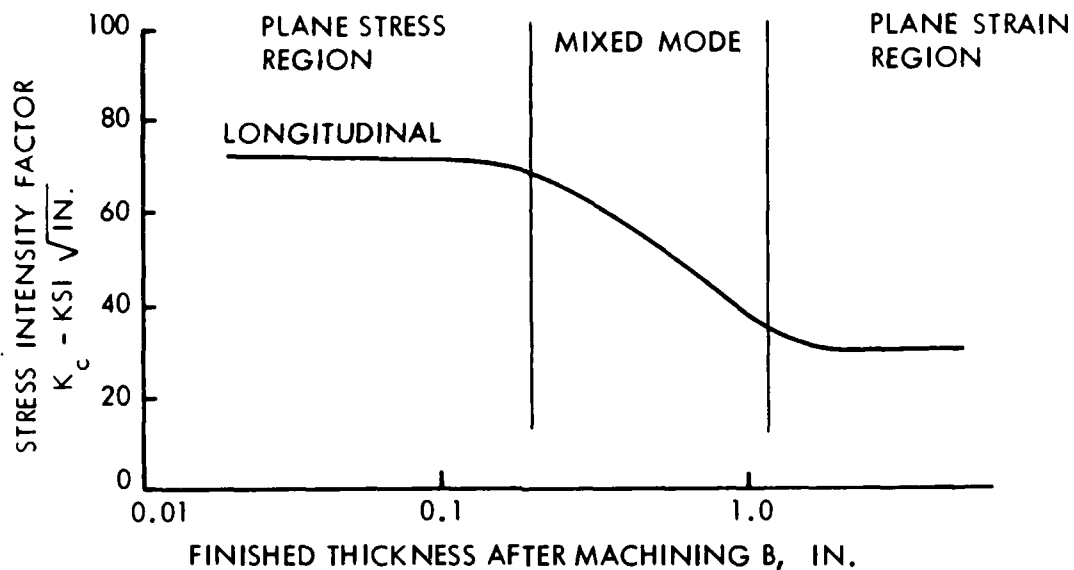


FIG. 1 STRESS INTENSITY FACTOR AS A FUNCTION OF THICKNESS FOR 7075-T6511 EXTRUSION

oped using a limited number of test specimens. The right hand side of the curve can be accurately established using the ASTM standard E-399 specimen, but currently there is no standard specimen for the mixed mode and plane stress regions.

PLASTICITY EFFECT

As discussed previously, linear elastic fracture mechanics is based on linear elasticity. Virtually all materials exhibit some ability to deform plastically without fracture. If the size of the plastic zone around the crack tip is very much smaller than all other significant dimensions of the structure and the crack length, the value of K elastically calculated is not very much changed. However, when the plastic zone becomes larger, as in a relatively ductile material, the value of K becomes questionable, and the effects of plasticity can be formulated as follows:

$$r_p = \frac{1}{2\pi} \left(\frac{K}{\sigma_y} \right)^2 \quad \text{for plane stress} \quad (2a)$$

$$r_p = \frac{1}{4\sqrt{2}\pi} \left(\frac{K}{\sigma_y} \right)^2 \quad \text{for plane strain} \quad (2b)$$

where r_p is the plastic zone radius at the tip of the crack, K is the fracture toughness stress intensity factor, σ_y is the material yield stress.

CRACK GROWTH EQUATION

The use of the concept of fracture mechanics in the design and analysis of structure assumes the existence of initial flaws or cracks. These cracks under repeated service loading conditions propagate and become unstable (fast fracture) when critical length is attained. The rate of crack propagation depends on many factors, such as material, environment, service load spectrum, crack geometry and local structural configuration. It is shown [16] that for a particular material the crack growth rate (da/dN) can be described as a function of stress intensity range ΔK as shown in Fig. 2. At present, there are large numbers of crack growth equations. The Foman crack growth equation [17], given below will be used in the present case study.

$$da/dN = \frac{c (\Delta K)^n}{(1 - R) K_f - \Delta K} \quad (3)$$

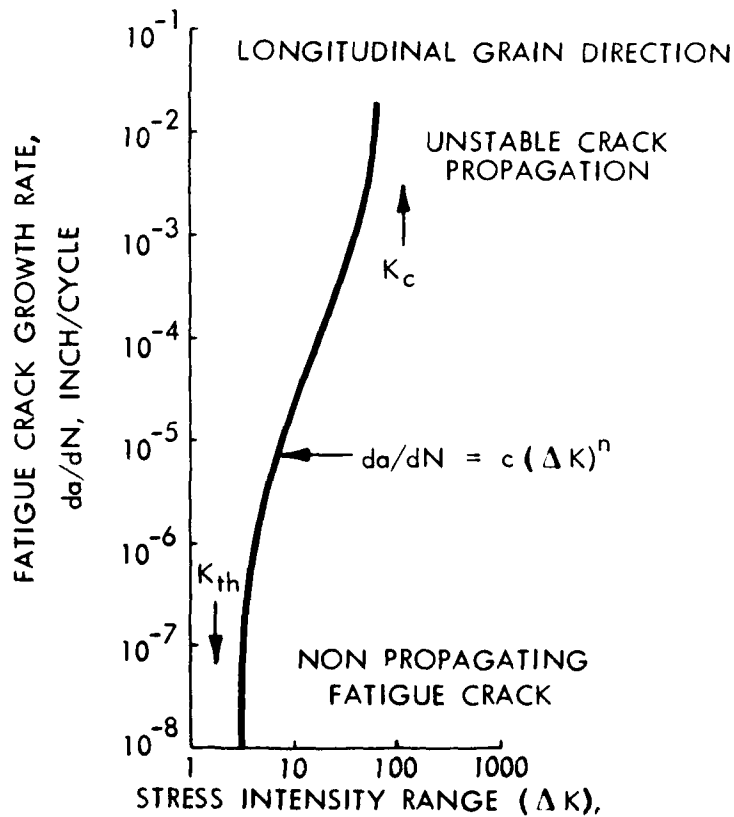


FIG. 2 CRACK GROWTH RATE AS A FUNCTION OF STRESS INTENSITY FACTOR RANGE FOR 7075-T6511 EXTRUSION

where, da/dN is the rate of crack growth, c and n are material constants, ΔK is the stress intensity range, R is the stress ratio defined as minimum stress divided by maximum stress and K_f is a critical stress intensity factor. The stress intensity range $\Delta K = \Delta\sigma\sqrt{\pi a} \cdot \beta_T$ where $\Delta\sigma$ is the stress range, a is the crack length and β_T is the product of various boundary condition correction factors.

The value of c and n (material constants) in Eq. 3 can be calculated from constant amplitude test data by applying the following rectification technique to the Forman equation.

$$\log \left[(1 - R) K_f \cdot \Delta K \right] + \log \left(\frac{da}{dN} \right) = \log c + n \log \Delta K. \quad (4)$$

For any two coordinate points, say $\Delta K_i, (da/dN)_i$ and $\Delta K_{(i+1)}, (da/dN)_{(i+1)}$, which represent a segment of the crack growth rate curve, one can solve two simultaneous equations for c and n .

LOAD INTERACTION

The crack growth analysis under constant amplitude cycling is fairly straightforward. On in-service structure the load conditions are quite complex. High and low loads are mixed. Therefore, to calculate the crack growth the load interaction must be taken into account. There are quite a few load interaction or retardation models to account for the load sequence effects. In this case study, only the Willenborg model [18] will be discussed and used. A peak load in the spectrum creates a plastic zone ahead of the crack tip. This plastic zone can cause retardation in the crack growth because there are compressive stresses in the plastic zone caused by tension stresses in the surrounding elastic material. In other words, the crack is operating at an effectively smaller alternating stress until the crack grows through the peak stress plastic zone.

The Willenborg retardation model accounts for the retardation effects by modifying the stress intensity range ΔK and the stress ratio R in the constant amplitude da/dN data to an effective stress intensity range ΔK_{eff} and an effective stress ratio R_{eff} . The effective stress intensity range and stress ratio are calculated as a function of the size and location of the current yield zone and the yield zone produced by the peak load. After the application of a peak overload the plastic zone can be calculated using Eq. 2a or 2b. If a peak stress σ_1 is encountered in the spectrum followed by another stress cycle σ_2 such that $\sigma_2 \ll \sigma_1$, the peak stress σ_1 will produce a plastic zone ahead of the crack tip.

Following the overload, the crack will continue to grow under a cyclic loading $\Delta\sigma_2 = \sigma_{2Max} - \sigma_{2Min}$. The growth rate, however, is delayed as long as no subsequent maximum stress greater than σ_1 is applied and as long as the growth remains within the zone of plasticity caused by the overload σ_1 . Assume that a third stress level $\sigma_3 = \sigma_{ap}$ (less than σ_1) occurs following the last cycle of σ_2 and that growth has not completely progressed

through the yield zone caused by the first overload. The retardation will be terminated when the value of applied stress is large enough compared to the first overload ($\sigma_{ap} < \sigma_1$) and the current crack length is of such an extent that the following condition exists:

$$a_c + r_{yap} = a_{p1} \quad (5)$$

where r_{yap} is the yield zone caused by σ_{ap} at current crack length, a_c . Using Eq. 2 for plane stress, the applied stress required to reach a_{p1} can be calculated as:

$$r_{yap} = \frac{1}{2\pi} \left(\frac{K_{ap}}{\sigma_y} \right)^2 = \frac{1}{2} \left(\frac{\sigma_{ap}}{\sigma_y} \right)^2 a_c$$

or

$$\sigma_{ap} = \sigma_y \sqrt{\frac{2 r_{yap}}{a_c}}$$

now inserting the value of r_{yap} from Eq. 5 in the above equation, we get:

$$\sigma_{ap} = \sigma_y \sqrt{2 \frac{(\sigma_{p1} - a_c)}{a_c}} \quad (6)$$

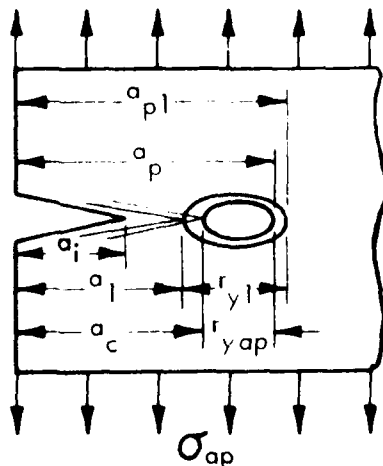


FIG. 3 YIELD ZONES FOLLOWING OVERLOAD σ_1 FOR ANY APPLIED STRESS σ_{ap}

σ_{ap} may be thought of as the effective portion of σ_1 remaining following the application of σ_1 . As retardation is a function of the differences in applied stresses, the amount that σ_2 is reduced is the difference $\sigma_{ap} - \sigma_2$ (Max) at any crack length, i.e.,

$$\sigma_{red} = \sigma_{ap} - \sigma_2 \text{ (Max)} \quad (7)$$

The effective reduced stress is dependent on σ_2 and variable with current crack length. Thus, following the overload, σ_2 (Max), σ_2 (Min) are reduced by the amount σ_{red} . These values are used to compute the reduced crack growth rate.

The limitations of this model are:

- 1 It does not take into account the negative stresses (compression stresses).
- 2 It cannot handle the negative overload effects.
- 3 It does not differentiate between single or multiple overloads.

DESIGN

For an efficient damage tolerant design structure, the designer must select a material as a compromise with strength and weight. Ideally, a material with high yield strength and high fracture toughness is desired. However, in reality this is not possible, as it is generally known [19] that fracture toughness K_{Ic} decreases with increasing yield strength for aluminum and many other materials. This variation is in part due to the inherent characteristics of impurities associated with the manufacturing processes of the material.

Another important parameter in the design of a structure is the establishment of an acceptable operating stress level so that critical length cracks do not occur for a specified number of flight hours. Generally, for 7000 series aluminum aircraft wing structure, the designer chooses 50 to 65 percent of the yield strength of the material as a design limit stress.

Using linear elastic fracture mechanics, and the available nondestructive inspection (NDI) capability for detecting flaws the designer can screen for the suitability of a particular material. Using the criterion that the structure will be inspected and crack lengths must be stable up to limit load stress and neglecting plasticity effects, the following relationship can be established between applied stress and critical crack length.

$$\sigma = \frac{K}{\sqrt{\pi a}} \quad \text{for very wide plate}$$

$$a_c = \frac{1}{\pi} \left(\frac{K_c}{.5\sigma_y} \right)^2 \quad (8)$$

Comparing the critical crack length a_c to the crack detection capabilities of the NDI techniques available for a particular design, the material can be accepted or rejected, i.e., if the crack becomes critical before it can be detected, another material will need to be selected, stress levels lowered, or design for the "non-inspectable category" as defined in MIL 83444 [4].

ANALYSIS PROCEDURE

The analysis of crack propagation requires a working knowledge of the stress intensity factor and the various other parameters in influencing it. Therefore, it is appropriate at this stage to discuss the "boundary condition" correction factors needed in the case study to modify the stress intensity factor. The majority of cracks in a typical wing structure emanate from fastener holes as corner cracks, where the influence of the hole and the fastener load transfer become important. There are no exact classical solutions for load transfer effect on the crack growth, however through recent application of detailed finite element models excellent two-dimensional approximations of load transfer correction factors have been derived. Assuming no load transfer, the modified stress intensity factor for a quarter circular corner crack emanating from the fastener hole can be written as follows:

$$K = \sigma \sqrt{\pi a} \cdot \beta_f \cdot \beta_b \cdot \beta_h \cdot \beta_w \cdot \frac{M}{\phi} \quad (9)$$

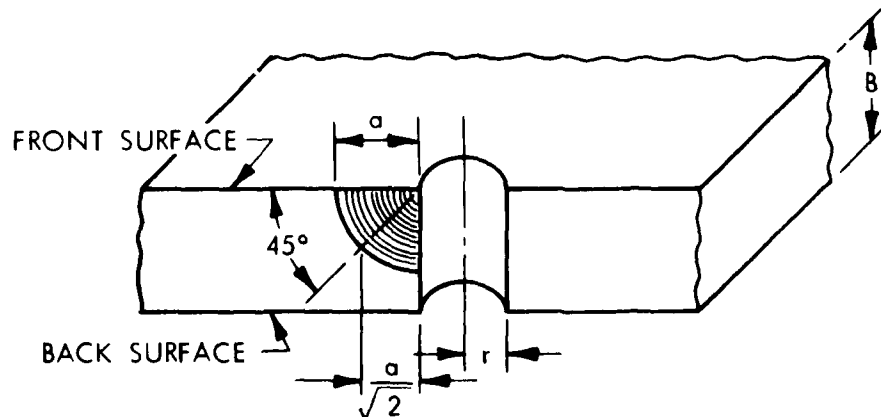


FIG. 4 CIRCULAR CORNER CRACK AT THE FASTENER HOLE

where β_f is the front surface (the free surface coincident with the initiation location of the crack) correction factor. This factor is [20] 1.12. β_b is a factor accounting the influence of the back surface [21] of the panel on a part-through corner crack. β_h accounts for the influence of hole and is a function of a/r , where a is the crack length and r is the radius of the hole. β_h may be modified to account for the influence of a fastener filled hole and load transfer. For a corner crack emanating from the fastener hole, crack growth predictions are more correct if β_h is considered a function of $a/\sqrt{2}r$, where $1/\sqrt{2}$ comes from the location of a point at 45° on the quarter circular corner crack [22].

β_p and β_w are the plasticity and width correction factors given by [23] and [24], respectively.

$$M = \left[(a/c)^2 \sin^2 \theta + \cos^2 \theta \right]$$

where c is the visible crack length and θ is the angle locating a specific point on the crack front with respect to the axis of symmetry. For a quarter circle crack, $M = 1$.

$$\phi = \int_0^{\pi/2} \left[1 - \left(\frac{c^2 - a^2}{c^2} \right) \sin^2 \theta \right]^{\frac{1}{2}} d\theta = \pi/2 \text{ for } a = c$$

Assuming a wide panel where finite width correction is not necessary and considering the plasticity effect minimum so that this correction can also be ignored, by using the quoted values of β_f and M/ϕ , Eq. 9 for a quarter circular crack becomes:

$$\begin{aligned} K &= \sigma \sqrt{\pi a} \cdot 1.12 \beta_b \beta_h \cdot 2/\pi \\ &= .712 \sigma \sqrt{\pi a} \beta_b \beta_h \end{aligned} \quad (10)$$

Further geometric correction factors needed for a specific problem are given in the next section.

CRACK GROWTH ANALYSIS

The damage tolerant design of an aircraft wing structure requires a reliable method of predicting the crack growth from some defined initial crack length to the size where unstable crack growth is imminent. In order to perform the crack growth analysis using linear elastic fracture mechanics, the following information is required.

- 1 Structural geometry
- 2 Crack geometry
- 3 Spectrum stresses
- 4 Material crack growth and crack stability data
- 5 Initial crack size

The accuracy of the crack growth predictions depends upon accurate da/dN versus ΔK data and the modified stress intensity factors discussed previously. da/dN versus ΔK for a typical material is shown in Figure 2. It can be observed that the log-log curve has three characteristic regions; lower, middle, and upper. The lower region corresponds to the limiting stress intensity factor value K_{th} , known as the threshold stress intensity factor, below which value crack growth does not seem to propagate for that particular material. The middle region of the curve corresponds to the stable crack growth region, where the rate of the crack growth seems to be linear. The upper region is near to the unstable crack growth point and the limiting value is the critical intensity factor K_c .

The stress ratio R and the environment have a significant effect on this curve. In addition the scatter in the basic crack growth data must be taken into account by repeating a realistic number of tests. The initial test crack length should be within the nondestructive inspection (NDI) capability [25].

For analysis the number of cycles or flight hours required for growth of the initial flaw to critical dimensions are calculated by a process of integration using Eq. 3. The stress intensity range ΔK corresponding to the initial crack length a_i and crack geometry is calculated using Eq. 9, assuming that the crack starts from the fastener hole. This value of stress intensity range ΔK is used with constant amplitude laboratory test data to determine the crack growth rate, da/dN . The crack extension increment Δa_i during a period, ΔN , can be calculated by integrating Eq. 3. This value of crack extension Δa_i is added to the initial crack length a_i to determine the new stress intensity range and a new crack growth rate. Eq. 3 is again used for another period to give further crack extension and iteration process is repeated until the critical crack length is achieved.

In order to take into account the retardation effect discussed previously, the stress intensity range and R value must be modified using Eq. 7, and the same iteration process applied.

DAMAGE TOLERANCE DESIGN CRITERIA

Fracture mechanics analysis is carried out on two types of structures: (1) new design and (2) existing structure. These currently have different criteria. On existing structure, analysis is carried out to determine inspection requirements, or safe operating life, while

analysis of new design is carried out to meet a specific set of criteria.

General requirements and detail criteria are defined in Refs. [3 - 5] for both types of structures. The example problem described in this case study consists of existing structure operating under a defined spectrum. The pertinent features of the criteria applicable to existing structure are:

- a What locations should be analyzed? The locations are chosen by reviewing test article failures, particularly the fatigue test articles. If no test article information is available, the analysis points must be selected by using static and/or fatigue analysis, by study of service or fatigue failures on similar structures, or by examination of drawings.
- b What size flaws should be assumed in the analysis? The size and configuration of the initial flaw is a very pertinent parameter in the fracture analysis. Some rationale, analytical or arbitrary must be used to select an initial flaw size and shape. A great deal of guidance, particularly for military aircraft, can be found in [4] where the size and configuration of the initial flaws are specified as a function of the category/slow crack growth, fail-safe multiement, or fail-safe crack arrest). For example, in the "slow crack growth category," the specified initial flaw in a hole is an .05 inch crack. For thickness greater than .05 inch, the assumed flaw is a .05 inch radius corner flaw, and for thickness less than or equal to .05 inch, the flaw is a .05 inch through-the-thickness flaw. Various other flaw sizes are similarly defined. The criteria allows reduction of the assumed initial flaw by taking into account special fastener and inspection procedures. The criteria also differentiate between the assumed initial flaw and the detectable flaw. An assumed initial flaw, a_i , or equivalent initial flaw, is the result of manufacturing and fabrication processes and a regression analysis of test results. The detectable flaw, a_{det} , is a flaw that a particular inspection technique can be expected to detect. The time to the first inspection is calculated using the assumed initial flaw established by specification or by agreement while the second and the subsequent inspection intervals are determined using the detectable flaw, a_{det} , corresponding to the applicable NDI inspection technique.

In the example problem shown later the assumed initial flaw is an .001 in radius corner flaw in a hole. In this instance, the small flaw is chosen just to generate the crack growth curve over the small flaw range and does not represent a realistic initial flaw for establishment of the inspection interval.

- c What maximum load level will crack instability be checked against? The maximum expected load level may or may not be in the crack growth spectrum. If crack arrest due to peak loads (retardation) is considered, it can be unconservative to include maximum expected peak loads or limit load, since the peak loads may not actually occur on a specific airplane. MIL-A-83444 [4] defines the load levels for which crack instability must be analyzed. The maximum expected load level

is defined as a function of "degree of inspectability and inspection interval," i.e., the shorter the inspection the less likely a limit load will be encountered during the interval.

In the example problem, limit load is used to determine the first (initial), the second and subsequent inspection intervals.

- d Crack metamorphosis? Since there is a large number of possible crack growth paths, the most critical (fastest growing) should be analyzed. Test data and/or finite element models and analysis must be used to determine the most critical crack path. As expected, cracks start at peak stress points and propagate in a direction perpendicular to the maximum principal stress. MIL-A-83444 lends significant guidance on determining crack path through specific requirements on continuing damage.
- e What safety factors, and/or test will be used to verify accuracy analysis? Obviously, safety factors and verification level are related. If a high level of confidence can be established in the analysis technique, a lower safety factor can be used than if a low or questionable level of verification exist.

Safety factors should also be related to inspection technique; for example, if a complex NDI inspection technique is required to detect relatively small flaws, a higher safety factor should be used than if a simple NDI technique is used to detect large flaws. Crack growth rate is more accurately predicted if load sequencing effect (retardation) is accounted for in the analysis; however, some form of spectrum test should be performed to verify the ability of the retardation model to predict the crack behavior. In the example problem a safety factor of 2 is used on the inspection intervals.

EXAMPLE APPLICATION

The example given below displays the use of fracture mechanics in analyzing an existing structural element. The crack growth analysis procedure is equally applicable to new or existing structure. The only difference is the damage tolerant design criteria which is briefly discussed in the last section.

EXAMPLE: Using fracture mechanics procedures described in the previous sections, perform residual strength and crack growth analysis for the given existing structural element of a front beam cap on the lower surface of a typical aircraft wing. The analysis will consist of deriving stability curves (critical stress σ_{cr} versus critical crack length a_{cr}) and growth curves (crack length versus flight hours). Using the stability curves, establish critical crack lengths for limit load stress (33 KSI) and establish the flight hours associated with crack lengths at this stress.

- Structural element: As shown in Figure 5, the grain directions are perpendicular to crack and parallel to load direction
- Material: 7075-T6511 extrusion
Yield stress = 70 KSI
Fracture toughness K_{Ic} for .2 inch thickness from Figure 1 is equal to $64 \text{ KSI} \sqrt{\text{in}}$
Plain strain fracture toughness K_{Ic} from Figure 1 = $23.0 \text{ KSI} \sqrt{\text{in}}$
 da/dN versus ΔK is given in Figure 2, constant amplitude data for $R = 0$
- Spectrum Stresses: Shown in Table I, adjusted to represent stresses perpendicular to crack growth and the sequence of missions is shown in Table III.

Assume four phases of crack growth analysis, start with Phase I part-through quarter circular corner crack from the wall of the hole and terminating at the back surface of the element. For Phase II, the initial crack is a 0.2 inch single edge through crack from the edge of the hole and terminating at the edge of the element. Initial crack length for Phase III is a 0.005 part-through quarter circular corner crack from the second wall of the hole and terminating at the back surface of the element. The beginning crack length for Phase IV is 1.356 inch edge crack which is composed of edge distance, hole diameter and the element thickness.

SOLUTIONS

Crack configurations and stress intensity factors for each phase are given below, using Eq. 8 with appropriate geometric correction factors:

Phase I Quarter circular, part-through corner crack from the edge of a hole of initial crack length $a_i = .001$ inch.

$$K = .712 \sigma \sqrt{\pi a} \cdot \beta_b \cdot \beta_h \cdot \beta_{sg}$$

Phase II Through single crack from the edge of a hole - initial crack length for this phase is .2 inch equal to the thickness of the part, $a_i = .2$ inch.

$$K = \sigma \sqrt{\pi a} \cdot \beta_h \cdot \beta_{sg} \cdot \beta_w$$

Phase III Quarter circular, part-through corner crack from the opposite edge of the hole wall of initial length $a_i = .005$ inch.

$$K = .712 \sigma \sqrt{\pi a} \cdot \beta_b \cdot \beta_s \cdot \beta_{sg}$$

Phase IV An equivalent edge crack of initial crack length of $a_i = 1.356$ inch.

$$K = \sigma \sqrt{\pi a} \cdot \beta_s \cdot \beta_{sg}$$

TABLE I CRACK GROWTH SPECTRUM

	MAX STRESS KSI	MIN STRESS KSI	CYCLES FLIGHT		MAX STRESS KSI	MIN STRESS KSI	CYCLES FLIGHT		MAX STRESS KSI	MIN STRESS KSI	CYCLES FLIGHT
MIS 0	20 327	-3 949	1 00	MIS 7	16 302	-1 630	1 00	MIS 11	8 758	000	1 00
MIS 1	9 974	- 997	1 00		9 282	7 282	335 00		5 373	3 373	1032 00
	4 816	2 816	219 00		10 294	6 294	72 00		6 626	2 626	155 00
	6 002	2 002	29 00		11 282	5 282	16 00		7 769	1 769	26 00
	7 057	1 057	4 00		12 236	4 236	4 00		8 758	758	5 00
	8 224	- 129	1 00		13 827	2 452	1 00		10 889	-1 257	1 00
	9 974	-2 214	10		16 302	- 342	10		13 828	-3 994	10
MIS 2	11 586	-1 159	1 00	MIS 8	18 717	-1 872	1 00	MIS 12	7 697	-1 367	1 00
	6 049	4 049	293 00		10 424	8 424	478 00		7 697	.000	1 00
	7 359	3 359	40 00		11 731	7 731	107 00		7 697	.000	1 00
	8 345	2 345	6 00		12 742	6 742	25 00		7 697	.000	1 00
	9 726	885	1 00		13 751	5 751	6 00		13 605	-1 367	1 00
	11 586	-1 314	10		14 699	4 699	1 00		8 690	.000	1 00
MIS 3	10 670	-1 067	1 00		15 942	3 392	1 00		8 690	.000	1 00
	7 030	5 030	420 00		18 717	271	10		8 690	.000	1 00
	8 030	4 030	60 00	MIS 9	18 541	-1 854	1 00		8 690	.000	1 00
	8 988	2 988	10 00		10 479	8 479	383 00		5 332	3 332	1008 00
	10 670	1 257	1 00		11 706	7 706	91 00		6 565	2 565	153 00
MIS 4	13 288	-1 329	1 00		12 670	6 670	22 00		7 697	1 697	26 00
	0 572	5 572	473 00		13 643	5 643	6 00		8 690	690	1 00
	9 860	5 860	85 00		14 578	4 578	1 00		10 791	-1 305	1 00
	10 906	4 906	16 00		15 759	3 309	1 00		13 665	-4 030	10
	11 916	3 916	3 00	MIS 10	16 556	-1 656	1 00				
	13 288	2 265	1 00		11 170	9 170	321 00				
MIS 5	13 735	-1 373	1 00		12 171	8 171	86 00				
	7 449	5 449	314 00		13 155	7 155	24 00				
	8 592	4 592	55 00		14 130	6 130	7 00				
	9 621	3 621	10 00		15 067	5 067	2 00				
	10 551	2 551	2 00		16 556	3 475	1 00				
	11 576	1 411	1 00	MIS 11	7 769	-1 383	1 00				
	13 735	-1 205	10		7 769	000	1 00				
MIS 6	15 767	-1 577	1 00		7 769	000	1 00				
	10 206	8 206	567 00		7 769	000	1 00				
	11 561	7 561	116 00		13 828	000	1 00				
	12 607	6 607	25 00		8 758	000	1 00				
	13 629	5 629	6 00		8 758	.000	1 00				
	14 591	4 591	1 00		8 758	000	1 00				
	15 767	3 329	1 00		8 758	000	1 00				

TABLE II GEOMETRIC CORRECTION FACTOR FOR VARIOUS PHASES

PHASE I $\beta_T - \beta_c, \beta_b, \beta_a, \beta_c$		PHASE II $\beta_T - \beta_c, \beta_a, \beta_c$		PHASE III $\beta_T - \beta_c, \beta_b, \beta_c, \beta_a$		PHASE IV $\beta_T - \beta_c, \beta_f$	
α	β_T	α	β_T	α	β_T	α	β_T
.001	4.01	.200	1.80	.005	10.23	1.356	1.63
.003	3.85	.250	1.75	.007	10.04	1.40	1.63
.005	3.70	.300	1.70	.009	9.86	1.50	1.54
.007	3.56	.350	1.69	.020	8.83	1.60	1.45
.009	3.42	.400	1.70	.040	7.53	1.70	1.39
.020	2.86	.450	1.76	.060	6.51	1.80	1.36
.040	2.33	.500	1.84	.080	5.79	1.90	1.35
.060	2.06	.550	1.93	.100	5.24	2.00	1.47
.080	1.88	.600	2.06	.120	4.88	2.10	1.65
.100	1.75	.650	2.27	.140	4.70	2.20	1.63
.120	1.67	.700	2.54	.160	4.54	2.30	1.63
.140	1.61	.750	2.84	.180	4.53	2.40	1.62
.160	1.58	.800	3.27	.200	4.89	2.50	1.58
.180	1.62	.850	3.82			2.60	1.57
.200	1.78	.900	4.80			2.70	1.56
		.950	7.10			2.80	1.54
		1.000				2.90	1.53
						3.00	1.53

TABLE III SEQUENCE OF MISSIONS IN 500 HRS PASS

SEQUENCE	MISSION								
1	7	25	8	49	4	73	12	97	2
2	8	26	6	50	7	74	8	98	1
3	1	27	11	51	12	75	7	99	12
4	2	28	1	52	8	76	5	100	5
5	12	29	12	53	11	77	2	101	7
6	7	30	7	54	5	78	4	102	8
7	5	31	8	55	7	79	1	103	9
8	11	32	2	56	1	80	8	104	2
9	8	33	5	57	2	81	7	105	7
10	9	34	7	58	12	82	12	106	11
11	7	35	1	59	8	83	11	107	12
12	1	36	9	60	7	84	9	108	1
13	12	37	12	61	0	85	7	109	8
14	2	38	8	62	3	86	8	110	5
15	7	39	11	63	5	87	2	111	7
16	8	40	7	64	1	88	5	112	2
17	11	41	2	65	7	89	1	113	12
18	5	42	5	66	12	90	12	114	8
19	1	43	12	67	8	91	7	115	7
20	7	44	7	68	2	92	10	116	9
21	12	45	2	69	11	93	8	117	1
22	4	46	8	70	9	94	11	118	11
23	2	47	1	71	7	95	3	119	4
24	7	48	9	72	1	96	7	120	12

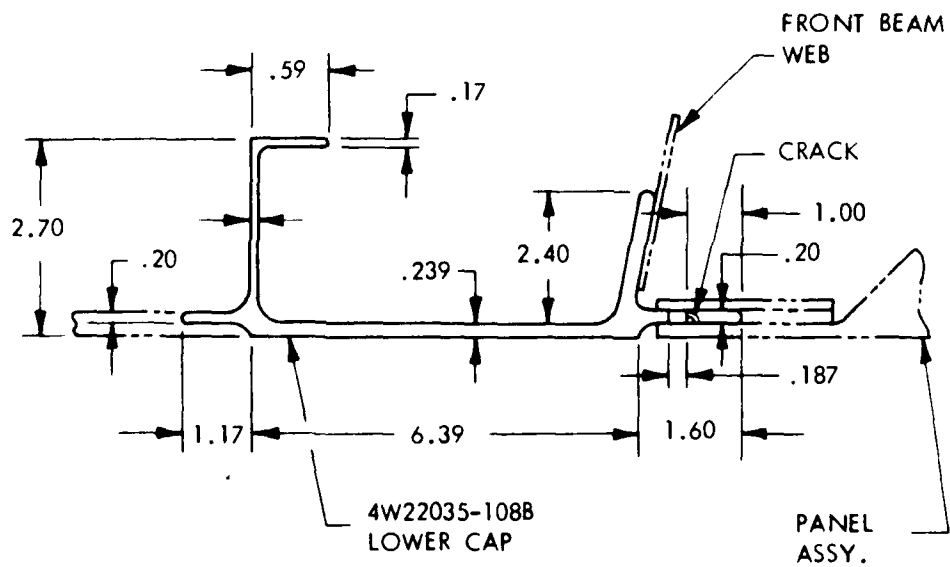


FIG. 5 STRUCTURAL DETAILS AT THE LOCATION OF ANALYSIS

β_b and β_h are as discussed before, β_s is the geometric correction factors for the slot effect (edge crack plus the hole) and is calculated using a cracked finite element model [26]. Note that $a/\sqrt{2}$ should be used for β_h and β_s for part-through Phases I and III for an equivalent crack length at 45° or at the mid point of the quarter circle. β_{sg} is the stress gradient correction factor due to the adjacent structural changes and it is calculated using the finite element model. β_w is the secant width correction factor. The various Beta factors (geometric boundary correction factors) are given in Table II.

The above stress intensity factors are modified to take into account the load interaction effect (variable amplitude spectrum) by using Eq. 7. The Forman equation and the Willenborg retardation model described in the previous section are used to evaluate the crack growth. A computer program [27] is used on a 500 hour repeating block spectrum to analytically generate a crack growth curve. The computer program "crack growth" uses a numerical integration technique [28-29] to generate a da/dF versus a curve where dF is an increment of the 500 hour block. Using Eq. 10 and making appropriate geometric correction factors for each phase, the critical stress for critical crack length can be calculated. The results are plotted in Figure 6. For limit load stress (33 KSI), the critical crack length is 1.3. The crack length versus flight hours is plotted in Figure 7. The critical crack length for limit stress is shown on the graph.

The primary objective of this analysis is to ensure the safety of the structure. Hence, the inspection of the structure in an economical way plays an important role. Economy of the inspection procedure depends on the procedure used and upon the criticality of the structure. The inspection intervals are established using a detectable crack length (based on the particular inspection procedure used) and the critical crack length. Assume for the present case study the initial flaw, a_i , is .05 and a_{det} is .15 inch and the critical crack length, a_c , at limit load is 1.3 inches.

Based on the above assumptions, the required inspections, including a safety factor of 2, and protecting the aircraft for limit load, the intervals are as follows:

$$\begin{aligned}
 \text{Initial inspection} &= \frac{\text{Time @ } a_c = 1.30 - \text{Time @ } a_i = .05}{2} \\
 &= \frac{23450 - 19000}{2} = \frac{4450}{2} = 2225 \text{ Hrs} \\
 \\
 \text{2nd and subsequent inspections} &= \frac{\text{Time @ } a_c = 1.30 - \text{Time @ } a_{det} = .15}{2} \\
 &= \frac{23450 - 21500}{2} = 975 \text{ Hrs.}
 \end{aligned}$$

Note: Inspection interval calculated as an example only, not to represent any specific aircraft.

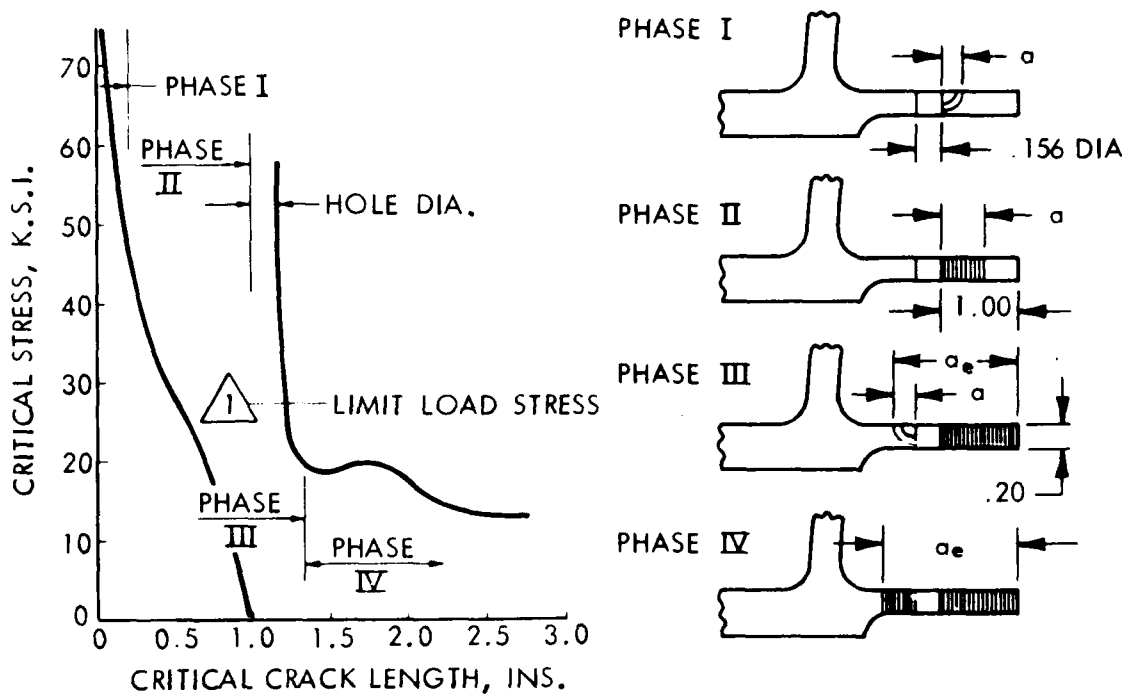


FIG. 6 CRITICAL STRESS AS A FUNCTION OF CRITICAL CRACK LENGTH

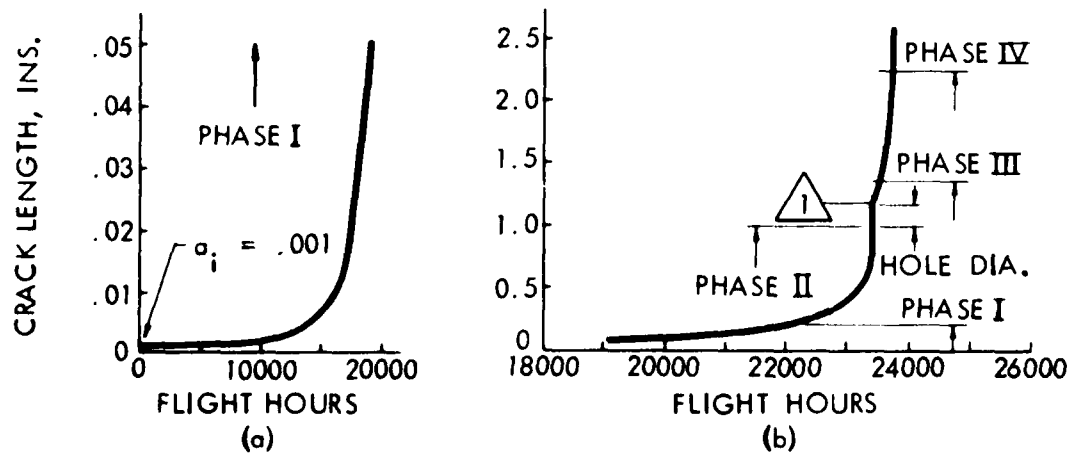


FIG. 7 CRACK LENGTH AS A FUNCTION OF FLIGHT HOURS

CONCLUSIONS

- 1 Basic fracture mechanics concepts and a sample analysis is described to establish inspection intervals that will ensure the safety of an existing aircraft structure. Longer inspection intervals can be realized by lowering the operating stress levels (aircraft restrictions) or if the short inspection intervals are confined to a few "hot spots" a "local beefup" may effectively be used to locally lower the stress. Any reduction in operating stress level has a very significant effect on crack growth since the minimum value of n for an aluminum alloy in the Forman equation is approximately 3, which is to say that the "time to grow" will increase as the cube of the stress reduction.
- 2 Parameters such as load transfer, spectrum derivation, load sequence effects (retardation) and special boundary conditions which effect crack growth characteristics are discussed only briefly in the text. There are a number of sophisticated techniques currently being developed and used to handle these parameters and are available in the "literature" but are considered outside the scope of this case study.
- 3 Fundamental fracture mechanics methodology that more accurately predicts the behavior of crack growth is developing at a very rapid rate. Therefore, the analyst should be aware of the current "state of the art" on such things as retardation models, effects of cyclic rate, threshold K 's and other parameters effecting crack growth behavior.

ACKNOWLEDGMENTS

This work was carried out at Lockheed-Georgia Company. The authors would like to thank Messrs. F. M. Conley, A. P. Shewmaker, S. C. Rogers, J. A. Neilson, and N. C. Appold for their encouragement in preparing this paper. The authors are also indebted to Mrs. Ruth Bowman for typing this document.

REFERENCES

- 1 "The Comets Accident", Report of the Court of Enquiry on the Investigation at the Royal Aircraft Establishment, *Aircraft Production*, v. 17, no. 4, April 1955, 136-137.
- 2 Hinders, V. A., "F-111 Design Experience - Use of High Strength Steel", AIAA 2nd Aircraft Design and Operations Meeting, Los Angeles, California, July 20-22, 1970.
- 3 MIL-STD-1530A (USAF), "Aircraft Structural Integrity Program Airplane Requirements".
- 4 MIL-STD-83444 (USAF), Airplane Damage Tolerant Design Requirements, July 1974.
- 5 MIL-STD-A-8866 (USAF), Airplane Strength and Rigidity, Ground Tests.
- 6 Inglis, C. E., "Stresses in a Plate due to the Presence of Cracks and Sharp Corners", *Proc. Inst. Naval Architecture*, 1913, 60, 219-230.
- 7 Tiffany, C. F. and Masters, J. N., *Applied Fracture Mechanics Fracture Toughness Testing and Its Application*, ASTM-STP-381, 1965, 249-277.
- 8 Gallagher, J. P., "What the Designer Should Know About the Fracture Mechanics Fundamentals", Paper 710151 presented at SAE Automotive Engineering Congress, Detroit, January 1971.

- 9 Wood, H. A., "The Use of Fracture Mechanics Principles in the Design and Analysis of Damage Tolerant Structures AGARD-LS-62, 1973, Paras. 4.1 - 4.13.
- 10 Wood, et al., "Current Practice on Estimating Crack Growth Damage Accumulation with Specific Application to Structural Safety, Durability and Reliability", Technical Report AFFDL-TR-75-32, 1973.
- 11 Toor, P. M., "A Review of Some Damage Tolerant Design Approaches for Aircraft Structures", Engineering Fracture Mechanics, v. 5, 1973, 837-880.
- 12 Toor, P. M. (Ed.), Fracture Mechanics Methodology and Analytical Procedures, Lockheed-Georgia Company, Report SMN-366, Rev. A, 1972.
- 13 Hoepner, D. W. and Krupp, W. E., "Prediction of Component Life by Application of Fatigue Crack Growth Knowledge", Engineering Fracture Mechanics, v. 6, 1977, 47-70.
- 14 Coffin, M. D. and Tiffany, C. F., "How the Air Force Assures a Safe, Durable Airframe", Metal Progress, v. 109, no. 3, March 1976, 26-32.
- 15 Gallagher, J. P., "Estimating Fatigue Cracks Lives for Aircraft - Techniques", Experimental Mechanics, v. 16, Nov. 1976, 425-433.
- 16 Paris, P., "The Growth of Cracks Due to Variation in Load", Ph.D. Dissertation, Lehigh University, 1962.
- 17 Foman, et al., "Numerical Analysis of Crack Propagation in Cyclically Loaded Structure", J. Basic Engineering, v. 89, 1967, 459-464.
- 18 Willenborg, J. D.; Engle, R. M.; and Wood, H. A., "A Crack Growth Retardation Model Using an Effective Stress Concept", TM-71-1-FBR, 1971.
- 19 Staley, J. T., "Fracture Toughness and Microstructure of High Strength Aluminum Alloys", The Metallurgical Society of the American Institute of Mining, Metallurgical, and Petroleum Engineers Spring Meeting, Pittsburg, Pennsylvania, May 23-24, 1974.
- 20 Wigglesworth, L. A., "Stress Distribution in a Notched Plate", Mathematika, v. 76, no. 4, 1957.
- 21 Kobayashi, A. S. and Moss, W. L., "Stress Intensity Magnification Factors for Surface Flawed Tension Plate and Notched Round Tension Bar", in Fracture 1969, Chapman & Hale, London, 1969.
- 22 Liu, A. F., "Stress Intensity Factor for a Corner Flaw", Journal of Engineering Fracture Mechanics, v. 4, no. 1, 1972, 175-179.
- 23 Irwin, G. R., "Plastic Zone Near a Crack and Fracture Toughness", Seventh Sagamore Ordnance Material Research Conference, 1960.
- 24 Feddersen, C. E., ASTM-STP-410, 1966, 77.
- 25 Packman, P. L.; Pearson, H. J.; Owens, J. S., and Young, G., "The Applicability of a Fracture Mechanics - NDT Design Criterion for Aerospace Structures", WESTEC Conference, March 10, 1969, L.A., California.
- 26 Lukaart, C. A., "Cracked Element Application", Lockheed-Georgia Company Report ER 0067, 1973.
- 27 Hsu, T. M., "Computer Program for Prediction of Fatigue Crack Propagation", Lockheed-Georgia Company Report SMN 370, 1972.
- 28 Brussat, T. R., "Rapid Calculation of Fatigue Crack Growth by Integration", Fracture Toughness and Slow-Stable Cracking, ASTM - STP 559, 1974, 298-311.

- 29 Brussat, T. R., "An Approach to Predicting the Growth to Failure of Fatigue Cracks Subjected to Arbitrary Uniaxial Cyclic Loading", Damage Tolerance in Aircraft Structures, ASTM-STP-486, 1970.

A POST-MORTEM WING STRENGTH ANALYSIS

R.J.H. Bollard and E.H. Dill
Professors, Department of Aeronautics and Astronautics
A.S. Kobayashi and R. Taggart
Professors, Department of Mechanical Engineering
University of Washington
Seattle, Washington 98195

INTRODUCTION

(i) Historical Background

The aircraft under study was a twin-engine plane which had been in service for approximately nine years and crashed during a normal descent. Inspection of the wreckage showed that the initial structural failure occurred by an upward bending mode of the right wing outer panel and that this failure was initiated by rapid crack propagation which originated from existing fatigue crack(s).

The purposes of this post-mortem analysis were to:

- a) Establish the actual structural geometry, including the extent of fatigue damage, prior to the failure of the wing.
- b) Predict the actual failure load (g-factor) under the application of aerodynamic forces associated with the most severe design conditions.

(ii) Technical Background

The wing beam structure consisted of a single box of laminated aluminum 7075-T6 sheets and extrusions bonded together into the geometry shown in Fig. 1. The moment of inertia of the original uncracked structure at this cross-section is 1409 in^4 and the principal axis of the moment of inertia is located at 10.68 inch above the stringer in the center of the access door and is almost parallel to the lower sheet chord line.

The design ultimate moment for the equivalent stowage condition at the time of the crash but with slightly less fuel, is 570,000 ft-lbs. An actual test conducted by the manufacturer with simulated load distribution on the wing demonstrated that this section of the wing without any fatigue cracks could withstand an applied moment of 639,000 ft-lbs.

The inboard portion of the right wing of the plane was retrieved at the crash site and the fatigue-fracture surface that existed both fore and aft of the access door in the lower surface of the right wing was examined.

The right-hand wing, outboard from the fracture surface, was not recovered at the crash site but was later found after much of the

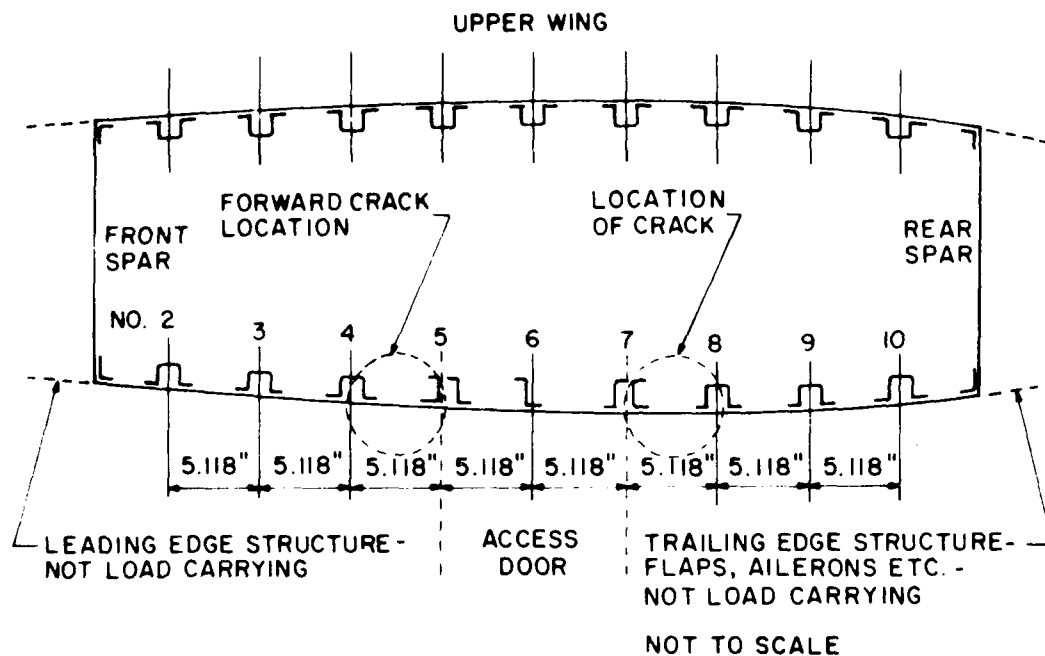


Figure 1 Cross-section of Wing Box at Fractured Section

preliminary analysis was completed. Major fatigue cracks were found in the lower skin of the right wing both fore and aft of the access door, in the inboard wing stub and in the vicinity of the bolt holes marked 1A, 2A, 1F and 2F in Figure 2.

Figure 3 shows a typical macroscopic detail of the fatigue cracks fore and aft of the No. 1 access door in the lower wing where macroscopic beach marks are clearly evident, consequently the length of the fatigue cracks can be estimated.

Since the wing section surrounding the No. 1 access door was identified as fatigue critical area by the manufacturer, this section of the wing was subjected to periodic X-ray inspection every 500 hours of flight time. A review of these X-ray records indicated the following.

1. X-ray inspection of the right wing at the access door 21 months prior to the wing failure revealed no cracks.
2. X-ray inspection of the right wing at the access door 6 months later revealed that a crack existed at bolt hole 1A and had grown at least as far as the vertical section of the J stringer.
3. Two X-ray inspections of the right wing at the access door in the next 12 months showed that the crack had extended from bolt hole 1A to 2A.

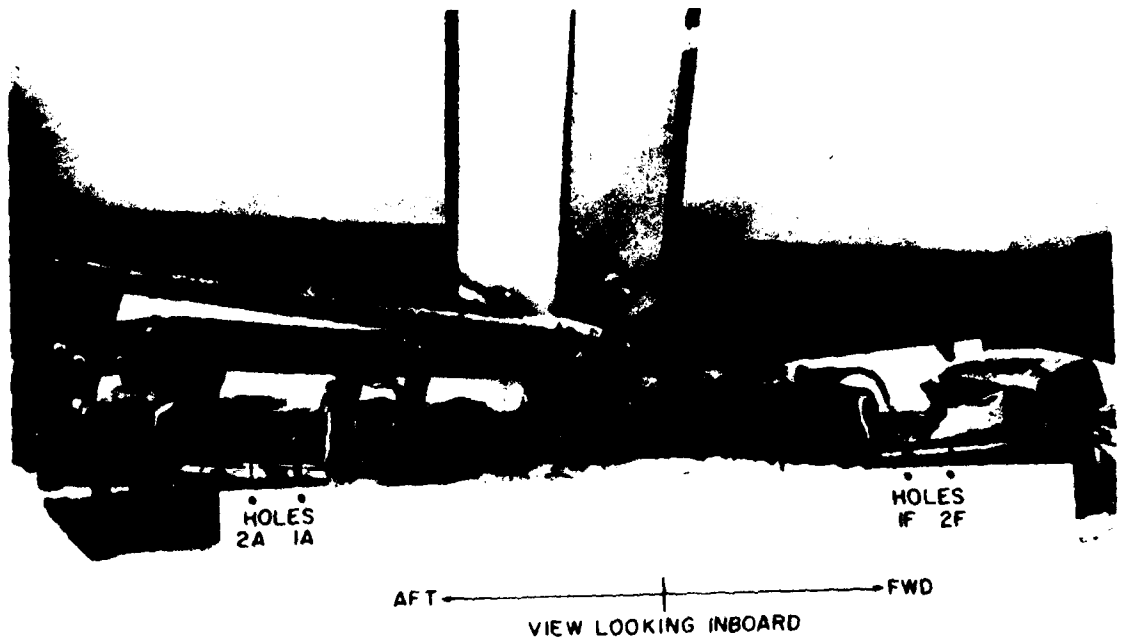


Figure 2 Fracture Surfaces of Right Wing Looking Inboard

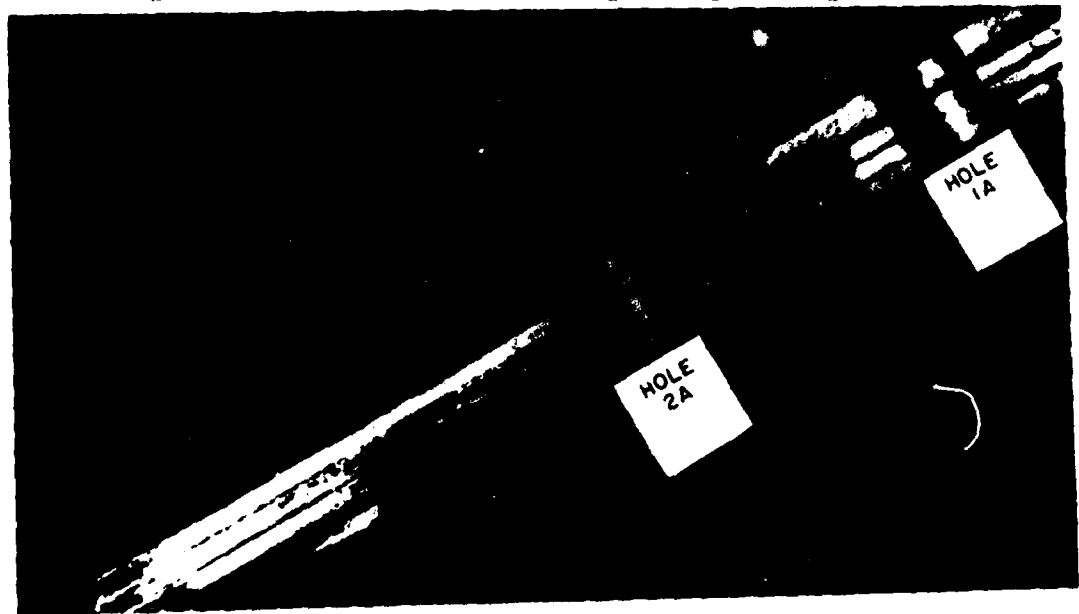


Figure 3 Fracture Surface Fore and Aft of Access Door

FORMULATION

(i) Macroscopic and Microscopic Examinations of Fracture Surfaces

The macroscopic details of the fatigue fracture surfaces on the salvaged outer wing panel are shown in Figure 4. These fracture surfaces



Figure 4 Fracture Surface Aft of Access Door, Outer Wing Panel

on the outer wing are close to the rivet hole 2A shown in Figure 2. The areas of fatigue fracture aft of the rivet in each doubler and in the toe of the hat section matched with the corresponding fracture surface on the inboard wing stub.

Two stage plastic replicas were prepared by standard shadowing techniques to permit their examination in a JEM-7 transmission electron microscope that was equipped with a tilting stage. The first series of replicas was taken from the inboard wing stub, and the second series of replicas was taken from the fracture surfaces of the salvaged outer wing panel. Representative fractographs from the first series of replicas are shown in Figure 5 and reveal the presence of micro-striations that are typical of a fatigue fracture which has grown under a sequence of random loadings. Figure 6 indicates the approximate positions from which replicas were taken. The length of the fatigue crack aft of the No. 1 access door is shown as 3.125 inches on Figure 6.

Fractographs that are representative of the second series of replicas are shown in Figure 7 and illustrate that the fatigue fracture in the skin of the outboard wing is identical in nature to the fractures in the doublers of the inboard stub. This fracture surface also shows random micro-striations.



Figure 5 Typical Fractograph of Fractured Surface

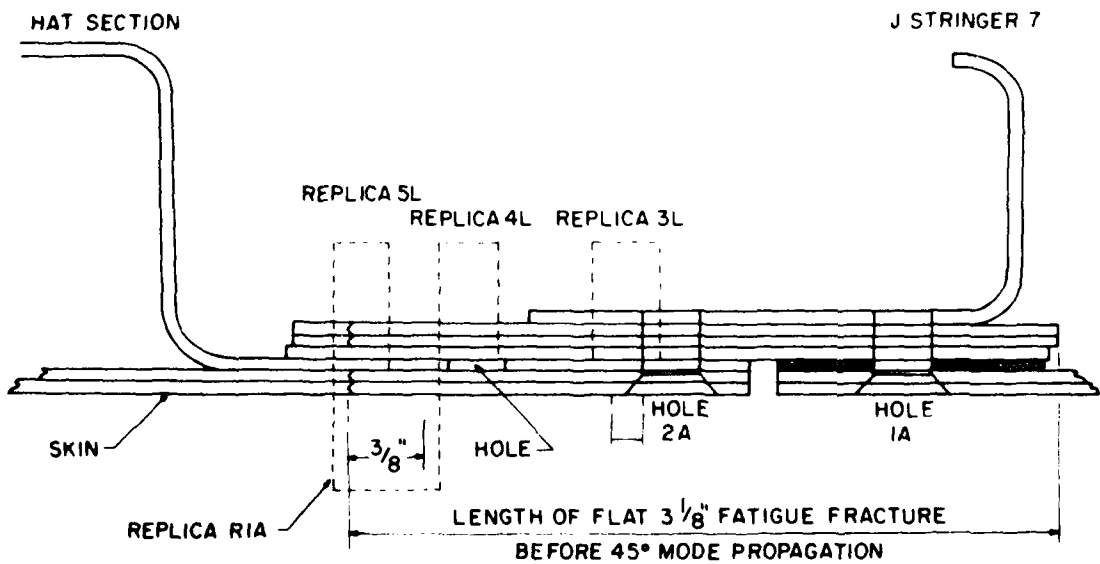


Figure 6 Position of Replicas in Relation to Fatigue Crack

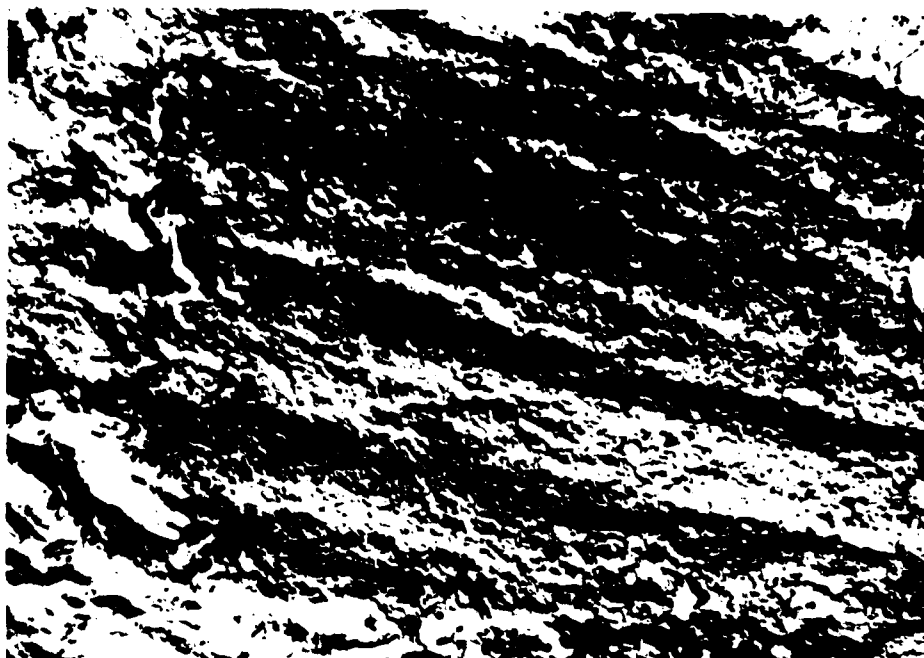


Figure 7 Typical Fractograph of Fractured Surface

(ii) Fractographic Analysis

By combining the details of the fractographic analysis from the inboard wing and the outboard wing panel with the X-ray records dating back to at least 21 months prior to the wing failure, it was possible to construct the sequence of fracture events preceding the final structural failure of the wing.

At least 15 months prior to the wing failure, fatigue cracks nucleated at hole 1A and grew towards the edge of the access door, as shown in Figure 8. Another series of cracks nucleated at hole 1A diametrically opposite to the first cracks and proceeded aft to hole 2A. Shear lips in the toe of the J stringer and the doublers are consistent with fatigue crack growth processes. A final series of fatigue cracks nucleated in all the doublers and the skin and grew aft towards the hat section. At a distance of at least 3.25 inches from the edge of the access door opening, the fracture mode changed from a predominantly fatigue, plane strain mode to a shear mode of failure. It should be noted that this transition occurs at the same place in all the doublers and the wing skin indicating that a crack at least 3.125 inches long existed aft of the access door prior to the final failure of the wing while the aircraft was in flight. The consistent nature of the pattern of macroscopic "beach marks" on the crack surfaces between holes 1A and 2A indicates that the doublers and the toe of the J stringer, between these two holes were cracked all the way through

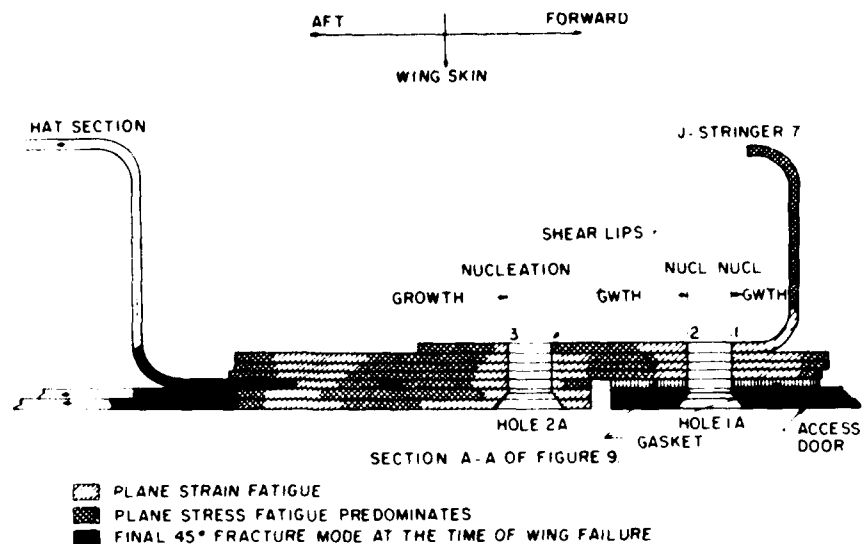


Figure 8 Fatigue Fracture Aft of the Access Door

at least as early as the second from last X-ray examination. Aft of hole 2A the macroscopic "beach marks" are very consistent and the matching of the areas of flat fatigue in the wing skin with the contiguous areas in the adjacent doublers is evidence indicating that a fatigue fracture grew simultaneously in all the doublers and the wing skin.

(iii) Estimate of Critical Crack Length at Wing Failure

Based on the above optical and electron microscopic examination and fractography analysis, the following conclusions were reached:

1. A fatigue crack at least 3.125 inches long existed in the lower wing surface aft of the access door. A similar investigation showed that another fatigue crack at least 2.625 inches long existed forward of the same access door in the lower wing surface prior to the in-flight failure of the right wing.

2. Both fatigue cracks grew by random loading which produced micro-striations on the fractured surface. Such micro-striations are evidence of progressive crack growth over an extended period of time. In the case of the aft crack this period extended over at least 14 months prior to the accident.

3. A comparison of both microscopic fracture surfaces and macroscopic details showed that the aft fatigue crack existed in the J stringer, all doublers, and wing skin prior to the final wing failure.

ASSESSMENT

(i) Residual Strength Analysis of the Wing

In order to determine the stress intensity factor associated with the crack geometry established by microscopic examination and fractography analysis, a two-dimensional finite element analysis of the idealized wing structure was conducted. Figure 9 shows the plan view of the lower panel of the wing in the vicinity of the fracture surface. The complex cross-section of the wing panel, as shown in Figure 8, was idealized into an assembly of axial force members and plane surface elements of different thicknesses in this two-dimensional finite element analysis. The hat

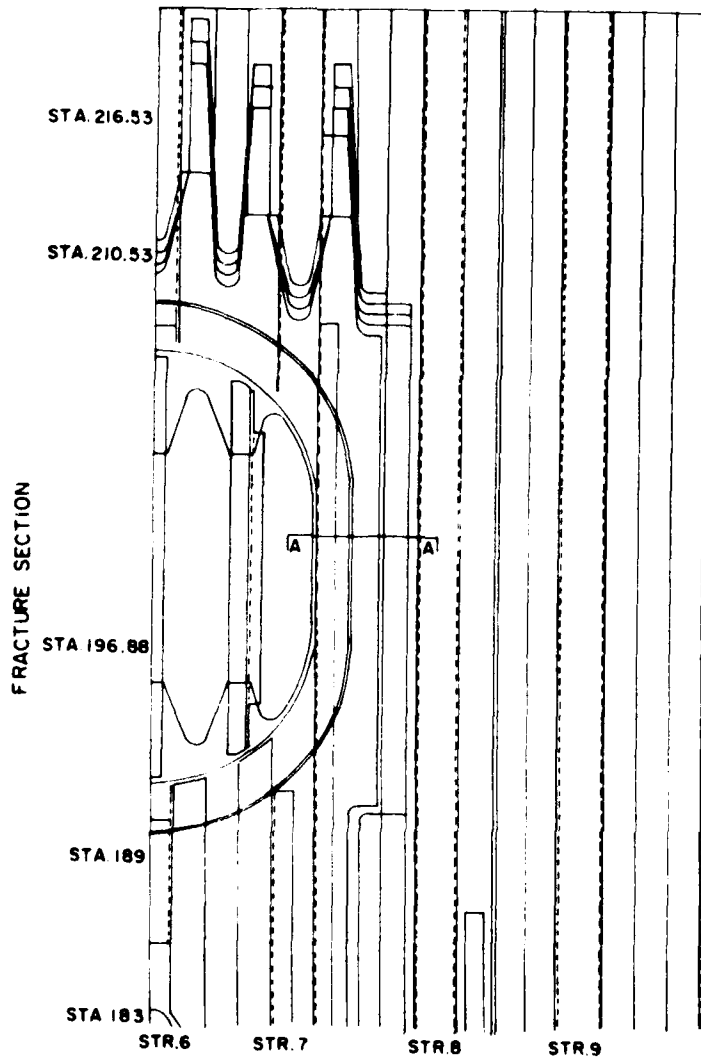


Figure 9 Plan View of Lower Wing Panel in the Vicinity of the Access Door

section was treated by lumping the webs of the hat into an axial force member. It was assumed that the door was designed such that the stringers could be continued through the door. A 3-inch crack was assumed to exist on both sides of the door at the fracture surface. Under these conditions the problem becomes a symmetric problem about the axis of stringer 6 and only the aft part of the panel was analyzed. That portion of the panel was divided into finite elements, as shown in Figure 10.

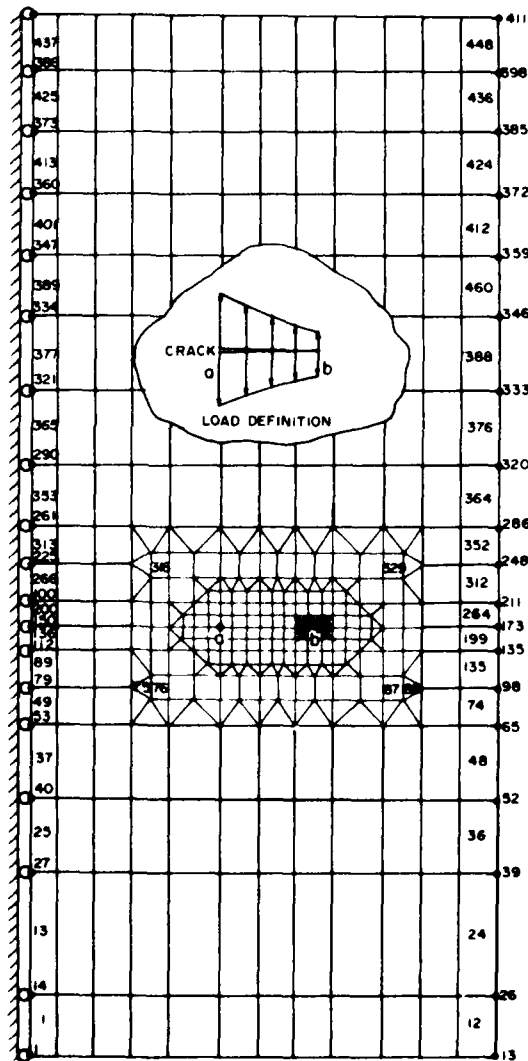


Figure 10 Finite Element Idealization of Lower Wing Panel shown in Fig. 9

The boundary condition used in this finite element analysis was the actual stress state which had been previously measured in an uncracked wing. This stress state is also shown as the prescribed boundary condition in Figure 10. The stresses increase approximately linearly at

the rate of 0.0059σ lb/in² per inch, where σ is the stress in Stringer 7. The stress in J Stringer 7 was found to be 1.32 times the stress near the door, as calculated by the elementary theory.

The calculated stress at Station 189 inches, identified in Figure 9, for the weight condition at the time of failure of the airplane in Stringer 7, also identified in Figure 9, is 47,000 psi for the design load which corresponds to a load factor of 4.5 g. The calculated stress is therefore 10,400 psi per g. Assuming the same stress concentration factor as measured at the adjacent door, the true stress at the Stringer 7 in the uncracked airplane would be 1.32 times 10,400 or 13,800 psi per g, and thus σ was taken to be 13,800 psi per g.

The stress intensity factor for the cracked structure was determined by the conventional procedure of "pressurizing" the crack with the stresses which exist in the corresponding portion of the uncracked wing and then computing the strain energy release rate. For the crack length of 3 inches, a normalized stress intensity factor of $K/\sigma = 2.5$ in^{1/2} was obtained.

In these calculations, the J section was assumed to be fully cracked. Additional calculations were conducted in which the outstanding leg of the J section was not cracked. The stress intensity factor was reduced by less than 6 percent and thus the above approximation of a fully cracked J section did not materially change the stress intensity factor. The solution showed negligible reactions along the line of symmetry in Figure 10, indicating that the two cracks at Stringers 5 and 7 could be analyzed separately. The stress state was also nearly symmetric about the line a-b of the crack. The small shear stress which would exist along a-b in the uncracked structure was neglected.

For 7075-T6 aluminum, the handbook value of fracture toughness for this thin gage is approximately $K_C = 70,000$ psi $\sqrt{\text{in}}$ [1]. Since $K = 2.5\sigma\sqrt{\text{in}}$, the crack will propagate at that load which would produce a stress at Stringer 7 of the uncracked structure of amount $\sigma = \frac{70,000}{2.5} = 28,000$ psi. As shown previously $\sigma = 13,800$ corresponded to a one- $\frac{2}{5}$ design condition and thus onset of crack propagation would occur at a load factor of $n = \frac{28,000}{13,800} = 2.03$ g.

The above study showed that the 3-inch pre-existing crack will become critical at a load factor of 2 g. Further calculations are necessary to predict crack arrest due to static unloading of the crack tip stress field of the stringers. For this purpose, stress intensity factors for various crack lengths, from 2.8 to 4.8 inches were calculated and at least through Stringer 8.

Since the first finite element study had shown the stresses to be nearly symmetric about the line a-b of the crack, only the portion of the panel from the fracture surface inboard of 23.2 in, which is longer and wider than the previous panel, was used in this second series of finite element analyses. Symmetry conditions were used along the fracture surface. The boundary conditions used are therefore the same as those shown in Fig. 10.

In this idealization the actual shape of the stringers and the doublers was taken into account. The thicknesses of plane stress elements were the mean thickness in the region of the elements. The construction of the access door was more accurately modeled. The portion of the hat sections which was lumped into an axial force member was slightly reduced. These changes provide increased accuracy of perhaps one or two percent.

The crack is assumed to increase at the same rate in all layers of skin and doublers. When the crack tip reaches the web of the hat stringer, two possibilities arise. The crack may continue to propagate in the skin and doublers leaving the hat section intact, or the crack may propagate into the web of the hat. Both situations were investigated.

If the crack did not propagate into the hat section, the above idealization of the hat section would provide a lower estimate of the wing strength. The hat section at Stringer 8 was therefore lumped into axial force members, one half at each side. A finite element analysis was then made for various crack lengths.

The stress which develops in the hat section is the stress which would exist if the wing were uncracked plus the extra stress due to the presence of the crack. The stress if the wing were uncracked, as described previously is 27,600 psi in the Stringer 7 at a load factor of 2 g. The stress in the hat section is .865 times the stress in Stringer 7 and thus σ_o is 23,900 psi at a load factor of 2 g. The extra stress corresponding to a stress of 27,600 psi in the J-section was found by the finite element solution to be as follows:

<u>Crack Length l Inches</u>	<u>Extra Stress σ_e psi</u>
3.0	14,100
3.2	24,000
3.4	37,400
3.5	56,100

The total stress in the hat section as the crack tip approaches the hat stringer is $\sigma_o + \sigma_e$:

<u>Crack Length l Inches</u>	<u>Stress in the Hat Section psi</u>
3.0	38,000
3.2	47,900
3.4	61,300
3.5	80,000

Since 7075-T6 has a tensile strength of about 77,000 psi, the stringer can be expected to fail and the crack will propagate into the web of the hat section.

A second analysis was done assuming that the crack would propagate into the hat section. The crack was assumed to grow at the same rate in the skin, doublers, and flange of the hat section until the web of the hat is reached. The crack is assumed to then grow in the hat up to the crown, and then propagate at the same rate in the skin, doublers and crown of the hat. The first model of the hat can be used to investigate this situation. This is shown in Figure 11 for the load factor 2 g; the load for which it was earlier found that $K = K_c$ for a crack length of 3 inches.

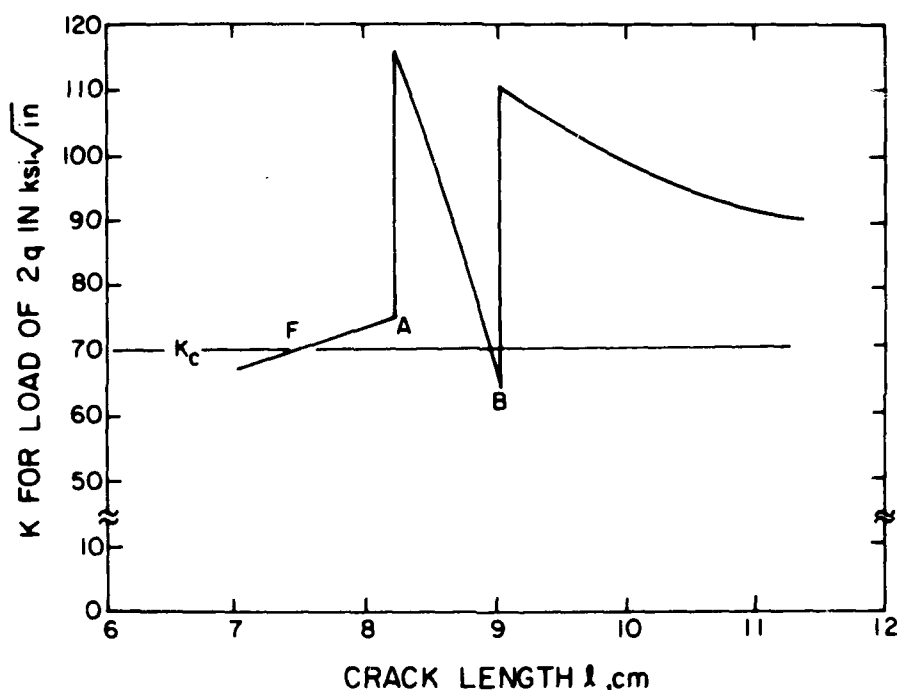


Figure 11 Variation in Stress Intensity Factor with Crack Extension

Little is known about the stress intensity factor which causes a propagating crack to arrest. Available experimental results are limited to laboratory materials, such as plastics and reactor grade steels, [2, 3, 4], reported to have arrest stress intensity factors, K_{1a} , varying from 0 to 15 percent lower than the fracture toughness of the material. The arrest stress intensity factor, K_{1a} , is said to be influenced by the stress wave effects and therefore varies with this problem [2, 3]. Nevertheless, one can expect that if a maximum arrest stress intensity factor, say 84 percent of the fracture toughness, is a necessary condition to arrest a crack in a single test specimen, a similar or even smaller stress intensity factor would be necessary to arrest a running crack in a complex structure such as the wing, which is subjected to dynamic loading.

With the reasoning outlined above, an arrest stress intensity factor of 58.8 ksi \sqrt{in} is used in conjunction with the results in Figure 11 to estimate the subsequent behavior of the propagating crack. Crack

propagation initiates at a load factor of 2 g (point F on the graph). Under the load of 2 g, the crack will propagate. The termination of the doublers at A, in Figure 11, causes the crack to accelerate; but as the crack approaches the hat section, it will slow down. The decrease in stress intensity factor to 63 at B, a decrease to 90 percent of K_c , is insufficient to arrest the crack. The stress intensity factor exceeds the critical value for all subsequent lengths, and the crack continues to propagate.

At the crack length of $l = 3.8$ inches, where the computation was terminated, the stress intensity factor is approximately 28 percent above the fracture toughness of $K_c = 70$ ksi $\sqrt{\text{in}}$. Extrapolating this stress intensity factor versus crack lengths curve to the 2nd web of the hat section will yield an approximate stress intensity factor higher than the $K = 63$ ksi $\sqrt{\text{in}}$ computed previously. Following the same reasoning as before, the running crack, although simultaneously decelerated at the 2nd web of the hat section, will continue to propagate through this barrier.

Subsequent arrest of this propagating crack under the assumed constant applied load of 2 g is not possible since the static stress intensity factor would have increased approximately 40 percent due to the doubling of the crack length alone. In addition, Stringer 9, in comparison with Stringer 8 will not offer any increased resistance to crack arrest, since these stringers are approximately identical structurally. Experimental results supporting this reasoning can be found in Reference 5.

CONCLUSION

The design stress analysis by the manufacturer had indicated that the stress in the J-section at the fracture section would be 10,400 psi per g. Subsequent measurements of the stress at the J-section showed a stress concentration factor of 1.32. Therefore, the stress at the point where the crack occurred is about 14,000 psi per g. The finite element analysis shows that the fatigue crack 3 inches long will propagate when the load is such that the true stress in the uncracked wing would be 28,000 psi. The fatigue crack will therefore begin to propagate at a load factor of 2 g. A separate finite element analysis shows that the crack will not arrest at Stringer 8, but will continue to propagate. Thus the ultimate load factor for the wing with the 3 inch fatigue crack is 2 g. The wing was designed to withstand a 4.5 g load factor.

REFERENCES

1. Allen, F.C., "Effect of Thickness on the Fracture Toughness of 7075 Aluminum in T6 and T73 Conditions," Damage Tolerance in Aircraft Structures, ASTM STP 486, 1971, 16-38.
2. Kobayashi, A.S., Emery, A.F. and Mall, S., "Dynamic Finite Element and Dynamic Photoelastic Analyses of Crack Arrest in Homalite-100 Plates," to be published in Fast Fracture and Crack Arrest, ASTM STP 627, 1977.

3. Hoagland, R.G., Gehlen, P.C., Rosenfield, A.R. and Hahn, G.T., "The Application of DCB-specimens for Measuring the Crack Arrest Properties of A533B and Other Steels," *ibid loc cit.*
4. Crosley, P.B. and Ripling, E.J., "Towards Development of a Standard Test for Measuring K_{Ia} ," *ibid loc cit.*
5. Wade, B.G. and Kobayashi, A.S., "Photoelastics Investigation on the Crack-arrest Capability of a Pretensioned Stiffened Plate," Experimental Mechanics, v. 15, no. 1, January 1975, 1-9.
6. Isida, M. and Itagaki, Y., "Stress Concentration at the Top of a Central Transverse Crack in a Stiffened Plate Subjected to Tension," Proc. of the 4th U.S. National Congress of Applied Mechanics, 1962, 955-969.
7. Isida, M., "On the Determination of Stress Intensity Factors for Some Common Structural Problems," Int. J. of Engineering Fracture Mechanics, v. 2, 1970, 61-79.
8. Isida, M., Tagami, S. and Itagaki, Y., "Stress Concentration Due to a Central Transverse Crack in a Strip Reinforced on Either Side," Journal of Japan Society of Aeronautics, v. 10, no. 100, 1961.

APPENDIX

Approximate Estimation of Critical Stress Intensity Factor

The stress intensity factor of the subject crack can be estimated by available analytical solutions. Such an estimate serves as a check on the more precise results obtained by the finite element analysis as well as being an indicator for areas where detailed further analysis by the finite element method are needed. The first step in such approximate analysis is to reduce the actual wing structure to a problem for which an analytical solution is available. The final results are critically dependent on this idealization process; which required considerable engineering judgment.

First, the lower skin shown in Figure 9 was assumed to be a tension member subjected to uniaxial tension. Furthermore, the built-up structure, as shown in Figure 8, was assumed to be in a state of plane stress and the stress concentrations due to abrupt discontinuity in thickness and riveted joints were ignored. The result of this idealization is an infinite strip with two longitudinal edge stiffeners on both sides, as shown in Figure 12.

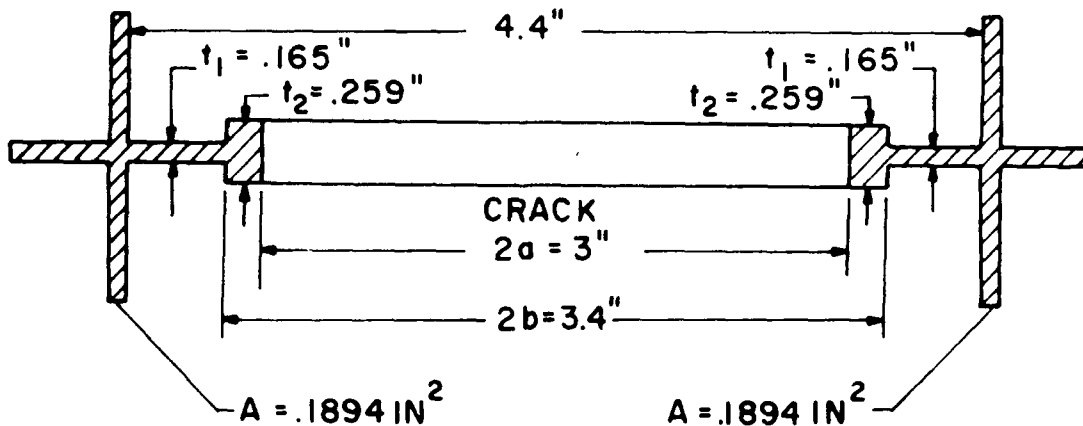
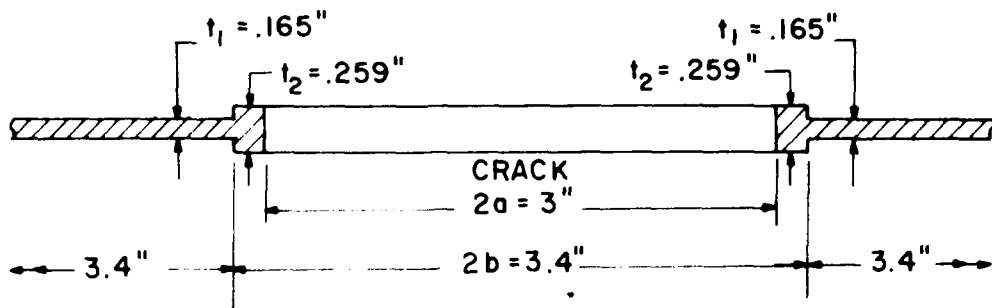


Figure 12 Cross-section of Idealized Cracked Plate with Cross-section Shown in Figure 8

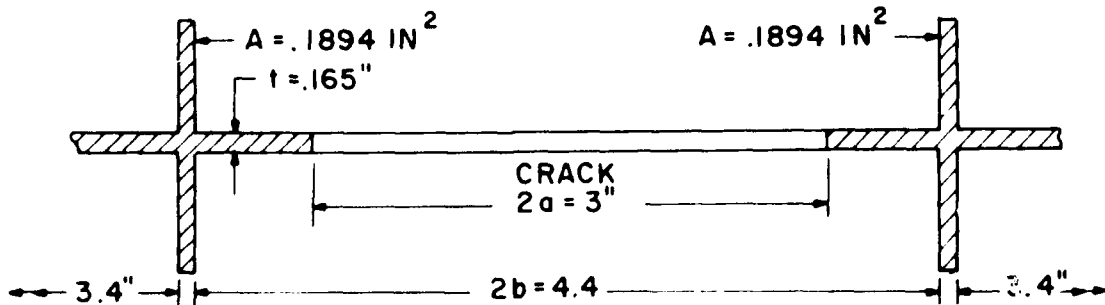
In this idealization, half of the stringer rigidity of the hat section is concentrated at its leg closest to the crack tip. In addition, the sudden change in skin thickness is accounted for.

Available analytical solutions related to this problem as derived by Isida [6, 7, 8] can be represented as $K = F(\lambda) \sigma \sqrt{\pi a}$, where λ is the ratio of crack length $2a$ to characteristic plate width of $2b$. $F(\lambda)$ which is the correction factor to the stress intensity factor of an infinite plate with

a crack of length $2a$ and subjected to uniaxial tension, σ , varies with each problem and can be obtained directly or indirectly from References [6, 7, 8]. Since the analytical solution to the problem represented by Figure 12 does not exist, a solution is constructed from the solutions of two known problems represented by Figures 13a and b. The product of the two $F(\lambda)$'s derived from these problems should be close to the $F(\lambda)$ of Figure 12.



(a)



(b)

Figure 13 Further Idealization of Cracked Plate

From Figure 13a we obtain $\lambda = \frac{a}{b} = .8826$ and a thickness ratio, $\beta = \frac{t_1}{t_2} = .6371$ with which we estimate $F_a(\lambda) = 1.28$ [7]. From Figure 13b, we obtain $\lambda = \frac{a}{b} = .6818$ and an area ratio $dk = \frac{A}{tb} = .5218$ with which we estimate $F_b(\lambda) = .97$ [8]. The resultant correction factor for the problem represented by Figure 12 is $F(\lambda) = F_a(\lambda) \cdot F_b(\lambda) = 1.24$, which agrees closely with the finite element results of $F(\lambda) = 1.15$.

FRACTURE MECHANICS CORRELATION STUDY
ON CRACKED AIRCRAFT STRUCTURES

J. B. Chang
Rockwell International Corporation
Los Angeles, California

INTRODUCTION

In the research, development, test, and evaluation (RD&E) phase of a military aircraft system, several design verification test (DVT) articles which represent major portions of the aircraft were built, and fatigue tests were conducted in the structural laboratory. The fatigue test loadings were variable amplitude loads which simulated the design flight by flight stress spectra of each test article. One such DVT article, identified as DVT-2 Aft Fuselage/Impennage Specimen (shown in figure 1), was tested in 1976. After the application of 991 flights of the fatigue spectrum loading, a 4-7/8 inch crack was detected on the exterior surface of the sideplate of the horizontal vertical stabilizer support fitting. The stabilizer support fitting and the cracked region are illustrated in figure 2.

This stabilizer support fitting is classified as an airplane safety of-flight structure which is a welded assembly of HP 9Ni-4Co .20 steel forgings heat-treated to 190-210 ksi ultimate tensile strength. The Republic steel alloy was selected because of its excellent toughness/strength characteristics. The weld joint was in a double U-groove configuration. Because of the large thickness of the part, more than 100 weld passes were required to make the joint. Weld run out holes were provided at the intersection of the web to the flange on both sides of the support fitting. A stress relief operation at 950° F for 2 hours was performed after the welding.

The cracked region was sectioned off from the test article. The test article was repair-welded and put back into test. It accumulated more than two life-times of the aircraft as of the end of 1976. Fractographic analysis was conducted on the cracked section. The crack was determined to originate from the inner-surface of the weld runout hole. The initial flaw was identified as an intergranular anomaly, elliptical in shape. The initial crack depth was 0.02 inch. Fracture mechanics analysis was performed in order to study the fatigue crack growth behavior in the welded airframe structure under the flight spectrum loading.

The fracture mechanics analysis was made employing the modified version of an existing crack growth calculation computer routine, the EFFGRO program

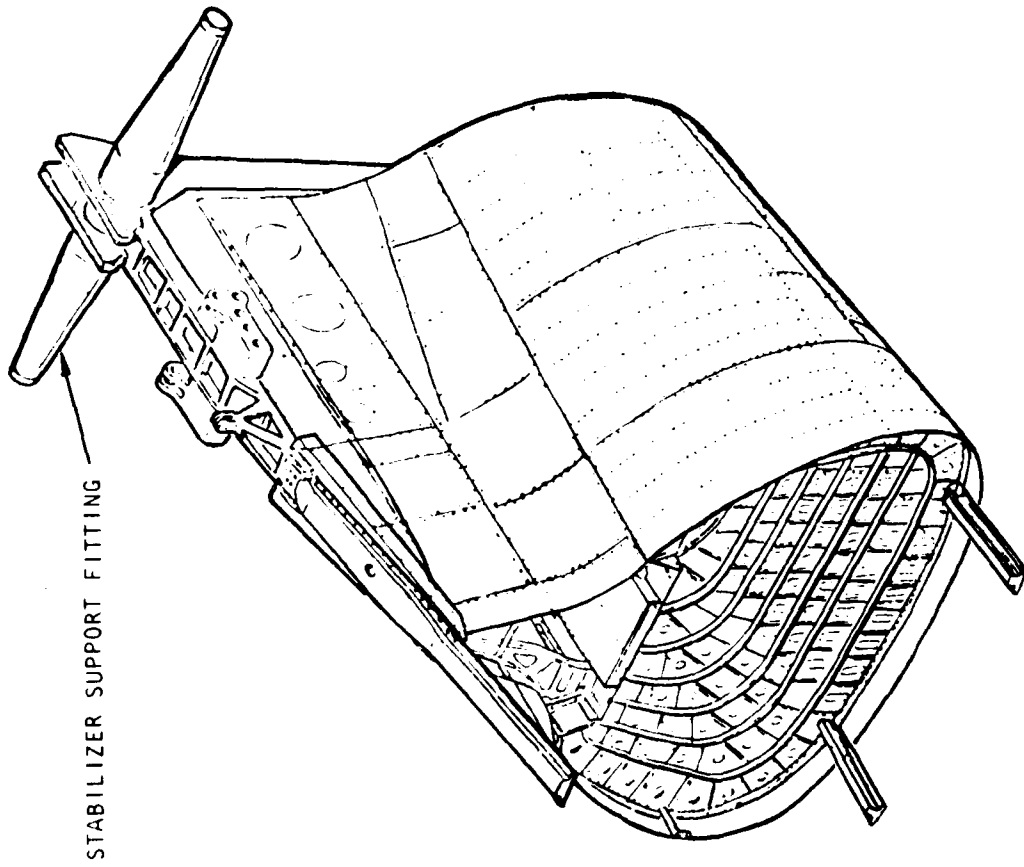


Figure 1. DWT-2 Aft Fuselage/Impennage Test Specimen

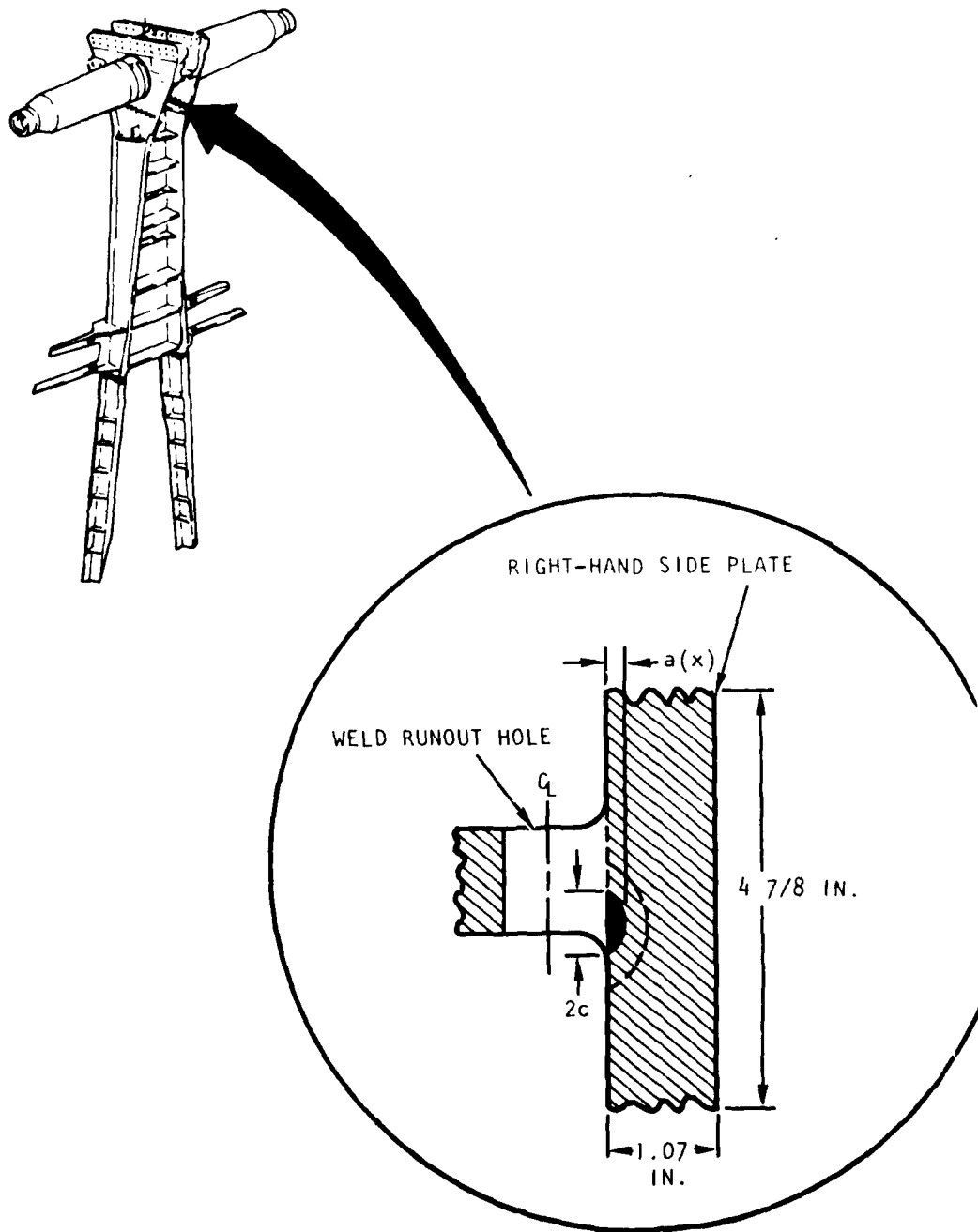


Figure 2. Spindle Support Fitting and Its Cracked Region

(reference 1), developed in-house at Rockwell International. This crack growth computer program is essentially a special integration routine where an initial crack size, a_i , is given and the cyclic crack growth rate, da/dn , is integrated to yield the relationship between "a" and "n" for a structure containing cracks subjected to a given stress spectrum.

The Paris-type fatigue crack growth rate equation (reference 2) with Walker stress ratio correction (reference 3) is employed in the EFFGRO. For tension-tension cyclic loadings, it is expressed as:

$$\frac{da}{dn} = C \left[\frac{\Delta K}{(1-R)^{1-m}} \right]^n, R \geq 0 \quad (1)$$

where C, m, and n are experimentally determined constants; $R = \sigma_{\min}/\sigma_{\max}$ is the cyclic stress ratio; and ΔK is the stress intensity factor range.

For tension-compression load cycles, the crack growth rate equation proposed by Chang (reference 4) is used:

$$\frac{da}{dn} = C \left[(1-R)^q K_{\max} \right]^n, R < 0 \quad (2)$$

where C and n are the same constants as in equation 1 for the tension-tension load cycles; K_{\max} is the stress intensity factor corresponding to the maximum cyclic stress; and q is the acceleration index, which is a constant for a specific negative stress ratio determined from constant amplitude, negative-R loading tests.

FORMULATION

To account for the effect of the residual stress existing in the welded structure on the fatigue crack growth behavior, the preceding rate equations were modified. The modification was on the stress intensity factor and the stress ratio in the rate equations by employing the "effective" stress approach proposed by Chang in his study of the growth behavior of cracks in the residual stress region of cold-worked boltholes (reference 5). The "effective stress intensity factor" in terms of the effective stress, $\bar{\sigma}$, for a surface flaw is expressed as:

$$\bar{K} = M_f(a/c) M_b(a/2c, a/t) M_w\left(\frac{c}{w}\right) \bar{\sigma} \sqrt{\frac{\pi a}{Q}} \quad (3)$$

where a is the crack depth, $2c$ is the crack length, t is the thickness, w is the width of the structure, and M_f and M_b are the front face and back face correction factors, respectively. The M_f and M_b for various a/c and a/t values are shown in tables I and II. They are derived from the results reported by Kobayashi and Moss (reference 6), and Shah and Kobayashi (reference 7). M_w is the width correction factor while Tada's modified secant function (reference 8) is adopted, which takes the following form:

$$M_w = \left[1 - 0.025 \left(\frac{2c}{w}\right)^2 + 0.06 \left(\frac{2c}{w}\right)^4 \right] \sqrt{\sec \frac{\pi c}{w}} \quad (4)$$

Table I. Surface Crack Front Face Correction Factor

a/c	0	0.1	0.2	0.4	0.6	0.8	1.0
M_f	1.12	1.11	1.1	1.08	1.06	1.04	1.03

Table II. Surface Crack Back Face Correction Factor

a/c \ a/t	0.0	0.2	0.3	0.4	0.5	0.5	0.7	0.8	0.9
0.1	1.0	1.02	1.04	1.05	1.08	1.13	1.2	1.36	1.76
0.2	1.0	1.0	1.02	1.03	1.06	1.1	1.16	1.27	1.53
0.4	1.0	1.0	1.02	1.01	1.04	1.07	1.13	1.20	1.37
0.6	1.0	1.0	1.0	1.01	1.02	1.05	1.09	1.16	1.28
0.8	1.0	1.0	1.0	1.01	1.02	1.04	1.07	1.13	1.24
1.0	1.0	1.0	1.0	1.0	1.01	1.02	1.05	1.10	1.19

The quantity "Q" is a combined factor which is expressed in terms of the elliptical shape normalizing factor, ϕ , and the ratio of the effective stress to the material yield strength, $\bar{\sigma}/\sigma_{ys}$, as:

$$Q = \phi^2 - 0.212 \left(\bar{\sigma}/\sigma_{ys} \right)^2 \quad (5)$$

Values of ϕ are the complete elliptical integral of the second kind, which can be expressed as:

$$\phi = \int_0^{\pi/2} \left(\sqrt{1 - (1 - 4\xi^2) \sin^2 \theta} \right) d\theta, \quad \xi = a/2c \quad (6)$$

For a structure containing the residual stress under a remotely applied tensile stress, σ_∞ , the effective stress is expressed as:

$$\bar{\sigma} = g(x)\sigma_\infty + \sigma_{\text{res}}(x) \quad (7)$$

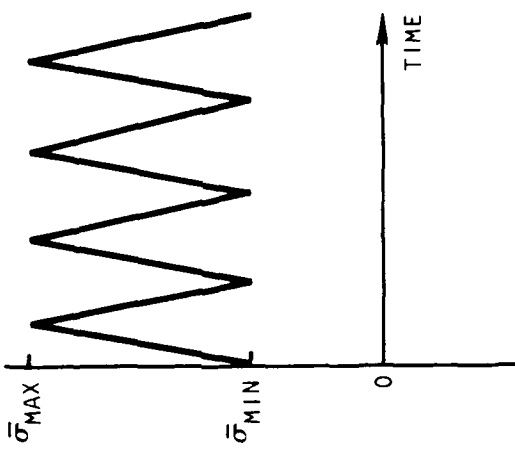
where $g(x)$ is the stress gradient for a nonuniform stress field, and $\sigma_{\text{res}}(x)$ is the residual stress distribution, either compression or tension.

The stress ratio, R , is also modified to account for the effect of residual stresses. In terms of the residual stress, the "effective stress ratio" is expressed as:

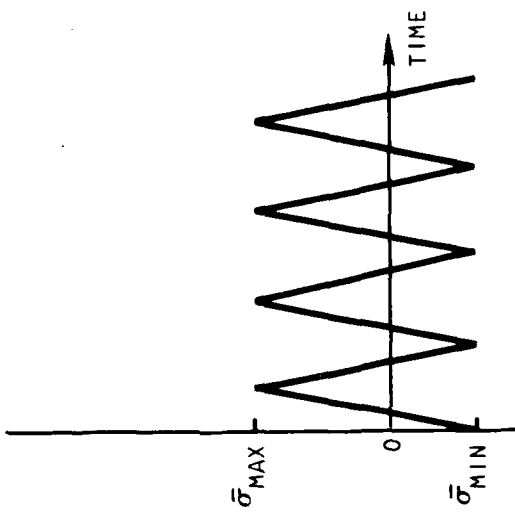
$$\bar{R} = \frac{\bar{\sigma}_{\text{min}}}{\bar{\sigma}_{\text{max}}} = \frac{g(x)\sigma_{\infty \text{min}} + \sigma_{\text{res}}(x)}{g(x)\sigma_{\infty \text{max}} + \sigma_{\text{res}}(x)} \quad (8)$$

where $\sigma_{\infty \text{max}}$ and $\sigma_{\infty \text{min}}$ are the maximum and minimum cyclic stresses remotely applied to the structure.

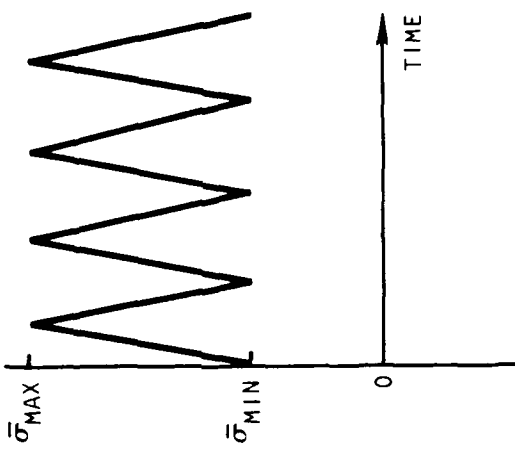
The modification of the stress intensity factor and the stress ratio to account for the residual stress plays the key role in the prediction of the fatigue crack growth behavior in welded structures. Figure 3 illustrates schematically the changes of the peak stress and the stress ratio values due to the existence of the compressive residual stress or the tensile residual stress. The reduction of the peak cyclic stress and stress ratio has been known as the major causative factor in the fatigue life improvement of cold-worked fastener holes (references 5, 9). The detrimental effect of the tensile residual stress to the crack growth has been observed by other investigators (reference 10).



(A)
REMOVEDLY APPLIED CYCLIC
SPECTRUM



(B)
"EFFECTIVE" SPECTRUM WITH
COMPRESSIVE RESIDUAL STRESS



(C)
"EFFECTIVE" SPECTRUM WITH
TENSILE RESIDUAL STRESS

Figure 3. Schematic Representation of a Cyclic Spectrum

In terms of the effective stress intensity factor K and effective stress ratio R , the crack growth rate equations 1 and 2 become:

$$\frac{da}{dn} = C \left[\frac{\Delta \bar{K}}{(1-\bar{R})^{1-m}} \right]^n, \bar{R} \geq 0 \quad (9)$$

$$\frac{da}{dn} = C \left[(1-\bar{R})^q \bar{K}_{\max} \right]^n, \bar{R} < 0 \quad (10)$$

Notice that, if the residual stress vanishes, the foregoing rate equations will resume their original form.

The existing crack growth computer program EFFGRO was modified to adopt the crack growth rate equations 9 and 10 for analytical predictions of the surface crack growth behavior in the welded structure.

CRACK GROWTH PREDICTION AND TEST DATA CORRELATION

Crack growth analytical predictions were performed by employing the modified version of EFFGRO which accounts for the effects of residual stresses. The inputs to the computer program are (1) the material's crack growth rate constants and its fracture properties, (2) the initial crack configuration and sizes, (3) the geometry of the cracked section, (4) the applied stress spectrum and the limit stress level, (5) the stress gradient, and (6) the residual stress distribution.

As described previously, the crack was determined to originate from the inner surface of a weld runout hole to grow through the thickness of the sideplate of the spindle support fitting as illustrated in figure 2. The key data were:

Thickness (t) = 1.07 inches

Width (w) = 8 inches

Crack depth (a) = 0.02 inch

Crack length ($2c$) = 0.06 inch

Elliptical shape normalizing factor (Φ) = 1.325

The crack growth rate constants of the HP 9Ni-4Co-.2C steel employed in the predictions are as shown in figure 4. The growth rate data were generated from the compact type (CT) specimens under constant amplitude loading. The

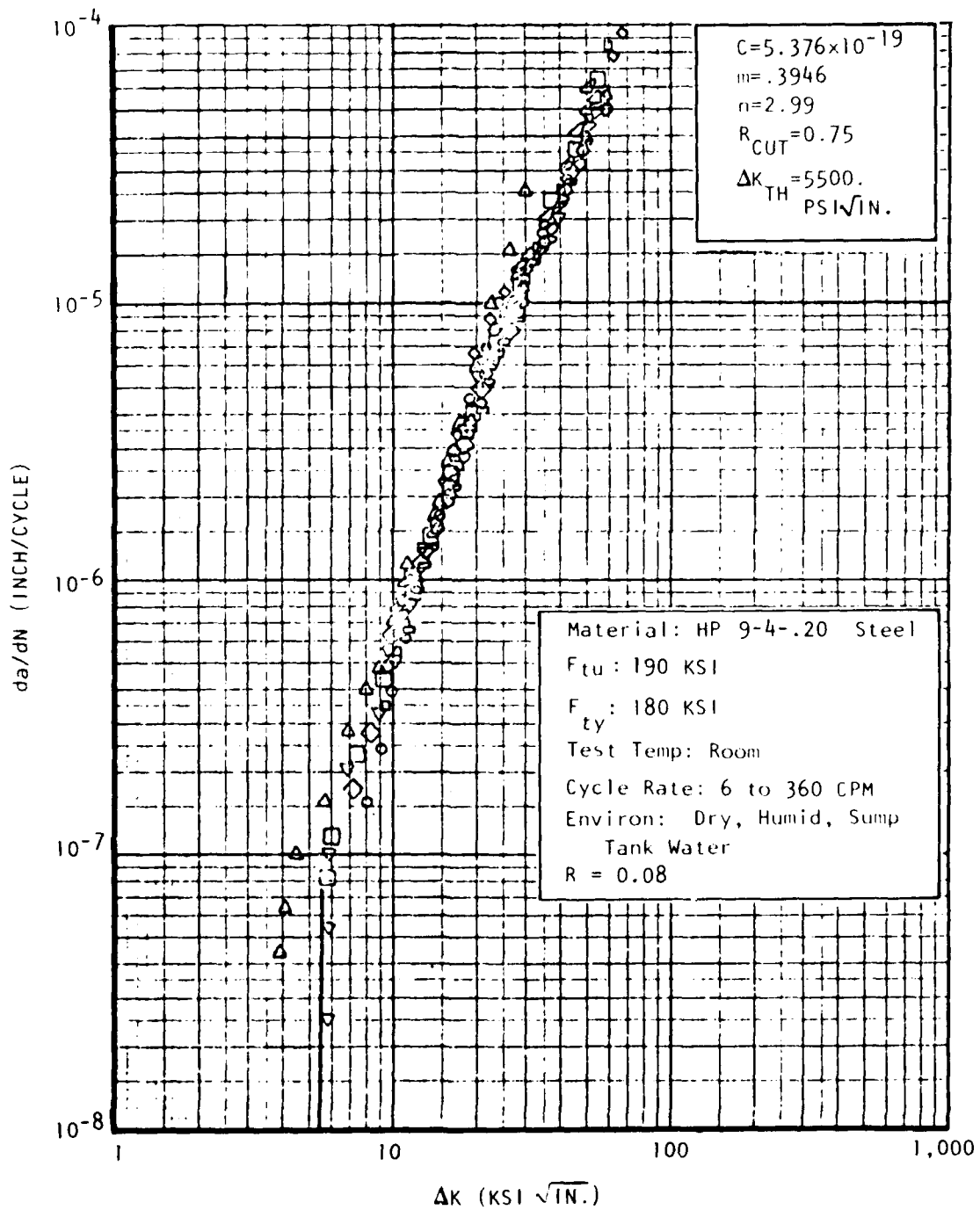


Figure 4. Material Properties, HP 9Ni-4Co-.2c Steel

fracture toughness and other material properties inputed in the computer program were:

$$\text{Plane strain toughness } (K_{IC}) = 165 \text{ ksi } \sqrt{\text{in.}}$$

$$\text{Plane stress toughness } (K_C) = 230 \text{ ksi } \sqrt{\text{in.}}$$

$$\text{Yield strength } (\sigma_{ys}) = 180 \text{ ksi}$$

The fatigue spectrum applied on the test article was the horizontal stabilizer spindle support spectrum in flight-by-flight format. Figure 5 shows the CRT spectrum chart of the test spectrum. Each flight of the spectrum contains 138 load steps and 259 cycles. The maximum nominal spectrum stress was 68 ksi, which applied once every 100 flights. The test flight spectrum was utilized in the analytical crack growth predictions.

The stress gradient across the thickness of the sideplate was determined through the known solutions of the static stress analysis. For a given crack size $a(x)$ measured from the surface as indicated in figure 2, the corresponding stress gradient $g(x)$ employed in the analytical prediction were:

<u>a(x), inch</u>	<u>g(x)</u>
0.0	1.50
0.1	1.32
0.2	1.23
0.3	1.18
0.5	1.14
1.07	1.30

The residual stress distribution across the thickness of the uncracked sideplate containing the double U-groove weld joint was best estimated from the X ray diffraction measurements as:

<u>a(x), inch</u>	<u>$\sigma_{res}(x)$, ksi</u>
0	-20
0.25	+40
0.5	-20
0.75	+40
1.07	-20

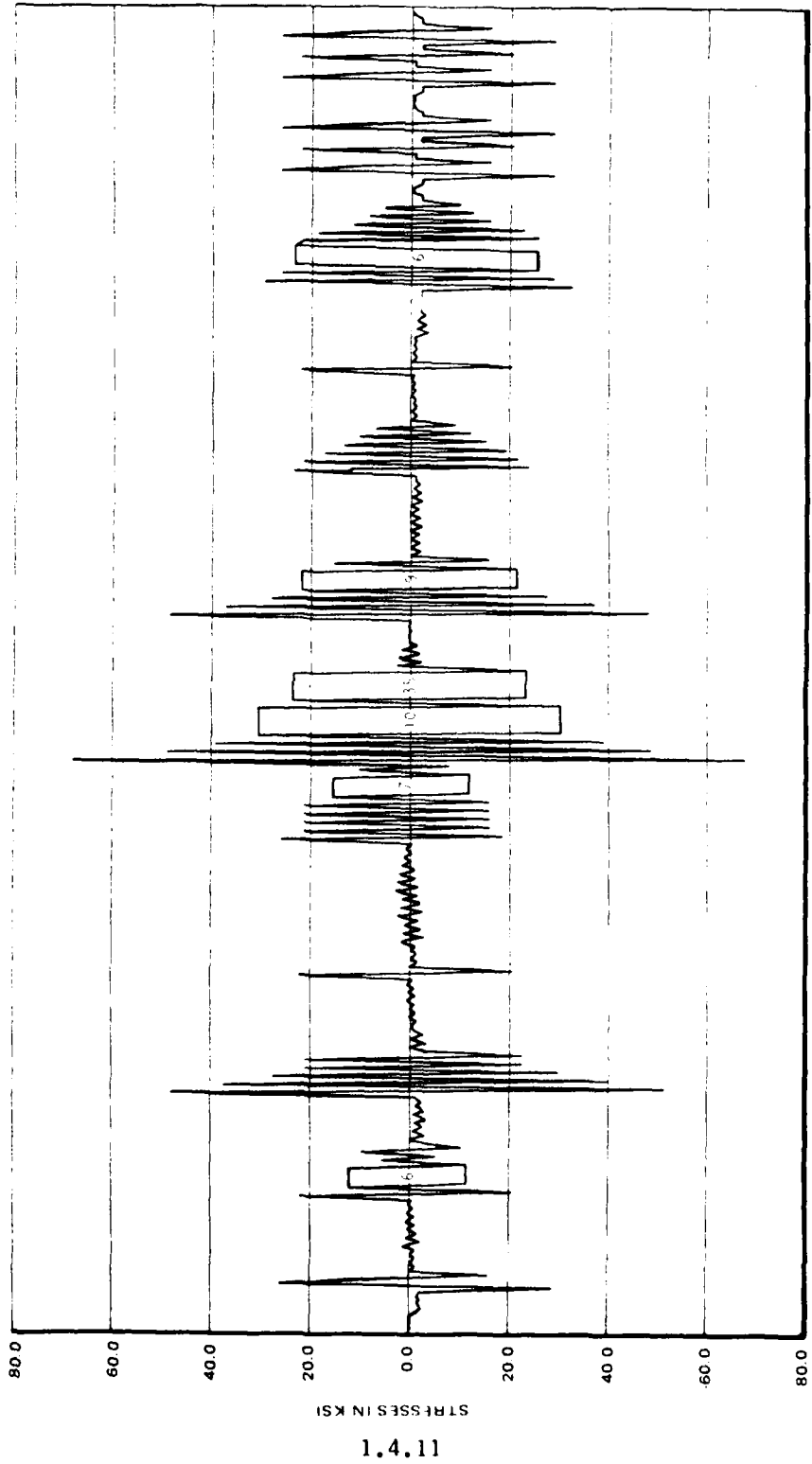


Figure 5. Stress Spectrum Chart, Spindle Support Fitting, one Flight

Several computer runs were made based on different assumptions on the effectiveness of the residual stress in conjunction with the preceding inputs. The first run was based on the assumption that the residual stress did not have any effect on the fatigue crack growth behavior. It implies that the applied cyclic stresses were the only driving force to the crack growth. The result of the analytical prediction was plotted in figure 6. The test data (reference 11) obtained from the fractographic analysis were also plotted for comparison. Based on the predicted result as shown in the figure, it would take 2,120 flights to grow the surface crack with an initial size $a_i = 0.02$ to its critical size. Compared to the test data, the prediction was off by a factor of 2. From this exercise, it was concluded that the residual stress did affect the crack growth behavior.

The second computer run was made by assuming that the estimated residual stress was 100 percent effective. Figure 7 shows the predicted crack growth behavior compared to the test data, it indicates the prediction was still off by a large percentage.

The subsequent computer runs were made based on the assumptions that the residual stress was relaxed under fatigue loading and also was redistributed as the crack propagating through the residual stress region. Limited research reports and technical papers have suggested the relaxation and redistribution of the residual stress when the crack is subjected to fatigue loading (references 12,13,14). However, there is no reliable analytical model available to determine the amount of relaxation and the redistribution pattern. Furthermore, it is very difficult, if not impossible, to measure the residual stress distribution with a crack propagating through the region. Thus, various residual stress distribution patterns which accounted for the relaxation and redistribution effects were assumed and inputted in the computer program. Figure 8 shows two residual stress distribution patterns where good correlations were obtained. The solid line in the figure represents the best analytical prediction.

CONCLUDING REMARKS

A case study of employing the state-of-the-art linear elastic fracture mechanics technology to correlate the fatigue crack growth behavior in a cracked aircraft structure has been presented. From the results of this study, the following were concluded:

1. The use of fracture mechanics provides a valuable tool for the understanding of the fatigue crack growth behavior in a welded aircraft structure.
2. Residual stresses play a very important role in the crack growth of the welded structure. Compressive residual stresses slow down the

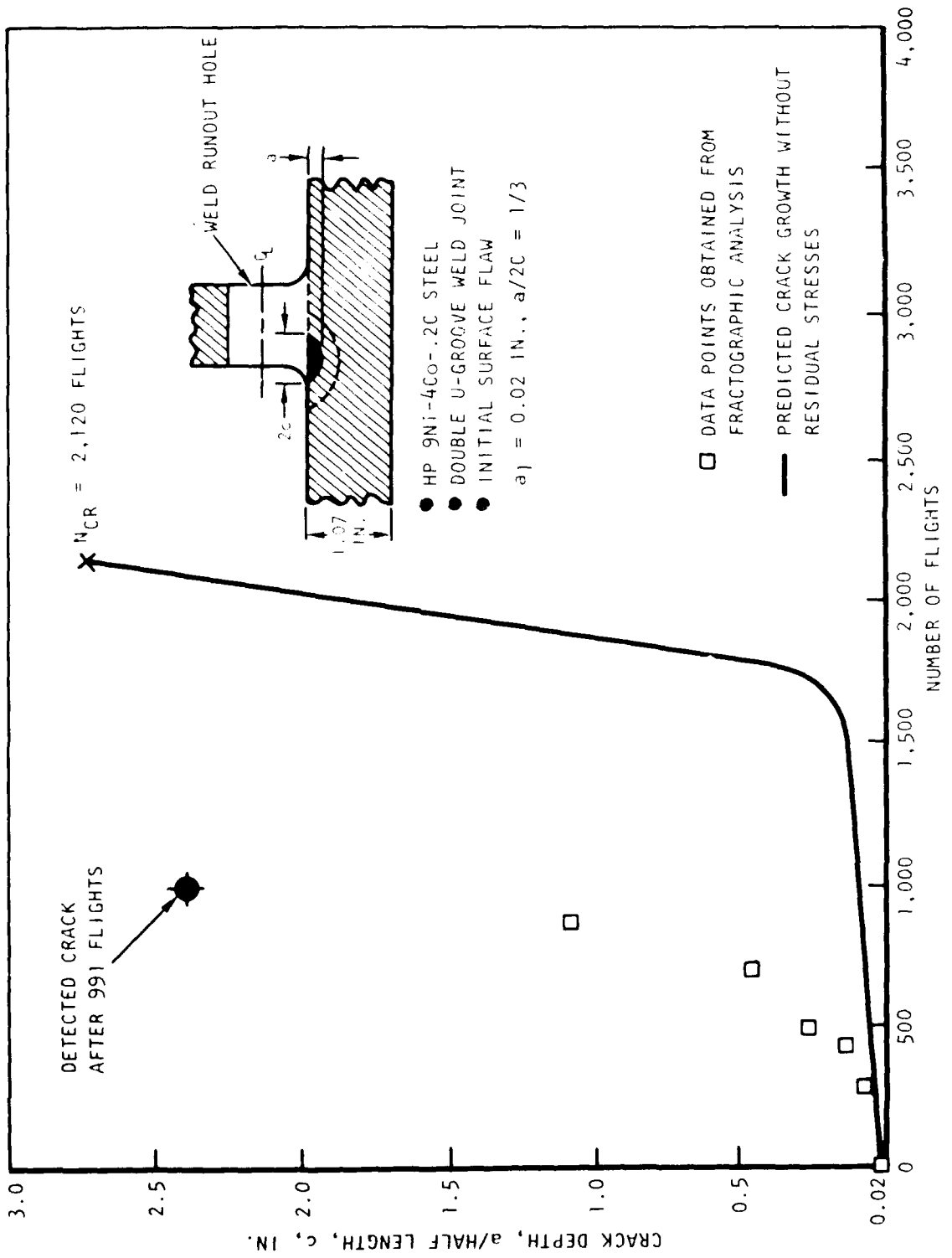


Figure 6. Test Data/Predicted Crack Growth Correlation, No Residual Stresses Assumed in Analysis

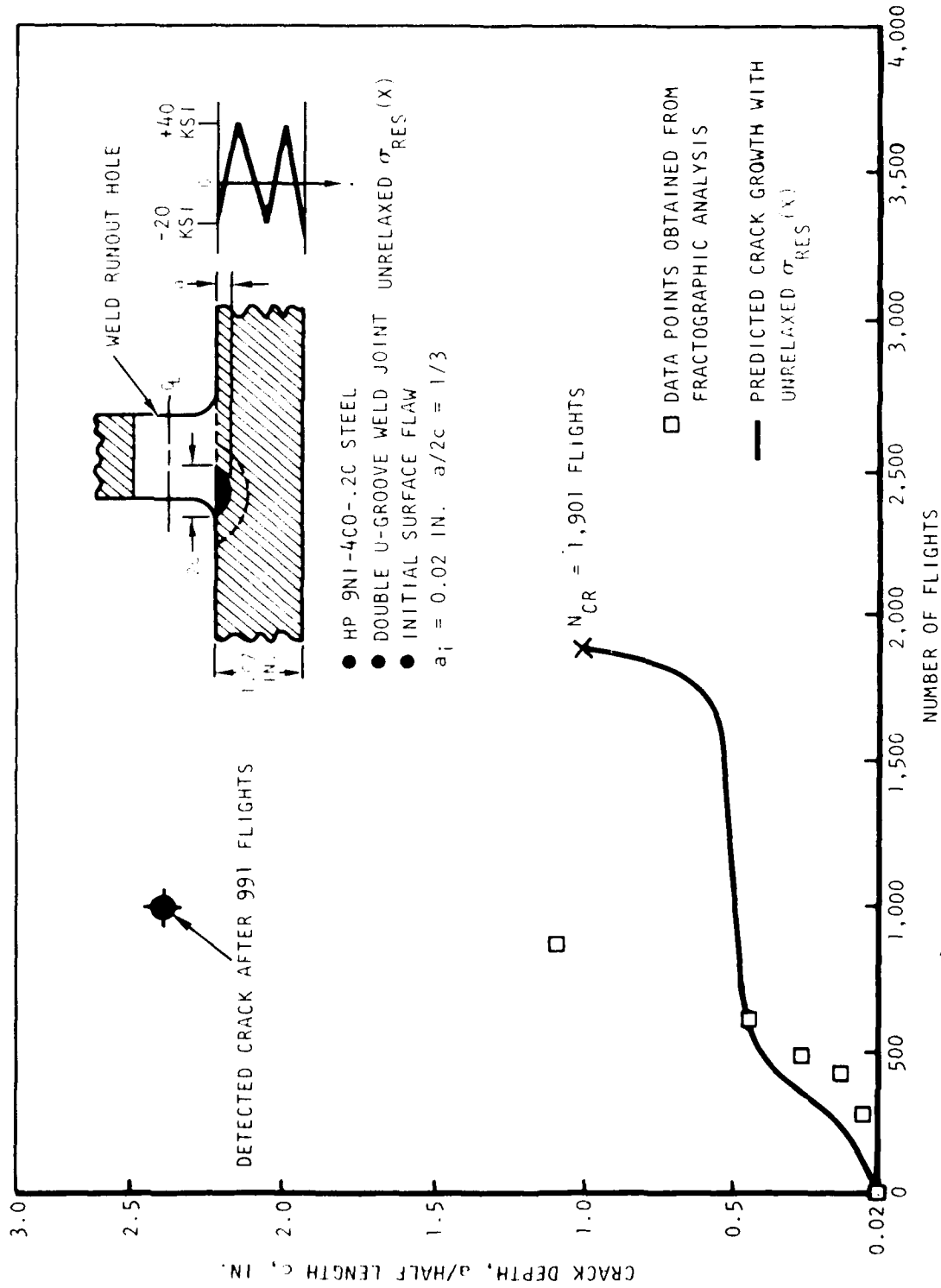


Figure 7. Test Data Predicted Crack Growth Correlation, Unrelaxed Residual Stresses Assumed in Analysis

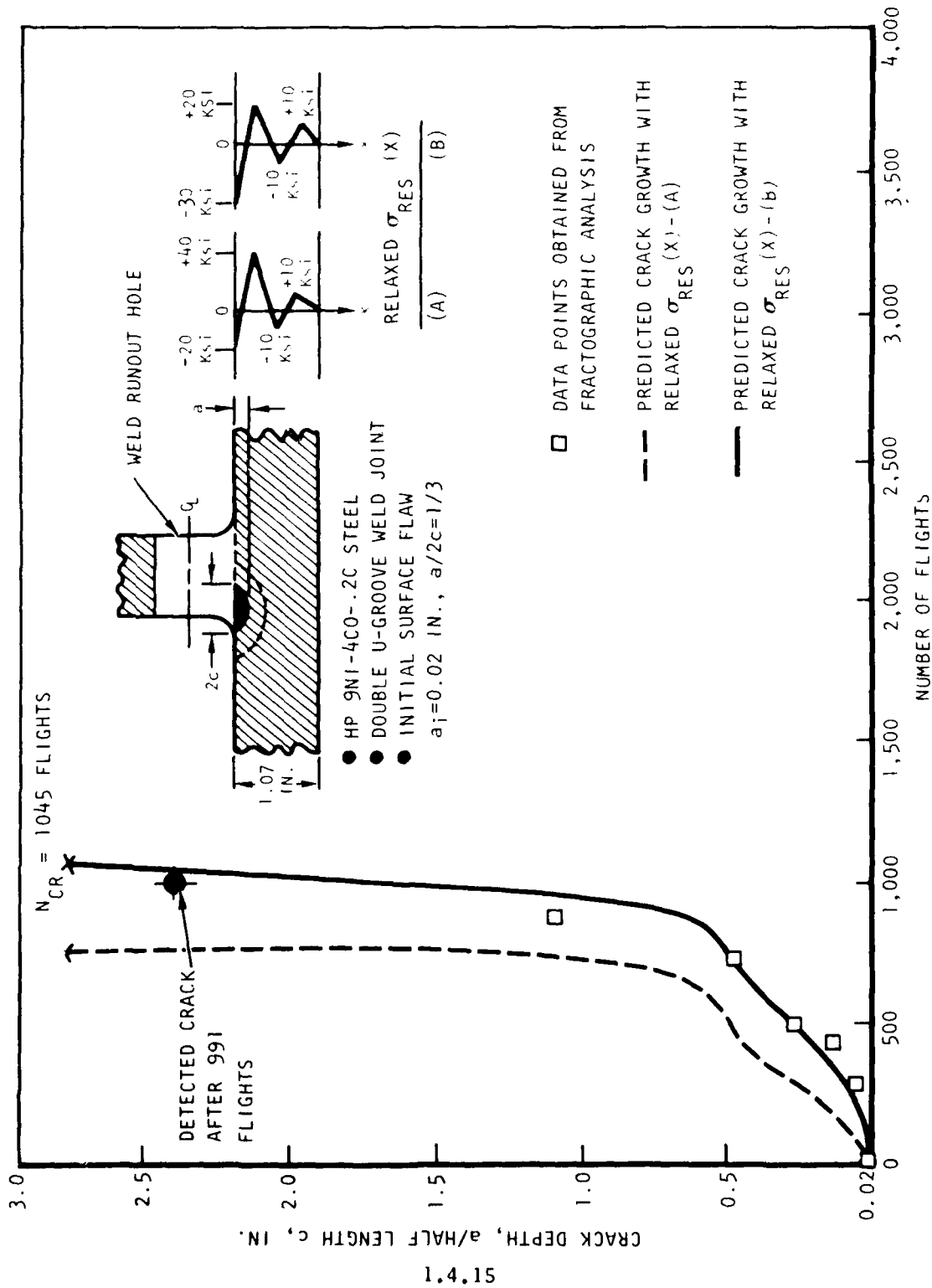


Figure 9. Test Data/Predicted Crack Growth Correlation, Released and Redistributed Residual Stresses Assumed in Analysis

crack growth, while tensile residual stresses speed up the crack growth rate.

5. Residual stresses could be relaxed under cyclic loading and could be redistributed when the crack propagates through the region. The amount of relaxation and the redistribution pattern of the residual stress should be accounted for in the analytical prediction. Further research in this area is urged.

REFERENCES

1. Szamosi, M., "Crack Propagation Analysis by Vroman's Model, Computer Analysis Summary, Program EFFGRO," NA-72-94, Rockwell International, B-1 Division, 1972.
2. Paris, P. C., Gomez, M. P., and Anderson, W. E., "A Rational Analytical Theory of Fatigue," The Trend in Engineering, Vol 13, No. 1, University of Washington, January 1961.
3. Walker, K., "The Effect of Stress Ratio During Crack Propagation and Fatigue for 2024-T3 and 7075 T6 Aluminum," ASIM STP 462, American Society for Testing and Materials, 1970.
4. Chang, J. B., "Development of Fatigue Crack Growth Model for Flight Spectra Containing Compressive Load Cycles," NA-76-858, Rockwell International, B-1 Division, 1977.
5. Chang, J. B., "Analytical Prediction of Fatigue Crack Growth at Cold-worked Fastener Holes," AIAA paper No. 75-805; presented at AIAA/ASME/SAE 16th Structures, Structural Dynamics, and Materials Conference; Denver, Colorado, May 27-29, 1975.
6. Kobayashi, A. S., and Moss, W. L., "Stress Intensity Magnification Factor for Surface-Flawed Tension Plate and Notched Round Tension Bar," Proceedings of the Second International Conference on Fracture, Brighton, England, 1969.
7. Shah, R. C., and Kobayashi, A. S., "On the Surface Flaw Problem," The Surface Crack: Physical Problem and Computational Solutions, American Society of Mechanical Engineers, New York, 1972.
8. Tada, H., The Stress Analysis of Cracks Handbook, Del Research Corporation, Hellertown, Pennsylvania, 1973.

9. Speakman, E. R., "Fatigue Life Improvement Through Coining Method," presented at the 72nd Annual Meeting, ASIM, Atlantic City, New Jersey, 22-27 June 1969.
10. Elber, W., "Effect of Shot Peening Residual Stresses on the Fracture and Crack-Growth Properties of D6AC Steel," ASIM SIP 559, American Society for Testing and Materials, 1974.
11. Young, J. D., and Kumar, A., "Failure Analysis of BW1-2 Aft Fuselage Horizontal Vertical Stabilizer Support Fitting Crack at R/H Weld Relief Hole," RFD-76-1086, Rockwell International, B-1 Division, April 1977.
12. Morrow, T., Ross, A. S., and Sinclair, G. M., "Relaxation of Residual Stresses Due to Fatigue Loading," SAE Transaction, Society of Automotive Engineers, Vol G8, pp 40-48.
13. Seppi, F. L., "Relief of Shot-Peened Compressive Layer by Fatigue Loading," Proceedings of a Work Shop on Nondestructive Evaluation of Residual Stress, NTIAC-76-2.
14. Underwood, T. H., Pook, L. P., and Sharples, T. K., "Fatigue Crack Propagation Through a Measured Residual Stress Field in Alloy Steels," Presented at the 10th National Fracture Mechanics Symposium, Sponsored by American Society for Testing and Materials, Philadelphia, Pennsylvania, 1976.

THE APPLICATION OF FRACTURE MECHANICS TO DECISIONS ON
STRUCTURAL MODIFICATIONS OF EXISTING AIRCRAFT FLEETS

John F. McCarthy, Jr.
Professor and Director, Center for Space Research, MIT
Cambridge, MA 02139

Charles F. Tiffany
Technical Advisor to the Deputy for Engineering
USAF Aeronautical Systems Division (ASD/EN)
Wright-Patterson Air Force Base, OH 45433

Oscar Orringer
Associate Director, Aeroelastic and Structures Research Laboratory, MIT
Cambridge, MA 02139

INTRODUCTION

The U.S. Air Force is currently in a transition period with respect to the philosophy of airframe structural integrity. New guidelines based on fracture mechanics [1] are being applied to design, test and force management of aircraft now under development. These criteria were developed as a result of service experience with older aircraft, which were designed for fatigue by Palmgren-Miner damage summation [2,3] based on material data from experiments which determined the number of cycles to failure in carefully prepared test specimens.

Early designs for jet aircraft, such as the B-47 (on the drawing boards in the 1940's), the commercial 707, and the original B-52 (manufactured from 1955 to 1962) did not even have a full-scale fatigue test to verify the analysis.* Full-scale fatigue testing subsequently became a standard procurement requirement (without a life guarantee) for Air Force aircraft. These tests often disclosed short-life structural details which had been qualified by calculation and/or laboratory tests, but which had to be redesigned to achieve reasonable life in the airframe. However, further surprises occurred in service. For example, the F-111 fleet had details redesigned on the basis of early failures in the full-scale fatigue test, and subsequent fatigue testing was conducted to greater than 40,000 cyclic test hours. In spite of these precautions, an F-111 was lost in 1969 on a training mission from Nellis AFB, Nevada due to catastrophic fracture in the wing with only 105 flight hours accumulated. The C-5A was the first Air Force aircraft to have a contractual life guarantee (full-scale fatigue test to four service lives), but the airframe experienced general cracking at about one half of a simulated lifetime. (At this point in time, the fleet had already accumulated a substantial number of flight hours.)

* In the case of the B-52, a full-scale fatigue test was added to the program after several aircraft were lost during low-level penetration training, a mission which had not been specified in the original operational concept.

Intensive structural reviews of the F-111 [4] and C-5A [5] brought to light the importance of damage-tolerance (the resistance of the airframe to propagation of flaws already present when the airplane enters service) as a subject distinct from resistance to crack-initiation. The philosophy of assuming the presence of initial damage was subsequently embodied in the Air Force structural integrity criteria [1], and has since been applied in retrospect to other existing fleets which have experienced cracking in service and/or which are planned to be flown beyond the original operational safety limit estimates [6-18]. Damage-tolerance assessments of older aircraft continue to be required as fatigue-cracking problems develop in these fleets, particularly in view of today's policy of extending the fleet service life when cost effective compared with new equipment buys.

Interpretations of the Air Force MIL-A-83444 damage-tolerance requirements have been published elsewhere [19]. The purpose of this paper is to highlight unknown factors in the technical analyses of older aircraft fleets, factors which result from the complexity of the systems, physical processes and analytical requirements. Recommendations for management to protect the structural integrity of the force must take these factors into account. In the body of this paper, several aircraft case histories are cited to illustrate the complexities associated with four major areas which strongly influence structural integrity assessment and decision making, viz: risk analysis, inspection intervals and techniques, definition of load histories, and ground testing.

LIMITATIONS OF RISK ANALYSIS

Risk analyses are made when fleet service experience indicates that structural integrity might be in question. Some examples were alluded to in the introduction. Fracture risk analyses involve integration of empirical crack growth-rate (da/dn) equations over the estimated typical service history of the aircraft, and beyond, to project the probable range of crack sizes which may exist in the fleet at future times.

However, even under the assumptions that enough growth-rate data in the proper chemical environments are available for good empirical da/dn fits, and that both past and projected aircraft load histories are well defined (we return to this point later), future crack-size distributions can be estimated only to the confidence with which the initial crack-size distribution is known. In some cases, e.g. risk analysis of the F-111 following the Nellis accident [20], no specific data for the fleet were available and the analysis had to be based upon general data. In other cases, there have been opportunities to obtain fleet-specific estimates by teardown inspection of critical parts from one or a few airframes. A teardown inspection is costly, time consuming, and may result in loss of the airframe for future service. Each critical part must be removed from the structure, cleaned and etched, and subjected to low-power optical microscopy to identify the current size and shape of each crack. From several dozen to several hundred of these cracks are selected for scanning electron microscope (SEM) fractography. SEM striation counts are then correlated with da/dn calculations to "retrograde" the crack. The striation count is usually lost close to the true initial-flaw size, which can be estimated by

extrapolating the da/dn calculation. One is then able to construct an estimate for the initial-flaw size distribution from the entire teardown sample (with da/dn calculations alone on those cracks not studied by SEM) by using standard methods of statistical analysis. The estimation procedure appears straightforward as outlined here, but is complicated in practice by the fact that some cracks in the sample may have initiated during service [21].

In spite of the time and cost required, the gathering of fleet-specific data is vital to avoid bias of the analysis by neglect of unexpected damage modes. The tendency of cracks to cluster and the effects of steel chips during drilling of steel/aluminum stackups in the F-5 airframe may be cited as examples [14].

Figure 1 illustrates a typical reconstruction of an equivalent initial flaw size distribution based on a sample of 104 cracks found during teardown inspection of an F-4 airframe [22]. A Johnson S_u distribution [23] was fit to these data by moment matching. One may estimate from this distribution that the probability of having an initial flaw larger than 0.03 inch is 2.5×10^{-8} . Hence, one might infer that the occurrence of 0.03-inch or larger initial flaws is highly unlikely, since the product of this probability, the number of airplanes in the F-4 fleet, and the number of critical locations per airplane is less than one. The foregoing analysis is typical of the results that have been obtained for other aircraft, and similar inferences could be drawn for those fleets as well.

However, it is unwarranted and dangerous to conclude that initial cracks larger than 0.03 inch will not occur in a fleet. In reality, initial-crack distributions are bimodal. What is observed in a teardown inspection is primarily the more populous mode of "average quality" flaws caused by the routine physical processes associated with metalworking (e.g., surface scratching by drill bits). These data cannot be used to estimate occurrence probabilities for the much less populous mode of rogue flaws* which result from unintended processes. That rogue flaws do occur is established by occasional observations, often in the course of accident investigations. The F-111 accident at Nellis AFB mentioned in the introduction is an example. The cause of this accident was determined to be an initial flaw nearly one inch long on the surface of the lower skin of the wing carrythrough box. The flaw, shown in Fig. 2, is about 90 percent through the skin thickness; the light band surrounding the initial flaw is the region of fatigue propagation which took place during the 105-flight-hour life of this airplane.

* We have adopted the term "rogue" from the literature of deep-water sailing. Masters of small ocean-going ships must watch intently for the occasional rogue wave (larger than usual, seldom occurring) which can swamp and sink a ship running before the wind in a stormy sea. The connotations of infrequency, unusual size, and dominance as a danger are appropriate for cracks as well as waves.

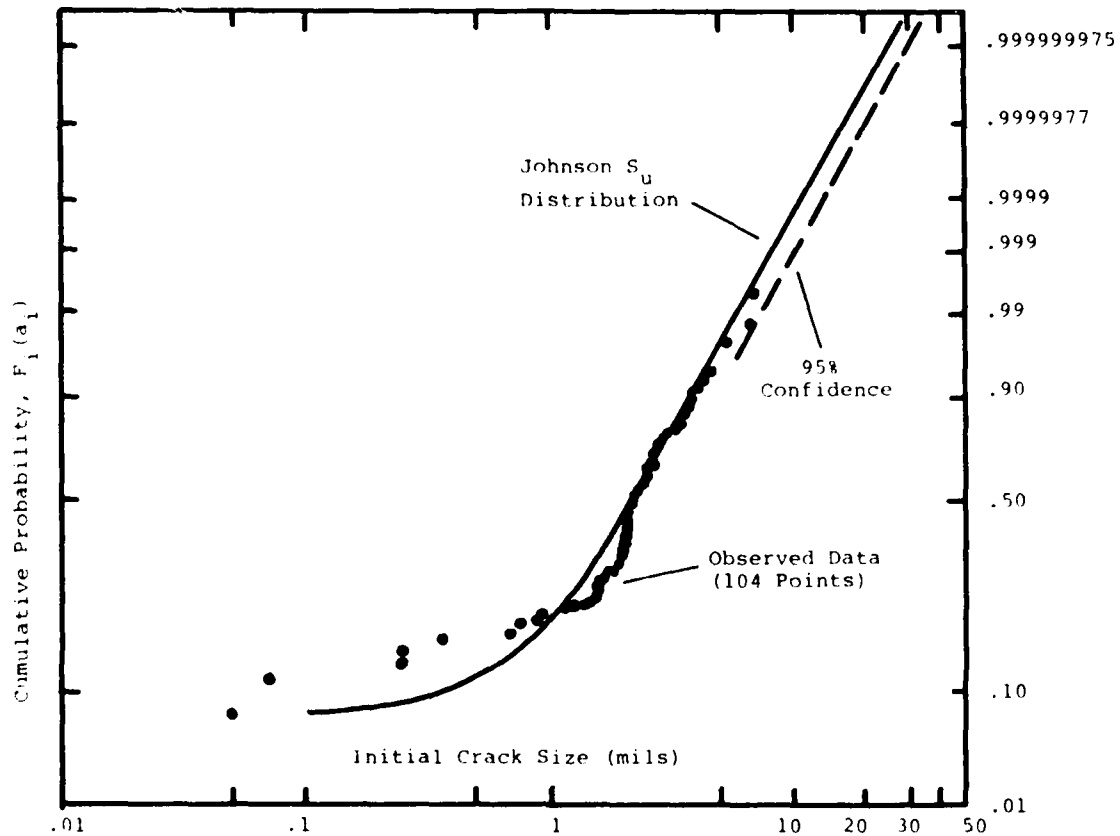


FIGURE 1. INITIAL CRACK SIZE DISTRIBUTION

The F-111 flaw is considered to be an extreme case in terms of size, but does not stand as an isolated instance. Figure 3 illustrates a case of initial tool damage (about 0.03 inch deep) near the wing root fillet of an F-5 which suffered wing failure at about 1,000 flight hours. Figure 4 illustrates several initial flaws discovered during manufacturing inspections of other aircraft. These flaws would have been rogue cracks in service, had they escaped detection. The figure indicates the nature of several unintentional processes which caused these flaws.

Another limitation of risk analysis arises from the complexity of airframe construction details, making it difficult to preassess the true degree of fail-safety in the structure. Fail-safety is an issue primarily for the large airframes of bombers and transport aircraft, which have traditionally been designed with commercial aircraft structural safety regulations (FAR, Part 25) as guidelines. A perspective view of part of the C-5A structure (Fig. 5) illustrates the complexity of large airframes which conform to FAR



FIGURE 2. ROGUE INITIAL CRACK IN F-111

F-5A WING FAILURE

(WILLIAMS AFB, APRIL 1970)

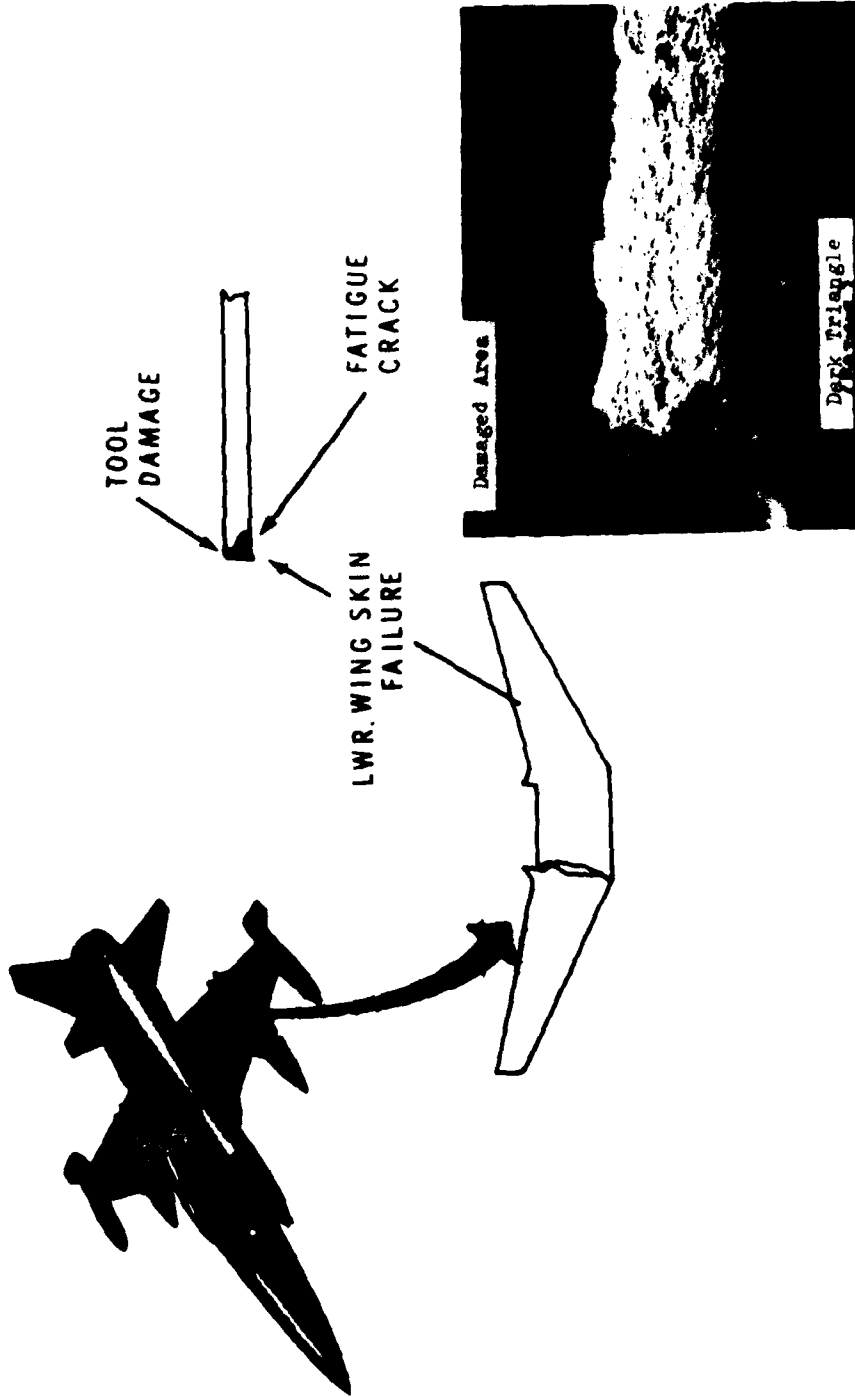


FIGURE 3. TOOL DAMAGE WHICH CAUSED F-5 LOSS

MANUFACTURING FLAWS:



FASTENER HOLE BURR TEARS



**SEVERE DRILLING DEFECTS
PLUS INSTALLATION DAMAGE**



**MISALIGNMENT &
INSTALLATION DAMAGE**



**MISALIGNMENT &
INSTALLATION DAMAGE**

FIGURE 4. TYPICAL INITIAL MANUFACTURING FLAWS

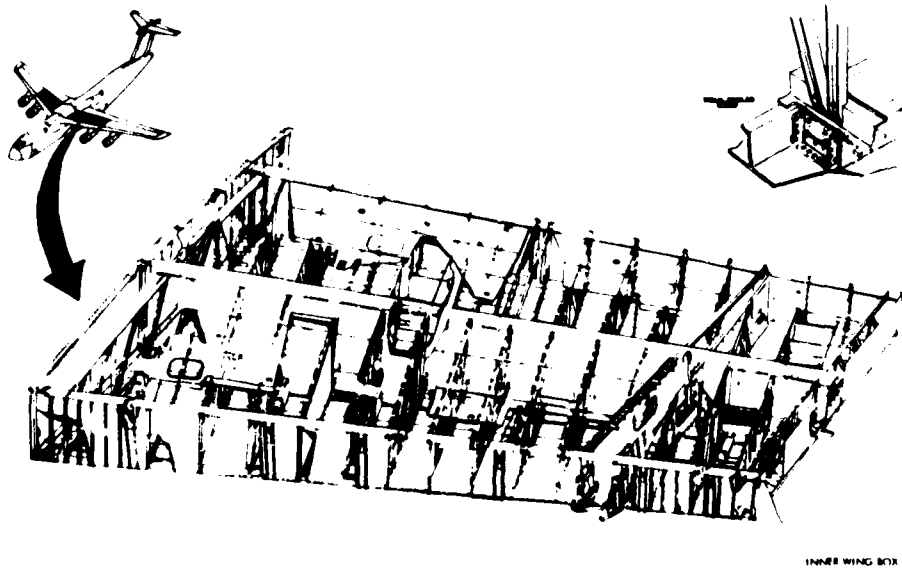
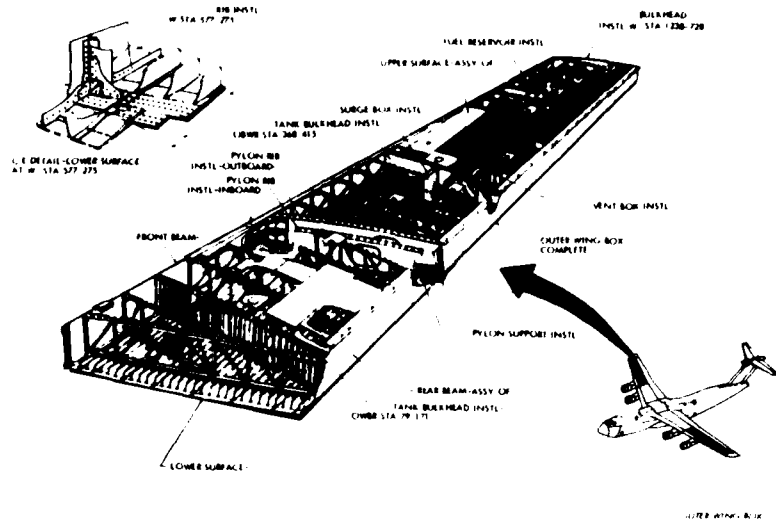


FIGURE 5. C-5A INNER AND OUTER WING BOXES

Part 25. Fail-safety in these multi-panel wing structures has traditionally been assessed by calculating the residual strength capability of the wing, assuming complete chordwise failure in one panel.

Two additional assumptions are made implicitly: that the adjacent panels are undamaged at the time of the failure, and that the cracked panel will be discovered and replaced before the airplane experiences a high load. The average quality metalwork inevitably associated with production lines makes the first assumption unconservative. Current assessments of transport fleets now assume that "average quality" initial flaws (Fig. 1) occur in all panels and that one rogue flaw can occur in any single panel. Also, rogue flaws could occur in two adjacent panels in a ship-lap type design where both panels contain common fastener holes, any one of which may have been damaged during the assembly drilling and reaming operation. A time to loss of fail-safety is established by estimating the flight hours required to grow the average-quality cracks to a size which would result in immediate fracture due to the overload caused by failure of the first panel (or two panels in the case of the common rogue flaw in ship-lap designs) [10,18].

The second assumption that the cracked panel will be discovered and replaced is also unconservative, but is less amenable to quantitative analysis. Although first-panel failures in wet-bay wing structure are likely to be seen by the escape of fuel, the bays near and inboard of the fuselage are usually dry and often difficult to inspect. Hence, there are concerns with respect to the transport fleets that a single dry-bay panel failure could go undetected until the airplane experiences a high load, or that a buildup of such failures could degrade the fail-safety of the wing below the expected once-per-flight load. Acoustic sensor detectors are now under development to reduce this risk.

In the final analysis, fail-safety is never completely proved until a part has failed in service without causing the loss of the airplane. Failures of single KC-135 wing skin panels on a number of different airplanes during flight operations over the past 20 years have illustrated in-flight fail safety. Also, a number of wing-attach-lug failures on the F-4 without loss of the aircraft have illustrated in-flight fail-safety. However, in 1973 an F-4 accident at Nellis AFB was caused by a lug failure which went undetected. Within six flights the adjacent lug failed, causing the loss of the wing and the aircraft (see Fig. 6). This further illustrates the point that a structure truly is not fail-safe unless the failed part is discovered expeditiously.

Proof testing has been proposed as an approach to the management of risk in existing aircraft fleets. However, it is generally not preferred, except as a last resort when there is an imperative strategic reason to keep the force flying. Proof testing is most effective for steel structure, in which cracks can be triggered during a ground test by applying low temperature and limit load. This procedure takes advantage of the smaller critical crack size due to reduced fracture toughness at low temperature. Proof testing is less effective for aluminum structure, and in fact must be supplemented by post-test flight restrictions to increase the critical crack size in

F-4 FAILURE

(NELLIS AFB, JAN 1973)

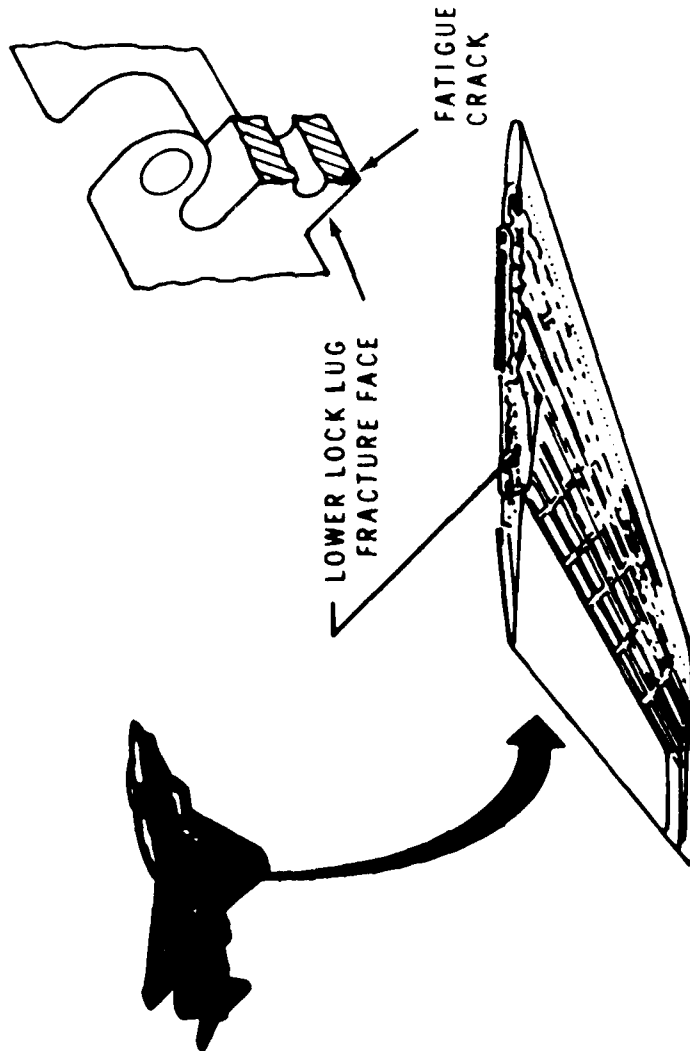


FIGURE 6. FAILURE OF F-4 WING LUG

service*. The F-111 fleet now undergoes periodic low-temperature proof testing [24]. The aluminum wings of the B-52D fleet were proof tested when fleet inspections indicated a high degree of fatigue cracking. In this case, the SAC peacetime mission requirements could be met with payload/flight restrictions sufficient to buy a reasonable time interval until a major modification could be accomplished. The complexity of proof testing is well illustrated by the B-52D test fixture (Fig. 7).

INSPECTIONS AND INTERVALS

The approach to maintaining fleet structural integrity by inspection can be summarized as follows. The manufacturing inspection method defines a "detectable" crack size (a_{det}). Cracks larger than a_{det} are presumed to be discovered and removed from the airframe. The subsequent safe operational limit for the airplane is then defined as the time to grow a crack from a_{det} to a_{cr} , the critical size for fracture corresponding to a specified residual strength load level which is generally equal to or greater than limit load. This safety limit is determined by spectrum crack growth calculations and laboratory tests, and the inspection interval is established as a fraction of the safety limit. The application of this concept to proof test inspections is obvious (a_{det} in this case is the smaller a_{cr} associated with the low temperature and/or test loads larger than subsequent flight loads). Naturally, the inspection interval thus derived must be a reasonable number of flight hours to make economic and operational sense.

The same concept has been applied to in-service aircraft nondestructive inspection (NDI). The inspection interval is generally required to be one half the safety limit to allow two chances to find a given crack before it reaches critical size. However, additional factors also need to be considered, and these factors are often times difficult to quantify.

The rationale for the establishment of inspection intervals assumes implicitly that: (1) every critical location is checked at every inspection; (2) cracks larger than a_{det} are found (at the worst, in the second inspection); (3) inspections are performed on schedule, and; (4) the inspection procedure is benign. These assumptions are convenient for the purpose of mathematical risk analysis (e.g., Ref. 25), but are often violated in the real world.

In many of the military aircraft designed and fabricated in the 1950's and 1960's the critical crack sizes are very small (e.g., the cracks become critical before they grow out from beneath the head of the fastener) and, of course, the crack that must be detected during NDI is even smaller. These complications have generally forced the use of fastener removals and inspections of the holes using an eddy current probe.

*The only way to reduce critical crack size in the test of aluminum structure is to increase the applied load. However, the test can be performed only slightly above limit load. Otherwise, the structure will undergo general plastic yielding.



FIGURE 7. B-52D PROOF TEST

To further complicate the inspection problem, some of the larger aircraft contain numerous critical fastener holes. For example, it has been estimated that there are about 22,000 critical fastener holes in the lower surface of the C-5A wing. Likewise, there are several thousand critical holes in other aircraft such as the KC-135 and B-52D. Even some of the smaller fighter aircraft have several hundred to several thousand critical holes.

Obviously, nondestructive inspections of large numbers of fastener holes per aircraft can be extremely expensive, tedious, time consuming and subject to error. The pressures to minimize maintenance costs and impacts on operational readiness combined with the inherent technical and human limitations of the NDI procedures all contribute to concern about what crack size might actually still exist in the airframe after in-service inspection. This concern has been a significant factor in the decisions that have been made by the Air Force during the past few years to protect the safety of several types of operational aircraft (e.g., the proof testing of the F-111 and B-52D aircraft, and the major modification programs on the B-52D, KC-135 and C-5A).

In spite of the fact that there very often is no practical alternative but to rely on in-service inspections and the safe-crack-growth concept for protecting the safety of the older operational aircraft, it is important that the major uncertainties be recognized. Also, these must be taken into account when making judgments with regard to probable post-inspection crack sizes, safe-crack-growth intervals, and modification requirements.

First, it should be recognized that there is often uncertainty as to whether all critical areas in each airframe are actually inspected when they need to be. Due to incomplete fatigue testing and/or insufficient post-test teardown inspection, all critical areas may not have been identified, and due to economic and operational pressures, all identified critical areas may not be inspected as completely or as frequently as desired. The desire to reduce costs and aircraft downtime combined with the sheer monotony of inspecting thousands of uncracked holes could lead to missing the one or two important cracks that may be present. Clearly, one might conclude that the probability of missing the rogue crack is high, and that thorough inspections are jeopardized by the incentive to reduce maintenance costs and aircraft downtime.

Second, there is significant uncertainty as to what is the maximum undetectable flaw size, because of the imperfect reliability of the NDI procedures. Figure 8 (drawn to full scale) illustrates the difficulty of detecting cracks which are small but still in the rogue category. Figure 9 summarizes the results of a test in which fastener holes were inspected by eddy-current probes, after which the parts were given a teardown inspection to estimate the true crack population more closely. These results clearly demonstrate the very low reliability for detection of rogue cracks in the range 0.04 to 0.08 inch. Furthermore, detection reliability for a single inspection appears to level off at about 80 percent for very large rogue cracks. In addition, comparison of the results for single and dual inspections indicates a significant number of cases in which the same crack is missed by both inspections. One may thus postulate the existence of some cracks which are immune to eddy-current

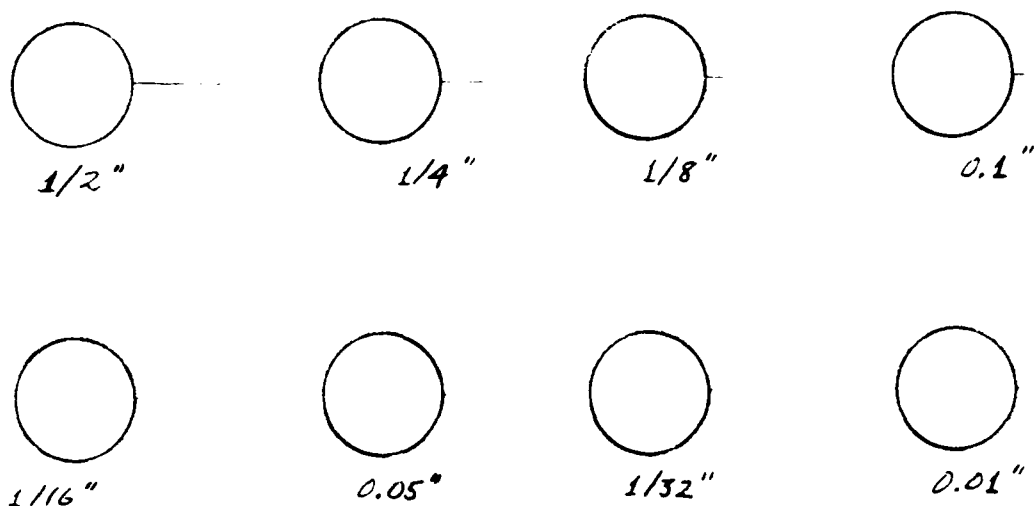


**FIGURE 8. THE CRACK DETECTION PROBLEM
(11/16 - INCH DIA. FASTENER HOLES)**

probe detection for physical reasons (cracks at faying surfaces are logical candidates). The risks of overlooking such cracks are obviously not reduced in the manner which a simple probability analysis would indicate. Efforts to improve NDI technology have tended to ignore the detectability problem by concentrating on reduction of the smallest crack size which can be detected. The real question which proponents of "improved" NDI techniques must face is, "What is the largest crack size that can be missed?"

Finally, there is uncertainty about the effectiveness of the fastener hole rework procedures and a concern about being too conservative in establishing inspection intervals where fastener removal inspections are involved. There are risks that the structure may be damaged during fastener removal, hole oversizing and fastener installation operations. Also, most areas designed with nominal edge margins will not allow more than one or two oversize operations. Thus, too-frequent inspections could lead to unnecessarily early structural replacement or retirement.

Based on the foregoing discussion, we believe it is clear that one cannot establish an inspection plan without recognizing the real-life limitations of in-service inspection, nor can one afford to be so conservative as to cause an excessively high maintenance burden, jeopardize aircraft operations, and perhaps cause early retirement of the aircraft. Truly, the formulation of a reasonable plan still remains in part in the province of engineering judgment guided by past experience.

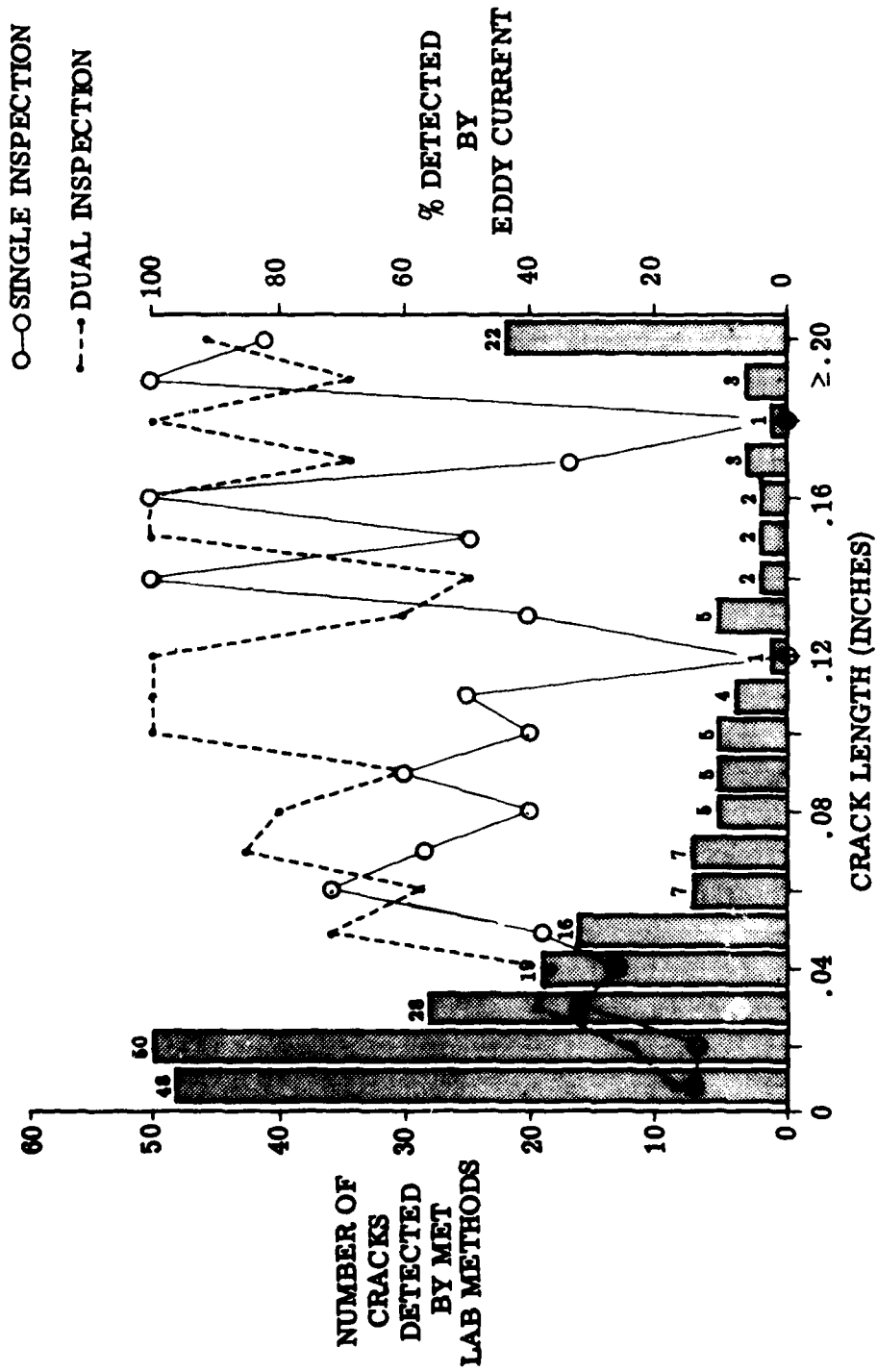


FIGURE 9. CRACK DETECTION RELIABILITY

LOAD HISTORIES

The preparation of a typical load history to represent aircraft service for the purpose of fatigue design and testing is an exacting task which requires detailed analysis of each flight segment (take-off, climb, cruise, etc.) and each mission (air/air combat, training, ferrying, etc.) which the aircraft is expected to fly [26]. This task is much more complex for military than for commercial aircraft because the latter do not have the mission variety required by combat and combat-support roles. The difference is well illustrated by comparing the boeing 747 design load mission profiles with those of the C-5A (Table I).

Table I. Design Missions for Boeing 747 and Lockheed C-5A

Mission	Duration, hr	Take-Off Load, lb	Flt. Str. Def. Mission	Take-Off Mission	Cruise Mission	Land Mission	% of Total	Total Fatigue Damage	Total Fatigue Damage
Boeing 747									
Intercontinental	11.5	1,100,000	1	60	100	1		100	
Medium-haul	4.0	1,000,000	1	40	14.4	1		40	
Short-haul	1.5	1,100,000	1	40	10.0	1		40	
Transoceanic	11.5	1,100,000	1	60	100	1		100	
Lockheed C-5A									
Intercontinental	11.5	1,100,000	1	60	100	1		100	
Medium-haul	4.0	1,000,000	1	40	14.4	1		40	
Short-haul	1.5	1,100,000	1	40	10.0	1		40	
Transoceanic	11.5	1,100,000	1	60	100	1		100	
Combat	1.0	1,100,000	1	40	10.0	1		40	
Training	1.0	1,100,000	1	40	10.0	1		40	
ferrying	1.0	1,100,000	1	40	10.0	1		40	
maintenance	1.0	1,100,000	1	40	10.0	1		40	
...									

1. The Boeing 747 and Lockheed C-5A are the only aircraft in the world that are designed to fly intercontinental routes. The Boeing 747 is the only aircraft in the world that is designed to fly intercontinental routes. The Lockheed C-5A is the only aircraft in the world that is designed to fly intercontinental routes.

Structural integrity problems not anticipated in design and test sometimes arise because of the changes in missions of a military aircraft. For example, the T-38 fleet was estimated to have an operational life limit of 15,000 flight hours of Air Training Command usage based on the results of the original full-scale fatigue test. About three years ago, a number of T-38's were assigned to the Tactical Air Command, and it was found that the limits for these aircraft are much lower (see Table II). These new estimates were based on usage data for the missions involved. The most severely used are the solo airplane flown by the Thunderbird aerobatics team and the aircraft assigned to fly the "aggressor" mission in the Dissimilar Air Combat Training Squadron. The latter

Table II. T-38 Estimated Operational Life Limits

Usage Category	Safety Limit (Flt. Hrs.)
Air Training Command	15,000
Tactical Air Command:	
Solo T-Bird	350
Diamond T-Bird	1,550
LIF	1,020
DACT	800

group is followed closely by the Lead-In Fighter Squadron, in which pilots newly assigned to TAC are given their initial training in air combat tactics.

While the T-38 TAC experience illustrates the potential effect of a major change in aircraft usage, there normally are significant usage variations within a specific force even when the aircraft is flown basically in the roles for which it was designed. This variation can only finally be determined after the aircraft has accumulated a significant amount of service experience. Table III illustrates the effects of variations in usage on the safe-crack-growth life of the F-4, where the baseline spectrum is a composite of several usages generated to represent the typical or average aircraft (i.e., it can be thought to be comparable to a design spectrum for a new aircraft).

Table III. F-4C/D Estimated Operational Life Limits

Spectrum	Safety Limit* (Flt. Hrs.)
Aircraft Structural Integrity Program Baseline	8,000
Air Combat Missions Baseline	6,800
Non-ACM Baseline	8,800
Southeast Asia	7,500
RF-4C (Southeast Asia)	10,600
RF-4C (Training)	14,400
* With recommended modifications and inspections.	

Although it is relatively easy to develop a representative operational spectrum for the older operational aircraft (assuming that there is adequate force tracking information), the problem of estimating what the design load

spectra should be beforehand is much more difficult. For example, in preparing the spectra for the Air Force's new F-16 fighter aircraft mission profiles and mission mixes were estimated by the operational command, past load-factor exceedance data from older fighter aircraft were reviewed, and estimates as to the possible increase in load-factor exceedances associated with the new "high g" inclined seats had to be made. While it is believed that the resulting spectra will be representative of the actual-force usage, this cannot be confirmed until actual operational data are obtained downstream. The Air Force Structural Integrity Program (ASIP) has the requirement that the contractor evaluate these flight data after three years of operational usage and develop new operational spectra. These data will then be compared to the originally estimated design spectra, and the aircraft life estimates and force maintenance plan will be updated accordingly. Obviously, should the flight data indicate that the usage is much more severe than originally estimated, the impacts could be significant.

Another factor that can have a significant effect on the design-loads spectra is the actual operational weight of the aircraft. Increased weight, of course, increases aircraft loads and reduces life. Thus, it is important that potential weight growth be properly assessed. An operational practice has often been overlooked in estimating fuel weights. In developing the load spectra it has sometimes been assumed that the aircraft fuel weight will be that required to perform the specific mission plus reserves. In fact, the fuel tanks are often topped off prior to every flight, thus resulting in much heavier aircraft.

For slow-crack-growth designs, where safety depends on preestablished periodic inspections, it is essential that individual aircraft be tracked, that the actual usage be compared with that assumed in the inspection-interval calculations, and that the intervals be adjusted accordingly. This precaution is particularly important for aircraft which can be subjected to a wide variation in usage. However, obtaining usage data is a difficult problem. Typically, 10 to 20 percent of each type of Air Force aircraft are equipped with multichannel recorders, which obtain sufficient flight data to allow reasonably accurate estimates of load spectra. However, the remainder of the force has much less sophisticated recording equipment. For example, fighter aircraft are generally equipped with counting accelerometers (g-counters) from which n_z exceedance data are obtained. To translate n_z exceedances into stress exceedances, which actually grow the cracks, it is necessary to make estimates of where in the sky (i.e., speed and altitude) the actual maneuver occurred and what the actual weight of the aircraft was. For example, the F-4 n_z exceedance curves (Fig. 10) indicate much less usage variation than what is found by crack-growth calculations based on stress exceedances (Table III). Obviously, such estimates are subject to errors which could lead to either overestimating or underestimating appropriate inspection intervals.

For transport aircraft (other than the C-5A which has 100 percent multichannel recorders) individual aircraft force-tracking typically has been accomplished with the use of flight logs supplemented with a limited number of Vgh or multichannel recorders. Probably the most significant data obtained

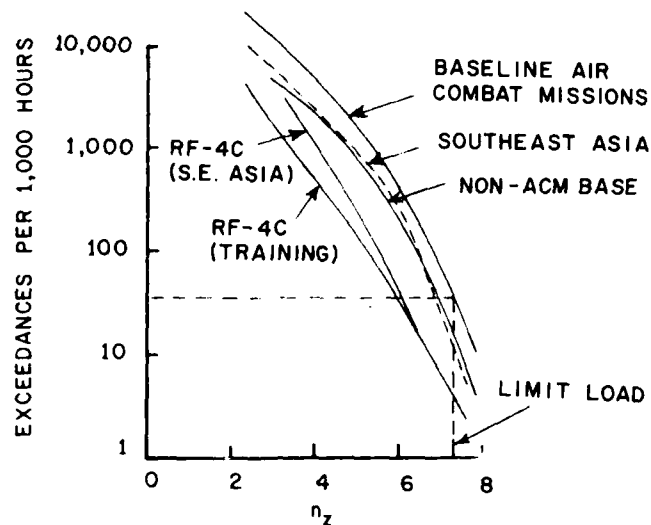


FIGURE 10. F-4C LOAD FACTOR FREQUENCY

from these logs are the reported numbers of landings which, of course, are extremely important to these types of aircraft (i.e., much of the fatigue damage is due to the ground-air-ground cycle). However, even here it has been found that there can be inaccuracies in reporting which can lead to errors in individual aircraft life estimates and inspection requirements.

Aircraft tracking has typically been plagued with equipment malfunctions and incomplete reporting, both of which result in gaps in the data thus necessitating estimation of the actual aircraft usage. Due to the increased emphasis placed on aircraft tracking as a result of new ASIP requirements, it is anticipated that many of the past problems will be substantially diminished in the future. Nevertheless, there will continue to be uncertainties requiring engineering judgments when establishing individual aircraft maintenance needs and life estimates.

Major mission changes, usage variation within the design mission profiles, and weight growth are factors which make the true safety limit of a fleet an unknown at the beginning of service. The safety limit estimate (based on design spectra) must be updated with actual usage spectra prepared from individual aircraft-tracking data gathered during service. Meanwhile, the pool of remaining safe operational hours which might be extended by modifications continues to shrink. This reduction in safe operational hours forces the fleet manager into a costly program of maintenance actions and/or major structural modifications as the only viable option by the time a structural integrity problem has been diagnosed and solutions have been assessed.

GROUND TESTING

Comprehensive ground testing is essential to assess both the economic life and flight safety of an aircraft. In particular, a full-scale fatigue test of the airframe is absolutely essential; it is impossible to analyze the fatigue performance of every potentially fatigue-critical location in time to influence the design. (Recall the complexity of the airframe, as illustrated by Fig. 5.) Also, fatigue prediction is still an expensive and inexact art, even with the aid of modern computers. Hence, the design must be progressed by estimating which will be the most critical locations in the airframe and subjecting these to analysis and prediction.

Essentially all full-scale fatigue tests have disclosed some local problem areas not previously identified by analysis. For example, the A-10 fatigue test article (Fig. 11) revealed a design deficiency in one of the fuselage wing-attachment frames (Fig. 12). The subsequent analyses showed that the loadings due to speed changes had not been properly accounted for. This location was not considered critical on the basis of the original calculations.

Figure 11 also illustrates the complexity of a full-scale fatigue test, even for a small airplane. Because of funding limitations, there is generally only one full-scale fatigue test article available for a program, and it must accommodate all mission profiles.

The aircraft manufacturer faces a basic dilemma: the detail design must be completed before full-scale fatigue test results establish that the design meets the required fatigue performance. This dilemma can be partially resolved by the use of design development tests (DDT). DDT articles are intended to represent typical structural details and to be tested in the laboratory. They are inexpensive, and they provide data quickly for design modifications, but they do not represent the structure as a whole. In recent designs an intermediate phase of design verification tests (DVT) has been added. DVT articles are full-scale representations of major portions of the airframe, and are subjected to both static and fatigue tests. The B-1 bomber provides a good example of the parallel progress of design with subcomponent and major component testing (Figs. 13 through 15).

In the case of a large complex airframe like the B-1, an iterative procedure between design and test must be followed in order to attain a reliable structural design at minimum cost. Many DDT's were tested during the early stages of the program, so that the structural designers had reliable data at their disposal. Once the design concept evolved in reasonably final form, DVT's, which are much more complex and expensive, were then tested in order to guarantee performance and to reveal design deficiencies early enough for economical modifications.

While it has been argued that full-scale fatigue testing of an aircraft should be delayed until the production configuration of the aircraft has been stabilized (and in some cases even until operational usage data has been obtained), this approach has one serious shortcoming. If major problems are



FIGURE 11. A-10 FATIGUE TEST

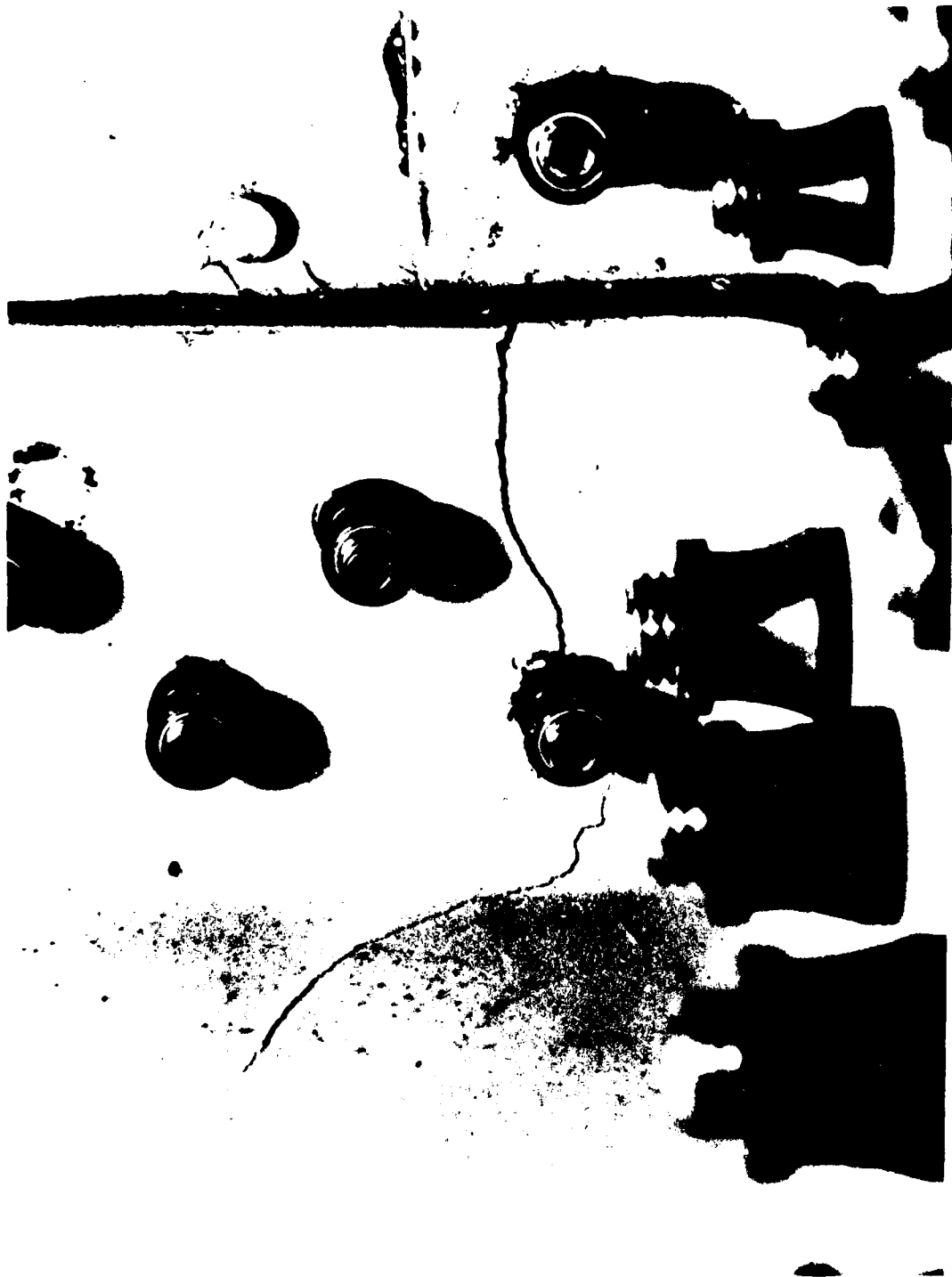
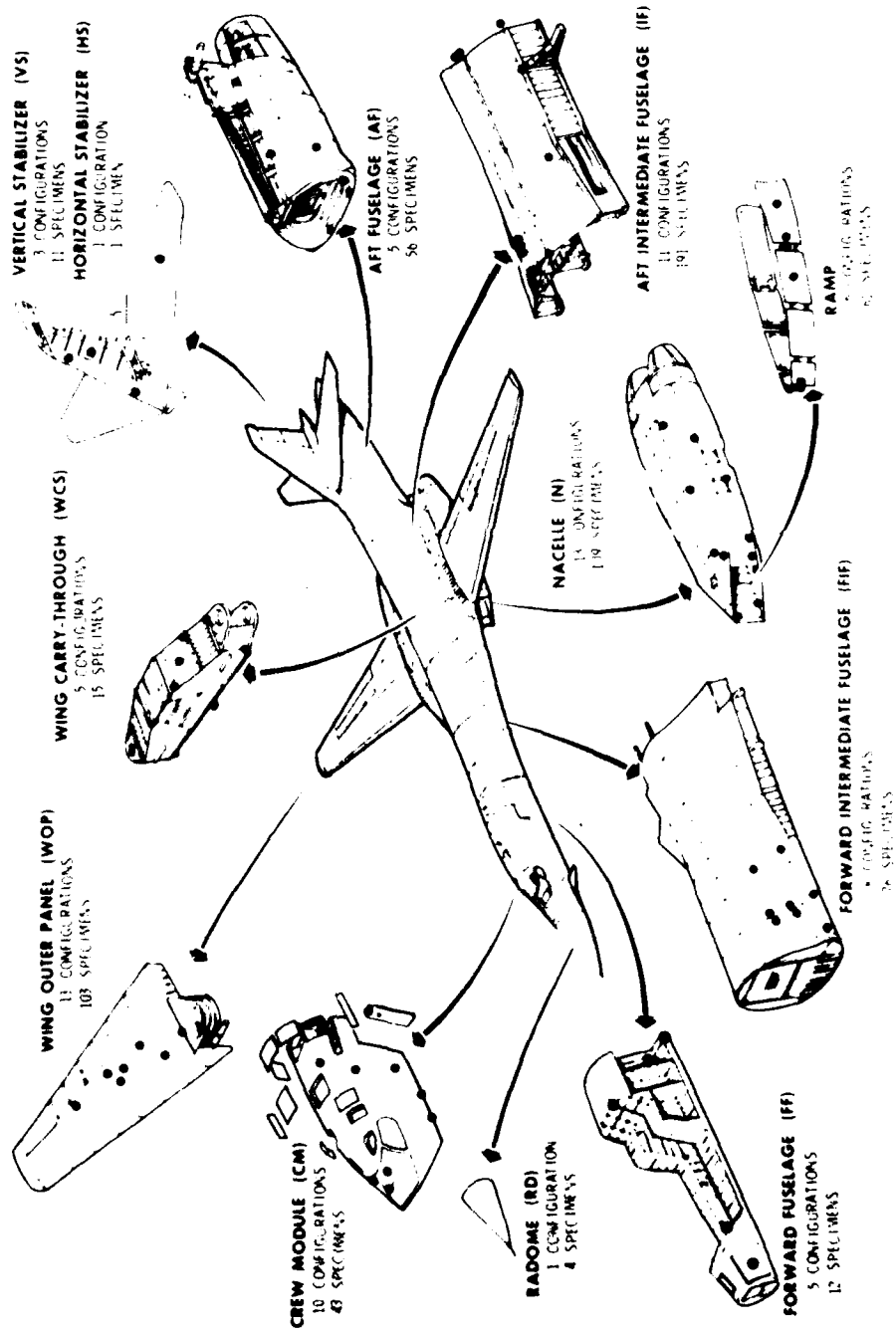


FIGURE 12. FATIGUE CRACK AT FS405

STRUCTURAL DESIGN DEVELOPMENT TEST PROGRAM

81 CONFIGURATIONS 682 SPECIMENS



NA-76-733 1-3

TS972-6191

FIGURE 13. B-1 DEVELOPMENT TEST PROGRAM

DVT-1 STATIC TEST ARTICLES

8 DEC '72 THRU 28 APR '75



AFT FUS / EMPENNAGE
30 APR 74



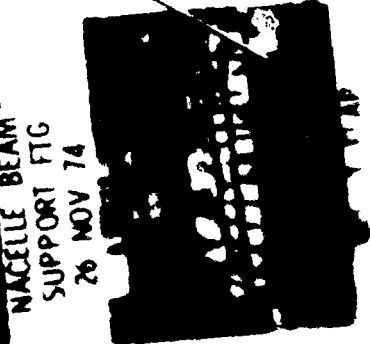
WING CARRY-THRU 28 APR 75



CREW MODULE
10 APR 75



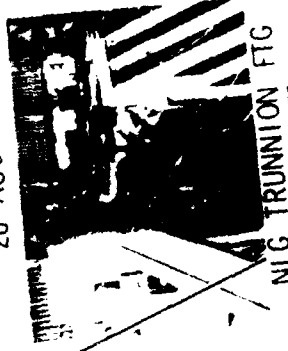
UARRSI
(REFUELING RECEPTACLE)
20 AUG 74



NACELLE BEAM
SUPPORT FTG
26 NOV 74



NO. 3 SLAT & TRACK
26 JUN 74



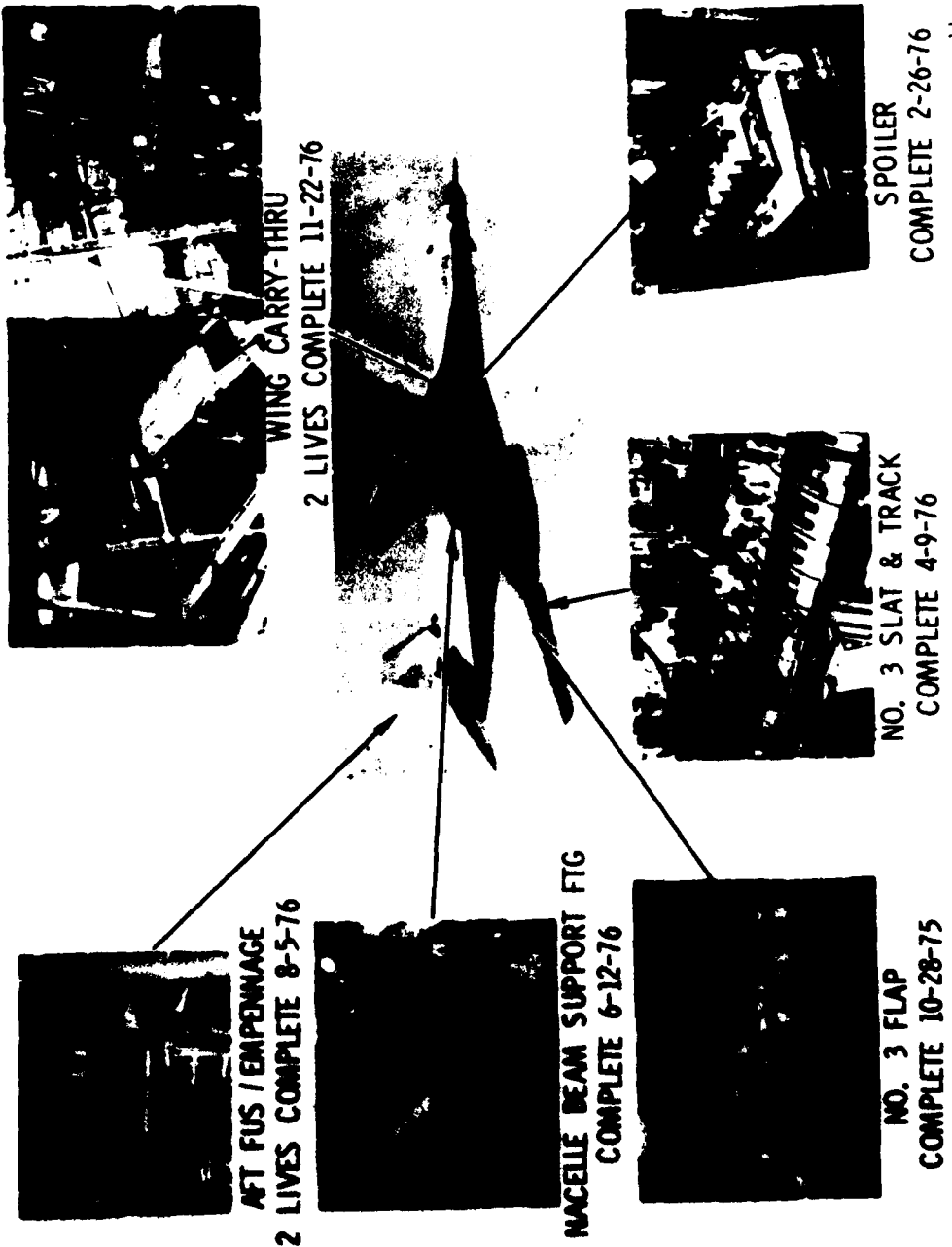
NLG TRUNNION FTG
28 AUG 73

11 16

RF 14 DVT STATIC TEST ARTICLES

100-4

DVT-2 FATIGUE TEST ARTICLES



TSP

FIGURE 15. DVT FATIGUE TEST ARTICLES

encountered during the test, as was the case for the C-5A, the Air Force is then faced with a costly retrofit program. Recognizing this shortcoming, the Air Force requirements now state that one lifetime of testing shall be completed prior to full production go-ahead (DSARC IIIB) and two lifetimes of testing (or the economic life should it occur first) shall be completed prior to first production aircraft delivery. Also, there are requirements for damage-tolerance testing of critical safety-of-flight portions of the airframe and comprehensive teardown inspection after completion of testing. Should there be major structural changes made between the development flight-test aircraft and the full-scale production aircraft, it is a requirement that these changes be subsequently fatigue tested--desirably at the full-scale component level.

CONCLUDING REMARKS

The achievement of aircraft structural integrity is a complex task which requires engineering judgments and management decisions based on estimates of what the technical data will eventually show when it is obtained. The current Air Force structural integrity requirements (as described in MIL-STD-1530A and supporting specifications) recognize much more of this complexity than did past criteria, but still cannot be treated as being inflexible. In fact, the current requirements allow a significant amount of flexibility. We have attempted to illustrate the complexity with examples from existing Air Force aircraft, and have pointed out a number of existing uncertainties which require application of judgments based on past experience. While risk and sensitivity analyses can be extremely helpful in making these judgments, they should not be treated as gospel. We briefly summarize some of the more important points here.

The rogue flaw occurs frequently enough to be an airplane-killer. Optimistic conclusions that rogues are not in the fleet, based on inspections of a few airframes, are not justified in view of the bimodal nature of initial crack size distributions.

New fleets and new methods of construction are often accompanied by unexpected damage-initiation modes. One case involving the F-5 fleet has been mentioned. Many other examples are available which illustrate their specific nature. The stress corrosion susceptibility of high strength titanium alloys in a number of different environments which were thought to be benign (e.g., methanol, freon, cleaning fluids and some propellents) was not anticipated when the alloys were first used. In the Boeing 727, joints in certain areas were both riveted and cold-bonded to improve their load-transfer characteristics and thus reduce fatigue cracking. However, the bondline attracted moisture and caused severe corrosion.

Fail-safety is usually taken as the design approach for large airframes. However, the degraded load-carrying capability after failure of one component can be an unconservative estimate of the true situation. First failures are not always caught and repaired quickly, as the analysis assumes. In addition, fail-safety will degrade with time, as cracks propagate in adjacent components.

The latter situation is further complicated by variations of fracture toughness from one component to another.

Proof tests generally have limited utility as an inspection procedure, and are thus used only as a last resort. Hence, most fleets must depend on NDI to maintain flight safety. Unfortunately, NDI may not check every critical location at every inspection, may miss cracks it is supposed to find, may not always be performed on schedule, and may be partially destructive in spite of its name.

Force damage-tolerance is always assessed in terms of estimated load spectra, which have in some cases turned out to be underestimates of usage in actual service. The lag time involved in getting actual-usage spectra, diagnosing the looming flight-safety problem, defining a "fix", and assessing its utility may in some cases approach the remaining safe-operational life of the force. This situation tends to severely limit the possible options.

Aircraft structures contain numerous complex details which are potential sources of in-service fatigue problems. Early full-scale testing is essential to disclose the critical details and avoid costly retrofits. On the other hand, many of the details may not be finalized early in the development program when the testing is needed. Thus, it may be necessary to repeat some fatigue testing when the production configuration is finalized.

The foregoing summary is not an exhaustive list of the complexities which affect airframe life and safety, but we believe it to cover the most important ones. Certainly the presence of these factors implies that the application of structural-integrity criteria to force management must be supplemented by good engineering judgments based on the specific operational characteristics, airframe design, and service problems of a particular fleet.

REFERENCES

1. Military Specification, "Airplane Damage Tolerance Requirements," MIL-A-83444 (USAF), 2 July 1974.
2. Palmgren, A., "Die Lebensdauer von Kugellager," Z.V.D.I., Vol. 68, 1924, 339-341.
3. Miner, M. A., "Cumulative Damage in Fatigue," J. Appl. Mech., Vol. 12, 1945, A159-A164.
4. Ashley, H., et al., "Report of the USAF Scientific Advisory Board Ad Hoc Committee on the F-111 on Lessons Learned from the F-111 Structural Experience," 26 October 1971.
5. Cleveland, F. A. and J. W. Lincoln, "Final Report, C-5 Independent Structural Review Team," Lockheed-Georgia Co., Marietta, GA, Report No. LG72ER0067, March 1973.

6. McCarthy, J. F., Jr., et al., "Report of the USAF Scientific Advisory Board C-5 Advisory Group," April 1973.
7. Clark, J. R., et al., "First Report of the F-4 Structures Committee," Division Advisory Group, USAF Aeronautical Systems Division (ASD/ENO), Wright-Patterson AFB, Ohio, March 1973. (Supplemental report, September 1973.)
8. Haviland, G. P., "Final Report of Ad Hoc Group Review of C/KC-135 Structural Integrity Program," USAF Aeronautical Systems Division (ASD/ENF), Wright-Patterson AFB, Ohio, 20 June 1973. (Supplemental report, 22 August 1973.)
9. McCarthy, J. F., Jr., et al., "[Report of the] B-52D/F Technical Assessment Group," Air Force Logistics Command (AFLC/OCAMA), Tinker AFB, Okla., March 1974.
10. Tiffany, C. F., "Report of the C-5 Structural Review Team," USAF Aeronautical Systems Division (ASD/ENF), Wright-Patterson AFB, Ohio, January 1975.
11. McCarthy, J. F., Jr., et al., "Report of the F-4 Structures Committee," Division Advisory Group, USAF Aeronautical Systems Division (ASD/ENO), Wright-Patterson AFB, Ohio, July 1975.
12. Tiffany, C. F., J. F. McCarthy, Jr., et al., "Reports of the A-10 Independent Structures Review Team," USAF Aeronautical Systems Division (ASD/ENF), Wright-Patterson AFB, Ohio, October 1975/March 1976/June 1976.
13. McCarthy, J. F., Jr., et al., "Report of Ad Hoc Committee on C-5 Structures," Division Advisory Group, USAF Aeronautical Systems Division (ASD/ENO), Wright-Patterson AFB, Ohio, March 1976.
14. Murnane, S. R., T. D. Stronge and O. B. Davenport, "Northrop/United States Air Force Durability and Damage-Tolerance Assessment of the F-5E/F Aircraft," Proc. 43rd Meeting of the Structures and Materials Panel, NATO Advisory Group for Aerospace Research and Development, London, UK, 28-29 September 1976.
15. Air Force Contract F09603-76-A-0612-001, "C-141A Durability and Damage Tolerance Assessment Program," Warner-Robbins ALC to Lockheed-Georgia Co., 1976.
16. Air Force Contract NPN3347R3, "T-38 Durability and Damage Tolerance Assessment Program," San Antonio ALC to Northrop Corporation, 1976.
17. Anon., "A-7D Damage Tolerance and Fatigue Assessment," Vought Corporation, Dallas, Texas, Report No. 2-53440/7R-5928, 31 January 1977.
18. Tiffany, C. F., "Report of the Structural Advisory Group for the -135

Aircraft," USAF Aeronautical Systems Division (ASD/ENF), Wright-Patterson AFB, Ohio, February 1977.

19. Wood, H. A., "Application of Fracture Mechanics to Aircraft Structural Integrity," J. Eng. Fract. Mech., Vol. 432, 1975, 1-8.
20. Maske, E. B., "F-111A/E/D/F Risk Assessment Sensitivity Analysis," General Dynamics Corp., Fort Worth, Texas, presentation to USAF Scientific Advisory Board, 25 June 1971.
21. Dempster, J. B., Chief of Technical Staff, The Boeing Airplane Company (Wichita Division), private communication, February 1977.
22. Anon., "Structural Review, F-4C/D/E ASIP, Volume I," McDonnell-Douglas Corp., St. Louis, Mo., 26-27 April 1974.
23. Hahn, G. J. and S. S. Shapiro, Statistical Models in Engineering, Wiley, New York, 1967.
24. Buntin, W. D., "Concept and Conduct of Proof Test of F-111 Production Aircraft," paper presented to the Royal Aeronautical Society, London, UK, 27 October 1971.
25. Yang, J. N. and W. J. Trapp, "Reliability Analysis of Fatigue-Sensitive Aircraft Structures Under Random Loading and Periodic Inspection," Air Force Materials Laboratory (AFML/LL), Wright-Patterson AFB, Ohio, AFML-TR-74-29, February 1974.
26. Holpp, J. E. and M. A. Landy, "The Development of Fatigue/Crack Growth Analysis Loading Spectra," NATO Advisory Group for Aerospace Research and Development, AGARD-R-640, January 1976.

FLAW PROPAGATION STUDIES OF
THE MINUTEMAN III THIRD
STAGE ROCKET MOTOR

by

William L. Hufferd & Harold R. Jacobs
University of Utah
Salt Lake City, Utah 84112

INTRODUCTION

The Minuteman III Stage III motor for the WS 133B weapon system was designed, developed and qualified by Aerojet Solid Propulsion Company (ASPC) in the 1960's. Subsequently, Aerojet has manufactured and delivered to the operational force 175 Stage III motors of the 1147372-69 or 89 configurations. The Aerojet Stage III motor consists of a solid rocket motor with a single fixed submerged nozzle. The propellant grain design incorporates a forward release flap but is bonded to the cylindrical section and aft dome. The propellant designation is ANB-3066.

During processing of the motor, the problem of casting motors without aft apex voids (voids within two inches forward of the nozzle bolt ring) arose. Prior to developing a casting technique to minimize these voids, a number of motors were cast with large apex voids. Motors with voids having a height greater than 0.2 inch but less than 0.4 inch and/or a total void area greater than 20 square inches were potted with SD-844-4 adhesive. Potting was accomplished by first drilling two 3/8 inch diameter holes through the propellant at each end of the void to be potted. The adhesive was then forced in one hole under pressure until it came out the hole at the other end. In most instances one or more holes would miss the void and additional holes would be required. The blind holes were also potted by forcing as much SD-844-4 adhesive as possible into the hole. It was later determined that many of these "Missed" holes were only partially filled and even for those that were successfully filled the mismatch of properties with the propellant caused local stress risers.

In 1969 TRW carried out an investigation of the anomalous ballistic performance of FTM-203 and FTM-301 and the burn-through of QT-3 [1]. The investigation concluded that the ballistic anomalies and the QT-3 burn-through were most likely caused by an "unzipping" phenomenon which was defined as a shear failure of the propellant-liner-insulation bond system in the motor aft end. During the course of this investigation, ASPC incorporated an aft end restrictor in the motor to modify the geometry of the burning propellant (Figure 1). The modified geometry increased the time required for the burning front to reach the location of maximum stress in the motor and reduced the stress transmitted to the bond line.

In subsequent flight and static test programs, it became evident with the failures of motors FTM-310, TMS-7 and OT-41 that motors with aft restrictors could also burn-through. As a result of the OT-41 failure on December 2, 1972,

TRW recommended a program to SAMSO to investigate the cause of Stage III burn-throughs with motors containing the aft end restrictor and to establish the impact of these failures on the operational force. The program planning was developed by SAMSO and TRW and reviewed with the Aerospace Corporation, OOAMA, AFRPL and ASPC. The ASPC supported the subsequent investigation by conducting correlation analyses, material property tests and motor cold pressurization tests [2]. In addition to the normal system engineering and technical direction support provided SAMSO, TRW modeled and analyzed the Stage III motor using the data generated by Aeroject to support the assessment of Stage III operational motors [3].

The significant findings of the investigations included:

- (1) "The Stage III propellant is highly notch sensitive relative to fracture initiation. The potting in the potted void motor introduces higher propellant strains due to the strain concentration factor associated with the holes (approximately two to three times higher). A strain concentration factor of 2.3 was demonstrated in the cold pressurization tests which was consistent with analytical predicted factors. Based upon these findings, it was concluded that all potted void motors will develop a cracked grain during firing. From the test results the crack path in the propellant appears to be a variable which explains why not all potted void motors burn-through" [3].
- (2) "Without the presence of potting holes, the aft end propellant is not sufficiently strained to cause grain cracking which would account for the ballistic anomalies associated with the non-potted motors. The analysis predicts separation of the aft end propellant-insulation bond line for both void and no-void motors. However, bond line separations are more likely to occur in the presence of apex voids. The results of the cold pressurization tests confirm the existence of this failure mode. Unfortunately, none of the tests demonstrated a clean separation mode since grain cracking preceded bond line separation in all cases. The bond line was sufficiently overloaded by the altered bond line separation in all cases. The bond line was sufficiently overloaded by the altered load path due to the grain cracks resulting in premature separation. Without notches in the grain propellant cracking is not predicted. The bond line separations observed in the cold pressurization tests would have undoubtedly occurred at higher pressured levels as observed in motor tests and as predicted analytically" [3].
- (3) "The propagation of the bond line separation appears to be constrained to the apex area and several inches outboard of the apex. This was observed in the cold pressure test results. The propagation analyses agree with observations. Provided that there is not significant change in the aging trends, there is a very low probability that bond line failure mechanism will lead to aft dome burn-through" [3].

Based upon these findings TRW recommended to SAMSO that:

- (1) "The potted void motors be removed from the operational force" [3].
- (2) "The non-potted void and no-void motors in the operational force be retained" [3].
- (3) The Stage III Surveillance Program be updated to track the propellant grain cracking and bond line separation failure modes.

Another investigation of the Stage III motor was also conducted by the Chemical Systems Division (CSD) of United Technologies Corporation* [4]. The CSD task included demonstration of a new grain analysis computer code, the Texas Grain Analysis Program (TEXGAP) on the Stage III motor.

During this same period of time (i.e., 1970-73) the University of Utah was conducting investigations to assess if a flaw, crack or debond would propagate mechanically due to combustion induced pressure loadings at a faster rate than the burning rate [5,6]. Thus, in January 1974 a task was added to assess the Third Stage Minuteman III motors susceptibility to failure due to burning flaws [7,8]. This investigation considered the above findings and recommendations within the context of the results of the crack criticality study. Assessment was made of two modes of failure:

- 1) Cracking of the grain in association with aft end voids.
- 2) Aft end bond line failure.

This analysis study differed from that of TRW and CSD in that pressure increases due to burning were considered in flaws having access to the main chamber.

FORMULATION

The propellant grain analyzed was a finocyl slotted design with a forward relief flap. Except in the slotted section the unflawed motor is symmetric. Flaws in a propellant motor are normally unsymmetric; however, experience has shown that flaws will normally propagate into a symmetric flaw before propagating axially. Based on this and the expense of a three-dimensional analysis, only axisymmetric analyses with axisymmetric flaws were conducted. A previous analysis indicated that the axisymmetric analysis yields acceptable stress levels when compared with a three-dimensional stress analysis [9].

The analyses for bond line failure were conducted for the 0.1 second burn configuration and those for grain cracking used the 10.5 second burn configuration with an axisymmetric void 2" by 1/4" located at the apex (Figure 2).

*Formerly, United Technology Center

The former was thought to be a critical situation if large scale debonding would occur while the second was shown previously by TRW [3] to be most critical in terms of maximum bondline shear stress. The 10.5 second burn configuration also corresponded to two cold pressurization tests conducted by Aerojet.

The finite element computer code used is valid for materials with Poisson's ratio in the range $0 \leq \nu \leq 0.49999$ with or without an axisymmetric elastic thin shell.

A basic grid size of 25 x 65 was chosen for the analyses. In order to obtain sufficient detail and accuracy two different basic grids were generated for each of the two burn-configurations; one for short crack lengths and one for long crack lengths. The grids for the 0.1 second configuration are shown in Figures 3 and 4 and the two grids for the 10.5 second configuration are shown in Figures 5 and 6.

The material properties used in the analyses were obtained from TRW. The case properties were obtained by matching calculated deflections with measured deflections from the cold-pressure tests conducted by Aerojet. The material properties used are presented in Tables I - III. The chamber pressure for the 0.1 second configuration was assumed to be 411 psig and that for the 10.5 second configuration to be 560 psig. Axial loads of 2120 psia and 3980 psia were applied to the nozzle boss to simulate nozzle thrust at 0.1 and 10.5 seconds, respectively.

The liner thickness was assumed to be 0.025 inches. In the propellant in the vicinity of a void, or close to the liner there existed a modulus gradient [3]. This gradient existed over a distance of approximately one inch into the propellant. A linear gradient from the high values to the bulk values of the modulus shown in Table I were used in the analyses over this distance.

The pressure loadings in flaws not open to the main chamber were assumed to be zero. Thus, if the void collapsed due to other loadings a modulus and Poisson's ratio were calculated which were sufficient to allow the void to close, but prevented overlapping of liner and propellant elements. The pressure distribution within a burning flaw is determined by the flaw opening and length. Thus, a flaw open to the main chamber was initially assumed to have the ambient chamber pressure acting within it to obtain an initial geometry which was used in calculating the initial internal pressure due to burning within the flaw. The final pressure and geometry were arrived at by iteration.

The pressure in a burning flaw was calculated using computer programs developed previously [5]. The loading time for a burning flaw was determined as the time necessary to reach a quasi-steady state flaw tip pressure,

$$t^* = 6.2 \times 10^{-6} (P_{t^*} - P_c)W \text{ (seconds)} \quad (1)$$

where P_{t^*} is the tip quasi-steady pressure in psi and W is the mean flaw width in feet.

For the 0.1 second burn configuration the $+3\sigma$ adhesive fracture energy was determined to be 2.5 in-lb/in² and $+3\sigma$ cohesive fracture energy was 10 in-lb/in² at 0.001 seconds and 8 in-lb/in² at 10.5 seconds.

Debond initiation or grain crack initiation was evaluated comparing strain energy release rates with the allowable fracture energies. Crack trajectory for grain cracking was determined using a maximum principal stress criterion and crack growth rate determined according to a previously developed local damage criterion [7],

$$a(t) = a_0 \cosh C(\sqrt{d} - \sqrt{d_c}) \quad (2)$$

where $d = \sigma_1^2 - 3\sigma_2$

$$\sigma_1 = (\sigma_1 + \sigma_2 + \sigma_3)^2$$

$$\sigma_2 = \sigma_1\sigma_2 + \sigma_2\sigma_3 + \sigma_3\sigma_1$$

$$C = 8.3 \times 10^{-6} \text{ psi for ANB-3066 propellant}$$

and

$$d_c = \frac{1}{a_0} \left(\frac{E\gamma_c}{1-\nu^2} \right) \quad (3)$$

ASSESSMENT

Debonding studies were primarily conducted for the 0.1 second burn configuration of the Third Stage Motor. The two finite element grids shown in Figures 3 and 4 were used for calculating strain energy release rates (dU/dA) from the bore to the case tangent point. The first grid shown in Figure 3 was used to obtain the energy release rate and stress distribution in the vicinity of the knuckle (Figure 2) while the grid of Figure 4 was used to obtain more accurate stresses in the vicinity of the tangent point.

Prior to investigating the debonding of the propellant from the liner the no debond configuration was evaluated. It was found [7,8] that the stresses along the bondline in the axial and radial directions were compressive except in the immediate neighborhood of the base of the knuckle where slight tension was experienced by the liner material and propellant.

The shear stress along the bondline as well as along the burning flaw surface is affected by the finite element representation; hence part of the reason for using two detailed grids for each configuration analyzed. Maximum shear stresses within the first four elements from the burning surface of Figure 3 were as high as 54 psi in the liner and 86 psi in the propellant but nominally around 20 psi. In the knuckle region a maximum shear stress of 207 psi occurs in the propellant. The shear stress capability is nominally 190 psi [2,3]. Thus, bond line shear failure in the propellant could occur in the knuckle region upon ignition; however, it may not propagate to the bore surface without a surface flaw present.

Stresses and strains along the bore for the 0.1 second configuration indicated that longitudinal cracking of the grain should not occur in the aft end.

In considering debonding, the flexibility of the case was such that shorter flaws were nearly at chamber pressure while longer flaws had significantly increased internal pressures due to burning in the flaws. Figures 7 and 8 show typical flaws subject to chamber pressure while Figure 9 and 10 indicate the final geometries with burning in the flaws. The 20 inch flaw has a quasi-steady flaw tip pressure of 1240 psi for the 0.1 second configuration. From Figure 10 it may be seen that the twenty inch flaw will close at the opening thereby giving use to an even greater pressure increase.

The strain energy release rate, dU/dA , was calculated both from evaluating the strain energy by releasing an additional node in the grid and by graphically determining the slope when the strain energy versus area was plotted to large scale. The resulting curves for the actual load and the chamber pressure only load are shown for the 0.1 second configuration in Figure 11. Figure 12 shows the equivalent chamber pressure only curve for the 10.5 second burn configuration, obtained by TRW [3]. For this latter situation it is doubtful that debonding would occur beyond the ten inch length based on $+3\sigma_a$; however, for the 0.1 second configuration the strain energy release rate exceeds the $+3\sigma_a$ beyond the point indicated by Figure 10.

From this analysis, it would appear that from a "criticality" point of view, the existence of a small flaw at the burning surface bondline would be most critical for the 0.1 second configuration. This is especially true since a flaw of one-eighth inch depth is nearly enough to exceed the $+3\sigma$ reported values of γ_a , ($\gamma_a = 2.5 \text{ in-lb/in}^2$ at 0.1 seconds).

For the twenty inch debond, which apparently closes after the full burning pressure is reached, the tip quasi-steady pressure is 1240 psia. Using a mean flaw width of between one and two inches, t^* is calculated from (1) to be between 0.0004 and 0.0008 seconds. Thus, the pressure build-up in such a flaw due to burning occurs less than one millisecond after the surface is ignited.

The conclusions drawn from this analysis is that all debonds in excess of 0.6 inches will fail if penetrated by flame.

Analysis of the 10.5 second burn configuration by TRW [3] indicated that in the presence of a void near the nozzle flange knuckle apex, cracking was possible. In fact both the AOP-3 and TMS-16 motors were subject to a combination of cracking followed by bondline separation. In addition a ballistic anomaly occurred at approximately 11 seconds in motor OT-41. Thus, this burn configuration was assessed for possible cracking and the extent of flaw propagation. To examine the likelihood of fracture the maximum strain was calculated along the burning surface both with and without a void of 2 in. by 1/4 in. located at the aft end apex. The results indicated a slight increase in the axial strain from 11 percent to 13.7 percent with the void present; however these values were considerably less than the propellant strain allowable. Thus, failure would not be expected except in the presence of a local stress riser, which the potting holes provided.

The crack path was taken to initiate at the peak strain location in the aft end and follow a maximum principal stress trajectory. The crack path is shown in Figure 13 by the double row of elements (boldline). The crack path terminates at the outermost element of the apex void. This path was typical of fractures observed on the cold motor tests conducted by ASPC [23].

The crack was allowed to open in the same manner as the debond by first assuming chamber pressure within the flaw to calculate an initial pressure increase due to burning which was used to calculate a new geometry and so forth until the final configuration and pressure were arrived at by iteration. Typical flaw openings due to burning within the crack are shown in Figures 14 to 16. The resulting strain energy release rate is shown in Figure 17. A crack length approximately 0.6 inch long is critical and should propagate. The initial crack speed was evaluated from (2). At 10.5 seconds, $\bar{d}_c = 180$ psi for a crack length of 0.6 inches, Figure 18. For an initial crack length of 0.3 inches, $t^* = 1.5 \times 10^{-5}$ seconds from (1) and $\bar{d}_c - \bar{d}_c = 60$ psi. Thus the initial speed is 0.005 inches per second. For a one-inch initial flaw size the initial speed is 0.28 inches per second. The burning rate was 0.33 inches per second; thus it would be anticipated that crack in the aft end would propagate at a slower rate than the burning rate and thus "burn-out" faster than they could propagate. For a 1-inch long crack the flame arrives at the case approximately 8 seconds after ignition compared to a normal time of 11 seconds. Thus unless a bondline failure occurs, the insulation receives only a three second excess exposure to flames.

CONCLUSIONS

Based on previous investigations, TRW recommended that all potted motors be removed from the operational force.

The present analysis indicates that motors with a potting hole do not appear to be critical due to burning in the flaw when the unfilled portion of the hole is less than one inch long. Flaws less than one inch long will open sufficiently to prevent over pressurization from burning in the flaw.

A more serious situation may result for debonding since the debonding may well propagate at a faster rate than the propellant burning rate. Data obtained on the bond line system were insufficient to obtain debond propagation rates.

REFERENCES

1. TRW, "Minuteman III Third Stage Ballistic Anomaly Investigation", TRW Report No. 14089-6558-T7-00.
2. Aerojet Solid Propulsion Company, "Final Report Minuteman III, Stage III Burn-Through Investigation, Weapon System 133B", ASPC Report No. 0162-III-SE-07, 21 December 1973.
3. Neely, R. B., et. al., "Final Report Minuteman III Stage III Burn-Through Investigation", TRW Report No. 23942-0462-TU-00, 15 January 1974.
4. United Technology Center, "Minuteman III Stage III Stress Analyses, Task V", UTC Report No. UTC 2439-TR.
5. Williams, M. L., and Jacobs, H. R., "The Study of Crack Criticality in Solid Rocket Motors", University of Utah, AFROL TR-71-21, January 1971.
6. Jacobs, H. R., Williams, M. L., and Tuft, D. B., "An Experimental Study of the Pressure Distribution in Burning Flaws in Solid Propellant Grains", University of Utah, AFRPL TR-72-108.
7. Jacobs, H. R., Hufferd, W. L., and Williams, M. L., "Further Studies of the Critical Nature of Cracks in Solid Propellant Grains", University of Utah, AFRPL-TR-75-14, March 1975.
8. Jacobs, H. R., Hufferd, W. L. and Anderson, G. P., "Propensity for Propagation of Cracks and Debonds in Third Stage Minuteman Propellant Grains", Proceedings of the JANNAF OSWG & SMBWG Combined Annual Meeting, CPIA Publication No. 264, The John Hopkins University, p. 383, May 1975.
9. Macbeth, A. W., "Third Stage Minutemann Propellant Grain Analysis," Thiokol Chemical Corporation, TWR-4177, 1971.

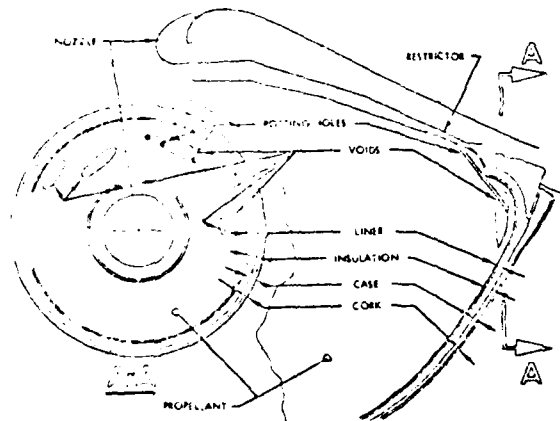


Figure 1. Typical Stage III Voids and Potting Hole

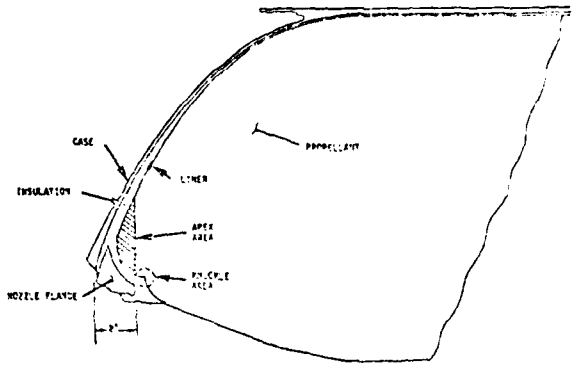


Figure 2. MINUTEMAN III Stage Aft End Configuration

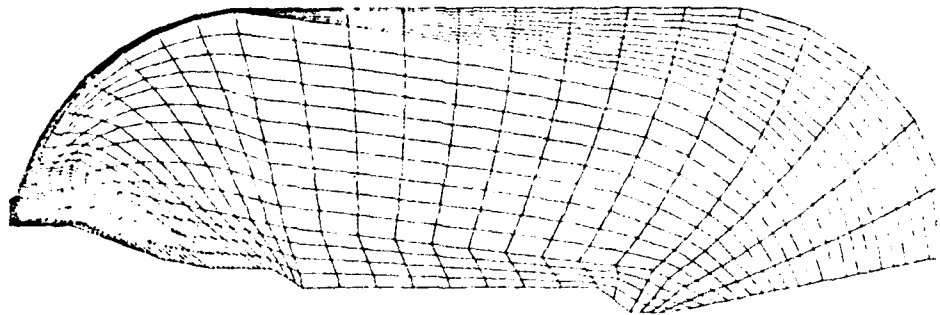


Figure 3. 0.1 Second Configuration, Grid No. 1, 3rd Stage Minuteman III

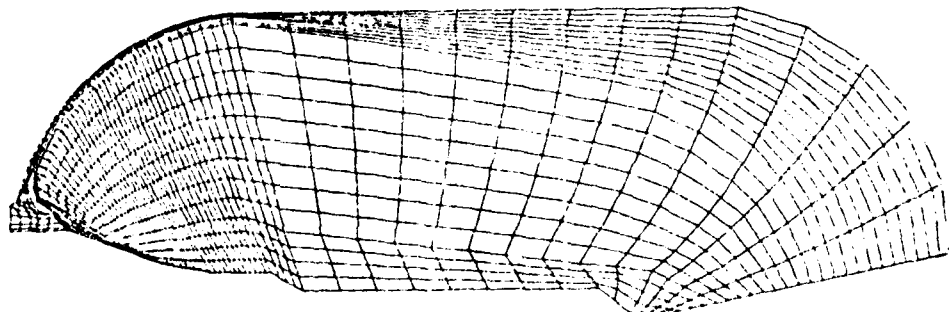


Figure 4. 0.1 Second Configuration, Grid No. 2, 3rd Stage Minuteman III



Figure 5. 10.5 Second Configuration, Grid No. 1 3rd Stage Minuteman III.

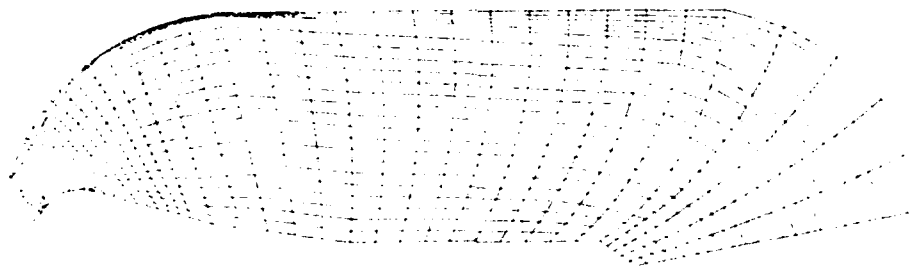


Figure 6. 10.5 Second Configuration, Grid No. 2, 3rd Stage Minuteman III.

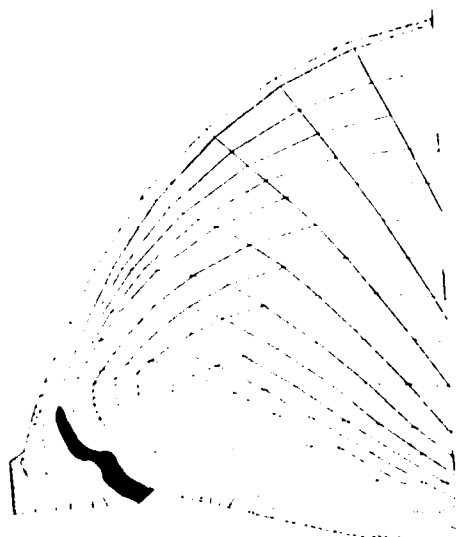


Figure 7. 5 in. Debond Subject To Chamber Pressure, 0.1 Second Configuration.

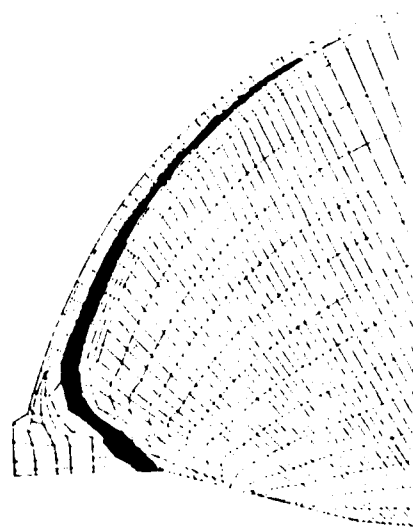


Figure 8. 22 in. Debond Subject To Chamber Pressure, 0.1 Second Configuration.

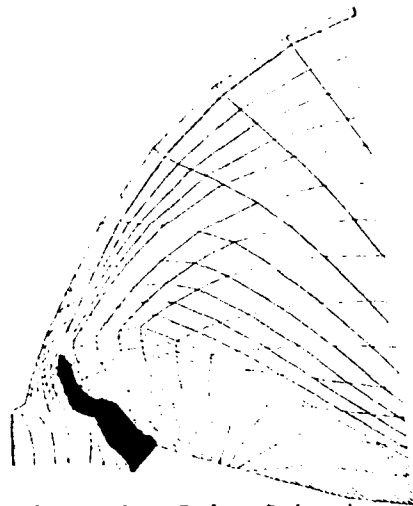


Figure 9. 5 in. Debond Subject To Burning Pressures, 0.1 Second Configuration.

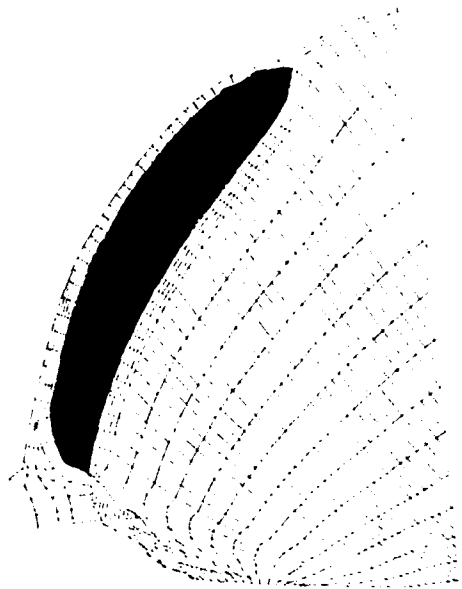


Figure 10. 22 in. Debond, Resulting Deformed Grid Using Burning Pressures (Note Closure) 0.1 Second Configuration.

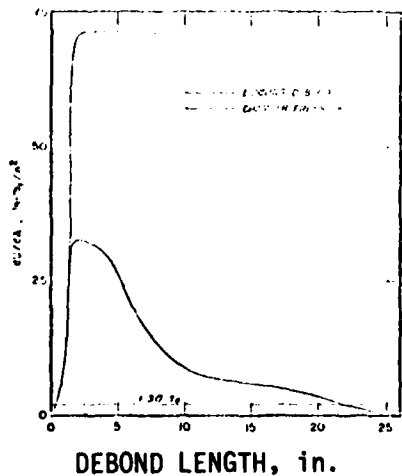


Figure 11. dU/dA Versus Bondline Crack Length 3rd Stage Minuteman III, 0.1 Second Configuration.

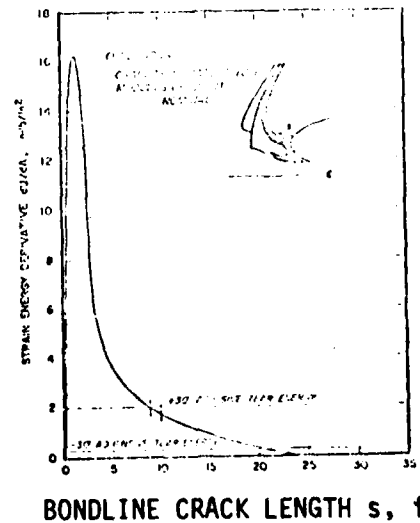


Figure 12. Change In Strain Energy Versus Bondline Separation Length for 10.5 Second Burn Configuration (initiation at bonding termination point). From TRW.

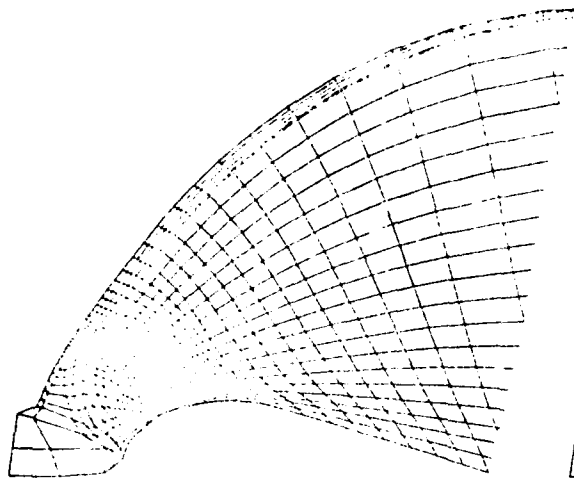


Figure 13. No Crack, 10.5 Second Configuration

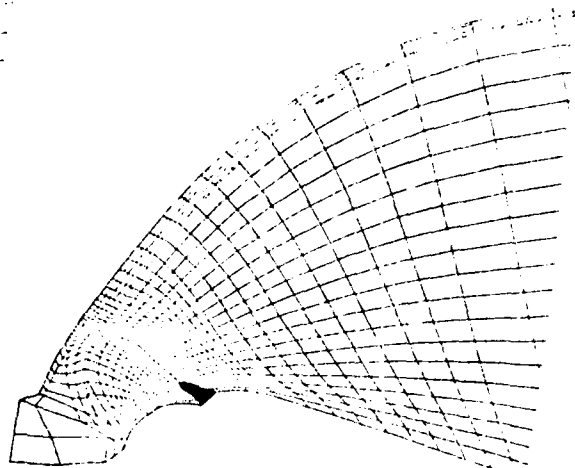


Figure 14. 1.0 in. Crack, Burning Pressure, 10.5 Second Configuration.

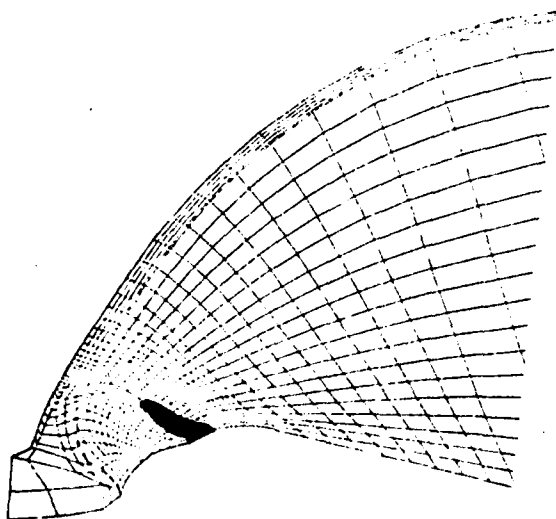


Figure 15. 2.2 in. Crack, Burning Pressure, 10.5 Second Configuration.

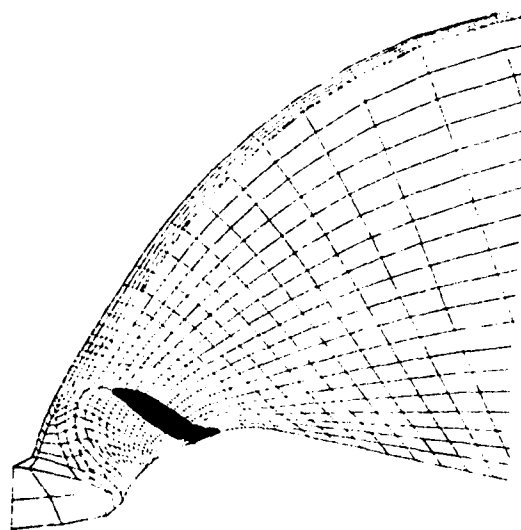


Figure 16. 3.2 in. Crack, Burning Pressure, 10.5 Second Configuration.

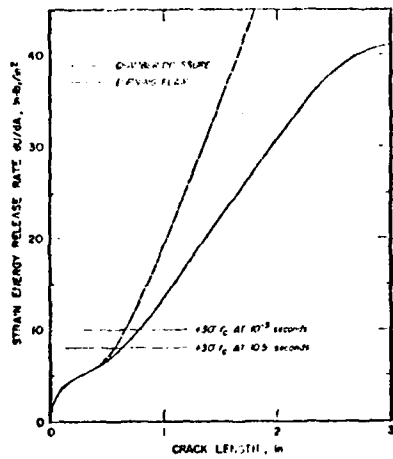


Figure 17. dU/dA vs. Crack Length
ANB 3066 Propellant, 3rd
Stage Minuteman. Void 2 in.
Long Symmetric 10.5 Second
Configuration.

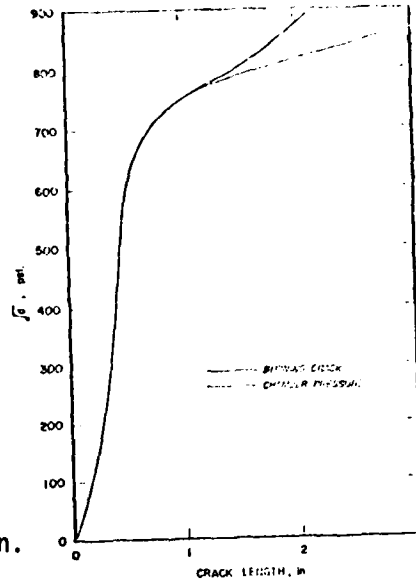


Figure 18. \sqrt{d} Versus Cohesive Crack
Length, 10.5 Second Con-
figuration III Stage
Minuteman III Motor Grain
Aft End.

TABLE I
MATERIAL PROPERTIES AT 77°F

MATERIAL	TIME	
	0.1 sec	10.5 sec
Insulation		
E (psi)	1607	1602
ν	0.499	0.499
Linear		
E (psi)	130	130
ν	0.499	0.499
Bulk Propellant		
E (psi)	2550	630
ν	0.499	0.499
High Modulus Propellant		
E (psi)	4000	7000
ν	0.4999	0.4999
Aluminum		
E (psi)	10.3×10^6	10.3×10^6
ν	0.33	0.33

TABLE II
CASE PROPERTIES, 10.5 SECOND CONFIGURATION

Location B (in)	Case Thickness (in)	E_0 ($\times 10^6$ psi)	E_1 ($\times 10^6$ psi)	ν_{00}	ν_{10}
17.29-17.72	0.590	8.51	1.31	0.2	0.01
17.77-17.97	0.570	8.54	1.31	0.2	0.03
17.99-18.25	0.560	8.50	1.31	0.2	0.04
18.27-18.41	0.510	8.50	1.31	0.2	0.01
18.43-18.72	0.470	8.54	1.31	0.2	0.01
18.74-18.90	0.450	8.54	1.31	0.2	0.03
18.92-18.95	0.390	7.30	4.75	0.2	0.05
18.95-18.98	0.380	7.30	4.75	0.2	0.07
18.98-18.98	0.360	9.00	8.52	0.2	0.13
18.98-18.97	0.315	8.81	5.18	0.2	0.20
18.97-20.06	0.301	12.00	17.03	0.2	0.29
20.06-22.07	0.075	15.45	30.00	0.2	0.39
22.07-24.37	0.070	14.40	30.90	0.2	0.42
24.37-25.37	0.065	17.00	31.00	0.2	0.49
25.37-25.83	0.077	14.16	18.45	0.2	0.11
25.83-25.83	0.076	6.25	3.85	0.2	0.17

TABLE III
CASE PROPERTIES, 10.5 SECOND CONFIGURATION

Location B (in)	Case Thickness (in)	E_0 ($\times 10^6$ psi)	E_1 ($\times 10^6$ psi)	ν_{00}	ν_{10}
12.27-12.97	0.530	8.5	1.31	0.2	0.03
12.97-13.45	0.460	8.5	1.31	0.2	0.01
13.45-13.94	0.390	8.5	1.31	0.2	0.01
13.94-14.04	0.355	7.5	3.00	0.2	0.10
14.05-14.15	0.327	7.5	4.00	0.2	0.127
14.15-14.77	0.310	7.2	4.90	0.2	0.119
14.77-15.22	0.270	7.2	4.90	0.2	0.119
15.22-15.64	0.200	7.0	4.70	0.2	0.134
15.64-15.91	0.170	9.0	6.00	0.2	0.122
15.91-16.72	0.150	10.0	8.00	0.2	0.160
16.72-18.99	0.130	9.0	6.40	0.2	0.187
18.99-19.01	0.105	8.3	9.40	0.2	0.227
19.01-19.37	0.100	10.0	6.00	0.2	0.260
19.37-20.10	0.095	20.0	12.00	0.2	0.330
20.10-20.96	0.090	29.0	16.00	0.2	0.349
20.96-21.89	0.080	30.0	16.00	0.2	0.375
21.89-22.06	0.075	30.5	15.40	0.2	0.396
22.06-23.85	0.075	31.0	14.20	0.2	1.437
23.85-24.76	0.070	21.8	12.20	0.2	0.477
24.76-25.46	0.065	32.3	11.20	0.2	0.512
25.46-25.83	0.073	16.4	14.70	0.2	0.114
25.83-25.83	0.076	3.85	6.25	0.2	0.123

METALLURGICAL EVALUATION OF PROOF TEST FAILURE
OF A SECOND STAGE MISSILE MOTOR CASE

Eric B. Kula and Albert A. Anctil
Metals Research Division
Army Materials & Mechanics Research Center
Watertown, Massachusetts 02172

INTRODUCTION

This report relates an investigation into the premature failure during proof testing of a second stage missile motor case. The proof testing was carried out as part of the certification procedure of a new producer for the missile. This investigation was to ascertain the cause of failure of this particular motor case, as well as to make general recommendations for preventing recurrence of failures in the future.

The case that burst had been subjected to five proof cycles at 1620 psi, above the operating stress of 1540 psi, and then failed at 1728 psi on a burst test. The expected burst stress was 1910 psi. Other burst stresses of 1980, 2080, and 2120 psi had been achieved in earlier tests by the original producer.

The motor case, about 43 inches in diameter, is made from 4340 steel quenched and tempered at 450 F to a yield strength of about 210 ksi and a tensile strength of 245 ksi. The chemical analysis of the case material meets the required specifications, although the sulfur content, 0.015%, is high for applications requiring maximum toughness at high strength levels. The cylindrical portion of the case is produced from plate with two longitudinal fusion welds made by the metal arc inert gas process. After preliminary sizing, the cylinder is heat treated, and then sized again. In this condition, the forward dome and aft funnel are inserted and each joined to the cylinder by two circumferential seam welds. A chart of the processing history is shown in Figure 1.

It should be emphasized that sizing and welding of steel such as 4340 in the quenched and tempered condition is not generally recommended. The fracture occurred in the forward end of the cylindrical portion of the case, in the heat-affected zone adjacent to the circumferential seam weld. It is believed that the origin was located in or near the intersection of a longitudinal fusion weld and a circumferential seam weld.

Available for inspection were a section of the case containing the suspected fracture origin, a metallographic specimen cut through the matching portion of the case and the dome, and two large pieces of the case and dome material. The inside view, Figure 2, shows the fracture path adjacent to a seam weld. An edge view of a section of the dome portion is shown in Figure 3. A schematic diagram shows the location of the fracture path with respect to the seam welds.

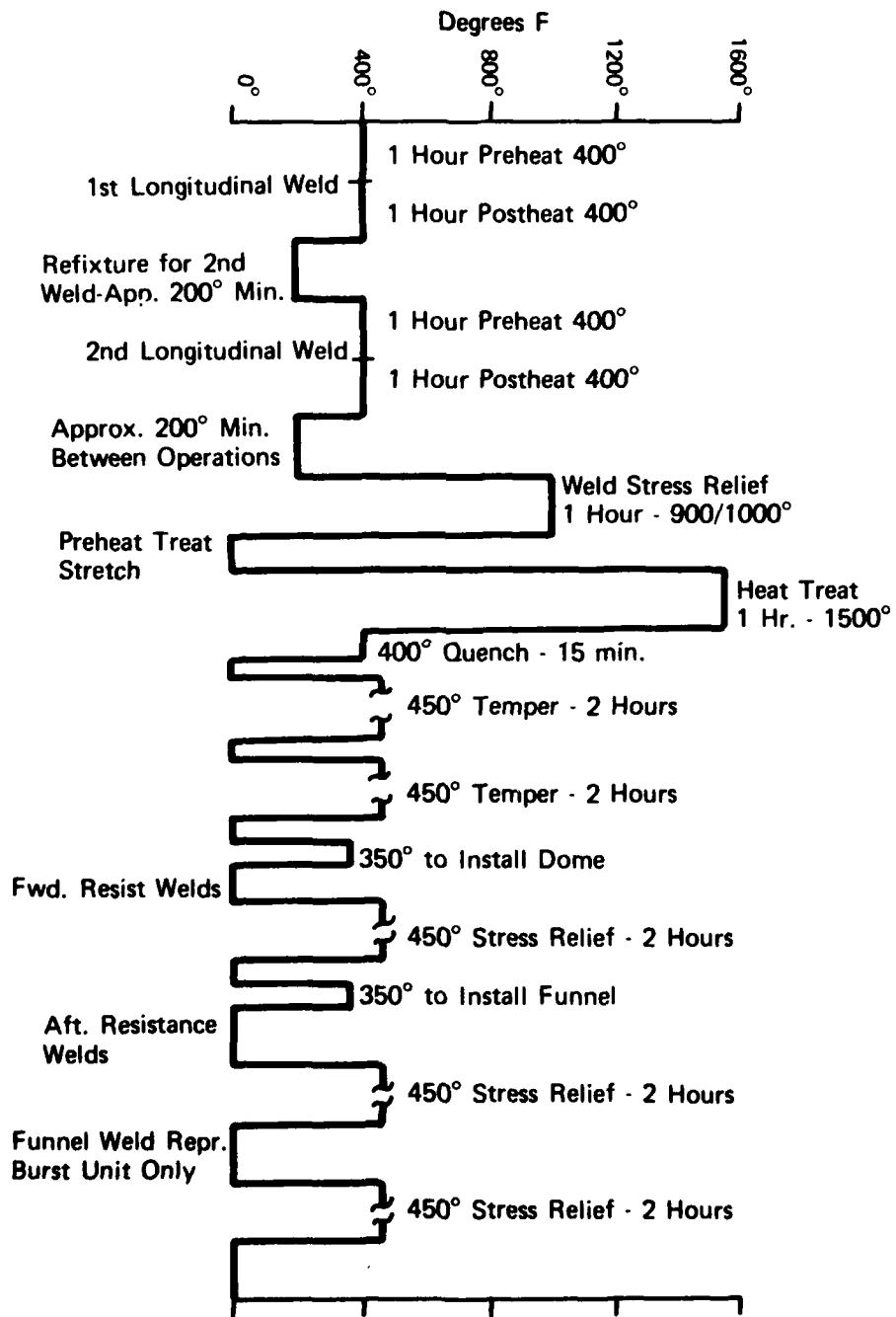


Figure 1. Processing history of second stage motor case

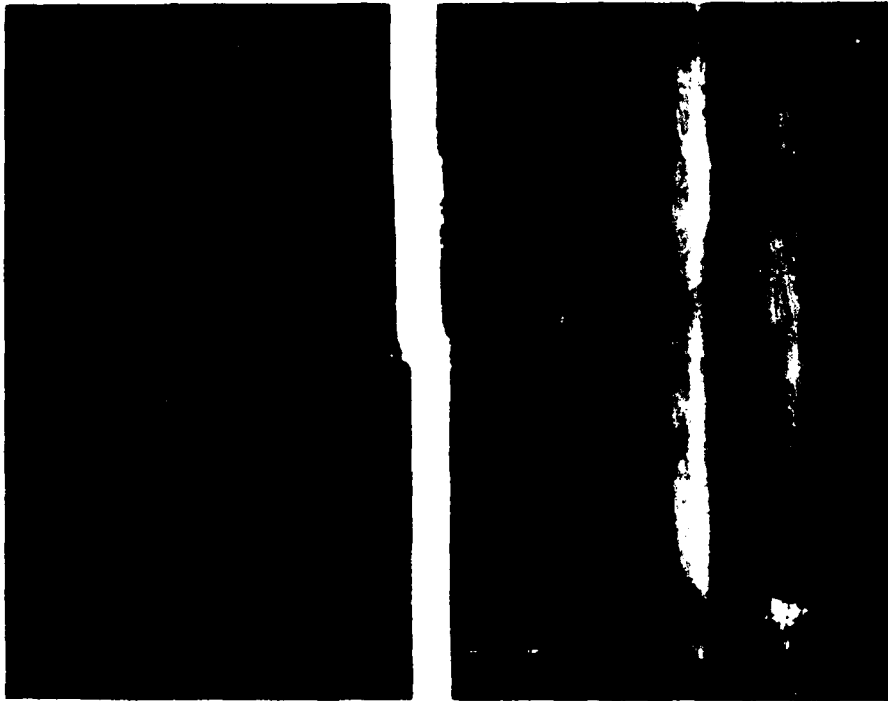


Figure 2. Inside view of section of motor case

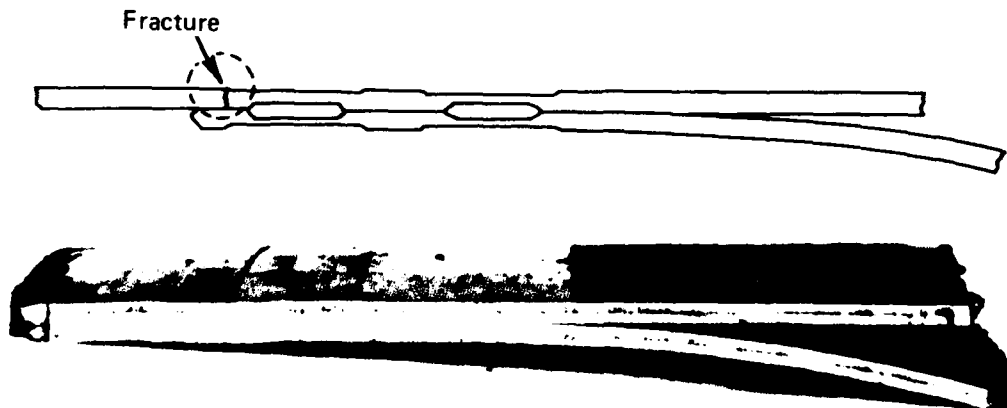


Figure 3. Edge view of dome portion of motor case

A fracture mechanics analysis and a thorough metallographic study of the fracture area, as well as a mechanical property study of the properties of the seam-welded region and the base metal in the case was performed. Properties determined included hardness, tension, fracture toughness, precracked Charpy impact, and stress corrosion.

FORMULATION

A picture of the fracture surface is shown in Figure 4. On the concave surface, a thumbnail-shaped region has been identified as the fracture origin.

This is reportedly in the heat-affected zone adjacent to the longitudinal fusion weld, which is in the center of the figure. The maximum depth of the crack is about 0.091 inch and the length on the surface about 0.530 inch, giving a depth to length ratio $a/2c$ of about 0.18. The remaining portions of the fracture surface that were examined showed a ductile, shear-type failure.

A cross section of the mating piece, in the dome portion, is shown in Figure 5. The weld nugget in the center is readily identifiable by the columnar grains. The fracture origin is in the case near the edge of the welded area perpendicular to the interface. From this region it propagated by shear. The unwelded interface, between the first and second seam welds, is clearly visible at the left.

At the end of the fracture origin in the cylindrical portion, the microstructure is somewhat different, Figure 6. Here weld cracks are clearly visible, surrounded by a white phase containing tempered martensite plates. Adjacent to this there is a region of tempered martensite containing small white carbide particles.

At this point one can speculate on the origin of this region, which clearly can be identified with the failure origin. It is a segregated region, high in carbon, chromium, and molybdenum. Excess carbide particles and plate martensite are both present. It contains weld cracks, and possibly other secondary cracks which occurred during the proof or burst testing. Furthermore, the microstructure shows a dendritic pattern, indicating a cast microstructure, which is unlike the cast structure of the weld nugget itself.



Figure 4. Failure origin on fracture surface of second stage motor case



Figure 5. Cross section through case and dome showing fracture origin



Figure 6. Microstructure near end of fracture origin, showing weld cracks

The location and appearance of this region suggest that weld cracks occurred during seam welding, as a result of mismatch between the dome and the case. The seam welding operation is not continuous, but is really a series of overlapping spot welds, with each portion of the weld melted and solidified as many as ten times. Some of this molten metal from the weld nugget could have been squeezed into the region of the weld crack, leading to the microstructure shown in Figure 6.

Specimens for mechanical property tests were cut from sections of the case and dome shown in Figure 2. The layout of the specimens in the dome section is shown in Figure 7, and in the cylindrical case in Figure 8.

Hardness, fracture toughness, and tension specimens were cut from the dome section containing the seam welds. In each case, the specimen included material from both the case and the dome. The 0.308 inch total thickness tension specimens in the dome section were a non-standard 3/8 inch wide, with a 1.5 inch gage length. They were located so that fracture could occur any place in the weld or heat-affected zone. For fracture toughness testing standard ASTM bend specimens were used [1]. The specimen width was 0.616 inch, with a 0.227 inch deep, 0.030 inch wide machined notch. The initial 0.003 inch radius at the crack tip was sharpened by fatigue cracking. As shown in Figure 7, the notches were located in the center of the weld, near the edge of the weld nugget, and in the heat-affected zone.

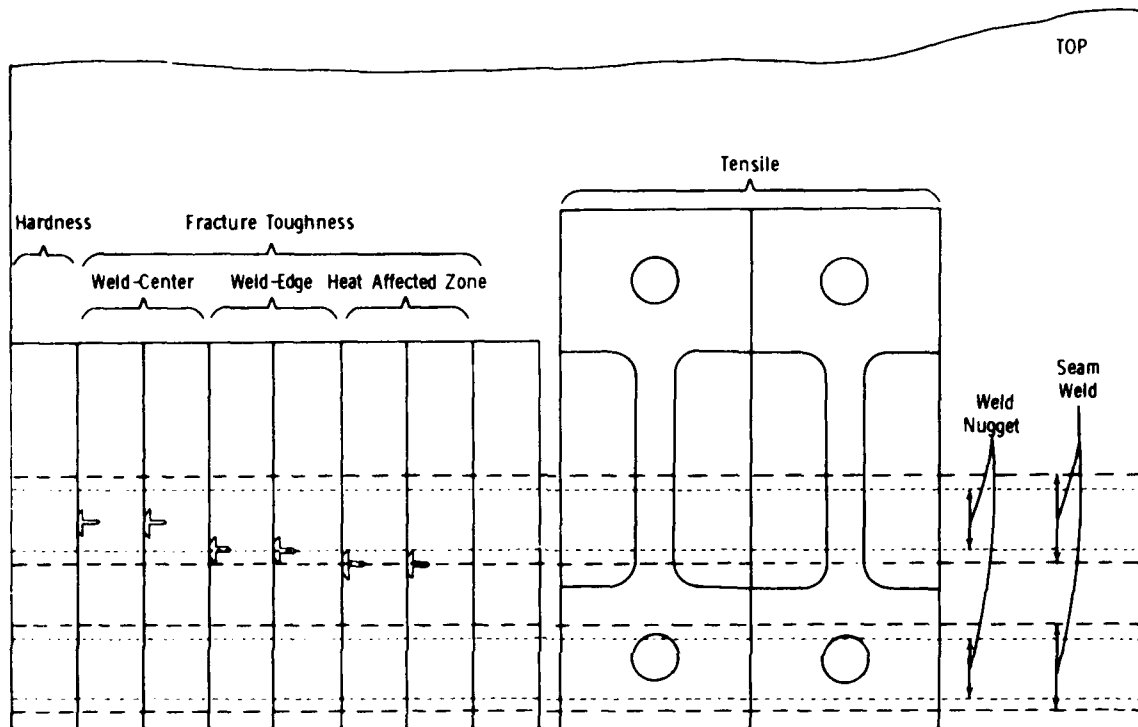


Figure 7. Layout of test specimens from dome section of motor case

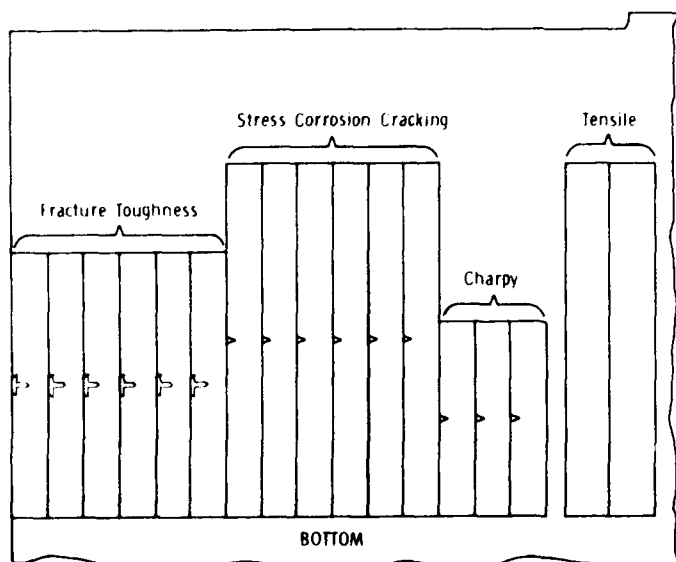


Figure 8. Layout of test specimens from case section of motor case

Tension, fracture toughness, precracked Charpy and stress corrosion cracking specimens were cut from the case section. The reduced thickness of this section, 0.158 inch, necessitated other specimen sizes. The tension specimens

were a standard subsize 0.250 inch wide with a 1 inch gage length. The fracture toughness bend bars were 0.316 inch wide with a 0.092 inch deep notch. Fracture toughness under dynamic conditions was determined from precracked Charpy bars, which had standard dimensions except for the reduced thickness. In addition, stress corrosion cracking tests were performed on specimens with the same geometry as the fracture toughness bend bars.

The results of a microhardness survey taken along a profile midsection through the case material in the vicinity of the seam weld are shown in Figure 9. The hardness readings range from a maximum of R_c 52 in the weld to a minimum of about R_c 33 in the heat-affected zone. This should be compared to a reported hardness for the case of R_c 52.

Tensile properties in the base metal and in the dome (seam weld) are listed in Table I. Note the sharply lower strength in the region of the weld in the dome section. The fracture occurred in the heat-affected zone, and since there was no welding between the dome and cylinder materials at this point, there were actually separate fractures in the case and dome materials.

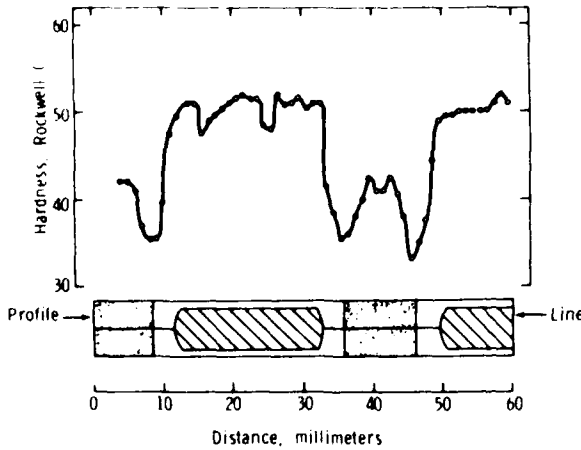


Figure 9. Microhardness profile through seam weld

TABLE I. TENSILE PROPERTIES

	0.2% Yield Strength (psi)	Ultimate Tensile Strength (psi)	% Elongation	% Reduction in Area
Base Metal	212,000	249,000	8	32
Weld Metal	164,300	174,400	4.7	30

Fracture toughness was measured in the precracked bend bars. K_Q , the stress intensity factor, was calculated from the expression

$$K_Q = \frac{P_Q S}{BW^{3/2}} Y \quad (1)$$

where

- P_Q = the offset load in pounds determined from a load-deflection curve where the slope is 0.95 times the initial slope,
 S = span length, in.
 B = thickness of specimen, in.
 W = depth of specimen, in.
 $Y = 2.9 (a/W)^{1/2} - 4.6 (a/W)^{3/2} + 21.8 (a/W)^{5/2} - 37.6 (a/W)^{7/2} + 38.7 (a/W)^{9/2}$
 a = crack length, in.

If the ratio P_{max}/P_Q does not exceed 1.10, where P_{max} is the maximum load, the test is a valid one, and the value of K obtained is the plane strain stress intensity factor K_{IC} . If the ratio exceeds 1.10, the test is not valid, and the K value is called K_Q . In such a case, a larger specimen would be necessary to obtain a valid reading.

The results in Table II, summarized in Figure 10, show that the toughness values for the base metal are marginally valid, with a K_Q averaging 56.0 ksi in.^{1/2}. The results for the center of the weld and the edge of the weld are probably close to being valid, and show a measurably lower toughness. The toughness of the HAZ was not valid, but in any case is significantly higher. It should be emphasized that the measured toughness values for the edge of the weld are for sound material, and are higher than what would be expected in the segregated region shown in Figure 6 where the actual failure origin was located.

Measurements were also made of K_{ID} , the fracture toughness under dynamic conditions, by testing precracked Charpy impact specimens on an instrumented Charpy machine. The specimens were representative of the base material in the

TABLE II. FRACTURE TOUGHNESS

	S	B	a	W	Y	P_Q	P_{max}	P_Q/P_{max}	K_Q
	in.	in.	in.	in.		lb	lb		psi in. ^{1/2}
Weld Center	2.5	.296	.289	.603	2.50	1100	1265	1.15	49,600
	2.5	.299	.305	.614	2.63	1200	1550	1.29	54,900
Weld Edge	2.5	.301	.306	.613	2.66	1135	1295	1.15	52,200
	2.5	.309	.297	.619	2.50	1225	1455	1.19	50,900
Heat- Affected Zone	2.5	.307	.290	.617	2.42	1535	2070	1.35	62,400
	2.5	.307	.286	.613	2.50	1480	1940	1.31	62,800
Base Metal	1.7	.158	.141	.316	2.28	389	448	1.15	53,600
	1.7	.158	.150	.316	2.46	393	438	1.11	58,400

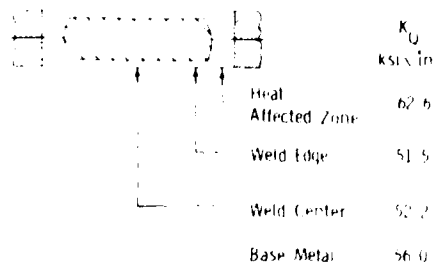


Figure 10. Fracture toughness of seam welded region of motor case

case. The values obtained, 53.5 and 56.2 ksi in.^{1/2}, compared to the static value of 56.0, show that there is only a minor effect of strain rate over this range.

Stress corrosion cracking tests were carried out in a 3.5% NaCl solution using the fracture toughness bend type specimens loaded as a cantilever beam. The results are shown in Figure 11, and show that K_{Isc} is about 22.0 ksi in.^{1/2}. Below this value of K , stress corrosion cracking will not take place in this environment. A 3.5% NaCl solution was used since it is a standard solution which simulates sea water. In the case of high strength steels, it has been found to be equally corrosive as sea water or distilled water.

A comparison has been made of the properties of this lot of 4340 steel with other heats of 4340. In general, the properties are adequate and are what would be expected for this processing and heat treatment. The toughness values appear to be on the low end of the range normally encountered, presumably because of the sulfur content, 0.015%. While this is not a high sulfur content, considering the levels up to 0.045% which may be found in common structural steels, it is high for a highly stressed critical application such as a motor case.

As would be expected, the mechanical properties of the weld and heat-affected zone are considerably reduced. The high hardness combined with the low toughness of the weld region, where the failure origin was located, should be noted as should the low strength of the HAZ, where the major part of the fracture path occurred.

A word of caution should be mentioned regarding the effect of the post heat treat stretching operation on the mechanical properties of the cylindrical case. It is well known that a quenched and tempered steel such as 4340 can undergo significant changes in properties if strained and aged [2]. For example, after a 400 F temper, a tensile strain of 3% followed by an age at any temperature up to 400 F, can lead to an increase in flow stress on yielding of over 100,000 psi over the unstrained value, or 30,000 psi above the flow stress after 3% strain. This strength increase is accompanied by a decrease in ductility and unknown effects on the toughness. The magnitude of the property changes is a function of the prior tempering temperature, the amount of prestrain, and the reheating temperature and time.

In the stretching operation used in manufacturing the missile, the average strain may range up to 3/4%. Because of composition differences and any mechanical discontinuity at the fusion weld, the local strain at any region may be

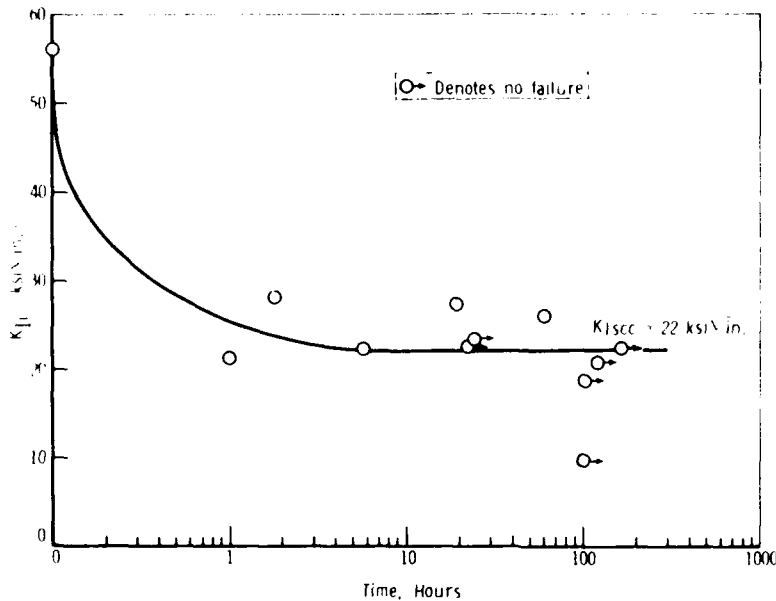


Figure 11. Effect of applied stress intensity on time to failure of motor case material in 3.5% NaCl solution

less or more than 3/4%. Again, during seam welding, temperatures reached in the HAZ may range from room temperature to the melting point. Accordingly, the actual properties in any local region of the case may vary over a considerable range.

ASSESSMENT

It has been shown that for a surface flaw [3], the stress intensity factor at the bottom of the crack can be related to the applied stress σ and the crack dimensions by the following equation:

$$K_{Ic} = \sqrt{1.21\pi} \sigma \sqrt{(a/Q)} \quad (2)$$

where

- a = the crack depth
- Q = a flaw shape parameter, which is a function of the crack depth and length $2c$ and the stress level, and can be obtained from Figure 12.

A schematic plot of Equation (2) is shown in Figure 13. If the applied stress and the flaw size lie below the solid line, fracture would not be expected; but if the combination of the two gives a point above the line, the applied K would be greater than K_{Ic} and catastrophic fracture would be expected. The dotted line gives recognition to the fact that, at low values of flaw size, failure will occur by general yielding.

From this equation, the fracture toughness required to sustain a flaw of the observed dimensions ($a = 0.091$ in., $2c = 0.503$ in.) at the burst stress can be estimated. A stress analysis for the dome end of the second-stage motor case was performed by Patrick and Smith at the U.S. Army Missile Research and Development Command. They found that a sharp maximum in the axial stress in

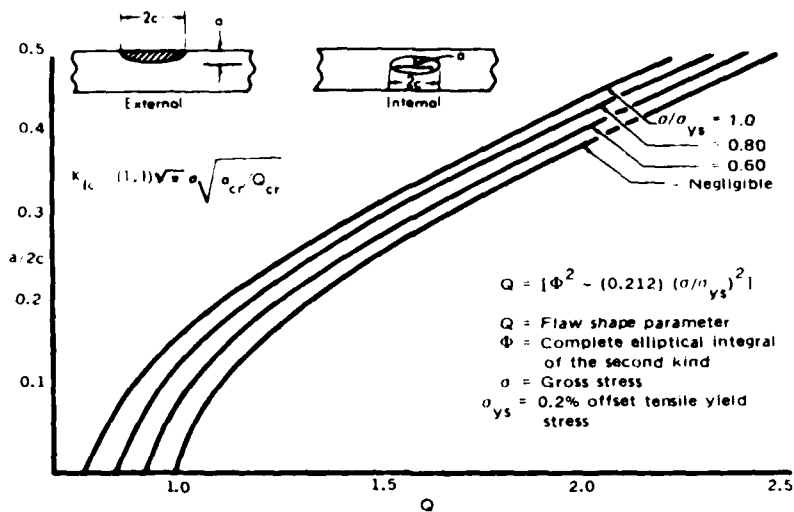


Figure 12. Flaw-shape parameter curves for surface and internal cracks

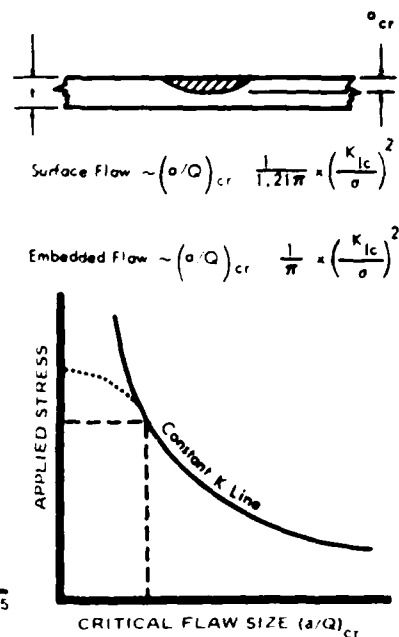


Figure 13. Applied stress versus critical flaw size

the cylindrical case occurred where the dome ended, on the inside wall of the case, i.e., at the observed failure origin. At a hydrostatic test pressure of 1620 psi, with an applied load on the forward skirt of 170,000 lb (8605 ksi), they reported the axial stress to be 127,000 psi. Since the stresses are linear at the observed burst pressure of 1728 psi, the axial stress at the failure origin would be 135,600 psi.

From Figure 12 and the crack dimensions and the yield strength, 212,000 psi, a value of the flaw shape parameter Q of 1.2 is obtained. Accordingly, from Equation 2:

$$K_{Ic} = \sqrt{1.21\pi} (135,600) \sqrt{\frac{.091}{1.2}} = 72,800 \text{ psi in.}^{1/2}$$

The results show that a fracture toughness of 72.8 ksi in.^{1/2} would be required to withstand the observed burst pressure, which is far in excess of the measured toughness of 51.5 ksi in.^{1/2} at the weld or 56.0 ksi in.^{1/2} in the base metal. The failure therefore is not unexpected.

For this weld toughness, failure might have occurred at an axial stress of 95,900 psi, corresponding to an internal pressure of 1220 psi. Alternatively, at the observed burst pressure, the critical flaw size parameter (a/Q) is 0.0379, which corresponds to a crack 0.046 in. deep and 0.253 in. long at an $a/2c$ ratio of 0.18. Thus a crack as short as 0.25 in. long and less than 0.05 in. deep located at this point could cause failure during proof testing.

To ensure against premature failure during proof testing or service, several general suggestions can be made [3]. In general, the case should operate below the solid line in Figure 13. This can be done by either:

- a. reducing the applied stress level during operation or proof testing,
- b. increasing the sensitivity of NDT techniques to detect smaller cracks, or
- c. improving the fracture toughness level K_{Ic} , which would allow larger stress level - flaw size combinations.

The fracture toughness can be increased by several methods. A common method with quenched and tempered steels is to decrease the tensile strength by increasing the tempering temperature, Figure 14 [4]. In this particular application, a reduction of strength level may not be possible without decreasing the safety factor. A second method of increasing the toughness without influencing the strength level is to increase the purity of the steel by reducing certain deleterious elements such as sulfur and phosphorus. Figure 15 shows the effect of sulfur content in the toughness of 4345 steel [5]. The steel used in this particular motor case contained 0.015% sulfur. Lower sulfur contents can be obtained commercially today.

A third method of improving toughness is by substitution of a different steel. The 18% nickel maraging steels generally have higher toughness than low alloy steels such as 4340 [6]. Figure 16 shows the effect of substituting a 250 grade maraging steel with a K_{Ic} value of 80 ksi in.^{1/2} on the applied stress - flaw size relationship. Since the critical flaw size varies with the square of the toughness, a small increase in the toughness can have a sizeable effect on the flaw size that can be tolerated.

In using fracture toughness concepts such as exemplified by Equation (2) and Figure 13, some caution should be exercised. The fact that a component does not have a critical flaw does not ensure that fracture will not occur on subsequent loading. In all materials, a repeated application of a stress will cause crack growth, at a rate governed by the stress level and material properties. Thus repeated loading during service, or even proof testing, can cause a subcritical flaw to grow to a critical size. Too many proof test cycles, or an improper load level during proof testing, can actually cause failure where otherwise no failure would be expected [3].

Another factor which can cause subcritical crack growth is stress corrosion. For stress corrosion cracking to occur, three factors are necessary: a susceptible material, a particular environment, and a stress; a quenched and tempered steel such as 4340 is such a material; water can be a deleterious environment; and the stresses may arise from either applied stresses or residual stresses from heat treatment or welding. The measured value of K_{Isc} of 22 ksi in.^{1/2} indicates that at any stress and crack length combination leading to a K value greater than 22 ksi in.^{1/2}, slow crack growth will occur, until such time as K_{Ic} is attained when rapid failure ensues.

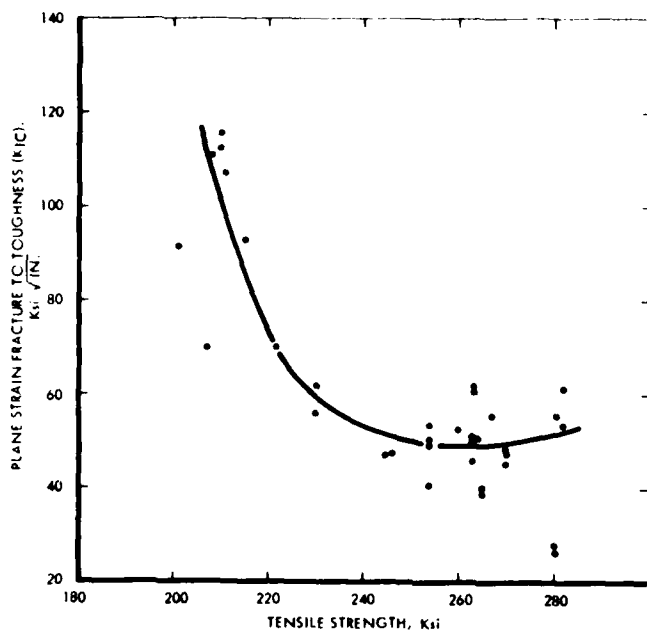


Figure 14. Variation of K_{Ic} with strength level for low alloy martensitic steels (6)

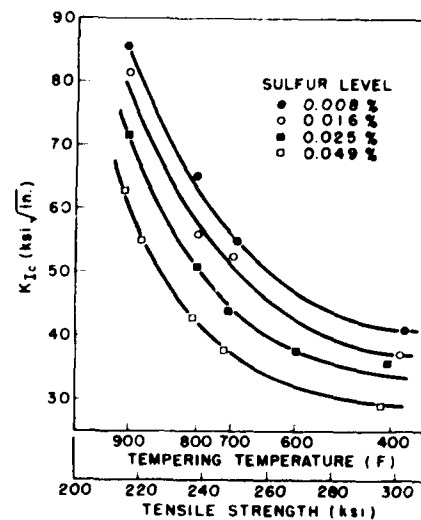


Figure 15. Influence of sulfur level on plane-strain fracture toughness of AISI 4345 steel (7)

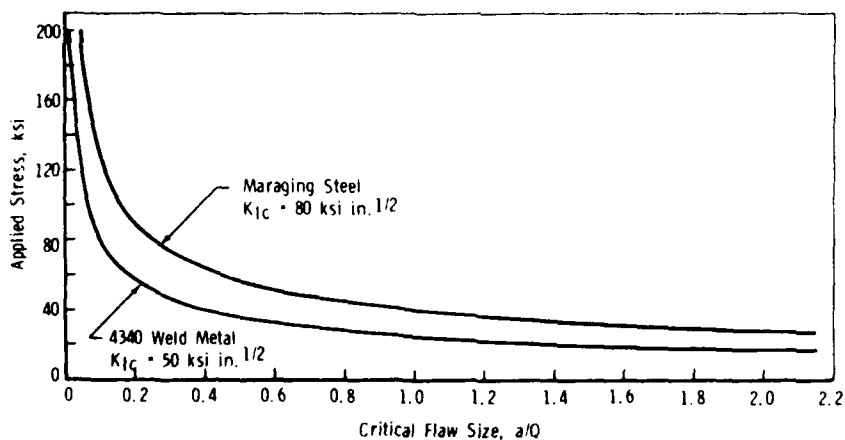


Figure 16. Effect of stress level on critical flaw size for 4340 weld metal and maraging steel

CONCLUSIONS

Portions of a missile second-stage motor case, which failed prematurely during proof testing, have been examined. The fracture origin has been identified. This was a thumbnail-shaped surface crack in the case, about 0.091 in. deep and 0.503 in. long, located at the edge of one of the seam welds, near the intersection with one of the longitudinal fusion welds. Fracture toughness calculations indicated that fracture at the burst pressure should have been expected.

A number of suggestions have been made for improving the present processing procedure for the motor case. Although implementation of these recommendations would improve the integrity of the case, there is no guarantee that a reliable case would be obtained. The use of 4340 steel, tempered at 450 F, and subsequently welded, is not recommended for applications that are highly stressed and where reliability is required.

If welding were carried out prior to final heat treatment, cracking problems would be minimized. Heat treatment after welding would produce a better structure in the welds, with greater toughness and strength. Some distortion problems may be anticipated, but these would be less with maraging steel than with 4340.

ACKNOWLEDGMENTS

The authors would like to acknowledge the helpful discussions with Dr. F. R. Larson, and the assistance rendered by F. L. Carr, heat treatment; W. W. Duffy, metallography; W. F. Czyrkliis, stress corrosion testing; T. S. DeSisto, toughness testing; and H. P. Hatch, welding.

REFERENCES

1. E399-72, Standard Method of Test for Plane-Strain Fracture Toughness of Metallic Materials, 1972 Annual Book of ASTM Standards, Part 31, 955.
2. Stephenson, E. T. and Cohen, M., "The Effect of Prestraining and Re-tempering in AISI Type 4340", Trans. ASM, v. 54, 1965, 72.
3. Tiffany, C. F. and Masters, J. N., "Applied Fracture Mechanics", Fracture Toughness Testing and Its Applications, ASTM STP No. 381, 1965, 249.
4. Steigerwald, E. A., "Crack Toughness Measurements of High-Strength Steels", Review of Developments in Plane Strain Fracture Toughness Testing, ASTM STP No. 463, 1970, 102.
5. Wei, R. P., "Fracture Toughness Testing in Alloy Development", Fracture Toughness Testing and Its Applications, ASTM STP No. 381, 1965, 279.
6. Damage Tolerant Design Handbook, MCIC-HB-01, Metals and Ceramics Information Center, December 1972.

IDENTIFICATION AND CONTROL OF FRACTURE
CRITICAL SOLID ROCKET BOOSTER (SRB) STRUCTURE

D. W. O'Neal, D. A. Deamer, R. M. Fujita and E. V. Wysocki
McDonnell Douglas Astronautics Company
5301 Bolsa Avenue, Huntington Beach, California 92647

(Work Sponsored by NASA Marshall Space Facility Center)
under Contract No. NAS8-31732

INTRODUCTION

The Solid Rocket Booster (SRB) stage of the NASA Space Shuttle Vehicle represents America's first reuse of a major launch vehicle booster. After the SRB performs its launch function, the two spent SRB structures are separated, parachuted into the ocean, recovered and towed back to the launch site by ship, and refurbished for future launches.

Marshall Space Flight Center (MSFC), the responsible NASA agency, was concerned about fracture control of the reusable SRB stage and drafted a Fracture Control Plan [1] for the SRB. One section of this plan required a fracture mechanics and fatigue analysis to determine the fracture criticality of all SRB parts. The analysis of SRB primary structure other than the solid rocket motor was contracted to McDonnell Douglas Astronautics Company (MDAC), and is the principal subject of this case study. A secondary, but closely related activity, involved the assessment of possible stress corrosion cracking in SRB structure. Only highlights of this activity will be covered.

This case study presents an approach to screen more than 1,400 SRB structural parts and identify which of these parts are potentially fracture critical. All parts identified as potentially fracture critical were subjected to in-depth linear elastic fracture mechanics analysis. Parts identified as fracture critical by analysis were again reviewed for new or additional non-destructive evaluations (NDE) to remove them from the fracture critical parts list. Any parts remaining after the screening process were identified and controlled as described in [1].

SRB structure will be subjected to 40 uses or missions. Using a factor of four for fracture analysis purposes, a lifetime of 160 missions was assumed per [1]. A mission consisted of the following design conditions:

<u>Condition</u>	<u>Approximate Flight Time</u>
Prelaunch	-
Lift-off	0 sec.
High dynamic pressure boost	40-60 sec.
SRB maximum acceleration	110 sec.
Pre-SRB staging	122 sec.
Reentry	Post separation
Parachute	(19,000 - 9,000 feet)
Water impact	-
Towback	-

Subsequent to the mission, SRB structure will be partially disassembled, inspected, and refurbished before the structure is certified for another mission.

Since the SRB is a new stage, no history was available to identify any fracture suspect designs. Another factor complicating the fracture analysis was that MDAC was not involved in the design and analysis of the SRB. MSFC was responsible for the design and stress analysis of the SRB structure.

FORMULATION

Screening of SRB Structural parts involved two major tasks. The first task included an in-depth drawing review and an assessment of part failure on mission success. Each SRB drawing was reviewed for the part material, surface and/or internal inspection requirements, part function, any redundant load paths that existed, mission effect due to loss of the part, and stress corrosion susceptibility. Mission effects were simplified into three categories: (1) Mission loss; (2) Unknown - Possible mission loss; (3) No mission loss. If no mission loss resulted from failure of a particular part, the review was terminated at that point and the part was identified as being non-fracture critical.

The second task was to review available stress analyses and establish the maximum tensile stress experienced by the part along with corresponding temperature. The maximum tensile stress was designated as σ_{op} . All stress analyses were supplied by MSFC. In the absence of stress analysis for a particular part, σ_{op} was established by selecting the lower of the following two design values: Allowable ultimate tensile stress divided by the design ultimate factor of safety ($F_{tu}/1.40$), and allowable yield tensile stress divided by the design yield factor of safety ($F_{ty}/1.10$). The maximum tensile stress was used to calculate allowable flaw sizes, as described in the Assessment section of this paper.

The foregoing information was collected on the survey form shown in Figure 1. This form summarized all pertinent design and analysis information, reduced recording time, and documented the information for future reference. Even when design changes were frequent, it was found that the survey form saved time because it contained information pertinent to the latest change.

Many different materials were involved in the parts which were surveyed. Material forms included sheet, plate, bar, extrusion, forging, and weld. Examples of material types were 2219 aluminum, 6061 aluminum, Inconel 718, A-286 corrosion-resistant steel, D6AC steel, MP35N multiphase alloy, 4130 steel, and 4140 steel. Material thicknesses varied from approximately 0.10 inch to 5.25 inches. Since 2219-T87 aluminum was predominantly used in the SRB, this material was selected for discussion in the ensuing parts of this paper. Plane strain fracture toughness, K_{Ic} , values for 2219-T87 aluminum alloy were as follows:

SAMPLE

FIGURE 1 SRB FRACTURE MECHANICS & FATIGUE ANALYSIS

PART NO.: 19A10XXX, REV. A PART NAME: INBOARD CAP SPICE, INTERM. RING, N/A: 19A11XXX
 MATERIAL: 2219-T87 AL ALLOY (88-A-25D/30) (FRUSTUM)
 INSPECTION REQ'D: ULTRASONIC INSPECTION PER MIL-I-8830B CLASS A NO SURFACE INSPECTION.*

REDUNDANT LOAD PATHS: NONE.	FUNCTION: INBOARD ANGLE SPICE FOR INTERMEDIATE RING.
MISSION EFFECT FROM PART LOSS: UNKNOWN - POSSIBLE MISSION LOSS.	ACCESSIBILITY: ONE SURFACE OF SPICE IS ACCESSIBLE FOR INSPECTION.
INSTALLATION STRESSES: LOW KSI HOLES DRILLED ON ASSEMBLY.	SUSTAINED TENSILE STRESSES: LOW KSI DUE TO IG LOADING.
S.C. THRESHOLD STRESS: 38.0 KSI (MIL-HBK-S) ACCORDING TO NASA/MSFC DWG/OMB3107, THIS MAT'L HAS HIGH RESISTANCE TO S.C. CRACKING.	S.C. EVALUATION: NO S.C. CRACKING PROBLEM.
CRITICAL DESIGN CONDITION: A. PRE-LAUNCH THRU SEPARATION: NOT CRITICAL MAX. TENS. STRESS (KSI): - TEMP (°F): - B. POST SEPARATION THRU RECOVERY: WATER IMPACT MAX. TENS. STRESS (KSI): 30.0 TEMP (°F): 75 (FROM R-27, SEE ATTACHED ANALYSIS)	
K_{Ic} = <u>NOT APPLICABLE</u> (KSI√IN.) RULE $d_0/dN = 2 \times 10^{-4}$ (IN./CYCLE)	ALLOWABLE FLAW SIZE (IN.) CRITICAL INITIAL MAXIMUM (INSP.) b _{cr} z _{cr} a ₁ z ₀₁ a _{max} z _{cmax}
	LOCATION Q SURFACE 1.0 0.085 0.723 0.053 0.449 * * INTERNAL 2.0 0.162 0.380 0.130 0.304 * * 1.0 0.120 0.512 0.056 0.237 0.047 < 1.000 2.0 0.230 0.269 0.166 0.194 0.078 0.078
DESIGN LIFETIME = 160 (CYCLES)	NOTE: FOR INTERNAL FLAWS, "a" REPRESENTS "2a".
DISPOSITION: NO STRESS CORROSION CRACKING PROBLEM EXISTS. SINCE THE SURFACE (Q=1.0 AND 2.0) ALLOWABLE INITIAL FLAW LENGTHS ARE RELATIVELY SMALL (LESS THAN 0.500 IN.), THE PART IS CONSIDERED TO BE FRACTURE CRITICAL. RECOMMEND FLUORESCENT LIQUID PENETRANT INSPECTION BEFORE ASSEMBLY.	

R

SOP
9/16/77
(21)

Table I - Fracture Toughness
For 2219-T87 Aluminum Alloy

Material Form	Avg. K_{Ic} (ksi $\sqrt{in.}$)		
	R.T.	200°F	300°F
◦ Sheet & Plate	30.0	28.1	25.3
◦ Extrusion (T8511), Forging (ST Dir.) and Weld	20.0	18.0	16.0

(From MSFC [2] and [3].)

This study made use of available cyclic data in two forms. Whenever possible, initial screening of a 2219 aluminum part was accomplished using the cycle life curve in [4], Figure 14, which shows normalized initial stress intensity, K_{Ii}/K_{Ic} , as a function of cycles to failure, N . Engstrom [4], Table 7, shows a sustained load threshold stress intensity, K_{TH} , of about $0.85 K_{Ic}$ for 2219-T87 aluminum at room temperature. To ensure that SRB parts were not susceptible to flaw growth from sustained load, the cyclic life of 50 cycles at $K_{Ii}/K_{Ic} = 0.85$ was added to the design life of 160 cycles. The resulting 210 cycles corresponded to $K_{Ii}/K_{Ic} = 0.76$, and was the basis for constructing allowable initial flaw size curves similar to Figure 2. For surface flaws, the equation used was,

$$(a/Q)_i = \frac{1}{1.21\pi} \left(\frac{0.76 K_{Ic}}{\sigma_{op}} \right)^2 \quad (1)$$

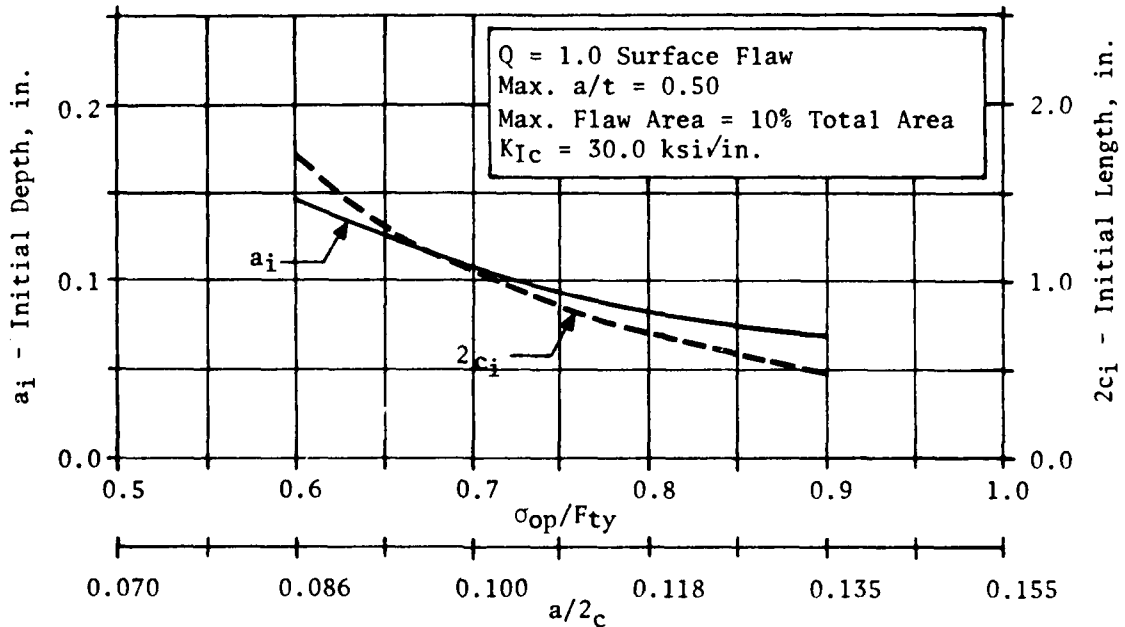
a = flaw depth
 Q = flaw shape parameter

Flaw length, $2c$, was also determined from Figure 2, based on Figure 1 of [5] at the appropriate Q and σ_{op}/F_{ty} . Similar curves were constructed for internal flaws by using 1.00π in the denominator. These curves permitted an analyst to quickly determine allowable initial flaw sizes from the applied stress and saved many hours of repetitive calculations.

The other form of cyclic data was flaw growth rate, da/dN , as a function of stress intensity. These data [6] were used when the critical flaw area exceeded 10 percent of the part cross-sectional area and when an in-depth analysis was performed on a potentially fracture critical part.

Potentially fracture critical parts subjected to high cyclic loadings for more than one design condition were analyzed with the MSFC crack growth computer program [7]. Three empirical flaw growth options were available in the program; Paris, Foreman, and Collipriest-Ehret. The Collipriest-Ehret

Figure 2 - 2219-T87 Parent Metal @ 75°F



equation was used for all calculations in this study. Equation constants were supplied by NASA/MSFC from test data on other Shuttle programs.

In order to assess the criticality of the allowable initial flaws, comparisons were made to maximum flaw sizes that could remain in a particular part after inspection. Methods of inspection delineated on SRB drawings or in material specifications included visual, liquid penetrant, ultrasonic, and radiographic. No proof tests were specified. Acceptance criteria were contained in the following specifications: QQ-A-250/30, Federal Specification, Aluminum Alloy 2219, Plate and Sheet; MIL-I-8950, Inspection, Ultrasonic, Wrought Metals; MSFC-SPEC-504, Specification, Welding, Aluminum and Aluminum Alloys.

ASSESSMENT

Criticality assessment of SRB hardware was conducted using procedures outlined in the SRB Fracture Control Plan [1]. The plan required a review of all hardware drawings, evaluation of mission effects in the event failures occur, and consideration of design stresses and required service lives with the purpose of deciding whether parts were or were not fracture critical.

Parts that had a service life factor of greater than 4.0 times the vehicle life cycle requirements were not fracture critical and did not require any fracture control. Parts that had a service life factor of less than 2.0

were designated for redesign. Parts that had a service life factor between 2.0 and 4.0 were considered to be fracture critical. These parts were either designated for redesign or recommended to the Fracture Control Board for fracture control implementation.

A previously described survey form (see Figure 1) summarized all pertinent information related to the fracture analysis. The form listed calculated critical and initial flaw sizes, allowable flaw sizes from specified inspections and the final disposition of the part based on evaluation of the tabulated data.

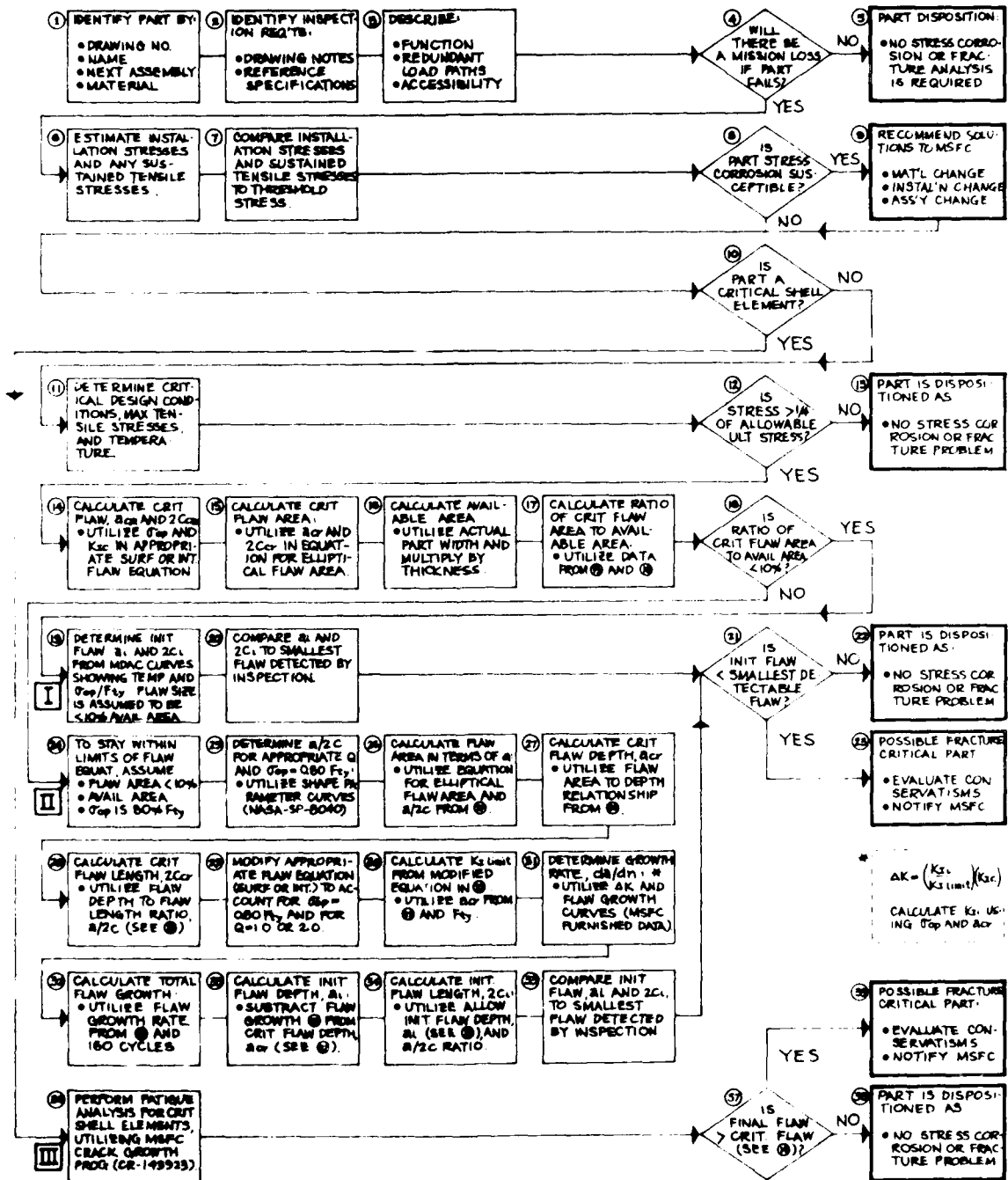
The flow chart shown in Figure 3 illustrates the logic used for assessment of stress corrosion and fracture criticality. Components such as nonmetallic gaskets, metallic washers, spacers, etc., whose failure would not affect the mission, were eliminated early in the review (steps 1 thru 5). Stress corrosion cracking (steps 6 thru 9) was evaluated on the basis of design criteria contained in MSFC document 10M33107 [8]. The evaluation considered material susceptibility to stress corrosion, service environment, and sustained tensile stresses resulting from fabrication, assembly, and/or prolonged operation or storage. Threshold stresses, to which the sustained tensile stresses were compared, were taken from [9].

Next, a determination was made as to whether the part was an element subjected to high cycles from multiple load conditions (step 10). A supplemental fatigue analysis was conducted for these high cycle parts (step 36), utilizing the NASA/MSFC Crack Growth Analysis Program [7], to account for a fatigue load spectrum that included both the prelaunch, flight, and post separation cycle requirements for 160 flight missions. MSFC supplied the fatigue load spectrum in tabular form with steady state and cyclic loads listed for each design condition.

When no high cycle part was involved, a review was made of the maximum design tensile stress. Whenever the stress was less than one-fourth of F_{tu} , the part was dispositioned as not fracture critical (step 13). This stress limitation was based on the flaw growth rate for 2219-T87 aluminum at this stress being less than 10^{-5} inches per cycle. For 160 cycles, less than 0.002 inch of flaw growth would occur. Historically, designs based on a factor of safety of 4.0 have been widely used for commercial applications with very high reliability without considering cyclic loads.

When the stress exceeded one-fourth of F_{tu} , calculations were made to determine the critical flaw size and ratio of the critical flaw size area to the total cross-section area of the element being analyzed (steps 14 thru 17). When this ratio was less than 10%, it was concluded that linear elastic theory applied, and the K_{Ic} value used in the analysis was valid (step 18). Initial flaw sizes were then determined using curves similar to Figure 2, as explained in the Formulation Section. These curves were drawn for two extreme flaw shape parameters, $Q = 1.0$ and $Q = 2.0$, to expedite the analysis. The maximum permissible ratio of flaw depth to part thickness was limited to 0.50 since higher ratios would require the application of a stress-

FIGURE 3 FRACTURE MECHANICS ANALYSIS LOGIC



intensity magnification factor (M_k).

Allowable initial flaw sizes were then compared to the maximum flaw sizes permitted by the specified NDE inspection (step 21) to disposition the part for fracture criticality (steps 22 and 23).

At step 18, if the critical flaw area was greater than 10% of the section area, a modified fracture analysis approach was taken to determine the critical and initial flaw sizes. Area of the critical flaw was limited to 10% of the section being analyzed, and the maximum operating stress was assumed to be 80% of the allowable yield stress. These values represent maximum values for application of linear elastic fracture mechanics theory and were used to define a limiting stress intensity. The following example illustrates the application of this approach. (See steps 24 thru 34).

Example: (Surface Flaw, $Q = 1.0$)

Part	: Splice, 1.94 in. x 0.25 in.	F_{ty}	: 51,000 psi @ R.T.
Material	: 2219-T87 Al Alloy	K_{Ic}	: 30,000 $\text{psi}\sqrt{\text{in.}}$ @ R.T.
Max Tension:	30,000 psi @ R.T.	A_{sect} :	$(1.94)(0.25) = 0.485 \text{ in.}^2$

From Figure 2, at $\sigma_{op}/F_{ty} = 0.60$,

$$a_i = 0.146 \text{ in. and } 2c_i = 1.70 \text{ in.}$$

$$A_{flaw_i} = (0.785)(a_i)(2c_i) = 0.195 \text{ in.}^2 \quad (2)$$

Since the critical flaw area, A_{flaw} , is greater than A_{sect} (10%), linear elastic theory has been exceeded. The modified 10% area method will be used.

$$A_{flaw} = A_{sect} (10\%) = 0.0485 \text{ in.}^2 \quad (3)$$

$$\sigma_{limit} = 0.80 F_{ty} = 40,800 \text{ psi} \quad (4)$$

From Figure 2 for $\frac{\sigma_{limit}}{F_{ty}} = 0.80$ and $Q = 1.0$, $\frac{a}{2c} = 0.118$ or $2c = 8.47a$.

For critical flaw depth and length, a_{cr} and $2c_{cr}$,

$$A_{flaw} = 0.785 (a_{cr})(2c_{cr}) = 6.65a_{cr}^2 = 0.0485 \text{ in.}^2 \quad (5)$$

and $a_{cr} = 0.085 \text{ in. and } 2c_{cr} = 0.723 \text{ in.}$

Introduce a stress intensity factor, K_I limit, which is consistent with $\sigma_{limit} = 0.80 F_{ty}$,

$$K_I \text{ limit} = 1.1(\sqrt{\pi}) (\sigma_{limit}) \left(\frac{a_{cr}}{Q} \right)^{1/2} \quad (6)$$

Assume conservatively that the following relationships hold,

$$K_{Ii} = 1.1 (\sqrt{\pi}) (\sigma_{op}) \left(\frac{a_{cr}}{Q} \right)^{1/2} \quad (7)$$

$$\frac{K_{Ii}}{K_{I \text{ limit}}} = \frac{\Delta K}{K_{Ic}} \quad (8)$$

or

$$\Delta K = \left(\frac{\sigma_{op}}{\sigma_{limit}} \right) (K_{Ic}) = 22,500 \text{ psi } \sqrt{\text{in.}} \quad (9)$$

From Figure 1 of [6], at $\Delta K = 22,500 \text{ psi } \sqrt{\text{in.}}$, $\frac{da}{dN} = 2 \times 10^{-4} \frac{\text{in.}}{\text{cycle}}$.

For 160 cycles,

$$a_i = a_{cr} - \Delta a = 0.085 - 160 \times 2 \times 10^{-4} = 0.053 \text{ in.} \quad (10)$$

$$2c_i = (8.47) (a_i) = 0.449 \text{ in.} \quad (11)$$

Calculated initial flaw sizes were then compared to the maximum flaw limits permitted by the NDE inspections (steps 21 and 35), and a disposition was made as to whether the part was fracture critical or not. The survey form in Figure 1 shows entries for the above example.

Final disposition of a part was based on consideration of all survey results. Susceptibility to stress corrosion cracking was reviewed and susceptible parts were flagged as being potentially fracture critical. Calculated initial flaw sizes were compared to the flaw limits permitted by the specified NDE inspection. When allowable initial flaws were greater than inspection limits, unacceptable flaws would be rejected so the part was not fracture critical. When initial flaws were smaller than the inspection limits, unacceptable flaws could exist so the part was dispositioned as potentially fracture critical.

All parts flagged as potentially fracture critical received additional attention. Since the screening analyses intentionally contained conservative approaches, conservatisms were evaluated and eliminated whenever possible. If the part was still potentially fracture critical, MSFC was notified.

Some thin parts and those made from extrusions were not subjected to an inspection. In the absence of inspection limits, engineering judgment was used to disposition these parts. Parts with initial surface flaw lengths less than 0.500 in. were dispositioned as requiring a liquid penetrant inspection following forming or machining and prior to assembly.

Parts considered to be marginal and accessible in the assembled structure were dispositioned with a recommendation for periodic inspections in service. All potentially fracture critical parts were subsequently reviewed by members of the MSFC Fracture Control Board.

Parts containing holes were analyzed with the procedure outline in [10] and [11]. At holes and cutouts, an initial flaw was assumed to be 0.050 inch through the thickness flaw at one side of the hole when the material thickness was equal to or less than 0.050 inch. The initial flaw for greater thicknesses was a 0.050 inch corner radius flaw at one side of the hole. With these assumptions, fracture mechanics analyses were performed using equations in [11], Tables 28 and 29.

Only one hole was identified as potentially fracture critical with this analysis. Since these areas are highly suspect, either the relatively small number of design cycles (160) is essentially negligible or possibly the assumptions and analysis are unconservative. In-service inspections after each Shuttle flight should identify any subsequent problems.

An MSFC supplied computer program, [7], was utilized to perform high cycle fatigue analyses of primary SRB parts subjected to cyclic loads for several load conditions, i.e., skin panels, rings, welds, and attach struts. Basic program input consisted primarily of part description, maximum number of SRB flights, stress influence coefficients, loads, geometry, material properties, description of initial flaw, selection of crack growth equation, and crack growth equation constants. The Collipriest-Ehret equation was used for all crack growth.

The crack growth program consisted of the following main steps:

- Consideration of each load condition within each flight in turn.
- Evaluation of stress intensity factors, using the appropriate stress for each load condition under consideration.
- Calculation of crack growth rate based on the stress intensity factors.
- Calculation of growth crack depth and length.

The calculation ended when one of the following events occurred:

- Critical stress intensity at either the crack surface or depth was exceeded. (Failure.)
- No crack growth occurred for an entire mission ($<10^{-8}$ inch). (No chance of failure).
- The required 160 flights were exceeded. (No failure.)

Since the forward skirt is attached to the External Tank (ET) at only one location, a subroutine was added to the program to input launch and ascent SRB/ET ball loads at the forward skirt attachment and to determine principal stresses. Stress coefficients within the forward skirt were available from a MSFC-generated SPAR computer model with axial, radial and tangential

unit loads applied at the SRB/ET ball. These coefficients were multiplied by the applied ball loads to obtain applied stresses. Applied stresses were then resolved into principal stresses for regular input into the flaw growth program. Only crack opening failure modes were considered in the analyses, but maximum tensile stresses for every condition were always conservatively assumed normal to the flaw plane, irrespective of principal stress direction.

The computer program output included the following information: A description of input data; surface crack half-length; crack depth; stress intensity factors at the surface and depth of the crack; surface growth rate; crack depth growth rate. Output was only printed every tenth flight for each load condition to limit output volume.

The forward skirt ring at Station 401 is a typical part which was analyzed by the computer program. The ring was made from 2219-T852 aluminum forging whose cross-section was comprised of a web and caps. Load spectrum and other pertinent input data are shown in Table II and III. The high cycle fatigue analysis showed that both the cap and web of the Station 401 ring were structurally adequate for 160 flights. The final flaw size was $a = 0.141$ inch and $2c = 1.007$ inch for the thinner 0.200 inch web.

CONCLUSIONS

Conclusions and observations of this study can be summarized as follows:

- Identification of potentially fracture critical parts in large structural assemblies is possible with simplified, conservative fracture analyses.
- The MSFC crack growth computer program [7] is a useful tool for analyzing structure subjected to a fatigue spectrum.
- Restricting critical flaw areas to 10 percent of the cross-sectional area is necessary when gross area stresses are used. Use of plane stress fracture toughness, when available, will eliminate some of the conservatism associated with analysis by this proposed method, since most of these parts are thin.
- Fracture mechanics analyses should be performed in the early design phase of single-load path and life-limited parts to identify pre-assembly quality control measures.
- Fracture mechanics will not solve all fracture problems. Engineering judgment is still a necessity in some instances.

Table II - Load Spectrum For Station 401 Ring
(Loads Applied at SRB/ET Ball)

Load Cond.	X-Dir. Load		Y-Dir. Load		Z-Dir. Load		Cycles (No./FLT)	Press. (psi)	Temp. (°F)
	Steady State (kips)	Oscil- lations (kips)	Steady State (kips)	Oscil- lations (kips)	Steady State (kips)	Oscil- lations (kips)			
Pre-Launch Empty	165	0.0	-86.0	10.0	74.0	8.0	20	0.0	70
Pre-Launch Empty	165	0.0	-7.0	0.7	6.0	0.6	2.75 x 10 ⁶	0.0	70
Pre-Launch Full	950	0.0	-37.0	4.0	32.0	4.0	20	0.0	70
Pre-Launch Full	950	0.0	-6.1	0.5	5.5	0.5	0.20 x 10 ⁶	0.0	70
Liftoff	1,000	396.0	-68.0	152.0	0.0	184.0	32	2.0	70
Max. Q	790	139.0	71.0	8.0	-32.0	3.0	70	11.6	140
Max. G	1,650	0.0	-115.0	0.0	75.0	0.0	1	11.6	212
Pre-SRB Sep.	-181	0.0	12.0	0.0	-12.0	0.0	1	14.7	300
D.C. Deploy.	11	0.0	0.0	0.0	0.0	0.0	1	0.0	300
Water Impact	10	0.0	0.0	0.0	0.0	0.0	1	0.0	212

(From MSFC Memorandum ED22-76-16, dated 18 March 1976)

Table III - Input Data For Station 401 Ring

Location Checked	Max. σ_{op} (ksi)	Max. Load Cond.	F_{ty} (ksi)	Available Area		Initial Crack Size*	
				w (in.)	t (in.)	a (in.)	$2c$ (in.)
Cap	18.00	Liftoff	35.00	3.00	0.500	0.078	1.00
Web	18.00	Liftoff	35.00	12.90	0.200	0.078	1.00

*Class B Ultrasonic Inspection per MIL-I-8950.

Analyses are still being performed at this time, but recommendations have been made to MSFC on some potentially fracture critical parts. Most SRB parts are subjected to quality ultrasonic inspections in stock form. When surface flaws caused problems, liquid penetrant inspections before assembly were often recommended to assure design life. Parts critical for unmanned load conditions and manned conditions with detectable critical flaws were considered for periodic in-service inspections with decisions dependent on cost, part accessibility and coating, and required type and frequency of inspection. On rare occasions, since MSFC designers were conscious of fracture control, a change in material or redesign was recommended. A proof test is presently being considered for a single load path assembly with several critical parts.

In summary, options available to remove parts from the critical list are redesign, rigorous non-destructive evaluation, restricted use, proof test or properly scheduled in-service inspections.

REFERENCES

1. MSFC SRB Fracture Control Plan, SE-020-002-2H, June 17, 1974.
2. MSFC Memorandum EE11 (75-468), "Minutes of SRB Fracture Control Board (FCB) Meeting", 21 October 1975.
3. MSFC Memorandum EH23 (76-203), "Updated SRB Material Properties", 9 November 1976.
4. Engstrom, W. L., "Determination of Design Allowable Properties, Fracture of 2219-T87 Aluminum Alloy", NASA CR-115388, March 1972.
5. NASA Design Criteria Document SP-8040, "Fracture Control of Metallic Pressure Vessels", May 1970.
6. MSFC Memorandum EH23 (76-11), "SRB Material Properties", February 1976.
7. Creager, Matthew, "MSFC Crack Growth Analysis Computer Program", NASA CR-143923, September 1975.
8. "Design Criteria for Controlling Stress Corrosion Cracking", MSFC Drawing 10M33107B, 20 August 1975.
9. "Metallic Materials and Elements for Aerospace Vehicle Structures", MIL-HDBK-5, 31 August 1973.
10. Military Specification - Airplane Damage Tolerance Requirements, MIL-A-83444 (USAF), 2 July 1974.
11. "Fracture and Fatigue Crack Growth Behavior of Surface Flaws and Flaws Originating at Fastener Holes", AFFDL-TR-74-47, Vol. 1, May 1974.

THE INFLUENCE OF FRACTURE MECHANICS
ON FAIL-SAFE DESIGN OF A LARGE SPACE STRUCTURE

James Gorman

Research Assistant, Aeroelastic and Structures Research Laboratory, MIT
Cambridge, MA 02139

Thomas R. Stagliano

Research Assistant, Aeroelastic and Structures Research Laboratory, MIT
Cambridge, MA 02139

Oscar Orringer

Associate Director, Aeroelastic and Structures Research Laboratory, MIT
Cambridge, MA 02139

John F. McCarthy, Jr.

Professor and Director, Center for Space Research, MIT
Cambridge, MA 02139

INTRODUCTION

The promise of reduced transportation costs to earth orbit and the potential for harnessing vast quantities of solar energy has revived interest in concepts of large space structures. The kinds of structures envisioned range from radio telescope antennas and solar arrays [1] to self-sufficient industrial communities in high orbit about the earth [2,3,4]. In the proposals publicized to date, two basic scenarios have been advanced to describe the direction of the space program in the period following the introduction of the space shuttle. The first proposes that both the material resources and manpower required for further ventures into space will be provided wholly from earth for the foreseeable future [5]. This concept involves the transportation of large masses from the surface of the earth to orbit, and manned missions of limited duration. The second scenario proposes that a bridgehead in space be established by the immediate fabrication of large structures from lunar or asteroidal material [4,6]. This requires the deployment of basic refining and manufacturing facilities in space at an early date in the overall program, and demands the provision of a permanent habitat in space for a substantial workforce. This paper addresses the problem of constructing a space habitat.

The work presented here was done in an advanced systems design class sponsored by the Department of Aeronautics and Astronautics at MIT in the Spring of 1976. The problem considered was the design of a prototype space habitat capable of supporting 1000 inhabitants. This limitation on the size of the structure was formulated as a compromise between the competing goals of rapid system deployment and similarity to the very large habitats being discussed in the current literature [2,3]. The location of the structure (the trailing Lagrange point of the Earth/Moon system, L5) has little bearing on the analysis required, as long as the habitat lies outside the radiation shielding provided by the earth's magnetosphere.

Certain basic criteria must be imposed upon the design of a structure providing permanent life support for a human population in the space environment. In addition to an atmosphere, thermal control, sustenance, and protection from micrometeoroids, the permanent aspect of this project requires the provision of radiation shielding, pseudogravity, a viable agriculture, and all the support services normally found in a small town on earth. Inherent in the above requirements and necessary for the psychological health of the inhabitants is the provision of an habitable volume for each individual far greater than that achieved in the previous history of the space program. Finally, it is necessary to consider the fact that a failure in the basic integrity of the proposed structure would have catastrophic consequences. Thus, such damage as might be encountered in the operation of a habitat, whether due to manufacturing defects or accidents, must be limited in its effect and repairable.* These criteria demonstrate that a fracture-mechanics assessment is an important part of the preliminary engineering design.

BASIC CONFIGURATION AND FABRICATION CONCEPTS

The midsection of the habitat is a cylinder with a radius of 100m and length equal to 100m. This midsection is closed by spherical caps of 100m radius. The habitat thus has the same diameter (200m) but is much shorter than O'Neill's "Model I" (1 km long) [2]. A rotation rate between 2 and 3 RPM about the cylinder axis provides 0.5 to 1 pseudo-"g" at the cylindrical surface. The pressure hull is subjected to biaxial tension due to both internal pressure and centrifugal loading.

Structural design of the pressure hull was based on existing steel and aluminum alloys. The deployment scenario assumed that the moon would be the principal source of raw material, and that refining facilities would be available at L5 to process the pressure hull alloys. The slag residue from the refinery would be used for the required radiation shielding (area density = 5000 kg/m^2 [7]). Calculation of the material requirements indicated that no significant structural mass constraint was necessary, since at least 10^9 Kg of slag were required for the shield. This estimate was based on lunar surface composition, as determined by analysis of Apollo samples [9]. The composition data, summarized in Table I, also show that the lunar surface is deficient in certain important alloying elements, notably carbon, nickel, and molybdenum. Approximately 2500 metric tons of these elements must be brought from earth to L5, together with an estimated 7470 tons of refining and metal-working equipment to establish a construction facility.

The fabrication scenario assumed that the O'Neill electromagnetic mass-launcher [3,6] would be available for transportation of raw material from the lunar surface. Various spacecraft including the NASA shuttle, shuttle derivatives, and "space tugs" were also assumed operational. Viability of a manned construction site at L5 was a further assumption, but the preliminary details

* The reader interested in additional background information should consult Refs. 7 and 8.

Table II Mass and Power Requirements for Construction Site

	Mass (Metric Tons)	Power (Kilowatts)
Construction shacks	316	---
Contents of first shack:		
Refinery	835	46,000
Contents of second shack:		
Blooming mill	2,700	5,000
Contents of third shack:		
Plate mill	1,300	2,500
Plate rolling machines	18	54
Contents of fourth shack:		
Billet mill	1,200	2,200
Light section mill	700	1,400
Fastener and nut machines	8	24
Major stiffener	24	72
milling machines	12	36
Minor stiffener		
milling machines		
Contents of fifth shack:		
Lay-up bed	312	100
ER welding heads	?	200
Drilling heads	42	112
Living quarters		
(Power = 10 kW/person)	134	1,600
Frame, crane, mast, and boom	2,740	1,000
Power plant (10 in Kw/kw)	603	---
TOTAL	10,946T	60,288KW

Table I Composition of Lunar Rock and Soil

Average compositions of rocks and soils returned by Apollo missions, excluding oxygen (43%) and elements present in amounts less than 1000 ppm.

Rock	Apollo 11	Apollo 12	Apollo 14	Moon 15	Apollo 16
Al	4.55	6.77	11.34	4.57	14.44
Fe	14.69	13.52	6.25	16.85	16.45
Ti	1.31	1.90	1.60	1.32	1.26
Si	18.73	22.00	20.20	21.63	21.47
Mg	4.67	4.11	4.43	4.31	3.44
Mn	1.19	1.17	1.53	1.33	1.39
Cr	1.25	1.21	1.15	1.33	1.19
Ca	1.77	2.16	2.14	1.74	1.15
Na	1.34	1.47	1.22	1.23	1.12
K	1.25	1.06	1.40	1.22	1.12
P	1.29	1.21	1.15	1.14	1.13
Soil					
Al	7.36	7.14	4.11	9.04	14.11
Fe	11.23	11.04	5.11	11.11	4.11
Ti	4.46	2.09	1.14	1.21	1.11
Si	19.63	21.61	22.11	21.11	21.11
Mg	4.76	5.11	5.11	4.11	3.11
Mn	1.16	1.16	1.11	1.11	1.11
Cr	1.20	1.11	1.11	1.11	1.11
Ca	1.59	1.51	1.11	1.11	1.11
Na	1.33	1.44	1.11	1.11	1.11
K	1.12	1.11	1.11	1.11	1.11
P	1.11	1.11	1.11	1.11	1.11

From J. L. Paster, et al., "Composition of Lunar Rocks Returned by Apollo 11-16 Samples," Proceedings of the Fourth Lunar Science Conference, Vol. 2, pp. 1111-1115.

Additional data in oxide weight percent.

of this facility were developed in parallel with the pressure hull design to enforce realism on the fabrication scenario. This procedure functioned as a constraint on the structural design, and resulted in the rejection of vapor deposition and deposition/filament-wound composite construction, concepts which had appeared promising based on structural calculations alone. Plate/stiffener construction similar to the construction of a ship hull was finally chosen as the scheme most compatible with recognized metalworking techniques. Some details of the construction equipment requirements are summarized in Table II. The fabrication scheme (indicated schematically in Fig. 1) involves refinement of ore, rolling and cutting of 1m x 1m plate, and production of other stock parts (stiffeners, fasteners, etc.) in a series of four construction "shacks" attached to a large trusswork frame. These stock parts are pre-assembled by electron-beam welding to form major sections of the pressure hull (20m x 20m) in a fifth "shack." The major sections are then delivered to the hull and held in place for final assembly by large cranes which traverse the frame structure.

STRUCTURAL DESIGN

We preface our review of the pressure hull design with a brief summary of how the final concept evolved. The hull began as a single skin supporting both the pressure load and the centrifugal load of the various internal masses. The 5000 kg/m² radiation shield was initially conceptualized as a separate, low strength, nonspinning structure surrounding the space habitat. A fail-safe approach quickly dominated the pressure hull design when the possible effects of impact accidents were considered. Internal platforms were then added to isolate the primary hull structure from corrosion by agricultural chemicals and waste products.* However, the platforms created unacceptably concentrated loads on the hull because of the small local bending stiffness of the thin skin. At this point, the design evolved to a double hull with axial and circumferential bulkheads which divided the 5m interspace into 510 compartments approximately 20m x 20m in the cylindrical midsection and with reduced dimensions in the spherical endcaps. The double hull configuration provided acceptable bending rigidity. In addition, it now became apparent that the structure could be designed with strength sufficient to bear the centrifugal load of the shield while retaining skins of reasonable thickness. At one end of this hull was emplaced a 40m diameter window, reflexed to absorb the pressure load in compression. This window was assumed to be a mosaic of silica glass panels supported by a frame structure. An 8m diameter docking port was positioned along the spin axis at the opposite end of the hull to facilitate the transfer of cargo from the various transport vehicles. Figure 2 illustrates the final hull design concept.

Attention was focussed on the highly stressed cylindrical section of the habitat, and the following structural analysis tasks were pursued: static and fatigue load estimation, stress analysis, design for residual strength, and

*The agricultural environment consists of aqueous nutrients and wastes containing Ca (NO₃)₂, H₂S, NH₃ and NaCl, all of which have been found to cause corrosion fatigue and stress corrosion cracking in steel alloys [10].

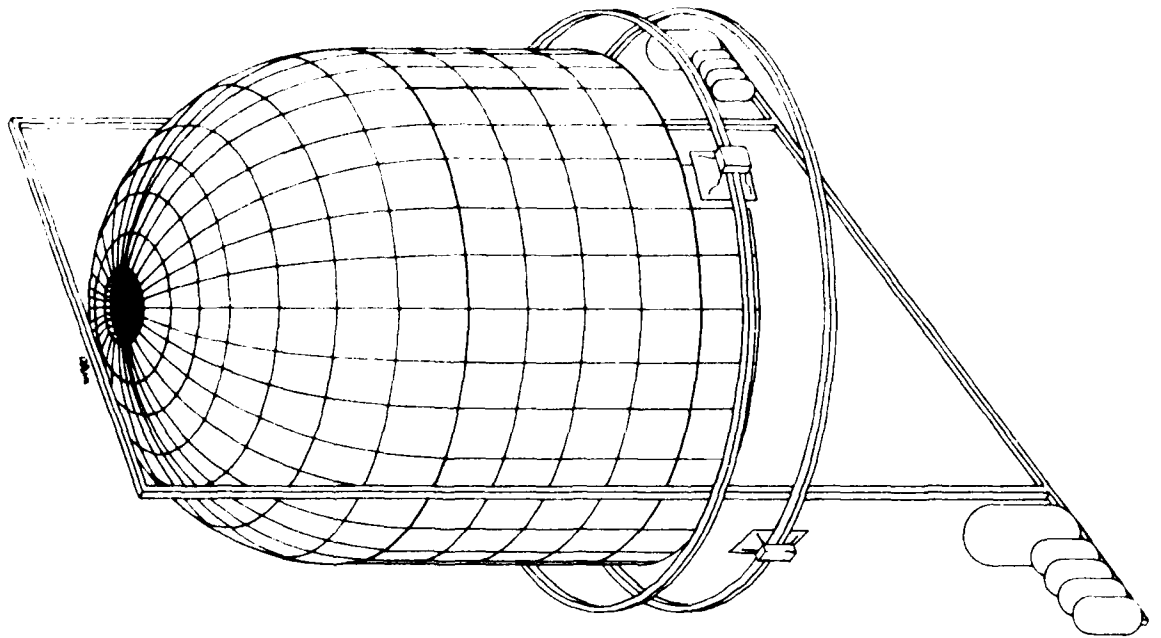


Fig. 1 Habitat Fabrication Scenario

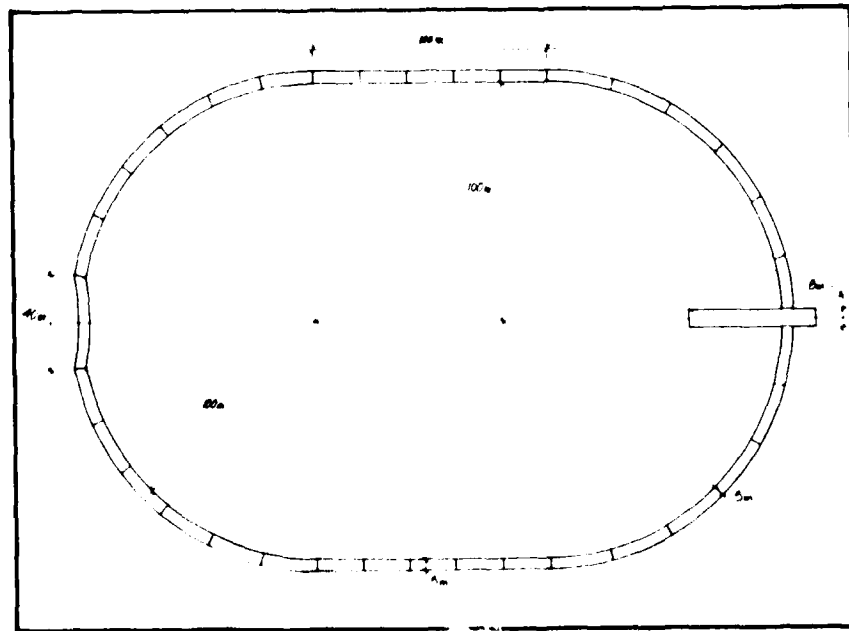


Fig. 2 Schematic View of Final Hull Design

crack propagation calculations to evaluate durability. Since only a preliminary design was intended, extensive simplifying assumptions were introduced at all stages of the analysis.

LOAD ESTIMATION

Components of the static load are provided by both internal pressure and centrifugal acceleration. These contributions are divided between the inner and outer hulls. Under normal conditions, the inner hull bears the load of the agricultural system, the buildings and support services, the inner hull mass, and a portion of the bulkhead mass. The outer hull supports those loads due to the shield, the outer hull mass, the remainder of the bulkhead mass, and the internal pressure. The composition of the habitat's atmosphere was formulated to minimize the biaxial tensile load induced by the atmospheric pressure. A 50/50 mixture of oxygen and nitrogen was adopted retaining the Earth sea-level partial pressure of oxygen and having a total pressure of 2/5 atm. The maximum one "g" (9.807 m/sec²) centrifugal acceleration was assumed for design purposes. The values of the static load components are presented in Table III.

It is apparent that the thin pressure shell (t/R = 0.05) cannot be modeled as a rigid body. Perturbations such as spin rate adjustment, pressure variation, the motion of internal masses, and the docking of massive cargoes will excite both dynamic elastic response and gyroscopic nutations. It was expected that the primary dynamic modes of the hull would be bending, torsion, and bulging. Calculations indicated that the bending and torsion frequencies would be approximately 6.8 and 1.2 Hz, respectively. Thus, a nominal 30-year lifetime might include 6×10^9 load cycles. Although the amplitude of the dynamic response was not accurately determined, further calculations demonstrated that a reasonable first assumption would be a constant amplitude alternating stress equal to +5% of the mean stress.

STRESS ANALYSIS

Having defined the loads applied to the hull, it is now possible to size the major components of the habitat structure. In the cylindrical section of the habitat, the applied static loads impose a hoop stress on each hull given by:

$$\sigma_{\theta} = \frac{RP}{t} \quad (1)$$

where R = radius, P = applied force/unit area, and t = hull thickness. The stress in the direction parallel to the cylinder axis is due to the internal pressure:

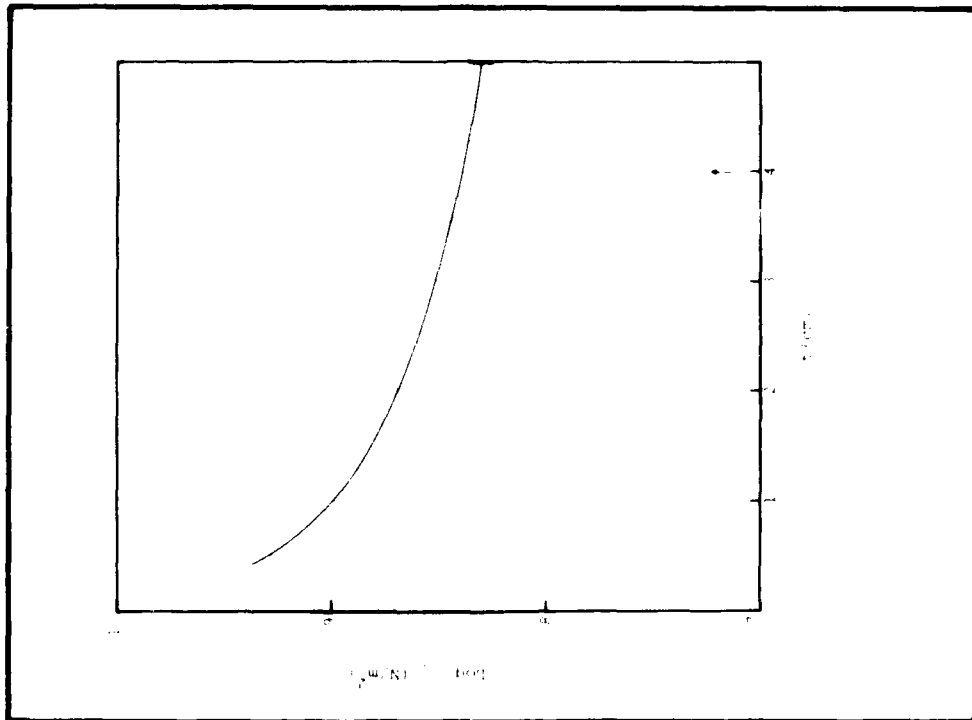


Fig. 4 Stress vs. Thickness
Relation for Outer Hull

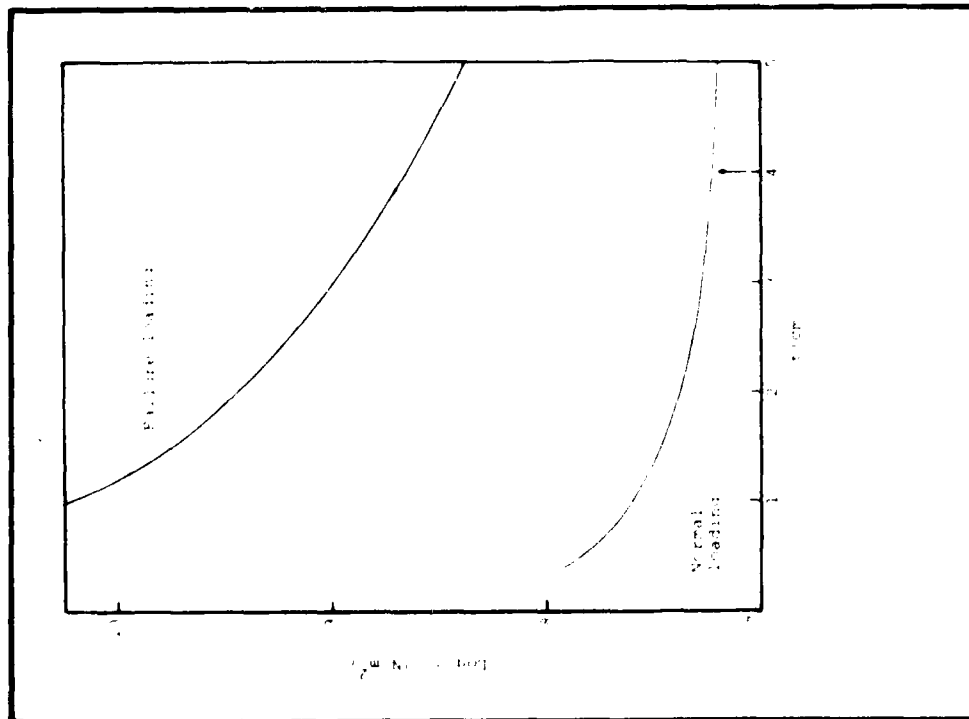


Fig. 3 Stress vs. Thickness
Relation for Inner Hull

$$P_1 = \rho_{Hull}(t_1)g + \rho_{Bulk}(t_1)g + M_{Ag}g \quad (3)$$

$$\sigma_\theta = \frac{R_1}{t_1} [\rho_{Hull}(t_1)g + \rho_{Bulk}(t_1)g + M_{Ag}g] \quad (4)$$

For the outer hull:

$$P_2 = \rho_{Hull}(t_2)g + \rho_{Bulk}(t_2)g + M_{Shield}g + P_o \quad (5)$$

$$\sigma_\theta = \frac{R_2}{t_2} [\rho_{Hull}(t_2)g + \rho_{Bulk}(t_2)g + M_{Shield}g + P_o] \quad (6)$$

Equations 4 and 6 are plotted on the lower curves of Figs. 3 and 4, respectively. The stress analysis of the bulkheads is complicated by differential radial expansion of the two hulls. Enforcing compatibility of radial displacements induces radial stresses in both the circumferential and transverse bulkheads. As is shown in the free body diagram in Fig. 5, the bulkhead radial force contributions must be added to the inner hull loading and subtracted from the outer hull loading. Since there are thirty bulkheads distributed about the hull circumference and six bulkheads distributed along the axis, the revised force/unit area parameters are given by:

$$\bar{P}_1 = P_1 + \frac{30 P_b}{2\pi R_1} + \frac{6 P_b}{100} \quad (7)$$

$$\bar{P}_2 = P_2 - \frac{30 P_b}{2\pi R_2} - \frac{6 P_b}{100} \quad (8)$$

In the above equations, P_b is the force per unit length contributed by the bulkhead radial stresses and is given by:

$$P_b = E \frac{\Delta(R_2 - R_1)}{R_2 - R_1} (t_3) = \sigma_b t_3 \quad (9)$$

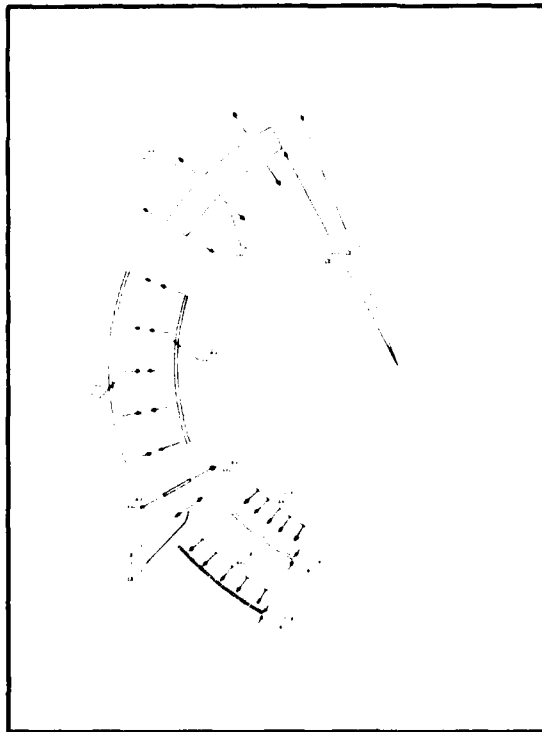


Fig. 5 Hull-Bulkhead Interaction Diagram

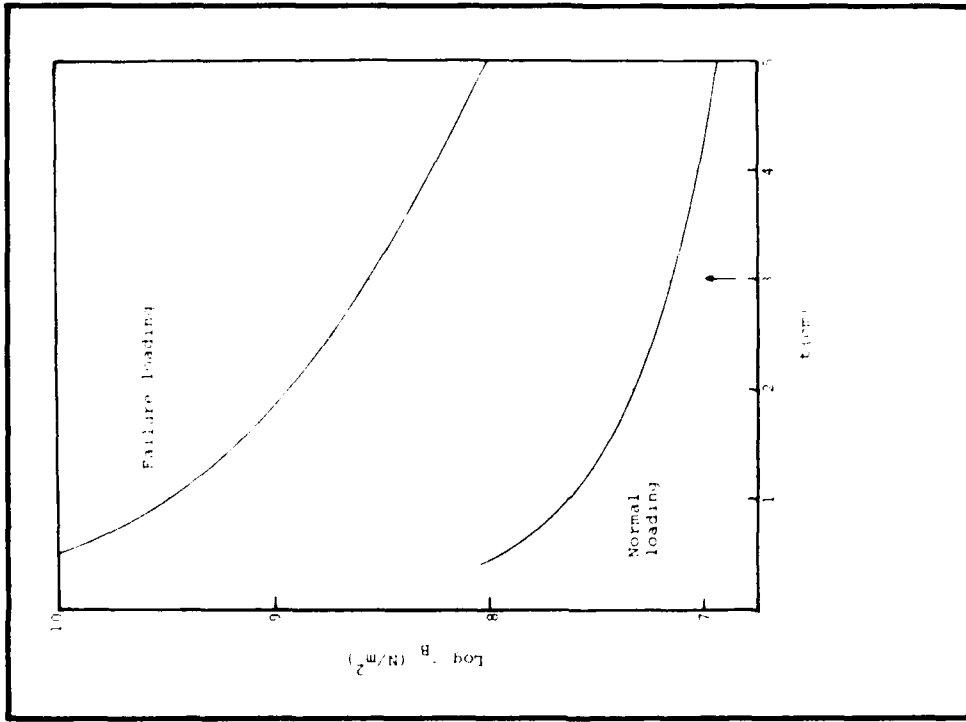


Fig. 6 Stress vs Thickness Relation for Bulkheads

Enforcing radial compatibility with the revised loadings now results in an expression for σ_b , the bulkhead radial stress, in terms of the loads applied to the hulls and the thicknesses, t_1 , t_2 , and t_3 .

$$\sigma_b = \frac{11,025 \frac{P_2}{t_2} - 10,000 \frac{P_1}{t_1}}{5 + 1163 \frac{t_3}{t_2} + 1077 \frac{t_3}{t_1}} \quad \text{N/m}^2 \quad (10)$$

The values of t_1 and t_2 must thus be specified before a relation between σ_b and t_3 can be defined.² The choice of design points is an iterative process involving considerations of residual strength and durability, as well as static strength. Further, it is desirable to load the outer hull more heavily than the inner hull to diminish the adverse effects of corrosion fatigue and stress-corrosion cracking on the inner hull. Finally, it must be recognized that substantial benefits are realized in fabrication if both the inner hull and outer hull are constructed from the same thickness of plate.

The final design points were thicknesses of 4 cm for both the inner and outer hulls. The relation thus defined between σ_b and t_3 is given on the lower curve of Fig. 6, together with the bulkhead³ design thickness of 3 cm. These points correspond to static stress levels of $1.74 \times 10^7 \text{ N/m}^2$ (2520 psi) for the inner hull, $2.45 \times 10^8 \text{ N/m}^2$ (35,600 psi) for the outer hull, and $1.41 \times 10^7 \text{ N/m}^2$ (2050 psi) for the bulkheads. Such stresses are low in relation to the yield strength of the construction material (AISI 4130 steel, $\sigma_y = 1.03 \times 10^9 \text{ N/m}^2$ or 150,000 psi) allowing a margin of strength to cope with^y both accidental and cumulative damage. In all cases, the usual stress concentration factor of three for holes and fillets is easily accommodated.

DAMAGE TOLERANCE

Residual strength after damage-induced component failures is provided by imposing fail-safety criteria on the structural design of the pressure hull. Accident scenarios envisioned involved primarily the penetration of one or both hulls by high-energy projectiles. These projectiles might be generated from the interior of the habitat by the rupture of high pressure pipes or bottles or by the failure of turbomachinery. The danger of meteoroid damage was considered and found to be slight in comparison with these other hazards [7,11]. The design maximum accident assumed in the fail-safety analysis was a four-panel corner joint failure in either or both hulls. A schematic view of this scenario is presented in Fig. 7. The leakdown rate associated with the penetration of both hulls provided the limiting condition on the hull panel sizing. It was determined that 40 minutes would be available before the oxygen partial pressure reached dangerously low levels in the event of a 4m^2 breach in both hulls. This was considered the minimum time necessary to

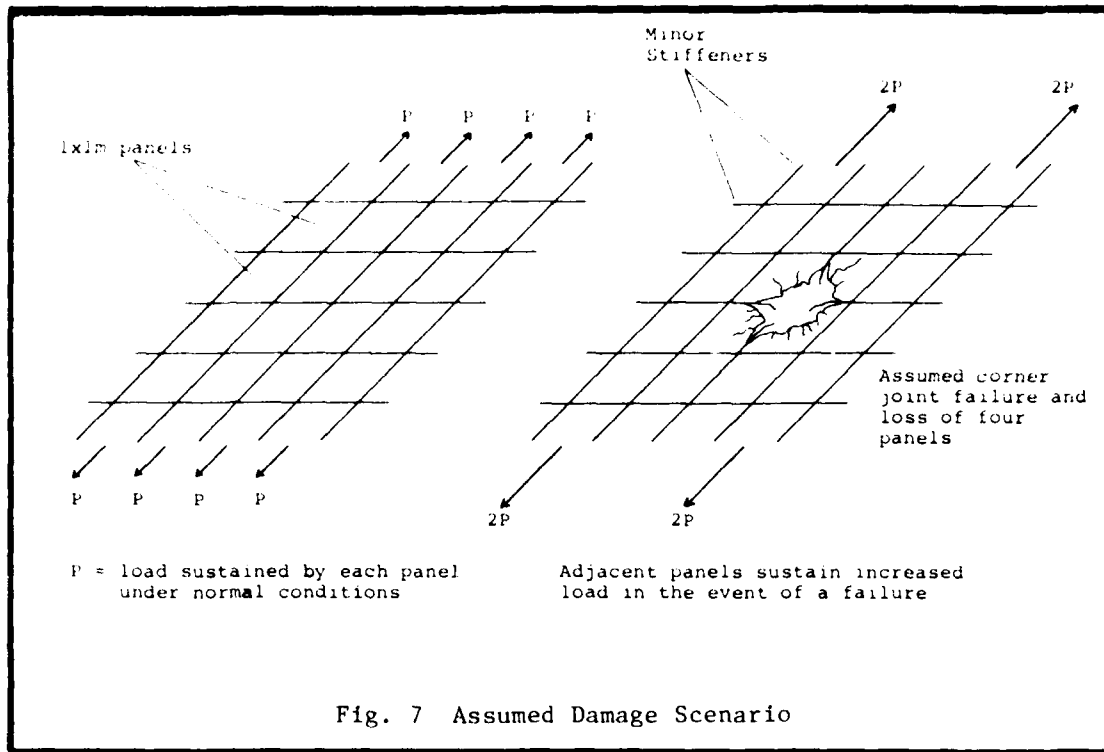


Fig. 7 Assumed Damage Scenario

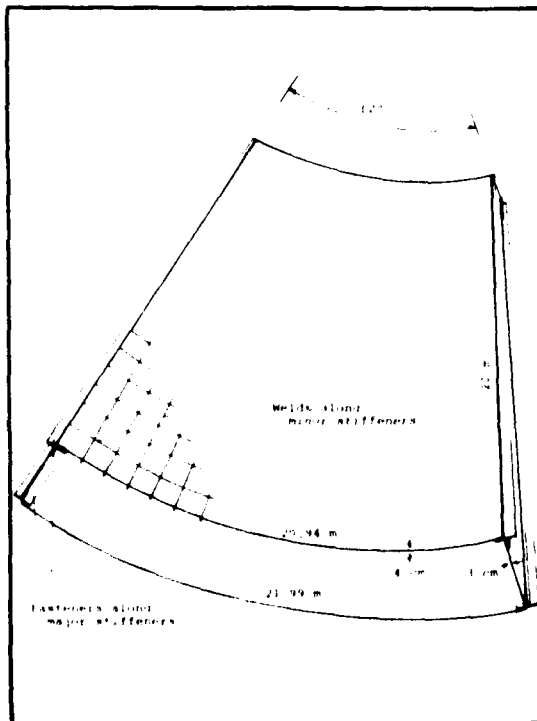


Fig. 8 Cylindrical Section Compartment

dispatch a repair crew and institute emergency procedures.* In order to limit the extent of unstable fracture in failed components, rectangular cross-section stiffeners are laid in an orthogonal grid between the 1m x 1m hull panels. These stiffeners are fabricated from a very high toughness alloy (HY-100, HY-130) and are electron-beam welded to the hull panels. Positive crack-arrest is achieved at the boundaries of the 20m x 20m hull sections by the use of fastened joints. Tee-section stiffeners of the same high toughness material are used to join the adjacent hull and bulkhead sections. Figure 8 illustrates the details of a cylindrical-section compartment.

In the event of a failure in the outer hull alone, the inner hull section and bulkhead sections surrounding the evacuated compartment must absorb the atmospheric pressure load in plate bending, as is shown in Fig. 9. The severity of the resulting bending stresses determines the sizing of the minor stiffeners. The upper curves of Figs. 3 and 6 represent the stress vs. thickness relations of the inner hull and bulkheads under this overload. The overload in a component, whether adjacent panel overstress or additional bending stress, does not exceed the material yield strength. Also, stresses at fillets or holes with a concentration factor of three do not exceed the material ultimate strength.

The fail-safe scheme proposed above requires that panels adjacent to an accidental failure absorb up to twice the load normally applied. This may not be possible if the adjacent panels are themselves near failure. It is thus desirable to reduce the incidence of panels weakened by the growth of large initial flaws. Therefore, a leak-before-break criterion was imposed upon the design of the hull panels. In order to formulate this criterion and gain some insight into the factors which affect the reliability of the hull structure, a modified Forman equation [13] was used with the assumed +5% alternating stress to determine the growth history of a large initial flaw:†

$$\frac{da}{dN} = \frac{C(\Delta K_1)^n}{1-R} \quad (\Delta K_1 \ll K_{1C}) \quad (11)$$

$$C = 0.627 \times 10^{-8}; \quad n = 2.25; \quad R = \frac{\sigma_{\min}}{\sigma_{\max}} = 0.9$$

The initial flaw was assumed to be a semicircular surface crack with a length (2c) equal to 0.1 inch (.0394 cm) and a depth (a) equal to 0.05 inch (.0197 cm). For a semi-elliptical surface flaw [14,15]:

* It was assumed that one or more of the interior structures would be fitted out as a pressure-tight "shelter."

† Equation in units of inch/cycle and ksi.

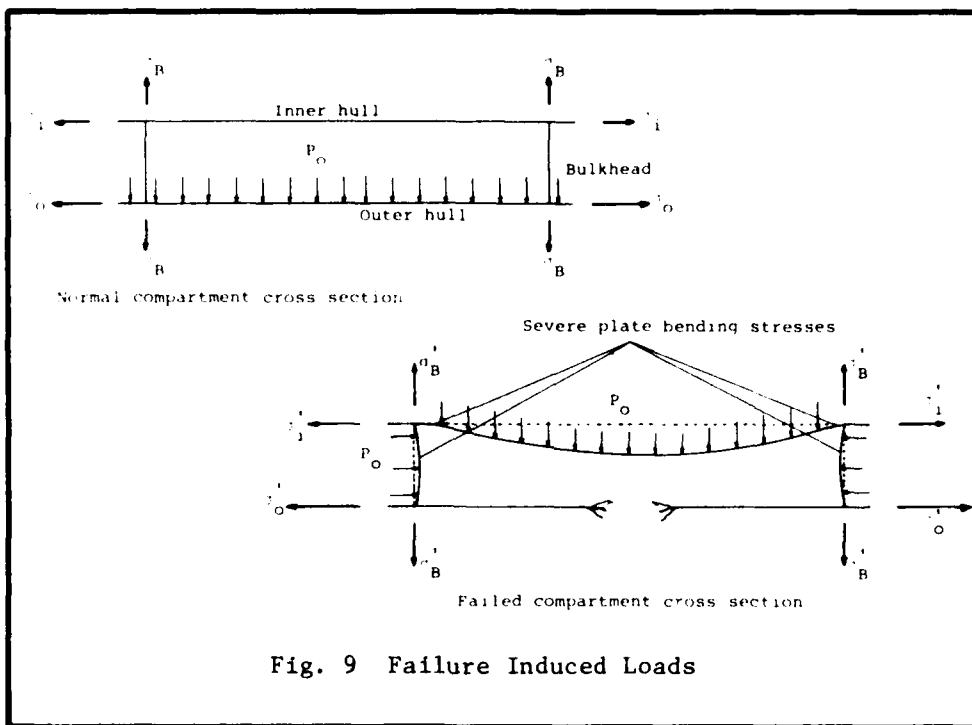


Fig. 9 Failure Induced Loads

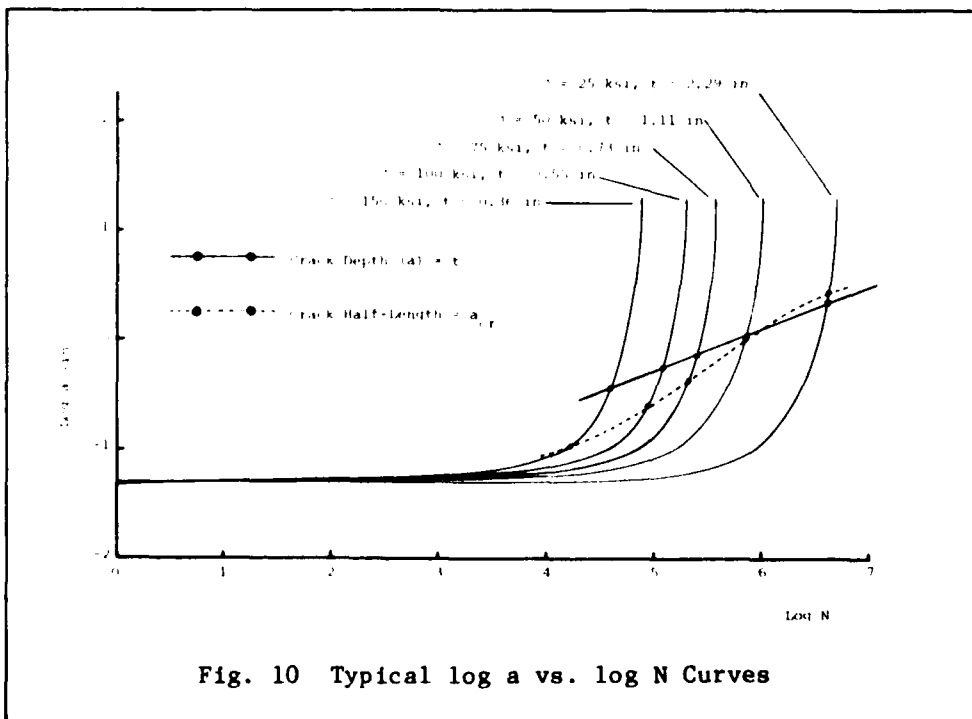


Fig. 10 Typical log a vs. log N Curves

$$\Delta K_1 = 1.1 \Delta \sigma \left(\frac{\pi a}{Q} \right)^{\frac{1}{2}} M_K \quad (12)$$

$$\Delta \sigma = 0.1 \sigma; Q = 2.3; M_K = 1.1$$

For a through-thickness flaw:

$$\Delta K_1 \approx \Delta \sigma \sqrt{\pi a} \quad (13)$$

The Forman equations for each crack-growth regime may be integrated from the initial flaw size to provide a composite a vs. N equation of the form given below:

$$N = \int^t \frac{1-R}{0.05 C \left[.11 \sigma \left(\frac{\pi a}{Q} \right)^{\frac{1}{2}} M_K \right]^n} da + \int^a \frac{1-R}{t C [0.1 \sigma \sqrt{\pi a}]^n} da \quad (14)$$

The appropriate σ vs. t relations can thus be used in Eq. 14 to obtain $\log a$ vs. $\log N$ curves for various values of plate thickness and operating stress. A typical set of outer hull plots for several operating stress levels is shown in Fig. 10. The critical crack size and the size at which the hull is first penetrated have been identified on each curve. Cross-plots of these points determine the maximum operating stress (minimum thickness) for which leakage precedes fracture.

An evaluation of the durability of the habitat structure is complicated by several factors. Chief among these is the fact that the number of load cycles experienced by the pressure hull (6×10^9) far exceeds the durations reported for experimental investigations. Also, an endurance limit for steel at a stress ratio of 0.9 is not well defined. Some justification for the assumption that no nucleation occurs may be found in the nominal static stress levels summarized in Table IV. The most severe loading occurs in the outer hull where the stress level is approximately 15% of the ultimate strength. For crack propagation, a threshold crack size at a fastener detail (SCF = 3) was established by solving Eq. 12 with $\Delta K_1 = \Delta K_{TH}$ (ΔK_{TH} assumed to be 5 ksi $\sqrt{\text{in}}$) and $M_K = 1$:

$$a_{TH} = \frac{Q}{1.21\pi} \left(\frac{\Delta K_{TH}}{3\Delta\sigma} \right)^2 \approx 0.13 \text{ inch} \quad (15)$$

Table IV Final Design Summary

Component	Quantity	Normal (N/m ² (psi))	Tension (N/m ² (psi))	Mass (Kg)
Inner Hull	4	1.74x10 ⁷ (2500)	4.57x10 ⁸ (64,300)	1.94x10 ⁷
Outer Hull	4	2.45x10 ⁸ (35,600)	5.15x10 ⁸ (74,800)	6.44x10 ⁷
Bulkheads	4	1.41x10 ⁷ (2050)	3.55x10 ⁸ (51,450)	2.55x10 ⁷
Cross Section (cm)				Mass (Kg)
Minor Stiffeners (Hulls)		4x16		1.96x10 ⁷
Minor Stiffeners (Bulkheads)		3x12		6.11x10 ⁶
Major "T" Stiffeners		cap - 44 cm flange - 20 cm thickness - 4 cm		4.77x10 ⁶
Fasteners		diameter - 4 cm		
Total Hull Mass (Kg)				2.0 x10 ⁸

ASSESSMENT

The long duration of the cyclic load history of the space habitat constituted a central factor in the structural integrity assessment. The combination of 6×10^9 cycles and a stress ratio of 0.9 brings into question the concepts of a fatigue endurance limit for crack nucleation and a threshold crack size for propagation.

Stress analysis calculations supported the potential fatigue endurance of the pressure hull, but the design does not depend on this potential. Instead, the leak-before-break criterion was applied to protect the structure against catastrophic panel failures due to routine defects and/or crack nucleation. Combination of leak-before-break with a requirement for reasonable plate thicknesses forced the material selection to steel rather than aluminum alloys. A balanced design was achieved, in the sense that similar hull and bulkhead thicknesses (for fabrication efficiency) resulted in low stress levels in the bulkheads and inner hull, i.e., those components most likely to be subjected to a corrosive environment.

Approximate residual strength calculations demonstrated that adjacent components could withstand the overloads caused by an assumed accidental failure of four panels plus intersecting stiffeners. In this respect, it is interesting to note that the residual strength design of a space habitat is unique, in that its operational loads cannot be reduced, as can be done for other aerospace structures, when an accident occurs.

A threshold crack size for propagation fatigue was calculated on the basis of an assumed semicircular surface flaw and the estimated cyclic loading.

Even if the threshold concept were accepted for the service duration of the habitat, the durability of the structure would still be in question because nondestructive inspection cannot be depended upon to detect cracks of this size (0.13 inch) with 100% reliability. Hence, other means must be sought to achieve the required durability. Leak-before-break design has already been mentioned in this respect. Other possible actions include proof testing and realistic inspection/repair schemes. An overspin/overpressure proof test is included in the habitat fabrication scenario [7].

A simple inspection scheme can be arranged by placing pressure taps in each interhull compartment, with operating pressures in the compartments set at two values, below the habitat pressure, in a checkerboard pattern. Comparison of pressure readings from adjacent compartments then locates any leak to within one major hull component. Realistic repair can be achieved by bagging the radiation-shield slag (for manual removal) and by design of a portable airlock which can be positioned, within the habitat, over an access hatch leading to the damaged compartment. The combination of measures outlined above provides a sufficient cushion against routine failures to make the structure independent of questionable fatigue endurance-limit concepts.

CONCLUSIONS

The design process has identified several areas which require further study. More detailed residual strength analyses of two types are needed: elastic-plastic strength calculations to assess the ability of lines of fasteners to withstand "domino" failure, and adjacent-panel cracking calculations. The threshold nature of the design prevents the estimation of time to loss of fail-safety by calculating the growth time for routine damage, as is presently done for airframes. Instead, such calculations must be based on inspection reliability. More sophisticated dynamic analysis is required to refine the service load history. In particular, nutation effects due to the motion of large masses within the habitat must be accounted for. A more detailed assessment of corrosion fatigue and stress-corrosion cracking on the inner hull is required. Finally, the effects of space processing must be evaluated, since the absence of atmosphere during refining and alloying may lead to mechanical properties better or worse than were assumed in this study.

However, the preliminary design calculations indicate that construction of a prototype space habitat is technically feasible with respect to long-term structural integrity. The achievement of structural integrity has resulted in a much thicker walled design with much less window area than was previously assumed by other investigators. In particular, the importance of considering more than static loads has once again been demonstrated.

ACKNOWLEDGEMENT

This paper is a portion of a student project in Systems Engineering pursued at the Massachusetts Institute of Technology during the spring of 1976 with the support of the William F. Marlar Memorial Foundation.

REFERENCES

1. Hagler, T., "Building Large Structures in Space", Astronautics & Aeronautics, May 1976, 56-61.
2. O'Neill, G. K., "The Colonization of Space", Physics Today, September 1974.
3. "System Design for Space Colonization", NASA Ames/ASEE/Stanford University Summer Study Report, NASA SP-413, 1975.
4. O'Neill, G. K., "Engineering a Space Manufacturing Center", Astronautics & Aeronautics, October 1976.
5. "Microwave Power Transmission Studies", 4 v., Raytheon Company, Equipment Division, Contract No. NAS 3-17835, Sponsor NASA Lewis Research Center, NASA CR-134886, ER 75-4368, 1975.
6. Proceedings of the 1975 Princeton Conference on Space Manufacturing Facilities, G. K. O'Neill and R. Miles, eds.
7. McCarthy, J. F., Jr., et al., A Systems Design for a Prototype Space Colony, 16.86 report, MIT Department of Aeronautics and Astronautics, 1976.
8. Crawley, E. F., Smith D. B. S., article to appear in Technology Review magazine, Massachusetts Institute of Technology, Cambridge, MA, July-August 1977.
9. Rose, H. J., Jr., "Compositional Data for Twenty-Two Apollo 16 Samples", Proceedings of the Fourth Lunar Science Conference, v. 2, 1149-1158.
10. Tetelman, A. S., McEvily, A. J., Jr., Fracture of Structural Materials, Wiley, 1967.
11. Cosby, W. A. and Lyle, R. G., The Meteoroid Environment and Its Effect on Materials and Equipment, NASA SP-78, 1965.
12. Military Specification, "Airplane Damage Tolerance Requirements", MIL-A-83444 (USAF), July 2, 1974.
13. Forman, R. G., et al., "Numerical Analysis of Crack Propagation in Cyclically Loaded Structures", Trans. ASME, Series D, J. Basic Eng., v. 89, September 1967, 459-464.
14. Tiffany, C. F. and Masters, J. M., "Applied Fracture Mechanics", Fracture Toughness Testing and Its Applications, ASTM STP 381, 1964, 249-277.
15. Campbell, J. E., et al., Damage Tolerant Design Handbook, WPAFB, 1972.

Section 2 JOINTS AND MOUNTINGS

FAILURE ANALYSIS OF SHRIKE MOUNTING LUGS

F. R. Stonesifer and H. L. Smith
Naval Research Laboratory
Washington, D. C. 20375

INTRODUCTION

The Naval Research Laboratory (NRL) has on a number of occasions provided failure analysis of missile components for the Naval Ordnance Systems Command. One such instance occurred in a development program to modify the standard Shrike Mk 39 air-to-air missile. In an effort to mass-produce and economize, a new model, Ex 53, was proposed as a replacement for the standard Mk 39. The proposed modification involved changes in both fabrication and attachment of the mounting lugs. These lugs, a forward tee-bar and two aft-hooks, on the Ex 53 motor case, were failing during the Navy acceptance test. This was unexpected since the Mk 39 motor cases had routinely passed these vibration tests. NRL was asked to study the problem and propose remedial measures.

FORMULATION

Two complete motor cases, a Mk 39 and an Ex 53, were sent to NRL for examination and comparison along with two (Ex 53) mounting lugs which had failed during testing. Three additional failed lugs were provided later from tests with better documentation.

The lugs function to attach the cylindrical exterior casing of the rocket to a launching track on the under side of the aircraft. The general configuration and location of the mounting lugs may be seen in Figure 1. All that was known about the first two failures, one in an aft-hook and one in a forward tee-bar, was that they occurred during vibration testing. A third specimen was obtained from an aft-hook which failed just prior to completion of the required forty-hour vibrational test at -65°F . Here crack growth had been detected by a decrease in resonant frequency as the crack extended. A fourth failure occurred in another aft-hook near the end of a forty-hour vibration test at $+160^{\circ}\text{F}$. Separation occurred in the lug while the loading frequency was swept back and forth between 500 and 2000 Hz with a maximum loading of 9G. This failure was reportedly different, having occurred very suddenly, unlike that of a normal fatigue failure. The fifth and final specimen was from a forward launch hook tee-bar which failed near the end of a forty-hour vibration test at room temperature.

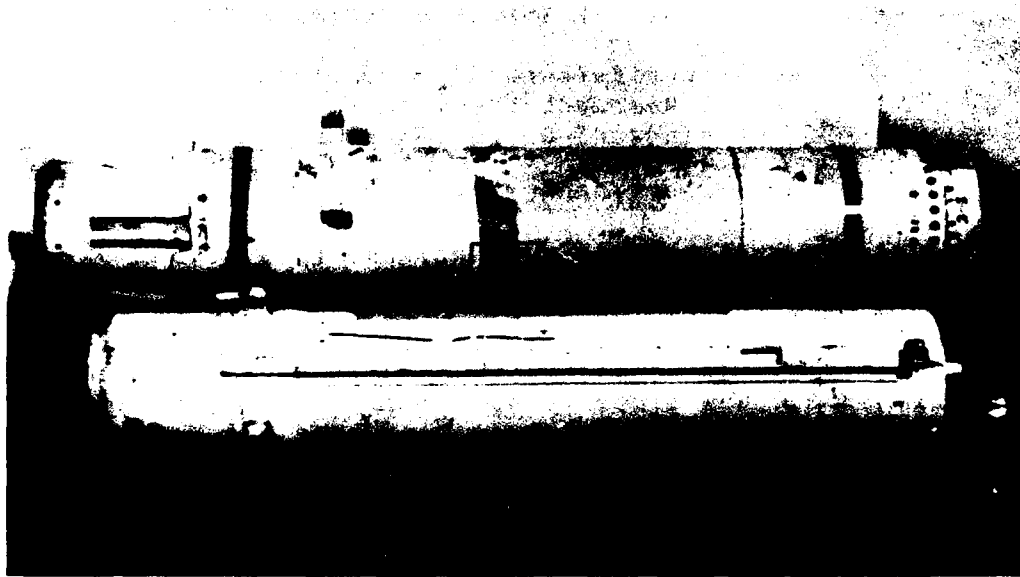


Figure 1: Shrike Mk 39 and Ex 53 motor cases.
(Ex 53 in foreground)

ASSESSMENT

Our study commenced with collection and consideration of available circumstantial evidence. The Mk 39 motor cases had been routinely passing vibration tests while the Ex 53 cases were frequently failing. The method of aft-hook attachment had been changed from a "strap-on" construction in the Mk 39 to a welded joint for the Ex 53. This change, as seen in Figure 1, was not under suspect as the culprit since failures were observed in the mounting lugs away from the lug-to-case weld; furthermore, the rigidity of the hooks had not been affected by the design modification.

The tee-bar and one aft-hook were removed from each of the two Shrike cases, Figure 2. Both tee-bar lugs were found to have standard acceptable radii. However, an additional bevel on the lower edge of the Mk 39 cross-bar should have reduced stress concentration at the end of the fillet. The external edges on the aft-hook are much sharper in the new design. It is common knowledge that radii in fillets contribute significantly to fatigue life of metal components. However, this is also true of external radii where fatigue cracks often initiate at highly stressed sharp corners. These external radii are shown as optional in the specifications.

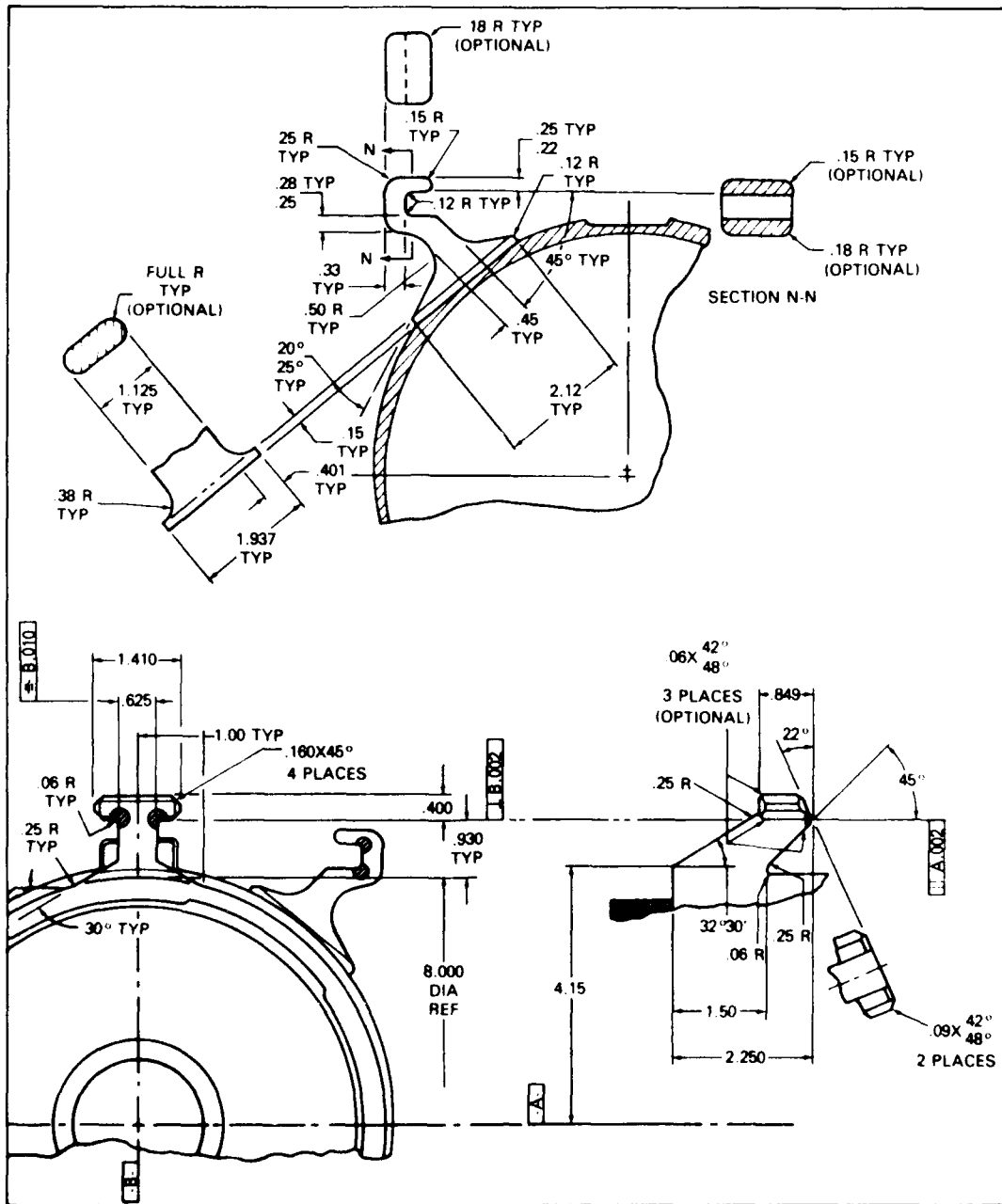


Figure 1(b): Dimensional details of the mounting lugs. Radii and bevels shown as optional were omitted for the Ex 53 model. The crack initiation zones are indicated by the shaded areas in the lower left-hand drawing.

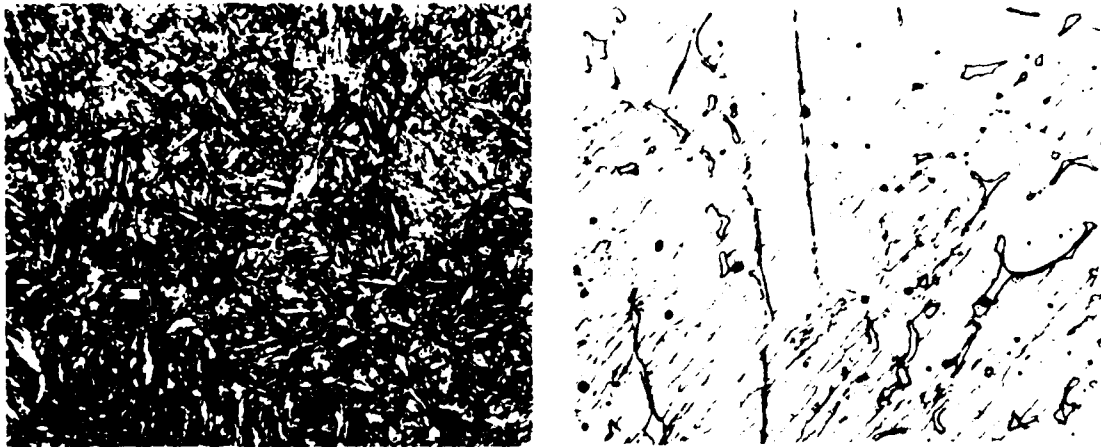


Figure 2: Aft-hook and tee-bar mounting lugs from Mk 39 (right) and Ex 53 (left) Shrike motor cases.

Results from chemical analysis, hardness tests, and micrographs of polished and etched sections reveal a number of discrepancies between the two cases, Table I. In particular, the lugs from Ex 53 cases were slightly harder and therefore probably more brittle. In order to avoid the more expensive forging and casting processes, the manufacturer was permitted to machine the lugs from extruded bar stock. This resulted in elongated inclusions and segregation oriented in the worst possible direction for the end product. Both the 4335V and 4340 steels showed the typical tempered martensite structure as

TABLE I. Comparisons Between Mounting Lugs on Shrike MK 39 and Ex 53 Motor Cases

		EX 53	MK 39
Tee Bar	Material	4335V	4340
	Hardness	50R _c	43R _c
	Approximate Tensile Strength (based on hardness)	243 Ksi	200 Ksi
	Grain size	ASTM #9	ASTM #9
	Structure	Tempered Martensite	Tempered Martensite
	Inclusions	A few rounded inclusions	A few small inclusions
	Remarks	Pronounced segregation parallel to notch. Probably bar stock.	Forging with slight segregation.
Aft Hook	Material	4335V	17-4 PH
	Hardness	46R _c	41R _c
	Approximate Tensile Strength (based on hardness)	215 ksi	188 ksi
	Grain size	ASTM #9	Coarse Grain
	Structure	Tempered Martensite	Age hardened martensite with some delta ferrite
	Inclusions	Elongated sulfide inclusions parallel to notch axis	
	Remarks	Practically no segregation	Casting



(a) Nitral etch, approx. 700x (b) Cupric chloride etch, approx. 350x

Figure 5: Typical microstructure (a) Tempered martensite of 4335V (Ex 53) and 4340 (Mk 39) lugs; (b) Islands of delta-ferrite in age-hardened martensite in 17-4 PH casting (Mk 39).

pictured in Figure 3a. The 17-4 PH casting had a somewhat different structure in which islands of delta-ferrite were surrounded by age-hardened martensite, Figure 3b. Figure 4 shows the elongated sulfide type inclusions typical of the

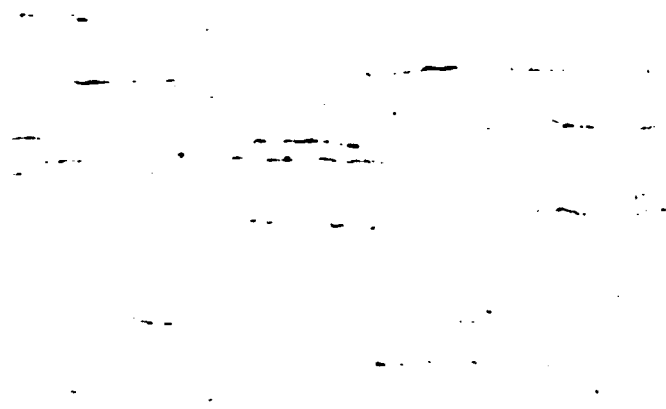


Figure 4: Longitudinal section through Ex 53 aft-hook showing typical sulfide type inclusions aligned parallel to notch axis (unetched, 70x).

longitudinal plane through the Ex 53 aft-hooks. Similar sections through the Mk 39 lugs showed only a few globular oxide type inclusions. Figure 5 illustrates the differing grain flow in the extruded Ex 53 and the forged Mk 39 tee-bars.

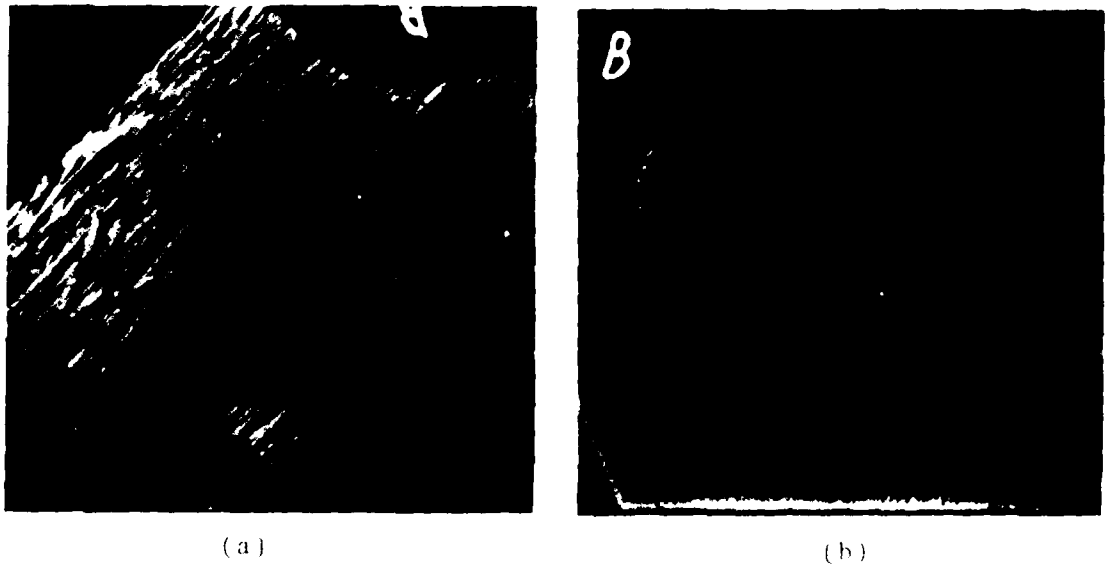


Figure 5: Longitudinal plane through tee-bar lugs (a) Ex 53, (b) Mk 39 (approx. 3.5x).

As stated earlier, five fracture surfaces were available for examination. All were from Ex 53 mounting lugs which had failed during various phases of the vibrational part of the acceptance testing. The first two specimens were received in poor condition. Removal of dirt and rust revealed typical fatigue type fracture surfaces as shown in Fig. 6. Each fracture originated from a single surface flaw near a corner at an internal radius, and showed considerable amount of slow crack propagation before fast fracture led to complete separation. Fig. 7 shows several views of two aft-hook lug failures. Both failures initiated at a fillet on the inside corner of the hook. One surface, shown on the left of Figure 7, shows a typical flat, relatively featureless, slow growth fatigue area to a point where the crack velocity became unstable. The resulting fast fracture then propagated quickly through the remaining section. The other failure, pictured on the right of Figure 7, was reported to have occurred very suddenly. The fracture surface has a pronounced woody texture, probably due to the presence of many elongated inclusions. The primary fracture origin, indicated by an arrow, is again at the surface of an inside radius near one edge of the hook. However, in this failure there is no evidence of fatigue



Figure 6: Fracture surfaces from two Shrike Ex 53 mounting lugs which failed during vibration testing (a) Tee-bar failure, (b) Aft-hook failure.

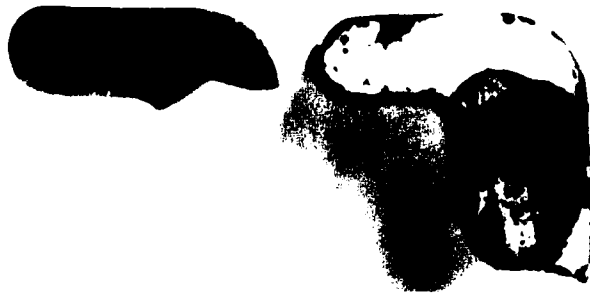
crack growth, thus substantating the reportedly sudden failure. Enlargements of the two fracture surfaces are shown for comparison in Figure 8.

The one remaining fracture surface, that of a forward launch hook (tee-bar) is shown in Figure 9. The primary origin, indicated by an arrow, is at an inside radius where a beveled edge of the tee-flange joins the center load bearing member. The crack propagated in fatigue for some distance before instability occurred.

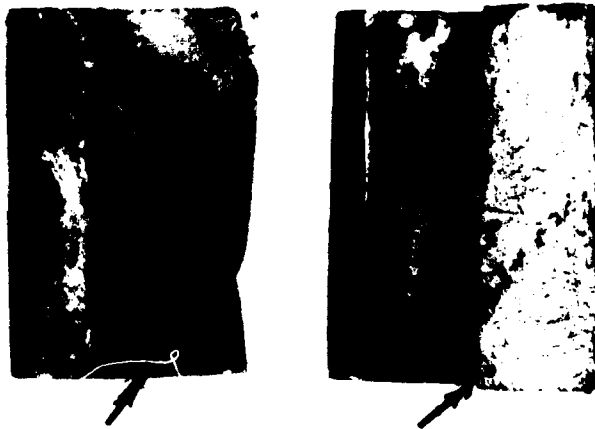
One finds, in each instance, grain flow and resultant elongated inclusions perpendicular to the principal stresses imposed in the lug. Such metallurgical defects could result in a lower fracture strength and shorter fatigue life. The fractures all originated at the surface of inside radii. These surfaces did not have a particularly good surface finish and tool marks were evident in most cases.

CONCLUSIONS

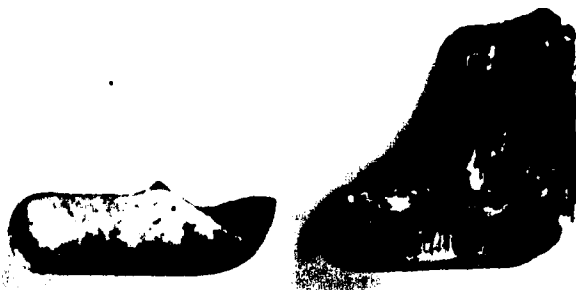
In attempting to eliminate mounting lug failures in the Ex 53 Shrike missiles and thus to ensure passage of the qualifying vibration tests, the following modifications were suggested.



(a) End view

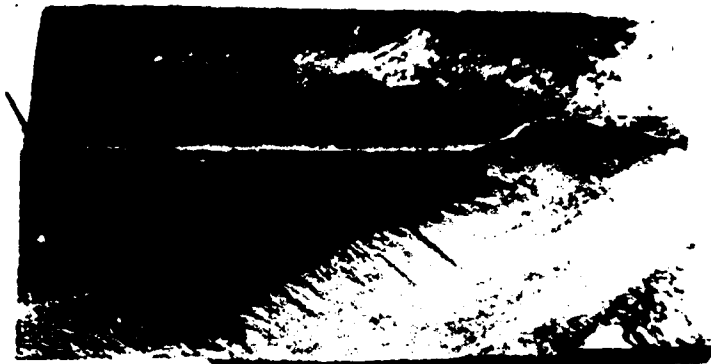


(b) Inside - Face view

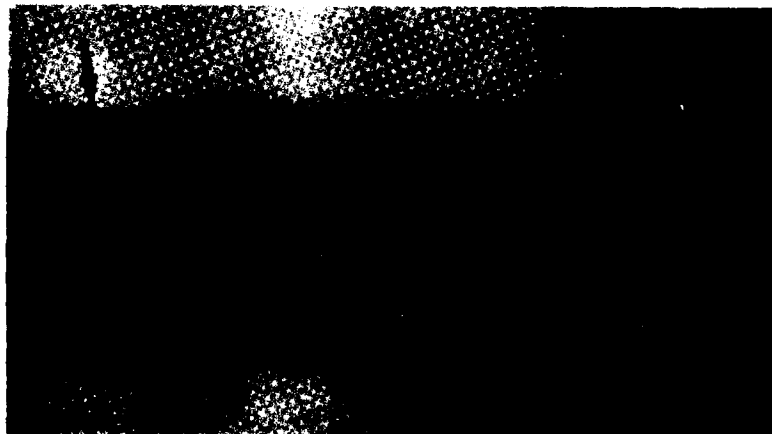


(b) Opposite - end view

Figure 7: Fractures from two Shrike Ex 53 aft-hook mounting lugs (approx 2x).



(a)



(b)

Figure 8: Fracture surfaces from two Shrike Ex 53 aft-hook mounting lugs. (a) Showing extensive fatigue-crack growth, (b) Showing a pronounced woody texture with no evidence of fatigue.

1) Change heat treatment for the mounting lug material so as to result in a strength level nearer the specified lower limit of 190 ksi (1.31×10^3 MPa.) Consider adding an upper limit to the specifications. The size of the slow growth areas on the fracture surfaces indicates that the sections are still being stressed well below the yield strength for the material. The additional strength is not required and the additional fatigue life of the softer material would be beneficial.

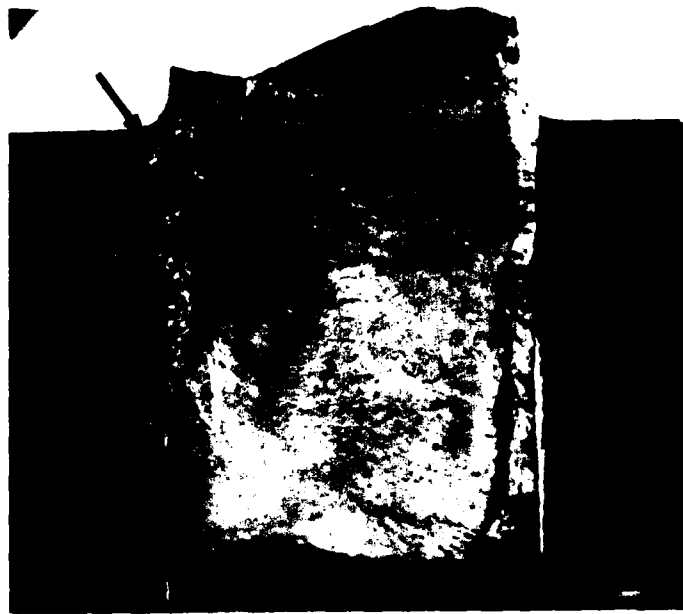


Figure 9: Fracture surface from tee-bar mounting lug on a Shrike Ex 53 motor case.

2) Increase the radius of curvature on lug sections and fillets wherever possible. Make such radii mandatory rather than optional.

3) Require a better surface finish to reduce tool scratches, especially in highly stressed fillet areas.

4) Make measurements of the magnitude and variability of stresses imposed during clamping in test stand. Establish some standard procedure to insure that stresses imposed during mounting are not excessive but realistic when compared to in-service conditions.

5) Change to the use of vacuum remelted material for the lugs if necessary. The additional cost will be justified by improved performance from the cleaner material.

REFERENCES

Stonesifer, F. R., Smith, H. L. and Romine, H. E., "Failure Analysis of Shrike Components," NRL Memorandum Report 1854, February 1968.

ANALYSIS OF HEAVY LIFT HELICOPTER (HLH)
ROTOR HUB LOWER LUG
Joseph C. Zola
Boeing Vertol Company
P.O. Box 16858
Philadelphia, Pennsylvania
19142

INTRODUCTION

The Heavy Lift Helicopter (HLH) rotor hub and crossbeam assemblies, figure 1, were designed for safe life capability and for fail safety.

Safe life is a design philosophy applied to fatigue critical helicopter components in which a service life is established and the component is removed from service at or before this interval to preclude catastrophic failures. The safe life design objective for the HLH hub and crossbeam is 3600 hours.

Fail safety is a design philosophy applied to fatigue critical helicopter components in which features are incorporated into the design which will permit the timely detection of fatigue damage and provide operational safety in a degraded mode. The hub and crossbeam were designed to be capable of sustaining limit load after one of the four lugs has completely failed and to have 100 hours of safe life based on mean -1 σ endurance limit.

Three rotor hub and crossbeam assemblies were fatigue tested in the laboratory to demonstrate capabilities of the design.

The safe life for the hub and crossbeam is 2645 hours based on the mission profile used and it is believed that additional testing and the elimination of fretting would demonstrate the achievement of the 3600 hour safe life goal.

In the three tests, fatigue cracks occurred in the hub lugs, crossbeam bosses and bushings, figure 2. The fail safety goal was partially achieved. The hub plate with fatigue-induced cracks in one lug and in the corresponding crossbeam boss sustained V_H level flight loads for an equivalent of ten flight hours in test. In addition, the capability to sustain limit load with a simulated complete failure in one lug was demonstrated.

Fracture mechanics theory was used in a failure analysis to demonstrate a correlation with test results that verified:



Figure 1. Heavy Lift Helicopter (HLH) Rotor Hub and Crossbeam Assemblies

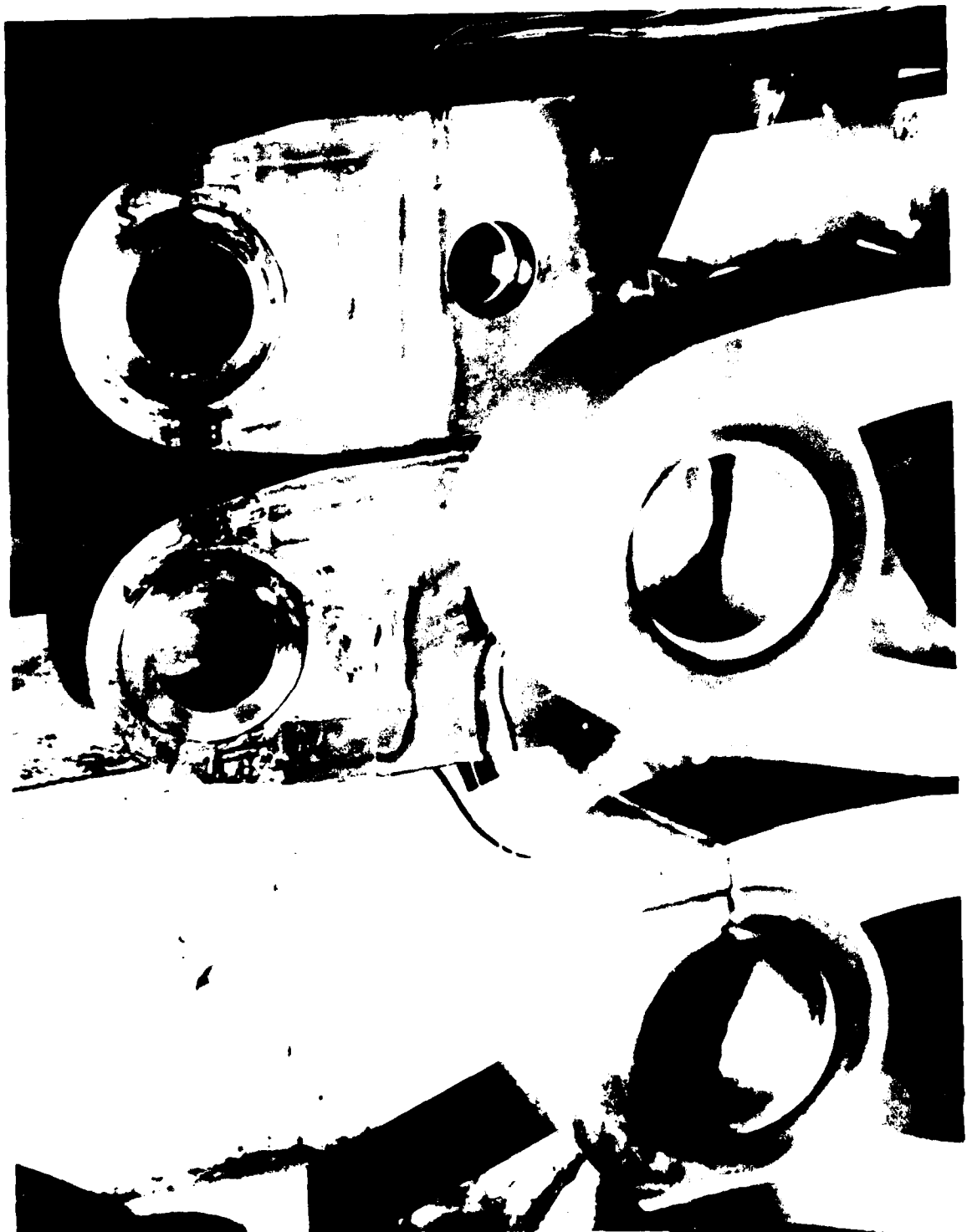


Figure 2. Rotor Hub Lower Plate Lug Cracks

1. Fracture toughness of the ($\alpha + \beta$) STOA 6 Al-4V titanium meets specification requirements.
2. The fatigue loads portion of the test spectrum loading produced rapid fatigue crack growth rates.

FORMULATION

Fracture of the rotor hub lower lugs was attributed to one of three possibilities:

1. low fracture toughness, K_C
2. rapid fatigue crack propagation rates at all operational stress levels, or
3. fretting (crack initiator)

Each of the three can be evaluated by using fracture mechanics theory, measured lug stress levels, and known fatigue crack propagation rates for titanium forging.

The fracture toughness, K_C , of a structure can be defined as the maximum stress intensity factor, K_{max} , at which the structural material will fail ($K_C = K_{max}$).

If the stress at failure is known, and a flaw shape is determined from the fracture surface it is possible to estimate the fracture toughness of a given structural component. In the case of the HLH rotor hub lower plate lead lug, the flaw shape at the onset of rapid fracture is a semi-circular flaw emanating from near one corner of the lug when viewed normal to the fracture surface, figure 3.

$$c = .188", \frac{2c}{b} = 3.09$$

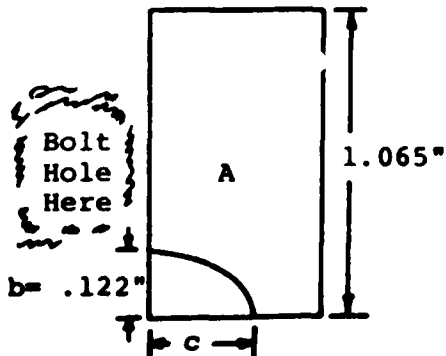


Figure 3. Fracture Surface Flaw Shape - HLH Lower Lead Lug

'A' represents the transition from fatigue crack propagation to the onset of failure of the lug. This boundary defines the flaw shape for describing the fracture of the lug. For the lug failure, the stress intensity factor at failure is determined from the following relationship:

$$K_{\text{maximum}} = \sigma_{\text{maximum}} \left(\frac{1.95}{\phi} \right) \sqrt{b} F\left(\frac{b}{r}\right) \quad (1)$$

where σ_{maximum} is the maximum gross stress in the section
 b is the depth of the crack into the bore of the lug
 $\left(\frac{1.95}{\phi} \right)$ is a value based on the shape factor, $\frac{2c}{b}$, of the flaw, figure 4.

$F\left(\frac{b}{r}\right)$ is a correction factor for the presence of a hole at the edge of the flaw with $r = 1.125$ inches, figure 5.

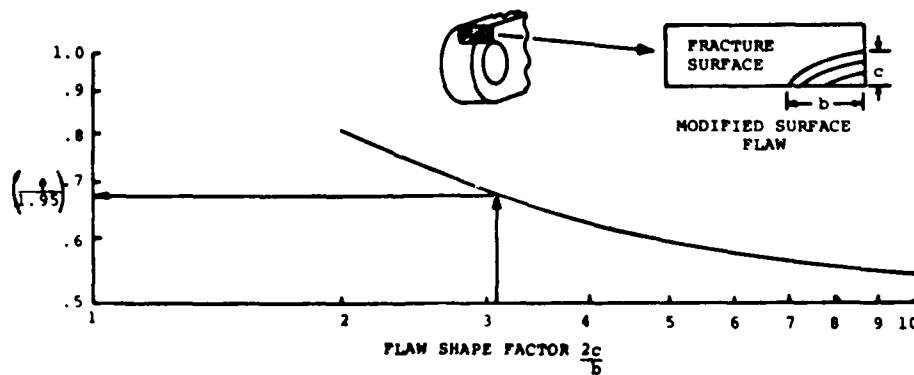
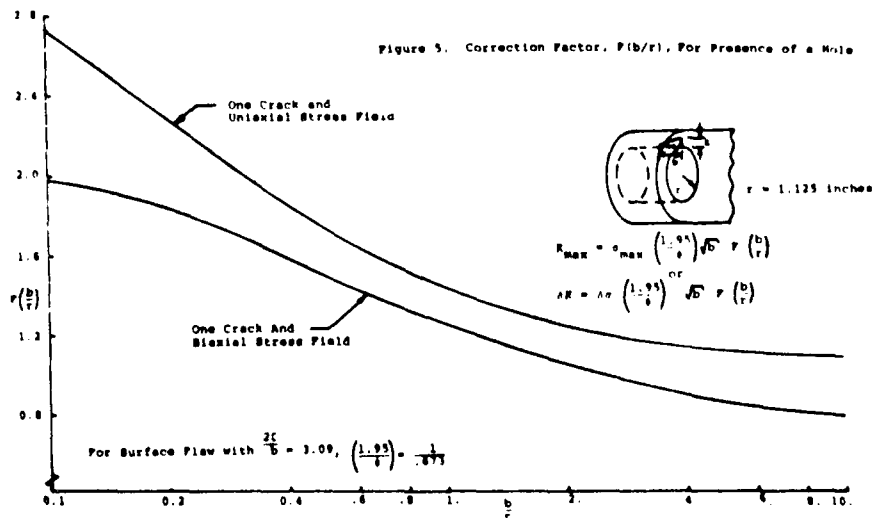


Figure 4. Variation of Surface Flaw Correction Factor, $\left(\frac{1.95}{\phi}\right)$, with Flaw Shape Factor, $\frac{2c}{b}$



Normally, the solution to equation (1) is based on the maximum gross section stress. However, the stress concentration effect due to the hole causes very high local stresses at the chamfer, and a calculation based on this stress level gives an indication of what is occurring very locally near the flaw initiation. As a result, both calculations define a range of K_C values to compare with basic material properties.

To provide answers regarding fatigue crack growth rates and crack initiation attributed to fretting, two fracture mechanics models were developed. A conservative model representing the actual geometry of the lug is used to predict crack growth for a corner flaw. As a check on the severity of this model, and its impact on predictions, a second model, labeled unconservative, which eliminates entirely the magnification factor in stress intensity factor due to the lug geometry (i.e., depth and width dimensions) but retains the corner flaw correction factor was also used. See figure 6.

- Conservative Fracture Mechanics Model-consists of a corner flaw originating from a lug, and includes a factor for the effect of the lug geometry (i.e., a boundary effect due to the dimensions of the lug).

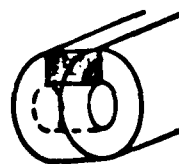


Figure 6a. Fracture Mechanics Models For Lug Analysis

growth rates associated with each stress level. From these calculations it is then possible to identify what combinations of initial flaw size and load conditions cause failure, and when failure would occur from these assumed initial conditions.

The initial flaw sizes selected are 0.02, 0.03, 0.04, 0.047, 0.048, 0.07, and 0.12 inch deep. The shape factor of $\frac{2c}{b} = 3.09$, figure 4, is assumed for all flaws.

The Heavy Lift Helicopter rotor hub material is an alpha-beta 6Al-4V titanium forging which has been solution treated and overaged (STOA). Predictions of the number of fatigue cycles for crack growth have been accomplished by using the 6Al-4V ($\alpha + \beta$) STOA titanium forging crack propagation characteristics shown in figure 7. This measured data is from the HLH ATC Titanium Materials Evaluation Program, Reference (1), and is representative of the stress ratios encountered in the load conditions of the HLH rotor hub fatigue testing.

The lug geometry, fatigue test loads, and lug measured stresses are presented in figure 8, and Table I.

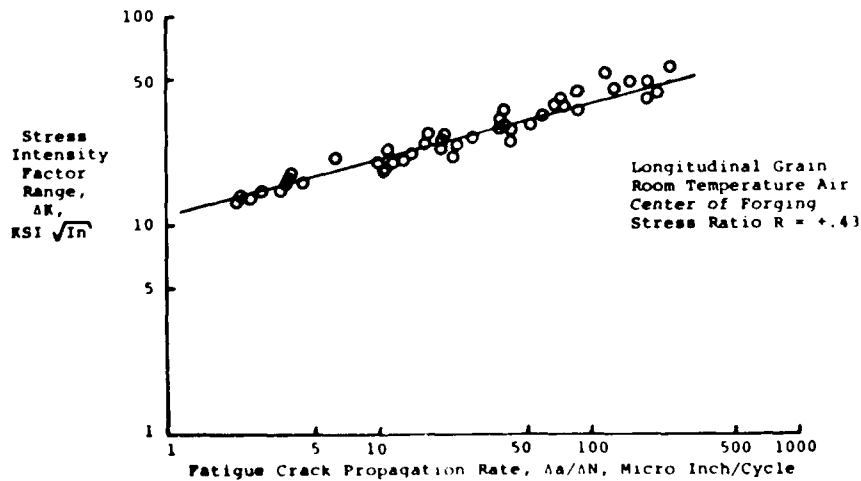
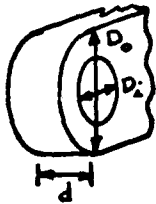


Figure 7. Fatigue Crack Growth Rate for 6Al-4V ($\alpha + \beta$) STOA Forging



$D_i = 2.25$ Inches
 $D_o = 3.00$ Inches
 $d = 1.065$ Inches

Figure 8. Rotor Hub Lug Geometry

Table I.
HISTORY OF HLH ROTOR HUB FATIGUE TEST

TEST SPECIMEN CONFIGURATION	LOADING CONDITION			CYCLES 10^6	RESULTS/COMMENTS
	CF (lbs)	VERT SHEAR (lbs)			
Fiberglass coated sleeve bushings - Lead Side FM/1000 coated sleeve bushings - Lag Side Washers (4 per side) (2 aluminum bronze (2 tungsten carbide coated Shear Pins: fiberglass coated - lead side FM/1000 coated - lag side	171,500	$\pm 27,800$	$\pm 44,540$ A	.078	
Aluminum bronze sleeve bushings Washers (2 per side): Aluminum Bronze/Ekonol Tungsten carbide coatings Shear Pin: ATC Configuration (Sermetal)	171,500	$\pm 10,590$	$\pm 13,060$ B	2.41	PRE-FATIGUE Endurance Test
	171,500	$\pm 27,800$	$\pm 44,540$ C	.104	FATIGUE TEST Shear Pins Failed
Aluminum Bronze/Ekonol coated Flange bushings with Sermetal O.D. Shear Pins: Increased flange thickness (shot peened)	171,500	$\pm 14,120$	$\pm 28,130$ D	.007	PRE-FATIGUE
	171,500	$\pm 13,300$	$\pm 22,410$ E	.161	Endurance
	171,500	$\pm 10,600$	$\pm 16,600$ F	2.25	Test
	171,500	$\pm 27,800$	$\pm 44,540$ G	.032	FATIGUE TEST Lower Hub Plate Lugs Failed Cracks Opened at 2,800 Cycles

ASSESSMENT

As shown in Table II, the average fracture toughness of the HLH rotor hub lower plate lead lug, assuming a uniaxial stress exists normal to the fracture surface, is 113400 psi $\sqrt{\text{in}}$.

Table II.
SUMMARY OF FRACTURE TOUGHNESS (K_{IC}) CALCULATIONS

$$K_{IC} = \sigma_{\max} \left(\frac{1.95}{\phi} \right) \sqrt{b} F \left(\frac{b}{t} \right)$$

LOAD CONDITION	STRESS, PSI σ_{\max}	$\left(\frac{1.95}{\phi} \right)$	CRACK DEPTH b INCH	\sqrt{b}	$F \left(\frac{b}{t} \right)$	FRACTURE TOUGHNESS K_{IC} PSI $\sqrt{\text{IN}}$	COMMENTS
G	At chamfer 67180	1.486	.85	.922	1.52	139890	One Crack Uniaxial Stress Model figure 5
	Average gross stress 41750					86900	Average value 113400
	At chamfer 67180	1.486	.85	.922	1.32	121480	One Crack Biaxial Stress Model figure 5
	Average gross stress 41750					75500	Average value 98500

Figure 9 demonstrates that the HLH rotor hub lower plate material is typical ($\alpha + \beta$) 6Al-4V titanium forging even on the basis of the lowest fracture toughness value calculated in Table II, and indicates that the material meets material specifications.

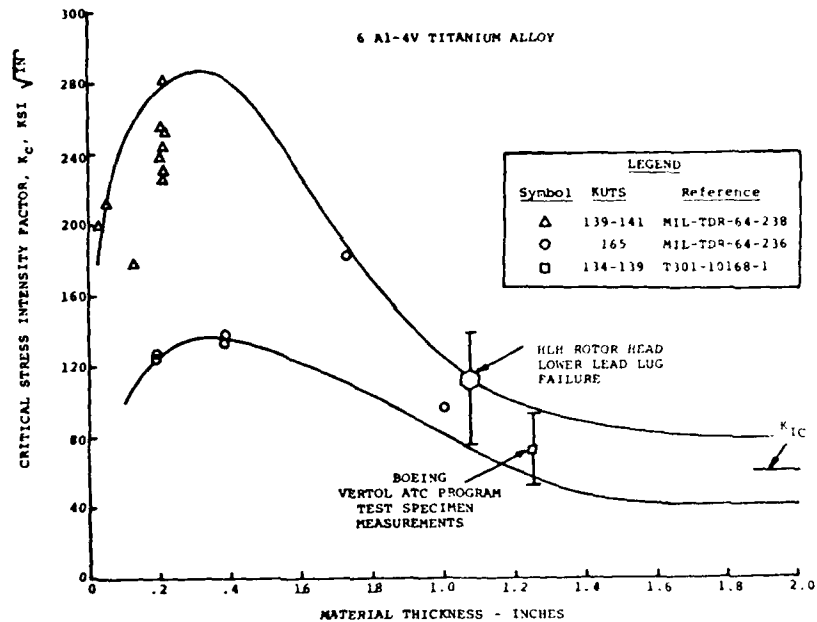


Figure 9. Variation of Critical Stress Intensity Factor, K_c , with Material thickness

Life predictions for the two lug models are summarized in Tables III and IV. Both models produce the same conclusions. Although the computed number of fatigue cycles for the two models differ for each condition, one can see by reviewing Tables III and IV that both models agree in the prediction of the load condition which causes failure. For example, if a 0.03 inch deep initial flaw existed at the initiation (I) of load condition A, the conservative fracture mechanics model shows failure of the lug in 37225 cycles into load condition B. The unconservative model also shows failure in condition B, but after 656240 cycles into load condition B.

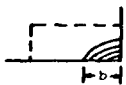
In Tables III and IV it is not important to place significance in the differences in numbers between the two models. These differences are reasonable for fracture mechanics calculations. The significant single conclusion which computations show by either method, and which is conveyed in the comparison of the two summary tables is that:

If any given initial flaw or defect size between 0.02 and 0.12 inch (and greater) existed during any load condition except the final two fatigue tests, a failure would have occurred much earlier than it did. All load conditions will cause a crack, once initiated, to propagate. The stress intensity range factors, ΔK , encountered are such that once a crack does start, the

TABLE III. FRACTURE MECHANICS MODEL FOR LUG INCLUDING GEOMETRY INFLUENCE

LOAD CONDITION	INITIAL FLAW STARTS AT INITIATION (I) OR TERMINATION (T) OF RUN	CONSERVATIVE FRACTURE MECHANICS MODEL					
		 (INCREASED STRESS CONCENTRATION EFFECT DUE TO A MAGNIFICATION FACTOR FOR GEOMETRIC BOUNDARIES OF LUG)					
		INITIAL FLAW SIZE, b, INCHES					
		0.02	0.03	0.04	0.047	0.07	0.12
A 78000 CYCLES	I	Failure 65500 Cycles into B	Failure 37225 Cycles into B	Failure 320 Cycles into B	Failure Occurs in 30540 Cycles	Failure Occurs in 2750 Cycles	Failure in 1400 Cycles
	T	Failure in 799000 Cycles	Failure in 652000 Cycles	Failure in 572000 Cycles	Failure 217330 Cycles into B	Failure 17900 Cycles into B	Failure 8400 Cycles into B
B 2410000 CYCLES	I	Failure in 799000 Cycles	Failure in 652000 Cycles	Failure in 572000 Cycles	Failure in 217330 Cycles	Failure in 17900 Cycles	Failure in 8400 Cycles
	T	Failure 89730 Cycles into C	Failure 83480 Cycles into C	Failure 80150 Cycles into C	Failure 10540 Cycles into C	Failure 2750 Cycles into C	Failure 1400 Cycles into C
C 104000 CYCLES	I	Failure occurs in 89730 Cycles	Failure occurs in 83480 Cycles	Failure in 80150 Cycles	Failure in 10540 Cycles	Failure in 2750 Cycles	Failure in 1400 Cycles
	T	Failure occurs 11540 Cycles into E	Failure occurs 11540 Cycles into E	Failure occurs 11540 Cycles into E	Failure occurs 11540 Cycles into E	Failure 3750 Cycles into D	Failure 1850 Cycles into D
D 7000 CYCLES	I	Failure Occurs 117200 Cycles into E	Failure Occurs 124000 Cycles into E	Failure Occurs 119000 Cycles into E	Failure 11540 Cycles into E	Failure 3750 Cycles	Failure in 1850 Cycles
	T	Failure 147900 Cycles into E	Failure 134000 Cycles into E	Failure 126600 Cycles into E	Failure 48290 Cycles into E	Failure 4300 Cycles into E	Failure 2120 Cycles into E
E 161000 CYCLES	I	Failure in 147900 Cycles	Failure in 134000 Cycles	Failure in 126600 Cycles	Failure in 48290 Cycles	Failure in 4300 Cycles	Failure in 2120 Cycles
	T	Failure 195900 Cycles into F	Failure 166500 Cycles into F	Failure 150400 Cycles into F	Failure 57250 Cycles into F	Failure 4900 Cycles into F	Failure 2400 Cycles into F
F 2250000 CYCLES	I	Failure in 195900 Cycles	Failure in 166500 Cycles	Failure in 150400 Cycles	Failure in 57250 Cycles	Failure in 4900 Cycles	Failure in 2400 Cycles
	T	Failure 89730 Cycles into G	Failure 83480 Cycles into G	Failure 80150 Cycles into G	Failure 12000 Cycles into G	Failure 2750 Cycles into G	Failure 1400 Cycles into G
G 12000 CYCLES	I	Failure in 89730 Cycles	Failure in 83480 Cycles	Failure in 80150 Cycles	Failure in 12000 Cycles	Failure in 2750 Cycles	Failure in 1400 Cycles
	T	-	-	-	-	-	-

TABLE IV. FRACTURE MECHANICS MODEL FOR LUG EXCLUDING GEOMETRY INFLUENCE

LOAD CONDITION	INITIAL FLAW STARTS AT INITIATION (I) OR TERMINATION (T) OF RUN	 UNCONSERVATIVE FRACTURE MECHANICS MODEL (REDUCED STRESS CONCENTRATION EFFECT BY ELIMINATION OF MAGNIFICATION FACTOR FOR GEOMETRIC BOUNDARIES OF LUG)					
		INITIAL FLAW SIZE, b, INCHES					
		0.02	0.03	0.04	0.048	0.07	0.12
A 78,000 Cycles	I	Failure Occurs In B at 837,100 Cycles	Failure Occurs in B at 656,240 Cycles	Failure Occurs into B at 77,900 Cycles	Failure in 32,000 Cycles	Failure in 5,200 Cycles	Failure in 3,300 Cycles
	T	Failure in 855,000 Cycles	Failure in 676,000 Cycles	Failure in 572,000 Cycles	Failure in 167,120 Cycles	Failure in 17,900 Cycles	Failure in 8,400 Cycles
B 2,410,000 Cycles	I	Failure in 855,000 Cycles	Failure in 676,000 Cycles	Failure in 572,000 Cycles	Failure in 167,120 Cycles	Failure in 17,900 Cycles	Failure in 8,400 Cycles
	T	Failure Occurs into F at 141,514 Cycles	Failure in 124,400 Cycles into F	Failed	Failure in 32,000 Cycles	Failure in 5,200 Cycles	Failure in 3,300 Cycles
C 104,000 Cycles	I	Failure Occurs into E at 141,514 Cycles	Failure in 124,400 Cycles into E	Failed	Failure in 32,000 Cycles	Failure in 5,200 Cycles	Failure in 3,300 Cycles
	T	Failure into E at 141,880 Cycles	Failure into E at 126,600 Cycles	Failure into E at 120,200 Cycles	Failure into E at 41,240 Cycles	Failure into E at 116 Cycles	Failure into E at 4,500 Cycles
D 7,000 Cycles	I	Failure into E at 143,880 Cycles	Failure into E at 126,600 Cycles	Failure into E at 120,200 Cycles	Failure into E at 43,290 Cycles	Failure into E at 116 Cycles	Failure into E at 4,500 Cycles
	T	Failure in 154,800 Cycles	Failure in 136,600 Cycles	Failure in 126,600 Cycles	Failure in 50,920 Cycles	Failure in 4,800 Cycles	Failure in 2,133 Cycles
E 161,000 Cycles	I	Failure in 154,800 Cycles	Failure in 136,600 Cycles	Failure in 126,600 Cycles	Failure in 50,820 Cycles	Failure in 4,300 Cycles	Failure in 2,133 Cycles
	T	Failure in 253,000 Cycles	Failure in 216,000 Cycles	Failure in 196,000 Cycles	Failure in 60,240 Cycles	Failure in 9,400 Cycles	Failure in 5,900 Cycles
F 2,250,000 Cycles	I	Failure in 253,000 Cycles	Failure in 216,000 Cycles	Failure in 196,000 Cycles	Failure in 60,240 Cycles	Failure in 9,400 Cycles	Failure in 5,900 Cycles
	T	Failure in 1,321,400 Cycles	Failure in 521,400 Cycles	Failure in 104,400 Cycles	Failure in 32,000 Cycles	Failure in 5,200 Cycles	Failure in 3,300 Cycles
F 12,000 Cycles	I	Failure in 1,321,400 Cycles	Failure in 521,400 Cycles	Failure in 104,400 Cycles	Failure in 32,000 Cycles	Failure in 5,200 Cycles	Failure in 3,300 Cycles
	T	-	-	-	-	-	-

progression is extremely rapid under constant amplitude loading conditions.

The extremely rapid mode of failure has been verified by metallurgical analysis and evaluation of the fracture surfaces of the lugs.

Failure at 32000 cycles into the last fatigue test is feasible in two situations. If a defect equal to or greater than .047 inch deep was introduced by some means during the early stages of the final fatigue test, a rapid failure could occur in 32000 cycles.

Now, theoretical calculations indicate that for the constant amplitude loading condition G, the flaw had to be at least as great as .047 inch deep, to propagate to failure in 32000 cycles. If the initial flaw was smaller than .047 inch deep, the flaw initiated during some earlier load condition. This earlier load condition might be one of the pre-fatigue load conditions D, E or F. The calculations show, however, for even the smallest flaw of 0.02 inch that if the flaw started in D, E, or F, failure would have to have occurred in load condition F.

By the numbers, then, it is not possible for the flaw to have initiated during the pre-fatigue endurance testing. Also, there is a practical consideration which must be included and which provides a logical explanation for the failure sequence.

Following the second fatigue test you note that the load conditions D, E, and F of the pre-fatigue endurance test step down in load levels. Stepping down in load will arrest crack growth.

The duration of arrestment cannot be predicted without test data, but in general, the arrest time increases as the step load increases.

The magnitude of the change in load conditions between the fatigue test condition C, and the pre-fatigue endurance test load conditions D, E, and F are such that without question, it is possible that a flaw or defect initiated during or at the end of the fatigue test, load condition C, was arrested during the pre-fatigue endurance test, and started to propagate immediately at the start of the final fatigue test, load condition G.

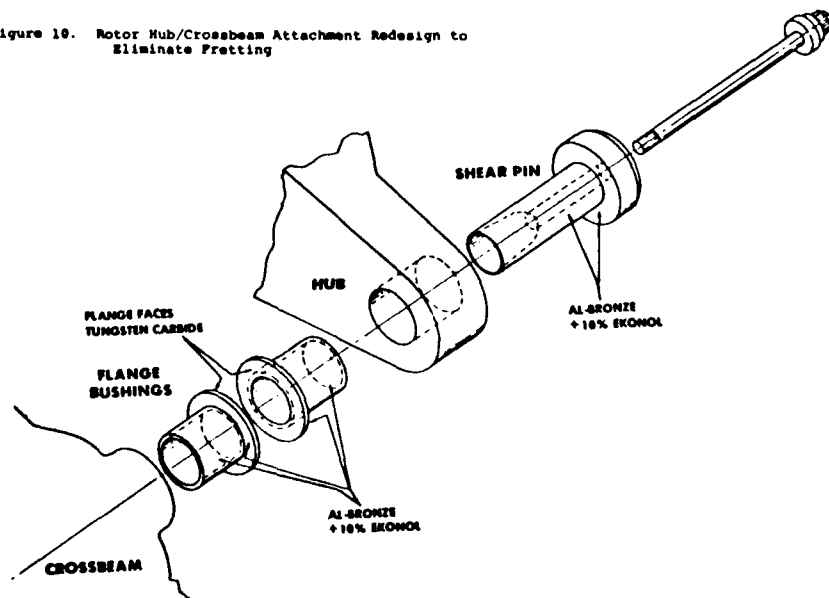
CONCLUSIONS

By using fracture mechanics theory, measured stress levels, and the known crack propagation rates for ($\alpha + \beta$) STOA 6 Al-4V titanium forging, it can be shown that the fracture toughness of the HLH rotor hub lower plate meets specifications for toughness, and crack growth rates are such that the failure of the lower lead lug occurs rapidly and most probably occurred in one of two ways:

- The crack initiated, and then propagated to failure during the final fatigue test
- The crack initiated during or at the end of the second fatigue test, was arrested during the pre-fatigue testing, and started to grow again in the final fatigue test where failure occurred in a relatively small number of cycles.

Crack initiation is attributed to fretting. Metallurgical examination of the fracture face of the lug confirmed that the initiation point of the flaw occurred in a region of fretting. The application of fretting inhibitors, tungsten carbide and aluminum bronze/ekonol, as shown in figure 10 would eliminate fretting, and the safe life goal of 3600 hours can be achieved.

Figure 10. Rotor Hub/Crossbeam Attachment Redesign to Eliminate Fretting



THE CHARACTERISATION OF CRACK GROWTH AND
FRACTURE IN A MILITARY BRIDGE

Dr N J Adams, Senior Inspector
Nuclear Installations Inspectorate
Thames House North, Millbank, London

and

D Webber, Principal Scientific Officer
Military Vehicles Engineering Establishment
Christchurch, Dorset

INTRODUCTION

The service environment of a military bridge is such that high quality defect free structures are not cost effective. However, at the same time, a structure should be designed and manufactured so that it will not fail prematurely when used in a hostile environment. The subject of this study is the tank launched bridge shown in Fig. 1, whose design was evolved in the mid-60s to comply with a number of specific requirements. The primary ones were that the bridge should meet military load class (MLC)* 60 demands, with a clear span of 22.8 metres, and when combined with its own transport vehicle should not exceed the MLC 60 limit.

The selected transport and launch vehicle was a Chieftain Tank without its gun turret. Thus, in order to meet MLC 60 limitations, the weight of the bridge was restricted to approximately 12 tonnes. In addition, to achieve an acceptable degree of mobility, a limitation of 1.8 metres was placed on the folded height. During the development program, an additional requirement was imposed of the bridge being capable of sustaining a minimum of 10 000 crossings of a MLC 60 vehicle at the maximum span.

In order to meet the requirements a material exhibiting high strength/weight ratio was essential together with a high modulus of elasticity to limit, to an acceptable level, the mid-span deflection. In addition, since climatic conditions could vary considerably, the material had to have good ductility at sub-zero temperatures. Notwithstanding these requirements, the selected material had to be readily worked and straightforward to fabricate. The material finally selected was 18% Nickel maraging steel with a nominal 0.2% proof stress of 1390 MNm⁻². This particular material posed no undue working problem in its annealed condition, could be readily welded by the metal inert gas (MIG) process without the use of preheat and aged to produce its optimum mechanical properties at about 480°C (1, 2, 3).

From the design evaluation the bridge evolved as an all welded basic girder section, consisting of a 4.7 mm thick stiffened plate web with a rectangular

* Military Load Class of a tank is approximately the weight in short tons.

top compression chord and a triangular bottom tension chord as shown in Fig. 2. A half span of one trackway comprises of a ramp and a center section. To form the full span the center sections are joined by a hinge. The hinge forgings are attached to the girders by means of slots that accept the web plate and have fillet welds on either side of the forgings, which are scarfed on to the chord sections with further fillet welds. The female forked hinge is 112 mm thick, whilst the male section is 45 mm thick. A similar arrangement is used to join the ramp to the center section, but the parts do not fold relative to each other although they may be hinged to improve traffickability. Two trackways are joined together to form a complete bridge (4).

In view of the large amount of welding involved it was inevitable, despite non-destructive examination of the more critical areas, that the bridge would contain defects. In addition, fretting of the hinges due to vehicles crossing produces a hostile environment at these details.

FORMULATION

Two mechanisms of failure are likely from a consideration of the thickness of the material used in the manufacture of a bridge; plane strain fracture in the heavy hinge sections and plane stress fracture in the bottom tension chord section, each preceded by subcritical fatigue crack growth. The former is now the subject of accepted standard material test methods both in the USA and United Kingdom (5, 6) but, at the time that the initial problems were being studied, these test standards were still being formulated. No completely acceptable test standard exists for the plane stress fracture mechanism, even to this day, although ASTM (7) have published a proposed method based upon the resistance curve concept.

It can be demonstrated that a material will fail in an apparently brittle and uncontrolled manner when the stress intensity at a crack tip reaches the critical value K_{Ic} , the plane strain fracture toughness. For the case of a partial penetration defect, failure can be defined by

$$K_I = S \sqrt{\frac{\pi a}{Q}} M_e = K_{Ic} \quad (1)$$

where a is the crack depth, Q is the elastic shape factor, M_e the elastic magnification factor which accounts for the influence of external boundaries and S is the nominal stress.

The definition of fracture in the plane stress regime is much less clear. The crack growth resistance method developed by Krafft (8), appeared to offer the only possible solution. It is an extension of the Griffith-Irwin energy balance analysis, to cases where stable crack growth occurs prior to instability. The crack growth resistance R is defined as the work required to produce a unit crack extension. In materials where the thickness permits stable growth, R is not a constant quantity but, in general increases as the crack extends



FIG 1 CNEFTAM FV 4205/AVLB BRIDGE LAYING VEHICLE.
(BRIDGE SPAN 22.8m)

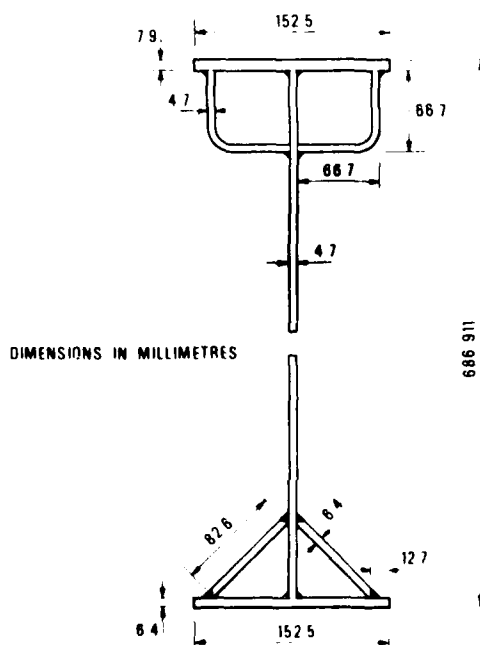


FIG 2 SECTION THROUGH BRIDGE GIRDER

from its initial length a_0 . This variation of R when plotted as a function of crack length, is referred to as a crack growth resistance curve or R-curve. Figure 3 shows an R-curve typical of thin section failure.

All structural materials have an initial resistance to crack growth in the presence of a flaw, that is failure does not occur at the initial application of a monotonically increasing load. Thus, in order that a crack can grow in a stable manner some energy must be supplied beyond that required to produce elastic crack opening and plastic deformation. The total quantity of energy, often referred to as the crack driving force, is equivalent to the elastic energy released per unit area of crack extension G , which is related to both the applied load and the instantaneous crack length. Thus, in Fig. 3, a family of G curves exists, each curve representing a specific load. When stable crack extension occurs, the elastic energy release rate must equal the crack growth resistance and this condition is represented by the points of intersection of the G curves with the R-curve, as shown in Fig. 3. Crack extension at these points is stable, since an increment of growth provides a greater increase in R than in G , and an increase in load is then required for further growth. Eventually, a point is reached where the G curve becomes tangential to the R-curve and the increase in R no longer exceeds that of G thus instability occurs. This point provides a critical value of the elastic energy release rate G_c which defines the critical fracture toughness, ($K_c^2 = EG_c$). An inescapable conclusion of the R-curve concept is that, at any particular material thickness, there is no single value of G_c , if that thickness is such as to permit stable crack growth. This result is a consequence of the shape of the G curves, which are derived from the elastic compliance of the cracked structure.

The resistance that develops against fast fracture is partly associated with the formation of the zone of plastically deformed material at the crack tip. The larger the plastic zone becomes, the greater the amount of irrecoverable work that must be done prior to fracture. It has been found that the toughness increases with increase in specimen width and approaches a maximum value asymptotically (9). Thus, the more readily a material yields, the wider the specimen must become in order to completely describe the R-curve and make the test meaningful in terms of elastic analysis.

The R-curve concept thus appears to offer valuable information in an investigation of thin sheet fracture. In cases where final failure occurs at a load considerably greater than that necessary to initiate crack extension, the concept can be used to determine both critical toughness values and their associated critical crack lengths.

The stress at failure on the remaining ligament, as defined by $W-2a_e$ where W is the specimen width and a_e is the compliance indicated crack length, must not exceed the material tensile yield strength according to the current ASTM recommended procedure for determining an R-curve. However, in materials which exhibit plane stress toughness levels as high as those in maraging steel, test specimens of very great width (exceeding the bridge depth) would be required to obtain so called valid results, but one cannot ignore the fact that these

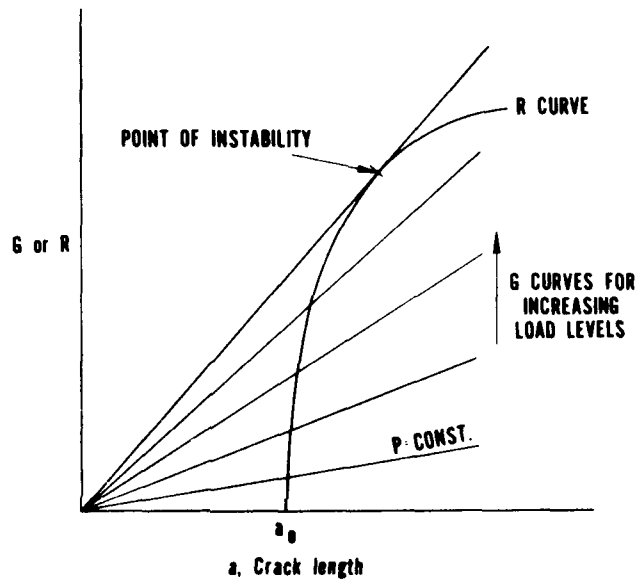


FIG 3 SCHEMATIC REPRESENTATION OF G-R CURVE RELATIONSHIP

materials will exhibit stable crack tearing even in small samples and when used within its context such laboratory R-curve test information on small specimens can be very valuable.

With regard to the fatigue aspect, in the case of the welds the cracks will be pre-existing defects, but in the bore of the hinge connections cracks have to be initiated at the points of high stress concentration aggravated by fretting. Growth of fatigue cracks has been shown to be a function of the crack tip stress intensity range and can be expressed as the $da/dN = C\Delta K^n$ (10) where C and n are material constants and ΔK is the stress intensity range. Thus it is clear that information, although not always simple to apply, can be generated from which it is possible to predict the fatigue life and crack length at failure under cyclic loading conditions.

Experience and data has been gained in programmes on structural and laboratory testing, which have overlapped, but for clarity they will be presented separately starting with development structural testing.

Two experimental trackway sections each comprising two girders, one without and one with a hinge cut from thick plate, were fatigue tested (11). Since those initial tests other tests have been carried out on prototype bridge trackways and a production trackway built by a commercial company. These tests have revealed a great deal of information about initial defects and crack growth. The results have been summarised, briefly, in Table 1. It is hoped to publish, in the near future, a series of detailed reports which will provide all of the information that has been obtained during the course of the tests, and so we have restricted what is presented here to the essential highlights.

The loads applied to the experimental sections were based on calculations but the loads required for testing the complete trackways were established by strain gauge measurements using an appropriate MLC 60 vehicle in a field test and the trackway was then loaded in the laboratory to reproduce these strains. In addition, the maximum load in some instances was increased by 13 kN to allow for the effects of mud and snow deposits that could form on the structure in service. The actual range of load was from a minimum of 10 kN, the latter being necessary to avoid slack in the testing system. In the case of the commercially manufactured bridge trackways these were subject to an initial production proof load of 1.25 x the maximum working load.

A variety of conventional inspection techniques were used in the course of testing, including visual (with a magnifying glass), dye penetrant, magnetic particle and pneumatic pressurising of the center section bottom chord. Because the hinge joints are scarfed into each end of the center section bottom chord, they form a sealed unit and an internal pressure of 276 kNm^{-2} could be applied. The outside surface was sprayed with a detergent solution, which indicated cracks or porosity by the formation of fine creamy lines of bubbles. The hinge lugs were most readily examined using the magnetic particle method with a small hand held permanent magnetic device. In addition, as part of an extra-mural contract, a center joint fatigue test was

Table 1 - Details of Structural Tests

Component	Girder Stress range MNm ⁻² *	Cycles	Brief Description
Center Girder	738	1 740 + 3 425	Experimental section of trackway made from air melted material but without jaws. Stiffener welds peened to prevent failure at transverse weld toes. Total crack length at failure 80 mm for each girder. Fracture analysis described in text.
Center Hinge	738	> 3 000	Experimental section of trackway using air melted material. After fatigue testing it was re-proof tested and failure occurred in one of the male jaws, from a pre-existing transverse weld crack that had grown during the fatigue test. Fracture analysis described in text.
Ramp Girder	264	> 35 000**	Failure initiated along the toe of a 150 mm long transverse fillet weld connecting a support bearing plate to the bottom flange of the girder. See Fig. 4 for detail of failure. The full extent of fatigue crack growth could not be determined.
Center Hinge	295 361	10 000 + 19 094	Test of prototype bridge made with air melted jaw material. Initial test on complete bridge with an MLC 60 tank. Continued testing in laboratory with one trackway comprising two center girders and a ramp girder with hypothetical design load. Male jaw failure shown in Fig. 5.
Center Girder	284	37 226	Production center trackways with double vacuum melted material used for manufacture of jaws. Failure initiated from toe of transverse stiffener welds, section failure shown in Fig. 6. The crack resulting in failure was detected 2726 cycles before failure occurred.
Center Hinge	264	47 000	Ramp joint manufactured from double vacuum melted material. Figure 7 shows extent of cracking 12 500 cycles prior to hinge failure.

* Estimated stress at maximum fibre distance R = 1.

** Predictive damage estimated for total life includes cycles at other stress levels.

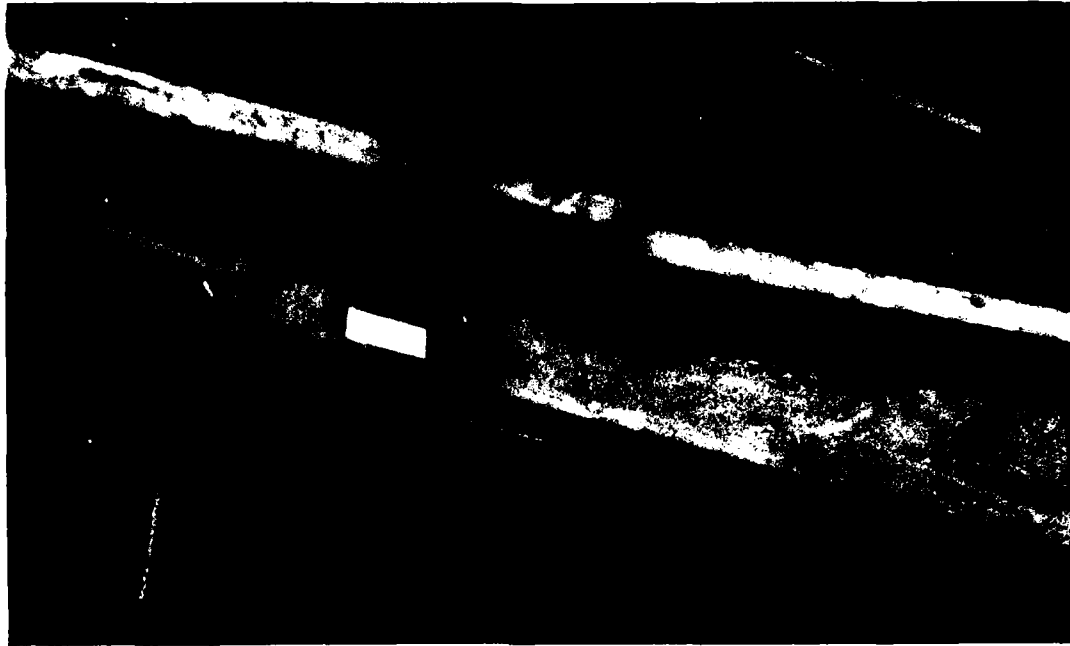


FIGURE 4 — RAMP UNIT FAILURE AT BEARING PLATE



FIGURE 5 — FRACTURE OF CENTER SECTION MALE LUG



FIGURE 6 - CENTER SECTION FAILURE ORIGINATING AT QUADRANT STIFFENER

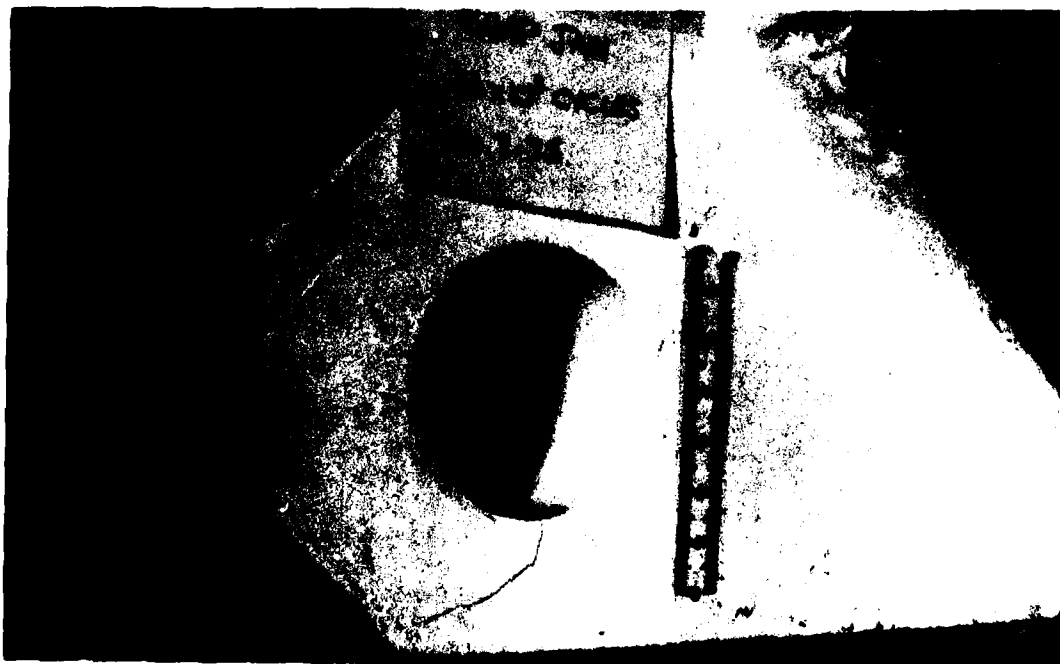


FIGURE 7 - EXTENSION OF FATIGUE CRACK IN MALE LUG OF RAMP JOINT

monitored by the acoustic emission method. Whilst the method was not successful in predicting imminent failure, retrospective examination of records revealed clear changes in output just prior to failure. It is still possible that the technique can be shown to be effective, but, one problem to be overcome is general noise isolation since there is a considerable amount of spurious noise generated in such a structure during a load cycle.

Basic material mechanical properties and fracture toughness data has been generated for both the hinge material and thin plate air melted material used in the prototypes and is recorded briefly in Table 2. This summarised information is recorded in detail in Reference (12). Table 2 also presents tensile mechanical and fracture toughness properties which indicate orientation and original thickness effects. Figure 8 shows the variation in fracture toughness of thin plate material expressed in terms of crack growth resistance R on specimens up to 280 millimetres wide, whilst Fig. 9 shows fatigue crack growth rates in the same material. Double vacuum melted material has been used for the hinges of production bridges. This has exhibited a considerable improvement in plane strain fracture toughness and some results are also quoted in Table 2.

ASSESSMEN.

A test section of trackway containing a hinge connection described earlier has been fatigue tested at maximum working load for more than 3000 cycles after which the trackway was used for weld repair trials. During subsequent re-proof testing, failure occurred at one of the male jaws. It appeared that a pre-existing transverse weld flaw grew during fatigue testing to a size that was critical on re-proof testing. The original crack had escaped detection by NDE. The shape and size of this flaw which could be approximated to a semi-ellipse was indicated by heat tinting arising from re-maraging after the weld repair. Using data for semi-elliptic cracks given by Tiffany & Masters (13) and stresses determined from photoelastic models, a plane strain fracture toughness of $86.8 \text{ MNm}^{-3/2}$ was calculated. It can be seen that this value is in reasonable agreement with toughness figures for 'air melted' material shown in Table 2.

In another test section of trackway a plane stress failure occurred which originated at the weld between the base and angled chord plates shown in Fig. 2. The fatigue crack length was approximately 48 mm into the flange and a fracture toughness value was calculated to be $500 \text{ MNm}^{-3/2}$ using the maximum bending stress (737 MNm^{-2}) and assuming that the section was a 152 mm wide single edge notch tension stript. This toughness value is equivalent to K_{CO} , (function of maximum gross stress and crack length a_0) calculated for center cracked plates, details of which are given in (11). Comparison can be made with some of the 200 and 276 mm wide specimens containing fatigue cracks approximately 75 mm long. Five 276 mm wide specimens failed at an average gross stress of 869 MNm^{-2} with an average K_{CO} of $312 \text{ MNm}^{-3/2}$. Seven 200 mm wide specimens failed at an average gross stress of 710 MNm^{-2} , with an average K_{CO} of $274 \text{ MNm}^{-3/2}$.

Table 2 - Properties of 18% Nickel Maraging Steel

AIR MELTED						
4.7 mm thick plate 0.2% proof stress	Ageing time at 480°C					
	1 h			100 h		
	1205 MNm ⁻²			1546 MNm ⁻²		
'As received' thick rolled plate after maraging	Ageing time 3 h at 480°C					
	Original thickness					
	100 mm			50 mm		
	Toughness MNm ^{-3/2} K _{IC}			80		
Orientation effects Toughness MNm ^{-3/2} K _{IC}	Direction					
	Ageing time 3 h at 480°C					
	L-S	L-T	T-L	T-S	S-L	S-T
	114.2	109.7	83.0	85.9	75.3	78.5
	DOUBLE VACUUM MELTED					
Ageing time	0.2% Proof stress MNm ⁻²	Toughness K _Q MNm ^{-3/2}		Thickness mm		
10 h at 460°C	1463	149-175		37.5		
3 h at 480°C	1382	168+		37.5		

It was appreciated that the simple approach adopted for assessing failure of the bottom flange was really not adequate and so an effort was made to examine theoretically the behaviour of cracks in flanged beams, since no suitable solutions exist. Several different configurations have been examined (14), but what is presented here is the more practical situation of a crack propagating across one side of a flange in a beam. There are a number of analytical techniques which can be used to determine stress intensity (15), however, complex boundary conditions in structures frequently preclude many of these methods. One method which does lend itself to both analytical and experimental determination is compliance analysis. Irwin (16) showed many years ago that the strain energy release rate G was related to the change in compliance by

$$G = \frac{P}{2B} \frac{d\lambda}{da} \quad (2)$$

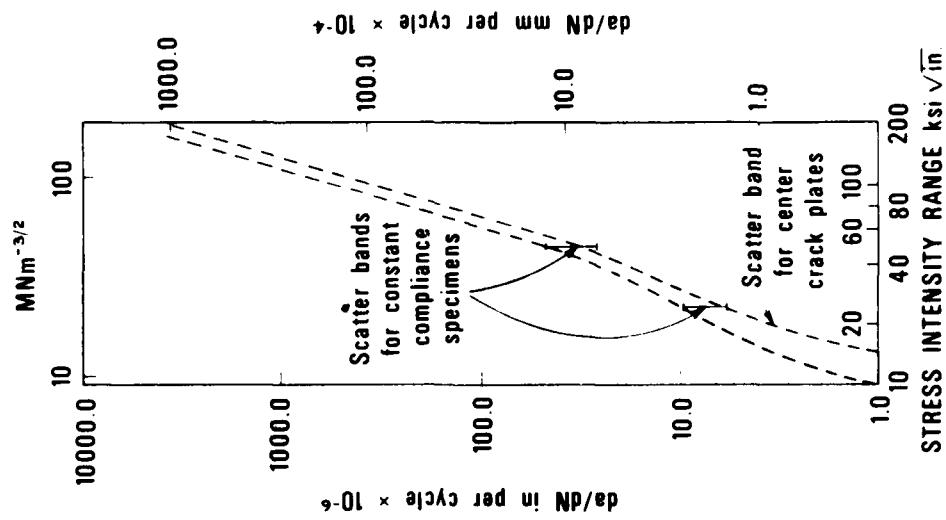


FIG 9 FATIGUE CRACK PROPAGATION RATES IN 18% NICKEL MARAGING STEEL

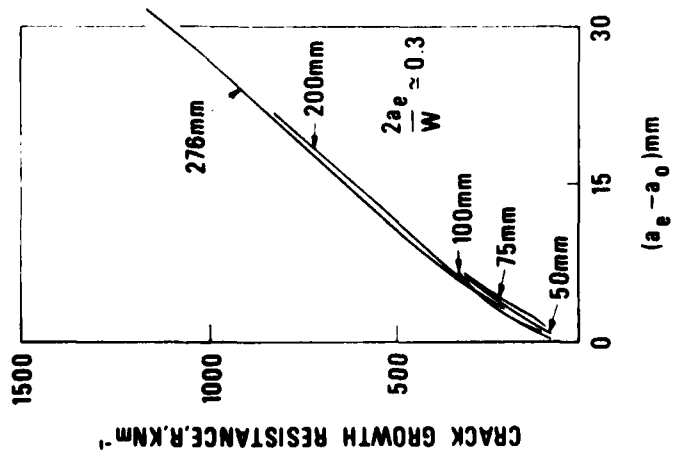


FIG 8 CRACK GROWTH RESISTANCE CURVES FOR SPECIMENS OF DIFFERENT WIDTHS

where P is the applied load, B the thickness and λ the structural compliance. The variation in strain energy release rate (stress intensity) is derived by measuring the change in stiffness of a structure as the crack length is varied.

By considering the bottom flange and part of the web of a beam in bending as a simple tension member, it can be shown that

$$K^2 = \left(1 + \frac{A_w}{A_f}\right)^2 \sigma^2 a \frac{W_f}{a} \left\{ \frac{df}{d} \frac{(a/W_f)}{(a/W_c)} \right\} \quad (3)$$

where A_w and A_f are the area of the web and flange respectively, σ is the remote stress and W_f the flange width. An example, which was examined is shown in Fig. 10, is an edge crack extending across the flange of an inverted Tee section towards the center web. The compliance variation with crack length was calculated using finite element methods employing an 8 node iso-parametric quadrilateral element with linear variation in strain to model the beams. At the same time an experimental programme was conducted to measure the compliance in perspex beams of the same dimension and as shown in (14) the results obtained by both methods were in good agreement. The results of the analysis are shown in Fig. 10 where the variation in stress intensity squared is plotted as a function of a/W and compared with the variation in a single edge notch tension configuration (17). This form of plot was chosen since it relates directly to the differential term in equation (3). It can be quite clearly seen that as the crack approaches the central web the crack tip stress intensity reduces. Although the bottom flange is normally in direct tension it was observed from measurements on the models tested and an examination of the finite element results that, some lateral deflection occurs and the edge opposite the crack tip becomes subject to compressive stress. This has been confirmed on low strength aluminium alloy I beams, tested in four point bending, where fracture could not be induced because the beam deflected laterally and twisted. However, it was possible to constrain the beam to fail by testing in three point bending. It was then observed that the crack would extend towards the central web and propagate into the bottom of the web before extending across the flange.

From consideration of Fig. 10, a revised value of Y for the case of a crack approaching the web in a beam can be obtained to re-calculate failure of the trackway described earlier. Taking an approximate value of $Y=2$, a stress of 737 MNm^{-2} and a crack length 48 mm, a value of K_{CO} equal to $312 \text{ MNm}^{-3/2}$ is obtained, which is in much closer agreement with the laboratory test results. In addition, observations of crack growth in the flange just prior to failure indicated growth rates exceeding 1 mm per cycle. This is greater than any measured values in laboratory tests recorded in Fig. 9 and indicates toughness in excess of $200 \text{ MNm}^{-3/2}$, which was the maximum stress intensity range reached during the fatigue crack growth tests. From the results it was concluded that the fracture toughness of an I beam is no greater than the toughness capacity appropriate to the width of the bottom flange. Unfortunately, it was not

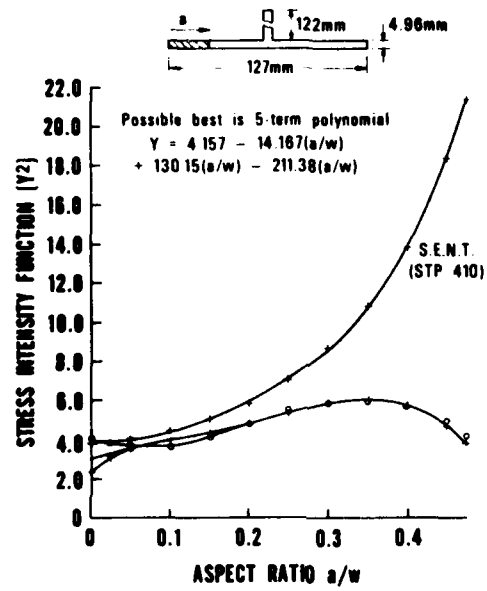


FIG 10 COMPARISON OF VARIATION OF STRESS INTENSITY (SQUARED) FOR SINGLE EDGE NOTCH TENSION SPECIMEN AND BOTTOM FLANGE OF A BEAM ASSUMED SUBJECT TO UNIFORM TENSION

possible to make similar calculations for the plane strain failures listed in Table 1, due to a lack of information on local stress conditions or final defect size, or for the other plane stress failures because of the lack of a suitable analytical solution.

Recently, Adams (18) has shown that fracture resistance is a function of specimen configuration and the results indicate that the toughness of a tension flange in a beam can be most easily and more realistically obtained from resistance curves determined using compact tension specimens which could well lead to lower values of K_{IC} . Furthermore, by careful measurements of the relationship between absolute crack length and stress it is possible to establish a resistance curve which does not include crack tip yielding. Such a resistance curve would be the most useful in structural analysis, both during design and for in-service assessment of postulated or actual cracks.

As reported at a TTCP meeting (19), a study was made on the influence of battle damage to stressed plates and subsequent fatigue crack growth from the penetrations. From this limited programme it was established that assessment of structural integrity following projectile damage can also be made in terms of fracture mechanics. It was observed that even in situations where penetration had a very ragged profile, fatigue crack growth required an initiation period.

CONCLUSIONS

The first and most significant conclusion from an examination of Table 1, is that user fatigue life requirements were exceeded by a sufficient margin to account for any scatter effects and small sample size. At the same time, structural testing revealed that no one area in the bridge could be identified as a particular area of weakness compared with the remainder of the structure. The second is that by choice of suitable simple inspection methods, aided by some knowledge of locations that require particular attention, it is possible to detect cracks likely to cause failure well before they can endanger the structure.

Failure occurs either across the bottom chord or in the hinge section, and a close examination of the results indicates ways in which the effective toughness of both areas can be improved. For thin plate, the R-curve analysis has demonstrated that toughness expressed in terms of K_{IC} increases with specimen width. Thus, if it was necessary to improve the strength of the bridge, increasing the bottom chord width would increase the toughness capacity. In the thick hinge material it has been demonstrated that a double vacuum melting can lead to a significant improvement in toughness and it may well be that an examination of the forging techniques used could contribute a further small increase in toughness. Alternatively, a double male lug would reduce the thickness of each protrusion below that in which plane strain fracture could occur, thus benefit could be derived from material deforming plastically.

Simple girder tests have revealed that asymmetric cracks lead to a failure involving lateral bending, thus cross-connection of the girders, by diaphragms

as in the present design, can be valuable by introducing stability and improving toughness capacity.

It has been established that ballistic damage, even for ragged penetrations, there is a delay period during which fatigue cracks initiate and treatment of the damage as a crack, using fracture mechanics concepts, is practical and includes a small measure of conservatism.

For future design studies more attention can now be paid to fracture analysis. This may be done by finite element methods, using the quarter node point isoparametric element which appears to offer considerable advantages in modelling crack tip conditions. Also the values of being able to see by use of visual display units what happens to a structure during a model analysis should not be ignored.

Crown Copyright Reserved.

DISCLAIMER

The views expressed in this paper are those of the authors and should not be taken as representing the official views or policy of the Nuclear Installation Inspectorate or the Military Vehicles Engineering Establishment (Christchurch).

REFERENCES

1. Roberts, C, "Mechanical Properties of 18% Nickel Maraging Steel", Welding and Metal Fabrication, v. 36, no. 3, March 1968, 111-118.
2. Bailey, N and Roberts, C, "Maraging Steel for Structural Welding", American Welding Journal, to be published. AWS 57th Annual Meeting, May 10-14, 1976.
3. Roberts, C, "Maraging Steel, Experience at MEXE Welding 90 tons/in² Grade Material", Welding and Metal Fabrication, v. 10, no. 11, November 1968, 405-409.
4. Napier, M A and Parramore, T S., "The Chieftain Bridge Layer", C.M.E. Journal, v. 22, no. 9, 1975, 69-72.
5. "Plane Strain Fracture Toughness of Metallic Material", ASTM E 399-72, Part 10.
6. "Methods for Plane Strain Fracture Toughness (K_{Ic}) Testing", British Standard Institution DD3, 1971.
7. "A Recommended Procedure for R-curve Determination", ASTM Book of Standards, no. 10, 1974.

REFERENCES (continued)

8. Krafft, J H, Sullivan, A H and Boyle, R W, "Effect of Dimensions on Fast Fracture Instability of Notched Sheets". Proceedings, Crack Propagation Symposium C of A, Cranfield, September 1961, v. 1, 8-28.
9. Srawley, J E and Brown W F, "Fracture Toughness Testing Methods". ASTM STP 381, 1964, 133-196.
10. Paris, P and Erdogan, F, "A Critical Analysis of Crack Propagation Laws". Trans ASME, J. Basic Eng, v. 2, no. 4, 1963, 528-534.
11. Munro, H G and Adams, N J "Fatigue and Fracture of a 200 ksi Grade Maraging Steel Proposed for Use in Military Bridging", Engineering Fracture Mechanics, v. 4, no. 3, 1972. 705-715.
12. Webber, D, Roberts, C, Adams N J I and Munro, H G, "Fatigue and Fracture of an 18% Nickel Maraging Steel Used for Military Bridging", MVEE Report 76504, February 1976.
13. Tiffany, C F and Masters, J N, "Applied Fracture Mechanics", ASTM STP 381, 1964, 249-277.
14. Adams, N J, "Fracture Toughness Characterisation in Military Construction Materials", Royal Military College of Science, Applied Mechanics Technical Report No. 77, 1976.
15. Rooke, D P and Cartwright, D J, "Compendium of Stress Intensity Factors", HMSO (1976).
16. Irwin, G R and Kies, J A, "Critical Energy Analysis of Fracture Strength", Welding Res. Supplement, v. 33, 1959, 193-198.
17. "Plane Strain Crack Toughness Testing of High Strength Metallic Materials", ASTM STP 410, 1966.
18. Adams, N J, "Influence of Configuration on R-curve Shape and G when Plane Stress Conditions Prevail", ASTM STP 601, 1975, 193-198.
19. Adams, N J I and Munro, H G, "Tests on the Effect of Ballistic Damage on Highly Stressed Plates and Subsequent Fatigue Crack Growth", Sumposium on the relevance of fracture toughness to design and reliability of military equipment, June 1973, sponsored by TTCP Working Panel on Metals (P1).

FRACTURE MECHANICS ANALYSIS WITH HYBRID "CRACK" FINITE ELEMENTS

Pin Tong

Staff Member, DOT Transportation Systems Center
Cambridge, MA 02142

Theodore H. H. Pian

Professor of Aeronautics and Astronautics, M.I.T.
Cambridge, MA 02139

Oscar Orringer

Associate Director, Aeroelastic and Structures Research Laboratory, M.I.T.
Cambridge, MA 02139

INTRODUCTION

For complicated structural components which include embedded cracks, it is imperative to apply numerical methods to compute the stress intensity factors at the crack tip. The most versatile method for such computation is the finite element method [1]. In principle, it is possible to use just conventional finite elements to determine the stress and displacement distributions near the tip of the crack and, in turn, to estimate the stress intensity factors. However, the rate of convergence is very slow, and a highly refined mesh must be employed near the crack tip [2]. A more efficient procedure is to utilize near the crack tip special elements which contain the correct stress singularity behavior. These "crack" elements may still be derived by methods which are based on assumed displacement distributions, although it is not always possible to maintain compatibility with the neighboring elements. A more rational approach is the use of a hybrid model which involves independently assumed field variables in the interior and along the boundary of the element. This paper reviews the history of the development of several hybrid crack elements for both two-dimensional and three-dimensional fracture analyses.

HYBRID MODELS IN FINITE ELEMENT ANALYSIS

Finite element methods can be formulated from variational principles in solid mechanics. Typical methods are the compatible and equilibrium models which are based on the principles of minimum potential energy and complementary energy respectively. The term "hybrid model" was first introduced to represent finite element methods which are formulated using modified variational principles with relaxed continuity conditions along the element boundaries [3,4,5]. Two such models which lead to element stiffness matrices and hence to the conventional matrix displacement method are a hybrid stress method and a hybrid displacement method.

The variational principle for the formulation of a hybrid stress model [3,6] is a modified complementary energy principle which specifies that the following functional π_{mc} is stationary:

$$\pi_{mc} = \sum_n \left[\int_{V_n} \frac{1}{2} \tilde{\sigma}^T S \tilde{\sigma} dV - \int_{\partial V_n} \tilde{T}^T u dS + \int_{S_{\sigma n}} \tilde{T}^T u dS \right] \quad (1)^*$$

where $\tilde{\sigma}$ represents equilibrating stresses, S the elastic compliance matrix, T the surface tractions (in equilibrium with $\tilde{\sigma}$), u the independent boundary displacements. In the finite element formulation the stresses $\tilde{\sigma}$ are approximated by a finite number of parameters $\tilde{\beta}$ and the element boundary displacement u are approximated by nodal displacements \tilde{q} . The stationary condition of π_{mc} permits the expression of $\tilde{\beta}$ in terms of \tilde{q} at the element level. Thus, π_{mc} can be written in terms of \tilde{q} alone:

$$\pi_{mc} = \sum_n \left[\frac{1}{2} \tilde{q}^T k_n \tilde{q} - \tilde{q}^T Q_n \right] \quad (2)$$

where k_n is the element stiffness matrix of the n th element. The resulting matrix equation is then in the form of

$$K\tilde{q} = Q \quad (3)$$

where K and Q are the assembled stiffness matrix and nodal force vector respectively.

The variational principle for the formulation of the hybrid displacement model [7] is a modified potential energy principle which specifies that the following functional π_{mp} is stationary:

$$\pi_{mp} = \sum_n \left[\int_{V_n} \left(\frac{1}{2} \tilde{\epsilon}^T C \tilde{\epsilon} - \tilde{F}^T u \right) dV - \int_{\partial V_n} \tilde{T}^T (u - \tilde{u}) dS - \int_{S_{\sigma n}} \tilde{T}^T u dS \right] \quad (4)$$

where the strains $\tilde{\epsilon}$ are expressed in terms of the displacements u , \tilde{u} are independent boundary displacements, \tilde{T} are boundary tractions for individual elements, and where C is the elastic coefficient matrix. In the finite element formulation \tilde{T} and u are approximated by a finite number of parameters $\tilde{\alpha}$ and $\tilde{\beta}$, respectively, while the boundary displacement \tilde{u} is interpolated in terms of nodal displacements \tilde{q} . By applying the variational principle at the element level both $\tilde{\alpha}$ and $\tilde{\beta}$ can be expressed in terms of \tilde{q} ; π_{mp} can then be expressed in terms of \tilde{q} and the element stiffness k_n , in the form of Eq. 2.

* The integration limits have the following meanings: V_n is the volume of the n th element, ∂V_n is the entire n th element boundary, and $S_{\sigma n}$ is that part of ∂V_n on which surface tractions are prescribed.

HYBRID "CRACK" ELEMENT I

An immediate application of Eq. 1 to the derivation of a "crack" element [8,9] is to include in the assumed stresses the singular terms which are governed by the stress intensity factors K_I , K_{II} and K_{III} which represent respectively the opening mode, the in-plane shearing mode and the out-of-plane shearing mode. Thus, the assumed stresses are written as

$$\tilde{\sigma} = P\tilde{\beta} + P_{\tilde{K}}\tilde{\beta}_{\tilde{K}} \quad (5)$$

where P may be simple polynomials, where $P_{\tilde{K}}$ represents the known distribution of the singular stress terms,* and where $\tilde{\beta}_{\tilde{K}} = \{K_I, K_{II}, K_{III}\}$. Since the parameters $\tilde{\beta}_{\tilde{K}}$ must be shared by several elements around the crack tip, they cannot be eliminated at the element level. Instead, a mixed system of matrix equations results:

$$\begin{bmatrix} \tilde{K} & \tilde{M} \\ \tilde{M}^T & \tilde{N} \end{bmatrix} \begin{Bmatrix} \tilde{q} \\ \tilde{\beta}_{\tilde{K}} \end{Bmatrix} = \begin{Bmatrix} \tilde{Q} \\ \tilde{O} \end{Bmatrix} \quad (6)$$

A "superelement" can be defined by pre-assembling the elements that contain $\tilde{\beta}_{\tilde{K}}$ and then eliminating $\tilde{\beta}_{\tilde{K}}$ by static condensation (see Fig. 1).

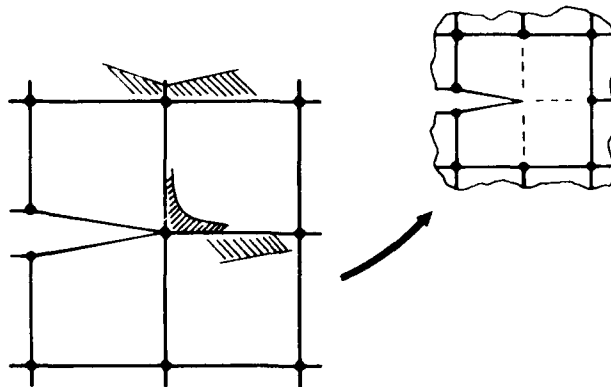


Figure 1 Assembly of Superelement from Four Hybrid "Crack" Elements of Type I or Type III

* In two dimensions each term in $P_{\tilde{K}}$ is proportional to $1/\sqrt{r}$, where r is the radial distance from the crack tip.

Upon substitution of Eq. 5 in Eq. 1, the term $\int_V \sigma_n^T S dV$ leads to terms of the form $\int_V P_n^T SP dV$, $\int_V P_n^T SP_K dV$ and $\int_V P_K^T SP_K dV$. The first of these can easily be evaluated by ordinary Gaussian quadratures, since the integrand matrix involves only polynomials. Quadratures cannot be used on the integrands containing the singular P_K matrix. However, it is apparent that these integrals may be expressed in terms of a compatible boundary displacement field u_K , corresponding to the stress distribution P_K :

$$\int_V P_n^T SP dV = \int_{\partial V} P_n^T u dS \quad (7)$$

$$\int_V P_K^T SP_K dV = \int_{\partial V} P_K^T u_K dS \quad (8)$$

Note that u_K is proportional to \sqrt{r} , since P_K is proportional to $1/\sqrt{r}$. As a result, the u_K integral in Eq. 8 involves only u_K polynomials, hence can be integrated by ordinary Gaussian quadrature. However, the integral in Eq. 7, could be obtained by a Gaussian quadrature determined through a coordinate transformation.

HYBRID "CRACK" ELEMENT II

Subsequent to the development of hybrid "crack" element I, it became obvious that if the assumed stresses also satisfy the compatibility equation, then the complementary strain energy integral over the element volume can be transformed to a boundary integral, so that the functional π_{mc} becomes:

$$\pi_{mc} = \sum_n \left[\int_{\partial V} \left(\frac{1}{2} T^T u - T^T \tilde{u} \right) dS + \int_S \tilde{T}^T \tilde{u} dS \right] \quad (9)$$

where T and u are associated with the assumed stress σ within the element and \tilde{u} are independent boundary displacements. Solutions for stress and displacement distributions for plane elasticity crack problems are available in the form of complete series expansions [10]. The complete series can also be written readily in terms of complex stress functions [11,12]. For two-dimensional problems, the series will include $r^{-1/2}$, r^0 , $r^{1/2}$, r , $r^{3/2}$ terms. A typical element in this case is a single element that has an embedded crack, as shown in Fig. 2. Since each term of the series solution also satisfies the stress-free condition over the crack surfaces, the boundary integral in Eq. 9 will not cover the crack surfaces and hence will not include any singularity in the integrand.

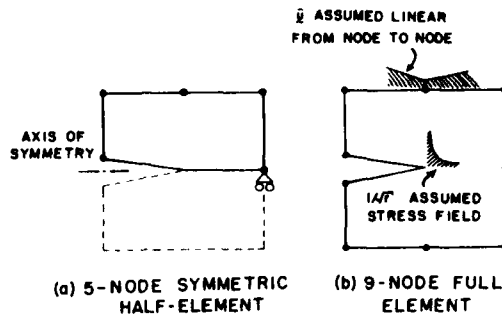


Figure 2 Hybrid "Crack" Elements of Type II

In the finite element formulation, both T and u in each element are expressed in terms of stress parameters β , which are the undetermined coefficients of the complete series solution. For two-dimensional problems, two of the β 's are the stress intensity factors to be determined. Since in this case the β 's are limited to the "crack" element only they can be eliminated at the element level. Hence, the element stiffness matrix can be obtained and used in a conventional finite element analysis program. Thus, this second hybrid "crack" element is superior not only in its completeness in the stress approximation but also in its simplicity for computer implementation.

HYBRID "CRACK" ELEMENT III

The use of the hybrid displacement model for the formulation of a "crack" element is similar to that of hybrid "crack" element I [13,14,15]. The correct singular displacement terms are included in the approximation of u in Eq. 4 and the displacement parameters are separated as β and β_K . Since β_K are shared by a group of elements the resulting matrix equation is again in the form of Eq. 6, and a superelement can be assembled as indicated in Fig. 1.

THREE-DIMENSIONAL "CRACK" ELEMENTS

Unfortunately, there does not exist any complete solution in the near field of the crack front for three-dimensional solids. The only available information is the two-dimensional singular behavior in the plane which is normal to the crack front. By designating this as the n - z plane where n is in the crack plane and z is perpendicular to it, and by using t to represent the direction normal to the n - z plane, then the singular behavior of the stress field and the corresponding displacement field near the crack front can be represented by the stress intensity factors K_I , K_{II} and K_{III} . The

stresses again possess $1/\sqrt{r}$ singularity while the corresponding displacements are proportional to \sqrt{r} .

It is obvious that for three-dimensional solids, if the assumed stress approach is used only the hybrid "crack" element I or III can be utilized. Indeed, several hexahedral elements with straight line edges and with different numbers of node points have been derived [16,17]. In this case, if the crack front is curved it must be approximated by straight segments. Each segment of the crack front then serves as the common edge of a group of four "crack" elements. The three stress intensity factors are common unknowns in this group of elements but can be eliminated so that a stiffness matrix of the superelement can be determined. A hybrid "crack" element III based on the hybrid displacement model has also been developed for three-dimensional solids [18,19].

COMPARISON OF THE TWO-DIMENSIONAL ELEMENTS

A square panel with symmetric edge cracks under uniform in-plane tension (Fig. 3) has been analyzed by all the two-dimensional crack elements discussed above. This problem also has an independent analytical solution obtained by Bowie [20], using the complex stress function and a boundary collocation method. Because of the double symmetry, only one quadrant of the panel needs to be modelled. Thus, only two type I or type III elements are needed to form a superelement at the crack tip, and the half-element of type II (Fig. 2a) is used.

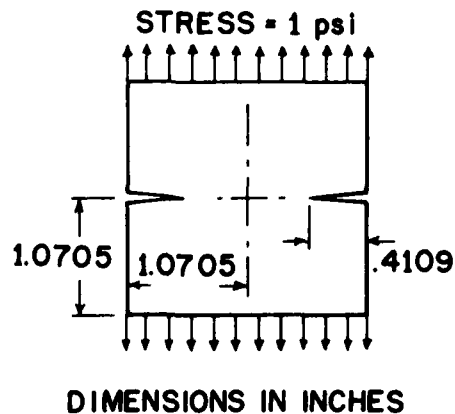


Figure 3 Test Problem for Comparison of "Crack" Elements

Table 1 compares the accuracy of the "crack" elements. It is clear that element type II is far superior, while types I and III are comparable. Similar analyses with conventional elements require 500 to 1,500 degrees of freedom to obtain comparable accuracy [1].

Table I Performance Test of Hybrid "Crack" Elements

"Crack" Element Type	Number of Elements in the Finite Element Model (One Quadrant)	Total Degrees of Freedom in Model	Error* in Computed Value of K_I
I	Two 8-Node Crack Elements and 22 8-Node Conventional Elements	184	0.5%
II	One 5-Node Crack Element and Four 4-Node Conventional Elements	17	0.1%
III	Two 8-Node Crack Elements and 22 8-Node Conventional Elements	184	1.0%

*Error calculated with respect to Ref. 20 analytical solution.

OTHER APPLICATIONS

The original hybrid "crack" elements were programmed for isotropic plane elasticity problems. Extension to orthotropic material is straightforward, since the stress and displacement distributions are available for stress-singularity terms, and orthotropic type I and III elements can be readily derived [8,9,14,15]. The corresponding complex stress function approach can be used to obtain a complete series solution for the corresponding type II element [21,22]. The complex variable method has also been extended to bi-material problems with cracks either normal to or along the interface [23,24]. The complex stress function approach to hybrid elements has also been used to determine stress intensity factors in panels with sharp notches having finite entrance angles. (The singularities for these cases are, of course, not of the order $1/\sqrt{r}$.)

Solids of revolution with axisymmetric cracks are also two-dimensional problems and have been solved with hybrid type II "crack" elements [25].

However, the series expansion for the stress distribution is not derived from the complex variable method in this case. Instead, the partial differential equation for the Airy stress function in real variables is solved by a perturbation Method.

There are two different theories for through cracks in plates subjected to bending. For thin plates, if the Kirchhoff plate theory is employed, a complex variable method has been developed to obtain the complete series expansion of the moment and displacement distributions to be used for derivations of a type II element [16,26]. In this case, only the K_I and K_{II} modes appear in the solution. A more rigorous approach is to apply Reissner plate theory, in which the effect of transverse shear is accounted for. However, in this case only the singular stress terms are available, and the resulting "crack" elements are type I [26,27]. Table II presents a current inventory of hybrid "crack" elements.

Table II Inventory of Hybrid "Crack" Elements
(Numbers in the table indicate references)

Type of Problem	Type I (Assumed Stress)	Type II (Assumed Stress)	Type III (Assumed Displacement)
Plane elasticity problems with sharp cracks:			
Isotropic material	8,9	11,12,25,28	13,14
Orthotropic material	8,9	21,22	14,15
Bi-material		23,24	
Plane elasticity problems with finite- angle sharp notches		29	
Axisymmetric solids		25	
Through cracks in plates subjected to bending:			
Kirchhoff theory*		16,26	
Reissner theory	26,27		
Three-Dimensional Solids	16,17		18,19
Elastic-plastic material (power-law hardening, two-dimen- sional problems)			30,31,32

*For isotropic, orthotropic and bi-material problems; also for plates with finite-angle notches.

The two-dimensional isotropic "crack" element type II was applied to several practical analyses of aircraft structural details during 1974-75 [33, 34, 35, 36]. This activity was motivated by the Air Force Aircraft Structural Integrity Program (ASIP), which requires K-solutions for the calculation of fatigue-crack propagation times in airframes. Some typical results of these analyses are summarized here. Figure 4 illustrates an attachment lug model subjected to either cosine or uniform bearing load [33].* Polar plots of K_I and K_{II} as functions of the angle θ to a radial crack in the bearing hole are shown. These models contain 400 to 600 degrees of freedom and require about 1 CPU minute to compute 32 solution pairs corresponding to 11.25° increments in θ from 0° to 348.75°. The attachment lug analysis was motivated by problems encountered in the C-5A engine mounts, and has also been applied to assessment of A-7 wing attachment lugs.

Similar nondimensional results for $K\sqrt{\pi a}/P$ are shown in Fig. 5 for a double chordwise wing skin splice. In this case, the outer mesh is quite coarse, and is connected to a refined inner mesh via a fastener hole element based on the conventional hybrid stress model given by Eq. 1 [37]. Again, each polar plot (24 solution pairs for a given a/R) requires about 1 CPU minute.

Figure 6 illustrates the finite element model and results for K_I for a three-dimensional analysis of a compact tension test specimen, using the solid "crack" elements of type I [16,17]. The computed results agree well with an independent analytical solution [38]. Further performance tests of these elements in analysis of semi-elliptical surface cracks, followed by application to ASIP analyses of three-dimensional attachment lug problems, are planned for the near future.

CONCLUSIONS

Three hybrid models have been utilized to formulate special "crack" elements and have proved to be a potent technique for obtaining fracture mechanics solutions to many singularity problems in two- and three-dimensional elasticity. Although hybrid "crack" element II has been demonstrated to be the most convenient and accurate model for plane elasticity problems, it is unfortunately not applicable to three-dimensional fracture mechanics. Initial success has been achieved for such problems using the hybrid "crack" elements type I and III. Further applications of these hybrid approaches to practical fracture mechanics problems will undoubtedly be forthcoming in the future.

ACKNOWLEDGEMENTS

The MIT element development work reported in this paper was sponsored by the U.S. Air Force Office of Scientific Research, with Mr. William J. Walker as technical monitor. The two-dimensional applications work was

*The total bearing load is 1,000 lbs.

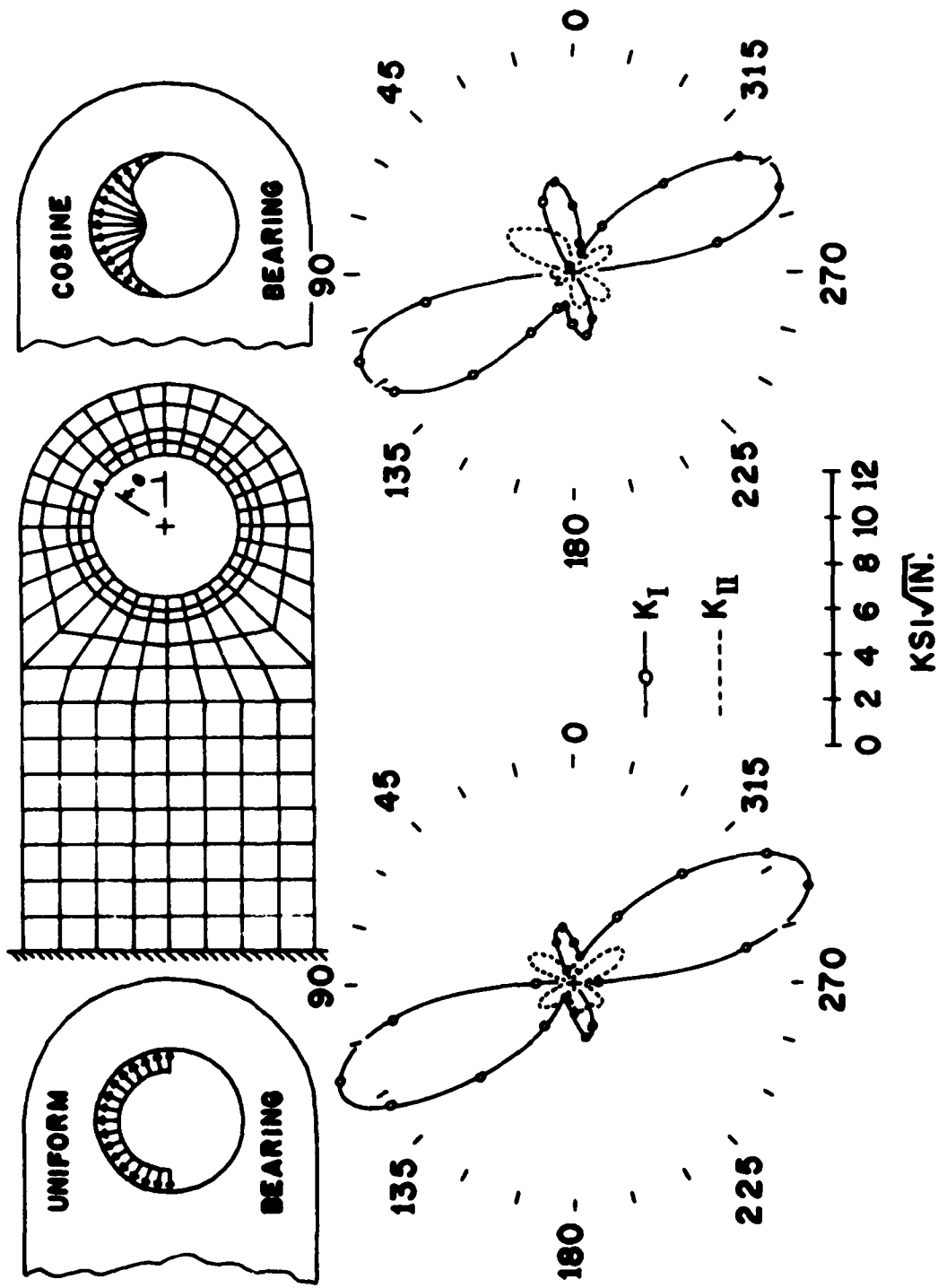


Figure 4 Attachment Lug Finite Element Model and Results

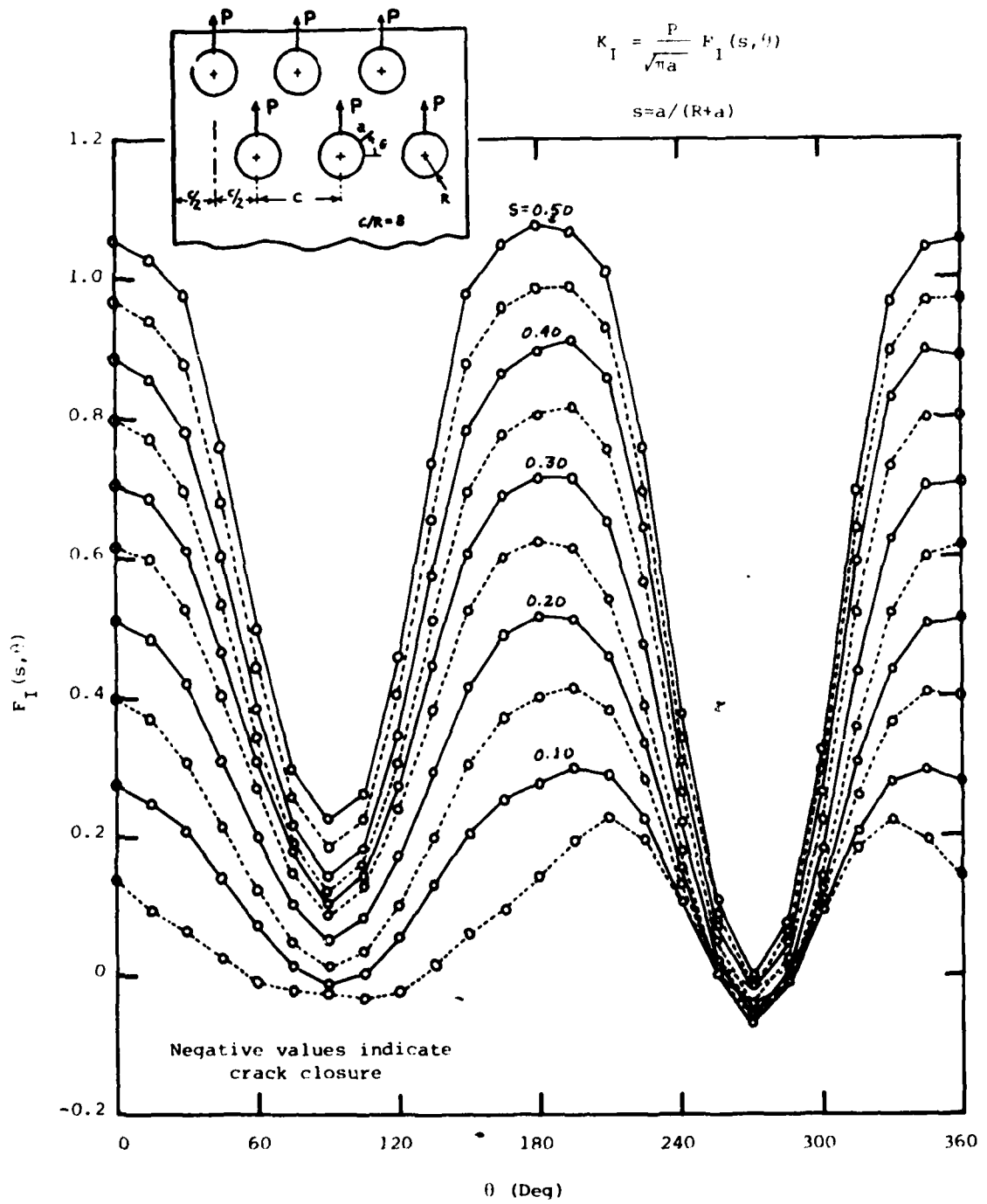
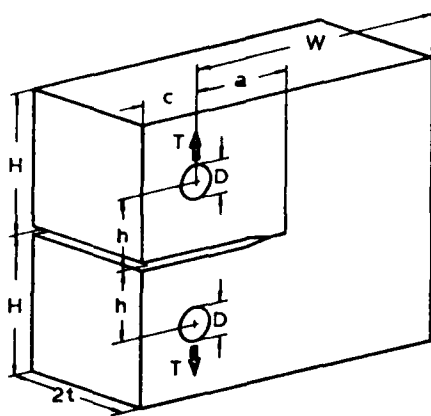
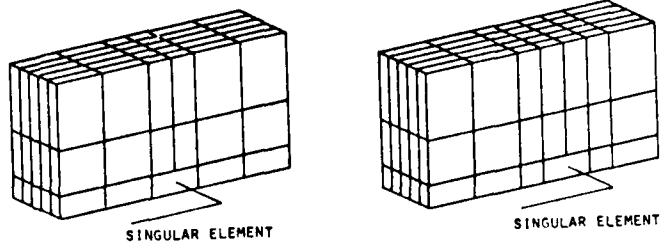


Figure 5 Mode I Stress Intensity Factors for Chordwise Skin Splice



$H = 0.6W$
 $h = 0.275W$
 $D = 0.25W$
 $c = 0.25W$
 $2t = 0.50W$



(1) $a/W = 3/8$
 85 ELEMENTS

(2) $a/W = 5/8$
 105 ELEMENTS

FINITE ELEMENT BREAKDOWN FOR THE ANALYSIS

STANDARD COMPACT TENSION SPECIMEN
 (ASTM STANDARD E-399-72)

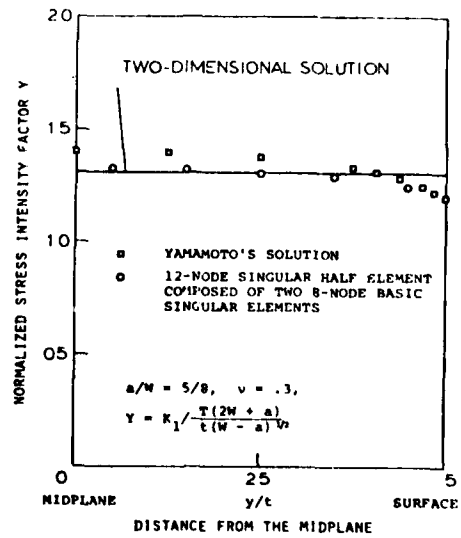
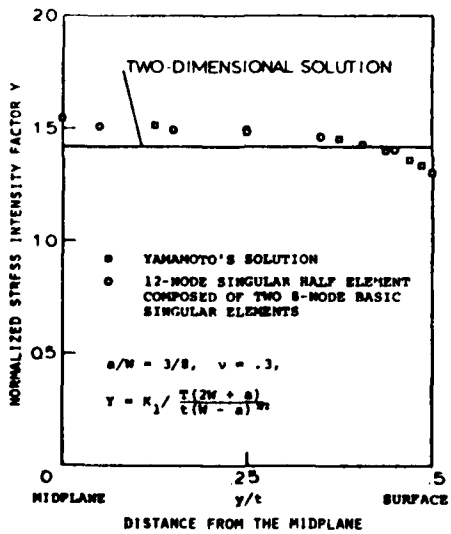


Figure 6 Finite Element Model and Results for 3D Analysis
 of Compact Tension Specimen

was sponsored by the Air Force Flight Dynamics Laboratory, with Mr. James L. Rudd (AFFDL/FBE) as technical monitor.

REFERENCES

1. Pian, T.H.H., "Crack Elements", Proc. World Congress on Finite Element Methods in Structural Mechanics, Bournemouth, Dorset, UK, 12-17 October 1975, pp. F1-F39.
2. Tong, P. and Pian, T.H.H., "On the Convergence of the Finite Element Method for Problems with Singularity", Int J Solids Structures, Vol. 9, 1972, pp. 313-321.
3. Tong, P. and Pian, T.H.H., "A Variational Principle and the Convergence of a Finite Element Method Based on Assumed Stress Distribution", Int J Solids Structures, Vol. 5, 1969, pp. 463-472.
4. Pian, T.H.H. and Tong, P., "Finite Element Methods in Continuum Mechanics", Advances in Applied Mechanics (C.S. Yih, ed.), Vol. 12, 1972, pp. 1-58.
5. Pian, T.H.H., "Finite Element Methods by Variational Principles with Relaxed Continuity Requirement", Proc. Conf. on Variational Methods in Engineering, Southampton University, 1973, pp. 3/1-3/24.
6. Pian, T.H.H., "Derivation of Element Stiffness Matrices by Assumed Stress Distribution", AIAA J, Vol. 2, 1964, pp. 1333-1336.
7. Tong, P., "New Displacement Hybrid Finite Element Model for Solid Continua", Int J Num Meth Eng, Vol. 2, 1970, pp. 78-83.
8. Luk, C.H., "Assumed Stress Hybrid Finite Element Method for Fracture Mechanics and Elastic-Plastic Analysis", Aeroelastic and Structures Research Laboratory, MIT, ASRL TR 170-1 (also AFOSR-TR-73-0493), December 1972.
9. Pian, T.H.H., Tong, P. and Luk, C.H., "Elastic Crack Analysis by a Finite Element Hybrid Method", Proc. 3rd Conf. on Matrix Methods in Structural Mechanics, Air Force Flight Dynamics Laboratory, Wright-Patterson AFB, Ohio, AFFDL-TR-71-160, December 1973, pp. 661-682.
10. Williams, M.L., "On the Stress Distribution at the Base of a Stationary Crack", J Appl Mech, Vol. 24, 1957, pp. 109-114.
11. Lasry, S.J., "Derivation of Crack Element Stiffness Matrix by the Complex Variable Approach", Aeroelastic and Structures Research Laboratory, MIT, ASRL TR 170-2 (also AFOSR-TR-73-1602), February 1973.

12. Tong, P., Pian, T.H.H. and Lasry, S.J., "A Hybrid-Element Approach to Crack Problems in Plane Elasticity", Int J Num Meth Eng, Vol. 7, 1973, pp. 297-308.
13. Atluri, S.N., Kobayashi, A.S. and Nakagaki, M., "An Assumed Displacement Hybrid Finite Element Model for Linear Fracture Mechanics", Int J Fracture, Vol. 11 No. 2, 1975, pp. 257-271.
14. Atluri, S.N., Kobayashi, A.S. and Nakagaki, M., "Fracture Mechanics Application of a Hybrid Displacement Finite Element Model", AIAA J, Vol. 13, 1975, pp. 734-739.
15. Atluri, S.N., Kobayashi, A.S. and Nakagaki, M., "A Finite Element Program for Fracture Mechanics Analysis of Composite Material", Fracture Mechanics of Composites, American Society for Testing and Materials, ASTM STP 593, 1975, pp. 86-98.
16. Moriya, K., "Hybrid Crack Elements for Plate Bending and Three Dimensional Solids", PhD Thesis, Department of Aeronautics and Astronautics, MIT, in publication.
17. Pian, T.H.H. and Moriya, K., "Application of Hybrid Finite Elements to Structural Mechanics Problems", Aeroelastic and Structures Research Laboratory, MIT, ASRL TR 170-5, January 1977.
18. Atluri, S.N., Kathiresan, K. and Kobayashi, A.S., "Three-Dimensional-Hybrid Finite Element Model", Trans 3rd Int Conf on Structural Mechanics in Reactor Technology, London, UK, 1975, paper L-7/3.
19. Atluri, S.N. and Kathiresan, K., "On a 3-D 'Singularity Element' for Computation of Combined Mode Stress Intensities", Advances in Eng Sci, Vol. 1 (13th Annual Meeting Soc. Eng. Sci.) NASA CP-2001, 1976, pp. 267-274.
20. Bowie, O.L., "Rectangular Tensile Sheet with Symmetric Edge Cracks", J Appl Mech, Vol. 31 Series E No. 2, 1964, pp. 208-212.
21. Lin, K.Y., "Fracture of Filamentary Composite Materials", PhD Thesis, Department of Aeronautics and Astronautics, MIT, February 1977.
22. Tong, P., "A Hybrid Crack Element for Rectilinear Anisotropic Material", Int J Num Meth Eng, Vol. 11, 1977, pp. 377-382.
23. Lin, K.Y., "The Stress Intensity of a Crack at an Interface Between Two Materials", Aeroelastic and Structures Research Laboratory, MIT, ASRL TR 162-5 (also AFOSR-TR-73-1917), June 1973.
24. Lin, K.Y. and Mar, J.W., "Finite Element Analysis of Stress Intensity Factors for Cracks at a Bi-Material Interface", Int J Fracture, Vol. 12, 1976, pp. 521-531.

25. Lin, K.Y., Tong, P. and Orringer, O., "Effect of Shape and Size on Hybrid Crack-Containing Finite Elements", Computational Fracture Mechanics, Proc. ASME Second National Congress on Pressure Vessels and Piping, San Francisco, CA, 23-27 June 1975, pp. 1-20.
26. Rhee, H.C., Atluri, S.N., Moriya, K. and Pian, T.H.H., "Hybrid Finite Element Procedures for Analyzing Through Flaws in Plates in Bending", to be presented at the 4th International Conference on Structural Mechanics in Reactor Technology, San Francisco, CA, 15-19 August 1977.
27. Rhee, H.C., "On the Accuracy of Finite-Element Solutions of Problems of Bending of Plates with Traction Boundary Conditions", PhD Thesis, School of Engineering Science and Mechanics, Georgia Institute of Technology, in publication.
28. Tong, P. and Pian, T.H.H., "Application of Finite Element Method to Mixed-Mode Fracture", Recent Advances in Engineering Science, Proc. 10th Annual Meeting of the Society of Engineering Science, 1975, pp. 255-263.
29. Nikfarjam, S.K., "Use of Special Finite Element to Evaluate Stress Intensity Factors at the Tip of a Notch in an Isotropic Solid", SM Thesis, Department of Aeronautics and Astronautics, MIT, February 1974.
30. Atluri, S.N. and Nakagaki, M., "Analysis of Two-Dimensional Fracture Problems Involving Large-Scale Yielding: A Displacement-Hybrid Finite Element Method", Proc. 12th Annual Meeting of the Society of Engineering Science, University of Texas at Austin, 1975, pp. 66-76.
31. Atluri, S.N., Nakagaki, M. and Chen, W.H., "Fracture Analysis Under Large-Scale Plastic Yielding", 10th U.S. National Symposium on Fracture, American Society for Testing and Materials, Philadelphia, PA, August 1975.
32. Atluri, S.N. and Nakagaki, M., "Post-Yield Analysis of a 3-Point Bend Fracture Test Specimen: An Embedded Singularity Finite Element Incremental Method", Developments in Theoretical and Applied Mechanics, Vol. 8, Virginia Polytechnic and State University, Blacksburg, VA, 1976, pp. 206-224.
33. Orringer, O., "Fracture Mechanics Analysis of an Attachment Lug", Aeroelastic and Structures Research Laboratory, MIT, ASRL TR 177-1 (also AFFDL-TR-75-51), January 1976.
34. Stalk, G. and Orringer, O., "Fracture Mechanics Analysis of Centered and Offset Fastener Holes in Stiffened and Unstiffened Panels Under Uniform Tension", Aeroelastic and Structures Research Laboratory, MIT, ASRL TR 177-2 (also AFFDL-TR-75-70), April 1976.

35. Orringer, O. and Stalk, G., "Fracture Mechanics Analysis of Single and Double Rows of Fastener Holes Loaded in Bearing", Aeroelastic and Structures Research Laboratory, MIT, ASRL TR 177-3 (also AFFDL-TR-75-71), April 1976.
36. Pian, T.H.H., Orringer, O., Stalk, G. and Mar, J.W., "Numerical Computation of Stress Intensity Factors for Aircraft Structural Details by the Finite Element Method", Aeroelastic and Structures Research Laboratory, MIT, ASRL TR 177-4 (also AFFDL-TR-76-12), May 1976.
37. Orringer, O. and Stalk, G., "A Hybrid Finite Element for Stress Analysis of Fastener Details", J Eng Fract Mech, Vol. 523, 1976, pp. 1-11.
38. Yamamoto, Y. and Sumi, Y., "Stress Intensity Factors for Three-Dimensional Cracks", presented at 14th International Congress on Theoretical and Applied Mechanics, Delft, HOLLAND, 1976.

CASE STUDY IN UTILIZATION OF FRACTURE MECHANICS IN THE
FAILURE ANALYSIS OF A HELICOPTER FLOAT CROSS TUBE

David W. Hoepfner, Ph.D., P.E.
Professor of Engineering
University of Missouri
College of Engineering
Columbia, Missouri 65201

BACKGROUND

During a reportedly normal landing, the float cross tube on a helicopter failed. It was the understanding that this failure was accompanied by no injuries and the damage to the aircraft was limited.

The failure occurred during a landing at Cooke Island in Alaska where the temperature was apparently below 0°F. The helicopter was being used in a petroleum exploration operation for transporting supplies and has been in service for 1619.4 hours. Two such helicopters were being operated in Alaska and both failed in the float cross tubes in similar manners. Five other helicopters of the same type were at the same time operating for a similar function in the Gulf of Mexico and no failures were reported on them.

The general position of the failure is shown in the sketch of Figure 1 and in more detail in Figure 2. As can be seen, the failures occurred in the aft cross tube adjacent to one of the support points. The helicopter is connected to these points by a strap which goes entirely around the cross tube and the helicopter is fastened to the cross tube only by six rivets. Rubber pads are placed between the helicopter body and the cross tube as well as between the cross tube and the strap.

The load in the helicopter at the time of the present failure is unknown; however, the load in the helicopter involved in the previous failure at the time it failed was 6101 lb at Station 131.1 inches (approximately 138.6 inches aft of the nose). The maximum total gross weight given for this type of aircraft is 8500 lb.

The cross tube is made of 7075-T6 aluminum alloy and the tube is formed after aging. The tube had an original wall thickness of 0.313 inch but was chem-milled between Plane "B" and Plane "A", as indicated in Figure 2, from 0.313 to 0.200/0.170 inch. The diameter of the tube was originally 3.25 inches but, due to the forming, it is slightly elliptical at various points along its length. The total length of the cross tube is 154 inches.

The fractures of both failures were reported to have similar appearances with small flaws apparent on them. These flaws were located at points corresponding to the bottoms of the tubes. The flaw in the previous failure had an area of about 0.16 square inch and the area of the flaw in the present failure is about 0.02 square inch.

Because of the unexpected nature of the failures, their propagation from apparently very small flaws, and because of the five additional helicopters of similar design that were in use in the Gulf, a failure analysis study was conducted.

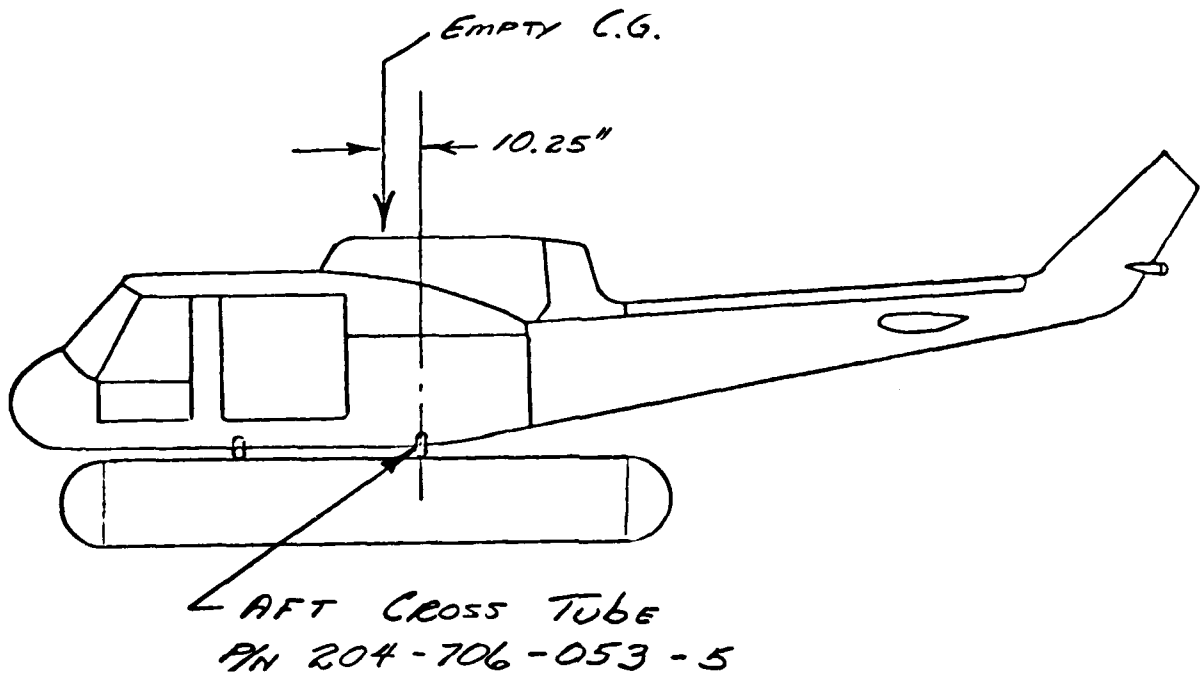


Fig. 1 -- General Position of Fracture

OBJECTIVES

- (1) To conduct a metallurgical, fractographic, and stress analysis investigation of the failed cross tube in order to determine, if possible, the cause(s) contributing to the failure.
- (2) To determine if potential failures from the same cause(s) exist in the other helicopters of the same design that are still in service.
- (3) To recommend corrective action that might be taken to eliminate the conditions causing the failure.

SUMMARY

A failure analysis study was performed on a failed helicopter float cross tube to determine the cause of failure. The failure was found to have formed on a fatigue-cracked flaw that had grown to a size which was critical for the stresses involved. Apparently, the fatigue crack initiated on a small surface crack, perhaps caused by corrosion or stress corrosion. However, the surface stresses in the tube under several assumed conditions of loading were found to be of sufficient magnitude to cause a fatigue crack to initiate and propagate without an additional stress raiser being present. Although the two failures occurred in Alaska, little influence of the temperature on the conditions of fracture is seen and, therefore, it is believed that the helicopters presently operating in the Gulf may contain potential failures.

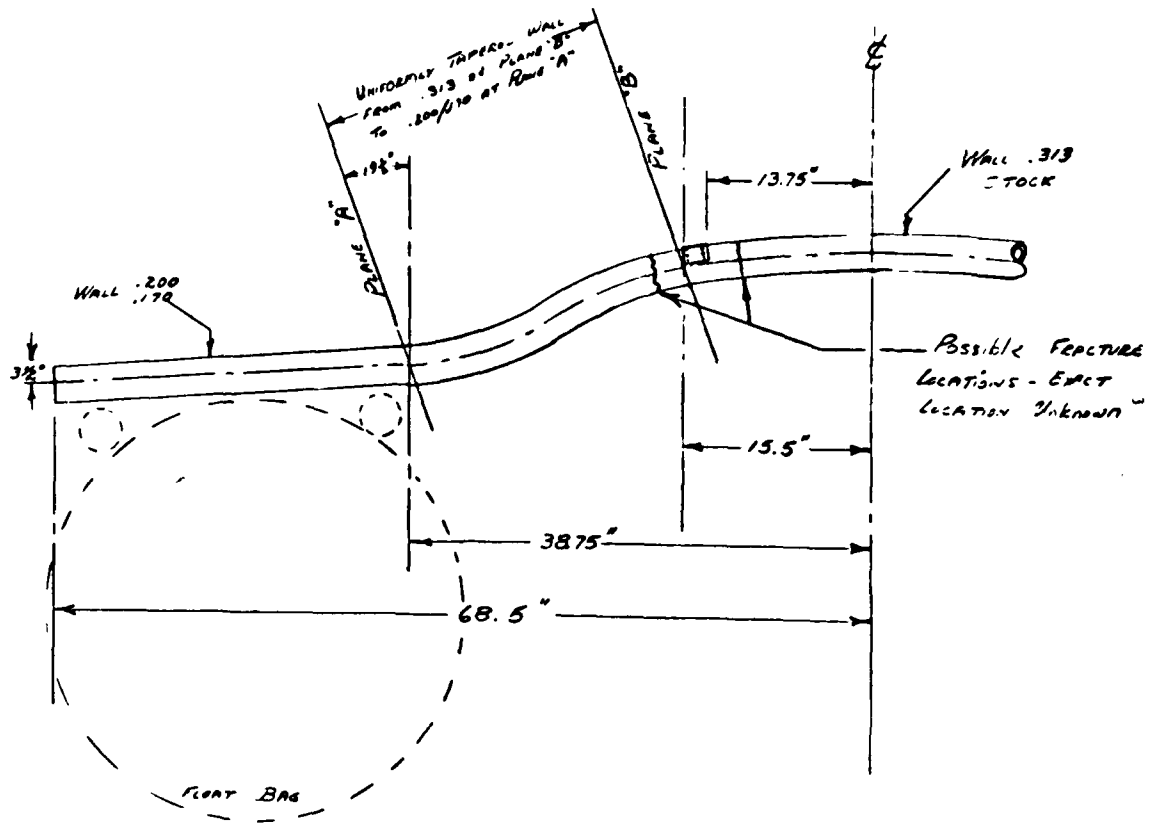


Fig. 2 -- Detailed Location of Fracture

FAILURE ANALYSIS

The laboratory studies pursued during the failure analysis of the failed float cross tube included visual examinations of the fracture, electron microscopic studies of the fracture, visual and microscopic examinations of the surface of the tube, and metallographic studies of cross sections of the tube.

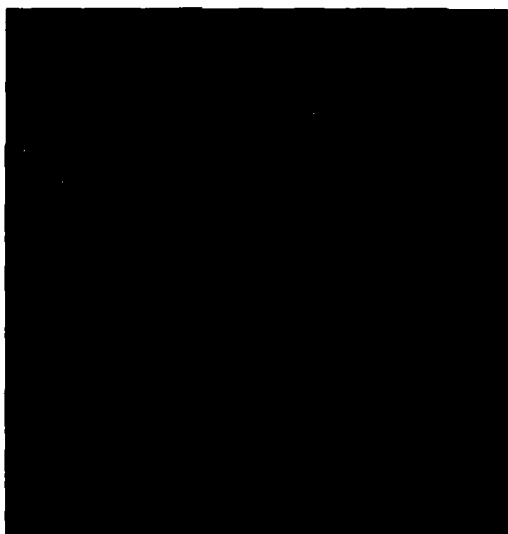
VISUAL EXAMINATIONS OF THE FRACTURE

Figure 3 contains photographs of the two halves of the fracture. Visual examinations of these revealed a flaw at the outside surface of the tube. The macroscopic markings on the fracture indicated that the flaw definitely was the origin of the fracture. This area is identified by the arrow in Figure 3 and is shown at higher magnification in Figure 4. The flaw was at the bottom of the tube as it is oriented when in service. This was determined since the flaw was about 180 degrees from the center rivets in the rubber pad that identifies the top of the tube.

Unfortunately, the flaw area was severely damaged on one half of the fracture, shown in the lower photograph in Figure 3, but appeared to be relatively undamaged on the other half, shown in the top photograph of Figure 3 and in Figure 4.



IX



IX

Fig. 3 -- Fracture in Float Cross Tube

The flaw where failure originated is identified by the arrow.



10X

Fig. 4 -- Fatigue Cracked Flaw on Fracture of Float Cross Tube

The flaw possessed a classical semi-elliptical shape. Its size was measured microscopically and found to be 0.183 inch along the surface (major axis) and 0.075 inch deep (one half the minor axis).

Macroscopically the flaw area had the appearance of fatigue, and this was verified by electron fractography as described below. It appeared to have an origin point at the surface approximately at the mid-point of the major axis. This point is identified by the arrow in Figure 4.

The remainder of the fracture was a typical overload type of fracture and was relatively flat except for the part of the tube corresponding to its top, which had a "V" type of fracture as shown in Figure 3. This area of the fracture was the last part to fail.

ELECTRON FRACTOGRAPHIC STUDIES

The flaw area was examined by electron microscopy in an attempt to verify that it formed by fatigue, to determine the approximate number of stress cycles involved, and to determine the nature of the origin of the flaw. For these studies, a strip of cellulose acetate was moistened in acetone and pressed onto the surface of the fracture. When this had dried, it was lifted from the fracture and shadowed with platinum-carbon, followed by a coating of carbon. The acetate was finally dissolved and the resulting replica examined in an electron microscope.

Figure 5 contains electron micrographs of typical areas of the flaw area. As can be seen, the typical striated appearance of a fatigue fracture was found. Since it has been shown that each striation is formed by a separate cycle of stress when they exist, a count of the total number of striations gives a value for the total number of stress cycles involved in the propagation of the crack. This is, of course, only true if there are not large amounts of cleavage or tearing present. This type of count was performed at selected points in the flaw, and the data integrated over the total length of the flaw. A value of about 6500 cycles was obtained. This value was determined from counting the rather well-defined striations that are shown in Figure 5. The spacing of these striations were found to be relatively uniform over the entire area of the flaw and this suggests that the magnitude of the cyclic stresses propagating the fatigue crack must also have been rather uniform. As will be seen in the stress calculations described later, it was suggested that a possible source of the cyclic stresses is the wave action that occurs while the helicopter floats on the water.

Close examination of the micrographs in Figure 5, particularly Figure 5a, reveals the suggestion of several very finely spaced striations between the striations mentioned above. If these are, in fact, fatigue striations, a low amplitude cyclic stress superimposed on the higher magnitude stress accounting for the more widely spaced striations would be indicated.

In addition to electron microscopic examinations of the propagation of the fatigue crack in the flaw area, examinations were made of the point of origin of the crack. Unfortunately, the outer edge of the tube in the entire area of the flaw was damaged and therefore examinations of the origin were prevented. The normals to the striations, however, usually point to the origin of a fatigue crack and this position was indicated on the cross tube. Striated fracture was observed up to the damaged edge which indicates that a large imperfection did not initiate the crack. The need for a significant stress raiser to start the crack also does not appear to be necessary as is shown by the stress analysis described below.

VISUAL AND MICROSCOPIC EXAMINATION OF THE SURFACE OF THE CROSS TUBE

Visual examination of the outer surface of the cross tube revealed that the paint on it contained numerous cracks in a band about 1 inch wide on the bottom side of the tube. The fatigue flaw that apparently initiated the failure was located approximately in the middle of this band. All of the cracks in the paint were short and oriented in the circumferential direction, i.e., normal to the length of the tube. No cracking was seen on other areas of the tube.

The paint was removed from the tube by immersion in acetone so that the surface below the paint could be examined for cracks. Essentially the same crack pattern as seen in the paint was seen on the surface of the tube. These cracks are shown in Figure 6. The long direction of the tube is indicated by the arrow in this figure.

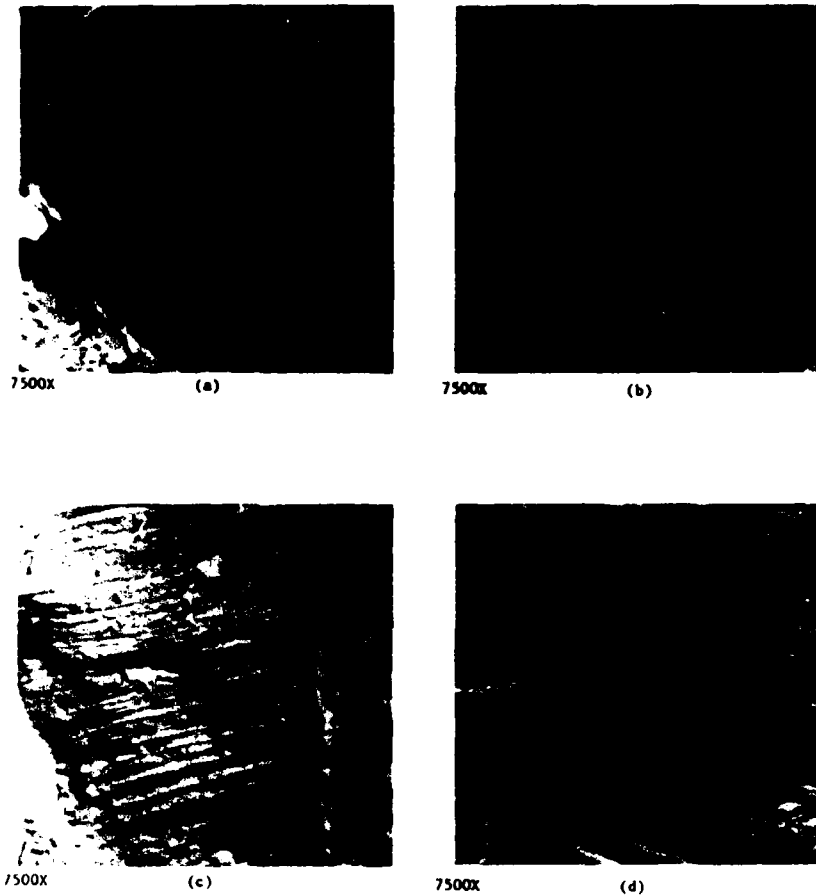


Fig. 5 -- Typical Electron Fractographs of Fatigue-Cracked Semi-Elliptical Flaw in Float Cross Tube

The arrows indicate the microscopic direction of crack propagation.

METALLOGRAPHIC STUDIES OF CROSS SECTIONS OF THE
OUTER SURFACE OF THE-CROSS TUBE

Metallographic sections were prepared of the outer surface of the cross tube in an attempt to determine the nature of the cracking observed on the surface. A typical area is shown in Figure 7. The entire surface was found to be cracked, but the cracks were very shallow, extending to a depth of only about 0.0005 inch. All of these cracks were found to be intergranular and, as such, were often oriented at various angles to the surface.

Because of their intergranular nature, it was suspected that they may have been caused by some type of a corrosion or stress corrosion

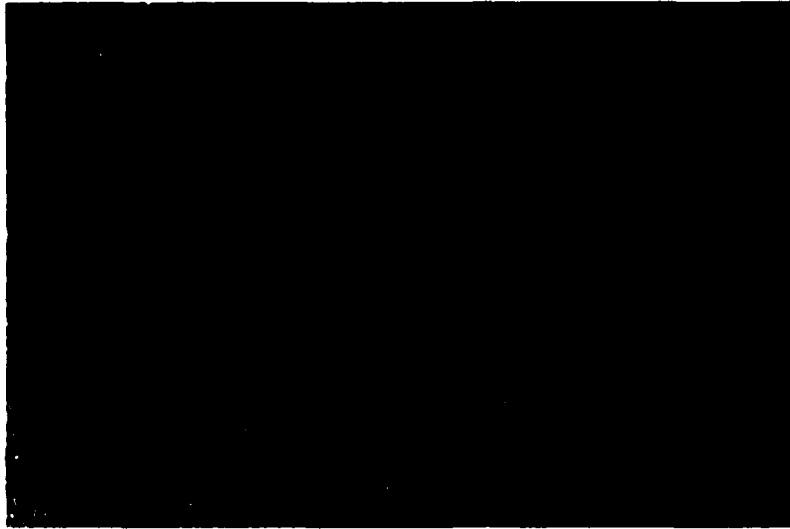


Fig. 6. -- Cracks on Surface of the Bottom of the Float Cross Tube

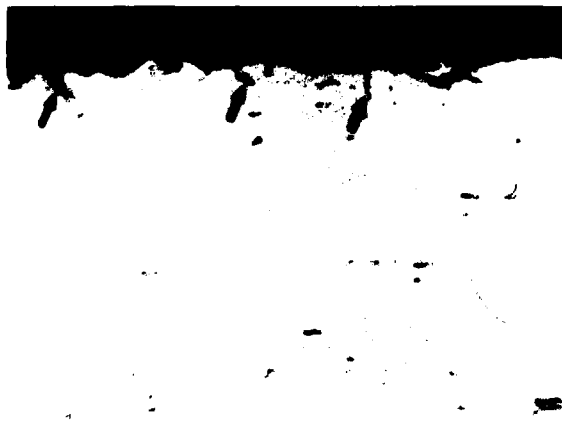


Fig. 7 -- Cross Section of Cracks Shown in Figure 6

mechanism and not by fatigue. However, no visible corrosion products were observed in them.

STRESS ANALYSIS

Based on the results of the examinations of the failed tube described above, a rather limited stress analysis was made of the tube to see if the failure could have been predicted from the stress conditions. This involved (a) determining if a fatigue crack of the type observed could have initiated and propagated and (b) determining if the size of flaw observed is of a critical size that should result in total failure.

Loading Conditions

For the analysis, two loading conditions have been considered since they both appear to strongly influence the stress levels in the tube and associated flaw behavior. Of primary interest is the landing condition when the cross tube apparently failed. However, as will be illustrated, there is a floating condition subject to wave action that also appears significant for fatigue crack generation.

Landing Condition at Failure. An aircraft weight of 6100 lb was assumed with the C. G. at Station 130 inches. This assumption was based on the known weight involved in the previous failure. From this, the load per aft cross tube arm is calculated to be 2030 lb. This assumes ideal and uniform landing under 1 G. conditions and should be very conservative. Full load landing with centered C. G. (i.e., at Station 120) would apply 2125 lb/arm.

Floating Condition. An empty aircraft floating in a gentle breeze (sea state 1) was assumed for this condition. An aircraft weight of 5600 lb was assumed with the C. G. at Station 140 inches. The load per aft cross tube arm was then 2330 lb. Wave action in sea state 1 may superimpose a ± 0.1 G cyclic loading.

Stress Conditions

The tube flexural stresses at the attachment area were determined from the loading geometry shown in the sketch of Figure 8. On this basis, the maximum moment occurs at and extends inboard of the attachment point and is equal to 38.2 P.

The tensile stress field is maximum at the underside of the tube where the surface flaw occurs and is calculated as

$$\text{Avg stress (at mid-wall)} = \frac{Mc}{I} = \frac{M}{\pi R^2 t} = \frac{38.2 P}{\pi (1.42)^2 (0.313)} = 19.8 P$$

$$\text{Max stress} = \frac{M(R + t/2)}{\pi R^3 t} = \frac{38.2 P(1.57)}{\pi (1.42)^3 (0.313)} = 21.9 P$$

Stress levels calculated for various possible loading conditions were then calculated and are listed at the bottom of Figure 8 in Table 1.

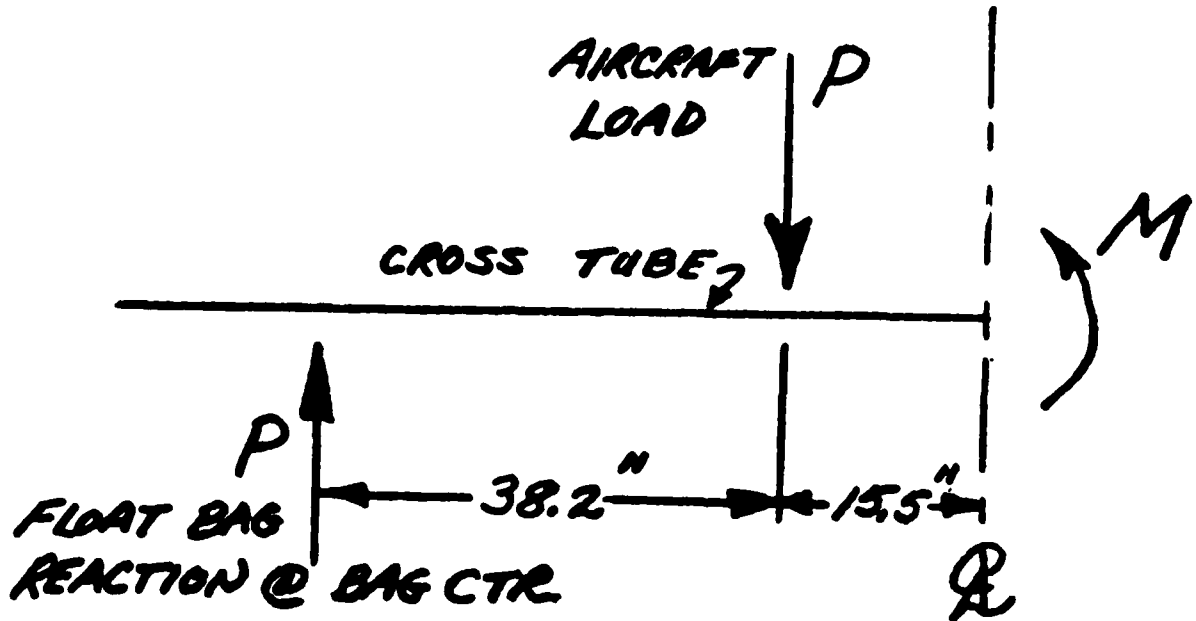


Fig. 8 -- Sketch of Loading Geometry in Float Cross Tube

Table 1. Calculated Stress Levels for Various Loading Conditions

Condition	Weight	Tube Load, lb	Mid-Wall Stress, ksi	Surface Stress, ksi
Landing	Partial, 6100	2030	40.2	44.5
Landing	Full, 8500	2125	42.1	46.5
Floating	Empty, 5600	2330	46.1	51.0
Floating	Cyclic, <u>high</u> <u>low</u>	<u>2563</u> <u>2097</u>	<u>50.8</u> <u>41.5</u>	<u>56.2</u> <u>45.9</u>

FRACTURE ANALYSIS

A fracture analysis was next made to determine if the size of the flaw observed was of a size that would be critical and thereby cause total failure. For this, I have considered only the landing condition since this is reported to be the condition when the failure occurred.

The stress levels determined above are believed to be extremely conservative and, since landing could impose a load factor of 1.5-2.0, I have used the lower value, 1.5, for the fracture analysis. Then, during landing a representative average stress field adjacent to the flaw is 60.3 ksi (1.5 x 40.2).

Using the idealized elastic surface flaw fracture model, K, the stress intensity is

$$K = 1.1 \sigma \sqrt{\frac{\pi a}{Q}}$$

For a flaw of the size observed, 0.075 inch deep by 0.183 inch at the surface, a value for Q of 1.25 is reasonable. Then,

$$K = (1.1)(60.3) \sqrt{\frac{\pi(0.075)}{1.25}} = 28.9 \text{ ksi-in.}^{(1/2)}$$

This value is within the critical 27 to 35-ksi-in.^{1/2} room temperature range indicated "for information only" for 7075-T6 aluminum in Mil-HDBK-5 (1969). Therefore, the crack appears to be of a critical size and failure would be expected when a flaw of this size exists. The conservatism of the above analysis further suggests that even smaller flaws may be critical under loading conditions that could exist in the cross tube.

DISCUSSION

The results of this analysis have shown that a flaw existed in the cross tube before the final failure occurred. This flaw was on the surface of the tube and at its bottom. It was shown by electron fractography to have propagated by fatigue due to cyclic stresses and that apparently about 6500 stress cycles of approximately uniform magnitude were involved; although the actual point of origin of the fatigue could not be examined because of damage on the surface of the fracture, the fractographic studies indicated the origin area must have been very shallow. The metallographic studies revealed that the bottom, outer surface, of the tube contained numerous cracks that extended into the material to a maximum depth of about 0.0005 inch. Although not confirmed, it was suspected that the fatigue-cracked flaw initiated on one of these small cracks. Furthermore, the origin of the small surface cracks could not be conclusively determined; however, because of their intergranular nature it was suspected that corrosion or stress corrosion was their cause. Because of this,

it was suggested that an examination of the effect of the chem-milling on the surfaces of the tubes be made.

The fracture analysis of the tube containing the flaw showed that, with the loading conditions assumed to exist in the tube, the fatigue-cracked flaw was of a critical size and total failure would be expected.

Since the only failures that had occurred did so in aircraft operating in Alaska, and those operating in the warmer environment of the Gulf had not failed, a brief analysis of the effect of temperature on the propagation of the fatigue crack and the size of flaw that would be critical was made. Realizing that several factors must be considered in this type of analysis, it was concluded that little effect should be realized from the temperature.

ACKNOWLEDGEMENT

The author is grateful to Professor (Emeritus) Henry Fuchs, Mr. J. McCall, Mr. C. Feddersen, and Dr. Kevin Kondas for various inputs and encouragement in writing this case for presentation.

FIGURE CAPTIONS

- Fig. 1 General Position of Fracture
- Fig. 2 Detailed Location of Fracture
- Fig. 3 Fracture in Float Cross Tube
- Fig. 4 Fatigue Cracked Flaw on Fracture of Float Cross Tube
- Fig. 5 Typical Electron Fractographs of Fatigue-Cracked Semi-Elliptical Flaw in Float Cross Tube
- Fig. 6 Cracks on Surface of the Bottom of the Float Cross Tube
- Fig. 7 Cross Section of Cracks Shown in Figure 6
- Fig. 8 Sketch of Loading Geometry in Float Cross Tube

APPLICATION OF FINITE-ELEMENT ANALYSIS TO DEVELOP
A BI-MATERIAL CRACK-PROPAGATION LABORATORY TEST SPECIMEN

Oscar Orringer
Associate Director, Aeroelastic and Structures Research Laboratory, MIT
Cambridge, MA 02139

Ken-Yuan Lin
Research Assistant, Aeroelastic and Structures Research Laboratory, MIT
Cambridge, MA 02139

James W. Mar
Professor, Department of Aeronautics and Astronautics
Cambridge, MA 02139

INTRODUCTION

During 1975 the MIT Aeroelastic and Structures Research Laboratory was asked by the Stowe-Woodward Company to assist in the development of a method for life-assessment of printing press rolls. The typical printing press roll is a large cylindrical component (about 48 inches in diameter) which consists of a structural metal drum with a thick exterior rubber layer. The rubber layer is adhesively bonded to the metal drum, and the sandwich is drilled with a square array of through-holes to permit ink to reach the printing plates. Figure 1 shows a schematic cutaway view of a small section of the roll.

The figure also indicates the predominant damage mode which has been experienced in service with this equipment: debond-cracking which propagates along the adhesive layer between the rubber and the metal. The objective of the MIT research program was to develop the data base and analysis required to predict the life of a roll from debond-crack growth-rate data.

Some preliminary experiments had been conducted prior to this program. In these experiments, ASTM-type compact tension specimens were constructed of one-half metal and one-half rubber, with a pre-crack introduced along the rubber-metal bond-line. With alternating tension loading applied to these specimens, an unsuccessful attempt was made to obtain the standard type of crack growth-rate data, i.e. a logarithmic plot of da/dn versus ΔK_I , where:

$$da/dn = \text{Crack growth-rate (inch/cycle)}$$

$$\Delta K_I = \text{Stress intensity range (psi}\sqrt{\text{in)}})$$

Observations of these experiments indicated virtually no difference between the threshold value of ΔK_I (below which no crack growth could be observed) and the critical value, at which the debond-crack would propagate across the entire test specimen within a few load cycles [1].

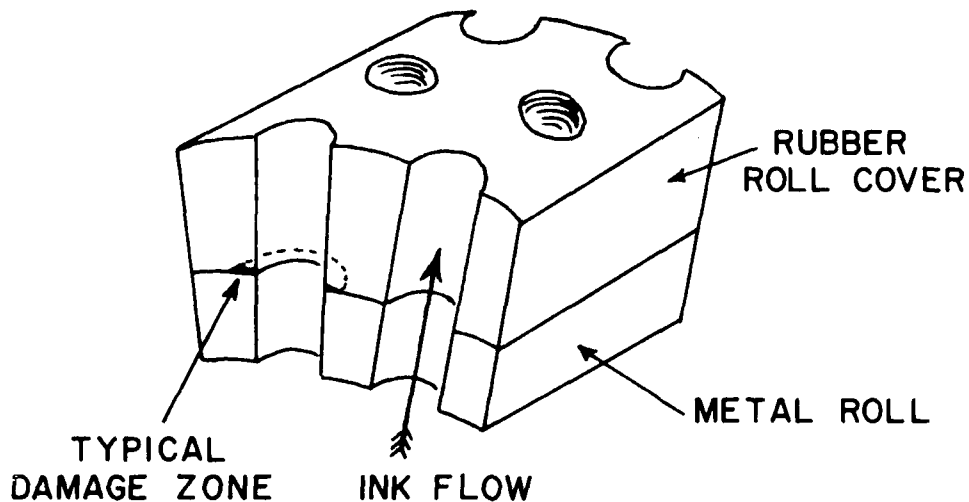


FIGURE 1. CUTAWAY VIEW OF PRINTING PRESS ROLL

One might conclude from these laboratory tests that the life of a printing press roll ought to be either infinite or (at slightly higher applied loads) only a few cycles. However, full-scale tests of the rolls demonstrated intermediate lives in the range of 10^5 to 10^6 cycles. Also, examination of the bond surface after removal of the rubber covers from rolls which had been cycled to endurance less than the fatigue life revealed annular zones of debonding around the ink holes, as shown in Fig. 1 [2]. Hence, debond-crack propagation must be accepted as the life-limiting damage mode in a printing press roll of this construction. The manufacturer's objective was to develop a design approach which could extend the life of a roll to the range of 10^7 to 10^9 cycles.

ANALYSIS

In view of the conflict between the laboratory experiments and the full-scale tests, it was hypothesized that crack-propagation in the roll was being driven by Mode II loads, i.e. shearing parallel to the plane of the debond crack. This hypothesis was reinforced by previous studies of the phenomenon of rolling contact [3,4]. These studies included stress analyses in which there were significant shear stresses at the edges of the zone of contact between two rollers, with the sign of the shear stress at contact exit reversed with respect to the sign at contact entrance. Hence, it is reasonable to assume that the adhesive bond-line in a printing press roll will experience one full reversed shear-stress cycle per revolution, while a compressive normal stress across the debond-crack is caused by the contact pressure.

Therefore, it was recommended that a Mode II laboratory test specimen be developed to acquire the necessary crack growth-rate data. It was assumed that, with such a specimen available, the experimental data could be correlated by a power law of the form:

$$da/dn = C (\Delta K_{II})^m \quad (1)$$

where ΔK_{II} is the Mode II stress intensity range and C, m are empirical constants fit to a logarithmic plot of the test data. Equation 1 is simply the application of a Paris equation to shearing-mode crack growth. Of course, before one can apply Eq. 1 to the correlation of test data, one must have an accurate relationship between the Mode II stress intensity, K_{II} , and the experimentally observable parameters, viz: applied load and crack size.

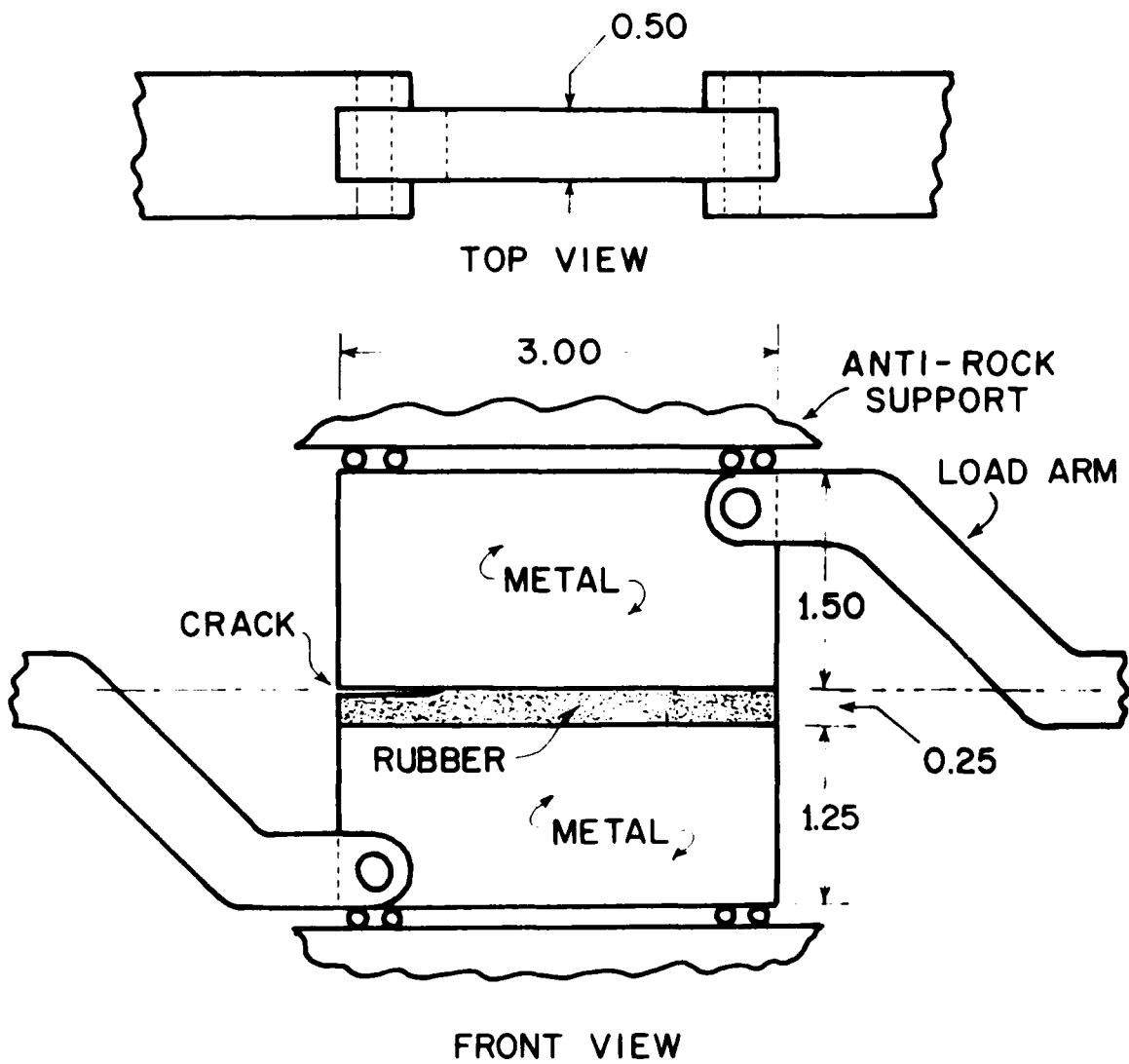
SPECIMEN DEVELOPMENT

Finite-element analysis was employed to obtain the required relation between K_{II} , applied load and crack size. Also, the analysis was used as a design tool to evaluate the ability of the test specimen to provide the stress environment required to produce stable debond-crack propagation.

Since the principal contribution to crack growth at the printing press roll adhesive bond is thought to be shear stress, the design activity focussed upon possible configurations for a Mode II test specimen. A bi-material "compact shear" specimen concept (Fig. 2) was selected as a promising candidate. This design is quite similar in general appearance to the ASTM standard compact tension specimen, which is widely used today for Mode I crack-propagation tests of homogeneous materials. The design illustrated in Fig. 1 consists of a 0.25-inch wide rubber layer bonded between two metal layers, with a pre-crack in the bond which lies along the load centerline. The offset load arms apply shearing forces to the specimen through two bearing pins. Since a moment is associated with these forces, the specimen must be placed on rollers between anti-rocking supports.

The primary condition which the test specimen is required to satisfy is that the Mode I stress intensity factor K_I must be much lower than K_{II} (ideally, the condition $K_I = 0$ is sought). This stringent design requirement calls for a careful analysis of the test specimen before any major commitment to an experimental program. The problem is compounded by the conflict between requirements for economy and realism* in the specimen design and the limitations of analytical stress analysis methods. The requirements usually dictate a design with no extreme dimensions and with different boundary geometries in proximity, configurations for which stress solutions cannot be calculated analytically. Also, the bi-material interface introduces its own complication, in that the fracture mechanics stress singularities associated with cracks at these interfaces have a general $r^{-\lambda}$ behavior instead of $r^{-1/2}$, where r measures radial distance from the crack tip. The value of λ has been shown to depend

* Realism: Can you grip it and load it?



(ALL DIMENSIONS ARE IN INCHES)

FIGURE 2. TEST SPECIMEN

upon the relative values of the elastic moduli and Poisson ratios of the two materials [5].

Although analytical solutions have been obtained for debond cracks between two infinite dissimilar materials [6], a numerical analysis is required to properly evaluate a test specimen such as the one illustrated in Fig. 2. Finite-element analysis is an obvious approach, but requires an accurate representation of the stress singularity behavior in the elements which surround the crack tip. It is well known that, without this representation, the solution convergence rates are so slow that the finite-element mesh must be refined beyond the bounds of computational economy, and that this situation cannot be improved by using displacement elements with higher-order interpolations [7]. However, a recently developed assumed-stress hybrid element (SKBP17) was available for this analysis. The SKBP17 element includes both displacement and stress interpolations, the latter derived from a stress-function solution for the near-field behavior of the actual bi-material singularity. The SKBP17 element was verified by comparison with the analytical solutions given in Ref. 6, and was shown to provide computed values K_I , K_{II} less than 1 percent different from the analytical values [8]. These tests were accomplished using meshes containing only a few hundred degrees of freedom. Additional details of the crack-element variational formulation appear in Ref. 9.

Therefore, the SKBP17 element was viewed as a practical tool for assessment of the proposed "compact shear" specimen design. A typical finite-element model of the test specimen is illustrated in Fig. 3. Note that the crack element is coupled to conventional displacement elements (TRIM3, QUAD4) in the surrounding mesh. Another special-purpose hybrid element (HOLEL) [10] is used to model the bearing pin holes to avoid wasting mesh detail in those areas. The entire finite-element model has approximately 520 degrees of freedom and is processed through an automated solution procedure in which the SKBP17 element moves from left to right to provide K-solutions for approximately 20 crack sizes. Several numerical studies were conducted with the boundary conditions varied to represent different physical possibilities for the anti-rocking supports. The boundary conditions shown in Fig. 3 correspond to ideally rigid supports of limited extent along the specimen's lateral edges. Rigid supports of full extent and combinations of rigid and spring supports were also studied.

RESULTS AND CONCLUSIONS

The reason for the extent of the investigation appears in Fig. 4, which illustrates the solution for Mode I and Mode II stress intensity as a function of crack size. The solutions shown correspond to the boundary conditions in Fig. 2 and represent the best effort to satisfy the essential design requirement $K_I \ll K_{II}$. For other support conditions, K_I tended to increase while K_{II} remained at about the level shown in the figure.

Thus, we failed to meet our main objective, which was to design a test specimen which could be used to study Mode II fatigue propagation of debond cracks in bi-materials. However, the study does provide a good illustration

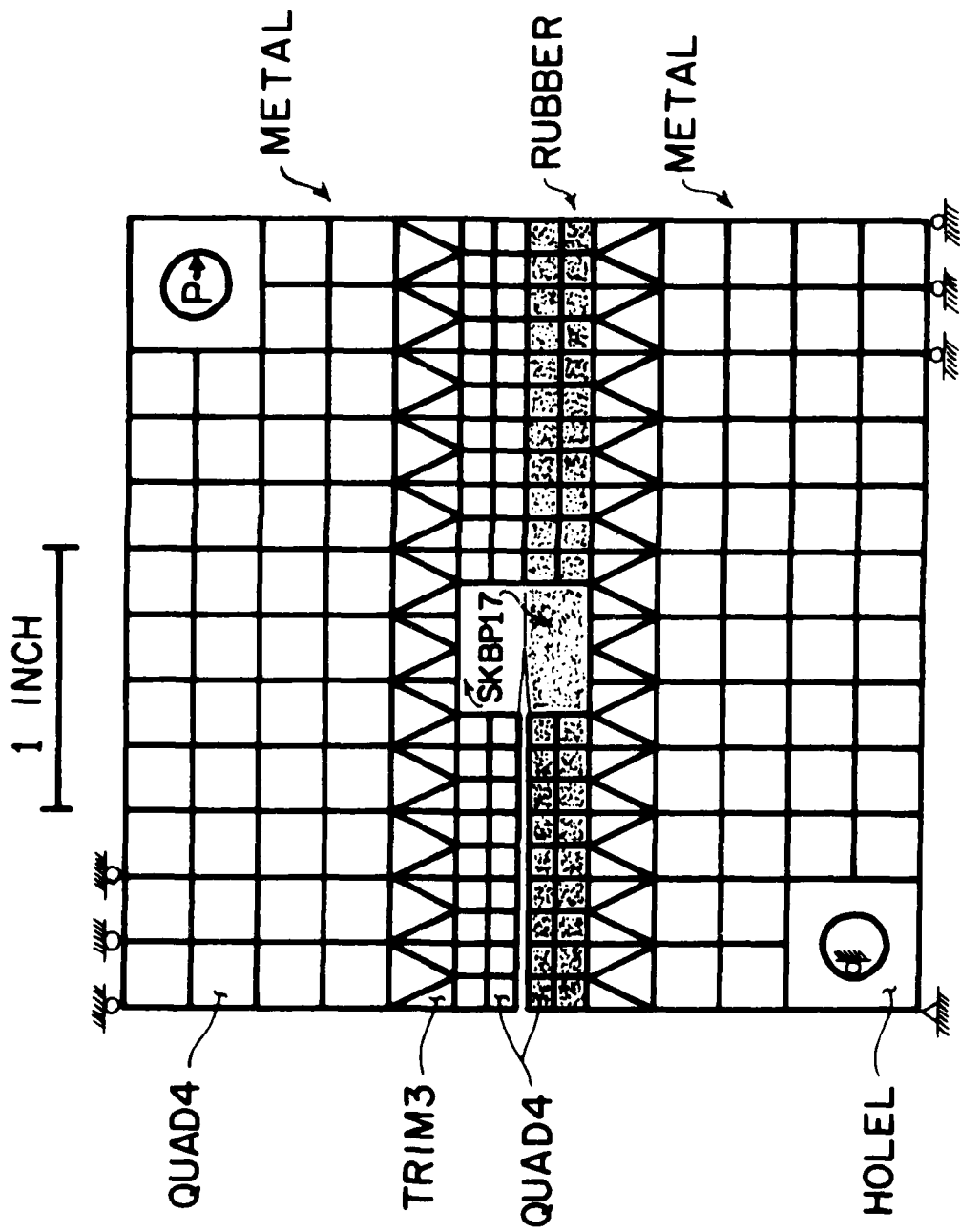


FIGURE 3. FINITE-ELEMENT MODEL

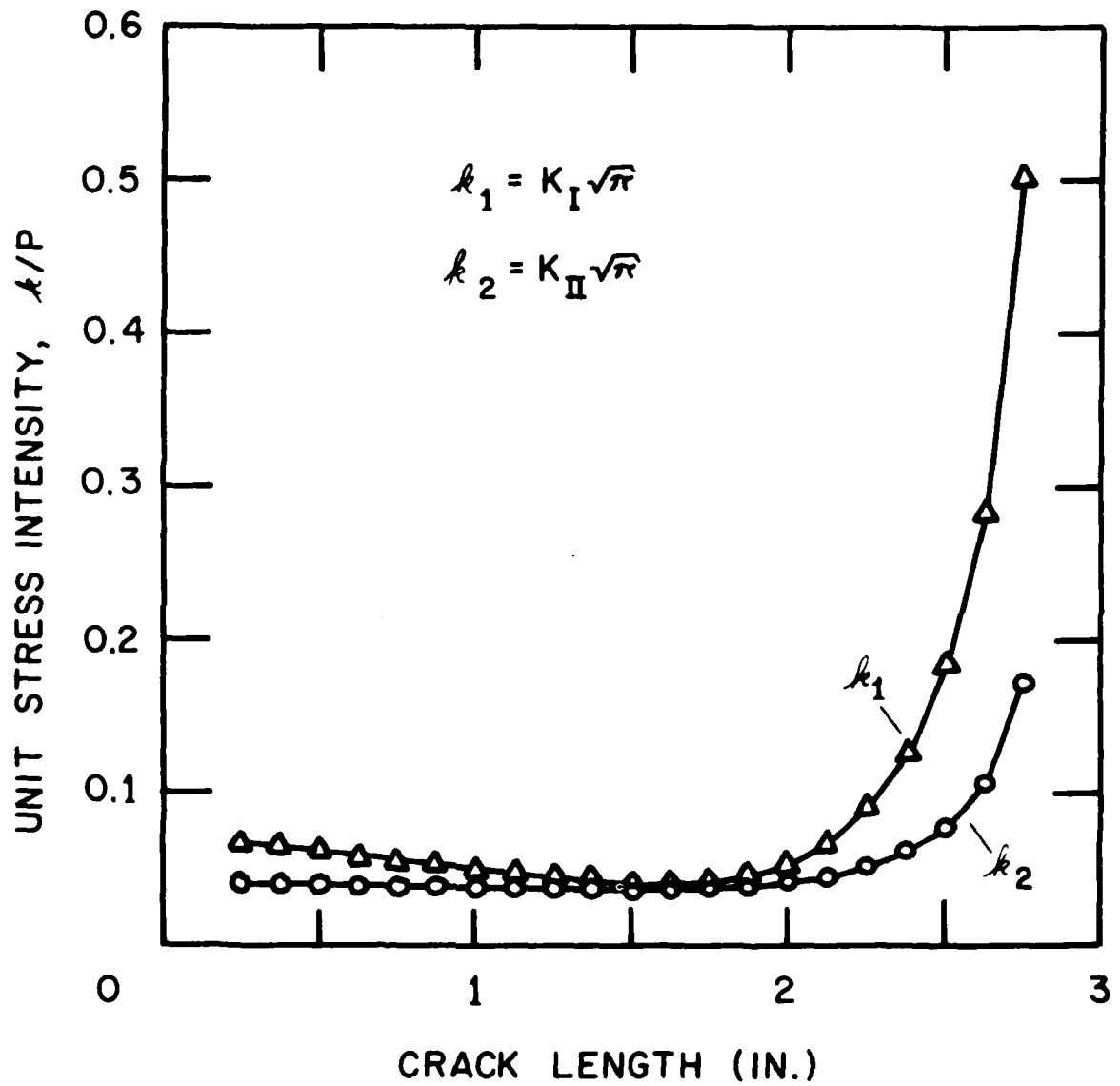


FIGURE 4. COMPUTED RESULTS

of the value of finite-element analysis as a tool for the assessment of fracture mechanics test specimen concepts. In the light of the results we obtained, the importance of making such an assessment before committing funds to an experimental program is obvious. A new study is now in progress to define and evaluate other test specimen configurations for this application.

ACKNOWLEDGMENT

The research reported in this paper was sponsored by the Stowe-Woodward Company, Newton, Massachusetts. The authors wish to express their appreciation to Mr. Joseph F. Cheatham, Director of Research, for providing pertinent experimental data and contributing to the design development.

REFERENCES

1. Pelloux, R. M., Department of Metallurgy and Materials Science, MIT, Cambridge, MA, private communication, 1975.
2. Cheatham, J. F., Stowe-Woodward Company, Newton, MA, private communication, 1975.
3. Bental, R. H. and K. L. Johnson, "Slip in the Rolling Contact of Two Dissimilar Elastic Rollers," Int. J. Mech. Sci., Vol. 9, 1967, 389-404.
4. Harris, A., "Finite Element Analysis of a Contact Problem," Aeroelastic and Structures Research Laboratory, MIT, ASRL TR 176-1, August 1974.
5. Williams, M. L., "The Stresses Around a Fault or Crack in Dissimilar Media," Bull. Seismological Soc. Amer., Vol. 49, No. 2, April 1959, 199-204.
6. Rice, J. R. and G. C. Sih, "Plane Problems of Cracks in Dissimilar Media," J. Appl. Mech., Vol. 32, Series E, No. 2, June 1965, 418-423.
7. Tong, P. and T. H. H. Pian, Int. J. Solids Structures, Vol. 9, 1973, 313-321.
8. Lin, K. Y. and J. W. Mar, "Finite Element Analysis of Stress Intensity Factors for Cracks at a Bi-Material Interface," Int. J. Fracture, Vol. 12, No. 4, August 1976, 521-531.
9. Tong, P., T. H. H. Pian, and O. Orringer, "Fracture Mechanics Analysis with Hybrid 'Crack' Finite Elements," Case Studies in Fracture Mechanics (T. P. Rich and D. J. Cartwright, ed.), Army Materials and Mechanics Research Center, Watertown, MA,
10. Orringer, O. and G. Stalk, "A Hybrid Finite Element for Stress Analysis of Fastener Details," J. Eng. Fract. Mech., Vol. 523, 1976, 1-11.

INVESTIGATION OF CRACKS IN REINFORCED CONCRETE BUILDING
Dr. Ardis White
Department of Civil Engineering
University of Houston
Houston, Texas 77004

INTRODUCTION

Historical Background

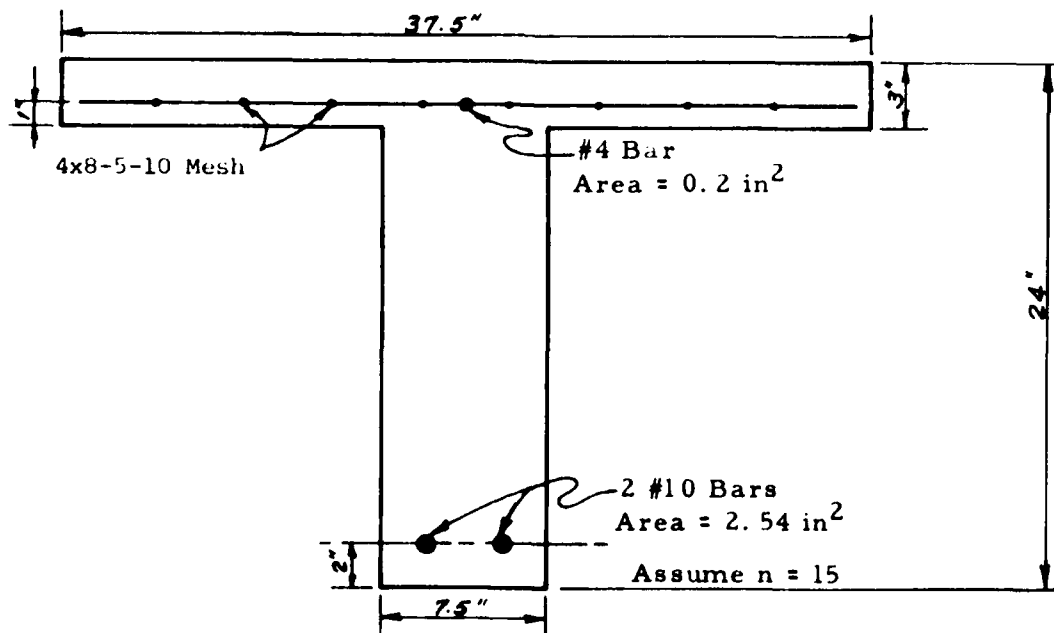
In the late 1950s, a seven-story parking garage of reinforced concrete was built in Houston, Texas, and after a few weeks, it was noticed that serious cracks (See Fig. 1) were occurring near the ends of the joists near the large 18-inch-by-18-inch columns on the outside perimeter of the floor, as well as in the same location on each side of these columns where the pan-joist type floor system was supported by the spandrel beam running between these columns. Some of these cracks ran not only throughout the depth of the stem of the joist, but through the slab depth as well. Inasmuch as there was no diagonal tension steel in the joist stems, only the dowel action of the bottom steel in the joist stems, the mesh in the floor, and the surrounding floor held up the floor and joists where the cracks extended both through the joist stem and floor slab. The presence of these cracks thus constituted a grave danger to the safety of the building.



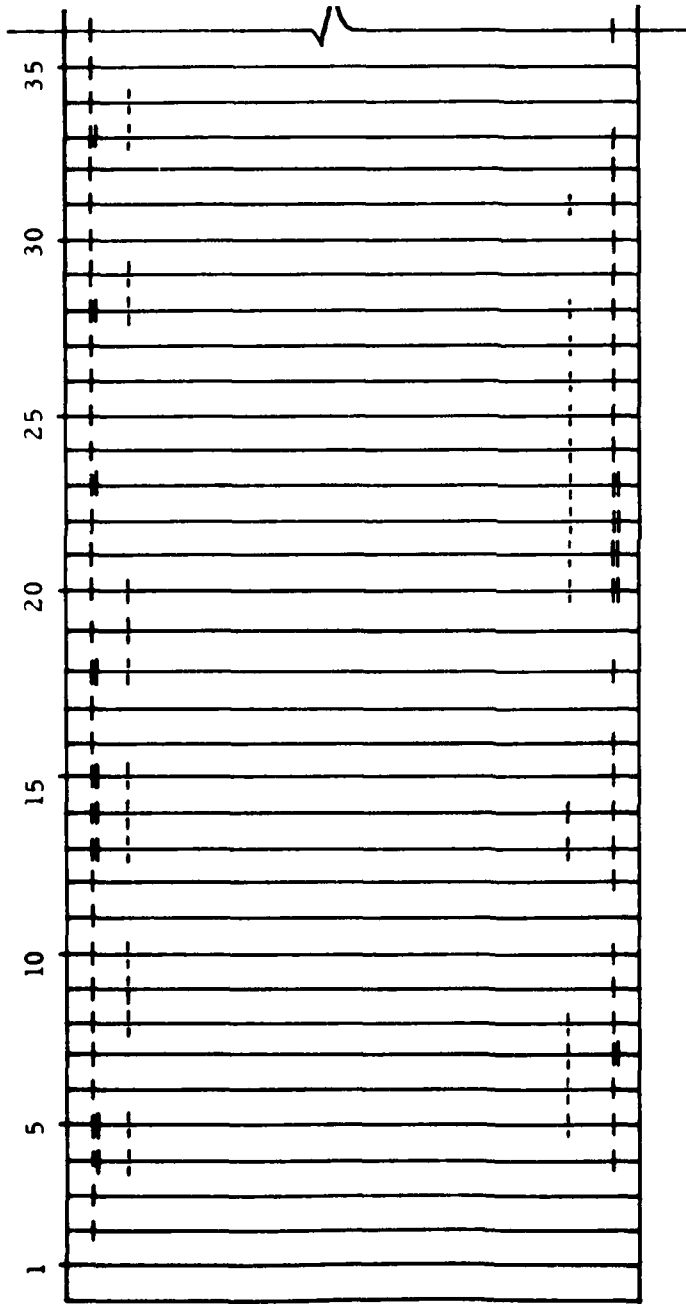
Figure 1. Cracks in Joists



Cracks in stems of joists--view from beneath 4th floor.
 Center joist is that of Fig. 1--No. 15, Fig.4.
 18" x 18" Column and spandrel beam at lower left. Figure 2.



Typical Joist Section
 Figure 3.



Definition of symbols for cracks of Figure 1:

- Small crack of type shown in Figure 1.
- - Large crack of type shown in Figure 1.
(These are cracks in stem of joists.)
- · - Cracks farther away from ends of joist---these go through the entire depth of the slab and connect with cracks in stems.

Distribution of Cracks

Figure 4.

The objective of the investigation was quite clear; it was to determine the cause of the cracks and to determine whether or not they could be repaired so that the building could be used safely.

Technical Background

The reinforced building under study was designed in strict adherence with the ACI code in effect at that time. The building consisted of extremely large (18-inch-by-18-inch) exterior and interior columns, and what is known as a pan-joist floor system. This is a system in which the floor and the joists are poured as a unit, or at one time. Apparently everything had been done in the way of design, in the use of materials, and in construction in accordance with accepted design criteria and construction procedures. The origin of the cracks thus presented quite a mystery at the beginning of the study, and, in addition, there were technical, legal, economic aspects, etc., to the problem.

FORMULATION

Definition of Tasks

It is the nature of ordinary reinforced concrete to crack, and it is extremely difficult to prevent it from doing so. Prestressed concrete is normally crackless concrete as it is designed to be so. As a matter of fact, if a reinforced concrete structure acts at the design load, it will certainly crack (although the cracks may not necessarily be seen with the naked eye) because of the difference in the stress-strain and strength properties of the plain concrete and the reinforcing steel.

The appearance and direction of the most serious cracks (Fig. 1) in the building suggested ordinary diagonal tensile stresses as the cause, but conventional computations for such stresses provided values obviously too low to be a single source of the cracks. Therefore, it was necessary to look elsewhere (many other places, in fact) for a more complete explanation.

Technical Data

The concrete used in the building was lightweight structural concrete, that is, concrete consisting of cement and water, a small amount of sand, and manufactured fine and course aggregates (burnt clay or shale). Structural concrete of this type is very commonly used today, but was not commonly used at that time. Shrinkage of lightweight concrete is slightly greater than that of ordinary sand and gravel (fine and course aggregates), a fact not as commonly known and appreciated at that time as it is now. The steel used in the structure was conventional reinforcing steel, and the construction procedures used were those commonly used throughout the industry for buildings of that type.

ASSESSMENT

A detailed presentation of numerical data obtained in this portion of the

case study would require much more space than is available. (The original source required a major portion of the 145 page report.) The work consisted primarily of the various computation procedures involved in determining the steel and concrete stresses required to permit a study of the stress conditions near the ends of the joists. These computations involved the following items:

- (1) Assumptions concerning joist-spandrel beam-column framework,
- (2) Dead load,
- (3) Live load,
- (4) Fixed end moments,
- (5) Moment distribution factors,
- (6) I/L for 3-joist unit,
- (7) Dead load and live load negative moments,
- (8) Selection of analysis points in failure zone,
- (9) Shear and bending moments in failure zone,
- (10) Summary of dead and live load shears and bending moments,
- (11) Steel and concrete stresses,
- (12) Properties of transformed sections,
- (13) Concrete stresses--dead plus live load,
- (14) Steel stresses--dead plus live load,
- (15) Stresses at top of slab, and
- (16) Principal stresses.

A detailed summary of the estimated stresses obtained was prepared, from which specific conclusions could be drawn regarding the safety of the building. Rather than presenting a small portion of the computations and results, the remainder of this case study is given primarily in narrative form, believed to be more appropriate.

The steps taken in obtaining information required for the conclusion decision regarding the safety of the building were as follows:

- (1) Obtaining a detailed survey of the cracks, with regard to extent, width, incidence, and then repeating this procedure at monthly intervals to determine whether or not the severity of the cracks was increasing, and if so, in what manner.

- (2) Concurrently with step one, many alternatives were considered in restoring the strength which had been lost due to the cracks. It should be noted that there were no stirrups (or vertical bars) in the stems of the joists to resist the diagonal cracks, and thus where the concrete was cracked both throughout the depth of the beam and the floor slab, as well, there was nothing to hold up the floor system and any live load except the dowel action of the continuous bottom steel reinforcement which extended into the columns or the spandrel beam on the outside perimeter of the building. From the very beginning, the writer was very doubtful as to whether or not the building could be saved, primarily because no immediate ideas came to mind as to how to restore the strength lost in the extensive initial cracking of the concrete. The owners and engineers were insistent in trying various methods of

injecting epoxy cements into the cracks in an effort to stop the cracking. This procedure did add temporary live-load strength to the floor system, but there were a number of additional factors (probably more important than the live load) which caused the cracks in the first place, and it was not believed that the injection of the epoxy had any influence on these factors. It was believed that cracks adjacent to those which had been filled with epoxy would occur; and this is exactly what happened. The epoxy-injection methods were soon stopped.

(3) Also, concurrent with the above, a detailed study was carried out, investigating every possible factor which could have led to the formation of the dangerous cracks in the floor system. Extensive discussions were held with the design personnel, material supplier personnel, and the construction personnel involved in the construction of the building. Extensive library work was also done regarding the properties of the materials involved. In the case of the construction procedures, extensive studies were made of the construction diary, the following leading, incidentally, to a rather surprising discovery. In the construction of a building of this type, the basement slab is poured first, then the basement columns are poured, and finally, shores of steel or timber are placed to support the first floor. After an appropriate time to allow curing of the basement slab and columns, the first floor is poured, and the forms are placed for the first-floor columns. After an appropriate curing time for the first floor, shoring is placed for the second floor. Then, depending on the waiting times involved, as well as the number of sets of shores available, the basement shoring may be removed and placed on the second floor as soon as the second-story columns are poured. This same procedure is repeated for the entire height of the building. The fact is, and can be demonstrated in a few minutes, that a floor dead load of more than twice the normal floor dead load can be placed on a given floor during construction long before the concrete is permitted to reach the normal 28-day design strength for which the concrete building is designed.

Many other factors were involved. Much study was placed on the shrinkage characteristics of the lightweight aggregate involved, the details of design which involved no stirrups in the stems of the joists (joists by definition, but perhaps more accurately described as "beams" with the widths and thickness involved--and the distinction is critical--the ACI code required stirrups in beams but not in joists). It was noticed very early in the investigation that the most severe cracks were in the slab and joists where the floor system ran into the extremely large columns. Similar cracks which were in the floor system near the spandrel beam between these columns were much less frequent and less severe, leading directly to the conclusion that the large negative moment caused by the difference in stiffness between the floor slab and the large columns was responsible for considerable negative moment tensile stresses in the top of the floor system. The termination of the cracks in the slab a few feet on each side of the columns was due to the decrease in the negative moment because of the much smaller torsional stiffness of the spandrel beam than the bending stiffness of the large columns. As a result, the negative moment and tensile stresses in the top of the slab and beam were much smaller where the floor system ran into and was supported by the spandrel beams.

Detailed study of the design also revealed an interesting feature. The code at that time required only a "hairpin" negative moment reinforcement bar at the columns, with the two legs of the hairpin being of unequal length. These were intended to take the nominal tensile stresses assumed to result from such construction. The closed end of the "hairpin" was embedded in the column, with the open ends facing away from the column and the ends ending at different distances from the face of the column. In many cases, the cracks which ran throughout the depth of the stem and through the slab, coincided with, or were very near one of the outer ends of the hairpin. The conclusion from this was that in addition to the negative moment tensile stress already existing in the concrete, there was a stress concentration at the end of the hairpin which increased the tensile stress in the concrete and contributed to formation of the crack. Computations were carried out to put approximate numbers on the tensile stress in the concrete at the end of the bars where the cracks occurred.

In summary, there were several factors which could have caused tensile stresses which led to the cracks in the concrete: (1) a very large negative moment causing tensile stresses in the top of the floor slab, stresses which would not normally be compensated for by the hairpin reinforcement there; (2) the stress concentration at the end of the hairpin bar in the region in which there were already high tensile stresses in the concrete due to the negative moment; (3) the floor system spanned fifty feet, which was rather long, as the pan joist system until that time had spanned only thirty-five to forty feet; (4) shrinkage in the concrete used was slightly greater than "hard-rock" concrete (concrete consisting of sand and gravel as the fine and large aggregate); (5) the construction process, which, according to diary dates, placed large floor dead load and thus large negative moments at the columns considerably earlier than the 28-day period at which the design strength of the concrete was to be obtained.

It was impossible to place precise quantitative values on any of the computations pertinent to the factors listed above, but they could be approximated, and they were. The considerations of the accumulative total of the effect of all factors acting together presented a rational explanation for the appearance of the cracks in the concrete. One question had thus been answered--why did the cracks occur? The second question was yet to be answered--whether or not the cracks could be repaired to restore the strength and safety of the building. This was a very difficult and agonizing decision to make, involving a great deal of money, legal matters, and other things. Reappearance of the cracks after repeated use of the epoxy revealed that this was not a suitably adequate procedure and that whatever phenomenon or phenomena had caused the cracks in the first place still existed. The extent and severity of the cracks continued to increase, and it was decided that one of two things were absolutely necessary. Either some way must be found quickly to strengthen the floor system, or else the building must be abandoned.

CONCLUSIONS

The final single conclusion in this case study was a very simple one.

Namely, that the building had to be torn down. This conclusion was based on the computations mentioned above, and the individual conclusions listed below.

The summary prepared from the computations mentioned at the beginning of the Assessment portion of this case study, together with other considerations led to the following specific conclusions:

(1) The primary cause of the serious cracks were the combination of stresses which arose from the greatly increased dead load during construction and shrinkage of the concrete at the early age of the concrete associated with this loading. This combination of stresses was believed to have started most of the cracks in the garage building.

(2) The second most important cause of the cracks was the combination of stresses which arose from the normal dead-plus-live loading plus long-time shrinkage. This combination of stresses was believed to be severe enough to cause some of the cracks in the joists, but the most probable effect of this combination of stress conditions was to cause progressive opening and extension of cracks initiated by the combination of stresses discussed in (1) above.

(3) The combination of stresses arising only from the normal dead-plus-live loading of the garage probably could not have started the serious cracks in the slabs and joists.

(4) Tests conducted at the University of Texas indicated that the diagonal tension strength of reinforced concrete beams was lowered when the percentage of steel was decreased to a low value, and that the diagonal tension strength was further decreased when bars were cut off near the end of the beam. These tests also indicated that the diagonal tension strength of light-weight concrete was less than that of sand and gravel concrete of the same compressive strength. Even though the research mentioned here was at that time limited in scope, the results indicated the very definite trends mentioned above, and were believed to be reliable. The items listed here were thus believed to be contributing causes of the cracks in the garage building.

Two footnotes should be added to this case study. At approximately the same time the study of this building was taking place, the air force had a number of failures of large concrete storage buildings across the United States, and as a result of these failures and others, the next version of the ACI code paid much more attention to shearing stresses in concrete members, and a number of changes were made pertinent thereto. Considerable attention was also given to the use of negative moment steel and reinforcing steel in general at connections.

Another footnote to this study is highly pertinent. If a designer walks securely in the footsteps of those who preceded him; using the same materials, the same structural systems, the same geometric proportions, and the same construction procedures, he is likely to run into little trouble. However, if any of these are changed, greater care and greater attention to fundamental

characteristics of the materials and other factors must be given. In this particular problem, the same structural system was used, but the geometric proportions were significantly different, and a new material was used. Disaster was the result, even though no violations of any existing codes or accepted construction procedures existed. All alternatives regarding restoration of the shearing strength of the joists at their ends were finally abandoned, inasmuch as they were extremely expensive, and because they did not address themselves to the questions of the stresses in the slab tensile stresses in either the slab or the joists. After more than a year of extensive study of all factors involved, it was concluded that the building was unsafe, could not be repaired at reasonable cost, and that it should be destroyed. The writer had concluded months before that the building would probably have to be destroyed, but work of several types had to be done before this same conviction could be passed on to the owner and designer of the building before preparation of the final report condemning the building.

Section 3

PRESSURE VESSELS AND ROTATING MACHINERY

APPLICATION OF FRACTURE MECHANICS
TO ROTATING MACHINERY

by

David W. Hoepfner, Ph.D., P.E.
Professor of Engineering
University of Missouri
College of Engineering
Columbia, Missouri 65201

BACKGROUND

Fracture mechanics has not been applied extensively to the design, maintenance and inspection of rotating machinery components - especially gas turbine engines. This is an interesting state of affairs inasmuch as Dr. Griffith is the progenitor of energy approaches to fracture prevention and he was apparently motivated in his classic fracture work by excessive numbers of engine failures. Furthermore, he made numerous contributions to the field of gas turbines. It is, therefore, somewhat paradoxical that in January, 1973 a second large fan disc failed on a large gas turbine engine that was manufactured by a company to which Dr. Griffith made numerous contributions.

This case is written to accentuate one of the major areas in which fracture mechanics was utilized as a tool to aid in life prediction related to this particular fan disc. In particular, emphasis herein is given to the necessity for using the correct fatigue-crack growth information when comparing materials, selecting manufacturing controls, establishing life limits, setting inspection intervals and establishing the configuration of structural components. Even though fracture mechanics considerations may be applied, if the incorrect material property information is supplied, errors in assessing the probability of failure may occur.

I have had the fortune of participating in evaluating many failures of rotating components. Some of those that I've worked on are cranks shafts for conventional internal combustion engines, soap flake rolls, pump impellers, ship screws and propellers, auxiliary power unit turbines, pump shafts, shipbased propulsors, rocket engines components, and gas turbine discs and blades. Two recent failures of interest relate to the broad objective of presentation of this case. Figure 1 shows a photograph I took of an engine that failed in flight over Colorado in January 1973. While the pieces of the fan disc that failed and the compressor blades were never recovered this failure was traced to an inflight burst of the fan disc. This was the second such event to occur. This failure is used as the basis of this case because of the emphasis it provided for increased application of fracture mechanics to the design and life verification testing of aircraft propulsion systems. Figures 2, 3, and 4 show photos

of the failed crankshaft that occurred in a conventional reciprocating engine in August 1976. The failure of this crankshaft led to the loss of six lives. These figures, taken from a recent National Transportation Safety Board (NTSB) report related to the incident, show that the crankshaft failed by fatigue. These two incidents point up the need for increased attention to structural integrity and reliability of aircraft engine components. If we were to check the FAA requirements on engines* we would find out that fracture mechanics considerations (i.e. damage tolerance requirements) are not required on aircraft propulsion systems. This is also true of military aircraft and ship propulsion plants. Even though the Air Force and FAA are both moving toward requiring damage tolerance analysis and verification on airframes, we have a long way to go before such requirements are introduced into propulsion systems. Hopefully, this case will provide a slight increase in stimulating us toward improving the methods we use to assure structural integrity of aircraft engines.

OBJECTIVES

Objective of case:

To accentuate the need for application of fracture mechanics based damage tolerance concepts to the design, inspection, maintenance, and replacement of rotating machinery. Emphasis in this case is directed toward gas turbines - those used in

- aircraft propulsion
- ship propulsion
- land based vehicle propulsion
- land based power generation

CASE

The failure shown in Figure 1 occurred when the L1011 aircraft was over Colorado at 37,000 ft. Failure of the fan disc occurred after approximately 200 flights. The design life for this disc was initially much greater than 5,000 flights.

* See, for example, Advisory Circular No. 33-3, FAA, D)T, 9/9/68

Obviously it became extremely important for the cause of the failure to be identified to formulate a fix. Since a spin pit test of the disc did not produce a failure of the disc until approximately 9500 cycles, for a five minute spin pit cycle, the lack of correlation between the spin pit tests, engine performance tests, engine verification tests and in-flight performance had to be explained. Actually, prior to this failure there had been another in-flight failure over Chesapeake Bay three days prior to the L1011 crash in December 1972. Thus, there obviously was a great deal of intensity applied to resolution of this failure.

As you all are aware, much fatigue data is generated using the sine wave shown in Figure 5.

However, we have recognized that we frequently must utilize the actual load (strain) spectrum applied to the structure. In the case of much rotating machinery, the use cycle can more closely resemble that shown in Figure 6b. Even though the load spectrum is greatly simplified here it is noted that a rotating component frequently is held at a fixed rpm for some period of time. Excluding vibration, gyroscopic, bending and aerodynamic loading on a rotating disc the centrifugal loads can be represented by a trapezoid. The length of dwell at maximum load after climb top-off will vary depending on the length of the flight. Rarely have fatigue data been generated with a dwell cycle at maximum load.

In the utilization of fracture mechanics for design it is important that the following factors related to the load (strain) spectrum be considered:

- Magnitude
- Frequency
- Wave Form (Carrier Function)
- Order of Occurrence
- Type - Positive, Negative
- Residual, Steady
- Alternating, R Value

Data on a material frequently are generated using a sine wave function, analyzed appropriately, and plotted on a log-log plot of fatigue-crack growth rate (da/dN) versus change in stress intensity (ΔK). Subsequently, a relationship that can be integrated to get life or the converse is employed. The most common parametric relationship used is of the form $da/dN = C(\Delta K)^n$. By evaluation of C and n from experimental data this equation can be integrated. However, if the incorrect values of C and n are used an estimate of life can result that is unconservative - that is, an unexpected failure can occur. Using the idea that the proper loading wave form must be employed to generate fatigue-crack growth data tests were conducted on the material employed in the fan disc that failed (Figure 1). It was necessary to utilize a trapezoid wave (Figure 6b) for these tests since the large difference in number of flight cycles to failure between the field failures and spin pit life verification failures had to be explained. It was believed that a potential acceleration of crack growth could result for this high strength titanium alloy based on previous experiences on the Appollo program.

Figure 7* presents data generated using a sine wave (solid lines) and using hold times as indicated in Figure 6b. Typical values in the C and n values assessed from the data shown in Figure 7 are:

<u>Baseline</u>	<u>Dwell</u>
10Hz, R = 0 Lab Air	Hold times indicated in Figure 7, R = 0 Lab Air
$C = 2.13 \times 10^{-13}$	$C = 9.79 \times 10^{-16}$
$n = 5.188$	$n = 6.854$

(da/dN in inches/cycle, ΔK in $\text{ksi}\sqrt{\text{in.}}$)

Thus, the previous results showed that, even though the alloy used in the fan disc was characterized using traditional fatigue data (S-N, ΔE -N), traditional mechanical properties, and fatigue-crack growth data generated using sine waves at frequencies greater than 10Hz, the differences in spin pit results and field results could be partially explained by the differences in fatigue-crack growth behavior under sine wave and trapezoid wave loading. Thus, using fatigue-crack growth data generated using test conditions that more closely simulated the disc use cycle, more accurate life predictions were performed. Thus, proper application of fracture mechanics led to greater reliability. We will be well advised to evaluate the load cycle effects on rotating machinery more carefully in the future.

In closing, it is important to emphasize that the load wave form effect on fatigue-crack growth was only one factor that related to the in-flight engine failures. There were many interesting aspects to this failure challenge that will be published in the future.

ACKNOWLEDGMENTS

The author is grateful to the following colleagues for continued encouragement and interaction: Mr. Robert Jeal, Dr. Glenn Bowie, Mr. J. B. Rittenhouse, Mr. W. Krupp, Dr. J. Ryder, Mr. D. Pettit, Dr. K. Kondas, Mr. D. Mauney, Mr. D. Alexander, Mr. W. Baumann, Dr. C. Hays, and A. L. L. People. I am indeed grateful to two of my students who were of significant help during preparation and delivery of this manuscript. Special thanks to Mr. Art Braun and Mr. C. Poon.

*J. T. Ryder, D. E. Pettit, W. E. Krupp, D. W. Hoepfner, "Evaluation of Mechanical Property Characteristics of IMI 685," Lockheed California Co. report, October 1973.

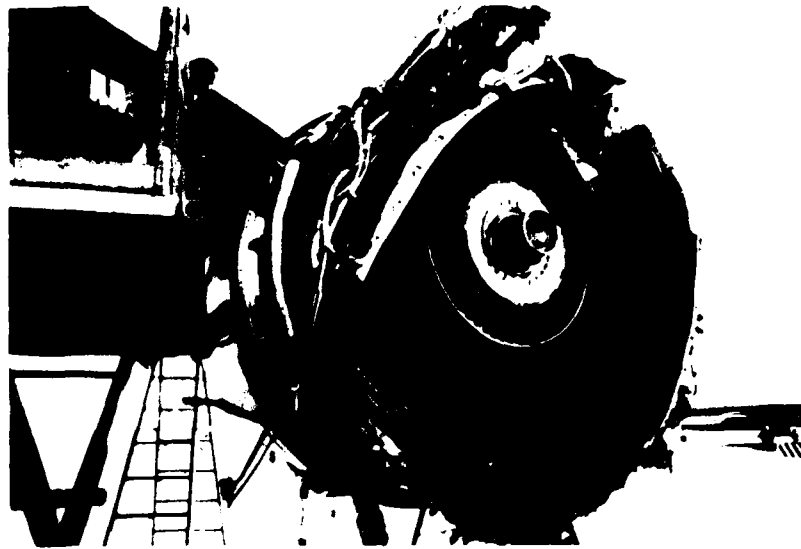


Figure 1 Photograph of large gas turbine engine that failed in flight -
D. W. Hoepfner, January 1973

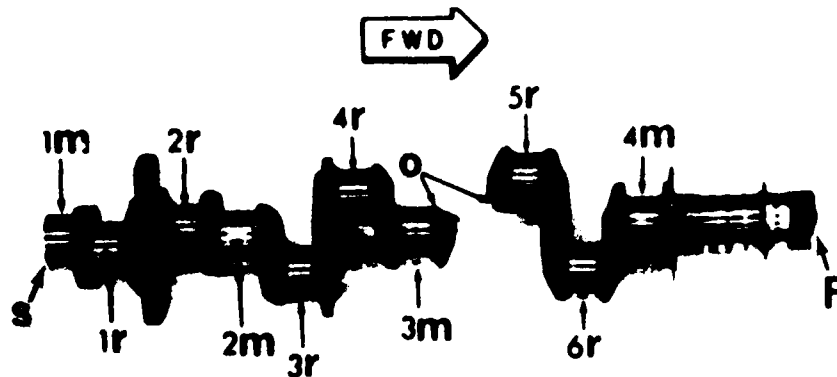


Figure 2 Figure of failed crankshaft from an aircraft engine - NTSB report (1976)

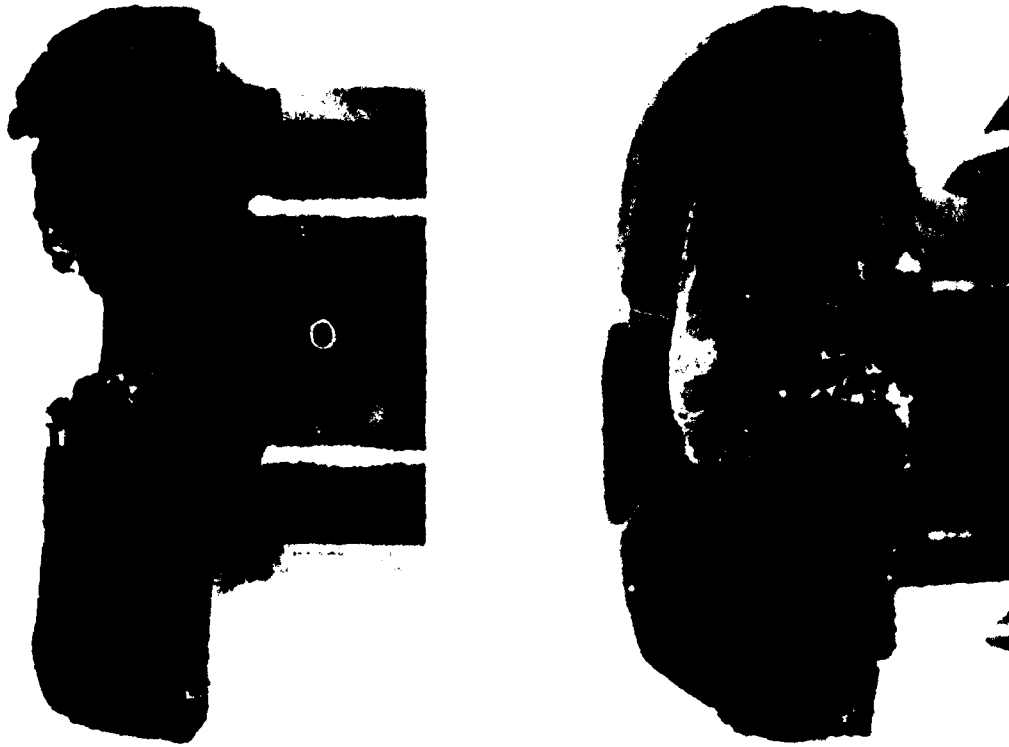
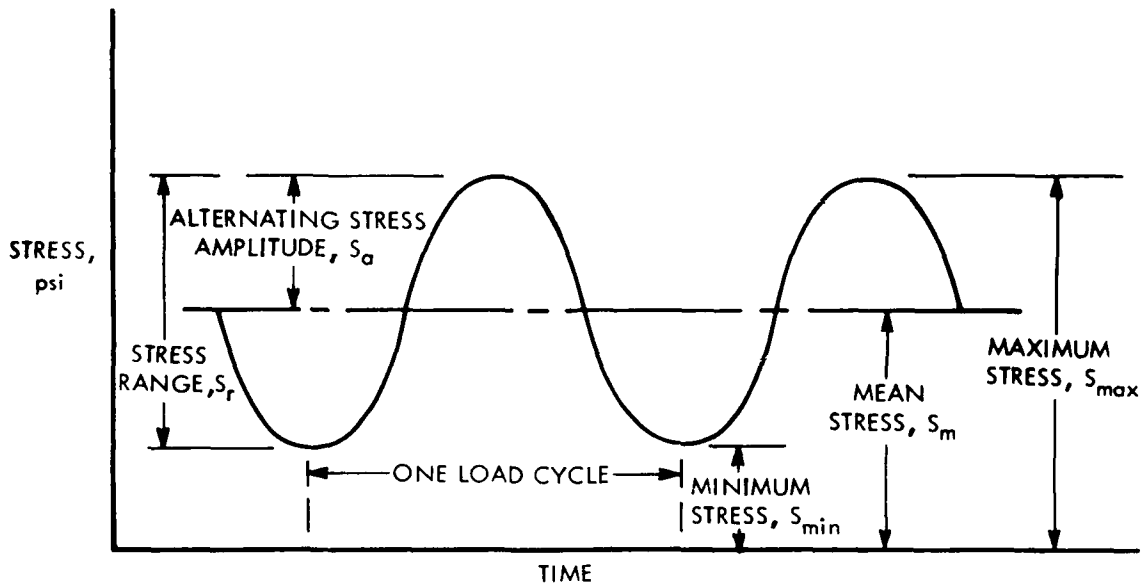


Figure 3
Mating fracture surfaces of break between No. 3 main journal
(far left) and No. 5 rod journal (far right).
Arrows "o" denote origin areas.
(NTSB report 9 1976)



Figure 4
SEM photograph of the origin areas shown in the left
photograph of Figure 3. Arrow "R" indicates journal radius. Note that
the fatigue origin is well below this radius surface.
(NTSB report - 1976)



NOTE THAT: $S_m = \frac{S_{max} + S_{min}}{2}$, $S_r = S_{max} - S_{min}$,

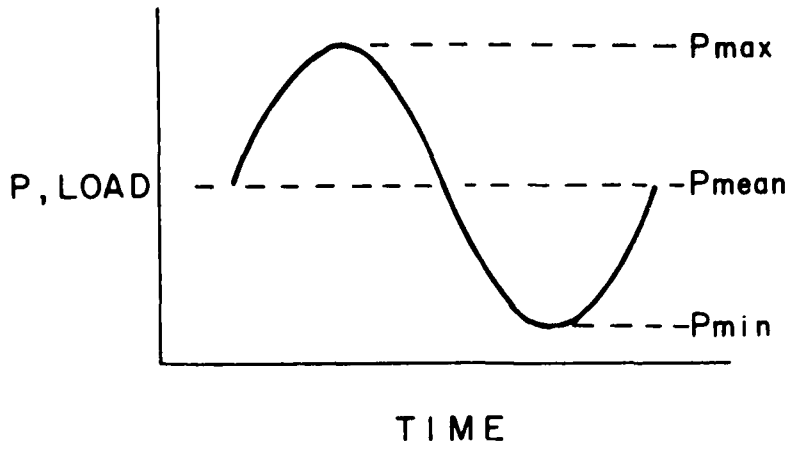
$$S_a = \frac{S_r}{2} = \frac{S_{max} - S_{min}}{2}$$

R OR A = STRESS RATIO

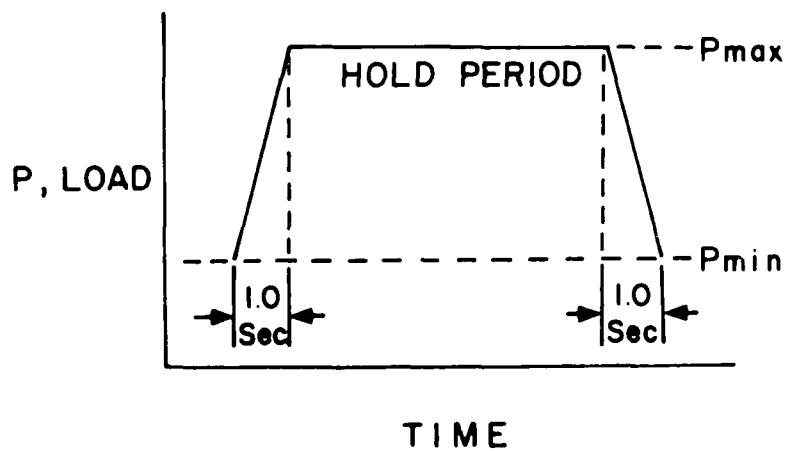
$$R = \frac{S_{min}}{S_{max}} \quad , \quad A = \frac{S_a}{S_m}$$

$$\text{AND } R = \frac{S_{max} - A}{1 + A} \quad , \quad A = \frac{1 - R}{1 + R}$$

Figure 5 Nomenclature used in fatigue



a. Sinusoidal Wave form, used for 10 Hz Frequency Tests



b. Trapezoidal wave form, used for Hold Time Tests

Figure 6 Comparison of sine wave and hold time loading spectrum

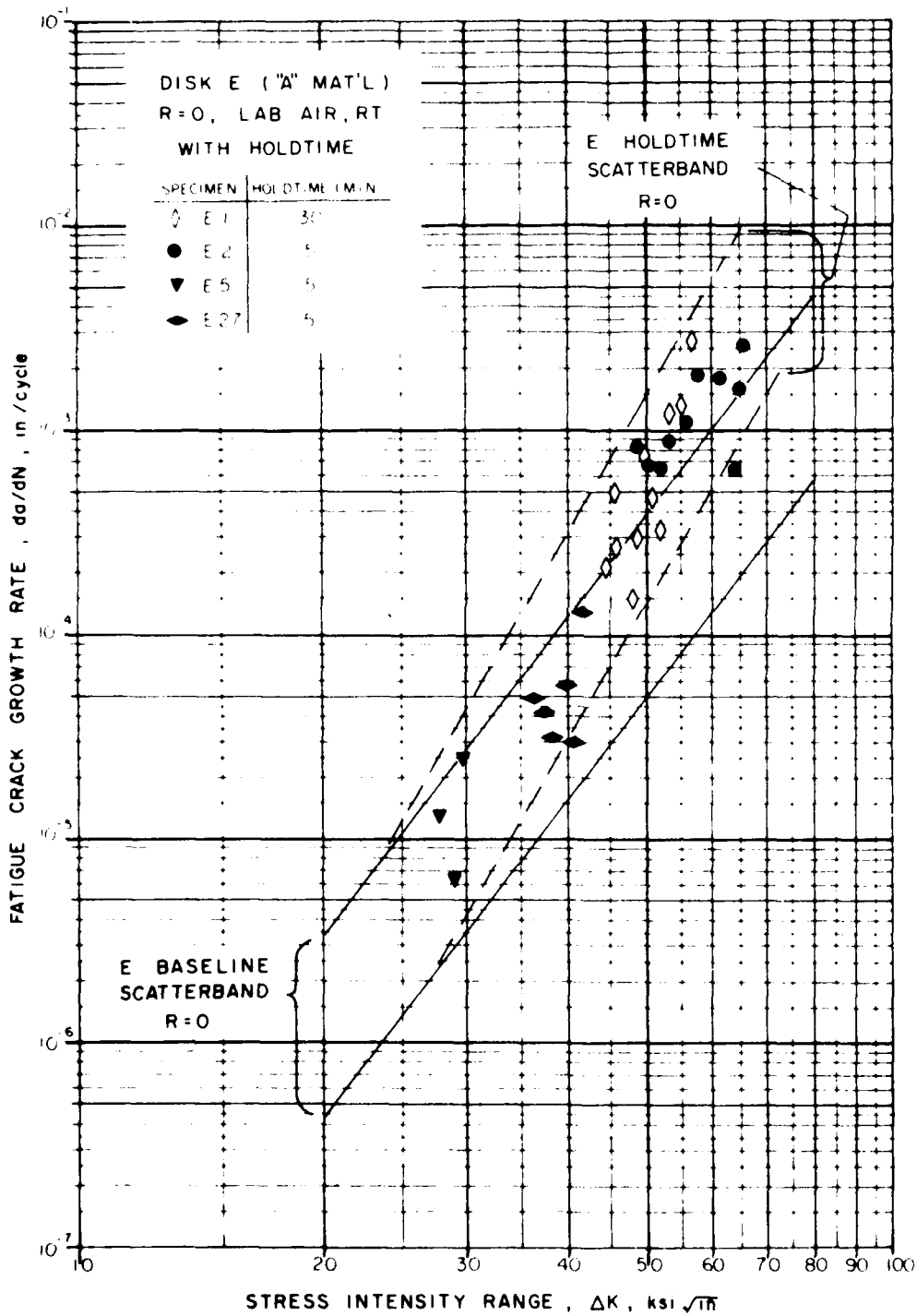


Figure 7 Effect of 5 and 30 minute hold times on fatigue-crack propagation in laboratory air

FRACTURE MECHANICS ANALYSIS OF ULTRASONIC INDICATIONS
IN CrMoV ALLOY STEEL TURBINE ROTORS

H. Craig Argo and Brij B. Seth

Materials Engineering, Steam Turbine Division
Westinghouse Electric Corporation
Lester Branch P. O. Box 9175, Philadelphia, Pa. 19113

INTRODUCTION

The two steam turbine rotors of 1Cr-1.2Mo-.2V alloy steel were retired after fifteen years of service. The rotors were made in 1953 using acid open hearth steel without the benefit of vacuum degassing which is employed today. Consequently, these rotors were expected to have high residual elements content, be less clean and have generally poorer properties compared with today's standards. Since these rotors were exposed during service to temperatures up to 1000 F, considerable degradation of properties due to temper embrittlement was anticipated. Further, these rotors, unlike modern rotors, were not ultrasonically inspected; therefore, their internal quality was unknown.

It was intended to use these retired rotors for shafts in a test facility. Since the shafts would be operating at room temperature under significant stresses, it was necessary to ensure their safety and reliability against catastrophic brittle failure. To perform the needed fracture mechanics calculations, information about rotor properties and indications in the rotors was required.

Both rotors were made from a single ingot of an average chemistry of .34C, .80Mn, .025P, .020S, .33Si, .19Ni, 1.05Cr, 1.21Mo and .21V. In subsequent discussion, the rotors will be identified as rotor A and rotor B. The original heat treatments of the rotors were:

	Rotor A	Rotor B
Austenitizing Temp Air Cooled	1850 F	1750 F
Tempering Temp & Time Furnace Cooled	1220 F, 52 hrs	1210 F, 45 hrs

The geometry of the rotors and test locations are shown in Figure 1. The original tensile properties are summarized in Table I.

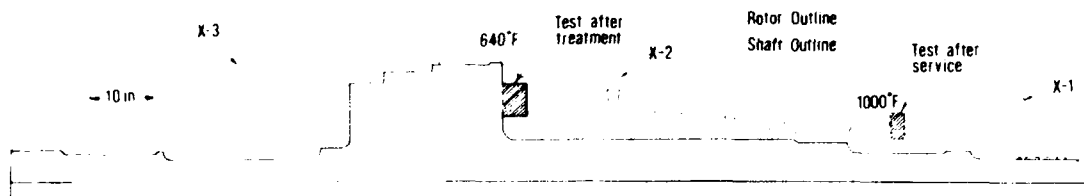


Figure 1 Schematic Outlines of the Rotor and the Shaft

Table I Original Tensile Properties

PROPERTY	Rotor A			Rotor B		
	X1	X2	X3	X1	X2	X3
0.2%YS, ksi	111.0	102.0	101.2	91.0	94.0	96.3
UTS, ksi	131.5	122.0	121.3	116.0	119.0	122.0
Elongation, %	12.5	16.0	12.8	15.5	16.0	14.0
Red. of Area, %	27.5	43.1	25.8	38.2	42.2	34.7

To establish the properties of these rotors after service, test material was removed from the location of maximum service temperature as shown in Figure 1. Tensile and impact tests were run on both rotors in the radial direction. The results are summarized in Table II.

Table II After-Service Mechanical Properties

PROPERTY	ROTOR A	ROTOR B
0.2%YS, ksi	98.6, 100.5	90.9, 91.9
UTS, ksi	123.3, 124.2	117.3, 118.3
Elongation, %	11.4, 10.0	15.8, 13.7
Red. of Area, %	19.2, 11.5	31.9, 23.4
RT CVN, ft-lbs	2	1
50% FATT, F	575	420

Considering that these rotors had lost ductility during service (compare Tables I and II) and had very high FATT's, the rotors were suspected of having undergone considerable temper embrittlement. The susceptibility of alloy steels to temper

embrittle is well known [1]. The fracture surfaces of after-service Charpy V-notch (CVN) impact specimens as examined by scanning electron microscope (SEM) showed a large percentage of intergranularity, refer to Figure 2, establishing that these rotors had undergone temper embrittlement. A series of CVN impact tests over the range from lower to higher shelf temperatures were used to estimate the fracture toughness versus temperature using the Begley-Logsdon correlation [2]. However, since these rotors were heavily embrittled, had very low room temperature (RT) impact strengths, had very high FATT's and low ductilities, it was thought that the Begley-Logsdon correlation would not be appropriate for converting impact values into K_{Ic} values. If the Begley-Logsdon correlation had been applicable, room temperature K_{Ic} 's of between 50 and 40 ksi $\sqrt{\text{in.}}$ would have been estimated. A conservative value of about half the estimated K_{Ic} values was used in the initial calculation which indicated the reliability of the shafts would be rather low.

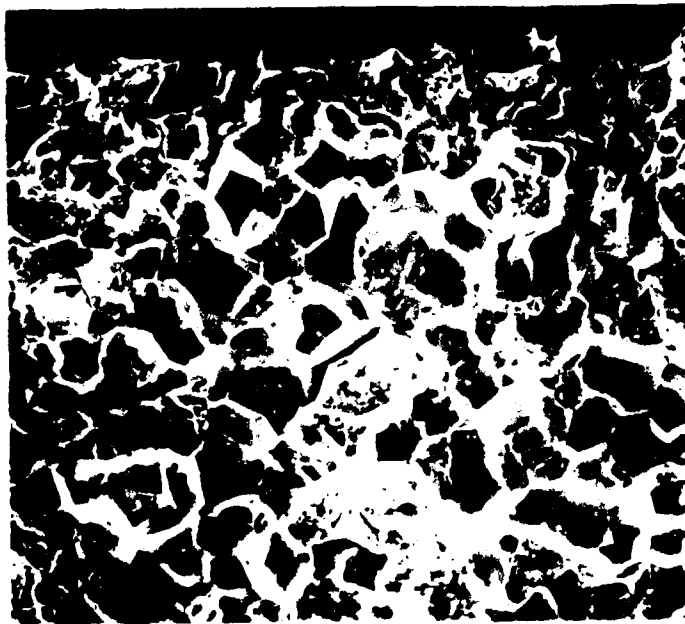


Figure 2 SEM view of impact specimen fracture at 50X. About 80% intergranular and 20% cleavage. 70F test having 2 ft-lbs.

In order to improve the fracture toughness, various de-embrittlement heat treatments were investigated in the laboratory and one was chosen for use on the rotors. The properties of the rotors after the de-embrittlement treatment were measured, the rotors ultrasonically inspected and fracture mechanics calculations performed to demonstrate that they would be quite safe for use as shafts.

FORMULATION

Analytical Equations

Basically, the test shafts have the potential for failure via two mechanisms: one, crack growth by high-cycle fatigue and, two, brittle fracture caused by critical crack size. To evaluate if crack growth by high-cycle fatigue was a possibility, the crack growth rate threshold concept as has been described by Paris et al [3] was used. Stress intensity at the indication is to be less than the threshold value in order for the indication to not grow in high-cycle fatigue. The stress intensity is given by the conventional equation noted by Greenberg et al [4]:

$$\Delta K = \Delta \sigma (1.21 \pi a / Q)^{1/2} \quad (1)$$

where ΔK = stress intensity range, ksi $\sqrt{\text{in.}}$.

$\Delta \sigma$ = alternating stress, ksi

a = crack depth, in.

Q = crack shape parameter is a function of the crack shape and the ratio of the applied stress to the yield strength of the material, refer to Figure 3 [4].

1.21 is included only when the crack is intersecting a surface

To evaluate the other failure mechanism possibility, the indication or crack size has to be compared with the critical flaw size given by the equation [4]:

$$a_{cr} = (Q / 1.21 \pi) (K_{IC} / \sigma)^2 \quad (2)$$

a_{cr} = critical flaw depth, in.

K_{IC} = fracture toughness, ksi $\sqrt{\text{in.}}$

σ = applied stress, ksi

The above equations are valid only for a single flaw in a given stress field. However, when there are several indications in the same general area, the possibility of their interaction has to be considered. The degree of interaction is a function of the size and spacing between the flaws. If there is an interaction between flaws, the stress intensity magnification can be determined and using Figure 4 [5].

Since the test shafts were to be used for only a few start-stops (less than 50 times), consideration of an initial defect depth a_i growing to a_{cr} was not necessary.

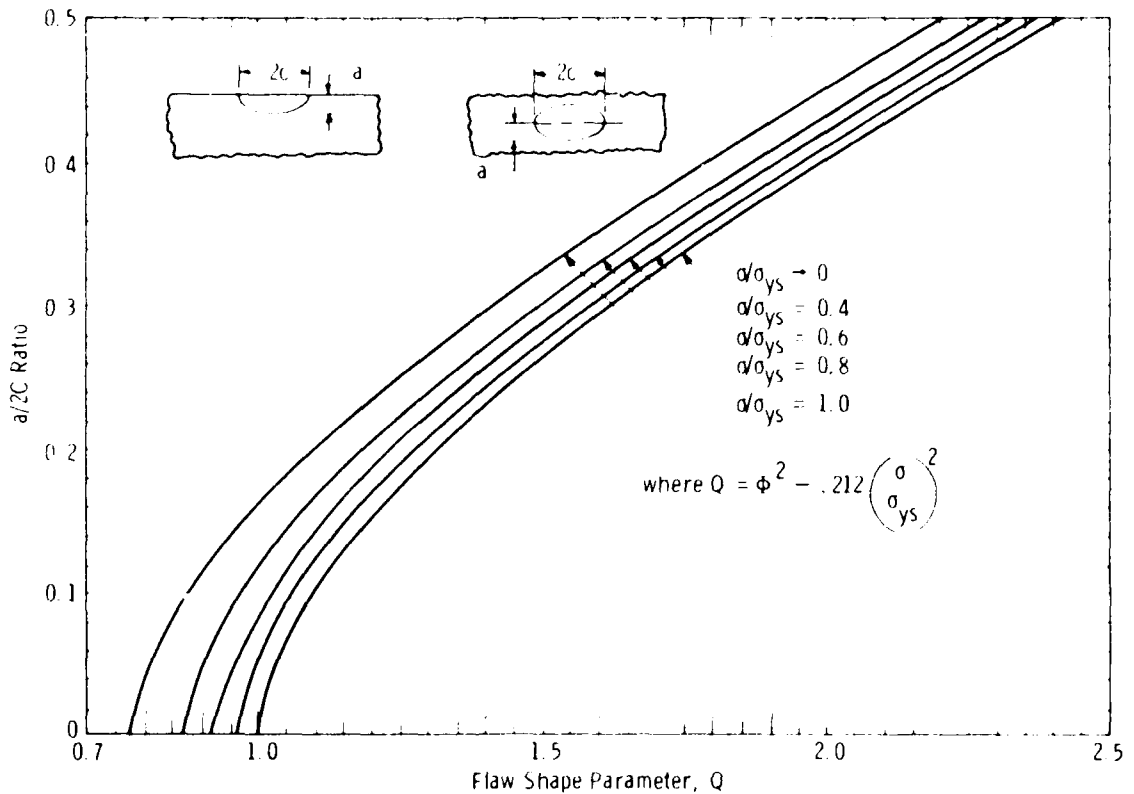


Figure 3 - Flaw shape parameter curves for surface and internal cracks [4]

In order to employ the above two equations for evaluating the reliability of shafts, it is necessary to know the mechanical properties, the ultrasonic indication sizes, and the duty requirements. These are discussed below.

(a) Mechanical Properties

Since the rotors were considered unuseable because of embrittlement, different heat treatments were evaluated in the laboratory using the after-service test material. One approach was to give a de-embrittlement/tempering treatment at 1230 F for 18 hrs followed by still air cooling so as to minimize the embrittlement and, at the same time, lower the strength level to improve the ductility. Another approach for improving the properties was to reheat treat the shafts completely. This was simulated by using material from the rotors which was austenitized at 1750 F for 18 hrs, controlled cooled at 100 deg or 300 deg F per hr to facilitate selection of cooling rate, and

tempered at 1250 F for 18 hrs followed by air cooling. The material was tested for tensile properties and impact strengths. The results are summarized in Table III.

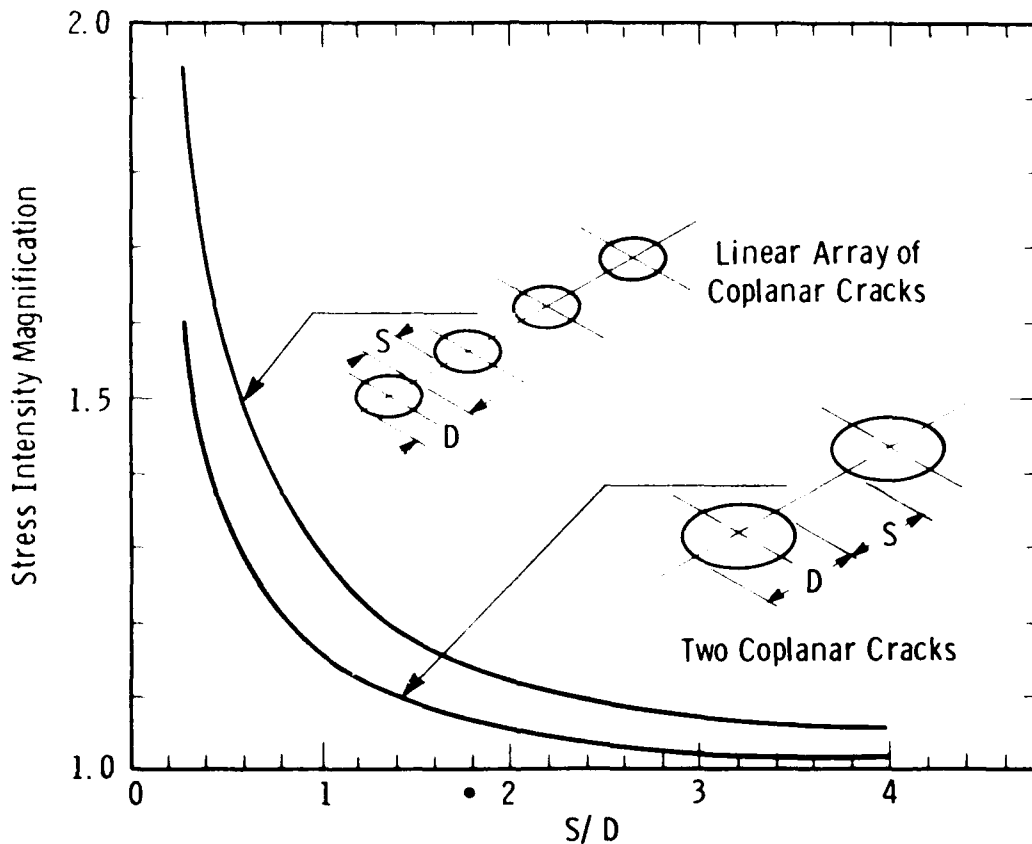


Figure 4—Stress intensity magnification at the approaching edge between adjacent circular defects in a tension stress field [5]

A marked improvement in room temperature impact strength values, FATT's and ductilities occurred as a result of these thermal treatments (compare Tables II and III). The de-embrittlement/tempering treatment properties were only slightly worse than the full heat treatment properties. The additional property improvement achieved by the full heat treatment was considered insufficient to justify its application since it would have required three weeks compared with four days for the de-embrittlement/tempering treatment.

Concurrent with the laboratory work, the rotors were machined near to the shaft configuration. An integral test location was left for providing test metal. The shafts were heat treated and ultrasonic inspected. Finally, the shafts were finish machined.

The shafts were de-embrittled at 1230 F for 32 hours followed by furnace cooling to 500 F. Below this temperature the shafts were air cooled. Test material was removed (from the after treatment test location, Figure 1) and tested for mechanical properties. The results are summarized in Table IV. Room temperature tensiles, room temperature Charpy V-notch (RT CVN) impacts, and the FATT tests were performed according to ASTM A370. The K_{Ic} tests were performed according to ASTM E399 using the compact tension specimens with B=1.00 in.

Table III Mechanical Properties of Laboratory Thermally Treated After-Service Material

Property	Rotor A			Rotor B		
	1230F 18 hrs	1750F 18 hrs 100 ^o /hr 1250F 18 hrs	1750F 18 hrs 300 ^o /hr 1250F 18 hrs	1230F 18 hrs	1750F 18 hrs 100 ^o /hr 1250F 18 hrs	1750F 18 hrs 300 ^o /hr 1250F 18 hrs
.2%YS, ksi	92.6	93.5	94.1	88.1	96.1	96.4
UTS, ksi	116.2	118.6	118.5	113.6	121.1	121.3
El, %	15.2	15.6	16.0	15.8	16.8	14.5
RA, %	32.1	35.6	37.9	36.6	37.9	30.5
CVN ft-lbs	4	8	6	6	8	6
50%FATT, F	250	200	205	215	205	205

Table IV Shafts' Mechanical Properties After Thermal Treatment

Property	Shaft A	Shaft B
0.2% YS, ksi	92.5, 90.9, 91.6	88.0, 88.4, 88.5
UTS, ksi	118.5, 115.7, 116.3	114.5, 113.6, 114.1
Elong, %	16.5, 14.8, 16.0	16.0, 17.8, 17.2
Red. of Area, %	40.7, 38.9, 36.9	43.4, 42.5, 41.6
RT CVN, ft-lbs	5	4
50% FATT, F	250	260
RT K_{Ic} , ksi \sqrt{in} .	40.0	48.0

The mechanical properties tabulated in Table IV are comparable to those obtained with laboratory thermal treatments as listed in Table III. The crack growth rate threshold value ΔK for this material is assumed to be 3.0 ksi $\sqrt{\text{in.}}$ based on data for other alloy steels [3].

(b) Ultrasonic Indication Sizes

Both shafts were ultrasonically inspected after being machined to near the shaft configuration, refer to Figure 1. The entire volumes of the shafts were inspected from the peripheral surfaces using a 2.25-MHz, longitudinal-mode transducer. Inspection sensitivity was calibrated against the amplitudes of 1/16-in. diameter flat bottom holes in reference blocks at two test distances. The amplitudes of the ultrasonic indications were corrected for test surface curvature and for metal path distances similar to the procedure described in ASTM A418. The description of the larger ultrasonic indications is summarized in Table V. The indications in shaft A were all located in the shaft end where the bore was 5.2-in. diameter; whereas, in shaft B the indications were located in the large-diameter section of the shaft where the bore was 6.7-in. diameter.

Table Va Ultrasonic Indications in Shaft A

<u>Indication No.</u>	<u>Dist from end*, in.</u>	<u>Dist from bore, in.</u>	<u>Angular Position</u>	<u>Area in.²</u>
1	141.0	0.25	220°	.0013
2	141.5	0.25	128	.0009
3	141.5	0.50	218	.0009
4	143.5	0.19	113	.0008

*Left side of Figure 1

(c) Duty Requirements

As shafts, the conditions would be to operate at room temperature and 3600 rpm as the normal speed and a possible 4320 rpm overspeed. The shafts experience an alternating bending stress during each revolution which create the high-cycle fatigue situation. This stress is maximum at the surface of the shaft and decreases towards the bore. The magnitude of the stresses at the locations of the ultrasonic indications in the shafts A&B are about 1 ksi and 4.25 ksi respectively.

The shafts will also experience a tangential stress which is maximum at the bore surface and is proportional to the square of the rpm. Each time the shaft is started and stopped, it will experience one cycle of this stress. The magnitude of this stress in the bore at the location of indications in shafts A and B at 4320 rpm is 6.3 ksi and 56 ksi respectively.

Table Vb Ultrasonic Indications in Shaft B

Indication No.	Dist from end*, in.	Dist from bore, in.	Angular Position	Area in. ²
1	62.4	.12	175°	.0014
2	62.8	.12	153	.0018
3	64.8	.62	15	.0014
4	64.9	.62	78	.0014
5	65.0	.62	84	.0014
6	65.0	.75	45	.0014
7	65.3	.75	30	.0018
8	65.3	.12	55	.0014
9	65.5	.25	70	.0014
10	66.0	.62	58	.0014
11	67.3	.38	145	.0014
12	68.0	.12	15	.0014
13	69.0	.12	358	.0018
14	69.6	.12	345	.0014
15	71.8	.25	270	.0015

*Left side of Figure 1

ASSESSMENT

Safety Against High-Cycle Fatigue Failure

Utilization of the shafts would subject the ultrasonic indications in the shafts to a very large number of fatigue cycles in only a few hours of operation at 3600 rpm. To evaluate the potential of failure via crack growth by high-cycle fatigue, a tolerable crack size was determined using equation (1) with ΔK equal to 3.0 ksi $\sqrt{\text{in.}}$ and solving for the crack depth value. The ultrasonic indications are reported as an equivalent area in comparison to the inspection sensitivity; hence, the tolerable crack size is to be an area. When intersecting a surface, an indication area is presumed to be a semi-elliptical shape, see sketches in Figure 3. The conservative area value is when the $a/2c$ ratio is 0.25 which is a Q value of 1.45 from Figure 3. The largest high-cycle stress was 4.25 ksi.

$$\begin{aligned}
 a &= (Q/1.21\pi) (\Delta K/\Delta\sigma)^2 \\
 &= (1.45/1.21\pi) (3.0/4.25)^2 \\
 &= 0.190 \text{ in.}
 \end{aligned}$$

The area of a semi-ellipse of $a/2c=0.25$ is πa^2 . The tolerable area for not having high-cycle fatigue crack propagation is $\pi (.190)^2$ or 0.113 in.². Indications in both shafts did

not interact as established by the criterion in Figure 4; hence, only the largest single indication needed to be considered. The tolerable area size is very much larger than the largest reported indication size of 0.0018 in². Thus, there is sufficient safety margin even with possible underestimation of the indication size found by Tu and Seth 6 .

A similar analysis could not have been made for the shafts before the de-embrittlement treatment because very little was known about the crack growth rate threshold value ΔK for embrittled materials.

Safety Against Catastrophic Failure

Since there were several ultrasonic indications in this shaft, it was decided to evaluate on the basis of the largest indication at the highest stress and near the bore. If this condition were safe then it would not be necessary to evaluate each individual indication. Based on the size and spacing of each indication, it was established that there was not any interactions between the indications by the criterion in Figure 4. Because toughness values were based on periphery properties only and because the bore properties are likely to be somewhat worse, the bore K_{Ic} values were calculated using 80% of the surface values. Thus, the bore K_{Ic} before and after thermal treatments were estimated as 25 and 38 ksi $\sqrt{\text{in.}}$ respectively. The critical flaw size for brittle bursting was calculated using equation(2).

$$a_{cr} = (Q/1.21\pi) (K_{Ic}/\sigma)^2$$

<u>Parameter</u>	<u>Before Treatment</u>	<u>After Treatment</u>
K_{Ic} , ksi $\sqrt{\text{in.}}$	25	38
σ , ksi	56	56
σ_{ys} , ksi	91	88
σ/σ_{ys}	.62	.64
a:2c	.25	.25
Q	1.35	1.35
a_{cr} , in.	.071	.164
A_{cr} , in. ²	.016	.084

Since the area of the largest indication detected ultrasonically was .0018 in.², the ratio of critical area to indication area before de-embrittlement treatment was only 8.9. This is approximately the degree of underestimating ultrasonic indications versus metallographic examination [6]; thus, there was insufficient safety margin before the de-embrittlement treatment. The ratio after de-embrittlement treatment increased to 47 which provided adequate safety against catastrophic failure.

CONCLUSIONS

1. Considerable temper embrittlement can occur in Cr-Mo-V alloy steel rotor material during service exposure. The embrittlement can be reduced by either a de-embrittlement treatment or a full reheat treatment.
2. The reliability of shafts was calculated using fracture mechanics principles and was found to be unsatisfactory before de-embrittlement treatment but satisfactory after applying the thermal treatment.
3. The operation of both shafts was satisfactory in the test facility.
4. The validity of the correlation of Begley and Logsdon for converting impact values into K_{Ic} is unknown for embrittled materials and should be examined.
5. The threshold ΔK values for embrittled materials should also be measured.

REFERENCES

1. Temper Embrittlement of Alloy Steels, ASTM STP 499, Philadelphia, Pa., 1972.
2. Barsom, J. M. and Rolfe, S. T., Fracture and Fatigue Control in Structures, Prentice-Hall, Englewood Cliffs, N. J., 1977, Chapter 6.
3. Paris, P. C., Bucci, R. J., Wessel, E. T., Clark, W. G., and Mager, T. R., "Extensive Study of Low Fatigue Crack Growth Rates in A533 and A508 Steels", ASTM STP 513, Philadelphia, Pa., 1972, pp. 141-176.
4. Greenberg, H. D., Wessel, E. T., Clark, W. G., Jr., and Pryle, W. H., "Critical Flaw Sizes for Brittle Fracture of Large Turbine Generator Rotor Forgings", International Forgemaster's Conference, 1970.
5. Hall, L. R., and Kobayashi, A. S., "On the Approximation of Maximum Stress Intensity Factors for Two Embedded Coplanar Cracks", Boeing Co. Structural Development Research Memorandum No. 9, May 1964.
6. Tu, L. K. L., and Seth, B. B., "NDT/Destructive Correlation and Fracture Mechanics Analysis", Journal of Testing and Evaluation, ASTM, Philadelphia, Pa., Sept. 1977.

DIESEL ENGINE CRANKSHAFT FAILURE

L P Pook

(National Engineering Laboratory
East Kilbride, Glasgow, Scotland)

INTRODUCTION

A large number of failure analyses are carried out at NEL and a fracture mechanics approach is used whenever appropriate. This investigation, which has been previously outlined [1] is a straightforward example of how quantification of flaw severity using fracture mechanics techniques can help to positively identify the causes of a failure. Only information which was available at the time of the investigation is used, but the accuracy of calculation is discussed in the light of more recent information. Proprietary detail has been omitted.

When the prototype for a new design of large diesel engine was being run under test conditions, the crankshaft failed after several hundred hours. A conventional metallurgical examination showed that the material was within specification and that failure was due to fatigue cracking, originating at a fillet. Nothing that accounted for the failure was revealed, although it was noted that grain flow in the vicinity of the failure was not as specified. It was suspected that the stress at the origin might have been higher than estimated during design, perhaps because of a resonance. There was however, no evidence of abnormal operation during the test. At this stage, NEL was asked to advise on the cause of the failure.

The crankshaft was a steel forging; the steel specification was not known at the time the calculation below was carried out. The site of the failure was a large radius fillet. The diesel engine had been run at constant speed, and the stresses in the fillet were largely due to inertial loads, so the loading could be regarded as a constant amplitude cyclic loading. The estimated stress level in the fillet was $0 \pm 90 \text{ MN/m}^2$. No surface treatments, such as surface hardening or shot peening, which could have introduced residual stress, had been applied to the fillet.

The metallurgical examination had shown that the grain flow in the fillet was roughly perpendicular to the surface, rather than parallel to the surface as specified. There were a number of small forging laps in the area, with depths measured perpendicular to the surface of up to about 2 mm. The incorrect grain flow and the presence of laps would not have been acceptable in a production engine, but the defects were not regarded as sufficiently serious to cause trouble at the stress levels involved. However, a fatigue crack had initiated at the root of one of the laps, resulting in fatigue failure of the crankshaft. The exact shape and depth of this lap had not been recorded and could not be ascertained because it had been destroyed during sectioning to determine the precise grain flow. However, it was believed to have been one of the deeper laps, that is about 2 mm deep. The sectioning had revealed a smaller fatigue crack at the root of another lap, again one close to 2 mm deep. Viewed on the surface the laps were approximately perpendicular to the maximum principal stress.

FORMULATION

Engine parts, such as a crankshaft, are subjected to very large numbers of cycles during service, so that once a crack starts to grow, fatigue failure is inevitable. The crankshaft failed after several hundred hours running, equivalent to roughly 10^7 cycles, that is about the knee of the S/N curve for the crankshaft. This suggested that the forging lap at which the fatigue failure originated was just severe enough to initiate crack growth under the actual stress in the fillet. The problem therefore resolved itself into determining whether or not the estimated stresses were sufficient to cause crack growth at the root of a forging lap 2 mm deep. The laps were crack-like in form so that a fracture mechanics approach was appropriate.

It is known [1] that a crack will not grow under a fatigue loading unless the range of opening mode stress intensity factor ΔK_I exceeds a threshold value ΔK_{Ic} . When a load cycle extends below zero, ΔK_I is conventionally calculated from only the tensile part of the load cycle. Relevant air threshold data which were available [2] are given in Table I. Lack of data for the crankshaft steel was felt to be unimportant because fatigue crack growth thresholds are largely independent [2] of a steel's tensile strength or composition; and ΔK_{Ic} was taken as $6.4 \text{ MN/m}^{3/2}$. The values of ΔK_{Ic} quoted in Table I were obtained as the fatigue limit of plates containing edge cracks between $\frac{1}{2}$ mm and 5 mm deep, but with ΔK_I rather than stress plotted against endurance in the S/N curve. They were therefore directly relevant to this type of problem. Certain precautions have to be taken [2] to obtain accurate results.

Table I Values of ΔK_{Ic} for Various Steels at Zero Mean Stress

Material	Tensile strength <u>MN/m²</u>	ΔK_{Ic} <u>MN/m^{3/2}</u>
Mild steel	430	6.4
Low alloy steel	680	6.3
18/8 authentic steel	665	6.0

ASSESSMENT

The expression for ΔK_I can be written in the general form:

$$\Delta K_I = \Delta \sigma (\pi a)^{1/2} \quad (1)$$

where $\Delta \sigma$ is the tensile range of applied stress across the crack,

a in this case is crack depth, and

α geometric correction factor of the order of one.

The forging laps were quite long compared with their depths, so α was taken as one, which is appropriate [1] for a semi-elliptical surface crack whose overall length is six times its depth. The laps were small compared with the fillet radius so β was obtained from the local stress [1]. Substituting the tensile stress range of 90 MN/m^2 and lap depth of 2 mm into equation (1) gave $\Delta K_I = 7.1 \text{ MN/m}^{3/2}$. This was somewhat (11 per cent) greater than the value of ΔK_{IC} , so it was clear that a forging lap only 2 mm deep was just sufficient to initiate fatigue crack growth. As with most loadings ΔK_I increased with crack size so that crack arrest could not occur, and as already stated, failure of the crankshaft was inevitable once crack growth started. The failure of the crankshaft after several hundred hours running, and the presence of a small fatigue crack at another forging lap, were therefore satisfactorily explained by means of a calculation based on the estimated stresses. Hence it was most unlikely that the premature failure was associated with any abnormal operating condition, such as a previously unsuspected resonance. Had residual stresses been present a different conclusion might well have been reached; residual stresses would alter the effective local stresses and hence ΔK_I .

At the time the calculation seemed to provide a sound basis for the explanation of the failure. With the benefit of hindsight it is possible to doubt the validity of this type of calculation, which inevitably involves various assumptions and approximations. Thus, for example, the assumption that the fatigue crack growth threshold is independent of steel type is only true to within engineering rather than scientific accuracy. No account was taken of the possible effect of the temperature, which must have been above ambient, or the oil environment, on the value of the threshold. In-air test results [3,4] show that moderately elevated temperatures have little or no effect on the threshold for various steels. Corrosive environments can have a dramatic effect on threshold behaviour; thresholds can be substantially reduced and frequency sensitivity introduced [4], and the knee in the S/N curve for a cracked specimen (or component) shifted to much longer endurance [5]. Fortunately, engine oil appears to be an inert environment for steels [4] so that the threshold is increased somewhat over the in-air value; for mild steel at zero mean stress, immersion in SAE 30 engine oil [6] increases ΔK_{IC} to $7.3 \text{ MN/m}^{3/2}$. This is very nearly the same as the calculated value of ΔK_I for the forging lap, and its use would perhaps have improved the quality of the failure analysis.

In failure analyses estimating the values of stress intensity factors for the usual irregularly shaped cracks is always a problem particularly when, as in the present case, the exact size and shape of the crack are unknown. Thus, a ten per cent error in the depth results in a five per cent error in the stress intensity factor. Making different, but still reasonable, assumptions about the shape of the crack can easily result in a ten per cent change. Similarly any error in stress level will result in a corresponding error in the stress intensity factor.

As already pointed out the forging laps were generally not perpendicular to

the surface. When this happens it is usual to estimate K_I by taking the resolved depth perpendicular to the surface. Comparison with numerical solutions, presented in graphical form, for inclined cracks [7], shows that this approach increasingly overestimates K_I as the angle of the crack to the perpendicular increases, but provided this angle does not exceed 30° the error is less than ten per cent. The edge sliding mode (mode II) displacements which appear for inclined cracks [7] are neglected by this approach, it being implicitly assumed that the value of K_I alone controls fatigue crack growth threshold behaviour. Available evidence [8] however indicates that this assumption can be unconservative if mode III displacements are also present. The complex situation is illustrated by Fig. 1, taken from Reference 4, which shows stress intensity factors for a crack growing from an initial crack inclined at 45° . As a general rule, fatigue cracks tend to grow such that only opening mode displacements are present, hence the radical change in stress intensity factors when crack growth starts.

CONCLUSIONS

The failure of the prototype engine crankshaft was due to a defect which would not be present in production engines, so no action was required. The analysis did, however, confirm the importance of using a forging schedule which would ensure correct grain flow in high stress regions, so that forging laps penetrating into the material would be avoided. The investigation introduced fracture mechanics techniques to a firm who were not previously aware of their utility.

ACKNOWLEDGEMENT

This paper is presented by permission of the Director, National Engineering Laboratory, Department of Industry. It is British Crown copyright.

REFERENCES

- 1 Pook, L. P., "Fracture mechanics - how it can help engineers", Trans. N. E. Coast Instn Engrs and Shipbuilders, v. 90, no 3, March 1974, 77-92.
- 2 Frost, N. E., Pook, L. P. and Denton, K., "A fracture mechanics analysis of fatigue crack growth data for various materials", Engineering fracture Mechanics, v. 3, no 2, August 1971, 109-126.
- 3 Pook, L. P. and Greenan, A. F., "Fatigue crack growth threshold for mild steel, a low alloy steel and a grey cast iron", National Engineering Laboratory, East Kilbride, Glasgow, NEL Report No 571, July 1974.
- 4 Pook, L. P. and Greenan, A. F., "Various aspects of the fatigue crack growth threshold for mild steel", International Conference on Fatigue Testing and Design, City University, London, April 1976, Society of Environmental Engineers Fatigue Group, v. 2, 30.1-30.33.

- 5 Pook, L. P., "Fracture mechanics analysis of the fatigue behaviour of welded joints", Welding Research International, v. 4, no 3, September 1974, 1-24.
- 6 Pook, L. P., "Fatigue crack growth data for various materials deduced from the lives of precracked plates", Stress Analysis and growth of cracks, ASTM STP 513, American Society for Testing and Materials, Philadelphia, Pa., 1972, 106-124.
- 7 Bowie, O. L., "Solutions of plane crack problems by mapping techniques", Sih G. C. (Ed) Methods of analysis and solutions of crack problems, Noordhoff, Groningen, 1973, 1-55.
- 8 Pook, L. P. and Greenan, A. F., "The Mode II fatigue crack growth threshold in mild steel", NEL Report, In preparation.

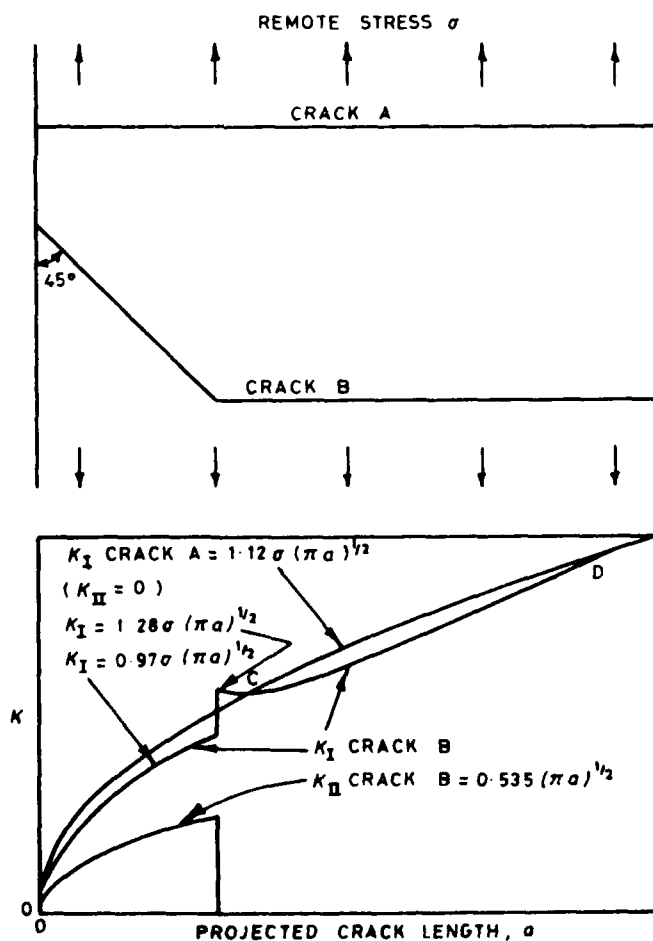


Figure 1 Stress Intensity Factors For Straight and Branched Short Edge Cracks

FRACTURE MECHANICS ANALYSIS OF STEEL
PIPE WELDS FOR STEAM TURBINES

L. K. L. Tu* and B. B. Seth

Advanced Engineer and Manager
Materials Engineering, Steam Turbine Division
Westinghouse Electric Corp., Phila., PA. 19113

INTRODUCTION

There were five types of shop welds used in the cross-around piping carrying steam from the high pressure turbine to the moisture separation reheaters (MSR) and from the MSR to the low pressure turbines. They were standard girth weld in straight sections of pipes, the girth weld attachment to a valve or ring, the true miter joint weld, the longitudinal seam weld, the attachment weld between pipe and turning vane assembly elliptical girders. Typical configuration of the crossaround pipes and welds are shown in Fig. 1. The longitudinal seam welds were made by automatic process and the other four types were welded by a manual shield metal arc welding process. The girth welds connecting carbon steel pipes were AWS E7018 and E70-1 carbon steels. Stainless steel E309 welds were used for joining 410 stainless steel turning vane to carbon steel pipes equivalent to ASTM A515 GR 65. The mechanical properties of these welds are given in Table I. Weld joints were visually inspected as well as magnetic particle and radiographically examined. Several types of defects were discovered in E309 stainless steel welds and carbon steel welds. The flaws were categorized into following five groups:

- a) spherical inclusion or void
- b) circular inclusion or void of elliptical cross section
- c) long elliptical slag line or lack of fusion line
- d) long surface groove, weld undercut and lack of penetration
- e) weld buildup or protrusion. The observed defect sizes and minimum radius of the defects in welds as revealed by X-ray films are summarized in Table II.

Since no standard ANSI or API standard could strictly be applied to this case, the safety as well as the need for any repair work of these defect containing welds were evaluated using ASME pressure vessel code fatigue design curve and fracture mechanics analysis employing the non-destructive test results, applied stresses and materials properties of the welds. The stress analysis included a combination of thermal expansion, dead weight, and local stress effects due to the presence of defects.

*Now with Exxon Production Research, Houston, TX

FORMULATION

A. Cyclic Life Evaluation According to ASME Pressure Vessel Code

Assume no crack propagation, the cyclic lives of various defect containing welds were obtained from ASME Pressure Vessel Code Section VIII, Division 2 fatigue design curve, Fig. 2. The effective stress concentration factor for cyclic loading (K_f) is:

$$K_f = q(K_t - 1) + 1 \quad (1)$$

where K_t = theoretical elastic stress concentration factor
 q = notch sensitivity factor.

According to minimum radii of the defects in welds detected by nondestructive inspection, the effective stress concentration factors K_f for various kinds of defects in stainless steel and carbon steel welds are given in Table II.

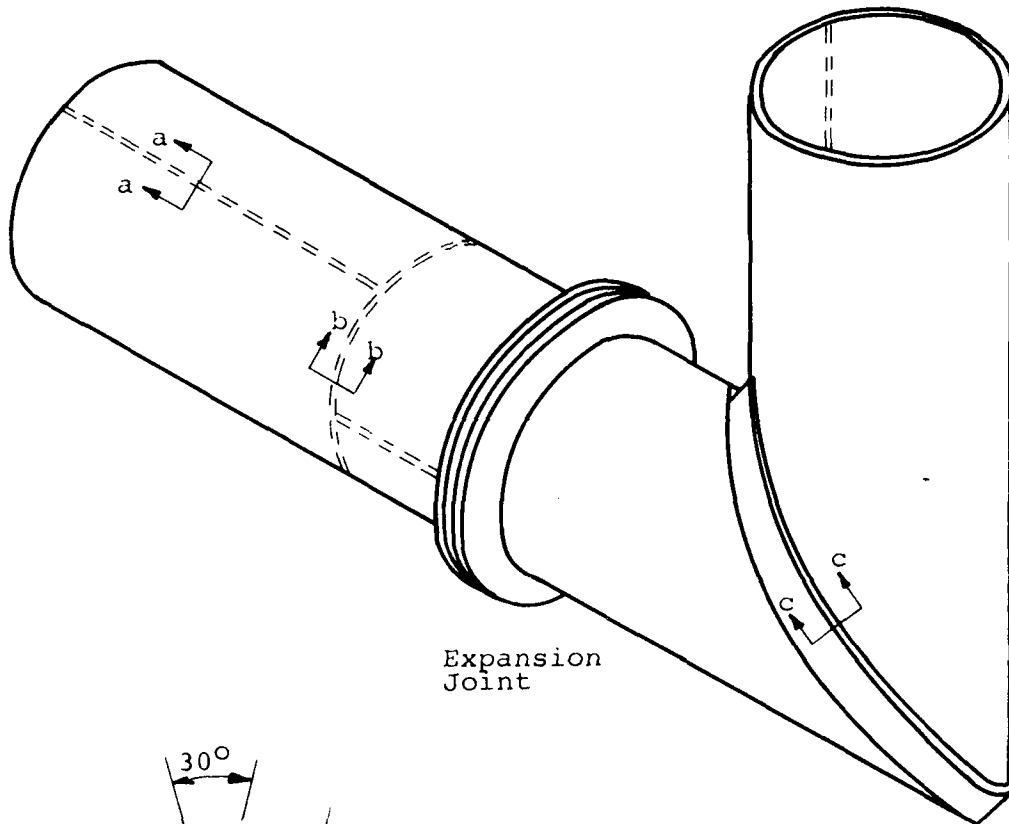
B. Static Fracture Mechanics Analysis

In the absence of any available test data, fracture toughness values of the welds were conservatively estimated from impact test data. The room temperature Charpy V-notch impact energy was $CVN \approx 90$ ft-lb obtained from literature [1, 2]. Fracture toughness value was estimated as follows: [3, 4]

$$\text{Upper shelf, } K_{IC} = \frac{\sigma_y}{115} \sqrt{5 (CVN / \sigma_y - 0.05)} \quad (2)$$

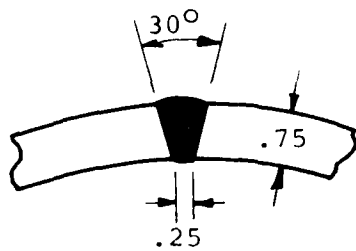
$$\text{Transition region, } K_{IC} = \sqrt{2E(CVN)^{3/2}} \approx 206 \text{ ksi-in}^{1/2} \quad (3)$$

Using $E = 25 \times 10^6$ psi at the maximum operating temperature of 373°F and $\sigma_y = 30$ ksi, it was found conservatively, $K_{IC} = 115 \text{ ksi-in}^{1/2}$. Although this approach is not strictly applicable to such ductile austenitic stainless steel, as it has been shown later the brittle fracture is not of concern, and therefore the great accuracy in estimating K_{IC} is not essential.

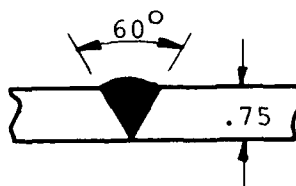


Expansion
Joint

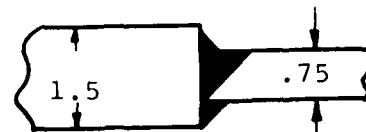
Turning
Vane



Section a-a



Section b-b



Section c-c

Fig.1 Typical Crossaround Pipe Assembly.

The critical flaw size for brittle fracture was calculated from [5] :

$$(a_{cr})_B = (1/M) (K_{IC} / \sigma_{max})^2 \quad (4)$$

for the assumed surface and internal cracks, Fig. 3.

where M = component geometry and flaw shape parameter

$$M = 1.21 \pi / Q \text{ (surface crack)}$$

$$M = \pi / Q \text{ (internal crack)}$$

$$Q = 1$$

C. Cyclic Fracture Mechanics Analysis

Assume in the worst case, all the defects presented were surface and internal cracks. The amount of crack growth in 10^4 cycles was calculated as follows:

Using an empirical fatigue crack growth rate equation [6]

$$da/dN = C_0 (\Delta K)^n \quad (5)$$

$$\text{and } \Delta K = \Delta \sigma (Ma)^{1/2}$$

the number of cycles for an initial crack to grow into a critical size was obtained by integration of equation (5).

Since $a/2c$ ratio is approximately the same during crack growth, it is reasonable to assume a constant M in the integration of the above equation.

Thus,

$$N = \frac{2}{(n-2) C_0 M^{n/2} \Delta \sigma^n} \left(a_i^{(2-n)/2} - a_{cr}^{(2-n)/2} \right), \quad n \neq 2 \quad (6)$$

$$\text{or } a_f = \left(a_i^{(2-n)/2} - N (n-2) C_0 M^{n/2} \Delta \sigma^{n/2} \right)^{2/(2-n)}, \quad n \neq 2$$

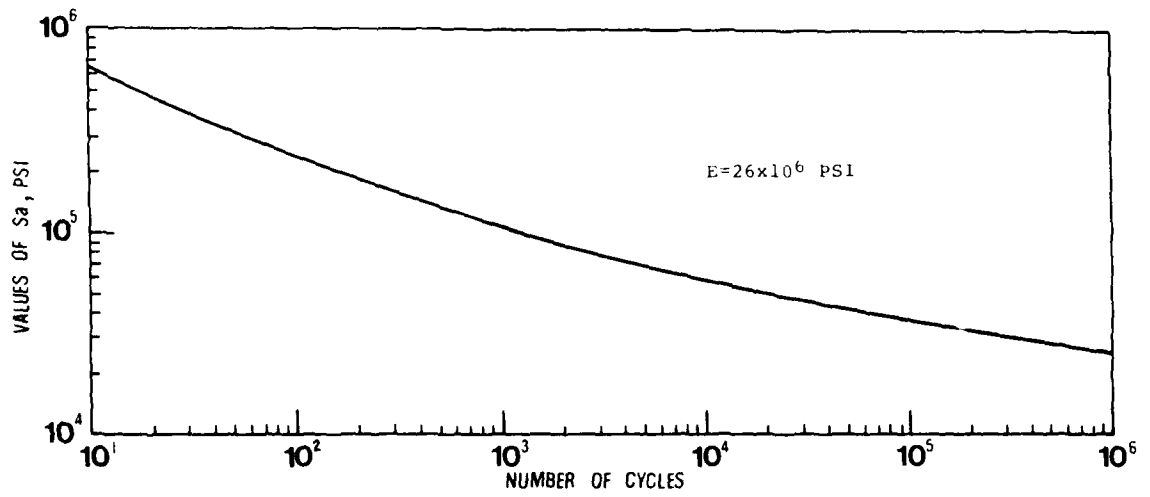


FIG. 2 DESIGN FATIGUE CURVE FOR SERIES 3XX HIGH-ALLOY STEELS, NICKEL-CHROMIUM IRON ALLOY, NICKEL-IRON-CHROMIUM ALLOY, AND NICKEL-COPPER ALLOY FOR TEMPERATURES NOT EXCEEDING 800 F

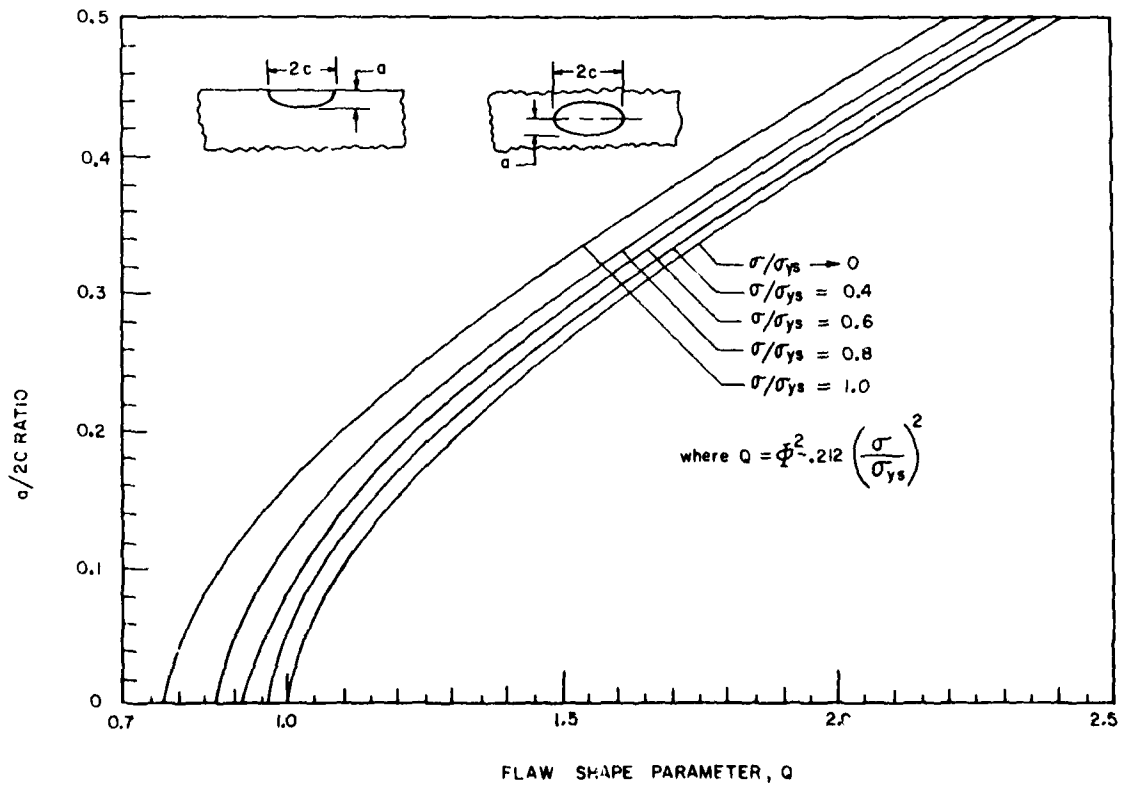


FIGURE 3 FLAW SHAPE PARAMETER CURVES FOR SURFACE AND INTERNAL CRACKS

where N = number of cycles for an initial crack to grow into a critical size.

n = slope of $\log da/dN$ vs. $\log \Delta K$ curve

C_0 = intercept constant

$\Delta\sigma$ = applied cyclic stress range

a_i = initial crack size

a_f = final crack size

ASSESSMENT

A. Cyclic Life Evaluation According to ASME Pressure Vessel Code

The cyclic lives of the stainless steel welds containing five types of flaws were calculated from the fatigue design curve, Fig. 2 and Table II.

a) spherical inclusion or void:

Since $\sigma_1 = 12.2$ ksi in axial direction and $k_f = 2$ from Fig. 2, we found $N_1 = 1 \times 10^6$ cycles.

Also, $\sigma_\theta = 17.9$ ksi in tangential direction and $k_f = 2$, from Fig. 2, we found $N_\theta = 1 \times 10^5$ cycles.

Similarly, lives for various other cases were calculated below:

b) circular inclusion or void of elliptical cross section:

$$N_1 = 60,000 \text{ cycles}, N_\theta = 10,000 \text{ cycles}$$

c) long elliptical slag line or lack of fusion line:

$$N_1 = 1.1 \times 10^4 \text{ cycles}$$

d) long surface groove, weld undercut and lack of penetration:

$$N_1 = 1.1 \times 10^5 \text{ cycles}$$

e) weld buildup or buildup and undercut:

$$N_1 > 10^6 \text{ cycles}$$

Hence, according to ASME Pressure Vessel Code, the E309 stain-

less steel welds are safe for the designed life (10^4 cycles) even with the presence of various kinds of welding defects. Similarly, the cyclic lives thus obtained for carbon steel welds are much longer than designed life and can be safely used.

B. Static Fracture Mechanics Analysis

Using the ASME Code procedure of multiplying the stress by a 2x to obtain the alternating stress resulted in a conservative stress of 35.8 ksi. This was the maximum applied stress employed in the calculation.

According to equation (4), it was found that $(a_{cr})_B = 2.71$ in. for surface crack and $(a_{cr})_B = 3.28$ in. for internal crack. The brittle fracture critical crack sizes in all cases were greater than the weld thickness (0.75 in.). Therefore, brittle fracture was impossible in the temperature range considered. The critical flaw size for ductile rupture, $(a_{cr})_D$, was obtained as follows:

Assume the crack propagates to $(a_{cr})_D$, the remaining weld thickness is t ,

$$\text{weld thickness} = 0.75 \text{ in.} = (a_{cr})_D + t$$

t is obtained by requiring that the stress on weld does not exceed the tensile strength. Using a minimum tensile strength of 75 ksi,

hence, $t = 0.358$ in.

and critical flaw size for ductile rupture was $(a_{cr})_D = 0.392$ in.

C. Cyclic Fracture Mechanics Analysis

(a) For a surface crack with $a_i = 0.100$ in.

Even though the actual indications were small, analysis was made assuming that the welds contain surface cracks with $a_i = 0.1$ in., $a_i/2c_i = 0.1$ and internal cracks with $2a_i = 0.2$ in., $a_i/2c_i = 0.1$. A conservative upperbound fatigue crack growth rate data for austenitic stainless steel [7] showed that $C_0 = 3 \times 10^{-10}$ and $n = 3.25$.

The number of cycles (N_0 , N_1) for a given crack to grow into a ductile fracture critical size $(a_{cr})_D$ in tangential and axial directions, and the final crack size

$[(a_f)_0, (a_f)_1]$ after 10^4 cycles of loading were calculated as follows:

i) surface crack

$$\begin{aligned} N_{\theta} &= 1.3 \times 10^5 \text{ cycles} & N_1 &= 4.7 \times 10^5 \text{ cycles} \\ (a_f)_{\theta} &= 0.107 \text{ in.}, & (a_f)_1 &= 0.102 \text{ in.} \end{aligned}$$

ii) internal crack

$$\begin{aligned} N_{\theta} &= 1.07 \times 10^5 \text{ cycles}, & N_1 &= 3.9 \times 10^5 \text{ cycles} \\ (a_f)_{\theta} &= 0.105 \text{ in.} & (a_f)_1 &= 0.101 \text{ in.} \end{aligned}$$

(b) For a surface crack with $a_i=0.25$ in.

$$\begin{aligned} N_{\theta} &= 3.1 \times 10^4 \text{ cycles}, & N_1 &= 1.14 \times 10^5 \text{ cycles} \\ (a_f)_{\theta} &= 0.285 \text{ in.} & (a_f)_1 &= 0.259 \text{ in.} \end{aligned}$$

Thus, if the initial crack is $a_i=0.1$ in., it will take larger than designed number of cycles to propagate it into a critical size; and less than 0.007 in. of maximum crack growth will occur in 10^4 cycles in axial and tangential directions. Even if the initial surface crack is 0.25 in., it will take larger than designed life to grow into critical crack size; and less than 0.035 in. of crack growth will occur in both axial and tangential directions under 10^4 cycles of loading. Carbon steel welds similarly showed adequate safety feature in the calculation.

CONCLUSIONS

A fracture mechanics analysis was performed for steam pipe welds containing nondestructively detected flaws. Both ASME Pressure Vessel Code fatigue design curve approach assuming no crack growth and fracture mechanics approach treating all the flaws as cracks were employed in the analysis. It was concluded that all the welds were safe for the designed life. Practical welds containing flaws with reasonable sizes and shapes can be safely used so long as careful analytical and experimental fracture mechanics evaluation has been conducted. The importance of the fracture mechanics analysis in the safety and economical evaluation of the welds has been demonstrated.

REFERENCES

1. Cr-Ni Stainless Steel Data, The International Nickel Co., Inc., Bulletin A, 1963.
2. ASM Metal Handbook, v. 1, 8th ed., 1961, 420.

5. Weld buildup or protrusion

r=	0.03 in.	0.03 in.
h=	0.75 in.	0.75 in.
K _f =	1.7	1.6

where r=minimum radius of defects in welds
t=circle of radius of elliptical inclusion
c=1/2 of major diameter of ellipse
h=weld buildup width

EXPLOSION OF AN AMMONIA PRESSURE VESSEL

A. R. Rosenfield
Metal Science Section
Battelle
Columbus Laboratories
Columbus, Ohio 43201

and

C. N. Reid
Faculty of Technology
Open University
Milton Keynes, MK7 6AA
United Kingdom

INTRODUCTION

Production of ammonia for the manufacture of fertilizers involves reaction of nitrogen and hydrogen at high pressures and slightly elevated temperatures ($\sim 120^{\circ}\text{C}$). The steel reaction vessel discussed in this paper exploded shortly before Christmas, 1965, during hydrostatic testing prior to being shipped to the chemical plant. Figure 1 shows that the damage to the vessel was extensive. The less obvious economic costs do not show up in the photograph. It is estimated that the cost of the failure (mainly from lost production due to the plant standing idle) was several million dollars. The vessel would cost about $\$4 \times 10^5$ today, about half of this sum being the cost of the steel plates from which it was fabricated. Thus, while material costs are not negligible, they play a minor role in the economics.

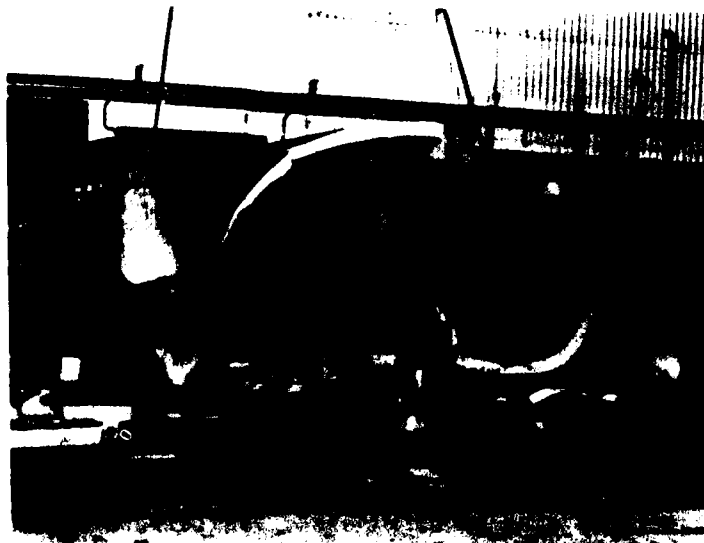


Figure 1. The Failed Vessel

The failure investigation had three main goals:

- (1) To determine whether the vessel could be repaired, and, if so, how,

- (2) To assess liability, and
- (3) To ascertain whether vessels already in service require modification.

The investigation was carried out by the British Welding Research Association (now the Welding Institute), who issued a full report [1]. A shorter report appeared in this country [2]. Starting in 1976, the Open University course, "Materials Under Stress", has used this failure to illustrate the use of fracture mechanics in engineering. This paper draws heavily upon the resultant text [3] which contains newer material and employs the case study format. A principal modification was the addition of fracture mechanics to the previous BWRA analysis. In fact, successful conclusion of the actual investigation involved more conventional tests, such as the Charpy. We have chosen to treat the investigation as it would have been carried out if the failure had occurred more recently, and the use of fracture mechanics had been included in the natural course of events.

Construction was by conventional techniques involving building up cylindrical sections by joining curved plates together with longitudinal electroslag welds. In turn, the cylinders were joined circumferentially by submerged arc welding. The end sections were forgings which were also joined to the remainder of the vessel by submerged arc welding (Figure 2). To minimize residual stress, preheat was used and the vessel was post-weld stress relieved at a nominal temperature of 650°C for six hours.

Fortunately the vessel failed during hydrostatic testing with no loss of life or serious injury. Under service conditions, with gas as the pressurizing medium, the damage would likely have been considerably more extensive [3]. By coincidence, the fracture occurred within 2% of the intended operating pressure, although the test was planned to run up to a level almost 40% higher. Furthermore, the visible damage seen in Figure 1 extended only along about one-third of the length. Thus, repair with replacement of the damaged forging and plates was a realistic consideration.

FORMULATION

Since the failure pressure was close to the design pressure an overload mechanism (plastic collapse) was out of the question (assuming that no error had been made in the design calculations). Neither would stress-corrosion be a reasonable hypothesis for a new vessel being tested under controlled conditions. Fatigue could also be eliminated. While References [1] and [3] show that a few load cycles had occurred, the severity of the strain reversals were quite modest. By the process of elimination, brittle (low stress) fracture must have occurred.

Under these circumstances, two kinds of deficiencies need to be sought out: physical defects, such as pre-existing cracks, and material deficiencies associated with low toughness. The combination of flaws and material leads to failure according to the well-known relations of fracture

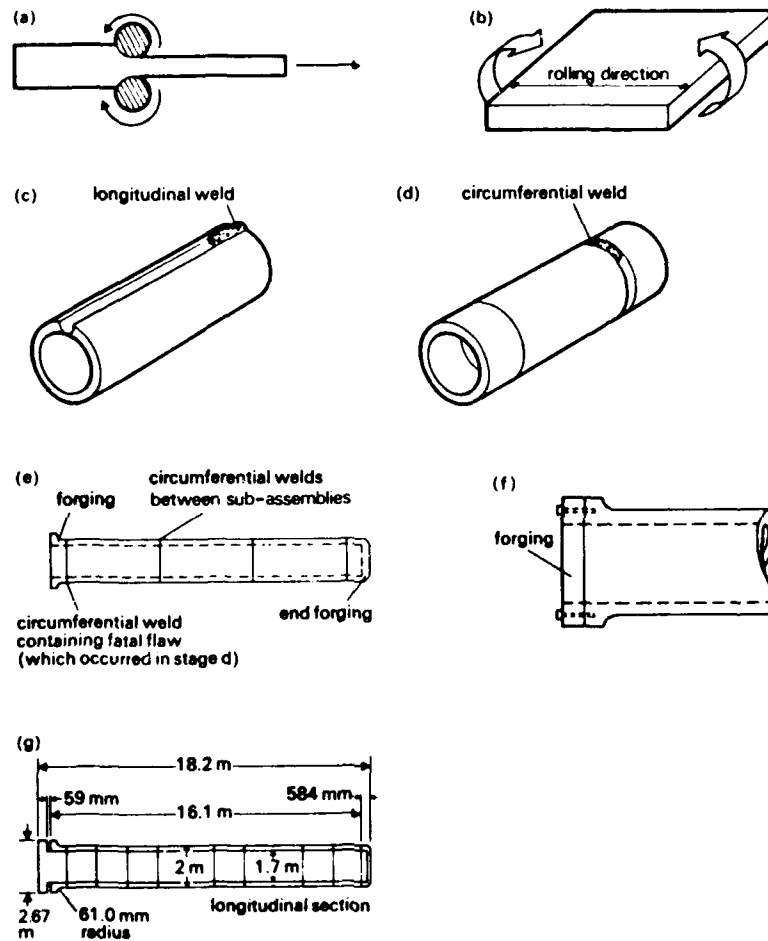


Figure 2. Fabrication Processes Used to Make the Vessel

- (a) Plate rolling
- (b) Plates bent to the proper curvature
- (c) Cylinders welded together from bent plates
- (d) Cylinders welded together to form sub-assemblies
- (e) Sub-assemblies welded together
- (f) End-cap bolted on
- (g) The completed vessel

mechanics. Assuming that the wall of a pressurized vessel acts as a center-cracked panel under uniaxial tension, failure will occur when

$$K_{Ic} \leq \psi \sigma \sqrt{\pi a_{eff}} \quad (1)$$

where ψ is a shape factor, σ is the nominal stress acting perpendicular to the crack, and a_{eff} is the effective value of crack length. In the case of this welded pressure vessel, both σ and a_{eff} have to be evaluated carefully:

- (1) The assigned value of stress must include applied stress plus any residual stress. In the case of the vessel in question it can be easily shown that the applied stress is close to the hoop stress for a thin-walled vessel whose radius is the mean radius of the actual vessel [3]. There is also a possible contribution due to discontinuities such as nozzles and ports, but examination showed that the origin of the failure was too far away from any such features to be of consequence. Residual stresses pose an even more difficult problem since their magnitude is not known. In developing the case study we assumed, along with Dawes [4], that the safest course was to set them equal to the yield stress of the base metal, σ_y (at the actual stress relieving temperature) for those instances where welds are not properly stress relieved. Realizing that this may be the most tenuous part of the analysis, we assume that

$$\sigma = \frac{PR}{t} + \sigma_{yB} \quad (2)$$

where P = pressure, R = mean radius, t = wall thickness, and σ_{yB} is the yield stress of the base plate at the stress relieving temperature.

- (2) The effective crack length will be equal to the actual crack length provided the local stress is a small fraction of the yield stress at the test temperature. When the local stress is a large fraction of the yield stress there are several ways of handling the problem. One can use Irwin's [5] approach and consider that the crack responds as if its length were larger by an increment equal to the plastic zone size. Alternatively, one could assume that the material obeys a critical crack-tip-opening displacement fracture criterion. In this case it is easily shown the resultant equations provide similar values to those obtained from the Irwin assumption. In either event the following relation gives an adequate description of the effect of crack tip plasticity on the failure criterion:

$$a_{\text{eff}} = a \left[1 + \left(\frac{\pi \sigma}{4 \sigma_y} \right)^2 \right] \quad (3)$$

When Equations (1), (2), and (3) are combined the failure pressure can be calculated.

The above equations show that the data required are the mechanical properties of the steels used, K_{IC} and σ_y , plus the size, shape, and location of the critical flaw, ψ and a . Table 1 provides the necessary strength and toughness as well as the steel composition. Note that both the base plate and the weld metal exceed specifications as to strength and that there is no required toughness level. At the time that the vessel was constructed, a "no-cracks" philosophy was current: Since no crack would be allowed it was unnecessary to insure that the steel had a particular fracture toughness. Since then the tendency has been to recognize that some small cracks will likely remain undetected and that materials should have a minimum toughness level to guard against them. While, in hindsight, the earlier approach would appear to be foolhardy, it must be remembered that pressure vessel failures have been quite rare for a number of years and that procedures such as stress-relieving of welds lend assurance that the toughness is sufficiently high. Some further assurance was required that the welds were sufficiently tough and this was done by making simulated production welds to qualify the procedure. Table 2 lists the results of this preliminary test and it is seen that the minimum Charpy energy is surpassed along the traverse.

The design parameters for the vessel are given in Table 3. It is interesting to reflect that the size is not far from that of the passenger compartment on a commercial airliner and that the stored compression energy of the gas is sufficient to propel the vessel vertically to respectable cruising altitude.

ASSESSMENT

As recreated in the Open University text [3], the failure analysis assembled information on all of the parameters of Equations (1) - (3). The first step was to locate the failure origin. Figure 3 shows a map of the break with two origins indicated. It was not a difficult matter to locate them by tracing chevron markings. A point of great importance is that both origins were associated with the weld indicated in Figure 2. Closer examination showed that these origins were within the heat affected-zone on the forging side of the weld and consisted of tiny pre-existing buried cracks. Figure 4 is a profile of such a crack which did not propagate. Although the origins were irregularly shaped as seen in Figure 5, for purposes of calculation they were taken to be circles of 8 mm diameter, for which the shape factor, $\psi = 2/\pi$. Note also that such a crack will escape detection by even the most sophisticated NDI procedures.

Table I Properties of the ammonia pressure vessel steels^a
 (a) CHEMICAL COMPOSITION (the figures give the weight %, the balance being Fe)

	C	Si	S	P	Mn	Ni	Cr	Mo	Cu	V
Plate	Specification	0.17	0.30	0.05	0.05	1.50	0.30	0.70	0.28	0.10
	Maximum from failed vessel	0.15	0.22	0.023	0.025	1.31	0.14	0.64	0.27	0.08
Forging	Specification	0.17	0.30	0.04	0.035	1.50	0.30	0.70	0.28	0.10
	Maximum from failed vessel	0.20	0.27	0.008	0.009	1.48	0.22	0.83	0.29	0.09
Weld Deposit	From failed vessel	0.08	0.31	0.020	0.025	1.05	0.12	1.34	0.83	0.010

(b) MECHANICAL PROPERTIES

	Yield strength at design temperature (393 K)/ Nmm^{-2}	Yield strength at room temperature/ Nmm^{-2}	Tensile strength at room temperature/ Nmm^{-2}	$K_{Ic}/\text{Nmm}^{-3/2}$ at room temperature
Plate	--	411	597	120
Forging	--	389	601	110
Weld	--	761	851	58
Minimum specified value	348	370	556	--

^a Based on data in References [1] and [3].

Table 2 Mechanical properties of simulated production welds*

	1	2	3	4	5	6	7	Specified
	Centre	HAZ	Midway	Centre	HAZ	Midway	HAZ	impact
	of weld		position	of weld		position		energy
Energy absorbed in Charpy test at 219 K / J	40	64	40	43	131	40	91	34

*Data from Reference [1].

Table 3. Geometry and Operating Pressure

Inner Diameter, D_1	=	1.70 m
Wall Thickness, t	=	0.149 m
Inner Length	=	16.7 m
Operating Pressure	=	35 MNm^{-2}

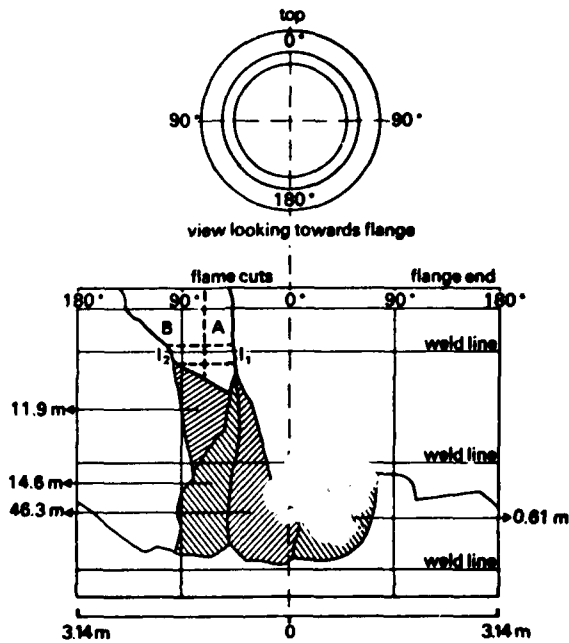


Figure 3. A Map of the Fracture Paths in the Vessel; the Shaded Fragments were Hurlled to the Distances Shown

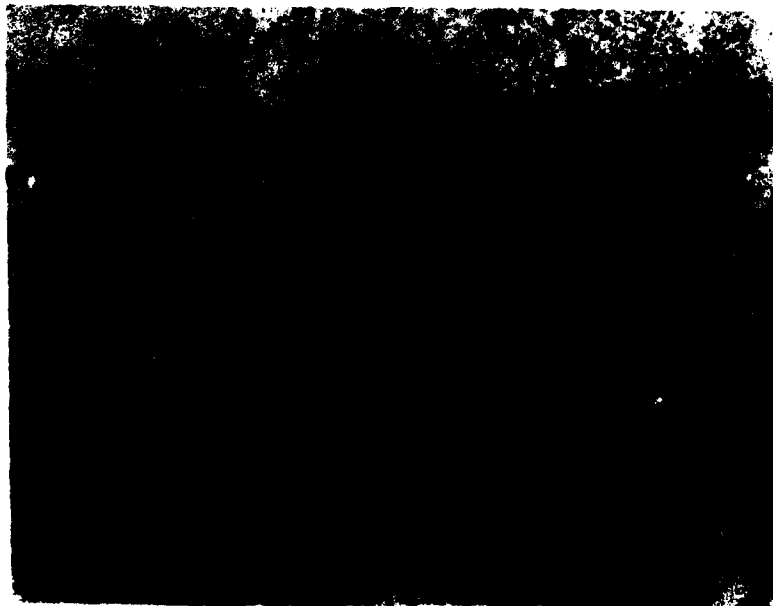


Figure 4. A Welding Crack in the HAZ of the Forging

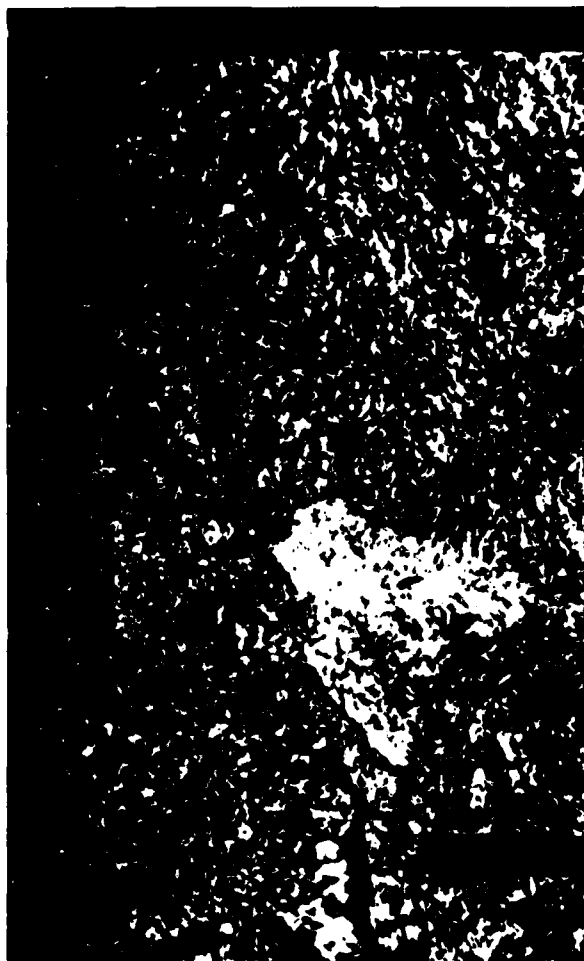


Figure 5. Flat Facet at the Origin I_1
(See Figure 3 for map.)

Attention then turned to the metallurgical conditions of the forging HAZ. A microhardness traverse showed that the location was considerably harder than either the base plate or the weldment (VHN \approx 430). When pieces were taken from it and tempered for two hours at various temperatures it was found that softening began at \sim 600°C. Clearly this location had not experienced the 650°C/6 hr. temperature/time combination it was supposed to have received during stress relief. This failure to stress relieve also led to low toughness as shown by the Charpy data of Figure 6. It was thus determined that there was an uneven temperature distribution within the stress relieving furnace and that the origin location was indeed cooler than required.

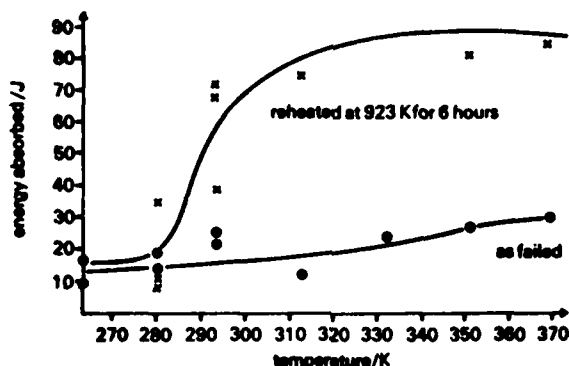


Figure 6. Results of Charpy Tests on the Weld Metal of the Failed Vessel

Having demonstrated that the HAZ was brittle, it remained to be determined whether the conditions were appropriate to trigger a low-stress fracture. There are several ways in which this might be done. We have chosen to calculate whether the test pressure was sufficiently high to grow the pre-existing cracks. The input data are summarized in Table 4. Equations (1) and (3) combine to give a 'predicted' failure stress:

$$\sigma = \frac{4\sigma_y}{\pi} \left(1 + \frac{\pi^3 K_{Ic}^2}{16 \sigma_y^2 a} \right)^{1/2} \quad (4)$$

whence $\sigma = 669 \text{ MNm}^{-2}$. From Equation (2), this converts to an expected failure pressure of 45 MNm^{-2} , about 30% above the actual value. Accordingly, the detailed treatment is consistent with failure occurring during hydrostatic testing although at a considerably higher pressure than the actual value.

There are several interesting points with regard to this calculation. Above, all, it is disturbing that the result is non-conservative. The most

Table 4. Evaluation of Fracture Mechanics Parameters

K_{Ic}	=	$58 \text{ MNm}^{-3/2}$
ψ	=	$2/\pi$
a	=	$4 \times 10^{-3} \text{ m}$
σ_y (forging)	=	761 MNm^{-2}
σ_{yB} (base metal)	=	389 MNm^{-2}

likely source of error is in the shape factor; the value for a circle is doubtless different from that of the actual crack. Secondly, the toughness level would have to be very high in order for critical cracks to be inspectible by routine NDI methods. Finally, it emphasizes the effect of residual stress which, in this case, is considerably larger than the applied stress.

CONCLUSIONS

Since the failure was limited to one end of the vessel and since examination showed that the remainder had not suffered damage, it was rebuilt. The vessel was finally put into service in 1968 and was still in regular use eight years later. Probably the major lesson learned is that the rules for pressure vessel construction assure safety provided they are adhered to strictly. However, even a very small deviation (in this case a local cool spot in the stress relieving furnace) has the potential of causing great damage. Because of the energy stored in such a structure the consequences can be serious. However, the requirement of pre-testing at elevated pressures is a major safety valve. Had the ammonia vessel not been pretested, the accident would have been many times more serious.

ACKNOWLEDGMENTS

ARR is grateful to Battelle Memorial Institute and to Battelle's Columbus Laboratories for having provided sabbatical leave at Open University in the summer of 1974. Special gratitude is offered to our fellow members of the Open University T351 course team.

REFERENCES

- [1] Anon., "Brittle Fracture of a Thick-Walled Pressure Vessel", British Welding Research Assn. Bull., 7 [6] (1966).
- [2] Clark, W. D., and Mantle, K. G., "Brittle Fracture of Ammonia Converter", paper presented at AIChE Fall Meeting (1966).
- [3] T351 Course Team, "The Stability of Cracks", Materials Under Stress, Units 5A-7A, Open University Press, Milton Keynes, U.K. (1976).
- [4] Dawes, M. G., "Fracture Control in High Yield Strength Weldments", Weld. Research, 39, 369s (1974).
- [5] Irwin, G. R., "Plastic Zone Near a Crack and Fracture Toughness", Proc. 7th Sagamore Ordnance Materials Research Conf. (1961).

APPLICATION OF FRACTURE MECHANICS
TO WELDED STRUCTURES DESIGN*

BY

D. A. Bolstad - Martin Marietta Corporation, New Orleans, La.
L. W. Loechel - Martin Marietta Corporation, New Orleans, La.

INTRODUCTION

This case describes the manner in which fracture control methods were used in the design, fabrication and test of the External Tank (ET) portion of the Space Shuttle Program. The ET is composed of two propellant tanks; a hydrogen tank and an oxygen tank which are joined together by an intertank section to form one element 154 feet long by 27.6 feet in diameter. Figure 1 is a sketch of the ET showing its main features. The ET is used to contain the liquid oxygen and hydrogen propellants used by the Space Shuttle Orbiter during ascent and serves as the structural backbone joining the Orbiter and Solid Rocket Boosters. This paper is limited to a discussion of the fracture control approach for the welded pressure vessels.

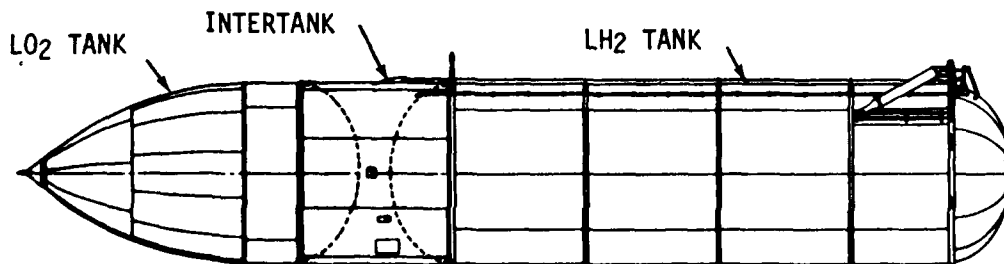


FIGURE 1 - THE EXTERNAL TANK

The liquid oxygen and hydrogen tanks are fabricated from 2219-T87 aluminum alloy sheet and plate with some 2219-T62 forgings and 2219-T8511 extrusions being used. 2219 was selected as the ET material because of its weldability, toughness, and good cryogenic properties. During launch the ET supports the Orbiter and Solid Rocket Boosters at attach points on the tank exterior. The ET must then absorb both the thrust loads from the Orbiter and the Solid Rocket Booster and, the internal pressure stresses of the tanks themselves.

* Work sponsored by the NASA, Marshall Space Flight Center, Alabama, under Contract No. NAS8-30300

Historical Background

For the ET program it was required that a Fracture Control Plan (FCP) be developed to define the manner in which fracture mechanics principles would be used in design, fabrication and testing of the ET. The constraints we considered to be appropriate in developing such a plan included the following.

Flight Reliability - The most important consideration in developing an FCP was to provide a positive demonstration of flight reliability. This was to be accomplished by a combination of proof test logic and non-destructive evaluation (NDE) techniques.

Low Cost - The manner in which fracture mechanics could contribute to low program cost lies basically in preventing proof test failures while maintaining the minimum NDE required to prevent such failures. Also it was envisioned that significant savings could result if the number of weld repairs required in the approximately 3,000 feet of ET welds could be minimized. Ambient temperature proof tests (GN₂ for the LH₂ tank and inhibited H₂O for the LO₂ tank) were selected to avoid costs.

Technical Background

The operational requirement for the ET is that it survive 1 flight with a scatter factor of 4. Operating and proof test environments include: liquid hydrogen, liquid oxygen, GN₂ and inhibited water; and temperatures ranging from -423°F to +150°F. A typical flight pressure profile is shown in Figure 2. In addition the tank sees external loads which include contributions from the other Shuttle elements and dynamically induced loads from engine noise, sloshing of the propellant, etc.

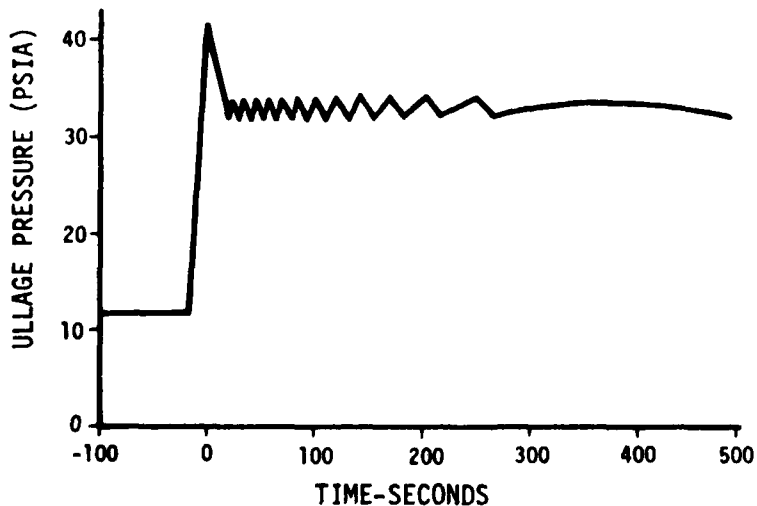


FIGURE 2 - FLIGHT PRESSURE PROFILE FOR THE ET

While earlier space programs had generated considerable fracture data on 2219 there was almost no data available for welds at cryogenic temperatures. A good deal of fracture data did exist in the literature for parent metal over the temperature range of interest and for welds at ambient temperature. Another variable recognized in the existing 2219 weld data was that the weld parameters varied from test to test and so no concrete conclusions could be reached regarding toughness and life behavior for the ET.

FORMULATION

From the previous section it can be deduced that three mechanisms of failure could be possible.

Static Overload - A failure could occur in proof test if a large enough flaw existed in the structure prior to proof test. Furthermore, failure could also occur in flight if proper screening of flaws was not achieved by the proof test and NDE.

Sustained Load - This mechanism of slow flaw growth under load was also possible both during proof test, storage, and flight if times above the slow-growth threshold were not controlled.

Cyclic - Once the tanks are proof tested, then they must be shown good for all the necessary leak checks, tankings, and flight conditions with a scatter factor of 4.

Additionally to reduce proof test failure risks, a program decision was made to design the ET weld land thicknesses so that a leak mode was to occur at proof in lieu of a burst mode. Technically this meant that the critical flaw depth exceeded weld land thickness at proof stresses and risk of failure during proof would be reduced.

Another important factor was that the design of the ET and the fracture control effort (both management and test) were starting at the same time. There was no luxury of having 2 years of test before the first draftsman drew his lines. Data trends had to be established early in the program, so as to have no impact on design that could adversely affect schedule and cost.

Empirical Approach

Since the ET was to be fabricated from 2219 aluminum which is very tough, it was recognized that expressions relating fracture strength to flaw size would be difficult to obtain and subject to criticism as would any calculation of a toughness value (K_{IC} , K_Q , etc.). Therefore, it was decided that a semi-empirical approach to the problem would be best. That approach was to generate specimens at the production facility with production welders, use production weld schedules, specimen thicknesses equivalent to tank wall thicknesses, test temperatures the same as flight temperatures, and to

determine critical flaws at the anticipated proof and flight stresses. The resulting curves of flaw size as a function of fracture strength were then used for design and analysis.

Test Program

Table I is a matrix of the tests that were run to verify that the ET met the specification requirements. A detailed description of the test program is presented in reference {1}. A brief summary of the specimens tested is as follows:

- 1) material was 2219-T87 per QQ-A-250/30;
- 2) semi-elliptical surface flaws with $a/2c = 0.20$ and 0.50 ;
- 3) flaws introduced by EDM or slitting saws and extended by low-stress high-cycle fatigue;
- 4) flaws in welded specimens were along the weld centerline and specimens were tested in the as-welded condition;
- 5) flaws in parent metal were parallel to long transverse direction;
- 6) specimen width for all temperatures except LH2 was 3.90 inches;
- 7) specimen widths for LH2 tests were 1.75 inch (0.125 thick), 3.00 inch (0.140 and 0.188 inch thicknesses), and 5.75 inch (0.375 inch thick);

TABLE I 2219-T87 TEST MATRIX

THICK (IN.)	CONDITION	+350°F	+250°F	RT	-320°F	-423°F
0.125	PARENT WELD	F F	F F	F,C F,C	F,C F,C	C
0.140	PARENT	F	F	F,C	F,C	F,C
0.188	PARENT WELD	F	F	F,C F,S	F,C F	C F
0.250	PARENT WELD	F	F	F F,C	F F,C	
0.375	PARENT WELD REPAIR WELD	F	F	F,C F,C,S F,C	F,C F,C F,C	F,C F,C F,C
0.500	WELD			F,C	F,C	
0.750	WELD			F,S		
1.00	WELD			F		

KEY: F = fracture test, C = cyclic test, S = sustained load test

- 8) for thicknesses to 0.500 inch, the welds were made with two passes - one penetration pass without filler wire and a second pass with 2319 filler wire using automatic DC GTA welding techniques. Multiple passes with 2319 were used for thicker welds.

Fracture Tests

All the fracture test specimens (except LH2) were tested in a 100 Kip load-capacity servo-hydraulic tensile machine. The LH2 tests were run on a 400 Kip unit. The toughness specimens were loaded at 100 (parent) and 50 (weld) ksi/min rates. The purpose of these tests was to develop the acceptable flaw lengths for the weld inspection criteria.

The results of these tests are presented in reference [1]. Figure 3 is a plot of fracture strength vs. flaw size for 0.375 inch thickness and is typical of data obtained for all thicknesses. This thickness approximates the most common thickness on the ET. These results (and the results from the other thicknesses) had three applications:

- 1) prediction of the largest flaws that would survive proof test;
- 2) determination of acceptable weld defects; and,
- 3) establishing leak before burst criteria.

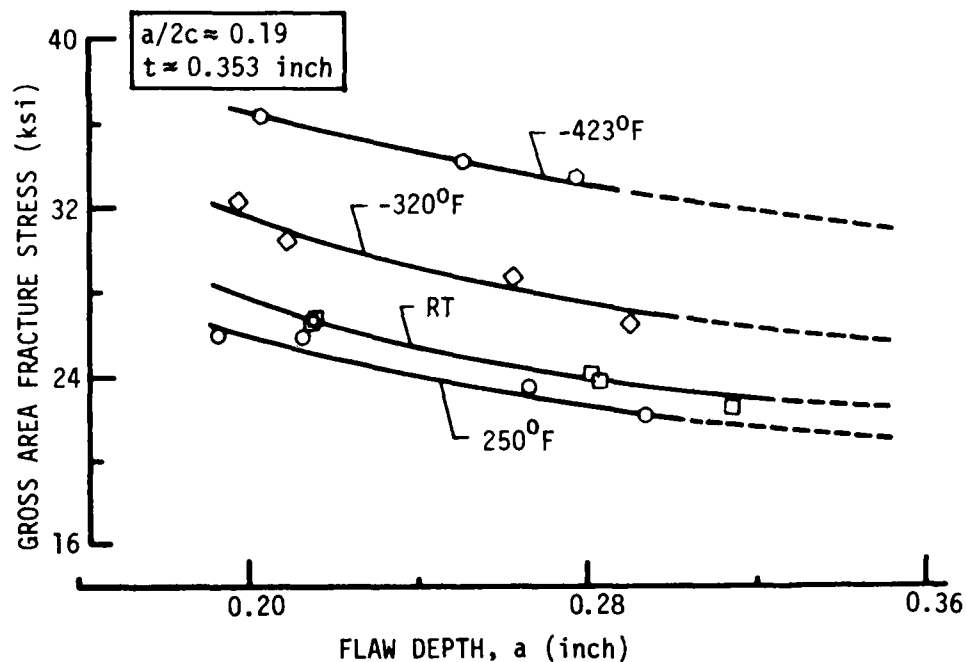


FIGURE 3 - THE EFFECT OF FLAW SIZE ON FRACTURE STRENGTH OF 2219-T87 WELDS

Sustained Load Tests

We ran a number of sustained flaw growth tests on welded specimens in air and dye penetrant to assure ourselves we did not have an aggressive environment to deal with. The literature {2,3} contained sufficient evidence that the flight and proof test environments were also non-aggressive. In addition, the proof (air) and flight cycle (air, LN₂* & LH₂) tests described in the following sections confirmed that this approach was correct.

Cyclic Flaw Growth

Because of the toughness of 2219 and unpredictable flaw growth during proof test, linear elastic fracture mechanics theory could not be used to predict the largest flaw surviving proof and da/dN data could not be used to predict cycles to fracture or leak. Therefore, it was determined to use a simulated-service test that incorporated a proof test on each specimen and "flying" the specimen on a number of missions. Each cyclic specimen had a flaw size (for that thickness and proof stress) that would just survive proof test. This critical flaw size was determined by 1) the fracture tests, 2) special instrumentation (strain gages and leak detectors), and 3) careful monitoring of the load-deflection readings of the tensile machine.

About one-half of the cyclic specimens "blew-up" in proof demonstrating that our simulated-service specimens started out with nearly catastrophic flaws. Figure 4 shows the profile of the proof and flight stresses of the specimens. At this point before any cyclic tests were run, a decision had to be made regarding the ET proof factor**. Based on preliminary data assessments, we selected a proof factor of 1.05. However, the major portion of the ET tanks would be at cryogenic temperatures and 2219 was known to exhibit higher toughness at these colder temperatures. Therefore, it was decided to take advantage of the cryogenic properties by establishing

$$\text{Proof Factor} = 1.05 \times \frac{\text{toughness at ambient}}{\text{toughness at cryogenic temperature}} \quad (1)$$

* Reference {2} presents data to show that LN₂ has similar flaw growth characteristics to LO₂ for 2219, so LN₂ was used instead of LO₂.

** Proof factor is defined here as the factor by which flight stress is multiplied to determine the proof stress.

A review of the literature (2) and early fracture results indicated that between room temperature and -320°F the toughness of 2219-T87 parent metal increased by at least 5%. Between room temperature and -423°F the data indicated at least a 10% increase. Therefore, the cyclic tests were established with the following proof factors.

<u>OPERATING TEMPERATURE</u>	<u>PROOF FACTOR</u>
ambient	1.05
-320°F	1.00 (1.05 x 1/1.05)
-423°F	0.955 (1.05 x 1/1.10)

No cyclic tests were run at temperatures above ambient because when these elevated temperatures occur on the ET, it is very late in flight and the stresses are inconsequential.

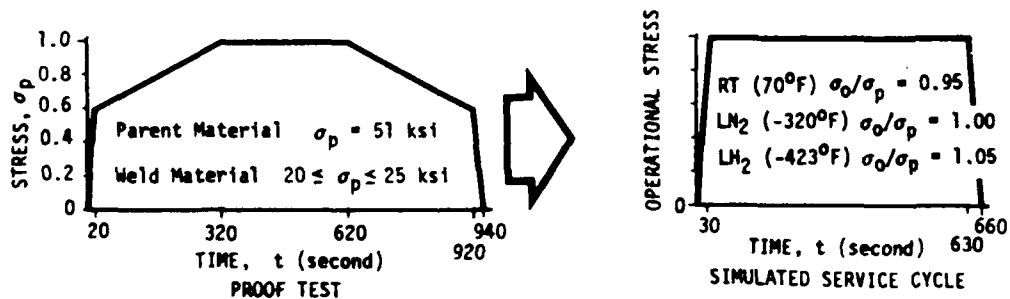


FIGURE 4 - TEST SEQUENCE

Table II presents selected cyclic test results. In all, 69 specimens survived proof and all 69 subsequently survived the required 4 flights. The test goal was to try to make twelve flights. The value of twelve resulted from a consideration of 1) anticipated changes in loads and stresses later in the ET program, 2) a possible requirement to show the ET good for more than one flight (i.e., test articles) and, 3) test budget restrictions (number of specimens vs. length of test).

TABLE II EXAMPLES OF SIMULATED SERVICE TESTS

THICK (IN.)	COND.	a	2c	a/2c	Proof (Ksi)		Test Temp.	Op. Stress / Proof Stress	Flights	Fatigue Cycles	
					Stress	Result				Leak	Fracture
0.122	P	0.055	0.405	0.14	51	OK	70°	0.95	12	293	306
0.138	P	0.075	0.438	0.17	51	OK	-320°	1.0	12	436	454
0.367	P	0.197	0.925	0.21	51	Frac.					
0.371	P	0.123	0.930	0.13	51	OK	-423°	1.05	12	NOT RUN	
0.233	W	0.195	0.920	0.21	24	Leak	70°	0.95	12	N.A.	118
0.357	W	0.240	1.255	0.24	24	OK	-320°	1.00	12		137
0.353	W	0.304	1.391	0.22	21.9	Leak	-320°	1.00	12	N.A.	204
0.366	W	0.324	0.688	0.47	24.7	OK	-320°	1.00	12	40	403
0.354	RW	0.243	1.230	0.19	24	OK	70°	0.95	12		58

ASSESSMENT

This section will discuss the test results, the impact of the test results on the ET design, and the implementation of fracture control on the ET.

Fracture Tests

By taking the individual data plots of fracture stress vs. flaw depth (for $a/2c = 0.20$) and extrapolating the data to where the flaw depth = thickness Figure 5 resulted. Figure 5 is used by the designers to determine the proper thickness to assure leak at proof. Remaining ligament tests have shown that leakage can occur at even higher stresses (4), which provides an added measure of conservatism in our approach.

There are some weld lands, that because of manufacturing limitations or complex loading, that will not be in a leak mode during proof. These welds receive no additional NDE effort, except that all cracks in these "burst" welds are referred to engineering for review before acceptance regardless of flaw length or stress in the weld. All tank welds are radiographed and penetrant inspected prior to proof test.

The next step in applying the fracture data to ET design was to establish a weld acceptance criteria. Here, we decided to consider every weld defect (porosity, dross, inclusions, ...) a surface crack. The most common defects associated with 2219 welding are porosity and oxide inclusions with an occasional crater crack in a weld repair area.

The thought process used to establish the defect criteria was as follows.

- 1) Review all the room temperature data for each thickness including weld repair data.

- 2) Determine the critical flaw depth (at $a/2c = 0.20$) for each thickness at 20,000 psi, 25,000 psi, and 30,000 psi fracture stresses. These stresses were chosen because they represented the most likely proof stresses. In actual fact, all proof stresses are less than 25,000 psi.
- 3) Convert the flaw depth to flaw length.
- 4) Divide this critical flaw length by two to provide a safety margin to minimize proof test failure risks.
- 5) Next, consider a flaw shape of $a/2c = 0.5$. Let a = thickness and calculate $2c$ (equals $2t$). This is the very deep flaw poised to leak or fracture.
- 6) Compare the flaw length in 5 to 4. Choose the smaller value.
- 7) Round off the number (i.e., 0.33 to 0.30) to simplify the task of the x-ray inspector.

Figure 6 was the result of this logic and was used to establish defect tolerance criteria.

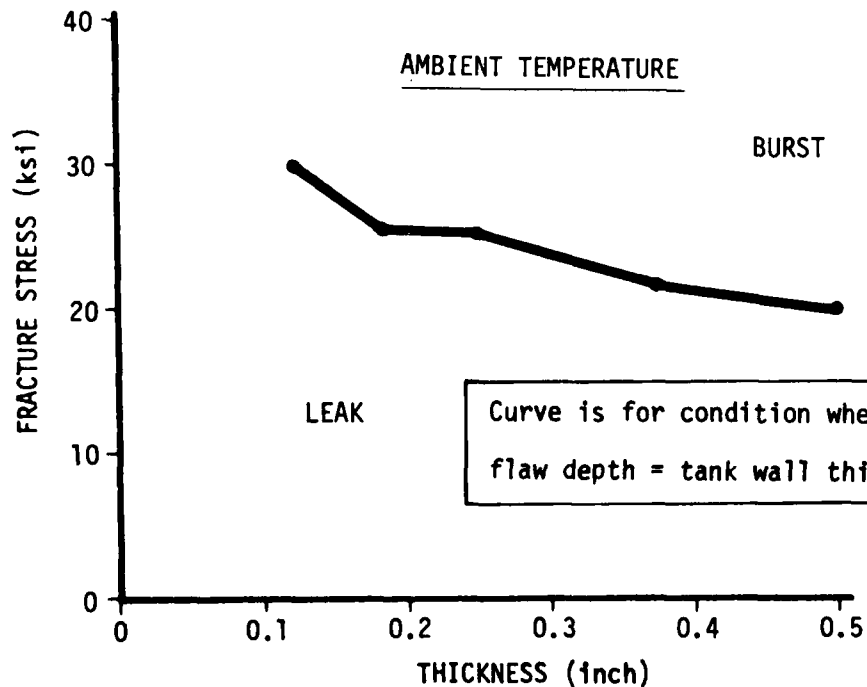


FIGURE 5 - LEAK/BURST CURVE FOR 2219-T87 WELDS

However, one additional step was still necessary so a weld grade system was established in the weld process specification in which defect lengths were assigned grade level numbers. Each grade level has a range of 0.050 inch. For example a grade 7 callout allows defects up to 0.300 inches in length. A grade 6 allows defects up to 0.250 inches. These grades are in turn specified on the engineering drawings.

This approach to establishing a weld acceptance criteria is conservative and yet allows the acceptance of defects considerably in excess of those that have been allowed in past pressure vessels. This has resulted in large ET cost savings through a significant reduction in weld repairs.

Cyclic Data

A review of Table II reveals two conclusions. First, that the flaw sizes that just survived proof are considerably larger than those allowed for that thickness during proof test, Figure 6. Secondly, that any ET that survives proof will be good for at least one flight with a scatter factor of four.

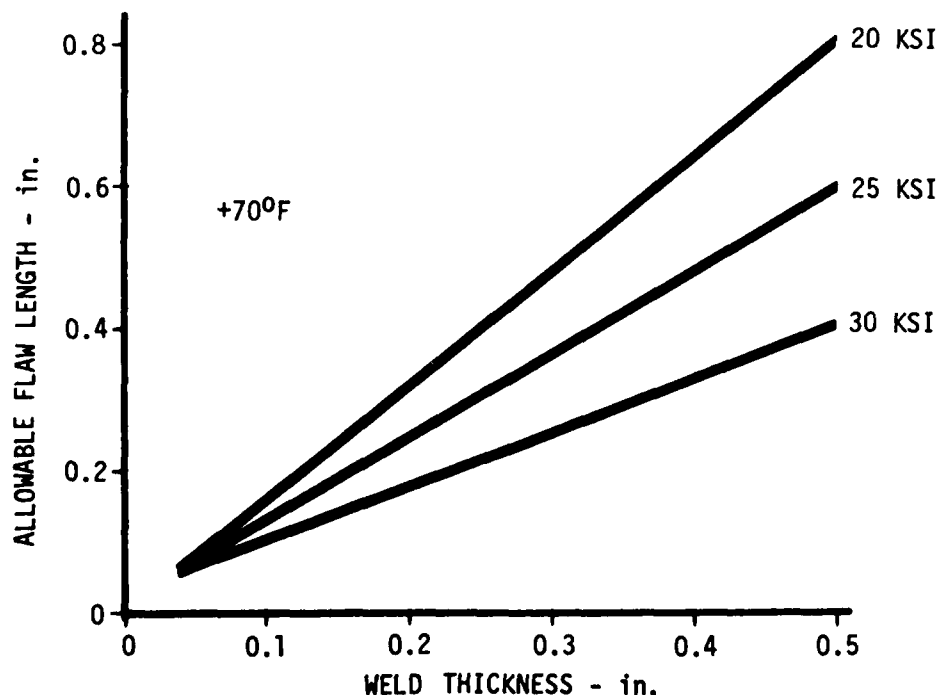


FIGURE 6 - WELD DEFECTS ALLOWABLE

As can be deduced from the data and knowledge of fracture toughness, this simulated service approach cannot assure that the ET will not leak. The test results show that a flaw may break through in proof, but will still not fracture for at least 12 flights. Still a leak is undesirable and therefore, each tank is leak checked either during or after proof test and acceptance grade levels for NDE are specified such that no flaw is accepted that will leak in service or proof test.

CONCLUSIONS

In the past the acceptance of internal and external defects in welds, (porosity, dross, cracks, inclusions, and lack-of-fusion) has been based on somewhat arbitrary and in general very conservative methods. For example, cracks (or crack-like defects), and lack-of-fusion have never been allowed for basic weld acceptance. The ET approach is to analyze all defects by fracture mechanics techniques as though they were cracks and allow these defects to remain in the weld if they are less than critical size. The defect acceptance length is specified on the engineering drawing. This approach has resulted in a weld acceptance criteria for the ET that although conservative, is much less stringent than that of other existing weld specifications. This approach has resulted in significantly fewer weld repairs and consequently lower cost for the ET.

We have minimized any risk of proof test failures by radiographic and penetrant inspection and by making welds leak mode where possible. Weld leakage is prevented by NDE. An empirical method in which no reliance is placed on theoretical analytical expressions that would be questionable for high toughness materials has been used to select proof factors that ensure successful flight operation.

REFERENCES

1. Fiftal, C. F., "Fracture Mechanics Data on 2219-T87 Aluminum for the Space Shuttle External Tank", Martin Marietta Aerospace - Michoud Operations Test Report, 826-2027, July 1975.
2. Engstrom, W. L., "Determination of Design Allowable Properties: Fracture of 2219-T87 Aluminum Alloy", NASA Report, CR-115388, March 1972.
3. Hall, L. R. and Finger, R. W., "Stress Corrosion Cracking and Fatigue Crack Growth Studies Pertinent to Spacecraft and Booster Pressure Vessels", NASA Report, CR-120823, December 1972.
4. Finger, R. W., "Proof Test Criteria for Thin-Walled 2219 Aluminum Pressure Vessels", NASA Report, CR-135036, Volume I, August 1976.

STRESS ANALYSIS OF AN OMEGA SEAL CONTAINING A CRACK-LIKE DEFECT

G. R. Sharp

Westinghouse Electric Corporation
Bettis Atomic Power Laboratory
West Mifflin, Pennsylvania 15122

INTRODUCTION

Historical and Descriptive Background

In the nuclear power industry, there are many applications for zero leakage seals. A seal of this type must usually provide a flexible connection between two independent components in order to accommodate their relative motions as well as to retain the applied internal pressure such that zero leakage is provided. One type of zero leakage seal frequently employed is called an "omega" seal. This seal is comprised of inner and outer seal halves which are fabricated into a complete toroidally shaped omega seal (the cross section of which resembles the Greek letter omega) by first welding or otherwise securing the bases of the seal halves to two components that move independent of one another. The two seal halves are then closure welded together at their "tops" to complete the omega.

The usual sources of loading on the seal are internal pressure and motion of the components to which the seal halves are affixed. The motion of the components is caused by pressure and temperature effects. Usually the displacements are large enough to produce exceptionally high stress levels in the seal. That is, for the given number of operating cycles the stress levels are frequently beyond those allowed in Reference 1. A low stress level with subsequent high fatigue life is obviously a more desirable situation. This has, in the past, frequently been accomplished by providing a thin flexible seal, particularly when the seal experiences large "bottom" end displacements. This lowering of the stress levels results from a thin seal which has negligible resistance to bending, hence, low bending stress. Thus, the more flexible the seal the lower the bending stresses will be and the higher the membrane stresses due to internal pressure will be. However, the membrane stresses are usually well within the limits established by Reference 1. Consequently, it is apparent that the best seal design will be a reasonably flexible seal which is capable of handling the various boundary conditions imposed on the seal. The strength and fatigue life of a thin seal is of course significantly affected by any linear defects (cracks) which may be present in the seal. Usually the material used in an omega seal is of high quality Alloy 600 and of course is carefully inspected for defects prior to installation. However, the final seal welding of the two halves of the omega seal is a possible source of defects because the underside of the weld cannot be inspected upon completion of the weld. It is for this reason that it is usually assumed by the analyst that a linear

defect of some prescribed depth exists, normally at one of the toes of the seal weld since that is the usual location of the highest stress level in the seal. Thus, in order to predict the stress levels and fatigue life of a seal that may or may not contain a linear defect, a fracture mechanics crack growth analysis of the seal with a defect is necessary.

Technical Background and Data

It was desired to perform a parametric study of an omega seal of Alloy 600, the cross section of which is shown in Figure 1. The material properties used in this analysis for the base metal were different from those used for the weld deposit metal as shown in Table 1. The weld underbead shape has been assumed; however, it does correspond reasonably well with the cross section of actual seal welds. The parametric study was to consist of both stress and fracture mechanics crack growth analyses to determine 1) the maximum depth of crack allowed at the toe of the weld so that crack growth would be less than five percent in an expected lifetime of 2000 cycles; 2) whether the remaining ligament could meet the primary membrane and primary membrane plus primary bending requirements set forth in Reference 1, and 3) whether ratchetting requirements (no rathcetting allowed) could be met. The analysis would be performed using finite element techniques. Further, the analysis of the omega seal would be performed on an axisymmetric basis and as such required that the cracks be circumferential. This of course creates a much more severe condition than isolated semi-circular or semi-elliptical cracks would create.

The boundary conditions imposed on the seal for this study are listed in Table 1 and correspond to the symbols indicated in Figure 2.

Table 1 Boundary Conditions and Young's Moduli

<u>Variable</u>	<u>Steady State</u>	<u>Initial Condition</u>
R_I (Rad. Displ.)	$9.1(10^{-4})$ in ($23\mu\text{m}$)	0.0
R_O (Rad. Displ.)	$2.8(10^{-4})$ in ($7.1\mu\text{m}$)	$-2.8(10^{-3})$ in ($-71\mu\text{m}$)
M_O (Displ. due to Mom.)	$1.34(10^{-3})$ radians	$1.26(10^{-3})$ radians
p (Pressure)	2500 psi (17.24 MPa)**	0.0
T (Temperature)	500°F (260°C)**	70°F (21.1°C)
E_W^* (Weld dep. Mat.)	$22.2(10^6)$ psi (153.06 GPa)	$23.7(10^6)$ psi (163.41 GPa)
E (Other Mat.)	$28.9(10^6)$ psi (199.26 GPa)	$31.4(10^6)$ psi (216.50 GPa)

One other condition (a limiting condition) imposed on the seal is that no ratchetting will be allowed.

* Assumed values of Young's Modulus for the weld deposit material.

**These values are representative of those used in either a pressurized water reactor or a light water breeder reactor.

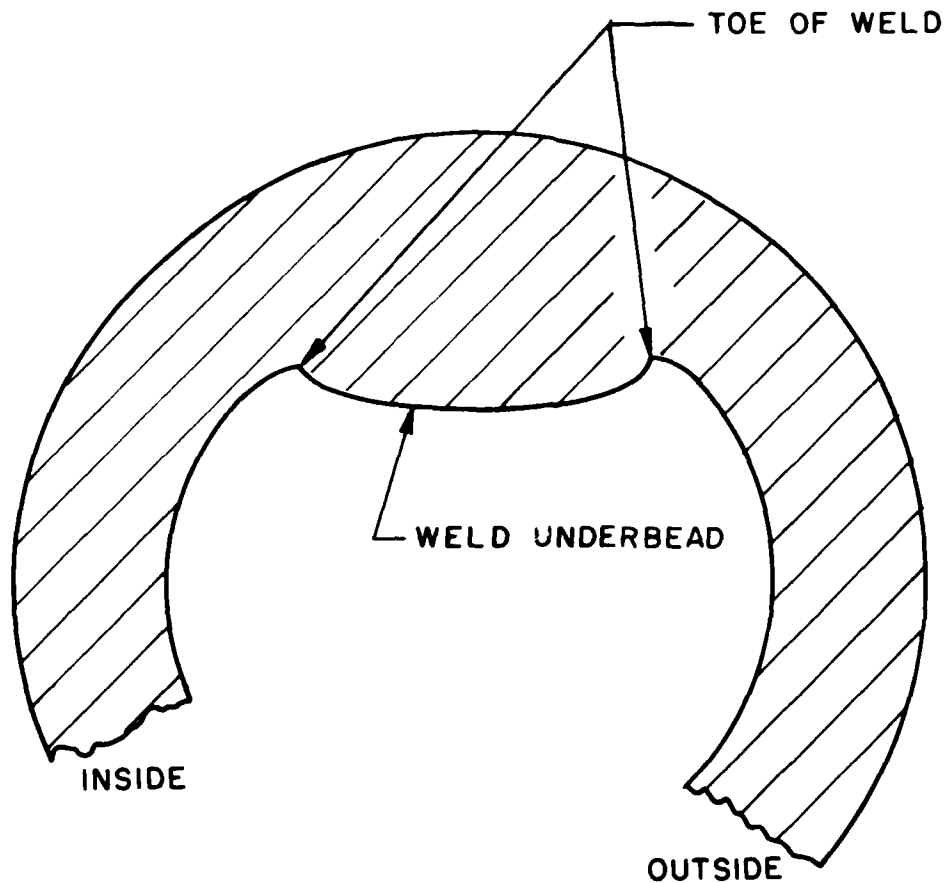


Figure 1 Cross Section of Omega Seal Scale 10/1

FORMULATION

Definition of Tasks

The first step in the analysis was to determine the point of maximum stress on the surface of the seal. An axisymmetric stress analysis using the finite element techniques described in Reference 2 and in Reference 3 was used to locate the maximum stress point. The next step was to create a new finite element model of the seal so that an explicit representation of the crack using finite element crack-tip elements could be inserted at the location of maximum stress, namely at the outside toe of the weld underbead.

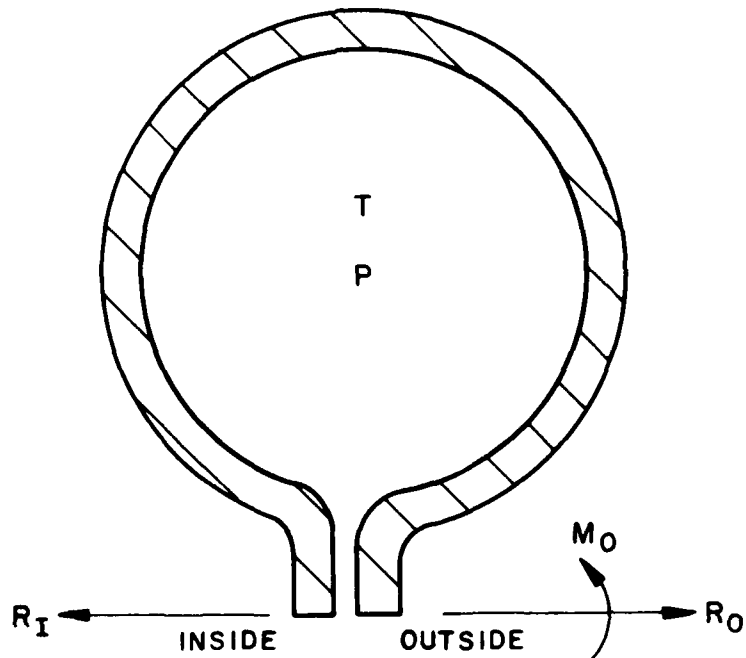


Figure 2 Sketch indicating pressure and temperature, and positive directions of displacements and moment

As stated above, it was necessary in the next step to know the crack growth rate for the maximum allowable depth of an axisymmetric crack located at the toe of the weld underbead. This was accomplished by using a nine node isoparametric brick finite element analysis in which the mode one stress intensity factor K_I was calculated first by means of the "J" integral method in the finite element domain and then by a displacement expansion method. The results of the two methods were then compared. The stress intensity factors for both initial and steady-state conditions were determined as indicated, then substituted into the expression

$$\frac{da}{dN} = C_1 (\Delta K)^n \quad (1)$$

where

- a = crack length in inches (m)
- N = number of cycles of stress amplitude (2000 in this case)
- C_1 = an experimentally determined material dependent quantity
(For Alloy 600 $C_1 = 4(10^{-13})$ in $[\text{cycle} (\text{KSI} \sqrt{\text{in}})^n]^{-1}$ or $1.016(10^{-14})$ m $[\text{cycle} (1.099 \text{ Pa} \sqrt{\text{m}})^n]^{-1}$)
- n = an experimentally determined material dependent quantity - 5.7 for Alloy 600
- ΔK = range of stress intensity factor (K_I at steady state minus K_I at initial conditions (assumed zero in this problem))
 $\text{KSI} \sqrt{\text{in}} (1.099 \text{ Pa} \sqrt{\text{m}})$.

The experimental data from which C_1 and n were determined were collected from specimens tested in air and subjected to maximum linearized stress levels in the range 68 to 104 KSI (469-717 Pa). These stress levels are considerably above monotonic yield and some were even above cyclic yield. Therefore, the empirical relationship of Equation (1) should be valid for stresses beyond yield such as are encountered in the problem under discussion. The value for C_1 was increased by a factor of 10 to account for the seal being in contact with water. The next step involved determining if the remaining ligament could withstand the steady-state conditions and meet the appropriate basic stress intensity limits of Reference 1. The final step was to investigate whether ratchetting takes place. For the omega seal under consideration, no ratchetting was allowed.

Technical Data

The technical data for the problem under discussion is presented in the Introduction under the heading Technical Background and Data.

ASSESSMENT

The cross-sectional geometry of the omega seal is shown in Figure 1. This geometry is basically the as-built condition with the assumed shape of the weld underbead corresponding reasonably well with observed weld cross sections. The cross-sectional geometry was converted to the mathematical (finite element) representation shown in Figure 3. This mathematical model consists of five free bodies which are fastened together at their respective interfaces. The free bodies (LHOMEG1, LHOMEG2, etc.) along with their respective s-t coordinate origins* are indicated in Figure 3. An axisymmetric stress analysis using References 2 and 3 was performed on the mathematical model. The data from the stress analysis of the complete seal was used to locate the point of maximum hoop stress on the boundary of the seal so that a crack could be placed in that location. That point is as indicated in Figure 3. The model shown in that figure was then modified to six free bodies to account for the crack-tip region which itself is a separate free body. To insert the crack-tip free body into the analysis, it was necessary to revise the free body CRAKEL to accept the additional free body. This involved certain changes in the mathematical model which can, for a representative crack length, be seen in Figures 4 through 8. Figure 4 is the crack-tip region itself. It consists of one element in the s-direction and 28 elements in the t-direction. Figure 5 is a modification of the free body CRAKEL from Figure 3 with five elements in the s-direction and 28 in the t-direction. The modification of CRAKEL consisted of changing the s-t origin and including a crack and a "hole" to receive the crack-tip region. As stated above, the free body of the crack-tip region is composed of a number of special crack-tip elements. These elements are triangular in shape so that the most acute angle of each element lies at the tip of the crack which is also the origin of the s-t axis in this free body. The purpose of this configuration is to provide that every element in the free body is common to the tip of the crack so that a $1/\sqrt{r}$ stress singularity,

* The coordinate system s-t is established as a convenient means for element and node numbering and is described further in Reference 3.

15 MIL CRACK IN OMEGA SEAL

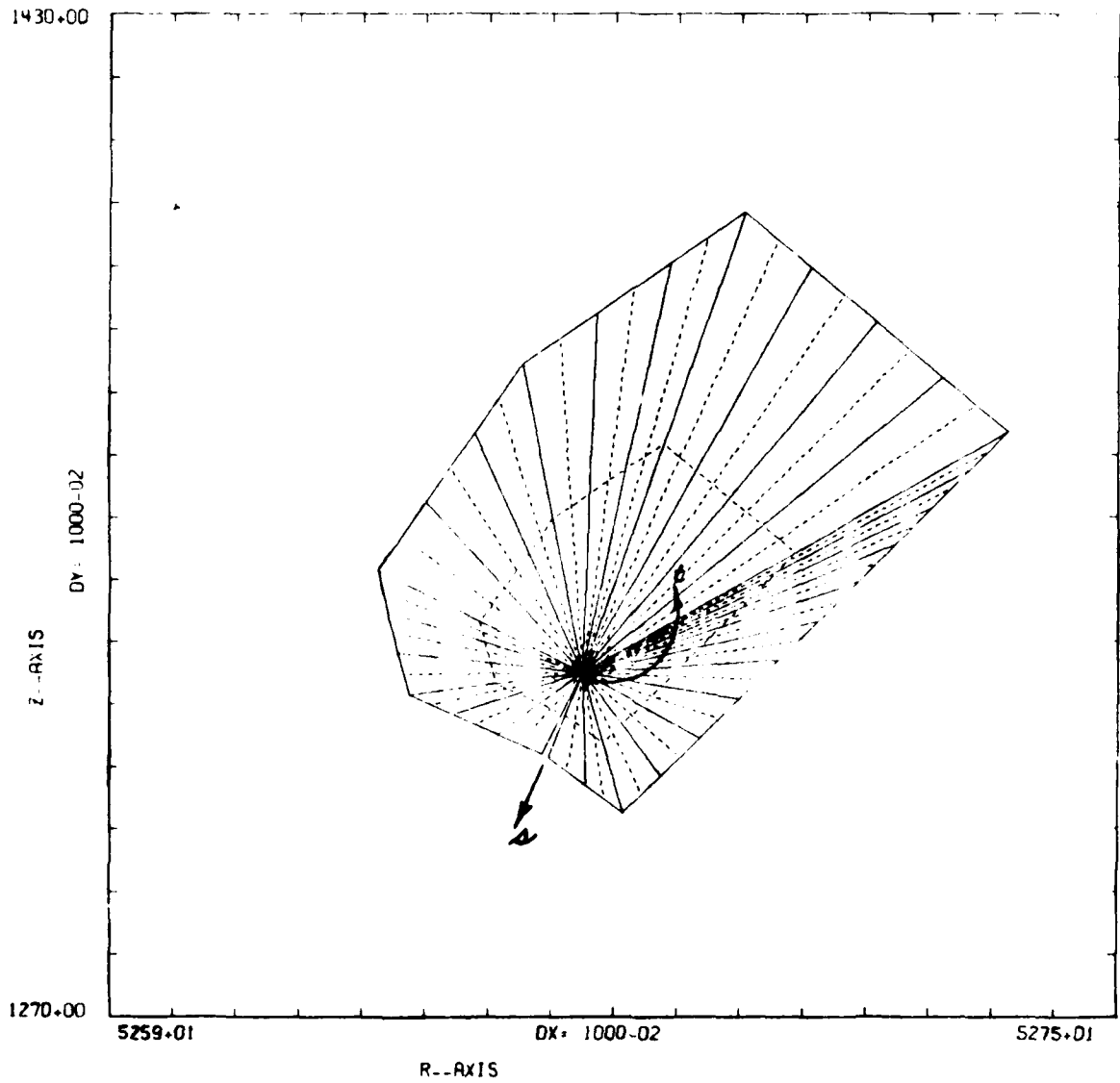


Figure 4 Free Body CRAKTIP (Crack-Tip Region)

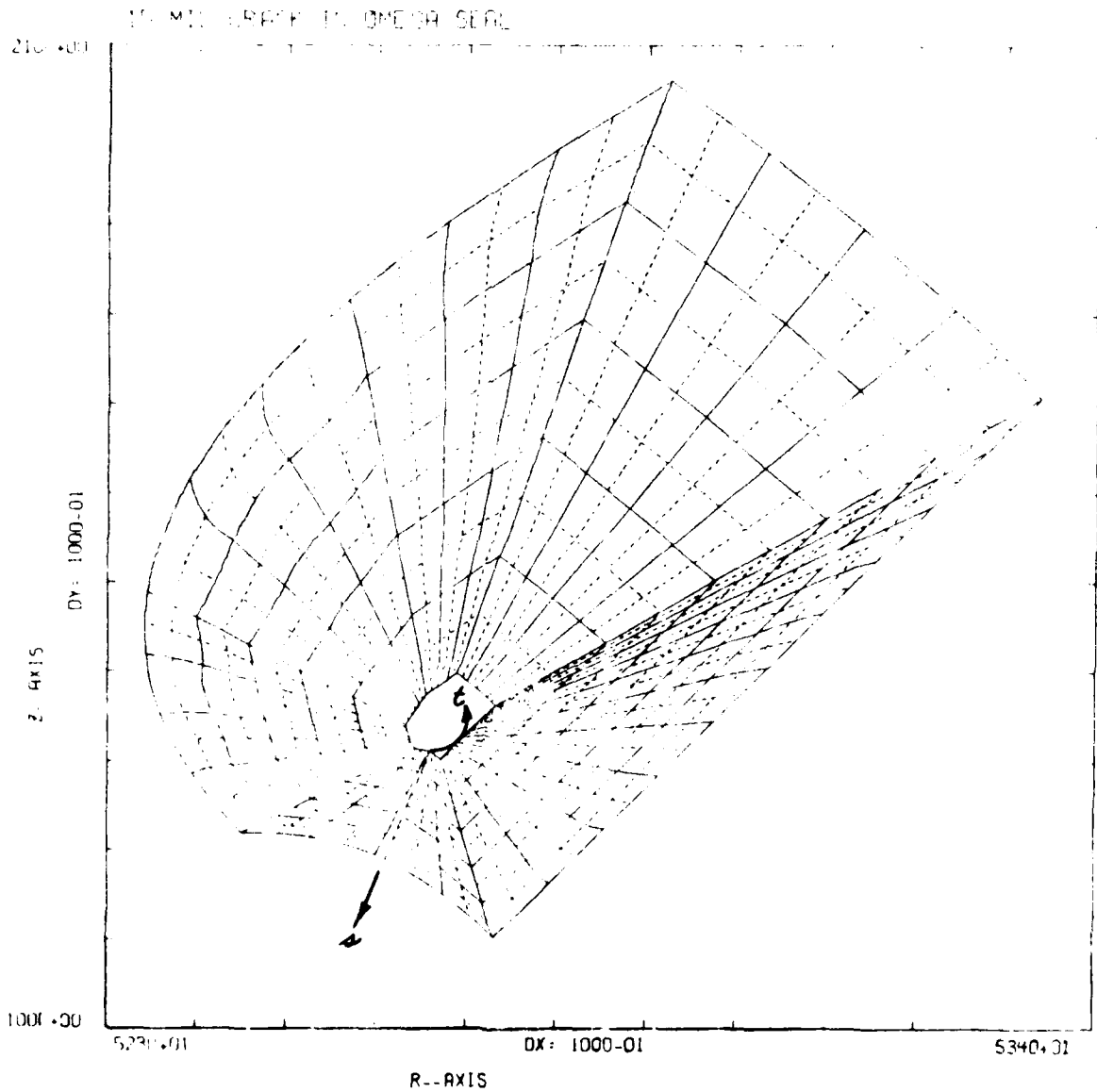


Figure 5 Revised Free Body CRAKEL

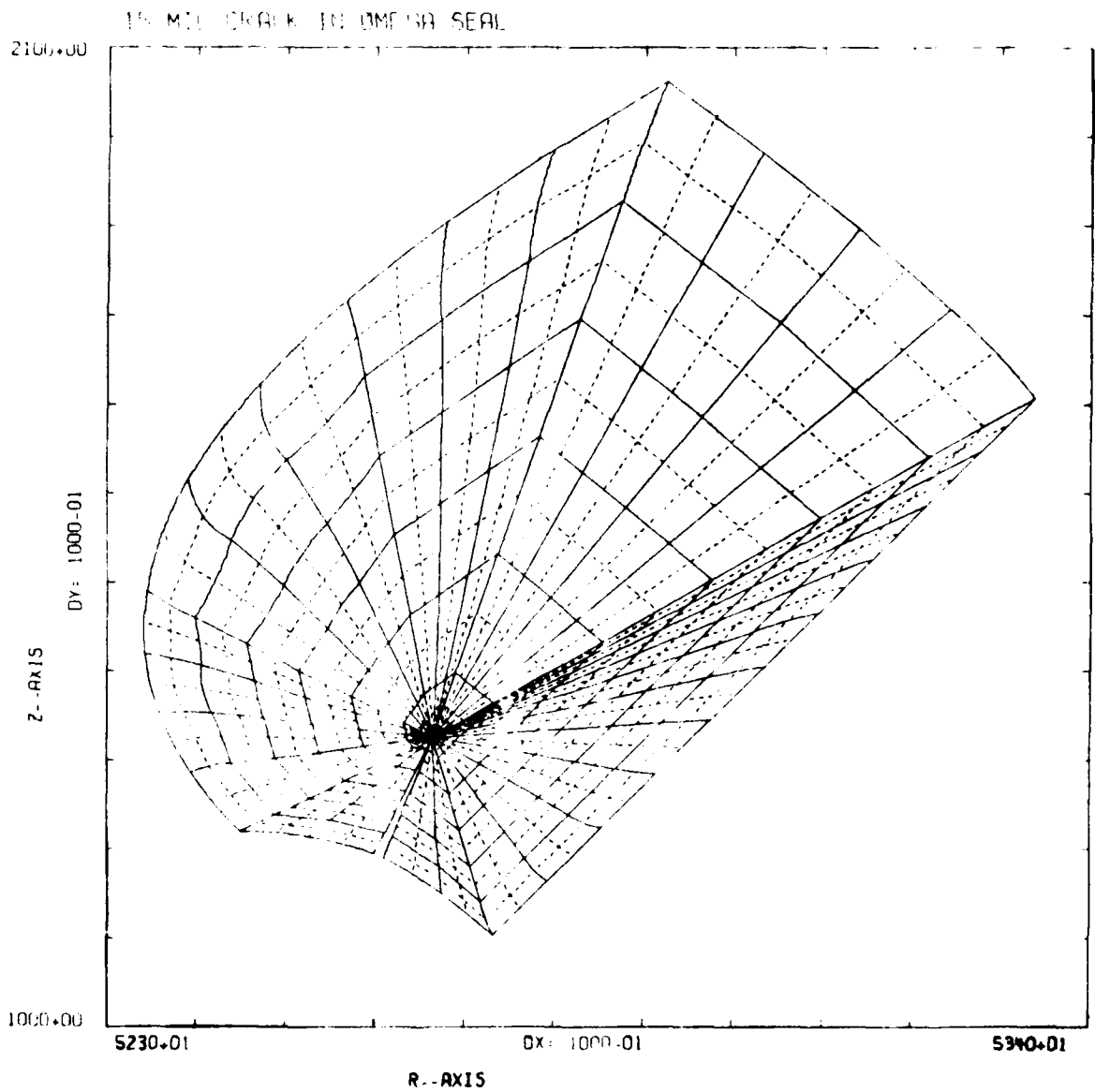


Figure 6 Assembly of CRAKEL and CRAKTIP Free Bodies
(Combination of Figures 4 and 5)

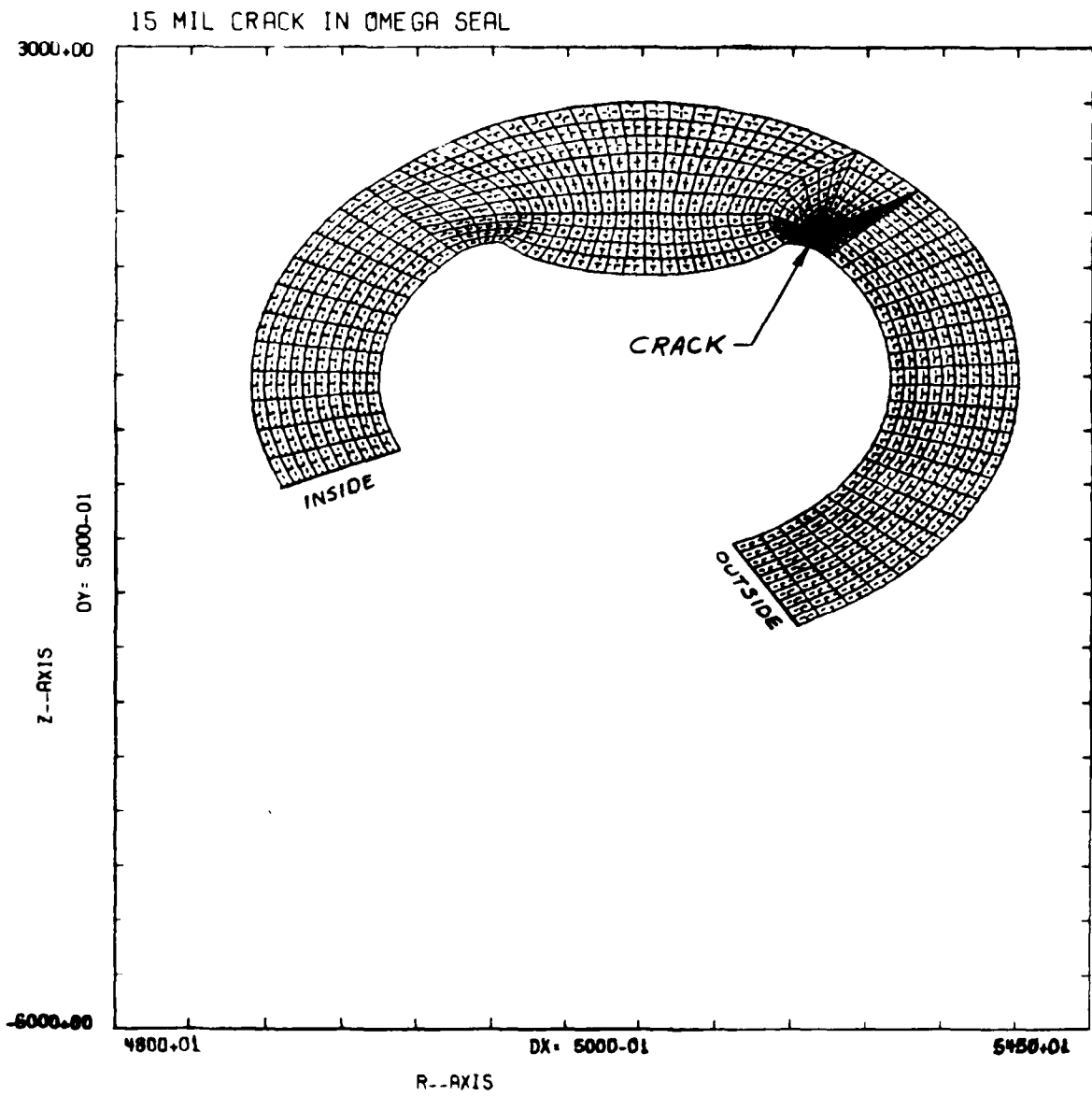


Figure 7 Cross Section of Omega Seal with Crack

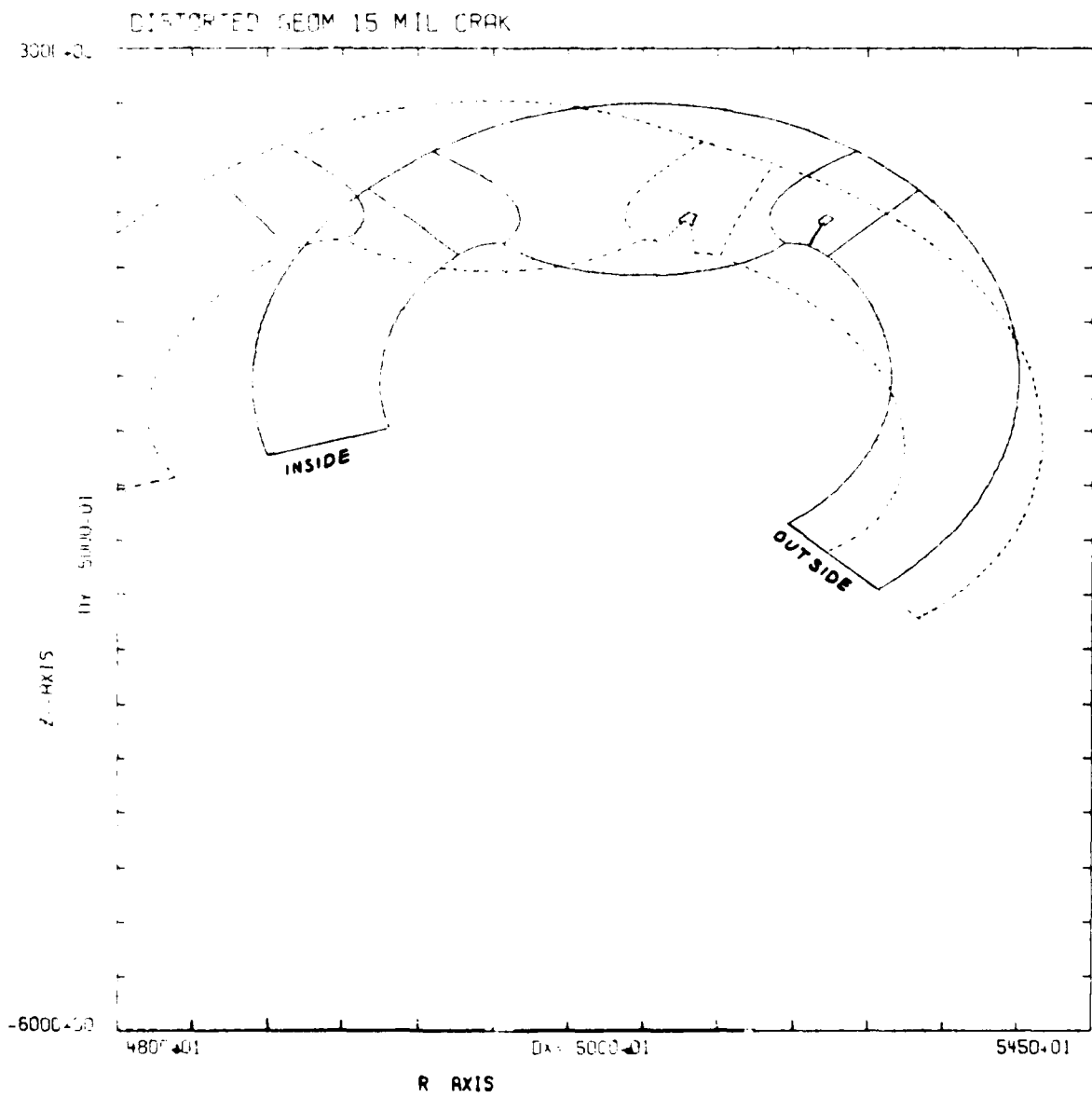


Figure 8 Distorted Geometry - Displacements Magnified 100 times
Steady State Boundary Conditions

presumed valid near the tip, can be modeled. This is shown graphically in Figure 4 where the free body resembles a Japanese fan, the pivot point of which would represent the near tip area of the crack. The edges of the triangular elements which form the periphery of the free body are exactly the same configuration as the mating quadrilateral elements of the surrounding free body CRAKEL shown in Figure 5. Thus, the free body CRAKEL is a transition region of quadrilateral elements which connects the free body containing the crack-tip to the remaining structure which is composed of basically rectangular elements. Figure 6 shows the assembly of the free bodies CRAKTIP and CRAKEL. Figure 7 shows the cross section of the seal with a crack at the outside toe of the weld and Figure 8 shows the displaced (dotted) outline relative to the undisplaced (solid) outline. The basic model shown in these figures was used to perform the parametric study to determine the maximum allowable crack depth for this seal and its associated boundary conditions. The following assumptions are used throughout the computer (finite element) analysis.

1. Linear elastic stress-strain relationship is valid.
2. Defect (crack) exists completely around the seal inner circumference.
3. The defect occurs in the area of highest hoop stress -- i.e., at the outside toe of the weld.
4. Poisson's ratio is 0.3.
5. Small strain, small displacement theory is valid.

The fracture analyses were performed following the same procedures and using the same computer program network as was used in the uncracked model except that a final module of the network was called to calculate the "J" integrals and then calculate the mode I stress intensity factor, K_I , for cracked elastic bodies by means of the expression

$$K_I = \sqrt{\frac{JE}{1 - \nu^2}} \quad (2)$$

where E is Young's Modulus and ν is Poisson's ratio.

A value for Poisson's ratio of 0.3 was used in all calculations. This produces the most conservative values for the J-integral since the problem is displacement controlled and the J-integral is proportional to the area under the force-displacement curve.

Equation 2 is the relation between K_I and J for the plane strain case and is not strictly valid for the axisymmetric problem considered here. However, since the ratio of torus radius to thickness is in the 55-60 range, the problem is reasonably close to plane strain. Therefore, the results of Equation (2) should be acceptable, although possibly a bit conservative.

The linear elastic fracture mechanics analyses of the omega seal were performed in a parametric fashion such that seals with circumferential cracks ranging in depth from 0.015 inches (0.381 mm) to 0.040 inches (1.02 mm) in increments of 0.005 inches (0.127 mm) were analyzed for both steady-state and initial conditions. To maximize the crack growth, it was assumed that the initial conditions produced no loading on the crack-tip. Hence, the K_I at initial conditions is zero. In accordance with Equation (1), the maximum calculated crack growth associated with a 0.040 inch (1.02 mm) crack normal to the inside surface of the seal at the outside toe of the weld underbead is 1.79 percent. This is based on a calculated stress intensity factor of 11.073 KSI $\sqrt{\text{in}}$ (12.17 Pa $\sqrt{\text{m}}$) at steady state conditions and the assumption that da/dN can be replaced by the difference expression $\Delta a/\Delta N$, where $\Delta a = a_f - a_i$ and $\Delta N = N_f - N_i$ for $f = \text{final}$ and $i = \text{initial}$. Substitution of these expressions into Equation (1) yields

$$a_f = a_i + N_f C_1 (\Delta K_I)^n \quad (3)$$

where N_i was set to zero.

Thus, substitution of the appropriate values into Equation (3) yields

$$a_f = .040 + 2000(4)(10^{-13})(11.073-0)^{5.7}$$

or

$$a_f = .0407168 \text{ in } (1.0342067 \text{ mm})$$

and the percent of growth for the 0.040 inch (1.016 mm) crack is

$$\begin{aligned} \% \text{ growth} &= \frac{.0407168 - .040}{.040} (100\%) \\ &= 1.79\% \end{aligned}$$

This is a small percentage growth and of course is less than the five percent limit set forth in the Technical Background and Data section. To corroborate this growth, the values of K_I calculated via the J-integral method were substantiated by hand calculation using the single term displacement expansion method discussed in Reference 4. In this method

$$K_I = \frac{v_i E}{4(1 - \nu^2)} \sqrt{\frac{2\pi}{r_i}} \quad (4)$$

where v_i is the displacement normal to the crack face at the i th node and r_i is the distance along the crack face from the crack-tip to the i th node. For instance, in the case of the 0.040 inch (1.02 mm) crack, the J-integral value for K_I was 11.073 KSI $\sqrt{\text{in}}$ (12.17 Pa $\sqrt{\text{m}}$) while the displacement expansion method of Reference 4 generated 16.056 KSI $\sqrt{\text{in}}$ (17.65 Pa $\sqrt{\text{m}}$). In Reference 5 the displacement expansion method was compared to test data and it was found that it over estimated the measured data. Thus, it is believed that the J-integral values of K_I are reasonable numbers for this case; hence, it is concluded that no appreciable crack growth will be caused by the loads considered.

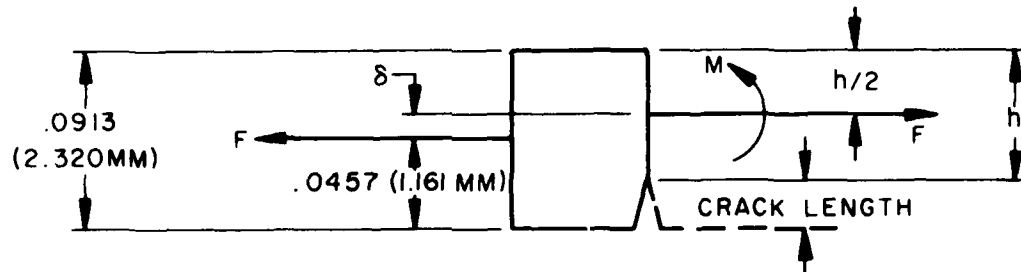
The portion of the seal between the tip of the crack and the outside surface of the seal is called the remaining ligament. It is now necessary to determine if the remaining ligament can withstand the steady-state conditions and meet the appropriate stress requirements of Reference 1. The stresses (as determined via References 2 and 3) within the seal, resulting from the boundary conditions of Table 1, contain a significant amount of secondary stresses due to thermal effects. Since the boundary conditions which produce primary stresses and those which produce secondary stresses were not stated independently, but rather were stated in a combined sense, i.e., given as total displacement or rotation, it is an extremely difficult if not impossible task to separate the primary and secondary components from the total stress determined by the finite element computer program. Consequently, a reasonable method of approximating the primary stresses is required. One approach to this problem is to observe that the only contribution to primary stress must come from internal pressure. Therefore, the primary stress intensity in the remaining ligament is due only to pressure. By considering the seal to be approximated by an uncracked torus, the membrane stress and hence the average membrane force can be determined by using the standard torus formula as shown in Reference 6 and reproduced below as

$$\sigma_{\max} = \frac{pb}{2t} \left(\frac{2a - b}{a - b} \right), \quad (5)$$

where

- p = internal pressure
- b = outside radius = 0.25 inches (6.35 mm)
- a = the torus radius = 5.15 inches (0.1308 mm)
- t = the torus thickness (remaining ligament in this case) = 0.046 to 0.076 inches (1.17 to 1.93 mm), depending upon depth of crack

For equilibrium, the membrane force must be transmitted across the remaining ligament. Referring to Figure 6, it was determined that the distance across the modeled seal along the line of the crack is 0.0913 inches (2.32 mm). Thus, by considering the free body diagram



it is seen that in transmitting the force across the remaining ligament the forces are offset an amount δ , thereby creating a moment $M = F\delta$. The maximum stresses per unit length can then be determined by the expression

$$\sigma = \frac{F}{A} \pm \frac{MC}{I} = \frac{F}{h} \pm \frac{6(F\delta)}{h^2} \quad (6)$$

where

F = membrane force/unit length
 A = area of ligament = $h(1)$
 $I = bh^3/12$, $b = 1$
 $C = h/2$
 h = remaining ligament

Using Equation (5), the maximum general primary membrane stress intensity S under a hydrostatic testing pressure of 3200 psi (22.064 MPa) (1.5 times operating pressure), a minimum remaining ligament h of 0.061* inches (1.55 mm) (a 0.030 inch (0.762 mm) crack), and a torus radius of 5.15 inches (130.81 mm) is determined to be

$$S = 13449 - \left(-\frac{3200}{2}\right) = 15049 \text{ psi (103.8 MPa)}$$

where the average stress due to internal pressure is subtracted from the toroidal stress to give the stress intensity. When compared with the S_m value of Reference 1 (the lower of $\frac{2}{3} S_y$ or $\frac{1}{3} S_u$), this stress intensity is well within the limits, e.g.,

* It will be shown on the following page that a crack depth of 0.030 inches (0.762 mm) is the maximum that can be allowed.

$$15049 \text{ psi (103.8 MPa)} < \frac{2}{3} S_y = \frac{2}{3} (35000) \approx 23333 \text{ psi (160.9 MPa)}$$

Using the stress in the remaining ligament of the torus, the membrane force/unit length used in Equation (6) can be determined. Thus,

$$F = \sigma h = 13449 (.061) = 820 \text{ lb/in (1.436(10}^5\text{) N/m)}$$

and Equation (6) now yields

$$\sigma = \frac{820}{.061} \pm \frac{6(820)(.015)}{(.061)^2}$$

or

$$\sigma_{\max} = 33276 \text{ psi. (229.4 MPa)}$$

By combining this value with the hydrostatic pressure stress, the maximum primary membrane plus bending stress intensity is determined to be 34876 psi (240.5 MPa). The limiting value of stress intensity in this case is $1.5 S_y = 1.5(23333) \approx 35000$ psi (241.3 MPa). Thus, this requirement on membrane plus bending stress intensity is satisfied for circumferential cracks of 30 mils (0.762 mm) or less in depth.

The primary plus secondary stresses in the remaining ligament were calculated by the computer in a coordinate system that was neither parallel nor perpendicular to the crack face. To separate the calculated stresses into membrane and bending components required a rotation of the computer determined stresses into a coordinate system which produced stresses normal and parallel to the crack face. It was then possible to use a numerical integration scheme on the normal, hoop, and circumferential stresses to separate the stresses into membrane and bending components. Normally this is done for purposes of differencing the components so that the stress difference range(s) between the two extreme conditions may be compared with the $3S_y$ limits of Reference 1. However, since Equation (1) was employed to determine the crack growth in one lifetime of 2000 cycles and since a fatigue analysis is intrinsic to this empirical equation, it is not appropriate to invoke the stress difference range limits and the fatigue limits of Reference 1. On the other hand, since the omega seal is subjected to both cyclic pressure and thermally induced displacement controlled loading, it is appropriate to investigate whether ratchetting takes place.

For the problem at hand, one of the "boundary" conditions stipulated that no ratchetting was allowed.

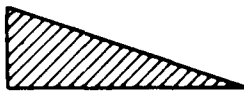
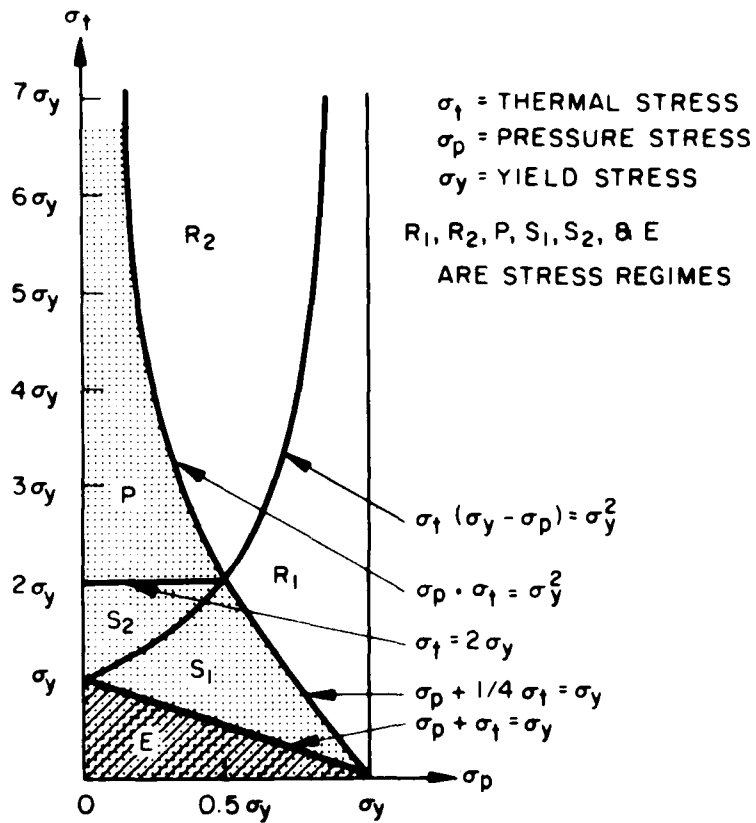
The investigation of ratchetting is accomplished basically by means of a graphical determination of the relation between primary membrane and primary plus secondary bending stress. The graph used is usually referred to as a "Bree" diagram (see Figure 9) after J. Bree (Reference 7). Both the ordinate and abscissa of Figure 9 are normalized on the yield stress. Even though Bree in his original paper (Reference 7), as well as subsequent authors on the subject, did not state which yield stress should be employed, it appears that if a cyclic phenomenon is under investigation the appropriate yield stress would be cyclic yield.

For the seal under consideration, σ_t (see Figure 9) will also include membrane stress due to thermal effects. It is assumed that the yield stress is the cyclic yield, in this case it is assumed that the cyclic yield is 45.0 KSI* (310.3 Pa) and that the pressure stress σ_p contains only the membrane stress due to pressure. Thus, since, for a 30 mil (0.762 mm) crack, the thermal stress is 128.9 KSI (888.8 Pa) and the membrane stress is 10.5 KSI (72.40 Pa), the ordinate and abscissa values are approximately 3 and .25 respectively. The resulting point of intersection lies in the regime P of Figure 9; hence, there is no ratchetting for this seal when it contains a 30 mil (0.762 mm) circumferential crack at the outside toe of the weld.

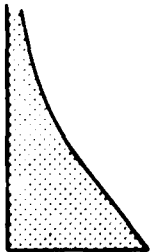
Summary and Conclusions

It has been shown that for the omega seal under consideration which contains a circumferential crack 0.030 inches (0.762 mm) deep at the outside toe of the weld, the primary membrane and primary membrane plus primary bending stress intensities are within the limiting values of S_m and $1.5 S_m$ respectively. Furthermore, there is essentially no crack growth in an expected life of 2000 cycles. Although the primary plus secondary and fatigue limits of Reference 1 are not explicitly invoked, the failure modes prevented by these limits are precluded as demonstrated by ratchetting and crack growth analyses. Further, by inference, a semi-elliptical or a semi-circular 30 mil (0.762 mm) deep crack at the toe of the weld would be well within the required limits. This, of course, implies that semi-elliptical or semi-circular cracks of greater than 30 mils (0.762 mm) depth could be tolerated. However, since it is not known to what depth they could be tolerated, if they are limited to 30 mils (0.762 mm) it will certainly be a conservative condition. It is therefore concluded that the seal analyzed in this report can meet the applicable stress limits, the ratchetting requirements, and the fracture mechanics requirements both for the given boundary conditions and for a worst case condition of a circumferential crack 30 mils in depth located at the outside toe of the weld underbead.

* This value of cyclic yield was extracted from Figure 1 of Reference 8 as a rough "average" of the cyclic yield between the knee of the curve and the 0.2 percent offset line.



E: REGIME OF NO CREEP RATCHETTING OR PLASTIC CYCLING
 (NOTE HOWEVER THAT CREEP DUE TO σ_p CAN EXIST).



$S_1, S_2, P \& E$: REGIMES OF BOUNDED CREEP/PLASTIC CYCLING

$R_1 \& R_2$: REGIMES OF PROGRESSIVE RATCHETTING

Figure 9 Stress Regimes (taken from Bree, Reference 7)

References

1. American Society of Mechanical Engineers, "ASME Boiler and Pressure Vessel Code", Section III or Section VIII.
2. C. M. Friedrich, "BESTRAN - A Technique for Performing Structural Analyses", Bettis Atomic Power Laboratory, WAPD-TM-1140, February 1975.
3. J. L. Gordon, "OUTCUR: An Automated Evaluation of Two-dimensional Finite Element Stresses According to ASME Section III Stress Requirements", ASME paper No. 76-WA/PVP-16, December, 1976.
4. J. J. Oglesby and O. Lomacky, "An Evaluation of Finite Element Methods for the Computation of Elastic Stress Intensity Factors", Report 3751, Naval Ship Research and Development Center, December 1971. AD-735874
5. H. J. Bellucci, "Three-Dimensional Elastic-Plastic Stress and Strain Analyses for Fracture Mechanics: Complex Geometries", MARC Analysis Research Corporation, Report No. 09177 (TR 75), November, 1975. ORNL/Sub/3821-1
6. R. J. Roark, "Formulas for Stress and Strain", McGraw-Hill Book Co., Fourth Edition, 1965.
7. J. Bree, "Elastic-Plastic Behavior of Thin Tubes Subjected to Internal Pressure and Intermittent High-Heat Fluxes With Application to Fast Nuclear-Reactor Fuel Elements", Journal of Strain Analysis, Vol. 2, No. 3, 1967.
8. A. L. Snow, et. al., "Low-Cycle Fatigue Strength of Notched Ni-Cr-Fe Alloy 600 and Low-Alloy Steel", Journal of Materials, JMLSA, Vol. 5, No. 3, September, 1970.

FATIGUE AND FRACTURE OF THICK WALLED CYLINDERS AND GUN BARRELS

By: B D Goldthorpe
Royal Armament Research and Development Establishment
Fort Halstead, Sevenoaks, Kent England

INTRODUCTION

Historical Background

Pressure vessels have always provided interest and an area of fruitful work for the engineer and scientist involved in fracture mechanics. The principal reasons for this are threefold; failure of pressure vessels always has serious consequences, the problems are usually interesting technically and they are usually amenable to some sort of solution. The approach used in this paper for predicting fatigue and failure of pressure vessels is primarily applicable to large calibre gun barrels although some of the results are of wider interest and application.

Historically the occurrence of fracture problems in gun barrels goes back a long way although these problems largely disappeared with the advent of modern forging and heat treatment techniques. Since that time the service life of gun barrels has been determined by wear since this produces a deterioration in accuracy and when this falls outside predetermined limits the gun is withdrawn from service.

In the intervening period there have been considerable changes brought about by demands for lower weight and higher performance. These changes have required an increase in working stress and an increase in the strength of steel used. The net result of this has been to reduce fatigue life through the increased stress intensity factor (ΔK) and the reduced fracture toughness. Originally the reduced fatigue life brought about by these changes was of little consequence since the wear life was shorter. However around the late 1960's the stress levels and strength levels had become such that in many cases the fatigue life was shorter than the wear life and the failure of a number of barrels occurred. This reduction in fatigue life required a fundamental change on the part of the user and designer since it meant that the fatigue life must be known with reasonable accuracy in order that the barrel could be withdrawn from service before failure occurred. It is the purpose of this paper to describe one of the methods of analysing and predicting the fatigue behaviour under these modern conditions.

Technical Background

One of the most important features of gun barrels in the context of fracture mechanics is that they are subject to thermal fatigue at the bore from hot propellant gases. This causes the bore surface to develop a network of craze cracks within the first few rounds and the crack depth reaches a maximum of about 1mm (0.04") after 200 rounds. Subsequent to this the cracks will

develop as longitudinal fatigue cracks growing radially as a result of the pressurisation and depressurisation of the barrel. The result of this is that fatigue in gun barrels is a particularly severe problem for two reasons. Firstly initiation of cracks is effected very rapidly and within a few rounds the ΔK value can reach $50-60 \text{ MNm}^{-3/2}$ ($40-50 \text{ ksi}\sqrt{\text{in}}$) at which fatigue crack growth rates are fairly fast. Secondly the pressure will act in the cracks as well as producing a hoop stress and since pressures can be in the range of $300-600 \text{ MN/m}^2$ ($20-40 \text{ tonf/in}^2$) this has a large effect on the ΔK value.

From observations on actual barrel failures or simulated failures the important features that appear relevant to an analysis of the problem are associated with the type of cracking that develops and the final failure. It appears that once the craze cracking is fully developed the mechanical fatigue cracks that grow from them are relatively straight fronted and can be large in number. This situation persists for a large part of the life but the curvature of the cracks increases as their depth increases. The final failure depends on the material and loading conditions but in the case of high pressure high strength barrels which first brought the problem to light the fractures can be fully elastic and often with fragmentation. In the case of low strength, low pressure barrels failure would normally be expected to occur by the leak before break mechanism.

FORMULATION

Definition of Tasks

The problem of predicting the fatigue life of gun barrels is in principle a simple one since we start with a truly initiated crack. It is therefore a standard procedure of integrating the crack growth equation between necessary limits. The difficulties that do arise are peculiar to this particular problem and can be listed as determination of appropriate stress intensity factor calibrations, whether these calibrations apply over the whole range of crack growth, effects of crack curvature and effects of residual stress (autofrettage).

Taking the non-autofrettaged case a K calibration does exist for the single crack (1) but the question arises as to whether this is applicable to the craze cracked gun barrel. Preliminary estimates of fatigue life showed that this model gave values which were lower than the expected or measured value by a factor of between 10 and 20.

A more realistic calibration had therefore to be obtained. A careful study of cracked gun barrels revealed that about 30-50 major cracks commonly developed and on this basis the best model would be one containing about 40 cracks. In order to calculate a K calibration for this model available data and approximation methods were examined and originally a technique by Williams and Isherwood (2) was applied to data for a star shaped crack published by Westmann (3). For the purpose of the present paper, however, an

approximation procedure by Cartright and Rooke (4) has been applied to the more accurate data for radial cracks from a hole in an infinite plate by Tweed and Rooke (5). The objective in this approximation procedure is that the multiple cracking shown in Figure 1 represents radial cracks growing from a craze cracked gun barrel. Using the general method outlined by Cartright and Rooke (4) the finite cylinder shown on the left hand side of Figure 2 which is loaded by internal pressure is equivalent to an infinite cylinder loaded by internal pressure plus a finite cylinder with external loading. The external loading is defined to be $-S$ where S is the stress where the external boundary for the finite cylinder would fall in the infinite cylinder.

If we take the example of a cylinder of diameter ratio 2.0 the stress S is given by

$$S = -P \frac{a^2}{r^2} \quad (1)$$

where r and a are the ratio of the external and internal boundaries. For the diameter ratio of 2.0

$$S = -\frac{P}{4} \quad (2)$$

$$\text{and } -S = \frac{P}{4}$$

Since this all round tension is equivalent to internal pressure then the cylinder on the right hand side is equivalent to one with internal pressure of $\frac{P}{4}$.

Now if the K calibration is in the form

$$\frac{K}{P\sqrt{a}} = f\left(\frac{a}{T}\right) \quad (3)$$

where a is the crack depth and T the wall thickness

Figure 2 gives us

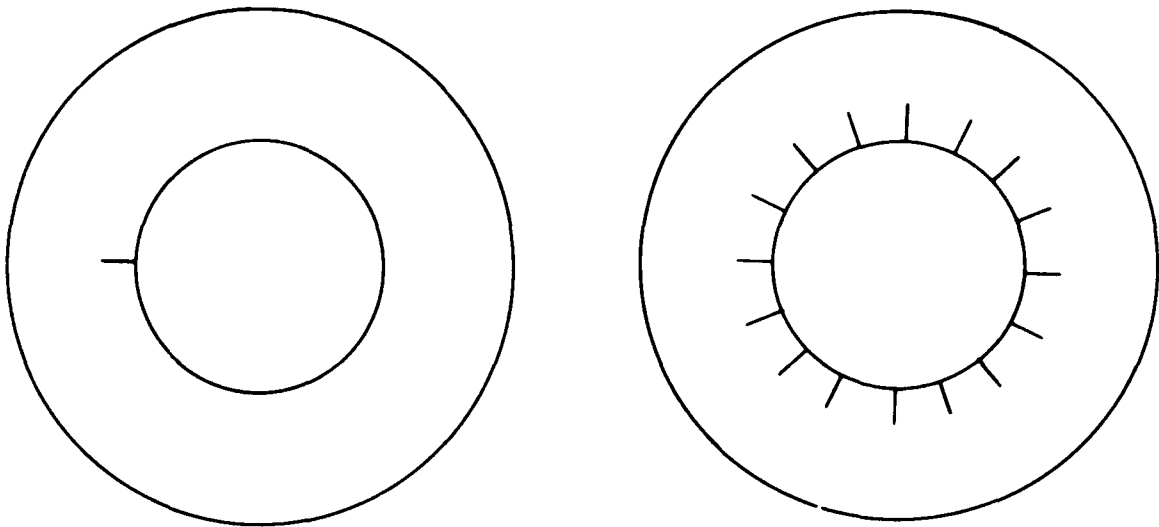


FIG.1 CRACK CONFIGURATION MODELS

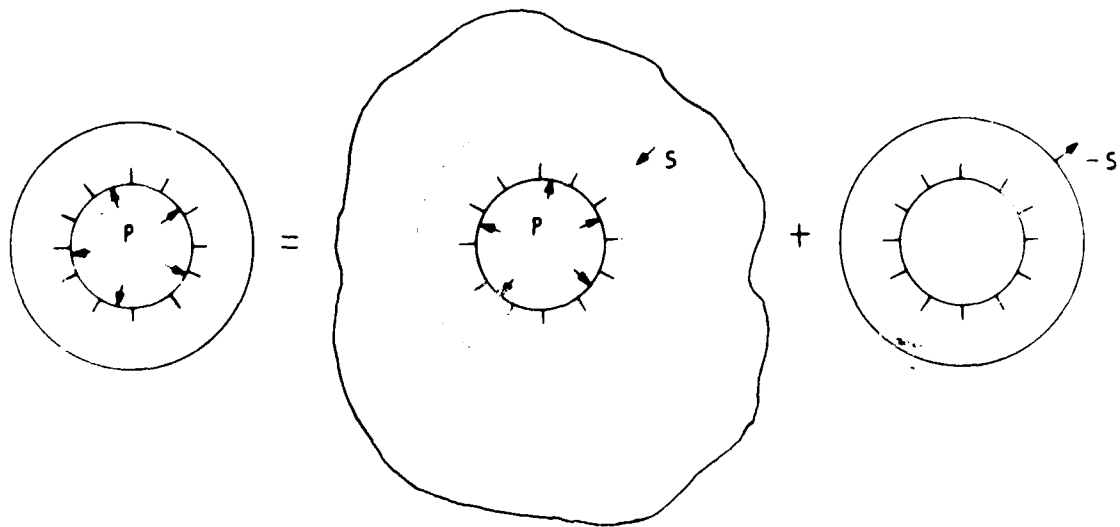


FIG 2 K_I CALIBRATION PROCEDURE

$$f\left(\frac{a}{T}\right)_f = f\left(\frac{a}{T}\right)_i + \frac{f\left(\frac{a}{T}\right)_f}{4} \quad (4)$$

where $f\left(\frac{a}{T}\right)_f$ is the calibration for the finite cylinder and $f\left(\frac{a}{T}\right)_i$ is the known calibration for the infinite cylinder. Consequently

$$f\left(\frac{a}{T}\right)_f = \frac{4}{3} f\left(\frac{a}{T}\right)_i \quad (5)$$

Equation 5 has been applied to the data of Rooke and Tweed (5) for a cylinder with diameter ratio of 2.0 and forty radial cracks. The results are given in figure 3 and compared with data for a single crack. It is evident that there is a very large difference between the calibrations and this difference increases as the crack depth increases.

To these curves have been fitted empirical formulae to be used in the integration procedure given in the next section.

The single crack model is represented by

$$\frac{K_i}{P\sqrt{a}} = 5.3 - 4.46 \frac{a}{T} + 3.8 \left(\frac{a}{T}\right)^2 - 7.63 \left(\frac{a}{T}\right)^3 \quad (6)$$

and the 40 crack model by

$$\frac{K_i}{P\sqrt{a}} = \frac{0.248}{\frac{a}{T} + 0.05} + 0.86 \quad (7)$$

$$\text{for } 0.01 < \frac{a}{T} < 0.7$$

$$\text{or } \frac{K_i}{P\sqrt{a}} = \frac{0.253}{\frac{a}{T} + 0.05} - \frac{0.001}{\frac{a}{T} + 0.001} + 0.86 \quad (8)$$

$$\text{for } 0.001 < \frac{a}{T} < 0.07$$

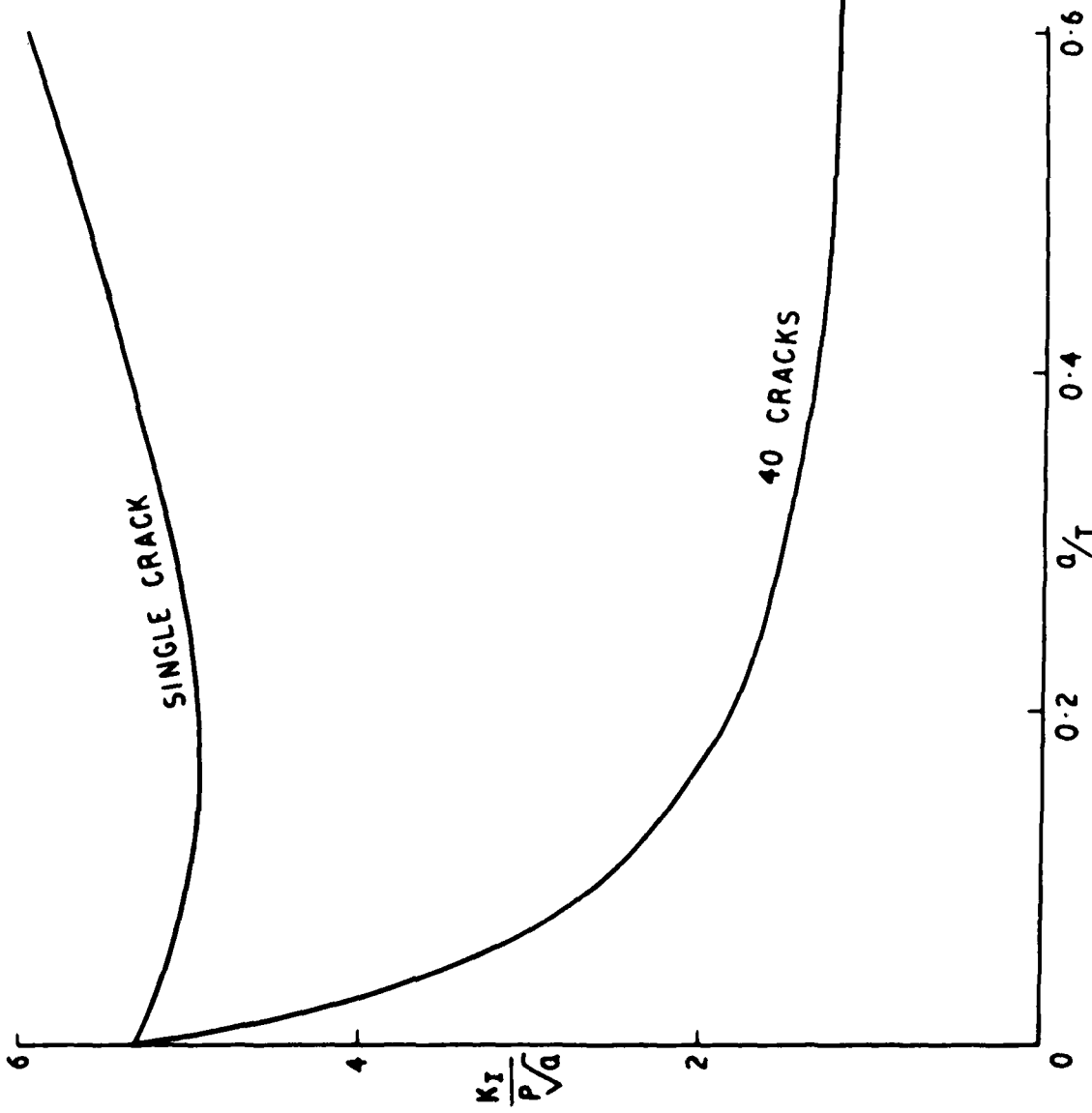


FIG 3 K_I CALIBRATION CURVES FOR DIAMETER RATIO 2.0

Technical Data

For the purpose of this paper the influence of three steels on fatigue life is examined. These are a low quality steel with high crack growth rate and low toughness designated steel A, a medium quality steel of intermediate fatigue crack growth rate and toughness designated steel B and a high quality steel of low crack growth rate and high toughness designated steel C. The properties of these steels in the transverse direction were as follows:

Steel	0.2%PS MN/M ²	UTS MN/m ²	%RA	%El	K _{IC} MNm ^{-3/2}
A	1225	1450	20	9.5	89
B	1170	1300	35	11	124
C	1185	1278	45	13.5	151

The fatigue crack growth data for these steels were represented in the form

$$\frac{da}{dn} = ae^{b\Delta K} - c \quad (9)$$

The reason for using this expression rather than the Paris equation is that the fatigue life of gun barrels starts well up the crack growth curve at a ΔK value of 40-50 ksi/in and therefore high ΔK values where the Paris equation does not apply are important in determining fatigue life. Equation (9) gives good representation up to high ΔK values as shown in figure 4.

The numerical values of the constants in equation (9) for the three steels using ksi units were as follows:

	Constants		
	a	b	c
Steel A	0.3	0.116	1
Steel B	1.6	0.071	2.4
Steel C	7.5	0.033	12.7

Assessment

The calculation of fatigue life can now be calculated by integration of equation (9) giving

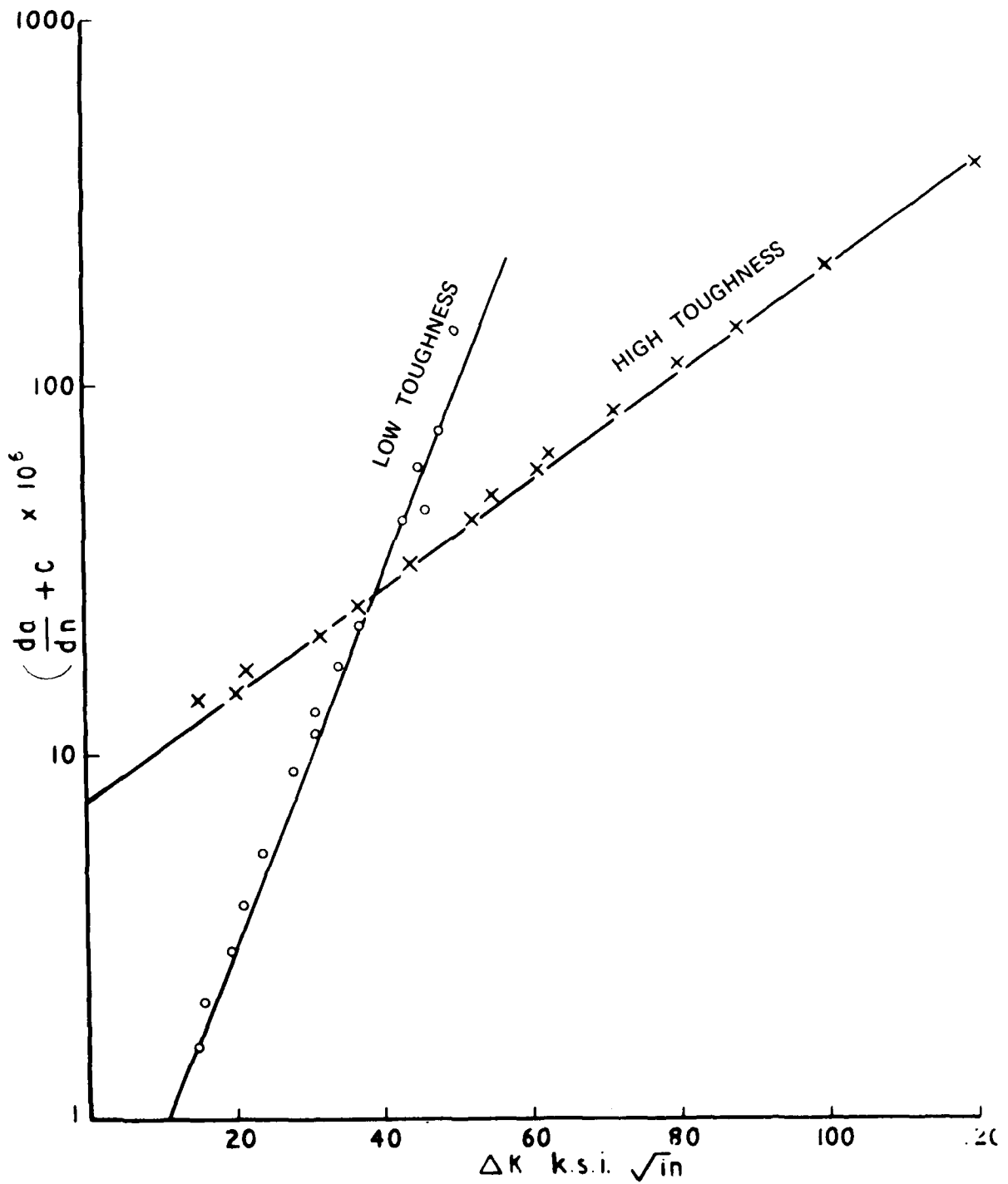


FIG. 4 FATIGUE CRACK GROWTH DATA FOR TWO STEELS

$$n = 10^6 \int_{a_0}^{a_c} \frac{da}{ae^{b\Delta K - C}} \quad (10)$$

where a_c is critical crack depth and a_0 is initial crack depth.

By modification of the variable to give

$$n = T \times 10^6 \int_{\frac{a_0}{T}}^{\frac{a_c}{T}} \frac{d\frac{a}{T}}{ae^{b\Delta K - C}} \quad (11)$$

the calibration can be used directly as

$$K = P\sqrt{a} f\left(\frac{a}{T}\right) \quad (12)$$

Here $f\left(\frac{a}{T}\right)$ is given by equations (6), (7) and (8).

Using the above data fatigue lives were calculated for the single crack model for all three steels and the results are shown in figure 5. Similarly the data for the 40 crack model was used with data from the three steels and the results are shown in figure 6. In all cases the initial crack depth was taken as 1mm (0.04") which is normal for craze cracking in gun barrels and the critical crack depth was calculated on the basis of the appropriate K_{Ic} value using equation (12). Also for all cases the diameter ratio was taken to be 2.0, the wall thickness 50.8 (2") and the pressure 344 MNm^{-3} (22.3 tonf/in^2), all about the values commonly used in gun barrels.

The objective in making these calculations here is not to deal with a specific failure but to show the range of fatigue lives that can occur as a result of variation in steel properties and crack configuration. The steels considered are actual gun barrel steels and the crack configuration models are developed from the observation of gun barrel failures.

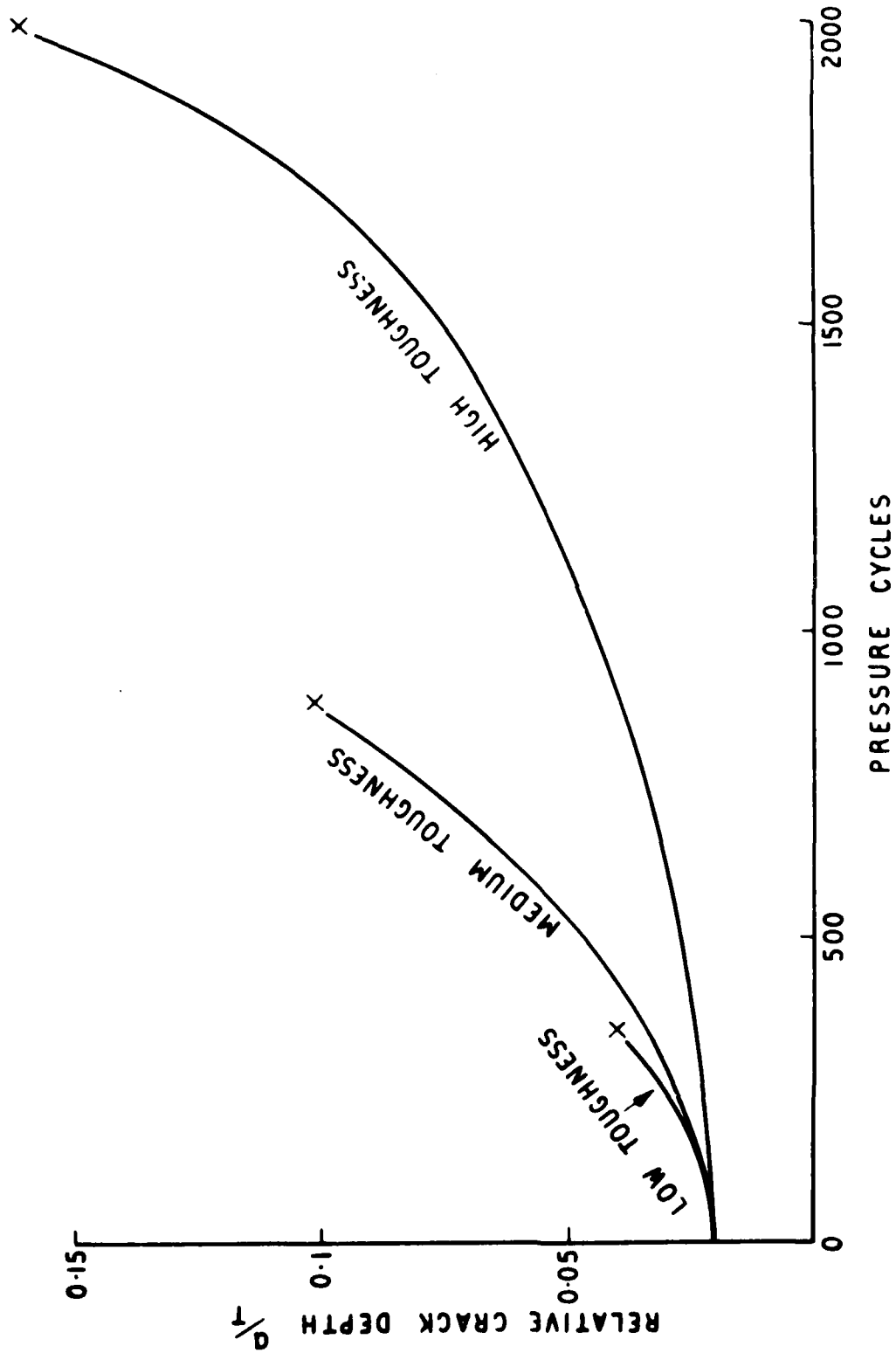


FIG. 5 PREDICTED FATIGUE CRACK GROWTH CURVES — SINGLE CRACK

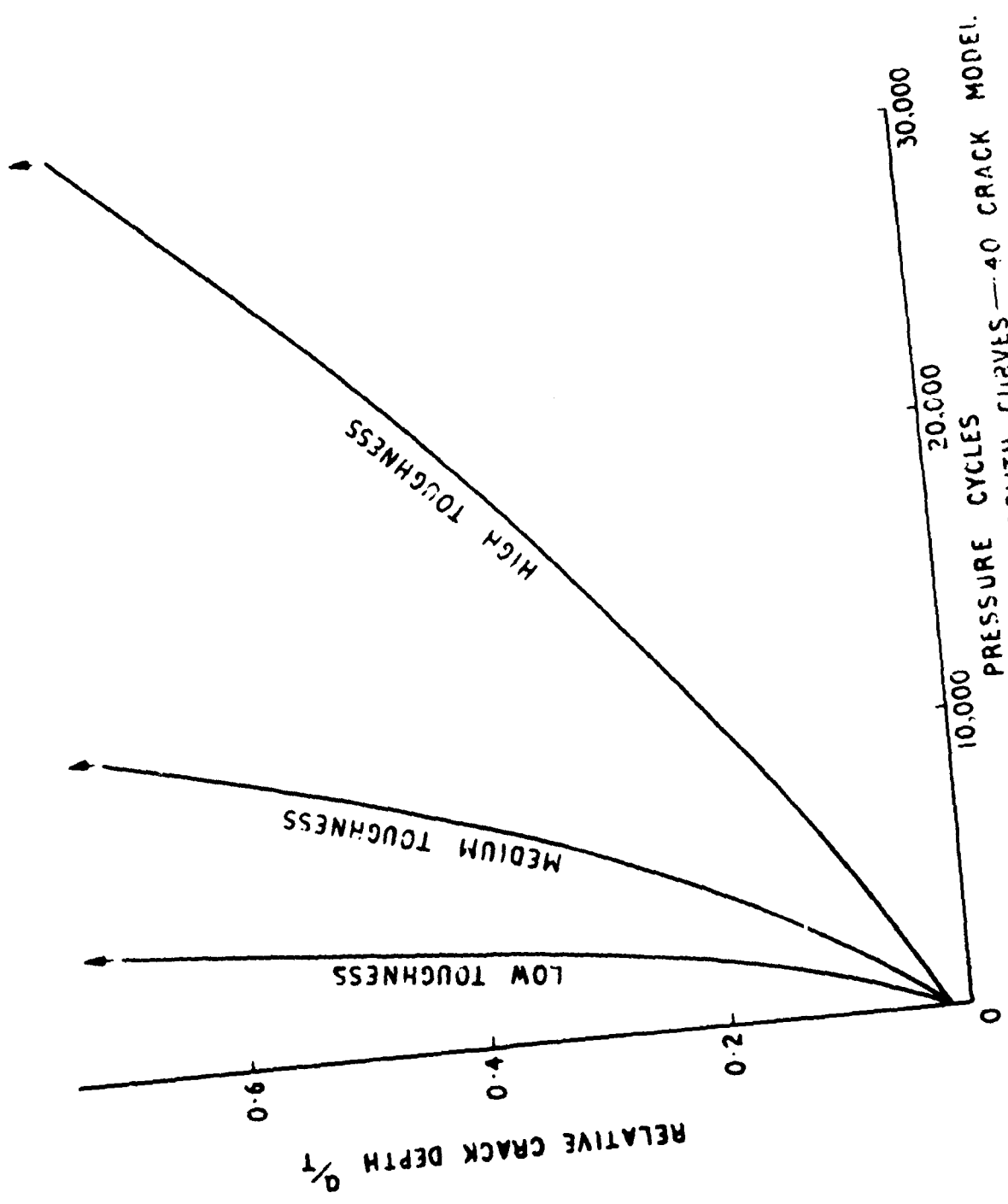


FIG. 6 PREDICTED FATIGUE CRACK GROWTH CURVES — 40 CRACK MODEL.

From figure 5 it is clear that with a single crack fatigue life for all steels is short although a factor of six improvement can be obtained by changing from a low quality steel to the best quality available. Also in all cases the crack depth at failure is very small ranging from 2mm (0.08") to 2.5mm (0.3") in a wall thickness of 50mm (2"). Therefore in all cases the fractures are fully elastic and in practice would be catastrophic.

For the 40 crack model the fatigue life is much longer, in fact for all steels the fatigue life is increased by a factor of about 15 over the single crack model. Also the critical crack depth at failure is greater than 36mm (1.4"), that is greater than the limit of the K calibration, and for the two higher toughness steels is almost certainly greater than the wall thickness.

The main implications of this analysis are that it provides for and explains failures from very shallow cracks after a few hundred rounds to failure from very deep cracks after tens of thousands of rounds. The short life failures would in practice be disastrous, whereas the very long lives take us back to the desirable state where the life is determined by wear and fatigue is no longer a problem. However, from a designers point of view it must be known how to make use of these effects since it is not clear what factors control the mode of failure. Obviously the choice of steel will be determined by economic and availability factors and the normal process of using the best quality that can be economically justified will be used. Unfortunately the more significant effect of crack configuration is not so easily dealt with. As pointed out earlier the normal mode of crack initiation in gun barrels is craze cracking which naturally leads to multiple cracking. This is only a metastable condition since any crack which momentarily grows deeper than the rest will have a higher ΔK value and therefore grow more rapidly. The process is, therefore, self sustaining and the situation would soon lead to a single crack condition with the consequent short fatigue life. It is known, however, from examination of fatigued gun barrels, that multiple cracking does persist to quite deep cracks and represents the major part of the fatigue life.

The life will therefore depend to a large extent on the stability of the crack pattern and some measure of this can be obtained in the following way. We take the measure of stability as the way $\frac{da}{dn}$ varies with a, that is

$\frac{d}{da} \left(\frac{da}{dn} \right)$. To simplify the analysis here the Paris crack growth law is used.

We have

$$\frac{d \left(\frac{da}{dn} \right)}{da} = \frac{d(CAK^m)}{da} \quad (13)$$

and from (3) this gives

$$\begin{aligned}
\frac{d\left(\frac{da}{dn}\right)}{da} &= \frac{dC \left[\frac{P\sqrt{a} f\left(\frac{a}{T}\right)}{da} \right]^m}{da} \\
&= C \left[m P \sqrt{a} f\left(\frac{a}{T}\right) \right]^{m-1} \left[P \sqrt{a} \frac{df\left(\frac{a}{T}\right)}{da} + \frac{P f\left(\frac{a}{T}\right)}{2a} \right] \\
&= m C K^m \left[\frac{1}{f\left(\frac{a}{T}\right)} \frac{d f\left(\frac{a}{T}\right)}{da} + \frac{1}{2a} \right] \\
\therefore \frac{d\left(\frac{da}{dn}\right)}{da} &= \frac{m da}{dn} \left[\frac{1}{f\left(\frac{a}{T}\right)} \frac{d f\left(\frac{a}{T}\right)}{da} + \frac{1}{2a} \right] \quad (14)
\end{aligned}$$

From equation (14) a number of conclusions can be drawn since the stability decreases with increase in the value of the right hand side. Obviously, therefore, high $\frac{da}{dn}$, that is rapidly growing cracks, will lead to instability.

This will include all such factors as high ΔK , poor material, as also reflected in the value of m , high pressure and large crack depth. Thus stability will always decrease as the fatigue life progresses and it would be expected that poor quality materials would lead to earlier breakdown than with good quality materials.

The other factors affecting stability are determined by the terms in brackets. Of importance is the calibration function $f\left(\frac{a}{T}\right)$ since $\frac{d f\left(\frac{a}{T}\right)}{da}$ will be strongly

negative at low values of a as shown in figure 3. Also how strongly negative this term is will depend on the number of cracks and as the number of cracks is increased the stability will be stronger. Values of

$$\frac{1}{f\left(\frac{a}{T}\right)} \frac{d f\left(\frac{a}{T}\right)}{da} + \frac{1}{2a}$$

have been calculated for three values of a from figure 3.

a (mm)	Stability function
1.25	1.39
5	0.31
16.5	0.10

These results give the surprising effect that the stability from this term will increase as the fatigue life progresses and it will therefore offset the rapid decrease in stability due to $\frac{da}{dn}$.

The overall conclusion on the stability of crack patterns is that all factors leading to longer fatigue will increase stability and further enhance fatigue life. Conversely factors leading to short fatigue life such as poor material and high pressure could produce a premature breakdown in stability with the serious consequence of very early fatigue failure. Therefore the variations in material and performance can have a much greater effect on fatigue life than would appear at first sight. The combination of high strength or poor quality material with high performance can lead to something approaching single crack type of failure from a very shallow crack. By use of better material with appropriate operating conditions (and autofrettage will be important here) the enhanced crack configuration stability will produce failure from deep cracks, generally leak-before-break, after a very long fatigue life.

Although this paper has treated two simple models it is now established that these are operative over much of the fatigue life. It should be mentioned for completeness, however, that there are important factors which have not been taken into account here. The most important, from the crack configuration point of view, is that of crack shape. It is well known that increasing curvature of cracks decreases the value of K. Also as cracks grow in gun barrels they tend to start straight fronted and eventually increase in curvature. Therefore for a fully accurate analysis this factor must be taken into account, particularly in determining crack depth at failure.

Finally it should be pointed out that little mention has been made of the important process of autofrettage. By this technique large compressive stresses can be induced in the bore of the barrel which reduce ΔK and increase fatigue life. Before the analysis used in this paper can be used in such cases it will be necessary to determine K-calibrations which taken into account these large compressive stresses.

Conclusions

The method of prediction of the fatigue life of gun barrels has been used successfully in a number of applications for both failure analysis and life prediction. It is particularly useful for examining the effects of pressure and diameter ratio at levels where no experimental data exists and the effects

of the use of new materials. As a consequence of the predicted material requirements for long fatigue life, that is low fatigue crack growth rate, high fracture toughness and homogeneous structure, alternative steels satisfying these requirements have been introduced resulting in substantial increases in fatigue life and reliable leak-before-break failures.

References

1. Bowie O L and Freese, C E, Elastic Analysis for a Radial Crack in a Circular Ring, Eng Fracture Mechanics 4 (2) 1972 p 315.
2. Williams, J G and Isherwood, D P, Calculation of Strain Energy Release Rates of Cracked Plates by an Approximate Method, Jnl of Strain Anal, 3 (1) 1968, p 17.
3. Westmann, R A, Pressurised Star Crack, Jnl of Math & Phys, 43, 1965, p 191.
4. Cartright, D J, and Rooke D P, Approximate Stress Intensity Factors Compounded by Known Solutions, Eng Fracture Mech, 6 (3), 1974, p 563.
5. Tweed, J, and Rooke D P, The Stress Intensity Factor for a Crack in Symmetric Array Originating from a Circular Hole in an infinite Solid. Jnl Eng Sci, 13, 1975, p 653.

FAILURE OF A 175MM CANNON TUBE AND THE RESOLUTION
OF THE PROBLEM USING AN AUTOFRETTAGED DESIGN

T. E. Davidson*, J. F. Throop, J. H. Underwood
*Chief, Materials Engineering Section
U. S. Army Benet Weapons Laboratory
Watervliet Arsenal
Watervliet, NY 12189

INTRODUCTION

History of Failure

In April of 1966 a catastrophic failure of a 175mm Army gun tube occurred during firing. The overall size of the 175mm gun tube is 7.0 in. inner diameter, 14.7 in. outer diameter in the region of the failure, 35 ft. long. A brittle fragmentary failure occurred near the breech end of gun tube no. 733 in the area from the point at which the breech assembly attaches to the tube to a point about 10 ft. from the breech. The tube broke into 29 fragments which were scattered over an area ranging up to 4000 ft. from the failure sight. Figure 1 shows the fragments reassembled in their appropriate axial position along with the breech assembly, still intact. This was the first such failure of the 175mm gun tube.



Figure 1. Fragments of 175mm Gun Tube No. 733

The extent of the fragmentation and distance to which fragments were thrown are both indications of a classically brittle failure. Apparently very little energy was absorbed in plastic deformation of the tube during failure. An indication of the lack of plastic deformation was the relatively flat fracture surfaces on the tube fragments; there was generally little or no indication of a 45° shear lip which nearly always occurs in a ductile fracture. The objectives of the investigation which ensued were to determine the cause of the brittle failure and to recommend both short range and long range changes in the gun tube specifications and design which would prevent any brittle failure from occurring.

Preliminary Technical Information

Information available to the investigators at the time of the failure

is the following. The chemical composition of the gun tube forging was not specified but was generally a Ni-Cr-Mo steel very similar to the composition of AISI 4335. The forging was made to the following specifications: 170-190 ksi yield stress, reduction-in-area single-test-minimum of 9% and minimum average of 15%, -40°F charpy energy single-test-minimum of 6 ft-lb and minimum average of 10 ft-lb. The ambient air temperature at the time of failure was 81°F. The gun was being fired at two minute intervals which resulted in a tube temperature of about 200°F. The firing history of the gun tube up to failure was a total of 600 rounds fired, 373 rounds at a nominal peak pressure of 50 ksi and 227 rounds at a nominal peak pressure of 22 ksi. The round being fired at the time of the failure was that with peak pressure of 50 ksi under nominal firing conditions.

The most pertinent information related to the failure was obtained from the fracture surfaces of the gun tube fragments. The brittle nature of the failure was shown in part by the flat fracture surfaces, as has been discussed. More important was the nature of the fracture surface at the location which appeared to be and was subsequently quite definitely shown to be the source of the failure. A photo of this failure initiation location is shown in Figure 2. The crack which initiated the brittle failure

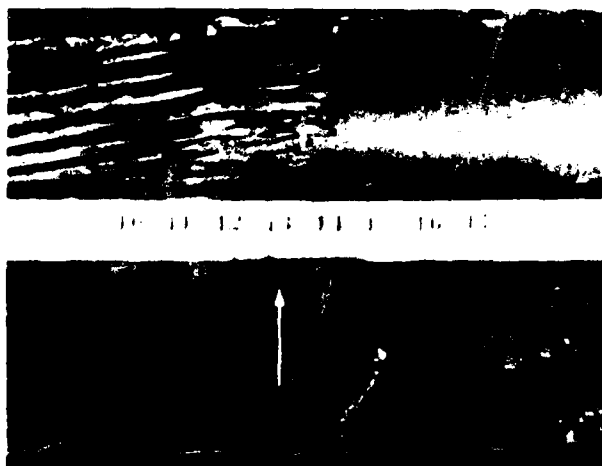


Figure 2. Failure Initiation Location of 175mm Gun Tube No. 733

could be clearly delineated due to its darkened surface, apparently due to combustion products deposited during firing. The crack was considered to be a fatigue crack due to its relatively smooth surface and the presence of combustion products. It was semi-elliptical in shape with a minor-axis depth into the tube wall of 0.37 in. and a length along the tube axis of 1.10 in. Two basic questions to be answered by the investigation were how did a fatigue crack grow so quickly to this size and how did a crack of this

size become the critical size crack for brittle failure.

FORMULATION

Possible Causes of Failure

As a result of the failure sight investigation and the analyses of existing and new test results pertaining to the 175mm gun tube, some possible causes of failure could be eliminated from consideration. An occurrence which could account for many of the features of the failure is a higher than expected pressure during firing. This could account for two items of primary concern, the faster than expected crack growth rate and the smaller than expected critical crack size. Inspection of the gun tube fragments and the breech assembly revealed no evidence of an overpressure; there was no indication of deformed rifling or deformation of the breech components which would be expected with an overpressure. Also significant was the lack of shear lips on the fracture surfaces, for if the gun tube had adequate toughness and failed due to an overpressure, shear lips would have been expected. Finally, several rounds of the group being fired at the time of the failure were available for inspection and testing. Nothing was found which could account for an overpressure.

The possibility of environmentally assisted fracture was considered. Embrittling environments were certainly present in the firing products, including water vapor and hydrogen sulfide, and firing products were present in the crack, as discussed in relation to Figure 2. But the nature of the loading can rule out most types of environmentally assisted fracture. The sustained tensile stress required for stress corrosion cracking and hydrogen embrittlement cracking is not believed to have been present. The tensile stress at the inner radius of the tube due to firing pressure is applied for about 20×10^{-3} sec., which is insignificant as a sustained loading time. No significant residual tensile stress due to heat treatment was expected, due to the low heating and cooling rates of such a large forging. Sach's boring-out measurements of residual stress (1) indicated a maximum tangential stress of +5 ksi at the inner radius which decreased to near zero in less than 0.1 in. from the inner radius. Using the maximum value of tensile stress and a crack length of 0.1 in., the calculated stress intensity factor is

$$K_I = 1.12\sigma\sqrt{\pi a} = 3.1 \text{ ksi } \sqrt{\text{in.}} \quad [1]$$

This value is an upper limit of the K_I due to the residual stress, because Eq. 1 is the expression for a constant value of stress, as opposed to the decreasing value which was measured. Nevertheless, the value of $3.1 \text{ ksi}\sqrt{\text{in.}}$ is still an order of magnitude below typical values of $K_{I_{\text{SCC}}}$ for alloy steels of the type considered here.

The type of environmentally assisted fracture which was considered possible is environmentally assisted fatigue crack growth, in which the presence of environment in the time period between firings lowers the

resistance to fatigue crack growth for subsequent firing. The most deleterious effect is envisioned to occur when there is a period of several days between groups of firing cycles, which can occur during typical service.

The effect of loading rate on the fracture of the gun tube was also considered as a possible contributing factor. However, it was eliminated as a possibility because the loading rate applied to the tube during firing is below the range in which there are significant effects. The pressure rise time for the tube is about 10×10^{-3} sec. If in this time the K_I associated with a typical crack in the tube increases to $100 \text{ ksi} \sqrt{\text{in.}}$, a reasonable upper limit as is shown in an upcoming section, the stress intensity factor rate is $10^4 \text{ ksi} \sqrt{\text{in.}}/\text{sec}$. Tests with the same type of material considered here (2) have shown generally less than 5% reduction in K_{Ic} for this loading rate.

Proposed Cause of Failure

In brief statement, the proposed cause of failure of the gun tube under discussion is (a) crack initiation from the inner radius due to a heat checking process, (b) a faster than expected fatigue crack growth rate due to locally poor fatigue-crack-resistance of the material and possibly due to the presence of an embrittling environment, and (c) final brittle failure at a smaller than expected critical crack size due to generally poor fracture toughness, K_{Ic} , of the material. In order to describe this failure process in more detail, we give the following general information regarding cracking in gun tubes and specific test results from the tube that failed and other similar tubes.

Thermally induced cracking, often referred to as heat checking, always occurs in gun tubes in which the hot firing products impinge directly on the inner radius of the tube. The 175mm tube is of this type. The heat checking occurs as the result of thermal stresses in a thin surface layer at the inner radius which has also undergone metallurgical transformations and related embrittlement by the thermal cycling. For the temperatures developed in the 175mm tube using the 50 ksi round, the heat checking becomes nearly fully developed after about 10 rounds. The heat checking results in a random network of cracks in a heat affected layer of up to 0.05 in. depth. So a 0.05 in. deep crack oriented normal to the tangential stress, the orientation of concern, must be considered to be present essentially from the first firing cycle.

Following initiation of the crack by heat checking, the cyclic growth occurred at a faster rate than expected, due primarily, we believe, to poor material properties. The microstructure of the material was acceptable, a tempered martensite structure as shown in the optical micrograph in Figure 3. But replica-electron-fractography showed predominantly intergranular and cleavage fracture on the fracture surfaces near the failure initiation point, see Figure 4. Temper embrittlement is believed to be a contributing cause of this brittle fracture mode.

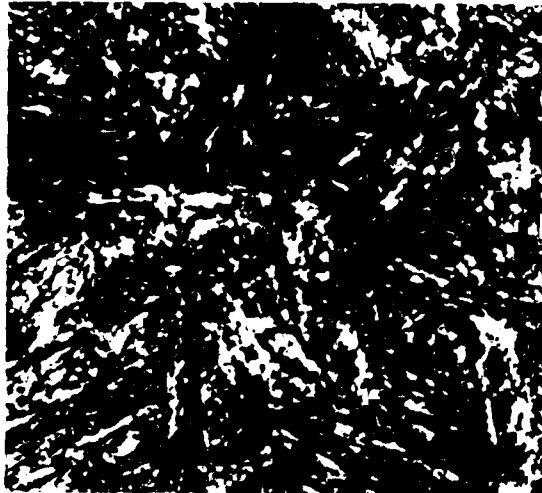


Figure 3. Microstructure of Tube No. 733 Near Failure, 1000X



Figure 4. Fracture Surface of Tube No. 733 Near Failure, 6500X

In addition, a second phase was often observed on the fracture surfaces at the prior austenite grain boundaries. These indications of brittle fracture modes provide the basic explanation for the faster than expected cyclic crack rate. Material properties measured from fragments near the failure location tend to verify the fractographic results. Table 1 shows the results of reduction-in-area, charpy energy, and fracture toughness measurements from locations as near as possible to the failure and locations about 4 ft. toward the muzzle and breech, respectively, from the failure.

TABLE 1. Fracture Related Properties of Tube No. 733

<u>Location</u>	<u>Near Failure</u>	<u>Toward Muzzle</u>	<u>Toward Breech</u>
+70°F reduction-in-area	9 - 28%	17 - 22%	18 - 34%
-40°F charpy energy	4.5-6.5 ft.-lb.	7.5-8.5 ft.-lb.	4.0-8.5 ft.-lb.
+70°F fracture toughness	81-83 ksi $\sqrt{\text{in.}}$	67-90 ksi $\sqrt{\text{in.}}$	-----

The generally lower reduction-in-area and charpy energy values near the failure location is apparent. This is in line with the fractographic results and also can explain how the properties measured by the manufacturer at the ends of the gun tube forging could be within specification while at the same time the charpy energy values near the failure location are significantly below specification. Table 2 shows the chemical composition and the tensile mechanical properties measured from the failed tube. No significant variation in these measurements was noted with respect to position in the tube.

TABLE 2. Chemical Composition and Mechanical Properties of Tube No. 733

<u>Weight %</u>							<u>Yield</u>	<u>Ultimate Tensile</u>	<u>Elongation</u>
Ni	Cr	Mo	Mn	C	V	S	Stress, ksi	Stress, ksi	%
1.79	1.16	0.68	0.69	0.36	0.14	0.008	171	201	10

With regard to the final fast fracture of the tube, the poor properties near the failure location, as described in the foregoing paragraph, certainly had a deleterious effect. Some indication of the effect of Charpy energy and fracture toughness on the crack size and total cycles at final fracture can be obtained from the data in Table 3. Shown here is a summary of fracture data (1,3) from a group of thirty-five 175mm gun tubes, some of which were being tested at the time of the failure of Tube No. 733. Data from 4 tubes with complete test information and typical data for the whole group are compared with the data from Tube No. 733. Each tube was fired several hundred 50 ksi rounds and was then cycled to failure in the laboratory at the same pressure. The general trend toward lower cyclic life and smaller critical crack size for tubes with low Charpy energy and fracture toughness can be seen in the data. The nominal value of 80 ksi $\sqrt{\text{in.}}$ shown for Tube No. 733 could be an overestimate of K_{IC} at the failure location because a value as low as 67 ksi $\sqrt{\text{in.}}$ was measured not far from the failure location.

TABLE 3. Fracture Data for 170-190 ksi Yield Stress 175MM Gun Tubes

Tube No.	Firing Cycles	Total Cycles to Failure	Yield Stress ksi	Charpy Energy ft-lb	Fracture Toughness ksi $\sqrt{\text{in.}}$	Critical a in.	Crack Size a/2c -
733	373	373	171	6	80	0.37	0.33
863	1005	1011	184	9	94	1.7	0.41
1131	330	9322	182	14	129	1.7	0.10
1382	1005	1411	185	11	98	1.5	0.36
1386	1705	4697	181	14	106	1.8	0.30
typical values from 35 tubes		4000	180	12	110	1.5	0.35

ASSESSMENT

By using the loading, the tube and crack geometry, and the measured material properties pertaining to the failed tube, it is possible to determine to what extent the proposed failure process is a realistic description of the actual failure. Then, based on this assessment, the changes in the specifications and design of the gun tube which are required to prevent brittle failure can be made with reasonable confidence.

Applied K_I Analysis

The most important step in analyzing the failure is the determination of the K_I which was applied to the tube. Bowie and Freese (4) have provided the solution for a loading and geometry close to that of concern here. They give K_I for an internally pressurized cylinder of finite wall thickness with a straight-fronted crack. This matches the gun tube failure conditions except for the semi-elliptical-shaped crack in the tube, and this can be taken into account. Their K_I results are in the form

$$K_I = f(a/w, r_2/r_1) P\sqrt{\pi a} \quad [2]$$

and results are given for a range of crack depth-to-wall thickness, a/w , and outer-to-inner radius, r_2/r_1 . Considering first the condition for the maximum extent of heat checking, the value of a/w is 0.05 in./3.90 in. = 0.013, r_2/r_1 is 2.10, the pressure, P , is 50 ksi, and the crack must be considered as straight-fronted. For these conditions K_I is

$$K_I = 2.87 P\sqrt{\pi a} = 57 \text{ ksi}\sqrt{\text{in.}} \quad [3]$$

For the condition at failure of Tube No. 733, a/w is 0.095, r_2/r_1 and P are the same, and K_I , if the crack were straight fronted, is

$$K_I = 2.70 P\sqrt{\pi a} \quad [4]$$

To account for the semi-elliptical shape of the actual crack, the ratio of K_I for the same shape crack in a finite thickness plate in tension to K_I for a straight-fronted crack in a finite plate in tension (5) can be applied to Equation 4. For the appropriate a/w and $a/2c$ values this ratio is 0.62. Applying this estimate of the crack shape effect to Equation 4 gives

$$K_I = 1.67 P\sqrt{\pi a} = 90 \text{ ksi}\sqrt{\text{in.}} \quad [5]$$

a reasonable estimate, we believe, of K_I at final failure of Tube No. 733.

Fatigue Crack Growth Analysis

A representation of the fatigue crack growth which occurred from the starting situation of a 0.05 in. heat checking crack to the final failure of Tube No. 733 can be obtained by integrating the fatigue crack growth rate expression

$$da/dN = C \Delta K_I^3 \quad [6]$$

The value of C in Equation 6 is taken as 3.4×10^{-10} with units appropriate to da/dN in inches/cycle and ΔK_I in $\text{ksi}\sqrt{\text{in.}}$. This value was obtained from fatigue-crack-growth-rate tests in steel of similar composition and mechanical properties to that of Tube No. 733 using laboratory specimens with a known K_I solution. The expression for ΔK to be used in the integral form of

Equation 6 is

$$\Delta K_I = 2.27 P\sqrt{\pi a} \quad [7]$$

which is the same form as Equations 3 and 5; the constant 2.27 is determined simply by using the average of the values from Equations 3 and 5. This gives a reasonable estimate of ΔK_I for the relatively short range of crack length considered here; a more sophisticated approach seems unnecessary, considering the approximate representation of crack shape effects in Equation 5. Using Equations 6 and 7 the estimate of cyclic life for the failed tube is

$$N_f - N_i = \int_{a_i=0.05}^{a_f=0.37} \frac{da}{C(2.27P\sqrt{\pi a})^3} = 2070 \text{ cycles} \quad [8]$$

Analysis versus Actual Fracture Behavior

With regard to the calculated values of K_I , Equations 3 and 5, we believe the analyses are good estimates of the actual K_I applied to Tube No. 733. This is based primarily on the good agreement between the calculated K_I at failure, 90 ksi $\sqrt{\text{in.}}$, and the high end of the range of measured K_{IC} , 67-90 ksi $\sqrt{\text{in.}}$.

With regard to the fatigue crack growth and life analysis, the large difference between the calculated cyclic life, 2070 cycles, and the actual life, 373 cycles, is attributed to the low fracture toughness of the material. Although fracture toughness is generally observed to have little effect on fatigue crack growth rate when K_{max} during fatigue is significantly below K_{IC} , a quite different situation is expected when K_{max} approaches K_{IC} , and this is the situation for Tube No. 733. Even at the start of fatigue crack growth the calculated value of K_{max} , 57 ksi $\sqrt{\text{in.}}$ (see Equation 3), is already only 10 ksi $\sqrt{\text{in.}}$ below the low end of the range of measured K_{IC} . So from the start, K_{max} was close to K_{IC} , and as a result, the fatigue crack was growing at a significantly faster rate than that represented by Equation 6. The constants in Equation 6 were determined for zero to tensile loading with K_{max} in the range 20-75 ksi $\sqrt{\text{in.}}$ but in a material with a K_{IC} of 130 ksi $\sqrt{\text{in.}}$; so no effect of K_{max} is included in Equation 6.

The significantly faster actual crack growth rate in Tube No. 733 could in part be due to the effect of environment already mentioned as a possibility. There appears to be no way to separate this effect from the K_{max} effect just discussed. We believe that the effect of K_{max} approaching K_{IC} is certainly more significant and could easily account for all of the difference between the actual cyclic crack-growth-rate and that predicted by analysis.

CONCLUSIONS

Short Range Changes in Specifications

Action was required within a matter of days following the failure of

Tube No. 733 in order to prevent any further failure. The decision made was to remove from service any gun tubes with fracture related mechanical properties, as reported by the forging manufacturers, in the same range as those of the failed tube. Considered were tensile elongation, reduction-in-area, and -40°F charpy energy, with emphasis placed on the latter. In general, tubes with values of charpy energy below 10 ft-lb were removed from service. In addition, for the tubes with charpy energy of 10 ft-lb or above, the fatigue life was lowered from 800 to 300 rounds, that is, the tubes were removed from service after 300 rounds with 50 ksi pressure. Following these actions no further field failures occurred.

An interim and still relatively short range decision was made to lower the yield stress specification from the original 170-190 range to a range of 160-180 and to raise the -40°F charpy energy minimum from 6 to 15 ft-lb. These changes could be made with no effect on the fabrication process nor on the configuration of the gun tube, so interchangeability of the weapon system was unaffected. The effect of these specification changes on the gun tube fracture behavior can be seen in the data (3) of Table 4, which summarizes the same tests as those performed on the 175mm gun tubes with the original specifications. Comparison of Tables 3 and 4 shows the significant

TABLE 4. Fracture Data for 160-180 ksi Yield Stress Gun Tubes

Tube No.	Firing Cycles at 50 ksi	Total Cycles to Failure at 50 ksi	Yield Stress ksi	-40°F Charpy Energy ft-lb	-40°F Fracture Toughness ksi $\sqrt{\text{in.}}$	Critical Crack Size a in.	a/2c
2108	400	12,377	167	32	121*	3.8 (thru wall)	0.27
1785	400	10,033	183	28	122*	3.8 (thru wall)	0.39
1910	400	7,677	171	31	126*	2.3	0.12

* invalid according to ASTM size requirements for a K_{Ic} test

increases in cyclic life and critical crack size as well as in fracture toughness which occurred as a result of the changes in material specification. However, it must be stated that the charpy energy values of the tubes listed in Table 4 were somewhat above the values from most production tubes, which were typically about 20 ft-lb after the specification changes.

Long Range Design Change - Autofrettage

The long-range design change in the 175mm gun tube, which resulted in part from the failure of Tube No. 733, was a change to an autofrettage design. A particular advantage of autofrettage, considering the brittle fracture problem with the 175mm tube, is that it makes possible a leak-before break failure condition for the tube. The interim change to 160-180 ksi yield stress material had shown that, at least for charpy energy values above normal, leak-before-break can occur, see Table 4. So, by lowering

the yield stress further and restoring the elastic strength of the tube using autofrettage, it is possible to routinely obtain a high enough fracture toughness to insure leak-before-break. An equally important advantage of autofrettage is that the residual compressive stress produced by the process reduces the fatigue-crack-growth-rate and thus increases the life of the tube.

The new design 175mm tube, which is the current design, is a partial autofrettage using a tube material of 140-160 ksi yield stress and 25 ft-lb minimum charpy energy. The tube is subjected to a hydraulic pressure (about 120 ksi) which causes plastic deformation up to halfway through the tube wall. The tangential residual stress distribution which results from this 50% autofrettage is shown in Figure 5. Also shown is the tangential stress

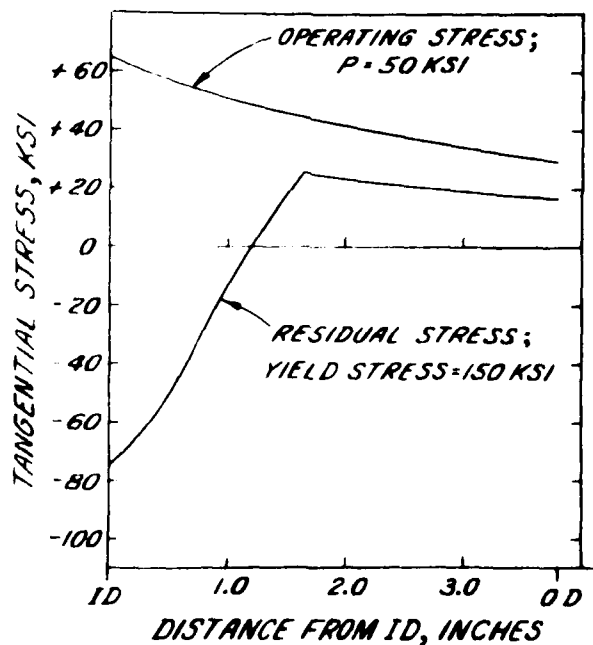


Figure 5. Residual and Operating Stresses in 175mm Autofrettaged Tube

produced by 50 ksi internal pressure. Notice that the residual, compressive stress at the inner radius is higher in magnitude than the operating tensile stress. The effect of this combination of residual and applied stress was investigated using the same type of tests as used with the non-autofrettaged tubes discussed in preceding sections. Table 5 summarizes the results from these tests. The tests did not include any firing cycles; at the first stages of development of the autofrettaged 175mm tube, partial length tubes were used, rather than full length tubes which are required for firing, However,

the autofrettaged tubes were compared directly with the original non-autofrettaged tubes under the same conditions, that is, with no preliminary firing cycles.

TABLE 5. Fracture Data for 140-160 ksi Yield Stress Autofrettaged Gun Tubes and for 170-190 Yield Stress Non-Autofrettaged Gun Tubes.

Tube No.	Firing Cycles at 50 ksi	Total Cycles to Failure at 50 ksi	Yield Stress ksi	-40°F Charpy Energy ft-lb	-40°F Fracture Toughness ksi√in.	Critical Crack Size a in.	a/2c
<u>Autofrettaged</u>							
1A	0	20,547	144	27	132*	3.8	0.20
4A	0	23,356	152	24	121*	3.8	0.20
6A	0	25,127	144	27	131*	3.8	0.20
7A	0	22,385	149	24	124*	3.8	0.14
9A	0	21,677	156	18	114*	2.7	0.27
11A	0	25,815	144	27	126*	3.8	0.22
<u>Non-Autofrettaged</u>							
4N	0	10,086	184	11	108	1.8	0.30
5N	0	10,630	185	12	102	2.0	0.33
6N	0	9,565	185	13	103	1.4	0.20

* invalid according to ASTM size requirements for a K_{IC} test

The considerably longer cyclic life of the autofrettaged tubes is apparent in Table 5. Autofrettage resulted in more than a factor of 2 increase in life. Equally significant is the trend toward stable fatigue crack growth all the way through the wall thickness and a leak-before-break failure mode. A typical fracture surface from the autofrettaged tubes is shown in Figure 6. The fatigue crack broke through the wall along a 2 inch length on the outer diameter. The only tube which failed by fast fracture with a critical crack depth of less than the wall thickness was tube no. 9A. As shown in Table 5, the charpy energy measured from this tube was well below the current specification of 25 ft-lb, and the fracture toughness was the lowest of the six tubes.

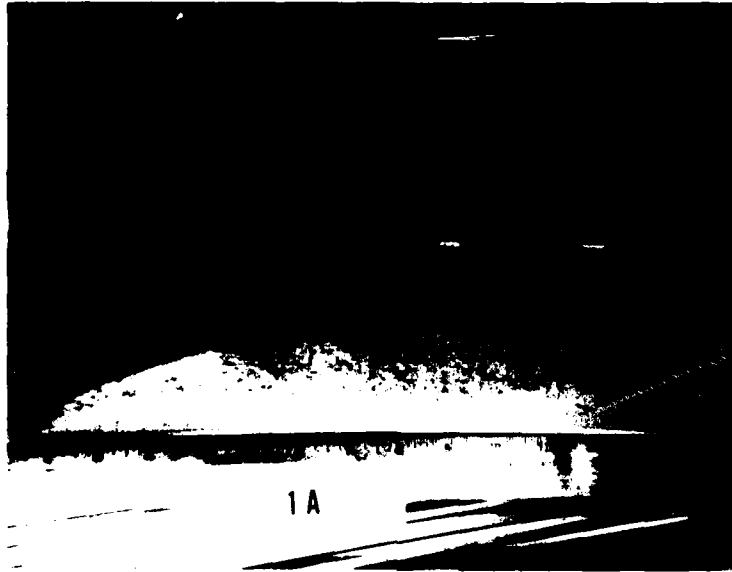


Figure 6. Fracture Surface of 175mm Autofrettaged Tube No. 1A

Closing

The high cyclic life and the leak-before-break failure observed in the autofrettaged tubes discussed here was observed in additional 175mm development tests, including tests with combinations of firing and laboratory cycling. For 175mm tubes with fracture toughness above 120 ksi in., which corresponds to the current charpy specification of 25 ft-lb, we have found that leak-before-break is always the mode of final failure. This experience and all the knowledge gained from the failure and the redesign of the 175mm gun tube has been applied to the fracture mechanics design of various gun tubes and other weapon components.

There are two key limitations in the application of fracture mechanics to weapons and to structures in general. The first is the lack of a general K_I solution of proven accuracy for surface cracks in finite geometries. With the large amount of experimental and analytical work in this area in recent years, it is becoming less of a problem. The second limitation is the lack of information on the effect on K_I of a residual stress distribution. Not only are there no solutions available, there seems to be no quantitative information available for use in analyzing crack growth in the presence of residual stress. This is an obvious area for future work.

REFERENCES

1. Davidson, T. E., Reiner, A. N., Throop, J. F., Nolan, C. J., "Fatigue and Fracture Analysis of the 175mm M113 Gun Tube", Benet Laboratories Technical Report, WVT-6822, Nov. 1968.
2. Kendall, D. P., "The Effect of Loading Rate and Temperature on the Fracture Toughness of High Strength Steels", Materials Research and Standards, v. 10, no. 12, Dec. 1970, 14-33.
3. Davidson, T. E., Throop, J. F., Reiner, A. N., Austin, B. A., "Analysis of the Effect of Autofrettage on the Fatigue Life Characteristics of the 175mm M113 Gun Tube", Benet R&E Laboratories Technical Report, WVT-6901, Jan. 1969.
4. Bowie, O. L., and Freese, C. E., "Elastic Analysis for a Radial Crack in a Circular Ring", Engineering Fracture Mechanics, v. 4, no. 2, June 1972, 315-321.
5. Rice, J. R., and Levy, N., "The Part-Through Surface Crack in an Elastic Plate", Journal of Applied Mechanics, v. 89, Mar. 1972, 185-194.

Section 4 SURFACE VEHICLES

A FRACTURE MECHANICS BASED ASSESSMENT OF THE RAILWAY RAIL FAILURE PROBLEM IN THE U.K.

D.F. Cannon C.Eng. M.I.Mech.E.

British Railways Board
Research and Development Division
Railway Technical Centre
Derby
England

INTRODUCTION

Despite the development of improved service flaw detection methods, such as the ultrasonic rail car, British Rail have experienced an increasing number of rail failures (1). On average about two rail fractures occur each day; however, the total number of "failures" reported, which includes cracked rails, is much higher than this, for example, in 1974 about 10 "failures" were reported each day. The replacement of cracked and broken rail costs BR a considerable amount of money; furthermore, broken rails have caused major derailments.

Most rail failures result from:

- (i) The initiation of a fatigue crack from a pre-existing defect or stress raiser.
- (ii) The stable propagation of the fatigue crack.
- (iii) The sudden unstable fracture of the rail when the fatigue crack reaches a critical size for a particular applied stress. The final fracture always occurs by the brittle cleavage mechanism.

In some cases the critical crack can be only 1-2 mm deep. The detection of cracks less than this size, on a rail system of 22 000 miles of running track is a formidable exercise.

The development of a fatigue crack and final fracture depends upon:

- (i) The existence of pre-existing defects and other stress-raisers.
- (ii) The stresses and strains, both active and passive, experienced by the rail.
- (iii) The material response to the imposed stresses and strains.

The locations of the more common cracks found in the rail section are shown in Fig.1. Failures resulting from the "star-crack" and the rail running surface crack arising from wheelburn (also known as engine burn) as particularly hazardous.

The "star-crack" failure originates from fatigue crack initiation at the periphery of fish bolt holes at rail joints. Fatigue crack growth occurs along a plane roughly at 45° to the horizontal and final fracture may initiate when this crack has extended only 1 or 2 mm (1). The unstable final fracture generally continues on the 45° plane so producing a triangular piece of rail which may fall out or become dislodged and form a ramp.

Wheel slip or spin results in heat being generated on the rail running surface. Rapid quenching by the bulk rail, when the wheel moves on, or stops spinning, may result in the usual ferritic/pearlitic structure of the rail steel being transformed to a martensitic one. The transformed material may extend to a depth of 2-3 mm and is soon found to contain cracks of this size. The formation mechanism of these cracks is unclear; however, they provide initiation sites for fatigue crack growth followed by fracture, or simply fracture. Since wheel spin tends to occur over a substantial length of rail it is possible for two or more fractures to take place near to each other and also within a very short time interval.

Both the "star-crack" and wheelburn fractures may result in an interruption of the running surface and clearly a derailment is threatened.

The solution to the rail failure problem is not a simple one and it has been confounded by a lack of knowledge of the service strain environment which is dependent upon variable load inputs and track support conditions. The wear characteristics must also be considered in view of the vast quantities of steel involved. The objectives of the fracture mechanics based assessment of this problem have been concerned with:

- (1) Increasing our understanding of rail failures.
- (2) The evaluation of the effect of modifications of the system on rail failures.

TECHNICAL BACKGROUND

The vast majority of rail steel used in the UK is made to the requirements of BS 11 (2). Specified chemical compositions and actual mechanical properties are given in Tables I and II respectively. The steel has a ferritic/pearlitic structure. Until recently rail steel was produced by the acid bessemer and basic open hearth processes. Almost all BS 11 rail steel is now produced by the B.O.S. concast process route. The steel is rolled to a section designated 113A (fig.1). This is a flat bottomed rail and has a mass of

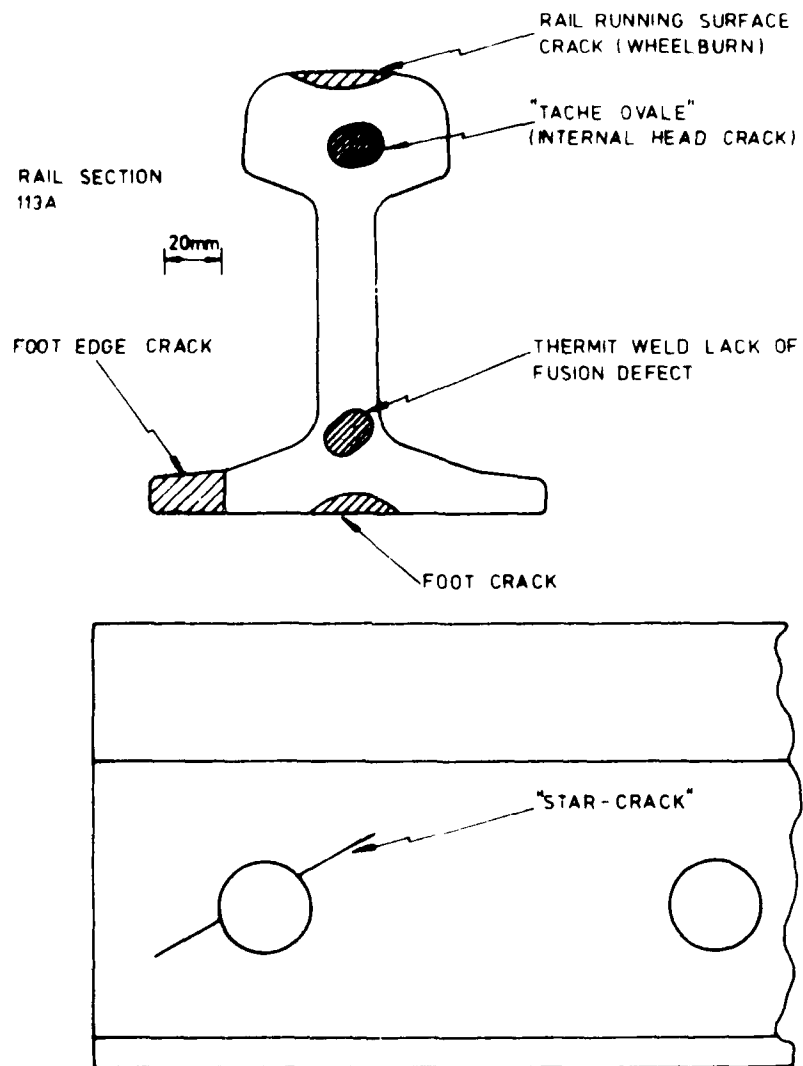


FIG. 1. SOME COMMON CRACK LOCATIONS IN THE RAIL SECTION.

TABLE 1 CHEMICAL COMPOSITIONS OF BS 11 RAILS
TESTED IN THE COLLABORATIVE PROGRAMME

Production Process	BS 11 Spec				Aim Levels*				Rail Maker	Actual C & Mn (approx)		Cast Ident
	C (%)		Mn (%)		C (%)		Mn (%)			C (%)	Mn (%)	
	Max	Min	Max	Min	Max	Min	Max	Min				
Acid Bessemer	0.50	0.40	1.25	0.95	0.50	0.46	1.05	0.95	Z	0.49	1.03	Z1
					0.44	0.40	1.25	1.15		0.44	1.16	Z2
Basic Open Hearth	0.60	0.50	1.25	0.95	0.60	0.56	1.05	0.95	Y	0.60	1.04	Y1
										0.51	1.19	Y2
					0.54	0.50	1.25	1.15	X	0.61	1.03	X1
										0.50	1.15	X2
					0.59	0.56	1.05	1.07	w1	0.59	1.05	w1
										0.56	1.07	w2

* Each rail maker produced two casts which were expected to meet the two aim levels

TABLE 11. TENSILE AND ELONGATION TEST RESULTS

Ball Number (as per Table 1)	Position (as per Table 1)	Condition (as per standard)	Tensile (150°)				Elongation		
			T.S. MPa	20% E.S. MPa	El %	R.A. %	at 150° %	at 150° Temp °C	
Z	Top	Head	797	470	21.1	45.4	4	108	124
	Middle	Head	751	442	16.0	47.0	4	98	111
	Top	Wet	701	411	20.7	55.0	-	75	-
	Middle	Wet	737	425	21.4	45.0	4	80	-
Z (Acid Resister)	Top	Head	775	440	18.7	39.0	5	80	115
	Middle	Head	810	470	17.1	38.0	4	98	125
	Top	Wet	931	486	8.0	15.0	-	>100	-
	Middle	Wet	771	417	19.1	45.0	-	85	-
Y	Top	Head	857	510	18.0	30.0	4	115	123
	Middle	Head	848	497	19.2	30.0	4	105	124
	Top	Wet	840	429	20.0	34.4	4	120	-
	Middle	Head	856	445	18.0	27.7	5	123	114
X (Basic Open Hearth)	Middle	Head	860	405	21.1	27.7	5	107	135
	Top	Head	803	454	18.6	40.0	4	111	110
	Middle	Head	810	473	20.3	40.0	4	111	122
	Top	Wet	811	305	21.1	38.2	-	65	-
W	Middle	Head	882	494	18.2	30.0	4	111	120
	Top	Head	845	406	18.6	30.0	4	128	115
	Middle	Head	845	420	19.4	35.0	4	135	122
	Top	Head	872	430	13.7	25.0	4	116	122
W (Basic Open Hearth)	Middle	Head	862	424	15.7	27.5	4	123	123
	Top	Wet	922	468	10.9	24.0	4	130	-

55.5 kg/m (113 lb/yd).

In the UK the rail experiences temperatures in the range -15 to $+50^{\circ}\text{C}$. To prevent track buckling in continuously welded rail (C.W.R.) the rails are pre-stressed when laid to give a stress free operating temperature of 27°C (80°F) i.e. at temperatures below this the rail experiences an axial tensile stress. Naturally the rail experiences all weather conditions and in some locations it is exposed to sea spray.

In addition to the thermally induced stresses the rail is subjected to:

(1) Active stresses:

- (a) quasi-static stresses arising from the normal running of trains.
- (b) dynamic stresses caused by wheel-rail vertical velocity differentials and ultimately loss of contact between wheel and rail. These stresses can occur because of rail joints, wheel flats, and depressions in the rail head caused by wheelburn.
- (c) dynamic stresses caused by lateral instability of vehicles.
- (d) high frequency stress oscillations caused by the sympathetic vibration of the rail.

(2) Residual stresses:

- (a) arising during manufacture
- (b) as (a) but modified due to the cold working of the rail running surface in service.

Although railways have existed for at least 150 years a full description of the strains experienced by rails has yet to be developed. Amongst others, Timoshenko and Langer (3) considered some aspects of loading and Satoh (4) described an experiment on the Tokaido Trunk Line in Japan which investigated the effect of wheel flats. However, neither of these, or other works known to the author provide sufficient data upon which to build a model of generalised rail strain behaviour. Recent experimental work at BR has now shown that active tensile stresses in the rail head (i.e. in the longitudinal direction) are higher than expected particularly when impact occurs between the wheel and rail. This experimental work was in fact stimulated by the analyses which are about to be described.

There is probably even more doubt as to the magnitude and distribution of residual stresses in rails. This question has been addressed by the European railway administrations through the offices of the O.R.E.

organisation (5) and an example of the results is shown in fig. 2. The generality of the O.R.E. findings has yet to be proven. Work at BR by Allen (6) suggests fair agreement with the O.R.E. work in new rail, but a substantial difference in used rail.

In brief, the only stress which can be reasonably predicted is that due to de-stressing and even that demands a knowledge of rail temperature.

FORMULATION

1. The Fracture Toughness of Newly Rolled Rails

Since practically nothing was known of the fracture toughness characteristics of rail steel an extensive collaborative programme was undertaken by the BRB and British Steel Corporation. The aim of the programme was:

- (a) To establish the potential variation in fracture toughness in both the head and web of rails produced within the limits of the BS 11 specification.
- (b) To provide basic data which could be used to compare:
 - (i) The toughness of rails that fail in service.
 - (ii) The toughness of newly developed rail steels.

In order to satisfy the aims of the programme, four works were asked to provide samples of 113 lb/yd BS 11 rails from two casts of steel. One cast was to have a carbon content near the top and a manganese content near the bottom of the BS 11 specification and the other to have a low carbon and a high manganese content. Two rails, both roller straightened, were to be supplied, one from the top and one from the middle of the ingot.

Fracture toughness tests were conducted at -15°C , the lowest expected service temperature, at low loading rates, on about 170 specimens taken from the rail head and web (fig. 3). Tests were conducted according to the requirements given in (7). Details of the results of this extensive programme are reported elsewhere (8) and are summarised below. Aim and actual analyses are given in Table I. Tensile properties and Charpy impact test data are presented in Table II.

The results of the fracture toughness tests are summarised in Table III. Approximately half of the fracture toughness tests yielded valid K_{IC} data. The most common cause of invalidity was that of excessive crack front curvature, particularly with the square section specimens. Many of the tests were also invalid due to the crack length and/or thickness being less than that necessary to ensure limited plasticity at the crack tip.

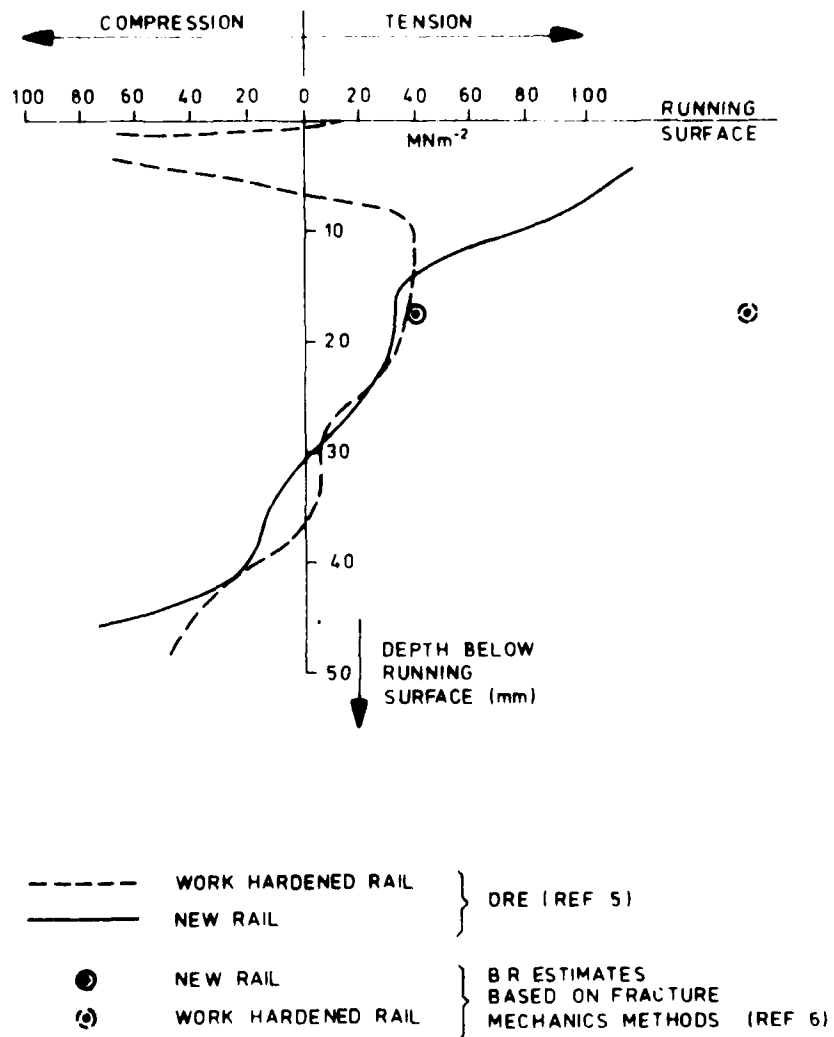
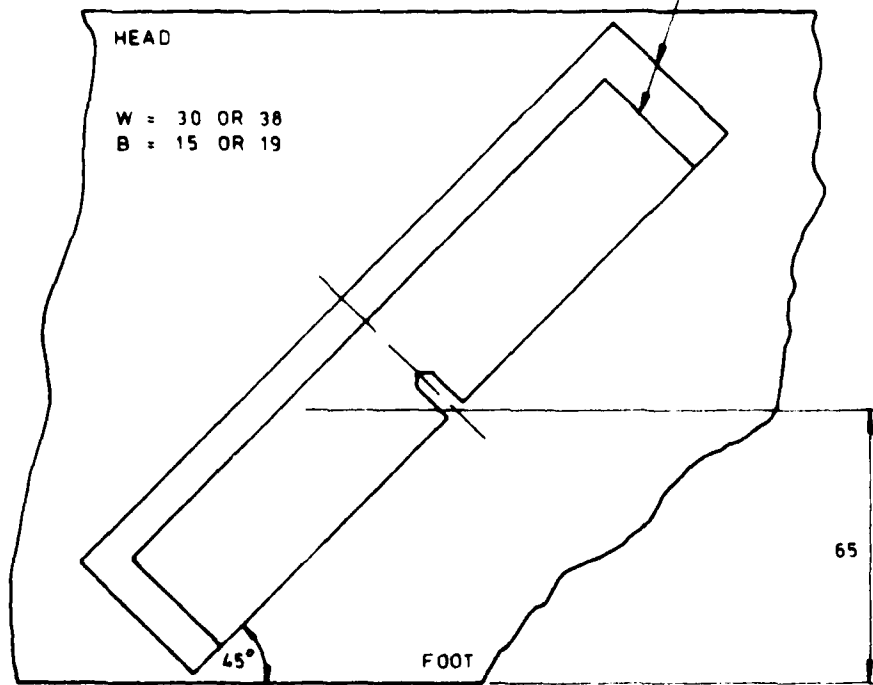
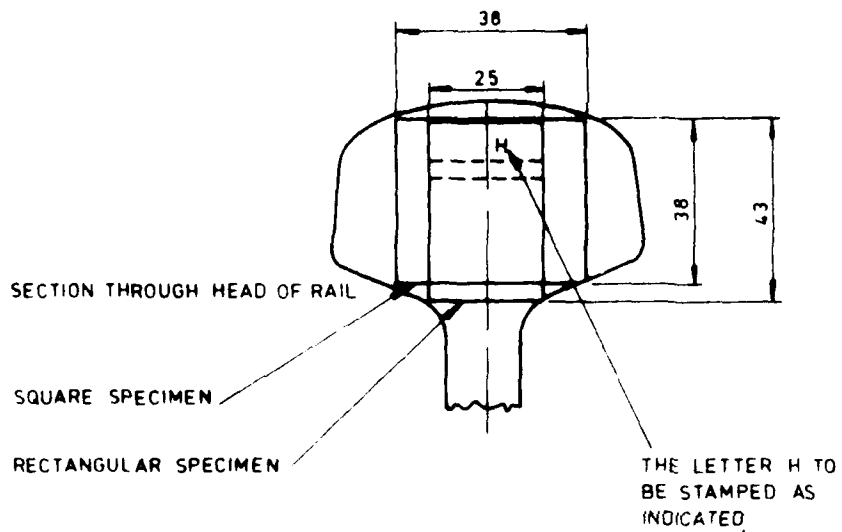


FIG. 2. VARIATION OF LONGITUDINAL RESIDUAL STRESS WITH
DEPTH BELOW RUNNING SURFACE ON THE AXIS
OF SYMMETRY.



ALL DIMENSIONS IN MM

FIG. 3 LOCATION OF TEST PIECES IN THE RAIL.

TABLE III FRACTURE TOUGHNESS (K_{IC}) DATA
(ALL TESTS AT -15°C)

Rail Maker and Process	Cast Ident (see Table I)	Position of rail in ingot	Specimen Position	Specimen Type	No. of K_{IC} results	Mean K_{IC} ($\text{MNm}^{-1.5}$)
7 (Acid Bessemer)	Z1	Top	Head	Square	2	29.1
				Rectangular	4	34.7
			Web	Rectangular	4	29.0
		Middle	Head	Square	6	32.4
				Rectangular	-	-
			Web	Rectangular	4	32.1
	Z2	Top	Head	Square	-	-
				Rectangular	-	-
			Web	Rectangular	4	29.5
		Middle	Head	Square	4	33.7
				Rectangular	2	36.9
			Web	Rectangular	-	-
Y (Basic Open Hearth)	Y1	Top	Head	Square	-	-
				Rectangular	1	41.6
			Web	Rectangular	3	34.3
		Not known	Head	Rectangular	5	35.1
		Middle	Head	Square	1	29.2
				Rectangular	-	-
	Y2	Top	Head	Square	2	33.6
				Rectangular	1	33.4
		Middle	Head	Square	1	35.4
				Rectangular	1	35.7

/Continued

TABLE III (Cont'd)

Rail Maker and Process	Cast Ident (see Table I)	Position of rail in ingot	Specimen Position	Specimen Type	No. of K _{IC} results	Mean K _{IC} (MNm ^{-1.5})
X (Basic Open Hearth)	X1	Top	Head	Square	3	28.4
				Rectangular	4	32.8
			Web	Rectangular	4	29.4
		Middle	Head	Square	2	33.8
				Rectangular	4	32
		X2	Middle	Head	Square	1
	Rectangular				4	37.8
	W (Basic Open Hearth)	W1	Top	Head	Square	-
Middle			Head	Square	2	31.7
W2		Top	Head	Square	-	-
				Rectangular	4	37.0
			Web	Rectangular	3	33.8
		Middle	Head	Square	-	-
				Rectangular	-	-

The fracture toughness data was subjected to a statistical analysis, broadly based on a small sample theory, in order to determine the effects of:-

- (a) Cast composition (principally carbon level)
- (b) Tensile and impact strength
- (c) Rail position in the ingot
- (d) Different manufacturing processes and material sources.
- (e) Position of the sample in the rail (head and web)
- (f) 'square' and 'rectangular' section test pieces on the apparent fracture toughness of the material.

Only the last two factors were found to influence the fracture properties. The average fracture toughness (K_{Ic}) of web material was lower than that of head material by about 12.5%, this figure being based on toughness data obtained from the rectangular type of head test piece. It was also found that the square section head test pieces yielded toughness data about 10% lower than the rectangular type. This may be a result of residual stresses within the rail head.

Since the results showed only limited variability in fracture toughness it is possible to summarise the data as shown in Table IV. It is anticipated that the fracture toughness of BS 11 rail steel at -15°C , will exceed the following levels 98% of the time. Values have been rounded down to the nearest $0.5 \text{ MNm}^{-1.5}$.

Based on the rectangular section head specimens:

$$27 \text{ MNm}^{-1.5}$$

Based on square section head specimens:

$$25.5 \text{ MNm}^{-1.5}$$

Based on web specimens:

$$24 \text{ MNm}^{-1.5}$$

2. Fracture Toughness of failed Rails

During a 12 month period BR Research and Development Division studied every rail failure which occurred within the railway network, the object being to check the composition and microstructure and to measure the initiating crack

size, tensile and fracture toughness properties of the rails concerned. Their fracture toughness was compared to that of unused rails and also, together with crack size, used to estimate the stress levels at fracture.

Fracture toughness specimens were machined from the fractured rails as close to the fracture as possible and orientated such that the fracture propagated in the direction and plane corresponding to that of the fracture in the rail. Tests were performed at the temperature associated with the service failure. This was done so that the most relevant estimate of fracture toughness could be made with respect to the failure thus facilitating the calculation of the failure stress. Examination of the data showed little effect of the temperature within the range encountered. Table V shows the current average fracture toughness of service failed rails together with results of the survey covering unused BS 11 rails previously described. It appears that both the new and failed rail samples are drawn from the same population i.e. that the average rail failure occurs in material which has a toughness typical of BS 11. The analysis of service failure data is still in progress.

The data described here were derived under slow loading whereas in service, cracks were most likely subject to dynamic loading conditions which can influence the toughness of a material. However, the results of dynamic tests (fig.4) show that the toughness of BS 11 rail steel is not influenced by high loading rates, hence the slow rate data may be used with confidence to determine failure stresses.

3. Fatigue crack growth rates

Fatigue crack growth rates have been studied in a variety of rail steels. Tests were carried out to determine crack growth rates as a function of ΔK on specimens tested under load controlled conditions. At BR, both single edge notch three point bend and centre hole notched specimens are used. Tests are conducted in either a high frequency Amsler Vibraphor ($f = 150-200$ Hz) or a servo-hydraulic testing machine ($f = 0.1-50$ Hz). Crack growth is measured either continuously using an electric potential drop method or at intervals optically.

Results for a number of rail steels using centre notched specimens (9) are shown in fig. 5. In general little difference is observed in the crack propagation rates of these steels at a given ΔK range. The figure shows the "scatterband" of the mean values of the $da/dN - \Delta K$ lines, showing a spread of about 3:1 on endurance. Overall differences are considered to be of secondary importance and would in practice be masked by scatter of the individual points.

TABLE IV
 SUMMARY OF BS.11 FRACTURE
 TOUGHNESS DATA

Item	Square Head Specimens	Rectangular Head Specimens	Web Specimens
Mean K_{IC} ($MNm^{-1.5}$)	32.2	35.2	31.1
95% Confidence Limits on the Mean ($MNm^{-1.5}$)	± 1.42	± 1.51	± 1.23
Standard Deviation ($MNm^{-1.5}$)	± 3.29	± 4.0	± 2.77
Number of Valid Results	24	30	23

TABLE V
 FRACTURE TOUGHNESS OF SERVICE FAILED RAIL
 COMPARED TO TYPICAL NEWLY ROLLED RAIL

Position in Rail Section	Average K_{IC} (at various temperatures) of BS.11 associated with rail fractures.	Average K_{IC} (at $-15^{\circ}C$) of Typical Newly Rolled BS.11
Head	36.1	35.2
Web	31.1	31.1

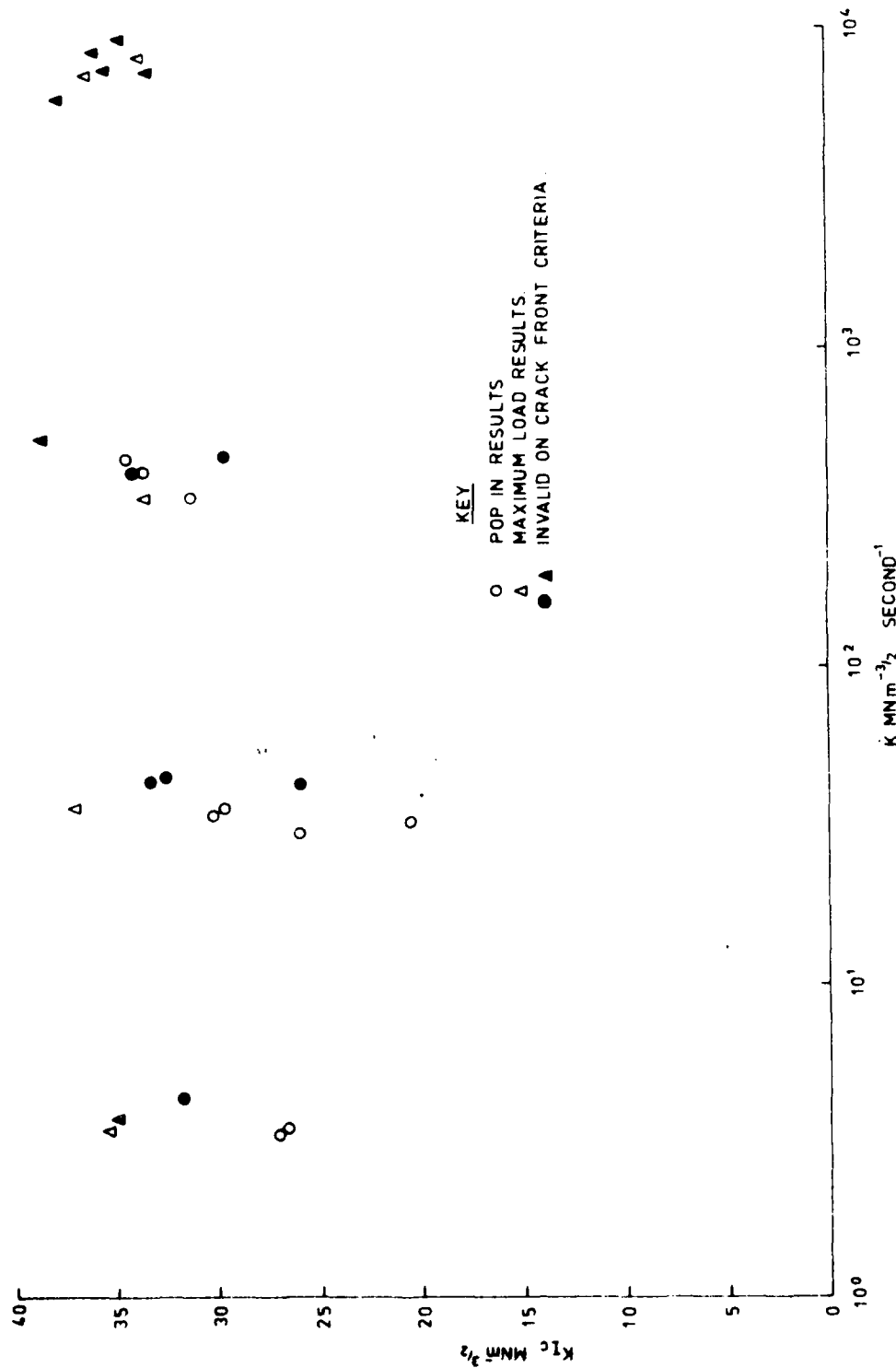
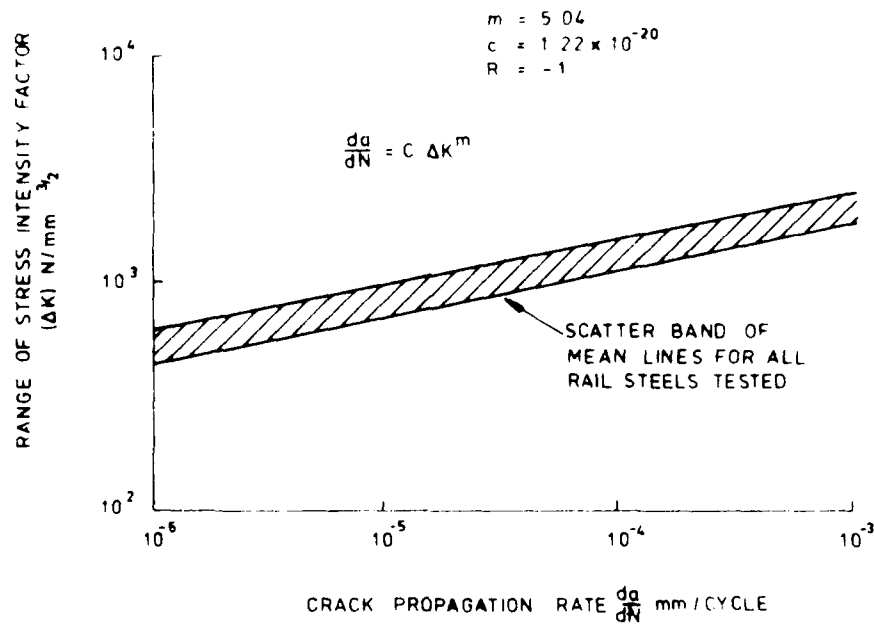


FIG. 4. THE EFFECT OF STRESS INTENSIFICATION RATE \dot{K} ON THE PLANE STRAIN
 FRACTURE TOUGHNESS K_{Ic} OF B.S.11 RAIL STEEL.



MATERIAL	SLOPE "m"	INTERCEPT "c"
BS 11	5.26	3.02×10^{-21}
BS 11 CONCAST	4.63	2.93×10^{-19}
UIC A	4.16	7.73×10^{-18}
UIC B	5.29	1.52×10^{-21}
1% Cr	4.09	1.19×10^{-16}

**FIG. 5. CRACK PROPAGATION RESULTS FOR SOME
RAIL STEELS**

ASSESSMENT

Service Failure Analysis

Because of the uncertainty surrounding the effective strains present in a rail, fracture mechanics was used to estimate the fracture stress associated with actual failures. Attention had therefore to be given to identifying or developing suitable crack tip stress-intensity functions for the common crack geometries and presumed stress distributions.

(a) Star-crack (fig. 1)

Since the fish bolt hole lies close to the rail neutral axis it was assumed that the stress field was predominantly pure shear. Solutions have been given by Bowie (10) for single and double cracks originating at a hole in a plate subjected to uni-axial and bi-axial stress. By adding the uni-axial solution for an applied stress of 2σ , to the bi-axial solution for applied stresses of $-\sigma$ and $-\sigma$ one arrives at applied stresses of $+\sigma$ and $-\sigma$ which is equivalent to pure shear. The solution is based on an idea by Wells and is shown in fig.6.

(b) Surface running cracks (wheelburn fig. 1)

Small semi-elliptic cracks originating at the surface of the rail may be treated using solutions given by Shah and Kobayashi (11) both for pure tension and bending. For deep cracks ($\gg 5$ mm) a solution was developed at BR. For the bending case a finite element energetic approach was used and for the tension case the Williams and Isherwood approximate method was employed (12). The two solutions are given in figs. 7 and 8 respectively. For the bending case (fig. 7) a comparison can be made between the finite element solution and the W and I method.

(c) Taches Ouales (fig. 1)

These defects which originate at hydrogen shatter cracks are totally embedded in the rail head and whilst they are small (say ≤ 25 mm diameter) they may be treated using data by Shah and Kobayashi (11). The actual 'K' calibrations for a rail section (BS 113A), subjected to a bending stress distribution is shown in fig. 9. The tension case can be treated in a similar fashion.

It is beyond the scope of this paper to discuss all of the service failure analyses undertaken. The following description of an analysis of a tache ovale type service failure is of particular relevance to our understanding of the stresses which can occur in service.

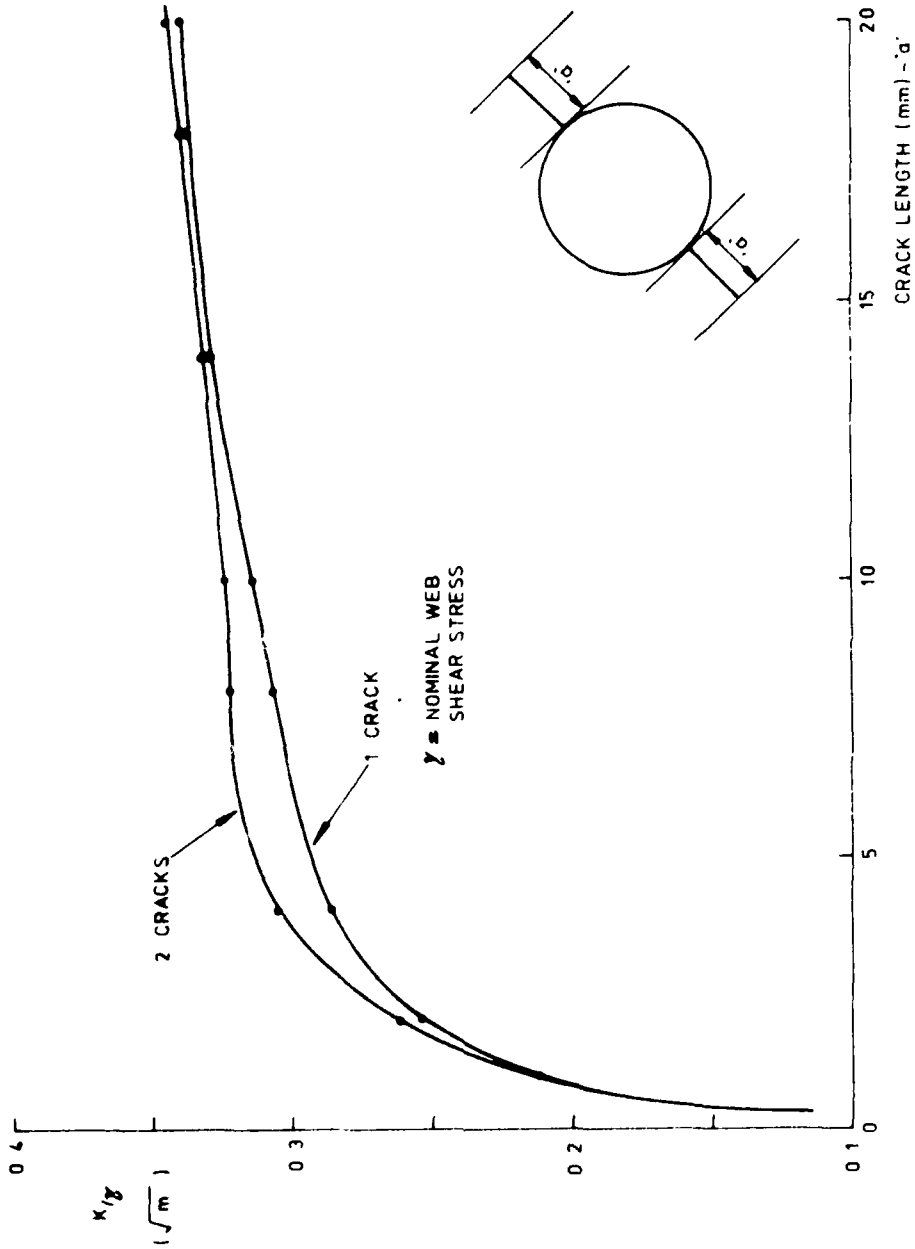


FIG 6. WELLS-BOWIE K-CALIBRATION FOR BOLT-HOLE CRACKS

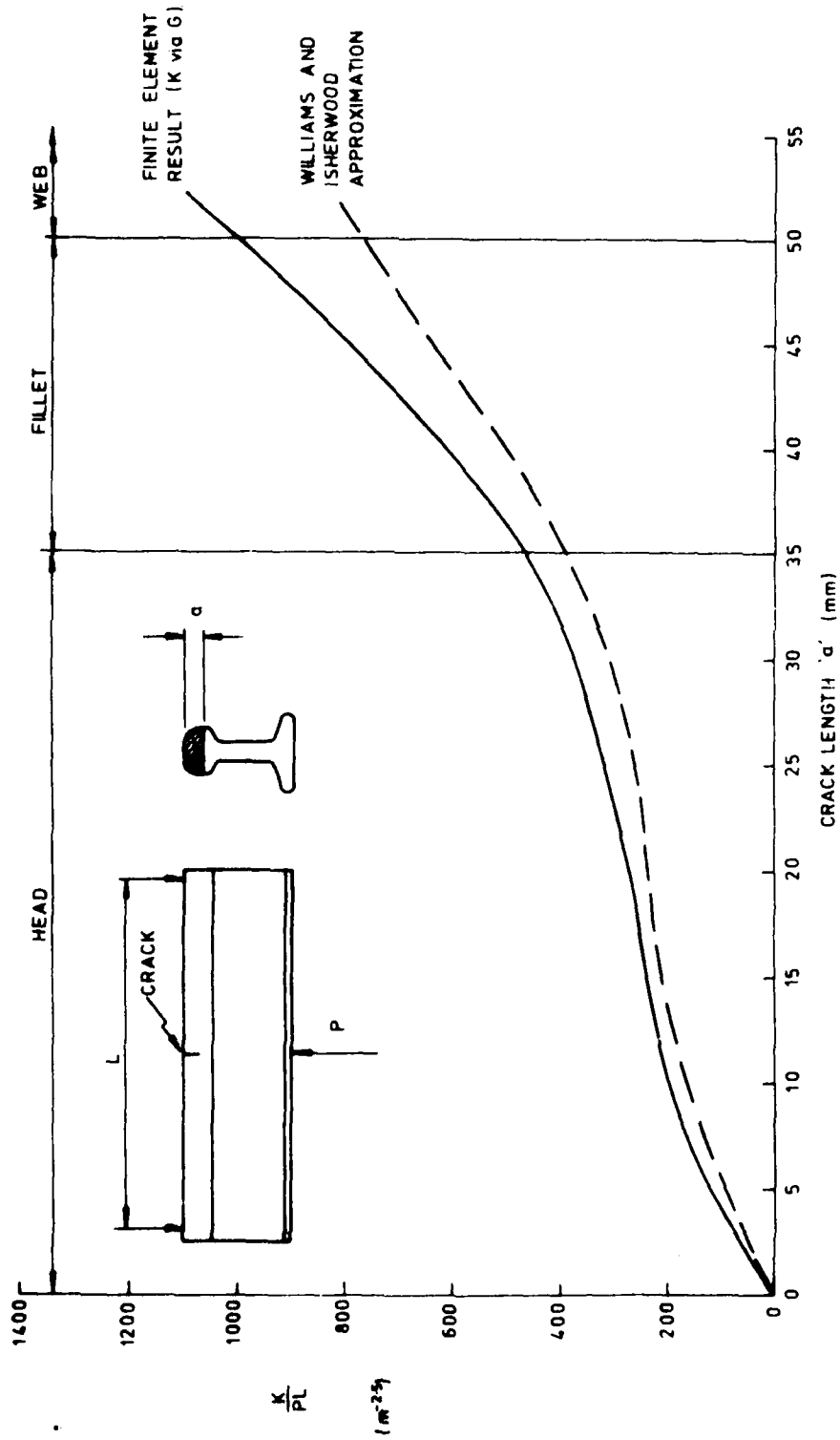


FIG. 7 'K' CALIBRATION RAIL HEAD CRACK IN B.S. 113A.

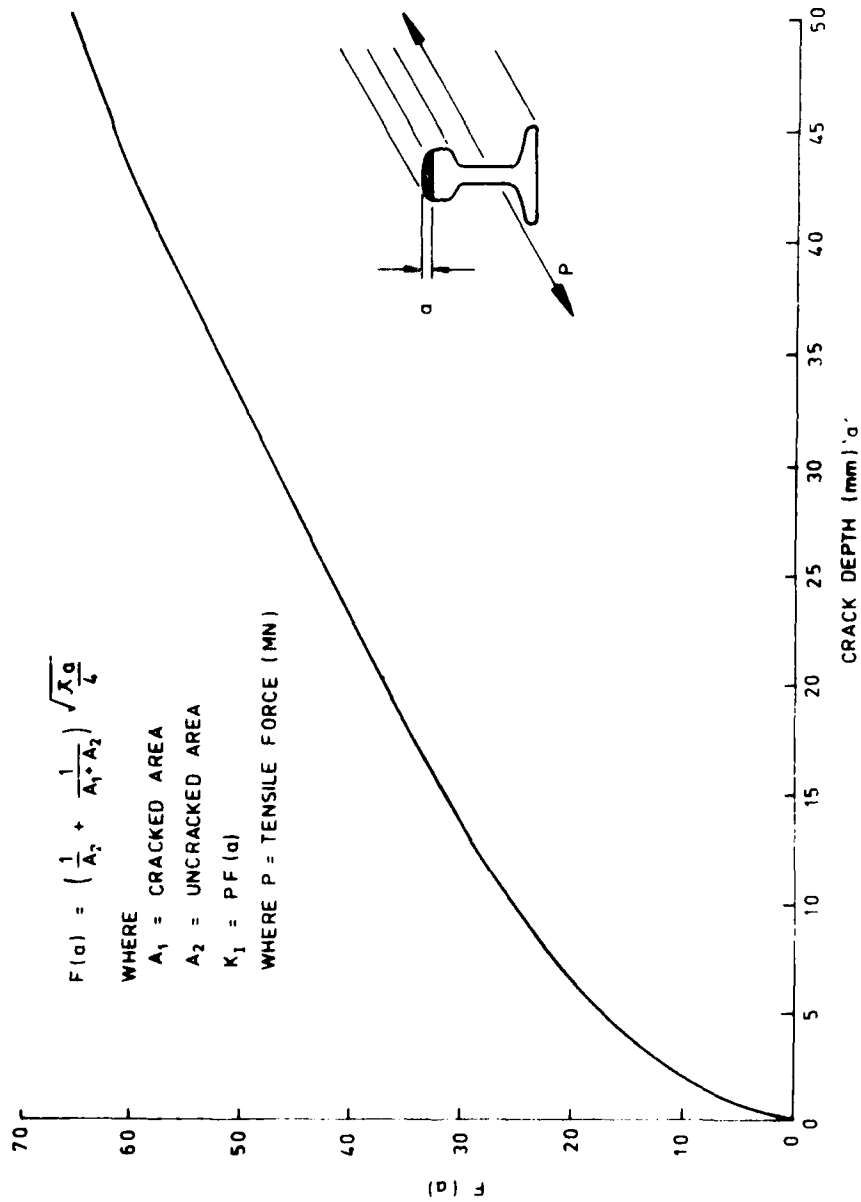


FIG. 8 K - CALIBRATION FOR THROUGH THICKNESS DEFECT IN RAIL HEAD SUBJECT TO UNIFORM TENSION (WILLIAMS AND ISHERWOOD METHOD).

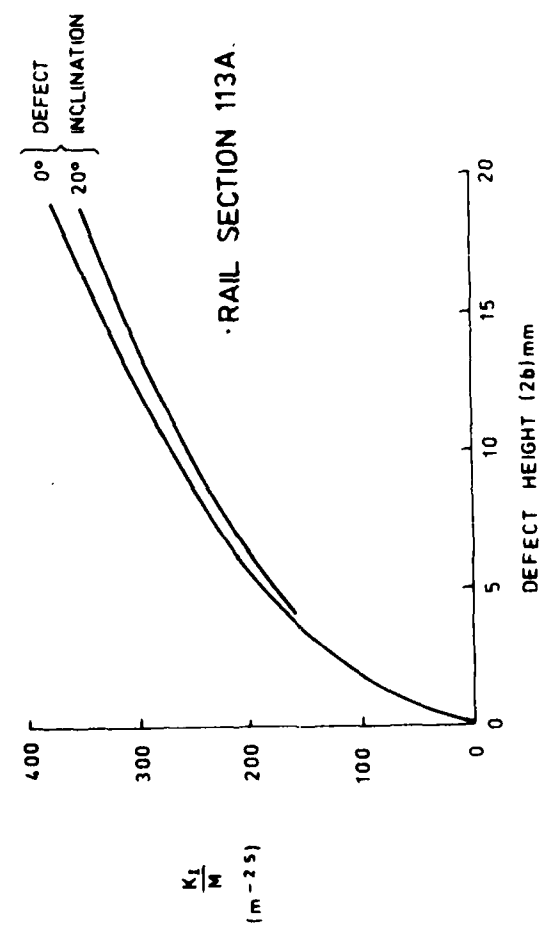
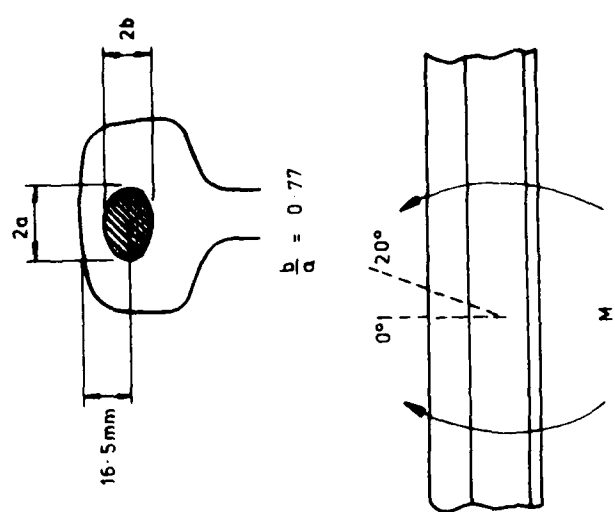


FIG 9 TACHES OVALES K_I CALIBRATION AS A FUNCTION OF DEFECT HEIGHT: MEAN VALUES FOR DEFECT POSITION AND ASPECT RATIO ASSUMED.

On BR the smallest size of tache ovale fatigue crack known to have caused fracture is about 14 mm diameter. The failure occurred between Lancaster and Preston on 2 Feb 71. The minimum temperature recorded on this date at the nearest meteorological office (Squires Gate) was -4°C . The rail had been destressed about one year previously at 27°C .

The K_I generated by thermal stressing ($+76 \text{ MNm}^{-2}$) is estimated to be $7 \text{ MNm}^{-1.5}$.

In order to estimate the K_I generated by residual stresses, values were selected at about the centre of the crack from the ORE work (5) and that of Allen (6). It was then assumed that these stresses were associated with a bending type stress distribution. The two equivalent outer fibre stresses i.e. on the running surface were $+49 \text{ MNm}^{-2}$ (O.R.E.) and $+195 \text{ MNm}^{-2}$ (Allen); the K_I 's computed were $5.2 \text{ MNm}^{-1.5}$ and $20.8 \text{ MNm}^{-1.5}$ respectively.

The average fracture toughness of rail steel at this temperature is $35 \text{ MNm}^{-1.5}$. Thus the K_I component contributed by the wheel, or wheels, of the train can be deduced to be either 22.8 or $7.2 \text{ MNm}^{-1.5}$ depending on the residual stress used in the calculations. Assuming the applied (or active) loads produce a bending type stress distribution the outer fibre stress associated with the failure can now be estimated. The active stress is found to be either 216 or 68 MNm^{-2} , depending on the residual stress contribution assumed.

Since the tache ovale crack associated with this failure is the smallest that is known it is probable that extreme service loadings caused the fracture. The maximum tensile stress deduced from theoretical track dynamic calculations performed at BR is $+50 \text{ MNm}^{-2}$ (6), however, recent experimental results obtained in track have shown that a wheelflat 120 mm long can induce tensile stresses in the rail head of 125 MNm^{-2} . Furthermore the bending wave caused by an impact travels at least 1.5 m along the rail from the point of impact with little attenuation of its magnitude. It seems likely therefore that any point in the rail will experience the induced stress cycle caused by a wheelflat impact at least once and may be twice.

Similar analyses of the "star-crack" type of failure have shown that the nominal shear stress in the rail web is around 200 MNm^{-2} when fracture initiates from the smallest fatigue cracks observed. Again dipped joints and wheelflats, resulting in impact loading, are probably the cause of these stress levels.

With some knowledge of the fracture toughness of current rail steels, defect sizes associated with failures, and the maximum stress levels likely to occur it is possible to consider solutions which will reduce if not eliminate the problem. Briefly, the possibilities are as follows:

(a) Re-design

The problems of introducing major design changes into a system such as the permanent way, which has evolved over the last 150 years, are formidable. Whilst in the long term these may be possible, e.g. paved track, this approach would not help the immediate, pressing problems.

(b) Improved Crack Detection

The critical crack size in BS 11 rail steel can be only 1-2 mm deep and bearing in mind that 22,000 miles of running track has to be inspected, it seems quite conceivable that crack initiation, crack growth and final fracture is possible within routine inspection periods. Further development of ultrasonic inspection techniques is possible and necessary.

(c) Reduced Stress Levels

The elimination, or reduction of, wheel flats would help to reduce the incidence of high stress levels in the track. However, impact conditions would still arise as a result of wheelburn depressions and rail joints (bolted and welded). In addition the service failure analysis programme has shown that temperature induced stresses, and residual stresses play a large part in the failure of a rail. The temperature stresses in continuously welded track are put there deliberately to avoid buckling in hot weather. A reduction of residual stresses, some of which arise in manufacture, and some as a result of service conditions, would be impracticable.

(d) Improved Fracture Toughness of Rail Steel

Because of the low toughness of current BS 11 rail steel (and this equally applies to European and American rail steels) there appears to be plenty of scope here.

Figure 10 shows the relationship between applied stress and critical crack length for a given level of fracture toughness for the "star-crack" failure. Two levels of operating stress are shown and a critical situation arises immediately the stress-crack length relationships drop below these stresses. It will be seen that for current rail steel ($K_{IC} = 31 \text{ MNm}^{-1.5}$ at -15°C) fractures can be expected when the fatigue crack length exceeds 0.5 mm. This is substantiated by service experience. However, if the rail steel had a K_{IC} of $80 \text{ MNm}^{-1.5}$ fatigue cracks of at least 20 mm length could be tolerated.

Experimental rail steels (13) have been developed jointly by the BRB and BSC and the fracture toughness of these steels are being determined over the range of operating conditions. An example of the effect of temperature and strain rate on the fracture toughness of one cast is shown in fig. 11. The determination of the toughness of these experimental materials has led to the

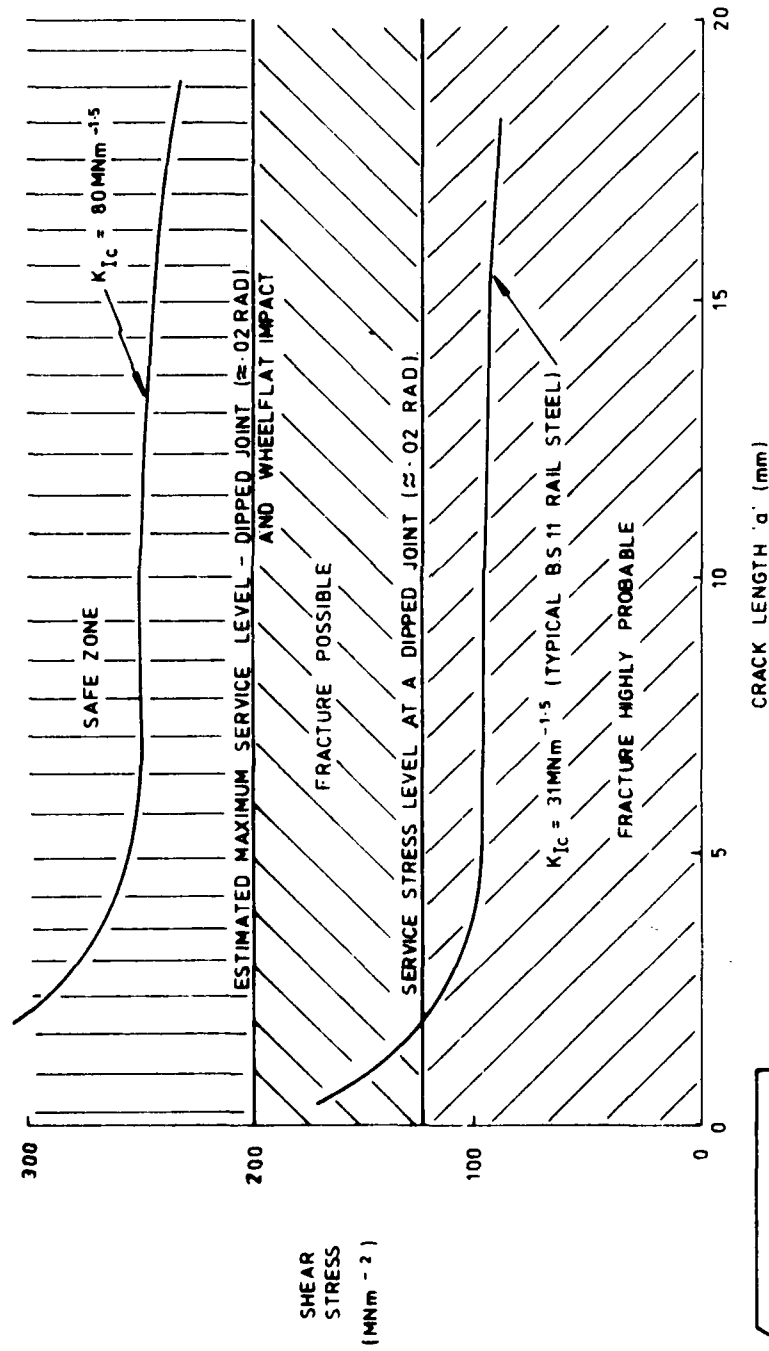


FIG. 10. EFFECT OF FRACTURE TOUGHNESS ON BOLTED RAIL JOINT CRITICAL CRACK LENGTH.

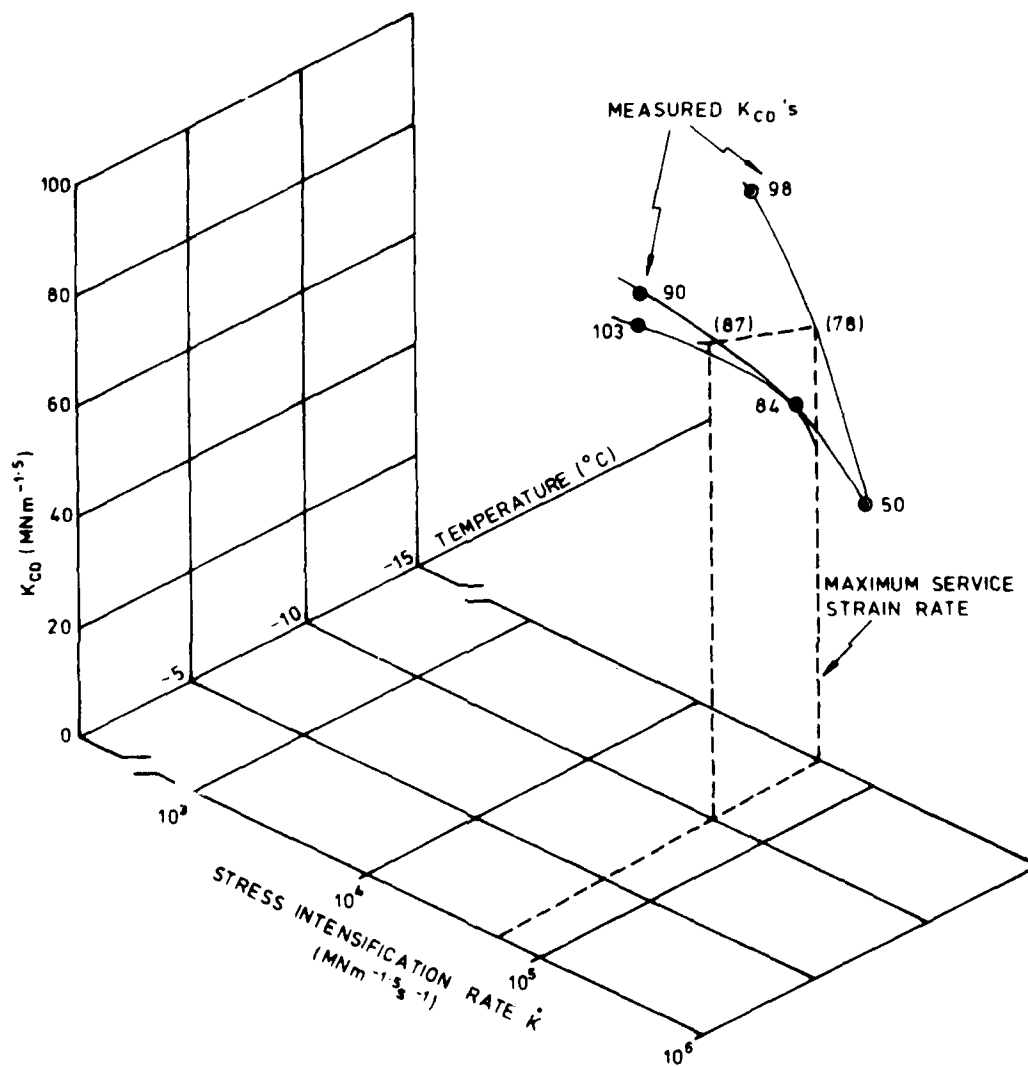


FIG. 11. EFFECT OF TEMPERATURE AND STRAIN RATE ON THE FRACTURE TOUGHNESS OF AN EXPERIMENTAL RAIL STEEL (CAST 4287).

development of a special dynamic test which uses a full rail section specimen. It is essential to test candidate replacement rail steels at the highest expected service strain rate since the toughness of these materials may degenerate as strain rate is increased. A special drop weight test facility has been built at the BR research laboratories to perform these tests. The test technique has been described elsewhere (9, 14).

The rail failure problem may be summarised as follows:

Although strain levels in rails are generally low fatigue crack initiation seems to be inevitable. Even supposing rail steel were free of material defects, fatigue crack initiation occurs, for example, from wheel-rail induced damage (e.g. wheelburn), mishandling, corrosion pitting and stress-raisers such as bolt holes. Of course material defects do occur, and this is hardly surprising in view of the large quantities of rail steel used (about 4.5 million tons in the UK).

Fatigue crack propagation studies have shown that for a wide variety of steels little variation in growth rate occurs at a given ΔK range. Thus there seems little prospect of modifying the fatigue crack growth period by material changes. However, analysis of strain data associated with a wheelflat impact has shown that the average fatigue crack growth rate per axle could be reduced substantially if wheelflats were eliminated or drastically reduced in size and frequency.

Although improved crack detection methods continue to be introduced the effect has been essentially to contain the failure problem at its present level. The critical crack length can be so small that the prospect of finding many fatigue cracks before final fracture is largely a matter of chance. The critical size of a fatigue crack determines the life of the rail following crack initiation and also determines the frequency and method of in-service inspection.

The rail fracture problem would undoubtedly be lessened if the critical crack length were increased. The effect would be "to buy time" - time to detect the cracks and take the necessary action to avoid an in-service fracture.

The fracture mechanics assessment of this problem suggests that substantial increases in critical crack length could be achieved by improving (even modestly) the fracture toughness of rail steel. A reduction in the size and number of wheelflats and other causes of impact would also be of benefit.

CONCLUSIONS

The fracture toughness of BS 11 rail steel at -15°C lies generally between $31-35 \text{ MNm}^{-1.5}$ and these values are not significantly affected by cast composition (within the BS 11 specification), rail position within the ingot, manufacturing process or rail source. Lower values of toughness are associated with web material.

The fracture toughness of BS 11 rail steel is insensitive to changes in crack tip loading rate over the range $10 \text{ MNm}^{-1.5} \dot{K} \leq 10^5 \text{ MNm}^{-1.5} \dot{K}^1$ at -15°C . The toughness of experimental, fracture tough, rail steels is dependent on crack tip loading rate.

Most rail failures occur in steel with toughness levels, and metallurgical properties, quite typical of BS 11.

The use of tougher rail steels would reduce the risk of in-service fractures. The BRB and BSC have developed a number of tougher rail steels which have been produced in rail form. These steels have not, as yet, been accepted for general use since many other factors have to be considered, e.g. wear, weldability, product uniformity, cost.

Fracture mechanics analyses of service failures have shown that residual and thermal stresses make a significant contribution to the total failure stress. The contribution made by impact induced stresses caused by wheel flats etc. to the fatigue and fracture of rails is becoming more clear. Active consideration is being given by the B.R. Research and Development Division to developing a wheel flat detector system which will determine the damage caused by wheel flats.

The application of fracture mechanics to rail failures has contributed considerably to our understanding of the problem and how it might best be resolved.

ACKNOWLEDGEMENTS

In preparing this paper the author has drawn upon the work of many of his colleagues at the BR Research Department in Derby. In particular he would like to thank Dr R.J. Allen, Mr K.A. Sharpe and Mr R.M. Tomlinson for their contributions. Some of the work described was performed in collaboration with the British Steel Corporation and in this respect the author wishes to thank Mr E.F. Walker and Mr D. James of the B.S.C. Special Steels Research Division, Sheffield. Finally, the author acknowledges the permission of the BRB to publish the paper.

REFERENCES

1. Davies, J. and Jones, E.G. "Experience with Rails on BR and the Requirements for Improved Rail Steel" I.S.I. Conference on Rail Steel Development, London, November 1972.
2. British Standards Institution "BS 11 : 1959 - Flat Bottom Railway Rails" 1959.
3. Timoshenko, S. and Langer, B.F. "Stresses in Railroad Track" ASME, Applied Mechanics Division, November 1937.
4. Satoh, Y. "Dynamic Effect of a Flat Wheel on Track Deformation" Permanent Way, No. 22 March 1964.
5. O.R.E. Report No. C53/RP 6/E "Behaviour of the Metal of Rails and Wheels in the Contact Zone," October 1970.
6. Allen, R.J. and Morland, G.W. "The Significance of Defects in BS 11 Rails : Bolt Hole Failures and Taches Ouales" I.S.I. Conference on Rail Steel Development, London, November 1972.
7. "Methods for Plane Strain Fracture Toughness (K_{Ic}) Testing" B.S.I. Doc. D.D.3. : 1971.
8. B.S.C./B.R.B. Fracture Toughness Testing Committee "Fracture Toughness of Rail Steels" Summary Report of B.S.C./B.R.B. Collaborative Test Programme on BS 11 Rails, August 1970.
9. Morton, K., Cannon, D.F., Clayton, P. and Jones, E.G. "The Assessment of Rail Steels: A.S.T.M. Conference on Developments in Rail Steels, Denver 1976.
10. Bowie, O.L. "Analysis of an Infinite Plate Containing Radial Cracks Originating at the Boundary of an Internal Circular Hole" J. Maths and Phys. 35, 60 (1956).
11. Shah, R.C. and Kobayashi, A.S. "Stress-Intensity Factor for an Elliptical Crack Under Arbitrary Loading" Eng. Frac. Mech. 1971 3(1) 71.
12. Williams, J.G. and Isherwood, D.F. "Calculation of the Strain-Energy Release Rates of Cracked Plates by an Approximate Method" J. Strain Analysis 3(1) 17 (1968).
13. Collinson, T.G., Hodgson, W.H., McNeely, V.J. "The Initial Development of Fracture Tough Rail Steels" I.S.I. Conference on Rail Steel Development, London, November 1972.
14. Cannon, D.F. "Fracture Research at High Strain Rates" Railway Engineer Vol. 1 No. 1 Jan/Feb 1976.

DEVELOPMENT OF DESIGN AND TEST CRITERIA FOR THE STRUCTURAL
INTEGRITY OF RAIL VEHICLE MECHANICAL SYSTEMS

Oscar Orringer
Associate Director, Aeroelastic and Structures Research Laboratory, MIT
Cambridge, MA 02139

Raymond Ehrenbeck
Staff Member, DOT Transportation Systems Center
Cambridge, MA 02142

Pin Tong
Staff Member, DOT Transportation Systems Center
Cambridge, MA 02142

INTRODUCTION

The Federal Railroad Administration is pursuing a program to improve the ride quality of the AMTRAK Metroliner. The program began in 1971, when AMTRAK took over the passenger service of 13 U.S. railroads. The Metroliner provides high-speed intercity service between New York City and Washington, DC. Current operations are limited to 105 mph maximum speed, with reduced speeds in many sections because of track conditions [1]. However, the track is being improved and future operations up to 120 mph are planned. FRA ride-quality improvement programs have included full-scale testing of new designs for the Metroliner railcar trucks [2,3] as well as review of proposed modifications to the existing trucks. The FRA evaluation resulted in a decision to minimize the improvement cost by modifying the existing trucks by adding vertical-motion dampers in the primary suspension, and by replacing the truck bolster and secondary suspension with a new design.

In 1976 FRA asked the Transportation Systems Center and MIT to conduct a structural integrity assessment of the Metroliner truck and to answer the following questions. What is the potential fatigue damage accumulation in the fleet? (The fleet consists of 60 railcars, i.e. 120 trucks, with an average service of 6 to 8 years. There are no spares for the major components of the truck.) How might the proposed modifications affect structural integrity (i.e., possible damage introduction and/or increases in cyclic stress levels)? What is the estimated post-modification fatigue life of the remaining existing parts and the new parts? What fatigue test plan should be followed to verify the structural integrity of the modified truck? The last question was crucial because of the lack of spares. If a repeat of the full-scale fatigue test of the entire truck were found to be necessary, this would have meant removal of one Metroliner car from service.

Looking to the future, FRA, also asked us to synthesize from the Metroliner case study a set of recommendations for structural integrity criteria for higher speed trucks which are planned as future acquisitions. Although current passenger trucks are conservatively designed, the advent of high

speed operations in the 130 to 160 mph range will force future designs toward lighter (and therefore more highly stressed) construction to avoid hunting instability [4,5] and to reduce the damaging effect of loads on the track [6]. Hence, the Metroliner trucks were subjected to crack-propagation analysis, as well as crack-initiation analysis, in anticipation of the probable requirements for future designs [7]. This paper focusses primarily on the results of the Metroliner case study, since the criteria recommendations are still under development.

The data available for the Metroliner were as follows. No fatigue failures had occurred in the truck frame (the major critical component for the structural integrity study). Yield strength, UTS, the notched endurance-limit strength (K_t not specified), and some chemical composition data were available for the truck frame alloy. Carbody acceleration and track roughness power spectra had been taken on short sections of the Metroliner route with the existing truck under the vehicle [2]. Load exceedance curves had been prepared based on run tests with Vought/SIG trucks [3]. Finally, track roughness power spectra taken by a special test vehicle were available for several additional short sections of the Metroliner route [8].

The investigation began in August 1976. A rapid and restricted analysis of the Metroliner truck structural integrity was required to meet a scheduled FRA decision-point in October. Also, time and cost constraints on the subsequent Metroliner test schedule dictated that existing equipment, able to provide only constant-amplitude loading, be used for any fatigue test of the modified truck.

GSI "GENERAL-70" TRUCK

The General-70 truck (manufactured by General Steel Industries, Inc.) currently rides under the Metroliner. Figure 1 illustrates this truck and indicates the proposed modifications: approximate placement of the primary-suspension damper (four per truck), and the bolster and bolster springs which are to be replaced. The truck frame (shaded in the side view) was the major component of concern regarding structural integrity. The frame is a single "H" casting with hollow sections. The section at the new damper location was selected for analysis because of concerns about the effects of welding a bracket to the frame at this point.

Load transfer through the primary suspension is quite complicated, but can be understood by review of the major paths for vertical, lateral and longitudinal components. Vertical and lateral loads enter the truck through the axle journals. The vertical loads are reacted by the gooseneck portions of the equalizer beams, and are passed to the truck frame through the equalizer springs. (In the modified design, a part of this load will be routed through the dampers, slightly increasing the vertical bending moments applied to the frame.) Journal guides which permit vertical motion of the journal are part of the frame. Lateral loads are passed directly to the frame at the journals. (This load path is not influenced by addition of the new dampers.) In practice, there will be some "play" between the axles,

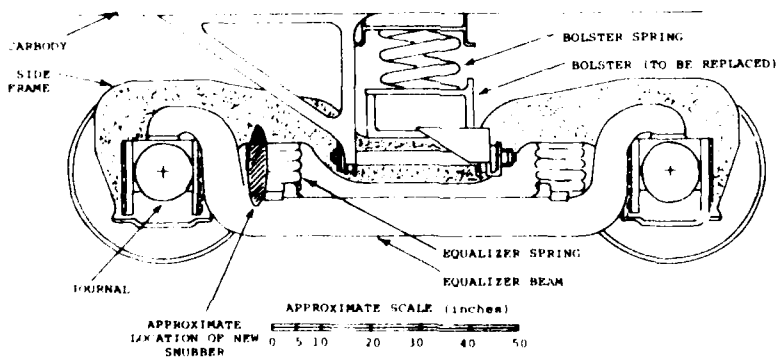
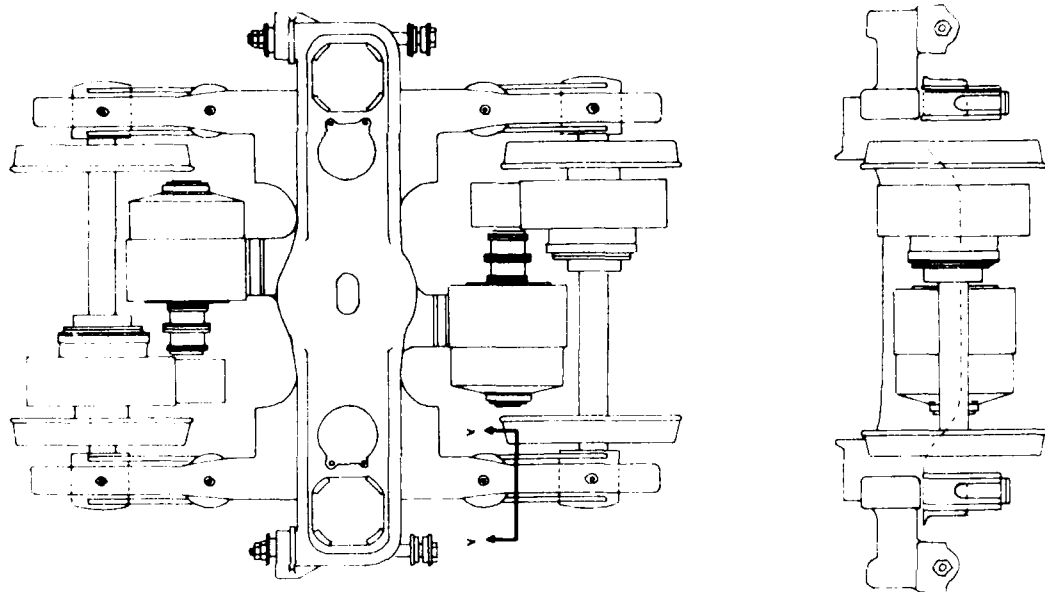
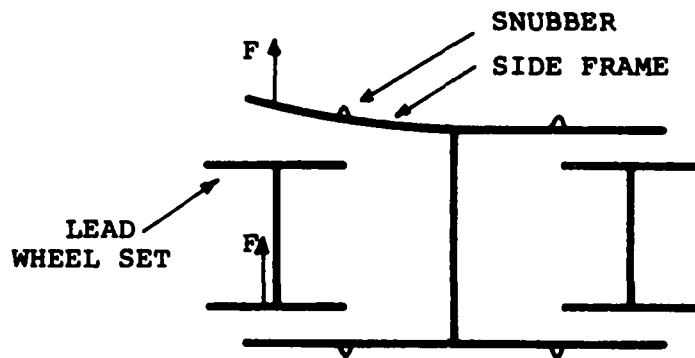
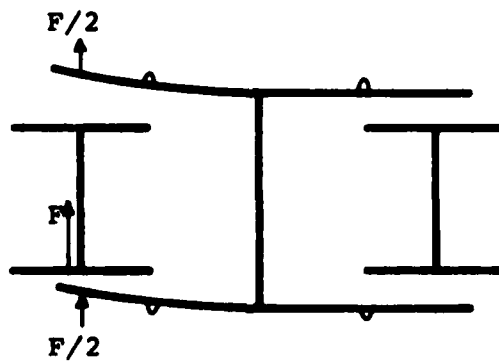


FIGURE 1. GSI GENERAL-70 TRUCK



(A) FREE PLAY ASSUMED IN JOURNALS



(B) NO PLAY ASSUMED IN JOURNALS

FIGURE 2. LATERAL LOAD TRANSFER

journals, and frame. However, the amount is unknown and probably varies from one truck to another. Hence, two extreme conditions can be visualized for the lateral loads, as indicated schematically in Fig. 2. At one extreme, the frame legs are alternately subjected to outward bending as the wheelset shuttles from side to side. At the other extreme, both legs are engaged continuously in zero-mean bending, at one half the bending moment of the first extreme. The bolster receives vertical and lateral loads through the centerpin and by side bearing at the sides of the truck frame. These loads are transmitted to the carbody through the bolster springs, and also through vertical and lateral dampers (not shown). Braking and traction forces are passed primarily through the journal guides, H-frame, and centerpin to the center of the bolster. (A secondary path exists through the gear boxes and motors, but is well isolated from the frame by rubber cushions in series in the motor mounts.) The longitudinal loads are then transferred from the centerpin, via bolster bending, through anchor rods at the ends of the bolster to triangular frames attached to the carbody.

ANALYSIS

The following engineering tasks were defined to meet the objectives of the study within the time allowed: (1) estimation of material fracture toughness and crack growth rate from handbook data; (2) preparation of a representative service load history from the data available in previous Metroliner studies; (3) fatigue-crack initiation and propagation calculations to estimate economic and safety limits, and; (4) formulation of a fatigue test plan. Comparison of the data on the truck frame alloy with metallurgical reference works [9,10] indicated that the material closely resembled AISI-2330 cast steel. Hence, the properties of the latter alloy (at 75 ksi UTS, 30 ksi unnotched endurance limit strength) were used in the analysis. Charpy V-notch data for AISI-2330 castings were correlated with K_{ID} values via an empirical relation developed by Barsom and Rolfe [11]:

$$(K_{ID})^2/E = 2(CVN)^{3/2} \quad (1)$$

where K_{ID} is the dynamic fracture toughness ($\text{psi}\sqrt{\text{in}}$), E is Young's modulus (psi), and CVN is the Charpy impact energy absorption (ft. lb.). These calculations resulted in average K_{ID} values of $124 \text{ ksi}\sqrt{\text{in}}$ at 75°F and $71 \text{ ksi}\sqrt{\text{in}}$ at 0°F .* The crack-propagation rate was estimated by fitting a combined Paris-Forman equation to data available for an alloy with crack-propagation behavior similar to AISI-2330, with the following results:

$$da/dn = 0 \quad \text{for } \Delta K < \Delta K_{TH} \quad (2)$$

* The 0°F value is used to determine critical crack size, under the assumption that fracture occurs during winter operations.

$$da/dn \approx 3.9 \times 10^{-9} (\Delta K)^2 \quad \text{for } \Delta K_{TH} \leq \Delta K \leq \Delta K_{TR} \quad (3)$$

$$da/dn \approx \frac{3.9 \times 10^{-9} (\Delta K)^2}{(1-R) \frac{K_C}{\Delta K} - 1} \quad \text{for } \Delta K \geq \Delta K_{TR} \quad (4)$$

where da/dn is in units of inch/cycle, where:

$$\Delta K_{TH} \approx 7(1-R) \quad \text{ksi}\sqrt{\text{in.}} \quad (5)$$

$$K_C \approx 110 \quad \text{ksi}\sqrt{\text{in.}} \quad (6)$$

$$\Delta K_{TR} \approx 55(1-R) \quad \text{ksi}\sqrt{\text{in.}} \quad (7)$$

and where $R = \frac{s_{\min}}{s_{\max}}$ is the stress ratio. The foregoing properties were also used for the new bolster material, except that K_{ID} was estimated to be only 45 ksi $\sqrt{\text{in}}$ at 0°F because the availability of the original alloy for the short-run production of new bolsters was in question.

No attempt was made to account for crack-growth retardation due to overloads. Hence, load-history preparation was confined to the development of appropriate exceedance curves. For this purpose, the action of the Metroliner carbody upon its trucks was treated as a stationary Gaussian process driven by the track roughness power spectrum and filtered by the carbody vibration modes. The dominant carbody motions are rigid body bounce and pitch, as far as vertical loads applied to the truck, although minor contributions are also made by the bending modes. Lateral truck loads are similarly influenced by rigid-body sway and yaw. The well-known formulae for calculating the exceedance curve of a stationary Gaussian process were employed [12]:

$$E(x) = \frac{1}{2} \bar{N}_0 \exp(-x^2/2\sigma^2) \quad (8)$$

where $E(x)$ is the expected number of exceedances per unit time of the level, x , of the parameter of interest, where:

$$\sigma = \left[\int_0^{\infty} G_{xx}(f) df \right]^{1/2} \quad (9)$$

$$\bar{N}_0 = 2 \left[\frac{1}{\sigma^2} \int_0^\infty f^2 G_{xx}(f) df \right]^{1/2} \quad (10)$$

and where $G_{xx}(f)$ is the power spectral density of x as a function of frequency, f , in Hz. We remark that the assumption of a stationary Gaussian process cannot be justified either theoretically or from the available test data in the present case; it was adopted merely as a convenience to obtain first-cut estimates of the load environment within the program schedule.

Exceedance curves were first estimated approximately by adjusting the short-run Metroliner test data [2] to correlate with the Vought/SIG estimates [3]. The first estimates were later confirmed by a more elaborate procedure, which is also of more interest and will be summarized here. Comparison of the track roughness spectra from the original tests [2] with spectra obtained several years later at 16 additional locations on the Metroliner route [8] indicated that the track roughness statistics could reasonably be treated as constants. An example is given in Fig. 3, which compares the track alignment spectra from the two data bases. (A similar observation was made for the profile spectra.) It was then postulated that exceedance levels are influenced primarily by operating speed, which varies considerably from one section of the route to another. Under this hypothesis, the load history was treated as a sequence of stationary Gaussian processes (one for each speed block) which could all be derived from the Metroliner test results as a "baseline" case in the following manner. Let $R(\lambda) = C\lambda^m$ represent the track roughness spectral density as a function of spatial wavelength, λ . (The constants C, m are derived by fitting the upper bound of the data in Fig. 3.) Then:

$$\lambda = v/f \quad (11)$$

$$G_{xx}(f) = G(f) = kR(\lambda) = kC(v/f)^m \quad (12)$$

where $G(f)$ is the measured baseline acceleration PSD and where v is the operating speed during the test. The parameter, k , is unknown but may be assumed independent of v because the acceleration response is determined primarily by fixed carbody vibration modes. In a similar manner,

$$G_i(f) = kC(v_i/f)^m \quad (13)$$

is the response PSD in the i th speed block, and both k and C can be eliminated to obtain the block response in terms of the baseline PSD:

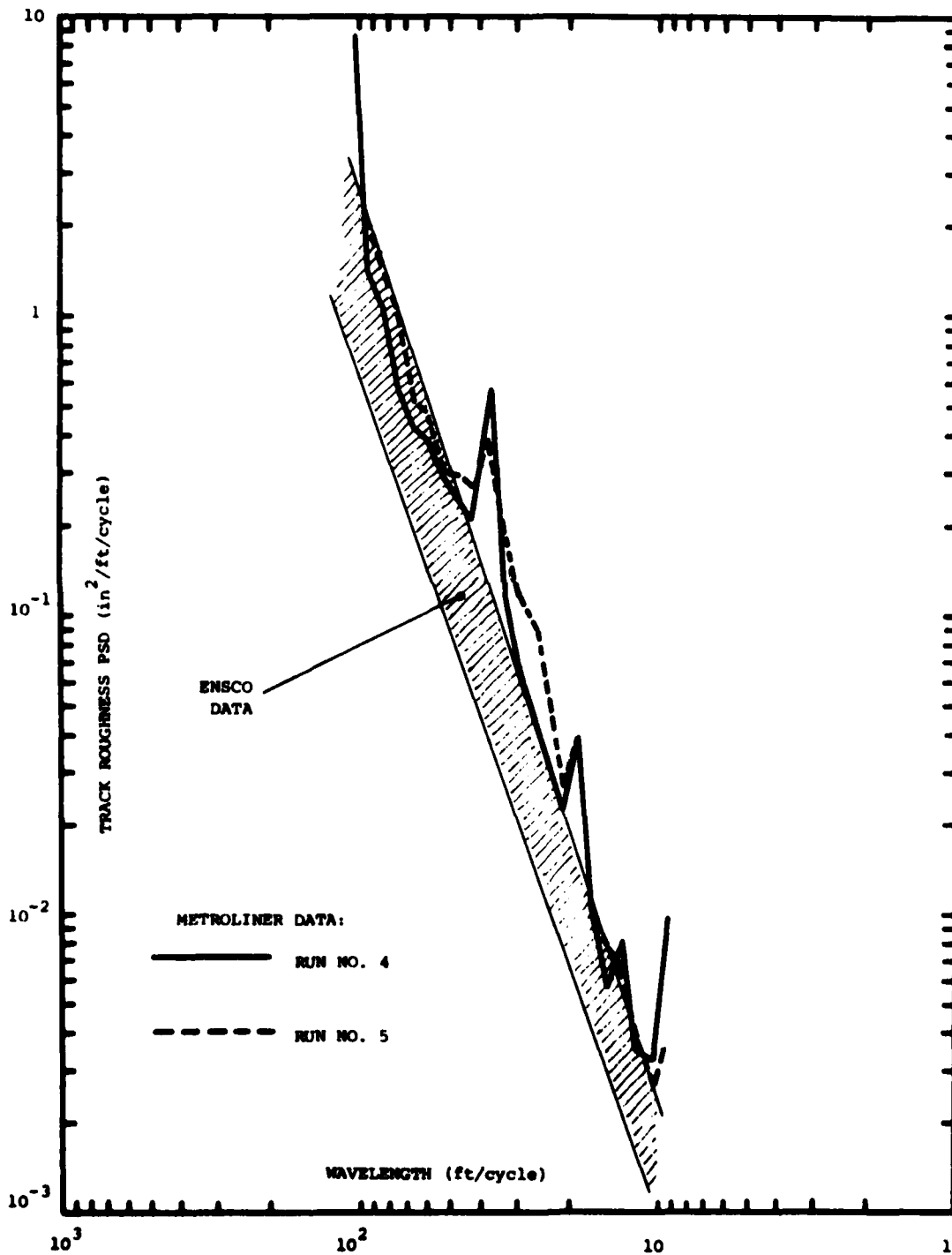


**FIGURE 3. NORTHEAST CORRIDOR
TRACK CONDITIONS (1971-75)**

$$G_i(f) = (v_i/v)^m G(f) \quad (14)$$

Block response statistics can now be obtained from Eqs. 9 and 10, and the route exceedance curve is derived by summing the blocks. Alternately, the zero-crossing rates can be expressed "per route mile" and a service-life exceedance curve can be given:

$$E(x) = \frac{1}{2} \bar{N}_0 [L_s / \sum_i L_i] \sum_i (L_i / v_i) \exp[-(v/v_i)^m (x^2 / 2\sigma^2)] \quad (15)$$

where L_s is the service life, L_i the block length, and where \bar{N}_0 and σ are the statistics of the baseline exceedance curve. Exceedance curve calculations were based on detailed operating speed-distance profiles for the Metroliner (current and projected) provided by AMTRAK.

Analysis for fatigue-crack initiation was conducted with Miner's linear damage-summation hypothesis [13]. When Miner's hypothesis is applied to Gaussian random-load fatigue, it can be shown that the expected rate of damage accumulation can be calculated from [14]:

$$D = \int_0^\infty \frac{-E'(s) ds}{N(s_a, s_m)} \quad (16)$$

where $E'(s)$ is the derivative of the stress exceedance curve, and where s is the total stress level consisting of a random alternating component, s_a , and a constant mean component, s_m . The denominator of Eq. 16 is simply the number of cycles to failure, taken from a constant-amplitude S-N diagram, for the load condition s_a, s_m . The damage rate D is per unit time if the exceedance curve is given in its usual form, or "per service life" if an expression like Eq. 15 is used. For lateral analysis of the truck frame legs, the correct process is zero-mean fatigue if no play is assumed in the axle journals (see Fig. 2). If free play is assumed, then s_m is not constant but the process is zero-to-tension, i.e. $s_m = s_a = s/2$ per cycle, and the correct value of N can be found from a Smith diagram for $R = 0$. For vertical loading, s_m is constant and corresponds to the static weight of the Metroliner carbody and passenger load.

Since the retardation effect has been ignored, crack-propagation as described by Eqs. 2 through 7 is also a linear damage-summation theory, and can be treated like crack initiation as far as the mathematical formulation is concerned. This is accomplished by assuming an initial crack size, a_i , and then integrating da/dn from a_i to the critical crack size determined by K_{ID} and a "once per life" or similar stress* to determine

*In the present case, K_{ID} at 0°F and the material UTS were used to make the analysis conservative.

the number of cycles to fracture, N. This calculation is done at constant amplitude, being repeated for several amplitudes to establish an equivalent "S-N" curve for crack propagation. Equation 16 can then be used to estimate D for propagation damage due to random loading. Equivalent "S-N" curves for several assumed initial crack sizes are compared with the ordinary S-N curve in Fig. 4 for AISI-2330 steel. The Tiffany formula for a semi-elliptical surface crack [15,16]:

$$K_I = 1.1 s M_K \sqrt{\pi a/Q} \quad (17)*$$

was used to determine when $K_I = K_{ID}$ and to compute ΔK (s replaced by $s_{max} - s_{min} = 2s_a$) for the da/dn integration. Results for the truck frame lateral analysis are shown in Fig. 5. The abscissa illustrates the benefit of high 0°F fracture toughness in the existing truck frame alloy (71 ksi \sqrt{in}). The figure also illustrates the high risk which would result from combining an alloy with no nickel ($K_{ID} = 45$ ksi \sqrt{in} at 0°F) with an inspection method not 100 percent reliable for detection of 0.15-inch-deep cracks.

ASSESSMENT AND FATIGUE TEST PLAN

The results of the fatigue calculations indicated that the General-70 truck frame is a very conservative design. The crack initiation damage rates were negligible, while the propagation rates indicated life limitation only for extremely large initial flaws. The largest assumed flaw (0.25 inch deep, 1.25 inch surface length) had a calculated safety limit of 140 operational hours, but initial damage in this size range could be ruled out as a consequence of the fact that no service cracking has occurred in the average 30,000 to 40,000 operational hours per railcar which have already been accumulated. Also, since the planned modifications would not influence lateral loading, we concluded that a new fatigue test of a complete truck was not necessary, and that smaller-sized initial damage which might affect structural integrity after modification could be effectively controlled by magnetic-particle inspection of the frames at modification time.

The bolster, being a new article, must be fatigue tested to verify the structural design. However, since the load-transfer paths to the bolster were simple and well defined, we felt that this article could be tested realistically as a separate component. The constraint to constant-amplitude testing (see Introduction) was of some concern because it is well known that constant-amplitude tests may be either conservative or unconservative when the test article contains cutouts, fastener holes, fillets, etc. [17]. Since the bolster design had not been finalized at this point, we chose a conservative approach, while keeping the proper

* Q, M_K are parameters which depend upon crack shape, wall thickness, and yield strength.

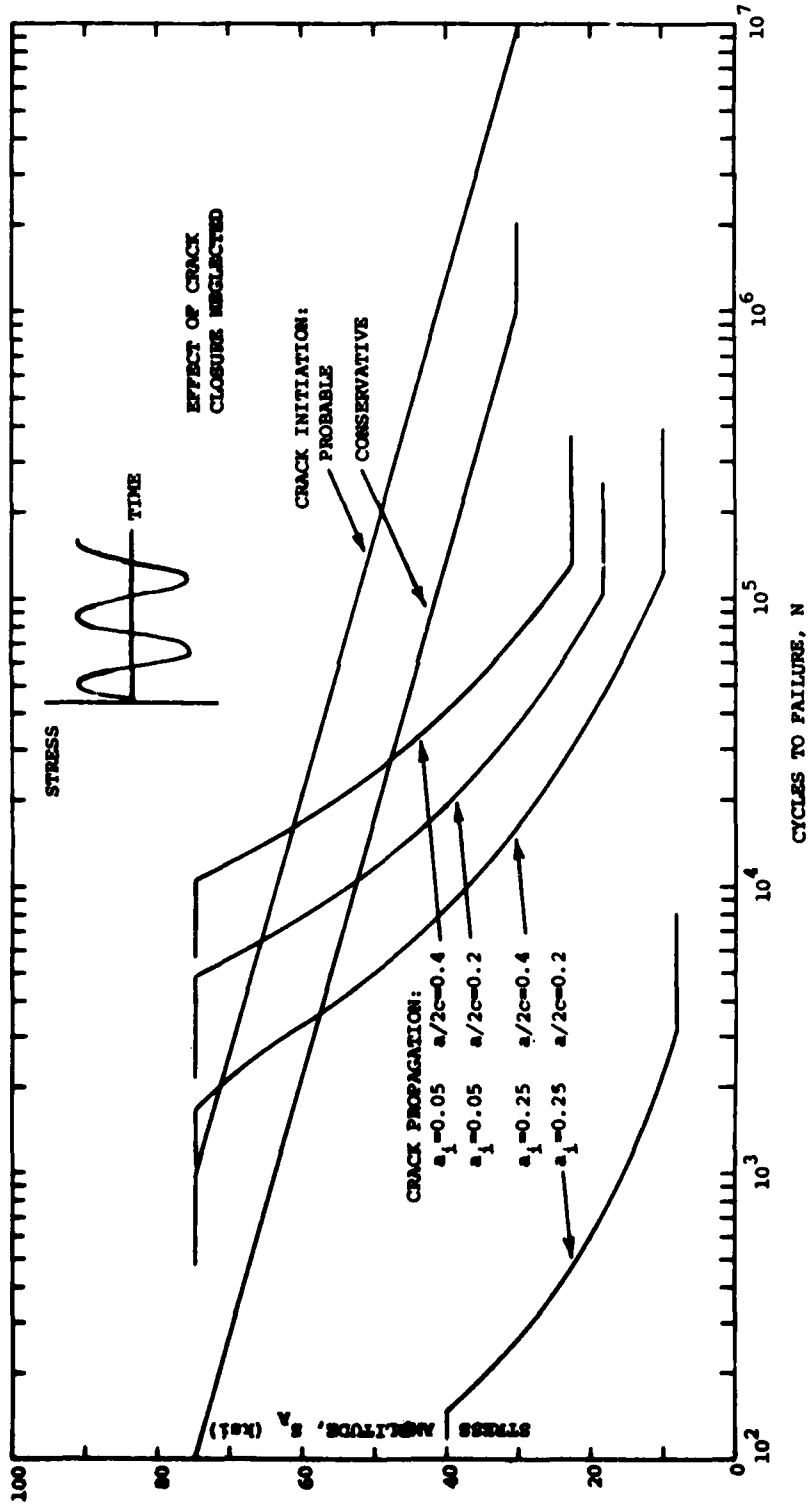


FIGURE 4. FATIGUE ENDURANCE VS. DAMAGE TOLERANCE (AISI-2330)

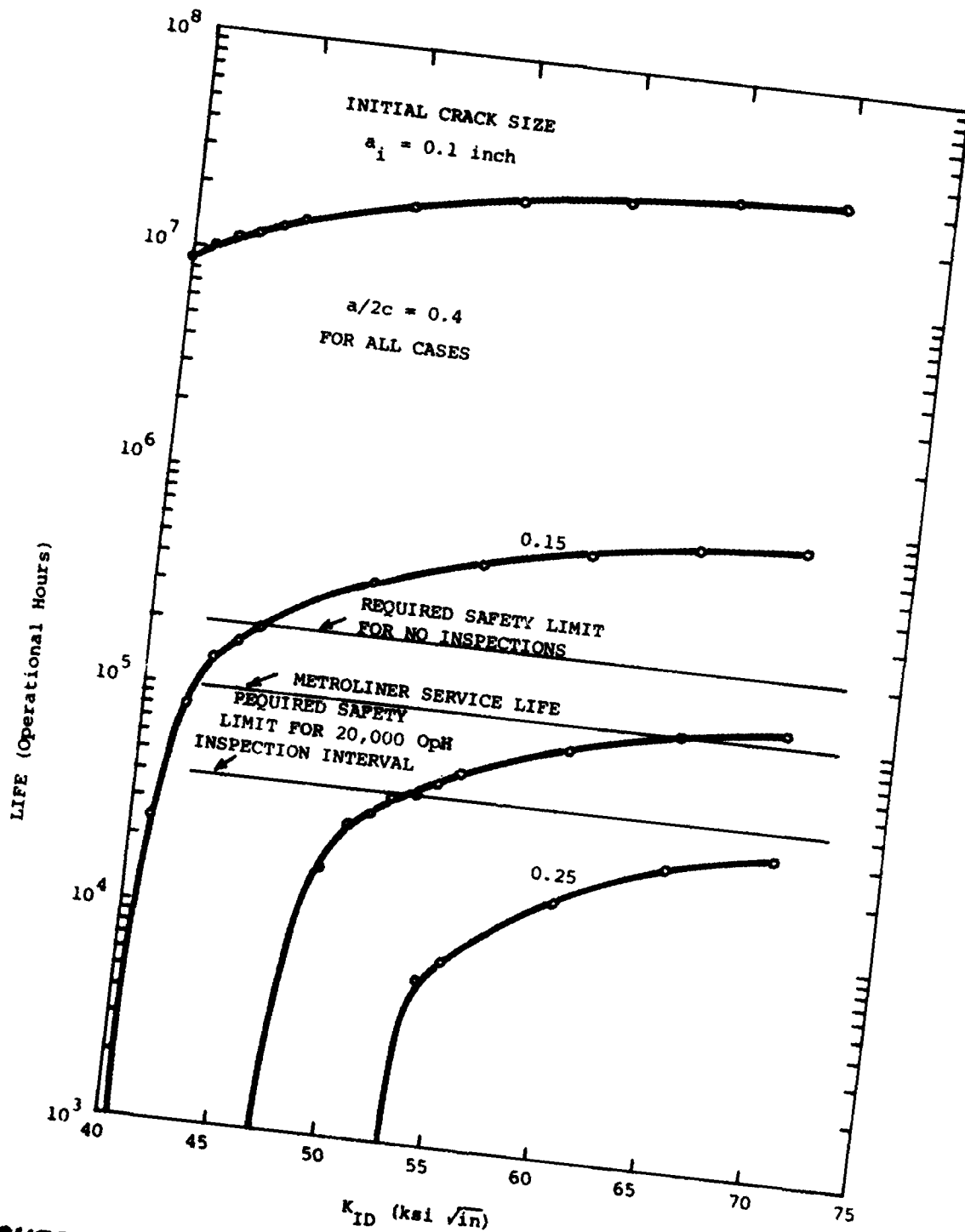


FIGURE 5. DEPENDENCE OF SAFETY LIMIT ON FRACTURE TOUGHNESS AND INSPECTION RELIABILITY

phasing between vertical, lateral, and longitudinal load cycles as derived from Metroliner tests:

$$\text{Vertical/Lateral/Longitudinal} = 2/1/1 \quad (18)$$

The longitudinal loading was established deterministically by counting the number of significant braking/traction events in the Metroliner operating profile (19 per one-way run) and by assuming that the wheels would engage at the maximum wheel/rail friction coefficient (0.15) for these events. Over the post-modification service life of the vehicle, these calculations resulted in 3.28×10^5 cycles at 0.15 "g". From Eq. 18, the corresponding figures are 3.28×10^5 lateral and 6.56×10^5 vertical cycles per life, these figures being used to enter the appropriate exceedance curves (Eq. 15) to obtain corresponding lateral and vertical acceleration amplitudes. A "scatter factor" of 4 was then incorporated* by extending the test plan to 4 times the number of cycles given above, with the final results:

Vertical:	2.6×10^6 cycles @ 0.3 "g"
Lateral:	1.3×10^6 cycles @ 0.15 "g"
Longitudinal:	1.3×10^6 cycles @ 0.15 "g"

CONCLUSIONS

The Metroliner case study was a useful learning exercise, even though the conservative design of its General-70 truck made fracture safety analysis somewhat of a minor issue. The study did suggest approaches to several areas in criteria development for future, higher speed designs.

In the materials area, cost-control for rail vehicle running gear, with its complex shapes, suggests continued use of castings. Also, high material test costs cannot be justified for each new design development. Hence, the criteria in this area should focus on extension of the handbook data base, together with a minimum set of quality-assurance tests from which all the mechanical properties can be correlated with confidence.

Load spectrum development has been given a good start, but further study of this area is needed. An experimental study with freight cars [18] has shown that truck loads on curved track depend upon the radius and are quite different from the loads on tangent track. Hence, a stationary

*The "scatter factor" concept assumes that the fatigue test article will be average and seeks to protect the fleet by placing mean fatigue life well above service life.

hypothesis may not be justified. Track roughness may or may not be Gaussian; additional data must be gathered and subjected to more thorough analysis to determine the process distribution. Also, realistic life models must take the realities of maintenance into account by assigning some fraction of life to "degraded-mode" operation. Degraded modes in railcar trucks are usually high-gain conditions caused by damper failures not spotted by maintenance personnel. Data need to be gathered by the operating organization to permit assessment of the frequencies and types of degraded modes which should be expected. As new designs become lighter and more highly stressed, the detailed load spectrum estimate should be used to establish more realistic multi-amplitude block loading for the full scale fatigue test.

Finally, perhaps the most important item is to recognize that railcar trucks are very different from airframes, ship hulls and other large structures, in that their dynamics are continuously nonlinear. Hunting motions are one example, but even below critical speed the numerous springs and dampers in a truck are engaged in their nonlinear ranges more or less continuously by design intent to provide good ride quality. Hence, the stress spectra in the truck's components will generally be non-Gaussian, even though the input may be Gaussian. Componentization of the full-scale fatigue test has been suggested as a cost-control measure [19], but the nonlinear effects on load transfer between components must be properly assessed to maintain test realism.

The next phase of the Metroliner Ride Improvement Program will provide answers to some of the questions which have been raised about load spectra and the effects of truck nonlinearities. After a prototype modification has been completed on one car, it is planned to include strain-gage instrumentation to pick up strain spectra, as well as the usual acceleration spectra, during the subsequent ride-quality tests. The Metroliner case study will then assess the accuracy of the simplified models and indicate how much these models should be refined for the general criteria.

REFERENCES

1. Aronson, R.B., "AMTRAK Begins to Roll", Machine Design, 22 January 1976.
2. Herring, J.M., "Metroliner Ride Improvement Program", Budd Company Technical Center, Fort Washington, PA, Report No. FRA-RT-73-30, February 1973.
3. Sandlin, N.H., "Development of Design Loads Criteria for High Speed Railcar Trucks", Proc. 4th Inter-Society Conference on Transportation, Los Angeles, CA, 18-23 June 1976.
4. Wickens, A.H., "The Dynamic Stability of Railway Vehicle Wheelsets and Bogies Having Profiled Wheels", Int J Solids Structures, Vol. 1, 1965, pp. 319-341.

5. Moron, P., "Basic Principles for the Design of Bogies for Passenger Rolling Stock", French Railway Techniques, No. 4, 1970, pp. 117-138.
6. Jenkins, H.H. et al., "The Effect of Track and Vehicle Parameters on Wheel/Rail Vertical Dynamic Forces", Railway Eng J, Vol. 3 No. 1, January 1974, pp. 2-16.
7. Orringer, O., "Structural Integrity for High Speed Passenger Railcar Trucks", Aeroelastic and Structures Research Laboratory, MIT, ASRL TR 185-4, in publication.
8. Jones, T., ENSCO, Inc., Springfield, V., private communication to D. Ahlbeck (Battelle-Columbus Laboratories, Columbus, OH), 15 December 1975.
9. Evans, E.B., Ebert, L.J. and Briggs, C.W., "Fatigue Properties of Comparable Cast and Wrought Steels", Proc. ASTM, Vol. 56, 1956, pp. 979-1011.
10. Forrest, P.G., Fatigue of Metals, Pergamon Press, New York, 1970.
11. Barsom, J.M. and Rolfe, S.T., "Correlations Between K_{IC} and Charpy V-Notch Test Results in the Transition-Temperature Range", Impact Testing of Metals, ASTM STP 466, American Society for Testing and Materials, 1970, pp. 281-302.
12. Bendat, J.S., Principles and Applications of Random Noise Theory, Wiley, New York, 1958.
13. Miner, M.A., "Cumulative Damage in Fatigue", J Appl Mech, Vol. 12, 1945, pp. A159-A164.
14. Burris, P.M. and Bender, M.A., "Aircraft Load Alleviation and Mode Stabilization (LAMS)", The Boeing Company and Honeywell, Inc., Report No. D3-7900-1 (AFFDL-TR-68-148), April 1969.
15. Tiffany, C.F. and Masters, J.N., "Applied Fracture Mechanics", Fracture Toughness Testing and Its Applications, ASTM STP 381, American Society for Testing and Materials, 1965, pp. 249-277.
16. Campbell, J.E. et al., Damage-Tolerant Design Handbook, Metals and Ceramics Information Center, Battelle-Columbus Laboratories, Columbus, OH, MCIC-HB-01, 1973.
17. Schjive, J., "The Accumulation of Fatigue Damage in Aircraft Materials and Structures", Proc. AGARD Conference No. 118, Symposium on Random Load Fatigue, Lyngby, Denmark, 13 April 1972.
18. Johnson, M.R., "Analysis of Railroad Car Truck and Wheel Fatigue: Part I - Service Load Data and Procedures for the Development of

Fatigue Performance Criteria", IIT Research Institute, Chicago, IL,
Report No. FRA-ORD&D-75-68, May 1975.

19. Cook, R.M., "Componentization for Fatigue Design and Testing (Provides Reliability for Modern Freight Cars)", IEEE-ASME Joint Railroad Conference, New York, NY (ASME Paper No. 71-RR-2), 19-21 April 1971.

AVOIDANCE OF FATIGUE CRACK GROWTH IN SHIPS' HYDRAULIC EQUIPMENT

L P Pook

(National Engineering Laboratory
East Kilbride, Glasgow, Scotland)

INTRODUCTION

This investigation, which has previously been outlined [1], is fairly typical of a number carried out at NEL over the past few years, in that a quick answer, based on limited information, had to be given. Only information which was available at the time of the investigation is included, and proprietary detail has been omitted.

In the manufacture of some ships' hydraulic equipment it was the usual practice to machine the port blocks required from heavy section plate. Care was needed in manufacture as a failure could disable a ship with serious safety and financial consequences. It was therefore standard practice to give the plate to be used for port blocks a 100 per cent ultrasonic examination. Any areas which had given ultrasonic indications were avoided when cutting out the port blocks to avoid ports intersecting flaws.

The equipment concerned was being made in a larger size than usual, and the ultrasonic examination of the 100 mm plate to be used gave indications of planar flaws in the region of the centre line. Sectioning through sample suspect areas uncovered laminations which might intersect the 25 mm diameter ports required at the centre of the plate, as shown schematically in Fig. 1.

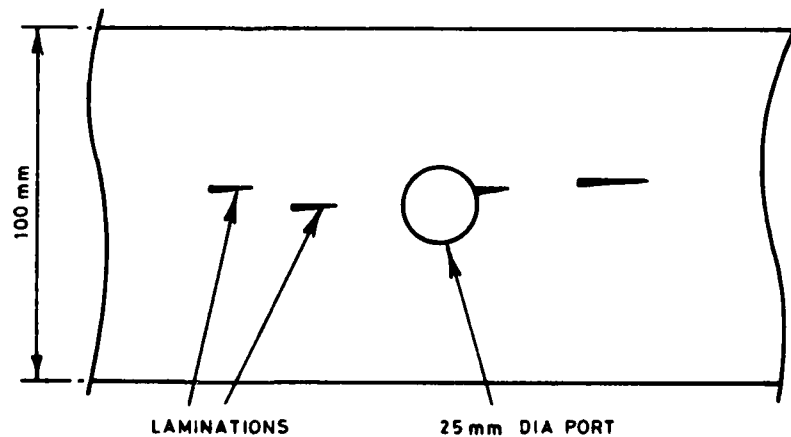


Figure 1 Schematic Section Through 100 mm Plate

It was impossible to avoid faulty regions when cutting out the port blocks required, nor could replacement plate be obtained in time to meet the delivery date. A possible alternative was to machine the port blocks from specially produced forgings. This was regarded as an emergency measure

involving a cost penalty. Work on the forgings would have to be initiated immediately if the delivery date were to be met. At this stage the firm telephoned NEL and was visited the following day.

The plate involved was a ship steel to BS 4360. Loading was cyclic in nature from zero to a peak pressure. The number of cycles during the expected life of the equipment, and the statistical distribution of the peak pressures were both unknown. The maximum operating pressure was 34.5 MN/m².

FORMULATION

In the absence of a detailed service pressure history the only safe course was to ensure that a port block would have an indefinite life under the pressure cycle 0-34.5 MN/m². The laminations can be regarded as crack-like flaws so that a fracture mechanics approach was appropriate. The problem amounted to the determination of the maximum permissible flaw size for the most severe type of crack which can be postulated. For the port block this was a crack intersecting a port block, both because a surface crack is more severe than a buried crack of the same size, and because fluid pressure can penetrate such a crack [1]. Indefinite life was required, so the permissible crack size was that which would just not grow under the pressure cycle 0-34.5 MN/m²; any fatigue crack growth would inevitably lead to eventual failure.

It is known [1] that a crack will not grow under a fatigue loading unless the range of opening mode stress intensity factor ΔK_I exceeds a threshold value ΔK_{Ic} . When a load cycle extends below zero, by convention, ΔK_I is calculated only from the positive part of the load cycle. Relevant threshold data that were available [2,3] are given in Table I; these are in-air data except where stated. No information was available for BS 4360 steel, but this was unimportant because fatigue crack growth thresholds are largely independent [2] of a steel's tensile strength or composition. They do depend on the value of R, where R is the ratio of minimum to maximum load in the fatigue cycle. Values for zero mean load (R = -1) are much the same as for zero to tension loading (R = 0), and immersion of mild steel in SAE 30 engine oil slightly increases the threshold. With these facts in mind, a ΔK_{Ic} value of 7.3 MN/m^{3/2} was selected for calculations.

ASSESSMENT

The expression for ΔK_I can be written in the general form

$$\Delta K_I = \Delta\sigma(\pi a)^{\frac{1}{2}}\alpha \quad (1)$$

where $\Delta\sigma$ is the tensile range of applied stress across the crack,

a in this case is crack depth, and

α is a geometric correction factor of the order of one.

Table I Values of ΔK_{Ic} for Various Steels

<u>Material</u>	<u>Tensile Strength</u> <u>MN/m²</u>	R	<u>ΔK_{Ic}</u> <u>MN/m^{3/2}</u>
Mild steel	430	-1	6.4
		0.13	6.6
		0.35	5.2
		0.49	4.3
		0.64	3.2
		0.75	3.8
Mild steel in tap water or SAE 30 engine oil	430	-1	7.3
Low alloy steel	680	-1	6.3
		0	6.6
		0.33	5.1
		0.50	4.4
		0.64	3.3
		0.75	2.5
Maraging steel	2000	0.67	2.7
18/8 austenitic steel	665	-1	6.0
		0	6.0
		0.33	5.9
		0.62	4.6
		0.74	4.1

For rough calculations it is often permissible [1] to take α as one, providing that $\Delta\sigma$ is a suitable nominal stress range. Assuming the crack to be small compared with port diameter this could be taken as the hoop stress range. The geometry was equivalent to a very thick walled cylinder under internal pressure, for which the hoop stress approaches the internal pressure as wall thickness increases, therefore the peak hoop stress could be taken as 34.5 MN/m^2 . However, in the geometry considered, pressure could penetrate the crack; this is equivalent to a stress equal to the pressure across the crack [1]. The pressure, therefore, had to be added to the hoop stress which gave a peak effective hoop stress of 69 MN/m^2 , and this, for the zero-to-pressure loading involved, was also the stress range.

Substituting $\Delta K_{Ic} = 7.3 \text{ MN/m}^{3/2}$ and $\Delta\sigma = 69 \text{ MN/m}^2$ gave $a = 3.6 \text{ mm}$ as the flaw depth which would just not grow. As with most loadings ΔK_I increased with crack size so that crack arrest could not occur and, as already stated, failure could be regarded as inevitable once crack growth started. The maximum permissible flaw depth was therefore 3.6 mm .

It was immediately obvious that such a flaw situated at a port was far too small for reliable detection with the available non-destructive testing

equipment, and as flaws had been detected the plate would have to be scrapped. Equally obviously there was no point in carrying out more refined calculations using more accurate expressions [4] for stress intensity factors, perhaps covering a range of postulated crack shapes. The practice of requiring plate for the manufacture of port blocks to be free of ultrasonic indications, using a particular set of equipment was confirmed as correct.

This is an example of how a simple 'back of an envelope calculation' based on apparently inadequate information can, and in fact often does, lead to a quick, clear-cut decision on the acceptability of a particular type of flaw. It could be argued that requiring an indefinite life at cycles of zero to the maximum working pressure introduced too much conservatism, and that an extensive investigation might have revealed that larger flaws, of an easily detected size, could have been tolerated. However, in this particular case, there was no time to obtain information, especially on the actual service pressure history. Moreover the cost of such an investigation into a one-off problem could not have been justified.

CONCLUSIONS

Within 24 hours of the original enquiry, a decision to scrap the plate material and replace with forgings had been taken by the firm concerned. Scrapping material containing defects is the obvious safe policy, but it can lead to unnecessary expense when material which would have been fit for the intended purpose is discarded. In this case it was possible to support the decision by a technical argument which helped convince a cost conscious management.

ACKNOWLEDGEMENT

This paper is presented by permission of the Director, National Engineering Laboratory, Department of Industry. It is British Crown copyright.

REFERENCES

1. Pook, L. P., "Fracture mechanics - how it can help engineers", Trans. NE Coast Instn Engrs and Shipbuilders, v. 90, no. 3, March 1974, 77-92.
2. Frost, N. E., Pook, L. P. and Denton, K. "A fracture mechanics analysis of fatigue crack growth data for various materials", Engineering fracture Mechanics, v. 3, no. 2, August 1971, 109-126.
3. Pook, L. P. "Fatigue crack growth data for various materials deduced from the lives of precracked plate", Stress analysis and growth of cracks. ASTM STP 513. American Society for Testing and Materials, Philadelphia, Pa., 1972, 106-124.
4. Underwood, J. H. "A note on cylinder stress intensity factors", Int. J. Pressure Vessels and Piping, v. 3, no. 3, July 1975, 229-232.

FAILURE AND SAFETY ANALYSIS OF CONTROLLABLE-PITCH PROPELLERS

Oscar Orringer
Associate Director, Aeroelastic and Structures Research Laboratory, MIT

Justin E. Kerwin
Professor of Naval Architecture, MIT

Regis M. N. Pelloux
Associate Professor of Metallurgy and Materials Science, MIT
Cambridge, MA 02139

INTRODUCTION

In the autumn of 1974 the USS Barbey (DE1088) lost its propeller during maneuvers off Long Beach, California. Just prior to the accident, the Barbey began a "crash-astern" evolution from full power ahead. The crew noted severe vibrations which increased as the evolution progressed, until about mid-way into the maneuver, at which time thrust was lost. Immediate investigation revealed that all five propeller blades had separated from the hub and had sunk in deep water, preventing recovery of the parts. Subsequently, the U.S. Navy asked MIT to conduct a technical investigation which included assessment of a similar twin-screw design for the USS Spruance (DD963). The Navy was primarily concerned with the latter ship, which was the forerunner of a destroyer class, and which was scheduled to begin sea trials in the spring of 1975. There was somewhat less concern about the Barbey, a prototype destroyer escort which was not to be produced as a class.

The objectives of the MIT investigation were to analyze the Barbey failure, to recommend modifications, and to assess the safe operational limits of three designs: Barbey (original), Barbey (modified) and Spruance. The task was complicated by the facts that the Barbey and Spruance propeller pitch-control mechanisms were developed by different manufacturers and were different in detail. Also, these were new designs, although controllable-pitch propellers had been installed on many commercial and some naval ships in Europe.

Figure 1 illustrates some of the mechanical details of a typical controllable-pitch propeller. The pitch mechanism, contained within the hub, is operated by a hydraulic system controlled through the hollow center of the shaft. Blade pitch is changed by spindle torques which the hydraulic system applies to crank rings located under each blade. The palm of the blade is secured to the crank ring by six or eight large-diameter blade bolts, which are installed with pre-tension to make the crank ring and blade palm act like a single solid piece. Pitch and RPM rates of change are quite severe in the high-speed maneuvers executed by destroyers and destroyer escorts, particularly because new ships in these classes combine gas-turbine engines with CP propellers. Since the revolution of a gas-turbine engine

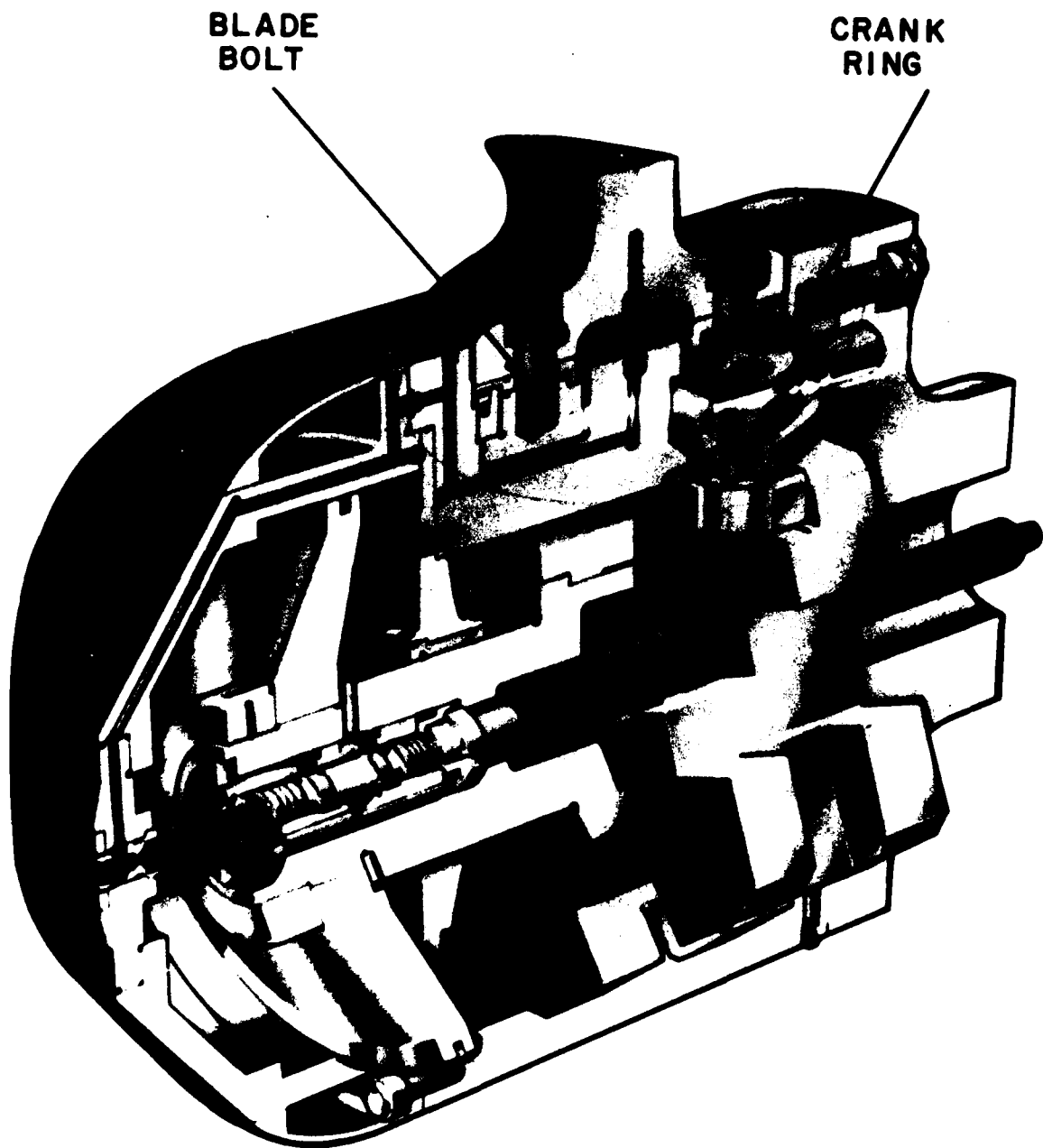


**FIGURE 1. PITCH-CONTROL MECHANISM
IN A TYPICAL CP PROPELLER**

cannot be reversed, the propeller shaft always spins in the same direction. Hence, in a crash-astern evolution such as executed by the Barbey, the propeller pitch is changed rapidly from forward to reverse while the ship is still steaming ahead. The large unsteady hydrodynamic forces thus created on the blades are reacted by the blade bolts and crank rings.

The Navy's investigation of the Barbey accident revealed the following information which bears upon the technical analysis. The Barbey had executed a few crash-astern evolutions during previous trials. The Barbey had accumulated about one year of service at the time of the accident. The blade bolts had been replaced during a dockyard inspection about 3 months prior to the accident. The original bolts (17Cr-4Cu-PH stainless steel) had apparently been insufficiently pretensioned in some cases and exhibited severe stress-corrosion cracking. New blade bolts of the same material were emplaced, but the installation procedure was changed from achieving a specified wrench-torque to achieving a specified shank elongation, as measured by a feeler gage inserted in a central hole bored into the shank from the bolt head. No bolts were recovered after the accident, but parts of some crank rings remained in the hub. After the Barbey had been towed back to port, these parts were removed and examined metallurgically. The metallurgical data indicated that the fracture toughness of the crank ring material (AISI-4340 casting) was considerably lower than the handbook value. A similar investigation of the Spruance crank ring material (AISI-4150 forging) also revealed low fracture toughness. Finally, measurements of shaft thrust were available for the Barbey from the earlier crash-astern trials. These measurements had been obtained from a shaft strain gage at approximately 10-second intervals.

In the light of the accident investigation data, fatigue-crack propagation was judged to be the probable cause of the loss of the Barbey's propeller. Both the crank rings and the blade bolts were deemed to be potentially critical parts. The MIT investigation therefore focussed on these parts. The Navy requested a rapid engineering assessment in order to have recommendations formulated prior to the scheduled sea-trials of the USS Spruance. Of necessity, many assumptions had to be made to complete the assessment on schedule, in view of the small amount of service data available. A detailed assessment was necessary because the crank rings and blade bolts are forced to be highly stressed designs by constraints on available volume within the propeller hub.

ANALYSIS

Five areas of pertinent engineering analysis were identified for the MIT investigation [1]. First, scale-model testing and dynamic hydroelastic analysis of the Barbey propeller were required to estimate the actual steady and unsteady blade loads during high-speed maneuvers. Second, an operational scenario for destroyers and destroyer escorts had to be constructed to define a typical cyclic service-load history. Third, stress analyses of the blade bolts and crank rings were required to relate applied loads to stresses and to identify the critical locations in these parts. Fourth, a crack propagation analysis had to be made to assess the safe operational life of each

design. Finally, metallurgical data and opinion had to be gathered and evaluated to justify recommendations for material selection, with particular reference to the seawater environment.

A dynamic finite-element analysis of one blade was conducted to estimate resonant frequencies for the Barbey's propeller. The finite-element model consisted of 72 triangular assumed-stress hybrid plate-bending elements [2] and 245 degrees of freedom. The first 5 resonant frequencies and mode shapes were calculated by the subspace iteration method [3,4]. The influence of centrifugal tension on blade frequencies was judged to be negligible for low-aspect-ratio CP propellers. However, the effect of the surrounding water as an apparent mass was included in the analysis. An upper-bound ratio of apparent mass-density to density of the blade vibrating in air:

$$\rho/\rho_0 = 4.46 \quad (1)$$

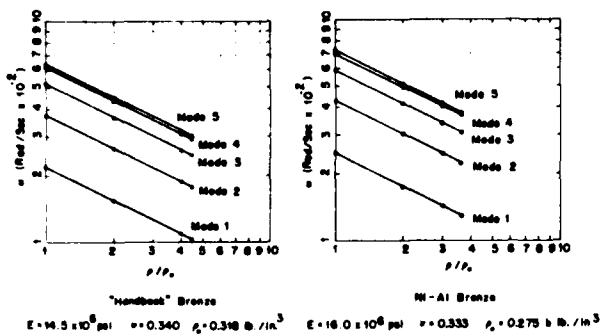
was calculated from high-aspect-ratio airfoil theory. A probable value:

$$\rho/\rho_0 = 3.64 \quad (2)$$

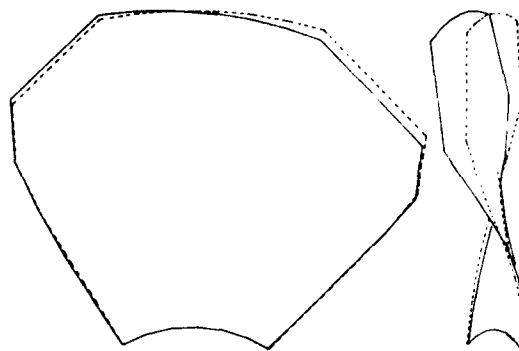
was estimated from low-aspect-ratio theory. Figure 2 illustrates the vibration frequencies and mode shapes for two blade materials: handbook bronze and the Ni-Al bronze alloy used to fabricate the Spruance blades. A study was made to evaluate the possibility of load amplification due to blade flexure. Classical flutter and stall-flutter were eliminated, but wake-induced flutter could occur at the lowest torsional frequency of the blade when the propeller operates in a ring-vortex mode [5], since this frequency coincides with the 9th to 11th multiples of shaft RPM. While not a direct cause of catastrophic failure, wake-induced flutter was judged to be a contributor to the general level of cyclic fatigue loads during crash-astern maneuvers.

Steady-state hydrodynamic calculations performed with the MIT-PINV-1 computer code [6] indicated that the Barbey propeller might operate in the ring-vortex mode during certain portions of a crash-astern maneuver. An order-of-magnitude estimate of the transient effect of the ring-vortex suddenly being blown away was made by running the same program with the vortex removed. The resulting thrust was approximately doubled (from 250,000 to 500,000 lbs.). This analysis can hardly be taken too seriously, but it indicates that transient-load increases of as much as 50 percent above steady state might occur in service.

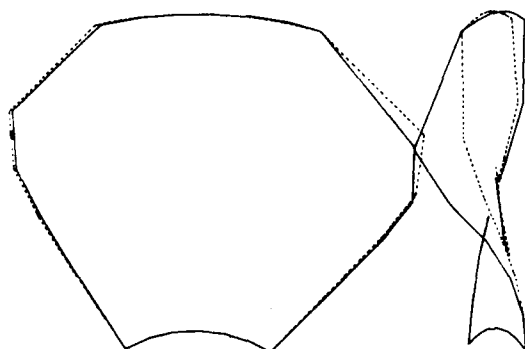
A reasonably close simulation of the Barbey's propeller and afterbody was set up in the 20-inch square test section of the MIT Water Tunnel. The blades from NSRDC Propeller No. 4402 (very close to the actual design) were combined with a hub, a splitter plate to simulate the hull above the propeller, and shaft struts built for scale tests of the Navy SEA-CONTROL ship.



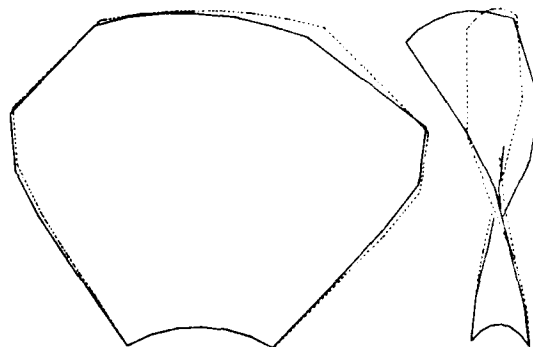
DE1088 CP PROP BLADE VIBRATION FREQUENCIES



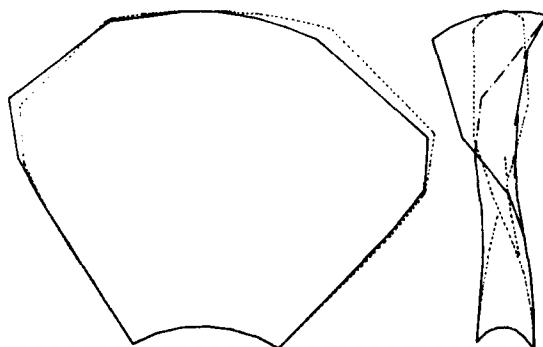
MODE 1 (BENDING)



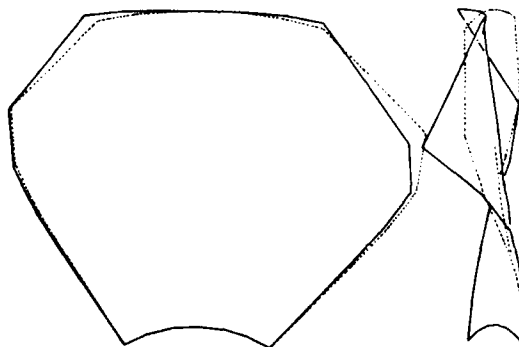
MODE 2 (TORSION)



MODE 3 (BENDING)



MODE 4 (BENDING)



MODE 5 (TORSION)

FIGURE 2. FREQUENCIES AND MODE SHAPES OF BLADE

Figure 3 illustrates the test configuration, together with photographs of the ring-vortex and cavitation phenomena observed in representative crash-astern simulations. At high forward speeds and negative pitch settings (corresponding to rapid pitch reduction from full speed), a highly unstable cavity flow develops, with the cavity "blowing out" to a radius much larger than that of the propeller. Pieces of the tip vortex are convected by the turbulent flow into the outer stream, where they either break away suddenly or strike the hull surface with a sharp cracking noise. The severe vibration levels could be felt by personnel standing on the laboratory floor, several feet from the water tunnel.

To complete the hydrodynamic analysis, the characteristics of the cavitating propeller obtained from the tunnel tests were used as input data to a one-degree-of-freedom computer program to calculate ship speed and propeller thrust versus time for any prescribed time-history of pitch and RPM. The first case studied corresponded to the pitch and RPM recorded during crash-astern trials for the USS Barbey. The prediction agreed well with both measured thrust (Fig. 4) and stopping time (120 seconds predicted, 110 seconds in trial). Other combinations of pitch and RPM were then tried to determine an upper bound on propeller forces. From these calculations, the worst case was estimated to produce a quasi-steady thrust of -393,000 lbs. and a torque of 300,000 lb.-ft., with unsteady components at 50 percent of the steady values. This resulted in an estimate of the extreme crash-astern load 60 percent greater than had been assumed by the designers.

An operational scenario was constructed from design data describing shaft RPM versus hours/year for the USS Spruance [7]. These data are summarized in Table I. At the 110-RPM condition (ship speed of 22 Kt), the hydrodynamic propeller loads were estimated to be 47 ± 10 percent of design-full-power-ahead (DFPA) loads, where the ± 10 percent represents unsteady loads [8]. This condition was taken to represent the state which precedes any high-speed operation, with a load minimum (37 percent DFPA) assumed to occur just before the first high-speed load peak. The shaft RPM values between 140 and 168 were taken to represent high-speed, high-stress operations (full-power ahead, full-power turn, and crash-astern). Summation of the RPM-time products for these 57.5 hours/year gave an estimate of 521 Kc/year of load cycles with high mean and small amplitude.* Low-high cycles (analogous to ground-air-ground cycles in airplanes) occur much less frequently, but are more damaging. The frequency of low-high cycles was estimated to be 2.2 Kc/year by assuming a "mission profile" of 10/1 full-power turns/full-power ahead, with average durations of 15 seconds per FPT (zig-zag maneuvers) and 15 minutes per FPA.

Static stress analyses of the crank rings were performed at the C. S. Draper Laboratory, using the MIT ICES/STRUDL-II finite-element code [9].

* For the USS Barbey, mean loads ranged from 120 to 172 percent DFPA and the alternating component was estimated to be ± 15 percent DFPA. The corresponding figures for the USS Spruance were 133 to 194 and ± 25 percent DFPA.

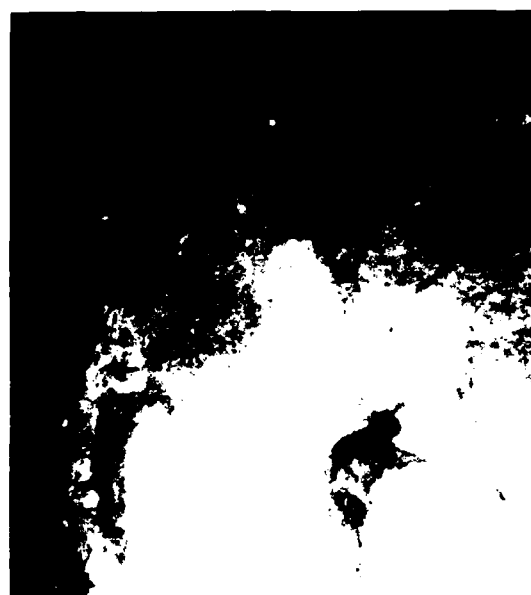


**FIGURE 3. MODEL PROPELLER AND OBSERVATIONS
OF CRASH-ASTERN SIMULATION**

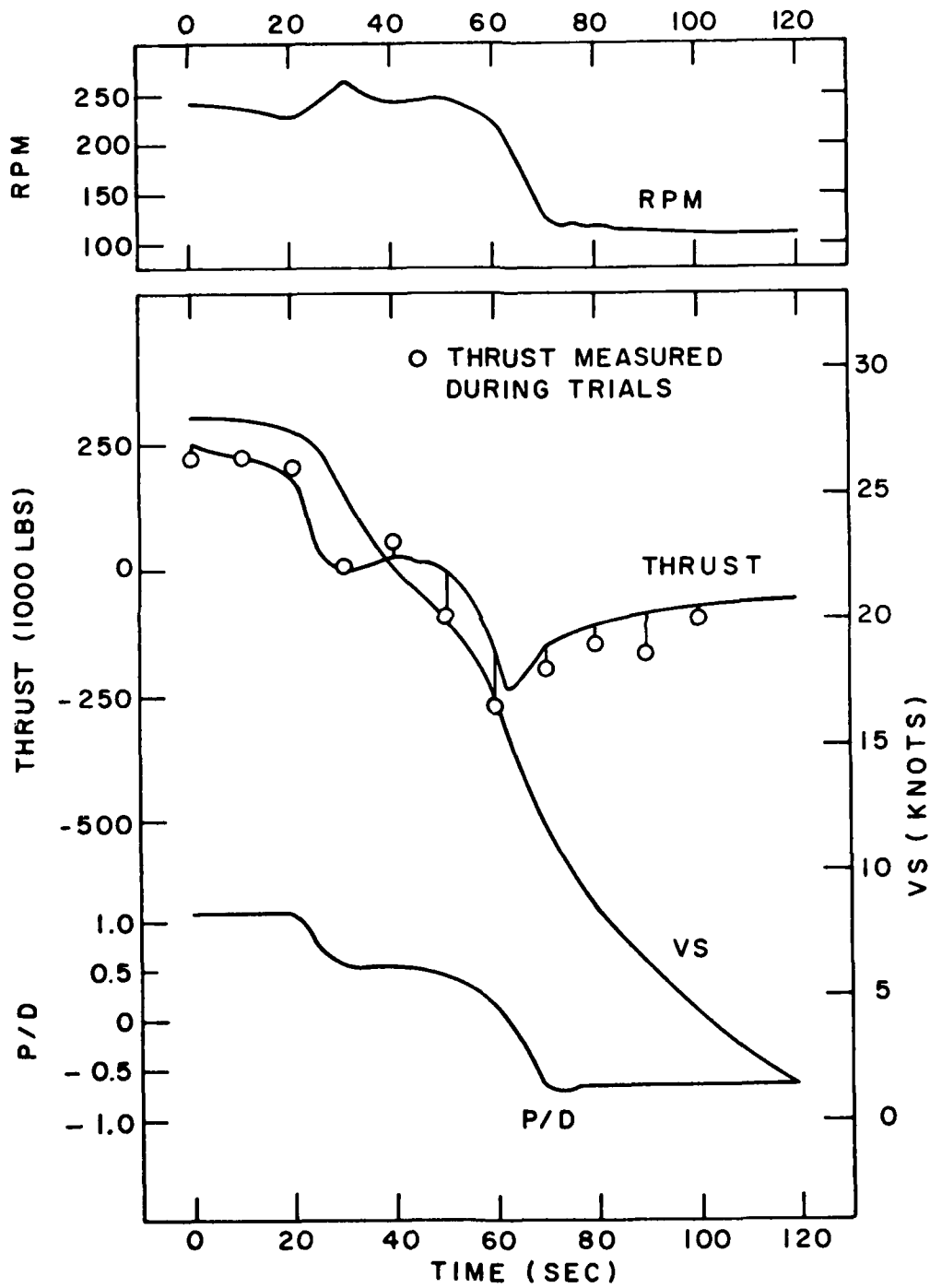


FIGURE 4. PREDICTED AND MEASURED SHIP DECELERATION DURING CRASH-ASTERN TRIAL

Table I
Hours/Year as a Function of Shaft RPM

RPM	Hrs/Yr	RPM	Hrs/Yr	RPM	Hrs/Yr	RPM	Hrs/Yr
55	584.5	80.2	297.1	110.0*	219.2	134.5	14.6
57	302.0	85	316.6	114.5	73.1	140.2**	14.6
61.5	326.3	90	350.7	119.5	63.3	148.0**	14.6
66	341.0	95	356.3	124.0	29.2	154.5**	14.6
70.5	345.8	100	433.5	126.5	26.7	160.0**	9.7
75.5	331.2	105	365.3	129.0	24.3	168.0**	4.0

*Corresponds to ship speed of 22 Kt.

**Assumed to be high-stress operations.

Separate analyses were conducted for the five principal load components imposed on the crank ring by blade loads and bolt pre-tension. Of these, three components (bending moment due to blade thrust, centrifugal blade forces, and blade-bolt pre-tension) were found to cause significant stress levels. The computed results were supplemented by applying handbook stress-concentration factors [10,11] to fillet and thread details in critical areas. The reason for the need to supplement the computer calculations can be seen from Fig. 5, which shows a perspective view of the finite-element model of one of the crank rings. The model is assembled from 3D isoparametric, linear assumed-displacement tetrahedra and hexahedra [12]. Restrictions on available computer core memory and CPU time limit the models to about 500 elements. However, the straight element edges reproduce the curved geometry of the part poorly. Also, many elements have elongated shapes, which reduces the accuracy of the analysis [13,14].

Figure 6 illustrates a schematic radial section through a typical crank ring, indicating the two stress-critical areas which were found in all designs. The principal contributor to short crack-propagation life is the relatively thin outer wall region between the blade bolt-hole and the crank ring bearing lip (0.44 inch for the Barbey, 1.5 inches for the Spruance). This is aggravated by the presence of cut-in oil grooves and fillets on the outer wall surface, and by thread grooves in the bolt-hole. None of these details can be adequately represented by the finite-element model.

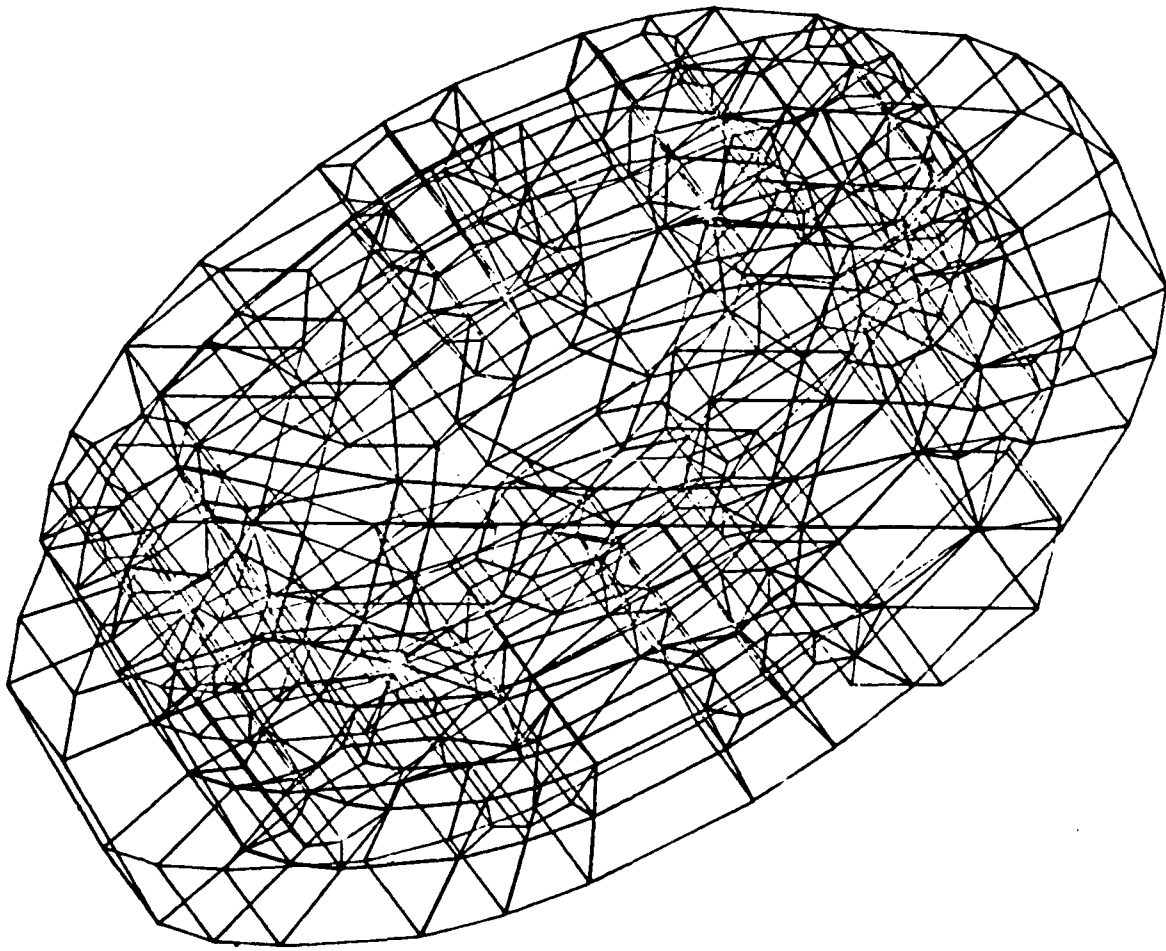


**FIGURE 5. USS BARBEY CRANK RING
FINITE-ELEMENT MODEL**

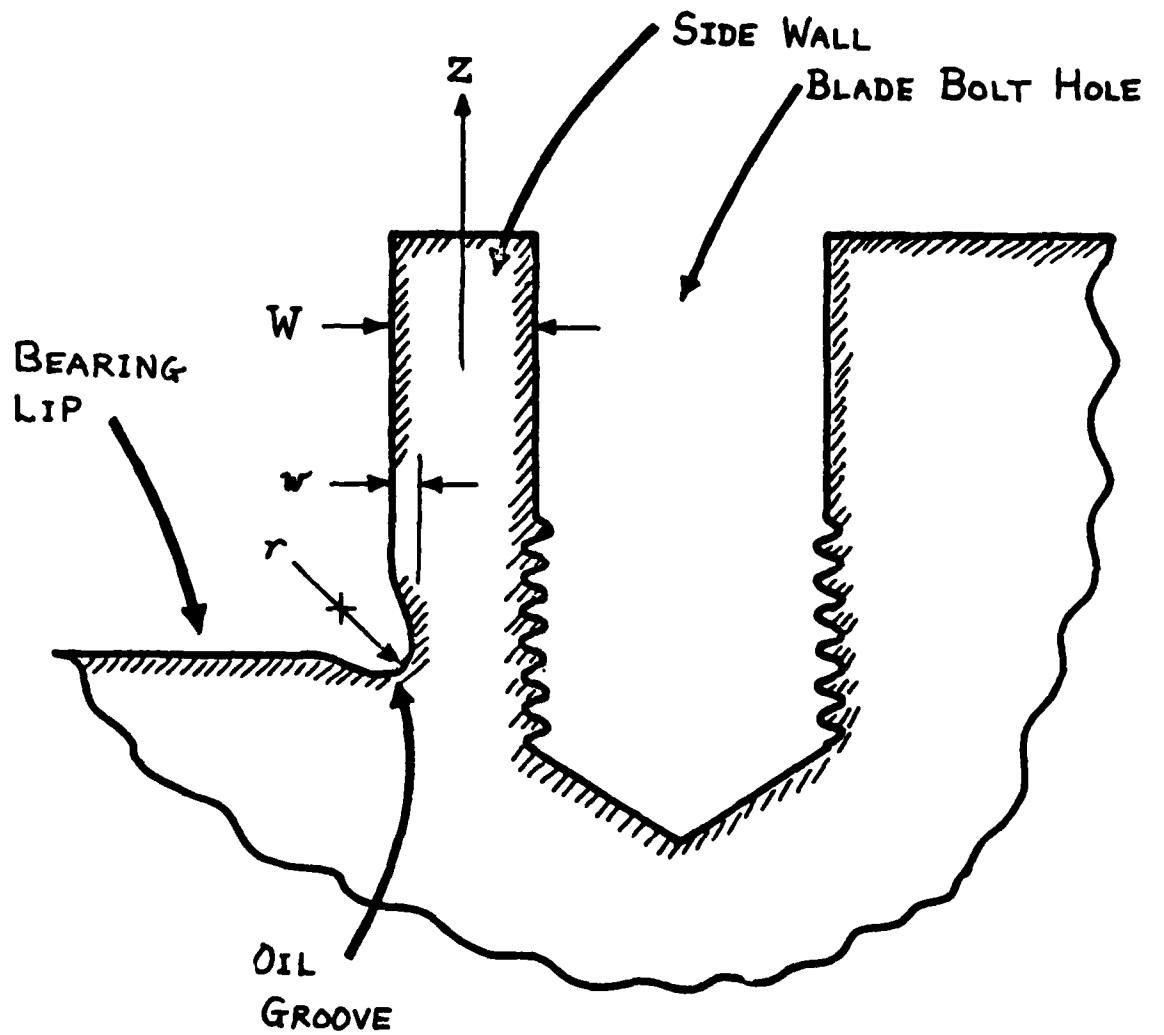


FIGURE 6. CRITICAL AREAS IN TYPICAL CRANK RING

Pre-tension was found to be the most significant contributor to blade bolt stress. Accordingly, the initial stress state in the bolts was analyzed by applying stress-concentration factors to the nominal shank tensions, using the bolt engagement scenarios as a guide. The bolt designs, materials and installation procedures are completely different for the two designs. Figure 7 illustrates the bolt geometries and summarizes the stress concentration factors which could be estimated from handbook data. The Barbey bolt is fabricated from 17% Cr - 4% Cu precipitation-hardening stainless steel aged to the H1100 condition ($f_{ty} \approx 115$ ksi). This bolt is installed by turning down to 70 ksi in the shank (as determined by center-bore dial-gage extension measurement correlated with measurements on bolts pulled in tension), and then backing off to 35 ksi pre-tension. The Spruance bolt is fabricated from intermediate-strength AISI-4340 steel ($f_{ty} \approx 180$ ksi) and has a large centerbore. A hydraulic system is installed over exterior threads on the bolt-head (not shown) and is pressurized to set up a prescribed shank tension (136,000 lbs. nominal, 190,000 lbs. maximum allowable). The bolt is then turned in "hand-tight", and the hydraulic system is depressurized. To complete the installation, the hydraulic system is removed and replaced by a plastic protective cover. The stress calculations for both bolts indicated that plastic yielding would occur in the top few turns of thread, until enough yielding had taken place to distribute the load uniformly.

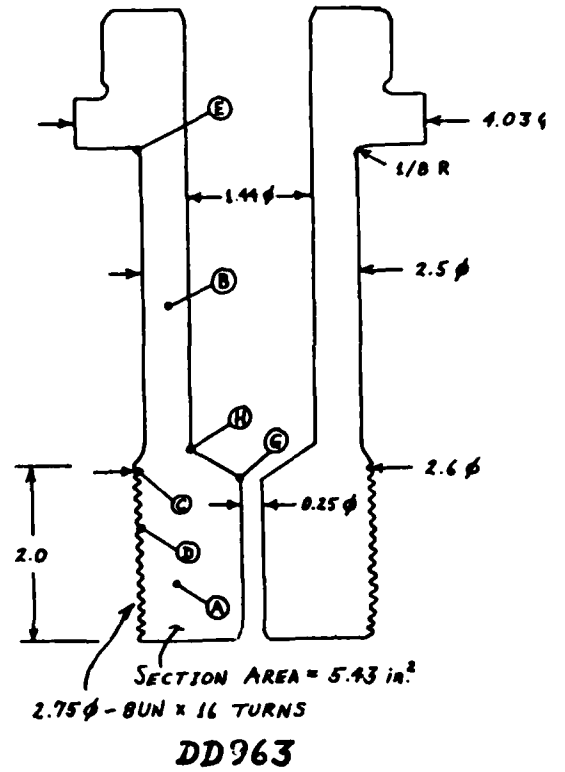
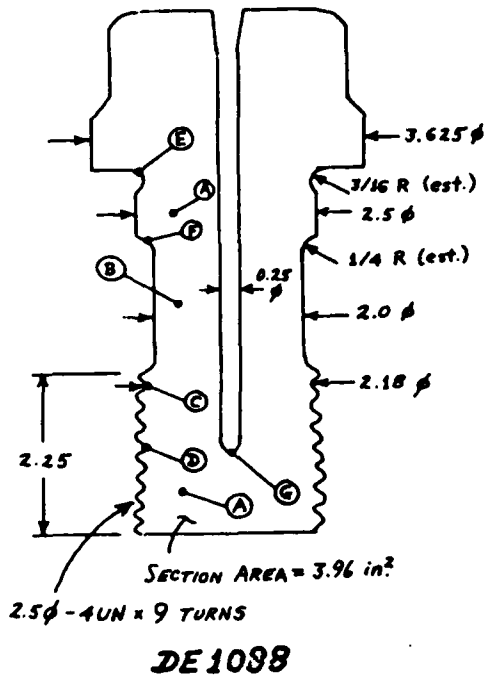
Crack propagation analyses were conducted for the blade bolts, both crank rings, and a proposed modification of the Barbey crank ring in which the oil groove was eliminated and the outer wall thickness increased from 0.44 to 0.84 inch. A restricted version of the Forman equation [15] was used in the analysis:

$$da/dn \approx \frac{C(\Delta K)^m}{1-R} \quad (3)$$

for $\Delta K \geq \Delta K_{TH}$ and $\Delta K \ll K_{IC}$, where:

- a = Current crack size
- n = Independent variable (number of load cycles)
- ΔK = Stress intensity range
- R = Stress ratio = S_{min}/S_{max}
- ΔK_{TH} = Threshold stress intensity range for crack propagation (material property)
- K_{IC} = Material fracture toughness

and where C, m are constants empirically fit to crack growth-rate data. Several low-carbon ferritic steels with a wide range of nominal fracture



BLADE BOLT STRESSES AND SCF

Location	DE1088			DD963		
	SCF	Stress at Max. Torque	Stress at Red. Torque	SCF	Stress for 190 KIPS	Stress for 136 KIPS
A		54 ksi	27 ksi		35 ksi	25 ksi
B		70	35		63.5	45
C	5.5	297	148.5	8	280	200
D	1.87	102	51	2.62	91.5	65.6
E	2.04	110	55	2.45	155	110
F	1.63	114	57			

FIGURE 7. COMPARISON OF BLADE BOLTS

toughness were considered for both ships (see Table II). On the basis of

Table II

Typical K_{IC} Values for Steels at 75°F

Alloy	K_{IC} (ksi $\sqrt{\text{in.}}$)	Remarks
AISI-4340	40	Worst handbook value
AISI-4140	60 - 80	Handbook range for high-strength alloy, f_{ty} to 220 ksi, CVN = 12 to 16 ft. lb.
AISI-4140	100 - 120	Intermediate-strength alloy, f_{ty} = 100 to 130 ksi, CVN = 30 to 40 ft. lb.
HY-130	150 - 300	Upper bound is controversial
17-4-PH (1100)	108	[18]
"4340"	60 - 80	NSRDC test of DE1088 crank ring; f_{ty} ~ 115 ksi, CVN = 6 to 11 ft. lb.
"4150"	55 - 70	NSRDC test of DD963 crank ring; f_{ty} ~ 120 ksi, CVN = 8 to 11 ft. lb.

dry-air crack-propagation tests at $R = 0.05$ [16,17], these alloys can be fit as a class with upper-bound values $C = 0.627 \times 10^{-8}$, $m = 2.25$, and with $\Delta K_{TH} \approx 5$ ksi $\sqrt{\text{in.}}$, with da/dn in units of inch/cycle and ΔK in ksi $\sqrt{\text{in.}}$. The data and fits are reproduced in Fig. 8, which includes data for 17Cr-4Cu-PH stainless steel as well [18]. As indicated in the figure, the values of $C = 2.7 \times 10^{-10}$ and $m = 3$ give a lower bound for 17Cr-4Cu-PH stainless steel.

Since no service data on initial damage were available, Eq. 3 was integrated from threshold crack sizes under scenarios which assumed simple crack and structure geometries. Cracks were assumed to start as semi-elliptical surface flaws, for which the stress intensity is given by [19]:

$$K_Q = 1.1 S M_k \sqrt{\pi a/Q} \quad (4)$$

$$\Delta K = 1.1 (S_{\max} - S_{\min}) M_k \sqrt{\pi a/Q} \quad (5)$$

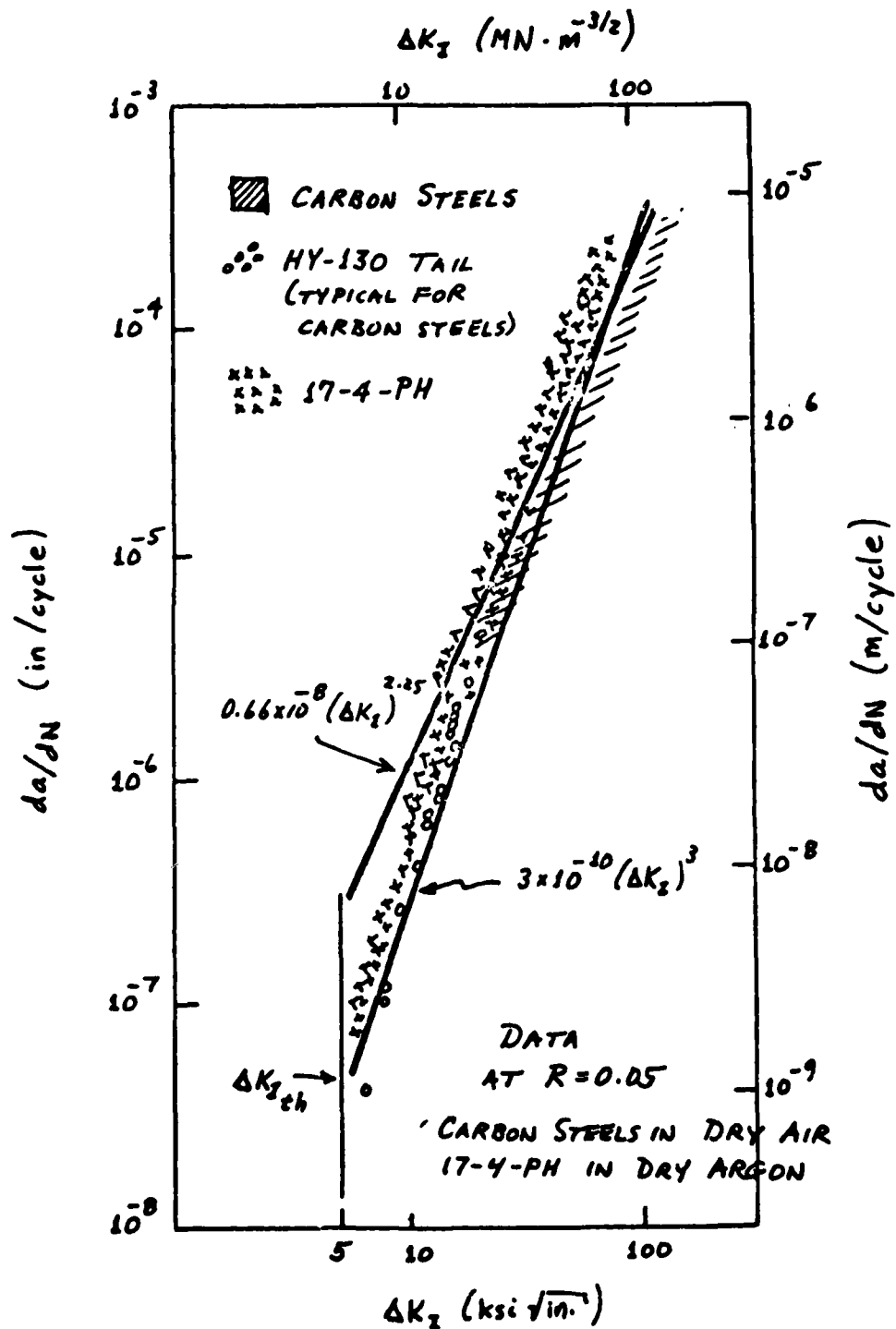


FIGURE 8. CRACK GROWTH RATE DATA [16,17,18] AND EMPIRICAL FITS

where M_k , Q are functions of crack size, crack shape, wall thickness, and f_{ty} , and where S is taken from the static stress analyses of critical areas. After growing through the minimum wall thickness of a crank ring, the crack was assumed to propagate around an annulus surrounding the bolt hole. Bolt cracks were arbitrarily and quickly transitioned to straight edge-cracks, based on the authors' experience with bolt failures in other applications. Equations 4 and 5 were then replaced by 2D K-solutions for through-cracks, a drastic approximation, but one which did not influence the results excessively because second-stage growth occurs quickly relative to the propagation of surface cracks. Crack growth was stopped when the first of two events ($K_{max} = K_{IC}$ or net-section failure by plastic yield) was reached.

Results for the crank rings are illustrated in Fig. 9. Separate curves for the high-speed and low-high cycles are shown, and the beneficial effect of wall thickness is evident for both load conditions. These data are cross-plotted in Fig. 10 to show the safety limit as a function of assumed initial crack size. The plots combine high-speed and low-high loading by linear damage-summation:

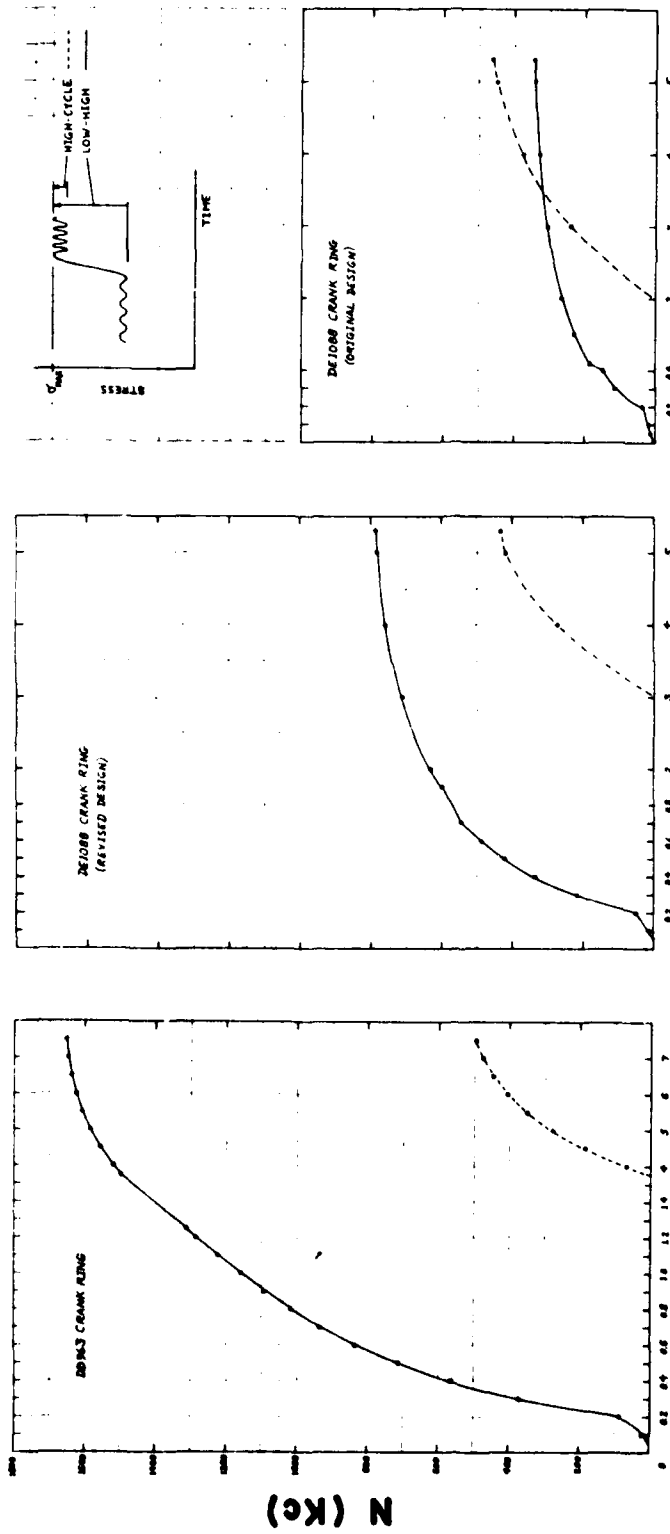
$$CY = \frac{\text{High-Speed Cycles}}{521 \text{ Kc/Year}} + \frac{\text{Low-High Cycles}}{2.2 \text{ Kc/Year}} \quad (6)$$

where CY is the number of calendar years to fracture.* Also, the Fig. 10 results have been adjusted downward to account for possible growth-acceleration due to corrosion. Figure 11 illustrates similar results obtained for the blade bolts.

Alloys outside the class of intermediate-strength low-carbon steels had never been considered for the crank rings. Hence, material selection for these parts was confined to a trade-off between fracture toughness and wall thickness. However, material selection for the blade bolts proved to be a controversial subject because of the different environmental sensitivities of low-carbon steels versus 17Cr-4Cu-PH stainless steel. The latter alloy was favored by the fabricator of the USS Barbey propeller and by some Navy personnel because of its good resistance to crack nucleation** (fatigue endurance limit of 20 ksi in seawater, compared with 3 to 9 ksi for the low-carbon steels). However, the stainless alloy is more sensitive than low-carbon steels to crack propagation (Fig. 8). Additional metallurgical data and opinions on the subject were gathered by informal consultation with several metallurgists in the aerospace, automotive, and metals industries. The details are too numerous to recount here, but the following generally accepted judgements are worth summarizing:

* Growth retardation was not considered in this study.

** Based on rotating bending fatigue test specimens.



CRACK SIZE VERSUS CYCLES FOR CRANK RINGS

FIGURE 9. CRACK SIZE VERSUS CYCLES FOR CRANK RINGS

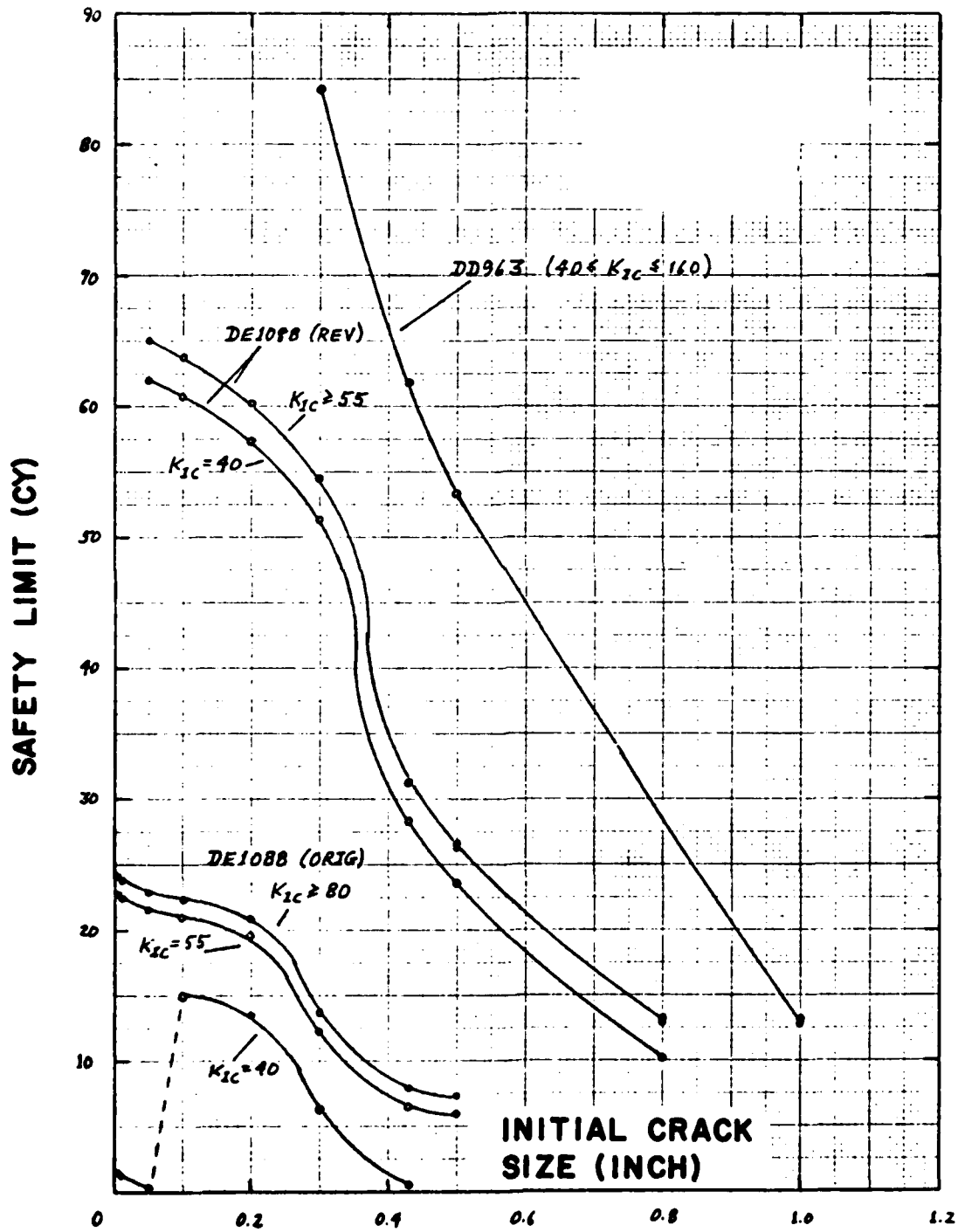


FIGURE 10. CRANK RING SAFETY LIMIT ESTIMATES

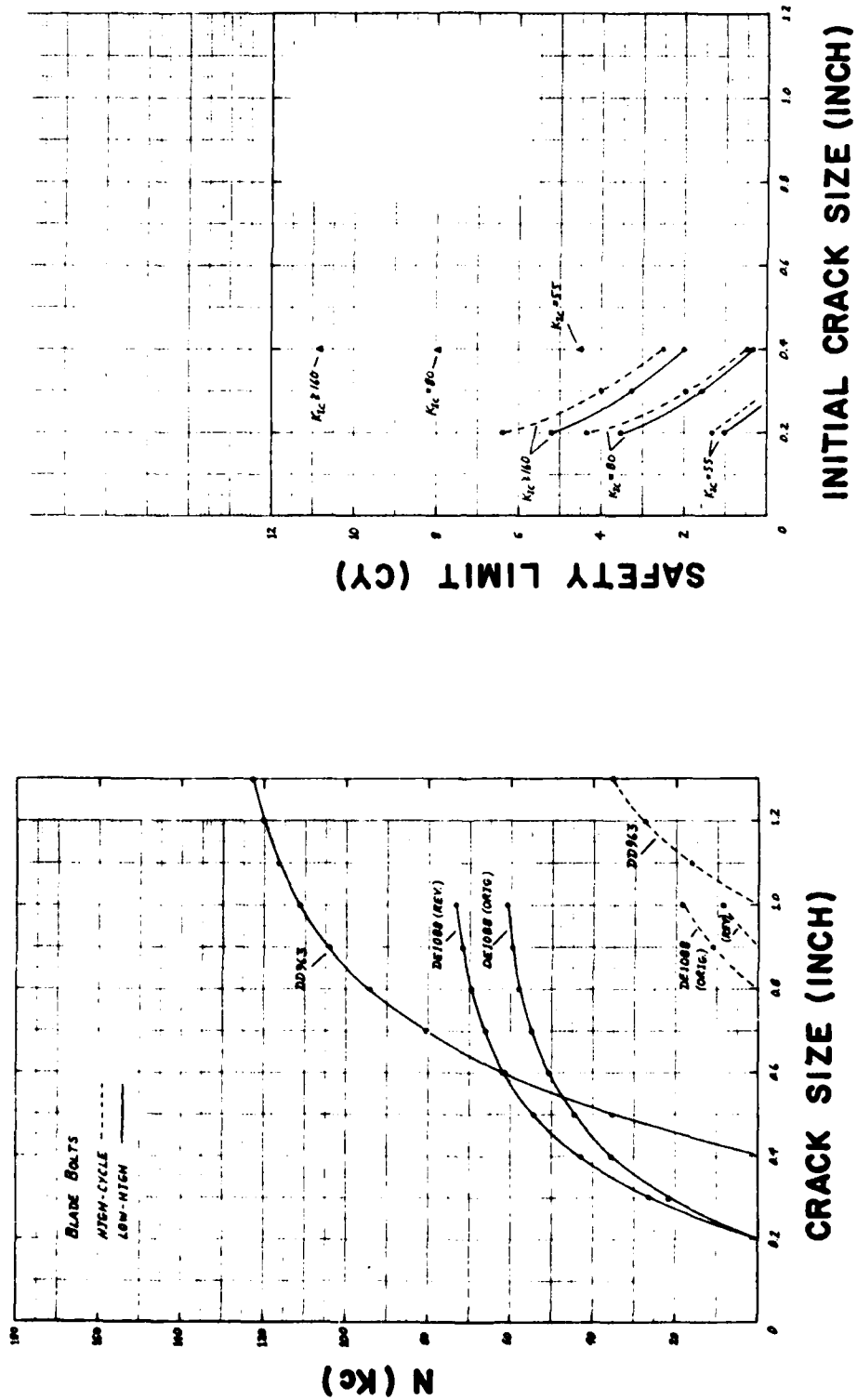


FIGURE 11. DAMAGE TOLERANCE OF BLADE BOLTS

1. Probable corrosion-damage modes are different. Low-carbon steels normally exhibit general area corrosion. However, 17Cr-4Cu-PH stainless is subject to pit-corrosion and localized galvanic stress-induced corrosion in stagnant seawater conditions, such as might be found underneath bolt-head protective covers.
2. The possibility of stress-corrosion cracking in AISI-4340 is of some concern ($f_{ty} = 180$ ksi, $K_{ISCC} < 50$ ksi $\sqrt{\text{in}}$). Achievement of good K_{ISCC} values in PH stainless steels does not correlate with overaging.*
3. The 17Cr-4Cu-PH alloy is considered to be highly sensitive to forging defects.

While gathering the above information, we also observed (as seems to be the case for many fracture mechanics assessments) that the environmental data were difficult to evaluate because they were almost invariably based on other alloy compositions and on test conditions with environments and measured parameters considerably different from those which were important to the subject of our investigation.

CONCLUSIONS

The following conclusions were drawn from the analysis of the USS Barbey and USS Spruance pitch-control mechanisms. Both steady and unsteady hydrodynamic loads during crash-astern maneuvers appeared to be much higher than assumed in the design cycle. These, together with loads corresponding to other high-speed maneuvers could cause higher cyclic stress levels in the critical parts than had been assumed in design. Fatigue crack propagation was therefore a concern in both designs, and a possible cause of the USS Barbey accident. Stress levels calculated for critical areas were generally below f_{ty} , but were high enough to permit crack propagation from initial damage. Blade-bolt pre-tension was found to be high enough in both designs to cause plastic yielding near the thread roots, a possible cause of initial damage. Poor installation procedure (e.g. accidental misalignment of the bolt during seating) was also considered to be a possible source of initial damage. The stress-concentration factors in the lower centerbore of the USS Spruance bolts were not quantified, but were of concern as a possible contributor to stress-corrosion cracking.

The representative load history constructed from Spruance operational design assumptions and the crack propagation analyses indicated that high-speed-maneuver stress cycles were generally below material ΔK_{TH} , except for very large crack sizes. On the other hand, low-high cycles could propagate quite small cracks, but were relatively infrequent. Hence, the safety limits tended to be quite large for small sizes of assumed initial damage, but they decreased rapidly for large initial cracks. With respect to the USS Barbey,

* K_{ISCC} is the threshold stress intensity for stress-corrosion cracking, i.e. propagation by chemical attack under static pre-tension.

the 1974 accident could be explained by an initial flaw in the crank ring with a characteristic dimension of 0.4 inch, since the accident occurred at about one calendar year of service (see Fig 10). A flaw of this size would have been almost through the crank ring wall thickness, and must be classified as an unusual forging defect which would occur infrequently. The remaining crank ring safety limit results demonstrated that the rings in the Spruance were tolerant to initial damage in the range 0.8 to 1.0 inch, and that the best way to achieve comparable damage-tolerance in the Barbey was to increase the wall thickness from 0.44 to 0.84 inch.

With respect to the blade bolts, the initial damage modes mentioned above were judged to be unlikely to cause cracks large enough to be above the propagation threshold for either high-speed or low-high cycles. However, forging defects above threshold size in 17Cr-4Cu-PH stainless round stock were thought to be possible. Corrosion fatigue (crack nucleation) in the bolt heads was not considered to be a problem, since these areas have little or no stress near the active surfaces. However, galvanic and/or pit-corrosion could be a problem for stainless steel bolts (USS Barbey). Also, stress-corrosion cracking in the lower centerbore (USS Spruance) was viewed as a potentially serious problem because of: (1) high pre-tension; (2) use of high-strength AISI-4340 alloy, and; (3) the possibility that the plastic centerbore covers might admit seawater by cracking or coming loose in service.

Finally, material selection was not a major issue for the crank rings, but was debated vigorously for the blade bolts. The principal conclusion drawn here was that combination of a high-risk material (17Cr-4Cu-PH stainless steel) with high static stresses near seawater (Sпруance bolts with cracked or lost covers) was inadvisable. The Barbey bolts were judged to have much less risk of centerbore stresses.

DISPOSITION

The MIT team made the following recommendations for disposition of the CP propeller systems of the USS Barbey and USS Spruance. Modification was recommended for the Barbey crank ring to eliminate the in-cut oil groove and to increase the minimum wall thickness from 0.44 to 0.84 inch. No dimensional modification was recommended for the USS Spruance, nor was a material change proposed for either design.

An inspection interval of 8 calendar years for both designs was recommended to coincide with existing Navy practice regarding ship survey schedules. This interval is unfactored with respect to the calculated safety limits based on 0.8 to 1.0-inch initial damage. The unfactored interval was deemed acceptable in this case because: (1) damage of this size is unlikely to escape detection, and; (2) propeller loss is not an accident as critical to operational safety as would be (for example) the loss of an airplane wing. The inspection interval was coupled with a recommendation to use improved manufacturing quality-assurance methods on all crank rings (e.g. X-ray scans).

The MIT team recommended retention of AISI-4340 for the blade bolts in the USS Spruance and accepted retention of 17Cr-4Cu-PH stainless steel for the bolts in the USS Barbey. Recommendation against the use of 17-4 in future ships was made (particularly in the case of production classes), at least until adequate service data should be available. As an added precaution with respect to the Spruance class, seawater soak-tests were recommended for the AISI-4340 bolts with: (1) 190,000-lb. pre-tension load; (2) Ni-Al-bronze material nearby to simulate galvanic coupling with the propeller blade, and; (3) no centerbore covers.

SUPPLEMENTARY RESULTS

Post-modification tests carried out by the Navy after completion of the MIT investigation disclosed other potential causes of fatigue damage [20]. These tests included a full-scale ground-vibration test of one blade and instrumentation of the propellers on both the USS Barbey and USS Spruance.

Static and alternating loads were obtained from strain-gage measurements at 0.35 blade radius and 50% chord. These measurements indicated that the alternating loads were much more severe than had been assumed in the analysis (approximately +50% DFPA instead of +15% to +25%). Also, the full-power turn maneuver was found to be more severe than the crash-astern condition.

Furthermore, deformations of the relatively soft blade palm material were found to change significantly the distribution of load among the blade bolts. The bolts appeared to be subjected to local bending, and one bolt nearest the trailing edge of the blade was found to bear 75 to 80 percent of the total loading in both designs. As a consequence, bolt failures were experienced both at the shoulder and in the top few threads.

These new findings illustrate two important points about failure analysis. First, loads and damage modes tend to be underestimated in the absence of test data. Second, full-scale tests are essential to obtain the required data.

ACKNOWLEDGEMENTS

The authors wish to acknowledge the contributions of the following individuals. Dr. Damon E. Cummings, Mr. Francois N.R. Ayer and Mr. Steven Allen led the C. S. Draper Laboratory group whose participation assured the completion of the study on schedule. Valuable contributions were also made by Messrs. S. Dean Lewis and Shou-kou Scott Tsao (Department of Ocean Engineering), Professors Norman D. Ham and Emmett A. Witmer and Dr. Peter L. Boland (Aeroelastic and Structures Research Laboratory), and Dr. Keto Soosaar and Mr. Stephen Anagnostis (C. S. Draper Laboratory). This research was carried out under Office of Naval Research Contract N00014-67-A-0204-0082, "Analytical Determination of CP Propeller Performance and Torque".

REFERENCES

1. Kerwin, J.E., Orringer, O. and Pelloux, R.M., "Failure and Safety Analysis of Controllable-Pitch Propellers for the USS Barbey (DE1088) and USS

- Spruance (DD963)," Department of Ocean Engineering, MIT, Report No. 75-7, April 1975.
2. Pian, T.H.H., "Element Stiffness-Matrices for Boundary Compatibility and for Prescribed Boundary Stresses," Matrix Methods in Structural Mechanics (J.S. Przemieniecki et al., ed), Air Force Flight Dynamics Laboratory, AFFDL-TR-66-80, December 1965, 457-478.
 3. Tong, P., "The SSIP Subroutine Package," Aeroelastic and Structures Research Laboratory, MIT, unpublished user guide, 1972.
 4. Mau, S.T. and Pian, T.H.H., "Linear Dynamic Analyses of Laminated Plates and Shells by the Hybrid-Stress Finite-Element Method," Aeroelastic and Structures Research Laboratory, MIT, ASRL TR 172-2 (also AMMRC CTR 73-40), October 1972.
 5. Jones, J.P., "The Torsional Oscillations of Airscrew Blades at Low Mean Incidences," Aeronautical Research Council, United Kingdom, Report No. 19.897, February 1958.
 6. Cummings, D.E., "Numerical Prediction of Propeller Characteristics," J. Ship Research, Vol. 17, No. 1, March 1973, 12-13.
 7. Letter from Litton Industries to Bird-Johnson Co., 12 April 1972.
 8. Ridley, D.E., Bird-Johnson Co., private communication, 12 February 1975.
 9. Logcher, R.D. et al., "ICES STRUDL-II, The Structural Design Language Engineering User's Manual," Civil Engineering Department, MIT, Vol. 1 (November 1968) and Vol. 2 (June 1971).
 10. Timoshenko, S. and Goodier, J.N., Theory of Elasticity, McGraw-Hill, New York, 1961.
 11. Roark, R.J., Formulas for Stress and Strain, McGraw-Hill, New York, 4th ed., 1965.
 12. Zienkiewicz, O.C. and Cheung, Y.K., The Finite Element Method in Structural and Continuum Mechanics, McGraw-Hill, New York, 1967.
 13. Desai, C.S. and Abel, J.F., Introduction to the Finite Element Method, Van Nostrand Reinhold Co., 1970.
 14. Wilcox, L.E., Gleason Works, Rochester, NY, private communication, 1973.
 15. Forman, R.G., Kearny, V.E. and Engle, R.M., "Numerical Analysis of Crack Propagation in Cyclically Loaded Structures," Trans. ASME, Series D, J. Basic Eng., Vol. 89, September 1967, 459-464.

16. Imhof, E.J. and Barsom, J.M., "Fatigue and Corrosion-Fatigue Crack Growth of 4340 Steel at Various Yield Strengths," Progress in Flaw Growth and Fracture Toughness Testing, American Society for Testing and Materials, ASTM STP 536, July 1973, 182-205.
17. Trican, G.P., "Fatigue Properties of HY130 Steel," SM Thesis, Department of Metallurgy and Materials Science, MIT, September 1974.
18. Rack, R.J. and Kalish, D., Met Trans, Vol. 5, July 1974, 1595-1605.
19. Campbell, J.E. et al., Damage-Tolerant Design Handbook, Metals and Ceramics Information Center, Battelle-Columbus Laboratories, Columbus, Ohio, MCIC-HB-01, 1973.
20. Allan, J., Naval Ship Engineering Center, Hyattsville, MD, private communication, April 1977.

ULTIMATE STRENGTH ANALYSIS OF "JANEK CHAIRLIFT"

Michael P. Wnuk

South Dakota State University, Brookings, SD 57006

FRACTURE MECHANICS APPROACH TO FRACTURE CONTROL AND PREDICTION OF LIFE

Objective of a good design is to ensure that fracture is unlikely to occur in the life of the structural component. Seemingly unpredictable phenomena, however, like notch embrittlement, local weakening of the material due to micro-structural defects, corrosion, initiation and spread of a dominant fatigue crack, do exist. Inability to predict them is reflected through common application of a variety of safety factors.

Fracture mechanics offers a more quantitative approach to prediction of the life of components subjected to either single loading, alternating loads, and/or aggressive environments. Perhaps the best illustration for a fracture mechanics approach to fracture control is consideration of fatigue. Experience shows that a dominant fatigue crack, initiated from a minute surface or a crystallographic defect, develops in a stable manner at nominal stresses well within the limits accepted as "safe". The propagating crack usually remains undetected until it reaches a certain critical size at which an abrupt transition to a catastrophic fracture occurs. Stress analysis carried out on the basis of fracture mechanics enables one to compute the rate of propagation of such a crack at each stage of its growth and to predict the useful life span of the component. Two kinds of design procedures are commonly applied: 1) finite life design, and 2) infinite life design. The information needed by the designer to apply these procedures combines a complete stress analysis for a component in question with no cracks present, an initial flaw size, and a K-calibration of the structure (i.e. a functional relation between the K factor and the current flaw size). The material data for finite life design include cracking rate da/dN as a function of ΔK and the critical level of K, denoted by K_{IC} from a plane strain condition and by K_C for plane stress situations. The infinite life design requires knowledge of only one material parameter, ΔK_{th} , that is the threshold value of the K-factor range below which crack extension will not occur.

To calculate the maximum tolerable flaw size in the structure it is advisable to first determine the critical length of the fatigue crack (a_c) at which fracture instability occurs. According to the available theory^c the critical size of a fatigue crack can be determined from the geometry of the structural member, maximum service stress, and - most importantly - from the material property K_C/K_{IC} referred to as plane stress/plane strain fracture toughness. This property serves as a measure of material sensitivity to stress concentrations induced by sharp corners, flaws, notches, high stress gradients at dislocations pile-ups, hard inclusions, etc. These and other micro-structural defects determine so called "notch brittleness sensitivity" of the material. Embrittlement of a metal may result in a number of ways under given service conditions, and it should be accounted for

a *priori* in the design procedures. This latter statement forms the rationale and the primary objective of the fracture mechanics approach to evaluation of strength of imperfect materials.

In selecting the proper material a following "rule of thumb" may be helpful: the higher the strength of a steel, the lower its fracture toughness is to be expected. In other words, notch-brittleness sensitivity increases for high-quality and high-strength steels. On the contrary, low strength steels exhibit high levels of toughness (K_C and K_{IC}) and thus they can withstand greater local stress concentrations. It should be noted, however, that a considerable deterioration of fracture toughness in a mild steel may occur at low temperatures and/or high rates of loading. Both these factors, plus the effect of corrosive environments should be taken into account in the course of a detailed fail-safe design analysis.

An example of a numerical analysis of a fatigue crack propagating through the square tubing which supports the chairlift is given below*. The estimated life of the tubing is given as 0.9 million cycles, while the other essential findings are as follows:

- (1) the smallest dimension of a surface defect at which the fatigue crack will start to grow is estimated as 8 mils.
- (2) the largest tolerable (critical) dimension of a crack on the tension side of the tubing is computed as 1.32".

FATIGUE ANALYSIS

Propagation of a fatigue crack developed on the tensile side of rod 1 at or near the cross section CC may be considered to consist of three distinct stages (see the Figure below):

Stage I: propagation of a semi-elliptical (or half-moon) crack across the thickness of the tubing:

Stage II: Transition to a fully developed through-width crack penetrating completely the side of the square-box section:

Stage III: lateral enlargement of the through-width crack up to the point of transition into a catastrophic fracture of the supporting element.

The number of load cycles required to complete each of these stages of fatigue crack growth is evaluated separately and their sum is expected to give an approximation to the total life span of the chair.

* For the detailed stress analysis of this structure see a South Dakota State University report on "Ultimate Strength Analysis of JANEK Chairlift, South Dakota State University, Brookings, South Dakota 57006. March 1976.

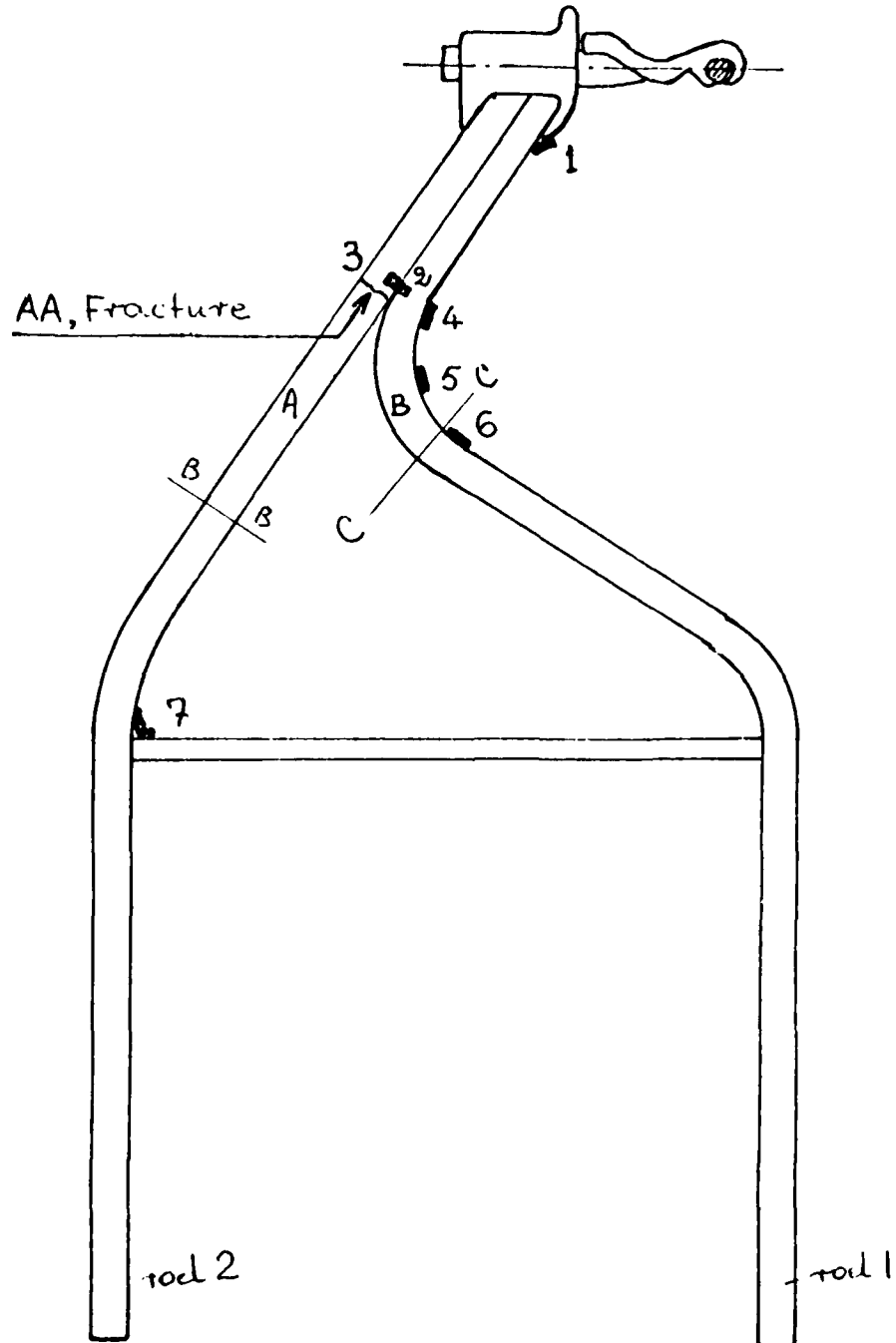
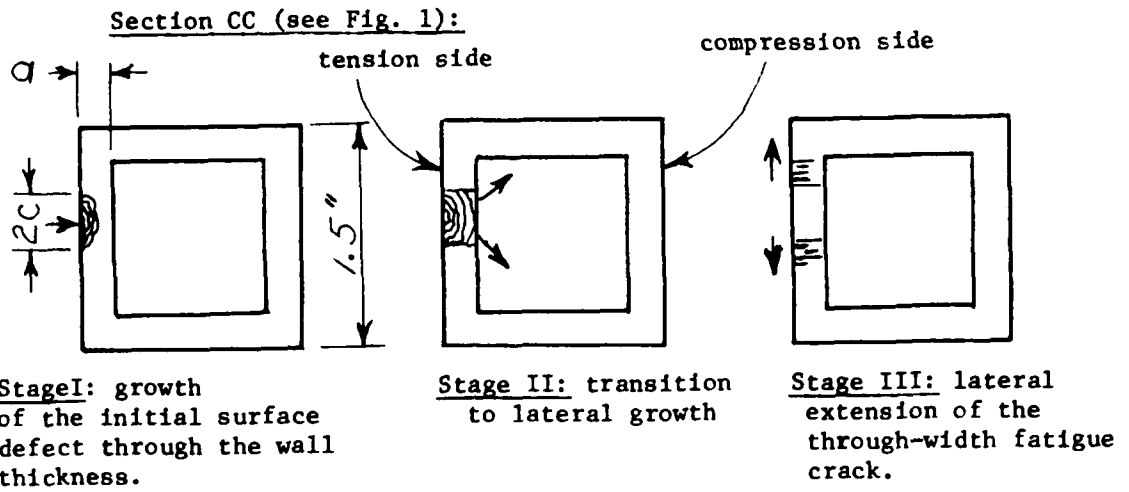
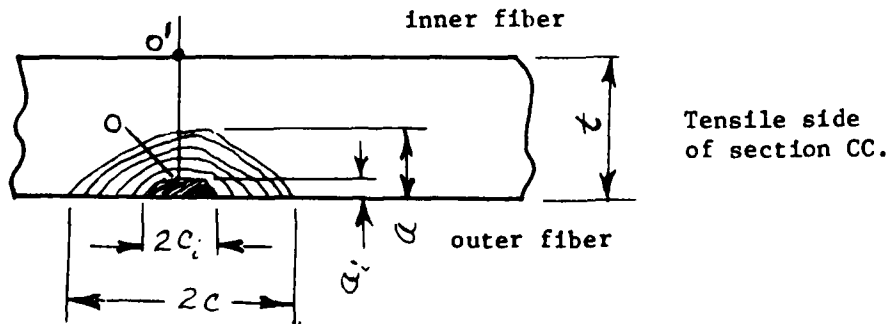


Fig.1 Sketch of the structural component subject to investigation. Numbers indicate location of the strain gages, while letters denote the cross-sections single-out for stress and fatigue fracture analysis.



(Arrows indicate the direction of fatigue crack growth)



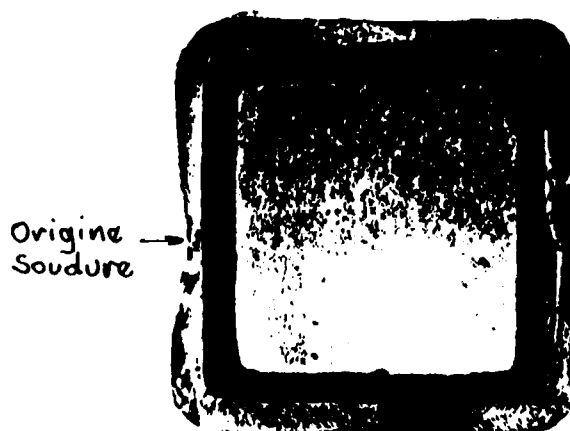


Fig. 2 Appearance of a component fractured during a fatigue test.

Stage I:

Propagation of the semi-elliptical crack (see Figure) is governed by the equation

$$\frac{da}{dN} = C(\Delta K)^m \quad (1)$$

where C and m are material constants, and ΔK is the range of the K-factor related to the geometry of the component and the range of the applied stress $\Delta\sigma$ as follows

$$K = 1.12 \sqrt{\frac{\pi a}{Q}} \Delta\sigma \quad (2)$$

$$Q = \left\{ \int_0^{\pi/2} \sqrt{1 - \frac{C^2 - a^2}{C^2} \sin^2 \theta} d\theta \right\}^2 - .212 \frac{\Delta\sigma^2}{R_e^2} \quad (2a)$$

Here R_e denotes the elastic limit, $2c$ is the length of the crack observed on the outer surface (see Figure above) while a is the crack depth which is bounded by the initial flaw size (a_i) from below and by the thickness of the tubing (t) from above

$$a_i \leq a \leq t \quad (3)$$

The rate of the fatigue crack is then the following function of geometry of the component and the loading range (combine eqs. (1) and (2)):

$$\frac{da}{dN} = \frac{C(1.12)^m \pi^{m/2} a^{m/2}}{\left\{ \int_0^{\pi/2} \sqrt{1 - \frac{C^2 - a^2}{C^2} \sin^2 \theta} d\theta \right\}^m} \quad (4)$$

Note that the correction term

$$.212(\Delta\sigma/R_e)^2 = (.212)(12.4/41.2)^2$$

is only about .019 and thus it has been omitted in the equation above (but retained for other considerations regarding such an important quantity as the initial flaw size).

The time, or the number of load cycles, used by the semi-elliptical crack to penetrate the thickness of the tubing can be obtained by integration of equation (1) as follows

$$N_I = \int_{a=a_i}^{a=t} \left(\frac{dN}{da} \right) da = (1.12\pi^{1/2} \Delta\sigma)^{-m} C^{-1} \int_{a_i}^t \left\{ \int_0^{\pi/2} \sqrt{1 - \frac{C^2 - a^2}{a^2} \sin^2 \theta} d\theta \right\}^m \frac{da}{a^{m/2}} \quad (5)$$

This form can be integrated numerically for any assumed functional inter-relation of the dimensions a and c . A case of a/c being constant during the entire stage I of crack propagation (proportional growth of both a and c is assumed) offers a possibility of a simple closed-form solution to the integral in eq. (5), namely

$$N_I = C^{-1} (1.985)^{-m} (\Delta\sigma)^{-m} E^m(k, \pi/2) \int_{a_i}^t a^{-m/2} da \quad (\text{if } a/c = \text{const.}) \quad (6)$$

Hence

$$N_I = \frac{E^m(k, \pi/2) / (\Delta\sigma)^m}{\left(\frac{m}{2} - 1\right) C (1.985)^m} \left[a_i^{1-m/2} - t^{1-m/2} \right] \quad (7)$$

Here the symbol $E(k, \pi/2)$ denotes a complete elliptic integral* of the second kind of modulus

$$k = \sqrt{1 - (a/c)^2} \quad (8)$$

For any given value of a/c the modulus k , and then the elliptic integral itself may be readily computed.

STAGES II AND III

The number of cycles used by the fatigue crack to complete the transition from the half-moon shape to a through-width shape (transition from stage I to stage III) is estimated as

$$N_{II} = \frac{.021}{(m/2 - 1) C (\Delta\sigma)^m} \quad (9)$$

For the stage III crack one may compute the life fairly accurately by integrating the expression

* Tabulated in e.g. "Handbook of Mathematical Functions with Formulas, Graphs, and Math. Tables", U. S. Dept. of Commerce, NBS, Appl. Math. Ser. 55, Washington, DC, 1964, p. 618

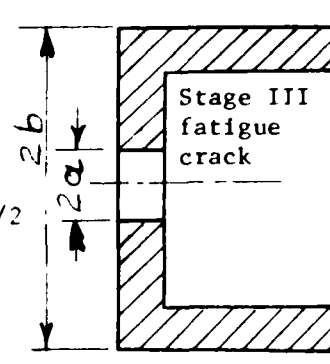
$$N_{III} = \int_t^c \left(\frac{dN}{da} \right) da \quad (10)$$

where now (see Figure)

$$\frac{da}{dN} = C(\Delta K)^m = c(\Delta\sigma)^m (\pi a)^{m/2} \{ \sec(\pi a/2b) \}^{m/2} \quad (11)$$

The two equations combine to give

$$N_{III} = \frac{1}{C(\Delta\sigma)^m} \int_t^c \frac{da}{(\pi a)^{m/2} \{ \sec(\pi a/2b) \}^{m/2}} \quad (12)$$



The integral on the right hand side of the last formula can be evaluated exactly through a standard numerical procedure. The following closed-form solution, however, will give the same order of magnitude for the number of load cycles spent at the final period of the useful life

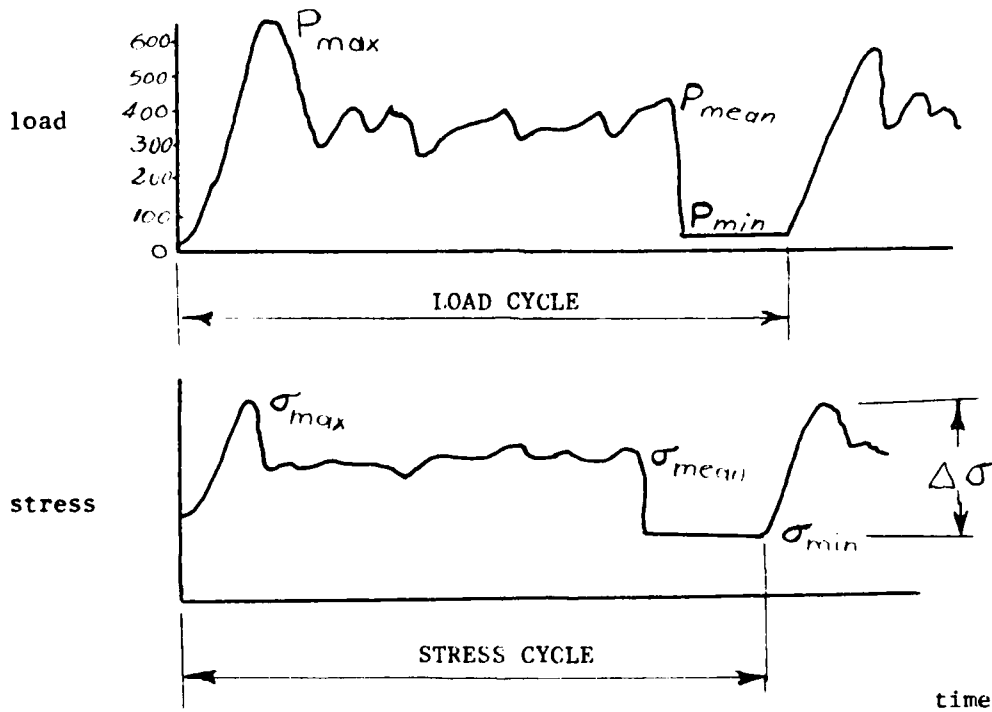
$$N_{III} \approx \frac{(\Delta\sigma)^{-m}}{(\frac{m}{2} - 1)C\pi^{m/2}} \left[\frac{1}{t^{m/2-1}} - \frac{1}{a_c^{m/2-1}} \right] \quad (13)$$

In order to apply the formulae for N_I , N_{II} and N_{III} derived here two sets of data are needed:

- (1) characteristics of the stress cycle, i.e. $\Delta\sigma$ and the R-ratio ($R = \sigma_{min}/\sigma_{max}$):
- (2) material data, namely
 - the constants C and m introduced by eq. (1).
 - the threshold value of the K-factor range, ΔK_{th} (necessary to compute the initial flaw size a_i),
 - fracture toughness K_{IC} or K_{IC} as described by an ASTM norm and appropriate for the thicknesses involved (necessary to predict the final crack length at which fracture becomes unstable).

Now we shall briefly discuss both groups of data.

FATIGUE LOAD AND STRESS CYCLES, EVALUATION OF THE STRESS RANGES AND R-RATIOS



ASSUMPTIONS:

load cycle

$$P_{min} = \text{weight of the chair}$$

$$P_{max} = (\text{weight of 2 passengers with equipment}) \times (\text{load factor}) = 632 \text{ lb}$$

$$P_{mean} = 400 \text{ lb}, \Delta P = 632 \text{ lb}$$

Stress cycle
at the tension side
of cross-section CC

$$\left\{ \begin{array}{l} \sigma_{min} = 8,937 \text{ psi}, \sigma_{max} = 22,402 \text{ psi} \\ \sigma_{mean} = 15,670 \text{ psi}, R = \sigma_{min}/\sigma_{max} = .399 \end{array} \right.$$

stress range at point 0: $(\Delta\sigma)_0 = 22,402 - 8,937 = 13,465 \text{ psi}$

stress range at point 0': $(\Delta\sigma)_{0'} = 12,267 - 915 = 11,352 \text{ psi}$

stress range averaged across
the thickness $(\Delta\sigma)_{AV} = 12,409 \text{ psi}$

SUMMARY OF DATA DESCRIBING THE FATIGUE STRESS CYCLE:

stress range in the outer fiber $(\Delta\sigma)_{\text{outer}} = 13,465$ psi
stress range in the inner fiber $(\Delta\sigma)_{\text{inner}} = 11,352$ psi
stress range averaged through thickness $(\Delta\sigma)_{\text{AV}} = 12,409$ psi

R-ratios:

$(R)_{\text{outer}} = .399$
 $(R)_{\text{inner}} = .081$
 $(R)_{\text{AV}} = .240$

MATERIAL DATA, EVALUATION OF INITIAL AND CRITICAL FLAW SIZES

Data pertaining to rate of fatigue crack growth (C and m):

Scarcity of the fatigue crack growth data leads us to apply as a first approximation the following equation tested by U.S. Army* for 19 different steels (mainly alloy steels containing chromium and nickel and molybdenum) of fairly high strength:

$$da/dN = .66 \times 10^{-8} (\Delta K)^{2.25} \quad \text{in/cycle} \quad (14)$$

in where the K-factor range (ΔK) should be expressed in units of ksi(in)^{1/2}. One should accept the eq. (2.1) only with certain reservations, since the steel under consideration is ASTM A500 Grade A, which is a mild steel. Nevertheless, it is expected that the application of eq. (2.1) will provide results on the conservative side, since a low strength steel exhibits better resistance to crack extension and, therefore, a slower fatigue crack growth. Condition of plane stress encountered in the walls of the square tubing (thickness of .12" equals roughly one half of the characteristic plastic zone size $r_y = (2\pi)^{-1} (K_{IC}/\sigma_{ys})^2$) will also tend to diminish the rate of the propagating crack.

THRESHOLD AND CRITICAL LEVELS OF THE K-FACTOR

The threshold value of the range ΔK is given for mild steels by the British** sources as

* J.M. Barsom, E.J. Imhof, S.T. Rolfe, "Fatigue crack propagation in high yield strength steels", Engn, Fracture Mechanics, Vol. 2, 1971.

** N.E. Frost, L.P. Pook and K. Denton, "A fracture mechanics analysis of fatigue for various materials", N.E.L. (England), Report No. 2, Febr. 1969.

$$\Delta K_{th} \approx 3 \text{ ksi } \sqrt{\text{in}} \quad (15)$$

This value, however, is diminished by about 20% in the presence of moisture, and it may be even further reduced if one accounts for stress corrosion cracking (i.e. slow growth of a corrosion crack under sustained load). Indeed, the tension side of the section CC is constantly subjected to a tensile stress of magnitude 8,937 psi (residual stress). This considerably facilitates initiation of a fatigue crack. Let us, therefore, assume the threshold level of ΔK to be 25% less than that given by Frost, Pook and Denton, i.e.

$$\Delta K'_{th} = (.80)(3) = 2.25 \text{ ksi } \sqrt{\text{in}} \quad (16)$$

The initial flaw is assumed to be a half-moon shaped surface defect for which the length observed on the outer surface ($2c$) is 10 times greater than the depth of flaw (i.e. $a/2c = .1$). Let us first compute the geometrical factor, namely the modulus k of the elliptic integral $E(k, \pi/2)$:

$$k = \sqrt{1 - (a/c)^2} = \sqrt{1 - (.2)^2} = .9798 \quad (17)$$

From tables (see foot-note on page 8) we find

$$E(.9798, \pi/2) = 1.0491 \quad (18)$$

Next, we evaluate the initial flaw size as follows

$$(a/Q)_i = \Delta K_{th}^2 / 1.2\pi(\Delta\sigma)^2 \quad (19)$$

$$Q = E^2(k, \pi/2) - (.212) \left(\frac{\Delta\sigma}{R_e} \right)^2 = (1.0491)^2 - (.212)(13.5/41)^2 = 1.0776 \quad (20)$$

Substituting this and

$$(\Delta\sigma)_{outer} \approx 13.5 \text{ ksi} \quad (21)$$

into the first of the foregoing equations, we obtain an estimate for the initial flaw size as follows

$$a_i = \frac{(Q)\Delta K_{th}^2}{1.2\pi(\Delta\sigma)^2} = \frac{(1.0776)(2.25)^2}{1.2\pi(13.5)^2} = .00794 \text{ in} \quad (22)$$

or

$$a_i = 8 \text{ mil.} \quad (23)$$

CRITICAL CRACK LENGTH

The critical flaw size can be readily computed for the geometry of crack in stage III from the following equation (compare Figure on page 6):

$$K_{max}(\text{stage III}) = \sigma_{max} \sqrt{\pi a} F(a/b) \quad (24)$$

$$F(a/b) = \{ \sec(\pi a/2b) \}^{1/2} \quad (25)$$

Let us denote a/b by x and combine both the equations above. Then

$$x \sec(\pi x/2) = \frac{1}{\pi} \left(\frac{K_{max}}{\sigma_{max} \sqrt{b}} \right)^2 \quad (26)$$

The right hand side of this equation is known if we agree to use the material fracture toughness as for a plane stress condition, $K_C \approx 80 \text{ ksi}\sqrt{\text{in}}$ (rather than the plane strain fracture toughness which for the steel involved is around $50 \text{ ksi}\sqrt{\text{in}}$). With σ_{max} denoting the maximum stress encountered during a load cycle (here σ_{max} is assumed to equal the average across the thickness of the maximum fiber stresses $.5(22,402 + 12,267) = 17,335$) we have

$$\frac{1}{\pi} \left(\frac{K_{max}}{\sigma_{max} \sqrt{b}} \right)^2 = \frac{(80)^2}{\pi(17.3)^2 1.5} = 4.5378 \quad (27)$$

It remains to solve the transcendental equation

$$x \sec(\pi x/2) = 4.5378 \quad (28)$$

for the unknown x . The approximate value of the root of this equation is found as

$$x = .8763 \quad (29)$$

Since x denotes the ratio of the half-length of the critical crack to the half of the outside diameter of the tube, we obtain the critical size

$$a_c = xb = (.8763)(1.5/2) = .6572 \text{ in.} \quad (30)$$

EVALUATION OF LIFE

Numbers of cycles needed to complete the stages I, II and III of fatigue crack propagation are now evaluated from the equations

stage I

$$N_I = \frac{(E(k, \pi/2))^m}{(\frac{m}{2} - 1)C(1.989)^m(\Delta\sigma)^m} \left[\frac{1}{a_i^{m/2-1}} - \frac{1}{t^{m/2-1}} \right] \quad (31)$$

stage II

$$N_{II} = \frac{.021}{(\frac{m}{2} - 1)C(\Delta\sigma)^m} \quad (32)$$

stage III

$$N_{III} = \frac{1}{(\frac{m}{2} - 1)C\pi^{m/2}} \left[\frac{1}{t^{m/2-1}} - \frac{1}{a_c^{m/2-1}} \right] \quad (33)$$

Substitution of the material constants

$$m = 2.25, \quad C = .66 \times 10^{-8} \quad (34)$$

and of the dimensions

$$\begin{aligned} a_i &= .008 \text{ in} \\ a_c &= .657 \text{ in} \\ t &= .120 \text{ in} \end{aligned} \quad (35)$$

leads to the following results (the elliptic integral $E(k, \pi/2)$ needed for stage I was evaluated previously and it equals 1.0491):

$$\begin{aligned} N_I &= \frac{(1.0491)^{2.25}/(\Delta\sigma)^m}{(.125)(.66)10^{-8}(1.985)^{2.25}} \times \left[\frac{1}{(.008)^{.125}} - \frac{1}{(.12)^{.125}} \right] = \\ &= \frac{1.516 \times 10^8}{(\Delta\sigma)^m} \end{aligned} \quad (36)$$

$$N_{II} = \frac{(.021) 10^8}{(.125)(.66)(\Delta\sigma)^m} = \frac{(.255) 10^8}{(\Delta\sigma)^m} \quad (37)$$

$$N_{III} \approx \frac{1/(\Delta\sigma)^m}{(.125)(.66) \times 10^{-8} (3.6249)} \left[\frac{1}{(.12)^{.125}} - \frac{1}{(.657)^{.125}} \right] = \frac{.835 \times 10^8}{(\Delta\sigma)^m} \quad (38)$$

Finally, if we choose to select the stress range as average of the ranges at inner and outer fibres

$$\Delta\sigma \approx (\Delta\sigma)_{AV} = 12.4 \text{ ksi} \quad (39)$$

and with $m = 2.25$, we obtain

$$\begin{aligned} N_I &\approx 5.26 \times 10^5 \text{ cycles} \\ N_{II} &\approx 0.88 \times 10^5 \text{ cycles} \\ N_{III} &\approx 2.89 \times 10^5 \text{ cycles} \\ \hline N_{\text{total}} &\approx 9.03 \times 10^5 \text{ cycles} \end{aligned} \quad (40)$$

The obtained estimate of roughly 1 million cycles for the total life of the component supporting the chair is based on the material data describing da/dN and valid for steels containing harder constituents like nickel and chromium. The mild steel is more "forgiving" as it is less sensitive to stress concentrations and it will slow down a fatigue crack. Experience indicates that the application of a mild steel may increase the total life, therefore, that the given above number of cycles to failure be considered as a conservative estimate of the actual life.

SUMMARY OF ESSENTIAL RESULTS OBTAINED BY FATIGUE ANALYSIS

total life	$N_{\text{tot}} \approx 0.9 \times 10^6$ load cycles
depth of the smallest surface defect that will act as a fatigue crack starter	$a_i \approx 8$ mil
critical size of the crack at which fracture becomes catastrophic	$2a_c \approx 1.32$ in
	* * * *

COMMENTS AND RECOMMENDATIONS

Although the stress evaluation shows that all stresses are within the safe limit (less than the yield point) a more detailed fracture mechanics

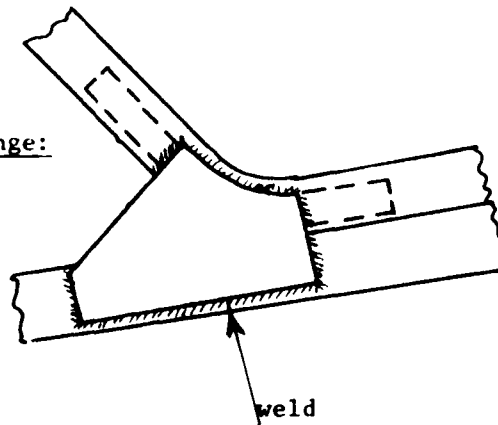
analysis shows that there exist a possibility of a fatigue problem. In this respect the present design of the chair appears to lead to two potentially dangerous sections:

- 1) section AA (rod 2): high stresses and high stress gradients exist in the vicinity of the lower end of the weld/joining both rods. Fatigue analysis for this section (not shown here) indicated the total life is on the order of 3.2×10^5 cycles. This is a conservative estimate when compared with the experimentally found $N_f = 3.6 \times 10^5$ cycles.
- 2) section CC (rod 1): high residual stresses are of the same sign as the stress induced by the service load. The tension side of this section is particularly prone to initiation of a fatigue or a corrosion crack that may develop from a minute surface crack of depth on the order of 8 mil, possibly introduced by cold forming and it may grow in some 0.9 million cycles to a flaw of catastrophic size (estimated as about 1.52 in).

It is concluded that a more precise analysis, combined with the experimental verification of assumed material characteristics, such as K_G , K_{IG} , and the da/dN vs. ΔK data, would be necessary to establish the actual life span and the load carrying capacity of the components supporting the chair.

Meanwhile, a simple remedy may be recommended: to strengthen both sections AA and CC a triangular plate should be welded at the upper corner of the frame under the consideration (as shown schematically in the figure below). Both strengthening and a beneficial stress redistribution effects leading to a structure of a more uniform strength and with lesser stresses and stress gradients are then expected.

Recommended design change:



Section 5 MATERIALS

CHARACTERIZATIONS OF MANUFACTURING FLAWS IN GRAPHITE/EPOXY[†]
George A. Hoffman and Don Y. Konishi
Los Angeles Aircraft Division of Rockwell International,
International Airport,
Los Angeles, CA 90009

OBJECTIVE: FLAW CATEGORIZATION IN COMPOSITES

The objective of this case study was the development of a representative set of flaw categories in composites. The assessment of the serviceability of graphite/epoxy requires determination of the effects of defects in structures undergoing a service environment and the flaw categorization or characterization allows setting NDE threshold and sensitivity goals, developing specific flaws for analysis of strength degradation, specifying critical and likely flaws for strength degradation tests, and provides a quantitative basis for a repair criterion.

INTRODUCTION: CONSEQUENCES OF DEFECTS AND THE USES OF FLAW CHARACTERIZATIONS

Composites for flight structures, such as graphite/epoxy, are inherently more flawed than aircraft metals of comparable cost, quality and intended use. The presence of flaws defects, cracks, voids, unintentional damage during processing, manufacture and assembly, is more abundant in graphite/epoxy than it is in aluminum and titanium. The consequence of these flaws may be the degradation of the serviceability, i.e., safety and durability, of composite structures via multiple routes through fracture micromechanics. Current empirical data indicates that graphite/epoxy might be relatively insensitive to degradation from many of these flaws. The measurements of the degradation, and ultimately of the fracture mechanics, due to flaws in graphite/epoxy are in the same terms as those of reliability, namely by probability estimates. Therefore the quantitative characterization of preflight flaws and damage should be in probabilistic terms, and the effectiveness of countermeasures to control and reduce flaws in graphite epoxy should be based on the likelihoods of their occurrence and criticality and on the costs to reduce the density of flaws.

By way of conclusion to these introductory remarks, it may be inferred that the aerospace industry's experience with flaw and defect occurrence is central to the eventual delineation the mechanisms and dynamics of fracture

[†]This effort is supported by the Air Force Materials Laboratory under Air Force Contract F33615-76-C-5344. The authors are grateful to Mr. P. Parnley, AF program monitor, for his continued encouragement.

and failure of graphite epoxy components. In the next section, the ingathering of this experience and evidence of preflight flaws, defects, errors and damage is described as a survey of case studies to characterize or set the scene for future failure analyses.

FORMULATION: INDUSTRY-WIDE SURVEYS OF GRAPHITE/EPOXY FLAWS

To achieve a better formulation of the character and likelihood of flaws, an industry-wide survey was conducted in two rounds of questionnaires. The first questionnaire was of a qualitative nature and consisted of soliciting a catalog of flaws, together with an inquiry into the likelihood of defect occurrence and into the criticality of the listed defects. The second round of the survey requested quantitative estimates of the most probable frequency of occurrence of those flaws that were deemed more likely and critical in the responses to questionnaire 1.

In the first questionnaire, (Figure 1), recipients were asked to enter additional common flaws to the submitted list, score two multiple-choice columns, and comment and anticipate the structural consequences of defects. The 35 responses to questionnaire 1 contained almost 1,000 data points and resulted in an expanded and more comprehensive list, Table 1, and in sets of individual opinions as to how often one ran across the listed flaws and how crucial they were, (i.e., the criticality effect of the flaw upon the structural integrity and performance).

The 36 returned questionnaires averaged 30 checks per entry for flaws 1 to 30. The survey asked respondents to choose among five grades of likelihood and criticality estimates for each flaw, as in Table 2 below.

TABLE 2. RESPONDENTS' GRADE CHOICES FOR FLAW LIKELIHOOD AND CRITICALITY

<u>Grade</u>	<u>Corresponding Estimate of Likelihood</u>	<u>Corresponding Estimate of Criticality</u>
0	Highly improbable	Negligible effects on strength
1	Rare, low likelihood	Minor effects
2	Occasional flaw occurrence	Possibly critical, intermediate effects
3	Fairly common occurrence	Critical flaw, of considerable concern
4	Flaw will occur very often	Most crucial flaw

The checks for each flaw of each respondent exemplified in Figure 1 were equally weighed, regardless of each individual's qualifications, affiliation,

INDUSTRY-WIDE SURVEY OF FLAW LIKELIHOOD AND CRITICALITY IN GRAPHITE/EPOXY

Respondent _____ Phone _____

ESTIMATE OF LIKELIHOOD
 100
90
80
70
60
50
40
30
20
10
0

ESTIMATE OF CRITICALITY
 100
90
80
70
60
50
40
30
20
10
0

OPINION AND COMMENTS ON ANTICIPATING ESTIMATES OF FLAW LIKELIHOOD, CRITICALITY, AND STRUCTURAL CONSEQUENCES

FLAW

- 1 External delamination core fibers protruding
- 2 Internal delamination B.S.P.
- 3 Coresides hole
- 4 Hole on side or end fibers protruding
- 5 Tear-out or pull-through in counterbores
- 6 Plying variabilities exceeding preset levels
- 7 Resin-stained bearing surface
- 8 Resin-rich or fiber-stained areas
- 9 Excessive porosity, voids
- 10 Scratch, fiber breakage
- 11 Dent, no fiber breakage
- 12 Fiber break-away from impact surface
- 13 Edge delamination, splintering
- 14 Overburdened or underwaxed fastener
- 15 Split hole, fiber separation
- 16 Edge notch or crack
- 17 Corner notch or crack
- 18 Mislocated hole -- not repaired
- 19 Mislocated hole -- resin refilled, roughed
- 20 Whimbles weariness miscommunication manual
- 21 Reworled area:
- 22 Missing ply
- 23 Foreign particle contamination inclusion
- 24 Out-of-round hole
- 25 Wrong material
- 26 Misoriented ply
- 27 Ply overlap
- 28 Fast ply failure or separation
- 29 Improper fastener seating
- 30
- 31
- 32
- 33

This questionnaire should be submitted also to:

1

2

3

Figure 1. Questionnaire 1. -- A separate instruction sheet asked recipients to check off likelihood and criticality, and solicited additions and commentary.

TABLE 1. FLAWS EXPERIENCED IN PRODUCTION OF GRAPHITE/EPOXY STRUCTURES

External delamination, loose fibers, disbonding
Internal delamination, blister
Oversized hole
Hole exit side broken fibers, breakout
Tearout or pull-through in countersinks
Prepreg variabilities exceeding preset levels
Resin-starved bearing surface
Resin-rich or fiber-starved areas
Excessive porosity, voids
Scratch, fiber breakage, damage done in handling
Dent, no fiber breakage, damage done in handling
Fiber breakaway from impact surface
Edge delamination, splintering
Overtorqued fastener
Split tow, fiber separation
Edge notch or crack
Corner notch or crack
Mislocated hole - not repaired
Mislocated hole - resin refilled, redrilled
Marcelled fibers
Wrinkles, waviness, miscollimation
Reworked areas
Missing ply or plies
Foreign particle, contamination, inclusion
Out-of-round hole
Wrong material
Misoriented ply
Ply overlap
Ply underlap, gap
First ply failure or separation
Improper fastener seating
Variable cure, poor spatial ΔT in oven, = inhomogeneous "miscure"
Figure 8 hole
Nonuniform bond joint thickness
Off-axis drilled hole (i.e., not perpendicular to surface)
Countersink on wrong side of laminate
Mislocated occurred assemblies in same tool
Tool impressions
Burned drilled holes from high-speed drilling
Pills and fuzz balls
Undersized fasteners
Dent, hidden fiber breakage, from production mishandling
Grossly nonuniform agglomerations of hardener agents
Misfitting parts cutting fibers in fillets, poor seating design
Metal-graphite/epoxy mating surfaces not shear balanced
Overwarpage of parts from poor tooling
Process control coupon thickness not constant or misrepresentative

experience, or reputation. The unweighed, median grade values of likelihood and criticality were calculated and rounded off to the nearest second digit. Next, the variation in the distribution of frequency of responses was rated at

- 4 = all respondents were unanimous in grades
- 3 = over half of grades fell in a single score box
- 2 = one-quarter to one-half of scores in one box
- 1 = less than one-quarter of scores in any one box of the questionnaire

Thus, the mean index of response variation was set at 2.5. Each raw mean grade entry was then multiplied by its respective variation index to give scores of likelihood and criticality to each flaw. Finally, the product of the likelihood score, --a probabilistic term--, times the criticality score --an impact severity term--, was calculated to give an index of the effects. This index of effects of flaws and defects, shown in the left-most column of Table 3 was purposely formulated to have a range from 0 to 100, 100 being the index for a very frequent flaw whose effects upon strength would be most crucial as illustrated at the end of the table. In conclusion, questionnaire 1 delineated 48 flaws that may occur in graphite/epoxy structures, a qualitative index of their effects, and preliminary indication of the likelihood of their occurrence, right-most column of Table 3, and wound up with 281 scores in the "frequent," X, category, 249 in the "intermediate," x, category, and 203 in the "infrequent," 0, category.

Turning our attention now to questionnaire 2 and remembering that its purpose was to obtain quantitative, numerical estimates of the frequency of occurrence of the worst-effect flaws reported in questionnaire 1, we will describe the degree of industry's opinion consensus in regards to these likelihoods of flaws and defects.

ASSESSMENT: THE FREQUENCY OF CRITICAL FLAW OCCURRENCE IN GRAPHITE/EPOXY

To make the second questionnaire more manageable, the 47 flaw types emerging from questionnaire 1 were pared down to 34 by eliminating those that scored less than 10 in the index of effects, and by omitting those defects or flaws that were clearly correctable design or stress errors. It was thus hoped that the probabilities of the apparently more critical flaws, defects and imperfections that occur during processing, manufacturing and assembly of aircraft components made from graphite/epoxy would be defined in this questionnaire, and would lay the groundwork for future investigations on the

Table 5. SCORES OF FLAWS IN GRAPHITE/EPOXY IN RESPONSE TO QUESTIONNAIRE 1

Index of Effects	Flaw type	Likelihood of Occurrence			
		Frequent	Intermediate	Infrequent	Dropped ^a
25	External delamination, loose fibers, disbonding		x		
25	Internal delamination, blister		x		
06	Oversized hole	X			
38	Hole exit side broken fibers, breakout	X			
30	Tearout or pull-through in countersinks			0	
62	Prepreg variabilities exceeding preset levels	X			
9	Resin-starved bearing surface				0
14	Resin-rich or fiber-starved areas	X			
10	Excessive porosity, voids		x		
10	Scratch, fiber breakage, damage done in handling				0
12	Dent, no fiber breakage, damage done in handling	X			
9	Fiber breakaway from impact surface				0
11	Edge delamination, splintering	X			
10	Overtorqued fastener				0
7	Split tow, fiber separation				0
18	Edge notch or crack			0	
19	Corner notch or crack			0	
15	Mislocated hole - not required			0	
28	Mislocated hole - resin refilled, redrilled		x		
27	Wrinkles, waviness, miscollimation	X			
28	Marcelled fibers	X			
29	Reworked areas	X			
20	Missing ply or plies			0	
24	Foreign particle, contamination, inclusion	X			
23	Out-of-round hole	X			
9	Wrong material				0
21	Misoriented ply			0	
15	Ply overlap	X			
19	Ply underlap, gap		x		
13	First ply failure or separation		x		
27	Improper fastener seating	X			
21	Variable cure, temperature inhomogeneities in oven		x		
24	Figure 8 hole			0	
25	Nonuniform bond joint thickness			0	
9	Off-axis drilled hole (i.e., not perpendicular to surface)				0
22	Countersink on wrong side of laminate		x		
25	Mislocated cocured assemblies in same tool		x		
15	Tool impressions	X			
9	Burned drilled holes from high-speed drilling				0
21	Pills and fuzz balls			0	
3	Undersized fasteners				0
25	Grossly nonuniform agglomerations of hardener agents			0	
20	Misfitting parts cutting fibers in fillets, poor seating		x		
16	Metal-graphite/epoxy mating surfaces not shear balanced				0
20	Overwarpage of parts from poor tooling				0
30	Process control coupon thickness not constant or misrepresentative				0

Index of Effects = (likelihood scores) x (criticality scores) on a scale of 1 to 100 as follows:

- 100 = (very frequent flaw) x (most crucial effects) = 2.5² x 4 x 4
- 75 = (fairly common experience) x (critical flaw) = 2.5 x 2.5 x 3 x 3
- 25 = (occasional occurrence) x (possibly critical flaw) = 2.5 x 2.5 x 2²
- 6 = (rare, low likelihood) x (minor effects) = 6.25 x 1 x 1

^aDropped or eliminated when index scored less than 10 or flaw is a design error.

damage to be expected during service lives. Next, the 34 flaws were rearranged into three classes of likelihood of occurrence:

- Most frequently experienced flaws
- Intermediate, less frequent flaws
- Infrequent, but still observable flaws

Questionnaire 2 displayed these rearranged flaws and asked the recipients to estimate the frequency of graphite/epoxy flaw occurrence expected in a normal aerospace production atmosphere based upon today's processing and manufacturing practices. To guide the respondent's thinking, each flaw had associated with it a range of score boxes with percentage units per parameter appropriate to the flaw, with the mid-range box being a first subjective assessment by the questioners. The questionnaire and the results are shown in Figure 2.

ANALYSIS: CHARACTERIZATIONS OF FLAWS FOR
FRACTURE MECHANICS ANALYSES

The results blocked out in Figure 2 bear out the 25 century old prophecy that "it is probable that the improbable will occur" (Agathon of Athens, 417 BC) and furthermore quantifies it for graphite/epoxy. The probability of flaw occurrence in Figure 2 were calculated by totalling the responses for each entry, finding the median and adjusting it by the shape of the histograms of responses in Figures 3a and b. This concluded the surveys, and with this data base the analysis of the effects and impacts of flaws can begin.

One approach toward the prediction of the consequences might be the linear program modelling of both the cost to detect flaws, $\sigma_1 \dots i$, and of the structural effects of flaws in a single causal and correlative formulation. The objective function would be

$$P_k(t, k, r, F, a_o, F_o, A_4, \dots, C, X, A, B, \dots)$$

subject to the constraints $AX \leq B$,

Figure 2. Questionnaire 2 and Its Results

FREQUENT FLAWS

Hole exit side broken fiber, breakout percent of drilled holes
<2 2-4 4-8 8-10 10-30

Overized hole percent of all drilled holes
<2 2-4 4-8 8-10 10-30

Prepreg variabilities exceeding preset levels percent of prepreg volume
<2 2-4 4-8 8-10 10-30

Vacilled fibers percent of ply surface area
<2 2-4 4-8 8-10 10-30

wrinkles, waviness, miscollimation percent of ply surface area
<0.4 0.5-1 1-2 2-4

Out-of-round hole percent of holes
<1 1-2 2-5 5-10

Too impressions percent of surface area
<10 1-20 20-30 30-45

Improper fastener seating percent of fasteners
<1 1-2 2-4 4-10

Handing dent, no visible fiber breakage percent of external area
<1 1-2 2-4 4-10

Reworked areas percent of visible surface areas
<2 2-5 5-10 10-20

Edge delaminations, splintering percent of edge length
<1 1-2 2-5 5-10

Resin-rich, fiber-starved areas percent of ply surface area
<2 2-5 5-10 10-20

Foreign particles, particulate contamination, inclusions
 between .05 and .04 inch in size particles ft² ply
<1 1-2 2-4 4-8

between .04 and .03 inch in size particles ft² ply
<2 2-5 5-10 10-20

between .03 and .02 inch in size particles ft² ply
<0.2 0.2-0.5 0.5-1 1-2

Ply overlap percent of ply area overlapping
<1 1-2 2-5 5-10

Undersized fastener passing inspection percent of fasteners
<2 2-5 5-10 10-20

INTERMITTENT, LESS FREQUENT FLAWS

External delamination, disbonding, loose fibers percent of external area
<0.1 0.1-1 1-2 2-5

Internal delamination, blister percent of internal ply area
<2 2-5 5-10 10-20

Excessive porosity, voids percent of volume of excess porosity and voids
<0.5 0.5-1 1-2 2-5

Mislocated hole, resin refilled and resealed percent of drilled holes
<0.5 0.5-1 1-2 2-5

Ply underlap, gap percent of ply area appears as underlapping gaps
<0.1 0.1-1 1-2 2-5

First ply failure or separation percent of first ply area separated
<0.1 0.1-1 1-2 2-5

Variable cure, oven temperature inhomogeneities percent of volume of resin variously cured
<1 1-2 2-5 5-10

Countersink on wrong side of laminate percent of countersinks
<0.1 0.1-1 1-2 2-5

Mislocated cured assemblies in same tool
 Mislocations of 1/4 to 1/2-inch percent of cured elements
<5 5-10 10-15 15-20

Mislocations of 1/2 to 1-inch percent of cured elements
<1 1-2 2-5 5-10

Mislocations of 1 to 2 inches percent of cured elements
<0.1 0.1-1 1-2 2-5

Grossly nonuniform agglomerations of hardener agents of volume
<0.1 0.1-1 1-2 2-5

INTERMITTENT FLAWS

Tearout or pull-through in countersinks percent of countersinks
<1 1-2 2-5 5-10

Edge notch or crack notches and cracks per 100-feet of edge
<1 1-2 2-5 5-10

Corner notch or crack notches and cracks per 100 corners
<1 1-2 2-5 5-10

Unrepaired mislocated hole percent of all drilled holes
<0.3 0.3-1 1-2 2-5

Missing ply or plies percent of designated plies
<0.5 0.5-1 1-2 2-5

Misoriented plies percent of designated plies
<0.5 0.5-1 1-2 2-5

Figure 8 hole percent of drilled holes
<0.5 0.5-1 1-2 2-5

Nonuniform bond joint thickness percent of bonded area
<2 2-5 5-10 10-20

Chips and fuzz balls percent of ply area is pilled
<0.1 0.1-1 1-2 2-5

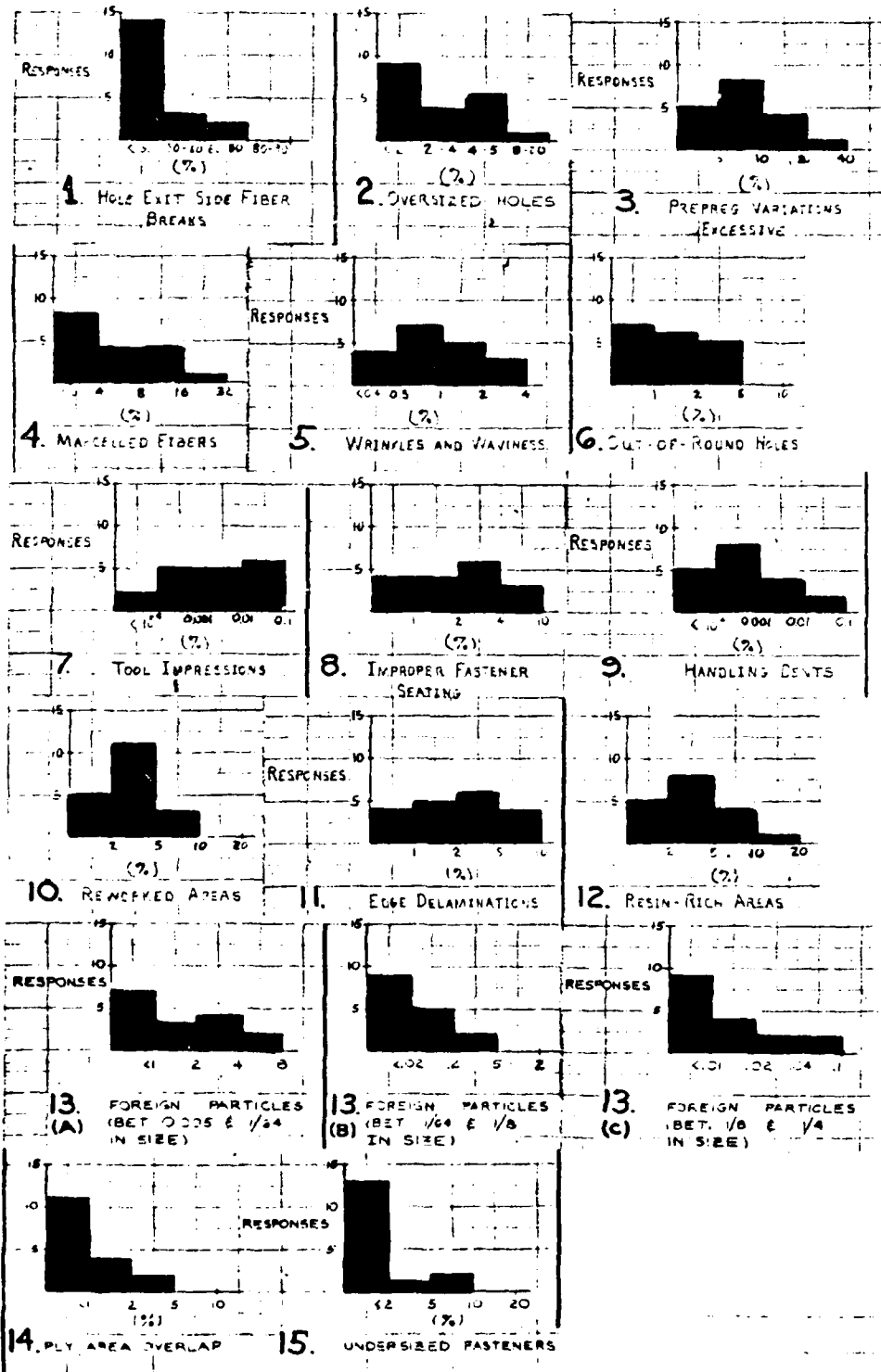


Figure 3a. Distribution of Responses to Questionnaire 2, Frequent Flaws

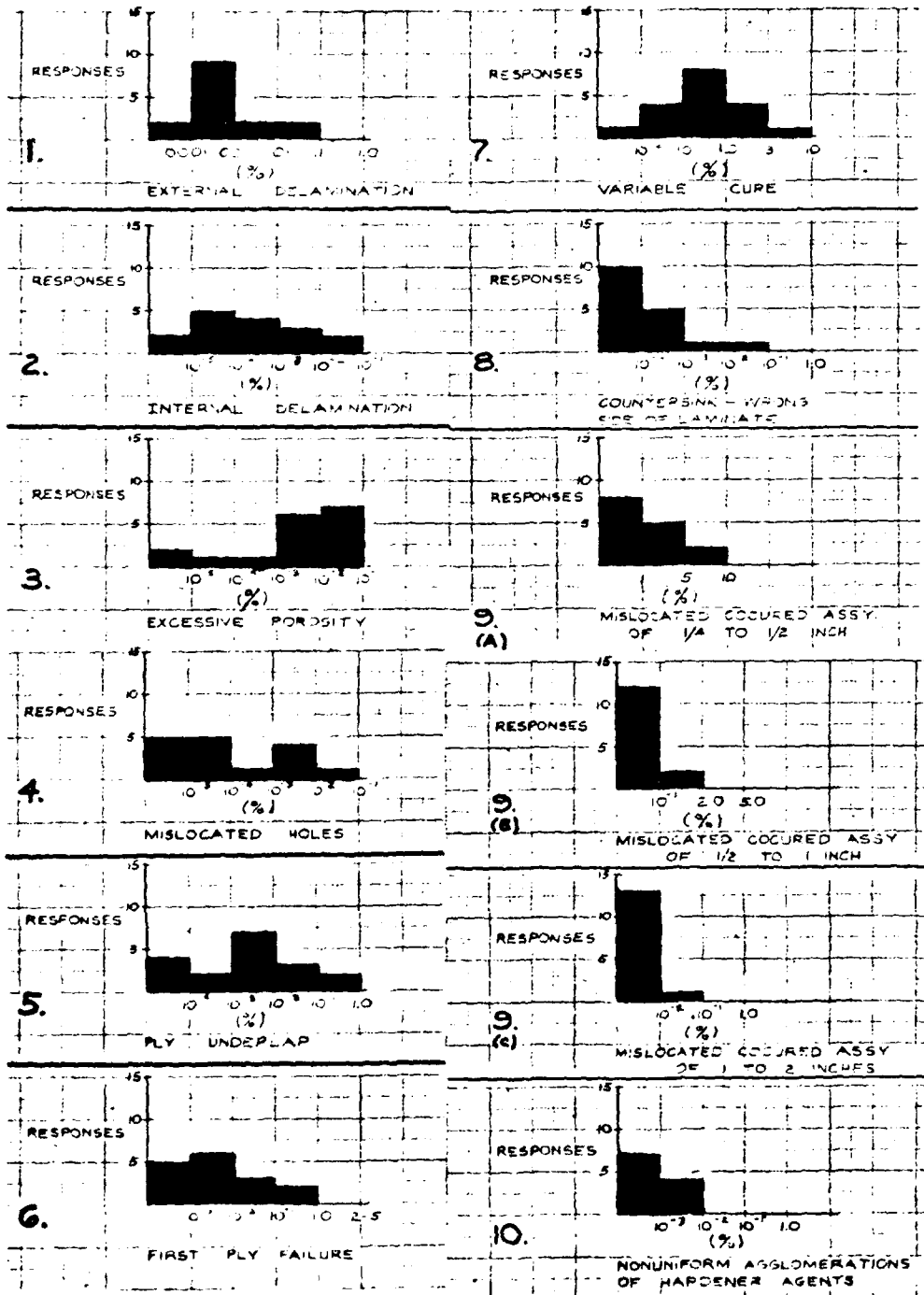


Figure 5b. Distribution of Responses to Questionnaire 2, Intermediate Flaws

where

P = residual load that can be sustained by the flawed component after t elapsed time in service.

$k = k_1, k_2, k_3 \dots$ = alternate sets of processes, manufacturing or non-destructive evaluation practices, with cost of $k_1 \neq$ cost of $k_2 \neq$ cost of $k_3 \neq \dots$

r = exponent characteristics of graphite/epoxy material.

F = stress with subscripts of F indicating stress associated with flaw.

a_0 = shape parameter for Weibull distribution function in the structural degradation formula

F_0 = scale parameter for Weibull distribution function

$A_4 = A_0 D^r K^{2(r-1)}$, where A_0 = constant coefficient

D = effective compliance

K = apparent toughness or work parameter

C = vector of contributions of all flaws to the loss of P_k , with $C_i(r, F, \dots)$ giving degradation of P_k caused by one flaw, X_i , acting singly.

X = index of flaws, X_i , where X_i = intensity of flaw occurrence = number of i th flaws expected in a component from specific manufacturing practice, expressed as n_i of flaw intensity X_i , as per Questionnaire No. 2 results.

i = enumerant of flaw type, category, size and location. $1 \leq i \leq 34$

A = matrix of A_{ij} coefficients indicating use of B_j by X_i .

B = vector of B_j constraints on several X_i 's.

B_j = limitations imposed by NDE₁ ... _j and their sensitivities and thresholds for detection versus cost of inspection and repair.

This linear programming approach is amenable to optimization for cost-effectiveness, and allows an algorithm to be formulated for structural accept/reject criteria, namely if

$$\Pi(P_{1N} \geq P_{XX}) \geq \Pi_0, \text{ then accept; and if } \Pi(P_{1N} \geq P_{XX}) < \Pi_0, \text{ then reject}$$

where

Π ; Π_0 = probability of event in parenthesis; prespecified serviceability probability delimiting acceptance or rejection

P_{1N} = probability that residual strength after one economic life exceeds design strength

P_{XX} = probability that maximum service load exceeds design load

CONCLUSION: CHARACTERIZATION OF MANUFACTURING FLAWS

By way of conclusion and characterization of these introductory investigations, the flaws were assigned to their characteristic stress field as shown in Table 4, and sorted into six types of stress fields associated with their occurrence:

<u>Type</u>	<u>Stress Field</u>
I	Localized, planar and sharp stress gradients
II	Localized, through the thickness stress gradients
III	Dispersed stress gradients
IV	Surface-localized high stress concentrations
V	Variable, fluctuating laminate stiffness and propensity for structural instability
VI	Miscellaneous

In summary we characterized graphite epoxy manufacturing flaws by both their likelihood of occurrence and by the stress field disturbances that they cause. This characterization can then pave the way for further studies on assessing the criticality of flaws so as to eventually develop criteria for acceptance or rejection.

TABLE 4. CHARACTERIZATION OF FLAWS IN GRAPHITE EPOXY BY STRESS FIELD AND PROBABILITY OF OCCURRENCE FOR THE PURPOSE OF SERVICEABILITY EVALUATION

Flaw Type Number	Flaw Type Description	Flaws	Measure of Occurrence
I	localized, planar and sharp	Oversized hole Mislocated hole-resin refilled, redrilled Out-of-round hole Figure 8 hole Edge notch or through crack Mislocated hole - not required	2-3% drilled holes .00006-.001% drilled holes 1.5% drilled holes 0.3-1.2% drilled holes 0.3-2% drilled holes
II	localized, through the thickness stress gradients	Tearout or pull-through in countersink Edge delamination, splintering Improper fastener seating Countersink on wrong side of laminate Internal delamination, blister Nonuniform agglomerations of hardener agents over small volume Nonuniform bond joint thickness Small external delamination, loose fiber, or disbond area Foreign particle, contamination, inclusion Dent, no fiber breakage, damage done in handling Pills and fuzz balls Misfitting parts cutting fibers in fillets corner notch or crack (thin specimen) Ply underlap, gap Ply overlap Tool impressions Resin-rich or fiber-starved condition over small volume Overtorqued fasteners	.13-2% countersinks 3.5% edge length 3.0% fasteners .0005% countersinks .0001-.0003% internal ply area 0-.001% volume 2-9% bond area .0005% external area 1-2% particles/ft ² /ply .0001-.0004% external area .12-1.3% ply area .9-6% per 100 corners .001-.005% ply area Less than 1.0% ply area .005% surface area 3.5% ply surface area
III	defects yielding dispersed stress gradients	Hole exit side broken fibers, breakout Tearout or pull-through in countersinks Reworked areas Marcelled fibers Wrinkles, waviness, miscollimation External delamination, loose fibers, disbonding Mislocated cocured assemblies in same tool Viable cure, temperature inhomogenities in oven Grossly nonuniform agglomerations of hardener agents Excessive porosity, voids Ply underlap, gap Ply overlap Resin-rich or fiber-starved areas	Less than 30% drilled holes .13-2% countersinks 3.5% visible surface areas .0005% external area 2.0% cocured elements 0.5% resin volume .001% volume .003% volume .005% ply area Less than 1.0% ply area 3.5% ply surface area
IV	Surface-localized, high stress concentration	Hole exit side broken fibers, breakout Improper fastener seating External delamination, loose fibers, disbonding Dent, no fiber breakage, damage done in handling Pills and fuzz balls Misfitting parts cutting fibers in fillets, poor seating Corner notch or crack Tool impressions Outer ply separation Scratch, fiber breakage, damage done in handling	Less than 30% drilled holes 3.0% fasteners .0005% external area .0001-.0004% external area .12-1.3% ply area .3-6.0 per 100 corners .005% surface area .006% outer ply area
V	Lower stiffness, asymmetry	Prepreg variabilities exceeding preset levels Marcelled fibers Wrinkles, waviness, miscollimation External delaminations, loose fibers, disbonding Misoriented ply Variable cure, temperature inhomogenities in oven Missing ply or plies Excessive porosity, voids Ply overlap Resin-rich or fiber-starved areas Outer ply separation	7.5% prepreg volume .0005% external area .05-8% designated plies .05% resin volume .08-.6% designated plies .003% volume Less than 1.0% ply area 3.5% ply surface area .006% outer ply area

CATASTROPHIC CRACKING IN DEPLETED URANIUM PENETRATORS

S. G. Fishman and C. R. Crowe
Naval Surface Weapons Center
White Oak, Silver Spring, Maryland 20910

INTRODUCTION

Heavy metal alloys are of great military interest as a result of their excellent penetration capability. Of the materials under consideration, depleted uranium alloys are among those with the greatest promise based on effectiveness, cost, and availability criteria. Each of the three services (Army, Navy, and Air Force) has at least one program in which a depleted uranium alloy is the prime candidate for the penetrator material.

One of the military requirements of munitions is a sufficiently long shelf life. Standard military environmental tests are carried out as a matter of course on every new munition prior to its introduction to service. Such tests were designed for munitions constructed of steel, brass, or other materials not susceptible to severe atmospheric attack. However, with the introduction into inventories of materials, which are susceptible to atmospheric corrosion such as depleted uranium, more comprehensive environmental tests must be carried out.

In order to determine if the DU-2 wt% alloy used for the DU-2 penetrator is susceptible to stress corrosion cracking (SCC) during long-term storage in a moist atmosphere, DU-2 penetrators from two of three procurement batches were subjected to moist air at 160°F and 95-percent relative humidity for varying lengths of time. Severe cracking of the penetrators from one of the lots resulted from these treatment, indicating the presence of a potential stress corrosion cracking problem in this particular alloy. A series of projectile ballistic limit tests were conducted on the uncracked penetrators following the temperature and humidity (T&H) treatment. The observation that the projectile ballistic limits are nearly the same for all the uncracked penetrators, independent of T and H treatment, was interpreted to mean that the rate of crack propagation is much faster than that of crack initiation. The fact that only one of the two batches investigated cracked during the T and H treatment indicated that there was some metallurgical difference between the batches. It was the purpose of the present program to investigate the mechanism of SCC in DU-2 penetrators and to ascertain the reason for the difference in behavior between the batches of penetrators when subjected to moist-air environments.

FORMULATION

In order to accelerate the SCC process, 20 specimens, as received, were placed under a controlled environment of 160°F \pm 2°F and 95% relative humidity \pm 2%. This treatment was sufficient to promote corrosion cracking

in all specimens. A detailed chemical analysis before and after the temperature-humidity treatment was carried out and the results for typical specimens are given in Table 1.

Metallographic samples were ground using standard techniques with final polishing of 6 μm diamond, 1 μm diamond and 0.5 μm Al_2O_3 on nylon, billiard cloth, and microcloth covered wheels, respectively. Specimens for the optical microscope were viewed both in the etched and unetched condition. A 50:50 nitric acid: acetic acid submersion etch was used. Scanning electron microscopy and X-ray dispersive analysis was carried out on a Cambridge MARK 2A SEM. The phase structure of the alloy was ascertained with a Phillips X-ray diffractometer.

ASSESSMENT

A macrosection of a typical specimen exhibiting corrosion cracks is shown in Fig. 1. The specimens possessed a large number of longitudinal stringers distributed throughout the component. Corrosion cracks were intimately associated with the stringers and propagated from stringer to stringer along the specimen. An optical microscopic examination confirmed that the stringers were composed of bulky, internally cracked inclusions, as shown in Fig. 2. During a hot rolling process, the more ductile matrix pulled away from the inclusions leaving voids between the two phases. This results in regions of potentially high localized internal stresses and low mechanical strengths which provide easy propagation paths for corrosion cracks through the specimens.

The two most probable sources of tensile stress sufficiently high to result in crack propagation may act independently or in combination. These are internal stresses due to fabrication and stresses due to corrosion product wedging. The internal stress profile of a DU-2 penetrator has been measured by the Sachs boring-out method. As shown in Fig. 3, high tensile stresses in the tangential directions are present on the surface of the penetrator.

A product of the uranium-water reaction is cathodically reduced hydrogen and uranium dioxide.



The corrosion oxide is considerably less dense than the uranium metal and as a result the subsequent "wedging" of corrosion product places the region of the crack tip under a state of tensile stress which increases the solubility of hydrogen there. This is a thermodynamic effect, with its origin in the material dilatation under elastic stress and the positive volume change that accompanies the entrance of hydrogen interstitials in the metal lattice. A mechanism is provided, therefore, for an increased concentration of hydrogen in the vicinity of a corrosion crack tip with a

TABLE 1

TYPICAL CHEMICAL ANALYSIS OF U-Mo ALLOY (wt.%)

Ti	--	0.001
Al	--	0.005
Si	--	0.014
P	--	<0.002
Fe	--	0.002
Ni	--	0.001
Cu	--	0.006
Mo	--	2.85
C	--	0.016
O	--	0.005
N	--	<0.0005
H	--	0.0001 before T and H
H	--	0.0022 after T and H
U	--	Bal.



Fig. 1. Longitudinal section of U-2 wt.-% Mo alloy specimen exhibiting corrosion cracks. 5X

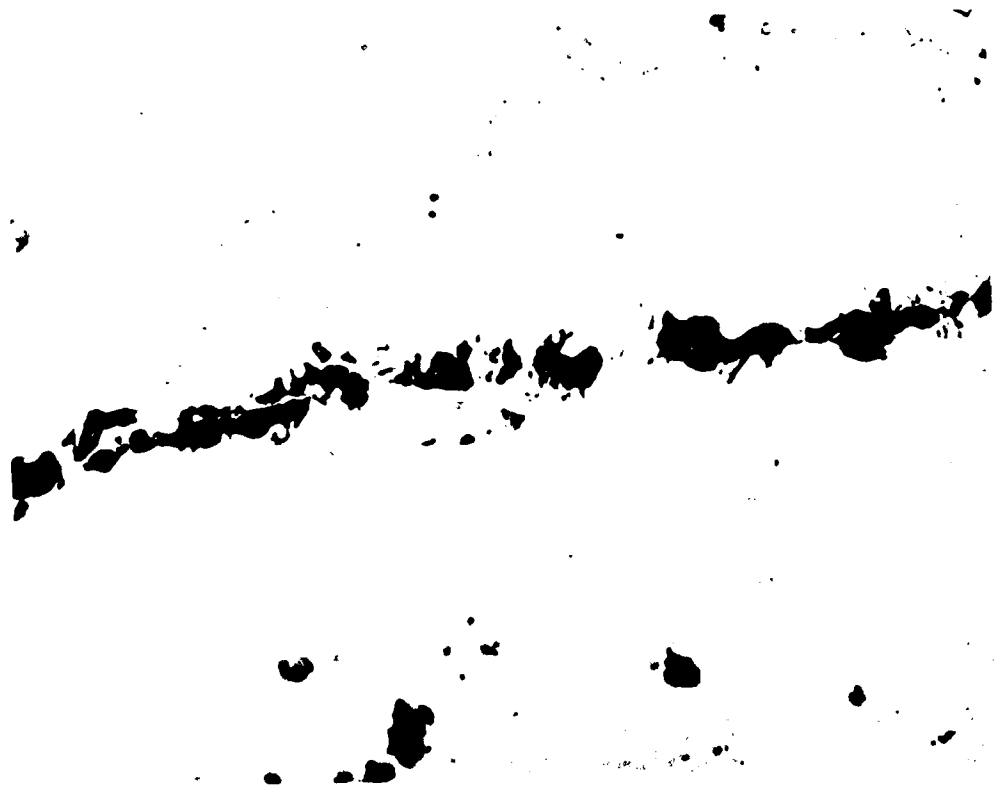


Fig. 2. Inclusions within corrosion cracking specimen. 800X

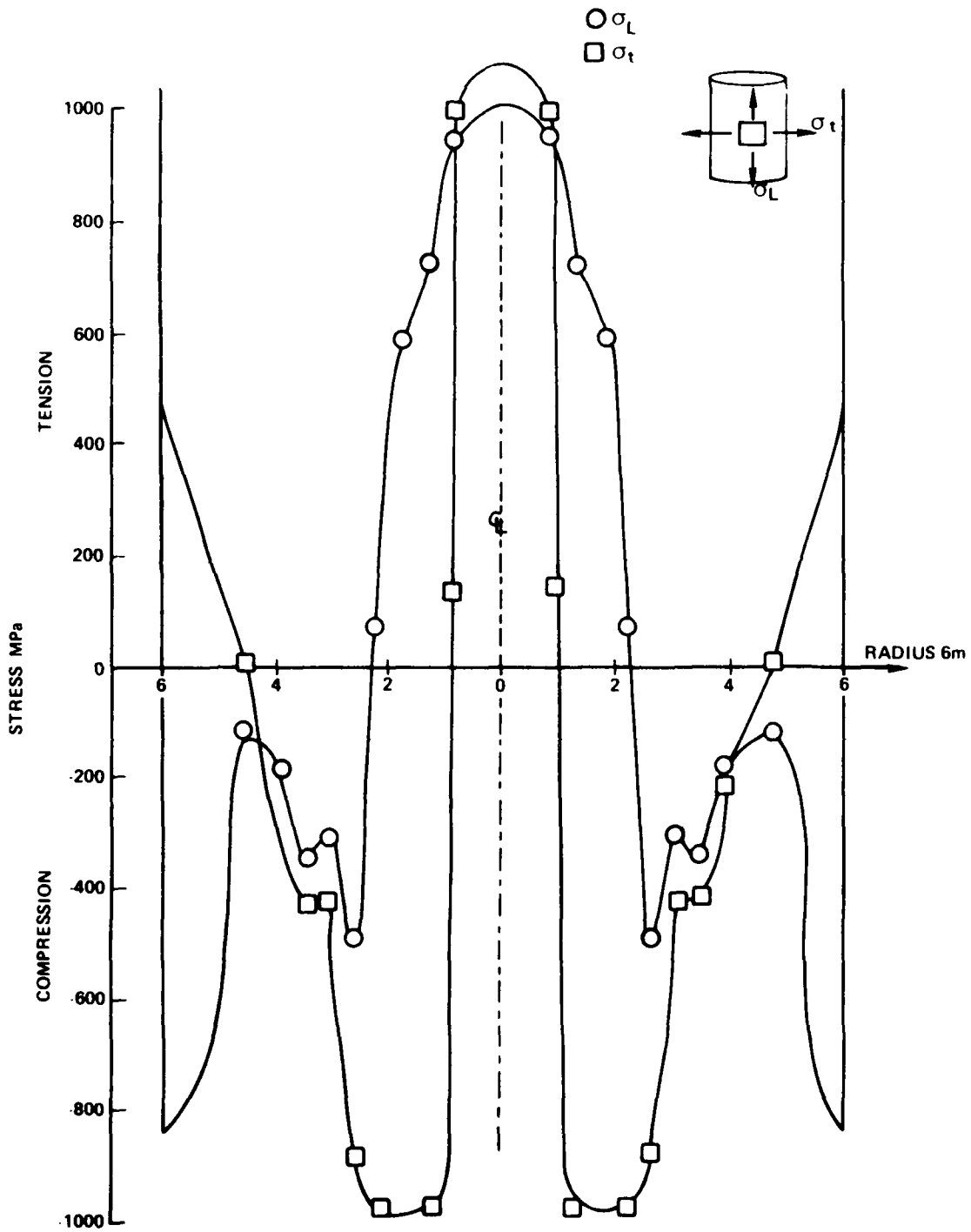


Fig. 3. Internal stress distribution in a penetrator

concomitant embrittlement of the uranium matrix. That this does indeed occur, is shown by the fact that the hydrogen content of the alloy increased from 1 ppm by weight prior to the 40 day temperature-humidity treatment to 22-26 ppm afterwards. As the solubility of hydrogen in α uranium is less than 0.5 ppm at room temperature, hydride precipitates nucleate ahead of the corrosion crack forming a path of easy crack propagation. Such a zone of UH_3 precipitates extending approximately 20 μm from a corrosion crack is illustrated in Fig 4. As the crack extends, new surface area of the metal is exposed and the corrosion and embrittlement process repeats in steps.

UH_3 particles by themselves do not provide sites of nucleation for corrosion cracks. In many cases hydride precipitates near the surface of the samples, such as those shown at the grain boundaries in Figure 5, were observed. In none was a crack initiating at these locations. U-2 wt.-% Mo alloys are usually not very susceptible to corrosion cracking in moist air. No cracking was observed in specimens without the presence of the stringer inclusions.

As previously mentioned, cracks have difficulty nucleating in media where the metal uniformly corrodes at high rates. In the present case, when a stringer of inclusions intersects the surface of the metal, a natural crevice is present which is subject to high tangential tensile stresses and which provides a site for a corrosion pit rapidly forms, as shown in Fig. 6. This occurs because of the more active nature of the metal at the base of the crevice than at its sides. Corrosion attack in the crevice with subsequent absorption of embrittling nascent hydrogen and formation of low density corrosion products produces a state of very high tensile stress causing crack propagation from the base of the corrosion pit.

Figure 7 shows a high magnification SEM photomicrograph of a typical inclusion. No discernable composition difference between the bulk of the inclusions and the matrix material was detected by X-ray dispersive analysis; however light elements such as oxygen and nitrogen are not detectable with this technique. The most likely identify of the inclusions are uranium oxides and/or nitrides formed during the melting and casting of the ingots as a result of an insufficient vacuum. Subsequent working of the material results in the formation of stringer inclusions. In isolated instances, X-ray dispersive analysis revealed the presence of sulphur, iron, and magnesium segregated in the inclusions. These elements were, however, observed only in widely distributed areas.

CONCLUSIONS

Components of a uranium-molybdenum alloy not usually susceptible to corrosion cracking in moist air were found to have a severe cracking problem. Metallographic examination indicated that stringers of blocky shaped, internally cracked inclusions were responsible. The inclusions, when intersecting the surface of the components, served to provide a site for accelerated corrosion attack, either due to crevice or galvanic corrosion effects. Cathodically produced hydrogen diffusing into the metal at these



Fig. 4. UH_3 precipitates around corrosion crack. 800X



Fig. 5. UH_3 precipitates in grain boundary near sample surface. 800X



Fig. 6. Corrosion pit and inclusions near sample surface. 800X

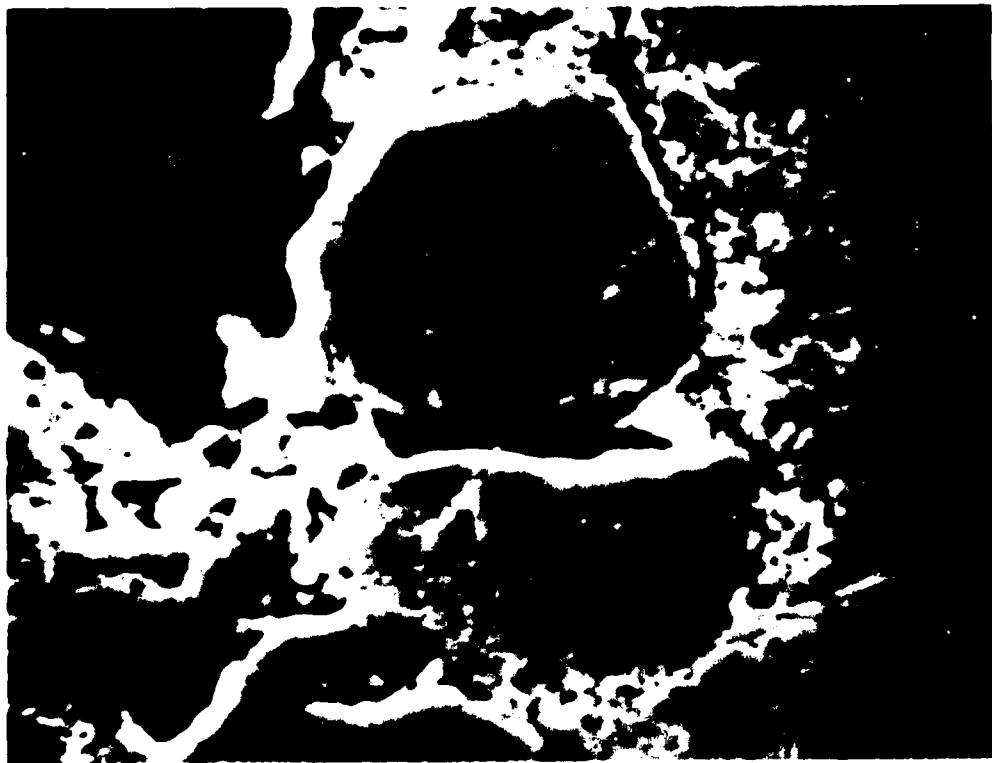


Fig. 7. Inclusion. 2,500X

sites caused the formation of hydride precipitates which resulted in alloy embrittlement. Tensile stresses responsible for crack propagation were provided by internal fabrication stresses and/or by corrosion products of lower density than the matrix alloy producing a wedging effect and subsequent crack propagation.

REFERENCES/LITERATURE

1. Burkart, M. W. and Lustman B., "Corrosion Mechanisms of Uranium-Base Alloys in High Temperature Water," Trans. AIME 212 (1956) 26.
2. Pridgeon, J. W., "Stress Corrosion Cracking in Uranium-Molybdenum Alloys" USAEC Report Y-1417 (1963).
3. Orman, S. and Picton G., "The Stress Corrosion Cracking of Uranium-Molybdenum Alloys," AWRE Report No. 015/70 (1970).
4. Peterson, C. A. W., "A Stress Corrosion Cracking Study of a Gamma Extruded U-8 wt.-% Mo-0.50 wt.-% Ti Alloy," USAEC Report UCRL-14132 (1965).
5. Hopkinson, B. E., Corrosion Technology 7 (1959) 337.
6. Davis, W. D., "Solubility Determination, Diffusion and Mechanical Effects of Hydrogen in Uranium," KAPL-1548 (Aug. 1, 1956).

THE DESIGN OF METAL-INFILTRATED POROUS CERAMICS
FOR MAXIMUM FRACTURE RESISTANCE

Richard A. Queeney, Associate Professor
Department of Engineering Science and Mechanics
The Pennsylvania State University
126 Hammond Building
University Park, PA 16802

INTRODUCTION

Specialized mechanical design applications suggest that ceramic materials might prove to be superior design choices as compared to conventional metallic alloys. Elevated temperature environments and wear-prone mechanisms are two of these applications. The current popularity of developmental efforts to produce fully-dense ceramic bodies, as reported in the ceramic literature, attests to the promise of these solids. At least two difficulties will remain even though such bodies are successfully fabricated--low fracture resistance and fabrication difficulties encountered in machining complex structural shapes. Metal-infiltrated, porous ceramics have been demonstrated to possess strength response levels superior to those of fully-dense bodies. Infiltrated solids can often be fabricated in a rough form close to finish dimensions and are comparatively facile to machine. Structural shapes have been fabricated and their production processes discussed[1]. Successful infiltration of a porous body implies interconnected pores; however, some porosity is not impregnated by the molten metal and residual porosity exists in such materials, usually less than 5.0% of the total volume. The residual porosity, coupled with cycling thermal and mechanical loads, leads to pore (or crack) growth and structural failure is produced by catastrophic crack extension. The design of a successful infiltrated body, then, must include a prediction and maximization of fracture resistance based upon the thermo-mechanical response of the composite's constituents and the distribution of these constituents.

Certain chemical effects must be considered for a successful ceramic-metal body. The molten metal must wet the ceramic pore surfaces; moreover, it has been found that the best infiltrants should form an intermediate layer of reaction in the pore[2]. The usefulness of the infiltrant is limited by its relatively low melting point; conversely, ease of infiltration is enhanced by lowered melting point. Given these material constraints, the fracture resistance of the resultant composite body will be determined by the metal's thermo-elastic and thermo-plastic response, by the spatial distribution of the metal (the average pore diameter and interpore spacing), and by the thermoelastic response of the ceramic matrix, assuming that the latter never achieves a state of phenomenological plasticity. These quantities should make possible a predictive design analysis of the mechanical response (fracture resistance) expectations inherent in the composite.

FORMULATION

There are two competing phenomena occurring to effect the fracture resistance of a metal-infiltrated ceramic as its temperature is increased. The first effect is the generation of tresselated stress fields around the pores as the temperature increase produces different strains in the metal pore than in the ceramic matrix: the second is the degradation of mechanical strength of the metallic phase, possibly extreme if its metallurgical state is not stable. Simplifying the complex interconnected pore structure to isolated porosity of spherical shape, we find from previous studies[3] that large, localized components of compressive normal stress are generated in the radial sense from the pore center in the brittle matrix. These stresses would not only reduce the tensile components present in a Mode I[4] crack extension process for a fully dense solid, but are even more advantageous than the concentrated stresses that would surround empty pores. If an average interpore spacing λ is present, and the thermal expansion misfit stresses act appreciably only to a distance of four average pore radii, $4a$, then the difference in strain energy release rate, ΔG , obtained relative to a fully dense matrix, is approximately:

$$\Delta G = \left(\frac{1}{\lambda}\right)^2 \frac{p^2 (4a)^3 \pi^2 (1+\nu_m)}{E_m} \quad (1)$$

$$P = \frac{(\alpha_m - \alpha_i) \Delta T}{\frac{1+\nu_m}{2E_m} + \frac{1-2\nu_i}{E_i}} \quad (2)$$

Here, α = linear coefficient of thermal expansion, ΔT at the change in temperature, ν poisson ratio, and E the modulus of elasticity. The subscript m refers to the ceramic matrix, and i to the infiltrant.

More important than the increase in fracture resistance expected from equation (1), however, is the eventual weakening effect brought about by the thermally-induced strength degradation of the metallic infiltrant. As long as the infiltrant can maintain the elastic stresses that give rise to equation (1), linear strengthening, as reflected in loads, with increasing temperature can be expected. When the sharp-notch stress fields, however, exceed the yield stress of the infiltrant in pores nearest the crack tip, departures from linearity in fracture resistance will ensue. When all pores within an average interpore spacing have stress states equal to the equivalent yield stress of the infiltrant, further strengthening cannot be expected unless the infiltrant possesses a high degree of work hardening.

The location of the elastic-plastic interface ahead of a sharp crack, in the plane of the crack, is given by[5]:

$$r_p \approx 2 \left(\frac{1}{6\pi} \right) \left(\frac{K_I}{\sigma_y} \right)^2 \quad (3)$$

where σ_y is the yield strength of the material and K_I is the Mode I stress intensity factor pertinent to the structural shape, crack geometry, and loading details. Equation (3) refers to plane strain constraints, certainly true for the infiltrant held in the pores. The maximum value for the plastic zone radius will occur for $K_I \rightarrow K_{IC}$ the critical value of stress intensity or fracture toughness. When this radius value reaches the interpore spacing λ , fracture resistance K_{IC} will have reached a plateau value.

Two metal-infiltrated composites were available for this study. One was a 2024 aluminum alloy infiltrated commercial graphite described elsewhere[2]. The other was a reaction-sintered Si_3N_4 similarly infiltrated. Both materials were prepared by Amos J. Shaler Associates, Park Avenue, State College, PA, 16801. The aluminum alloy can be presumed to be overaged, as the composite samples were air cooled after infiltration. Bulk mechanical response quantities are available in the literature for such alloy forms[6] and the temperature dependence of the aluminum yield stress is given in Table I.

Yield Stress(ksi)	47	45	36	19	9	6	4
Temperature($^{\circ}C$)	24	100	150	205	260	315	370

Table I. Yield strength levels and temperature for 2024-T7 (overaged) Aluminum

Infiltrated pore sizes and dispersion were directly measured on plane polished sections at 500X magnification. The average infiltrated pore diameter was 4.1×10^{-4} inches for the Si_3N_4 and 2.8×10^{-3} inches for the graphite: the interpore separations averaged 2.2×10^{-3} inches for Si_3N_4 and 2.8×10^{-3} inches for the graphite. Typical photomicrographs are shown in Figure (1) below. It should be possible, via equation (3), to predict upper limits to the fracture toughness K_{IC} for both materials.

ASSESSMENT

The results of testing for fracture resistance are given in Figure (2) below. The fracture toughness measurements were made on beams subjected to 4-point bend loading. The test samples had a cross-section 0.25 inches square and a span of 2.0 inches between the outer most bearing points. The innermost bearing points were 0.5 inches from the outermost, bearing a 0.08 inch deep notched constant moment center span of 1.0 inches. Notch radii were finite, less than 10^{-4} inches for graphite, 10^{-3} inches for the Si_3N_4 . The samples were placed in a loading jig with thermocouple attached, lowered into the thermal jacket already at temperature, and tested when the sample

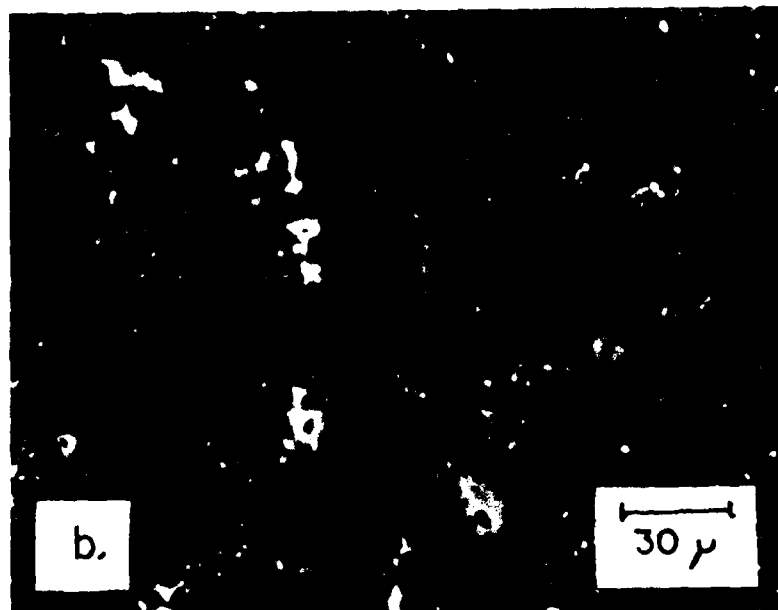
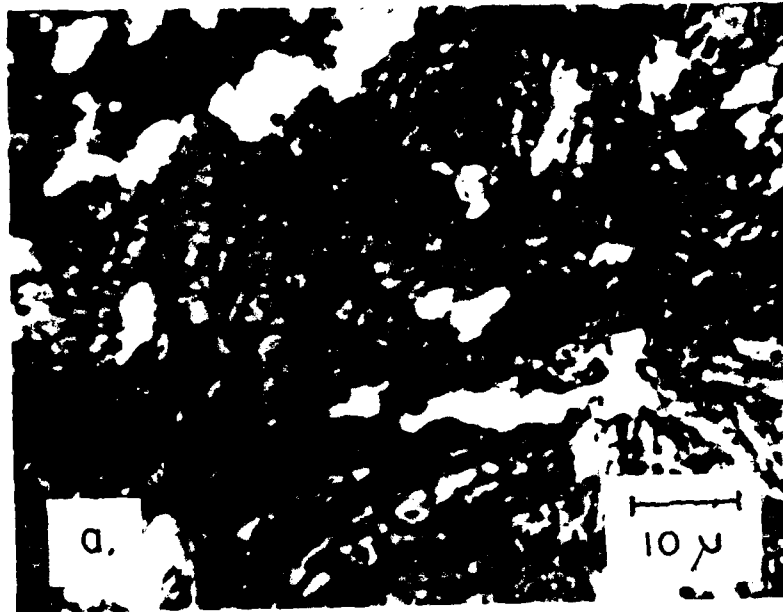


Figure 1. Infiltrated Ceramic Microstructures a. Graphite
b. Si_3N_4

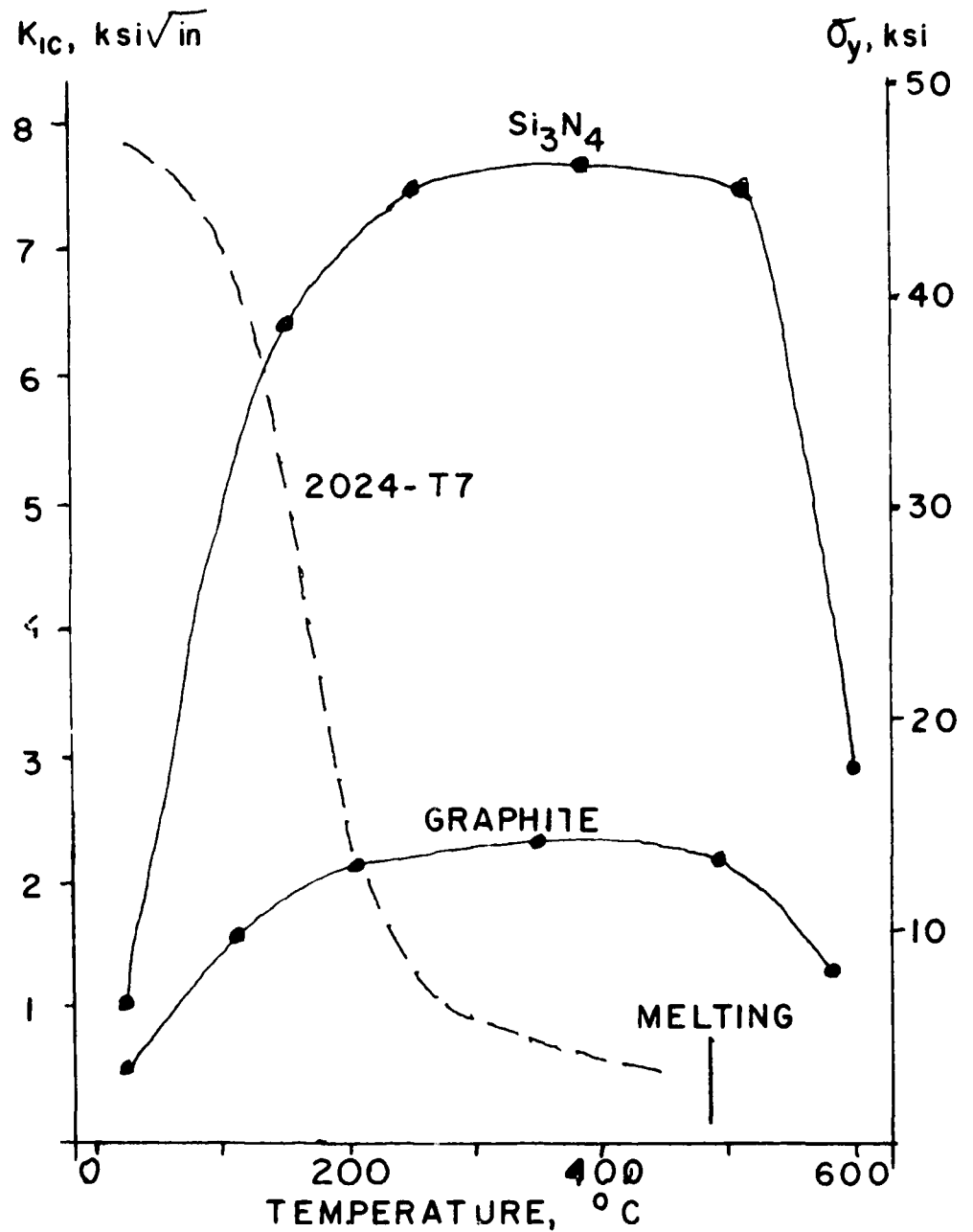


Figure 2. Measured Fracture Toughness (K_{1C}) Values and Infiltrant Yield Strength vs. Temperature for Two Infiltrated Ceramics.

reached the desired temperature. Fracture toughness values were calculated using maximum load values and specimen geometry measures in a suitable stress intensity factor formula for the configuration[7].

Applying equation (3) to the experimentally determined K_{IC} values, and using tensile yield strength data for the infiltrant (Table I), we find plastic zone sizes to be 0.0031 and 0.002 inches for the graphite and Si_3N_4 , respectively at the maximum K_{IC} values for the two materials. These values agree closely with the measured values of 0.0028 and 0.0022 inches for graphite and Si_3N_4 . Clearly, then, the maximum fracture resistance will occur when a complete pore sample, included within an average interpore spacing ahead of the crack tip, carries the maximum elastic stress (yield stress) for the infiltrant. It should be noted that previous attempts[2] to explain the fracture resistance at room temperature, without using fracture mechanics concepts, were unsuccessful.

In summary, then, it appears that knowledge of the filled pore spatial distribution in a metal infiltrated porous ceramic, as well as characterization of the metallic alloy mechanical response at elevated temperatures, will suffice to predict the maximum expected fracture toughness of the composite. Suitable alloys can be chosen to suit application demands, provided that the molten metal wets the ceramic. The above treatment is rather brief and not complete, however. The task still remains for the fracture mechanics analyst to provide the materials engineer with a more complete thermo-elastic stress analysis of sharp flaws imbedded in multiphase media.

CONCLUSIONS

With the preceding analysis as a guide to future design of metal-infiltrated ceramics, it only remains for engineers to find applications for which the adoption of these materials represent not only a technological, but also an economic, improvement over existing design options. New material fabrication processes, including ultrasonically-aided infiltration, are currently being investigated to realize the technological potential of these solids by ameliorating economic difficulties.

REFERENCES

1. Conway, J. C., and Shaler, A. J., "Development and Analysis of Modified Graphites for Deep Dea Submergence", Am. Ceram. Soc. Bull., V.50, No.8, August 1971, 656-658.
2. Queeney, R. A., and Turner, R. L., "Fracture Resistance of Metal-Infiltrated Porous Graphites", Fracture Mechanics of Ceramics, V.2, Plenum, New York, 1974, 807-815.
3. Selsing, J., "Internal Stresses in Ceramics", J. Amer. Ceram. Soc., V.44, No.8, August 1961, 419.

4. Paris, P. C., and Sih, G. C., "Stress Analysis of Cracks", ASTM Special Technical Publication 381, Philadelphia, 1965, 30-58.
5. Irwin, G. R., "Plastic Zone Near a Crack and Fracture Toughness", Proceedings of Seventh Sagamore Ordinance Material Research Conference, Syracuse University, 1960, 4-63.
6. Aluminum Standards and Data, The Aluminum Association, New York, 1969, 31.
7. Tada, H., Paris, P., and Irwin, G., The Stress Analysis of Cracks Handbook, Del Research Corp., Hellertown, PA, 1973, 2.13.

Army Materials and Mechanics Research Center,
Watertown, Massachusetts 02172
CASE STUDIES IN FRACTURE MECHANICS -
Thomas P. Rich and David J. Cartwright

AD
UNCLASSIFIED
UNLIMITED DISTRIBUTION

key words

Monograph Series AMMRC MS 77-5, June 1977,
470 pp, illus-tables, D/A Project 11865803M75
AMCWS Code 685803.7290012

Aerospace craft
Aircraft engines
Airframes

A collection of more than thirty case studies is presented covering a wide range of practical engineering applications of fracture mechanics to design, inspection, maintenance, and failure analysis. The case studies are written by individual specialists within industry, government, and academia from the United States and Great Britain. The collection is divided into five sections corresponding to (1) Aerospace, (2) Joints and Mountings, (3) Pressure Vessels and Rotating Machinery, (4) Surface Vehicles, and (5) Materials. Most of the case studies are between twelve and fifteen pages in length and written to a standard format. The interdisciplinary nature of fracture applications is reflected in the case studies, and the reader is brought through a sequential development and solution of actual engineering problems in an interesting and economical manner.

Army Materials and Mechanics Research Center,
Watertown, Massachusetts 02172
CASE STUDIES IN FRACTURE MECHANICS -
Thomas P. Rich and David J. Cartwright

AD
UNCLASSIFIED
UNLIMITED DISTRIBUTION

key words

Monograph Series AMMRC MS 77-5, June 1977,
470 pp, illus-tables, D/A Project 11865803M75
AMCWS Code 685803.7290012

Aerospace craft
Aircraft engines
Airframes

A collection of more than thirty case studies is presented covering a wide range of practical engineering applications of fracture mechanics to design, inspection, maintenance, and failure analysis. The case studies are written by individual specialists within industry, government, and academia from the United States and Great Britain. The collection is divided into five sections corresponding to (1) Aerospace, (2) Joints and Mountings, (3) Pressure Vessels and Rotating Machinery, (4) Surface Vehicles, and (5) Materials. Most of the case studies are between twelve and fifteen pages in length and written to a standard format. The interdisciplinary nature of fracture applications is reflected in the case studies, and the reader is brought through a sequential development and solution of actual engineering problems in an interesting and economical manner.

Army Materials and Mechanics Research Center,
Watertown, Massachusetts 02172
CASE STUDIES IN FRACTURE MECHANICS -
Thomas P. Rich and David J. Cartwright

AD
UNCLASSIFIED
UNLIMITED DISTRIBUTION

key words

Monograph Series AMMRC MS 77-5, June 1977,
470 pp, illus-tables, D/A Project 11865803M75
AMCWS Code 685803.7290012

Aerospace craft
Aircraft engines
Airframes

A collection of more than thirty case studies is presented covering a wide range of practical engineering applications of fracture mechanics to design, inspection, maintenance, and failure analysis. The case studies are written by individual specialists within industry, government, and academia from the United States and Great Britain. The collection is divided into five sections corresponding to (1) Aerospace, (2) Joints and Mountings, (3) Pressure Vessels and Rotating Machinery, (4) Surface Vehicles, and (5) Materials. Most of the case studies are between twelve and fifteen pages in length and written to a standard format. The interdisciplinary nature of fracture applications is reflected in the case studies, and the reader is brought through a sequential development and solution of actual engineering problems in an interesting and economical manner.

Army Materials and Mechanics Research Center,
Watertown, Massachusetts 02172
CASE STUDIES IN FRACTURE MECHANICS -
Thomas P. Rich and David J. Cartwright

AD
UNCLASSIFIED
UNLIMITED DISTRIBUTION

key words

Monograph Series AMMRC MS 77-5, June 1977,
470 pp, illus-tables, D/A Project 11865803M75
AMCWS Code 685803.7290012

Aerospace craft
Aircraft engines
Airframes

A collection of more than thirty case studies is presented covering a wide range of practical engineering applications of fracture mechanics to design, inspection, maintenance, and failure analysis. The case studies are written by individual specialists within industry, government, and academia from the United States and Great Britain. The collection is divided into five sections corresponding to (1) Aerospace, (2) Joints and Mountings, (3) Pressure Vessels and Rotating Machinery, (4) Surface Vehicles, and (5) Materials. Most of the case studies are between twelve and fifteen pages in length and written to a standard format. The interdisciplinary nature of fracture applications is reflected in the case studies, and the reader is brought through a sequential development and solution of actual engineering problems in an interesting and economical manner.

Army Materials and Mechanics Research Center,
Watertown, Massachusetts 02172
CASE STUDIES IN FRACTURE MECHANICS -
Thomas P. Rich and David J. Cartwright

Monograph Series AMMRC MS 77-5, June 1977,
470 pp, illus-tables, D/A Project 11865803M75
AMCMS Code 685803.729001.2

A collection of more than thirty case studies is presented covering a wide range of practical engineering applications of fracture mechanics to design, inspection, maintenance, and failure analysis. The case studies are written by individual specialists within industry, government, and academia from the United States and Great Britain. The collection is divided into five sections corresponding to (1) Aerospace, (2) Joints and Mountings, (3) Pressure Vessels and Rotating Machinery, (4) Surface Vehicles, and (5) Materials. Most of the case studies are between twelve and fifteen pages in length and written to a standard format. The interdisciplinary nature of fracture applications is reflected in the case studies, and the reader is brought through a sequential development and solution of actual engineering problems in an interesting and economical manner.

AC
UNCLASSIFIED
UNLIMITED DISTRIBUTION

Key Words

Aerospace craft
Aircraft engines
Airframes

Army Materials and Mechanics Research Center,
Watertown, Massachusetts 02172
CASE STUDIES IN FRACTURE MECHANICS -
Thomas P. Rich and David J. Cartwright

Monograph Series AMMRC MS 77-5, June 1977,
470 pp, illus-tables, D/A Project 11865803M75
AMCMS Code 685803.729001.1

A collection of more than thirty case studies is presented covering a wide range of practical engineering applications of fracture mechanics to design, inspection, maintenance, and failure analysis. The case studies are written by individual specialists within industry, government, and academia from the United States and Great Britain. The collection is divided into five sections corresponding to (1) Aerospace, (2) Joints and Mountings, (3) Pressure Vessels and Rotating Machinery, (4) Surface Vehicles, and (5) Materials. Most of the case studies are between twelve and fifteen pages in length and written to a standard format. The interdisciplinary nature of fracture applications is reflected in the case studies, and the reader is brought through a sequential development and solution of actual engineering problems in an interesting and economical manner.

AC

UNCLASSIFIED
UNLIMITED DISTRIBUTION

Key Words

Aerospace craft
Aircraft engines
Airframes

Army Materials and Mechanics Research Center,
Watertown, Massachusetts 02172
CASE STUDIES IN FRACTURE MECHANICS -
Thomas P. Rich and David J. Cartwright

Monograph Series AMMRC MS 77-5, June 1977,
470 pp, illus-tables, D/A Project 11865803M75
AMCMS Code 685803.729001.2

A collection of more than thirty case studies is presented covering a wide range of practical engineering applications of fracture mechanics to design, inspection, maintenance, and failure analysis. The case studies are written by individual specialists within industry, government, and academia from the United States and Great Britain. The collection is divided into five sections corresponding to (1) Aerospace, (2) Joints and Mountings, (3) Pressure Vessels and Rotating Machinery, (4) Surface Vehicles, and (5) Materials. Most of the case studies are between twelve and fifteen pages in length and written to a standard format. The interdisciplinary nature of fracture applications is reflected in the case studies, and the reader is brought through a sequential development and solution of actual engineering problems in an interesting and economical manner.

AD
UNCLASSIFIED
UNLIMITED DISTRIBUTION

Key Words

Aerospace craft
Aircraft engines
Airframes

Army Materials and Mechanics Research Center,
Watertown, Massachusetts 02172
CASE STUDIES IN FRACTURE MECHANICS -
Thomas P. Rich and David J. Cartwright

Monograph Series AMMRC MS 77-5, June 1977,
470 pp, illus-tables, D/A Project 11865803M75
AMCMS Code 685803.729001.1

A collection of more than thirty case studies is presented covering a wide range of practical engineering applications of fracture mechanics to design, inspection, maintenance, and failure analysis. The case studies are written by individual specialists within industry, government, and academia from the United States and Great Britain. The collection is divided into five sections corresponding to (1) Aerospace, (2) Joints and Mountings, (3) Pressure Vessels and Rotating Machinery, (4) Surface Vehicles, and (5) Materials. Most of the case studies are between twelve and fifteen pages in length and written to a standard format. The interdisciplinary nature of fracture applications is reflected in the case studies, and the reader is brought through a sequential development and solution of actual engineering problems in an interesting and economical manner.

AC

UNCLASSIFIED
UNLIMITED DISTRIBUTION

Key Words

Aerospace craft
Aircraft engines
Airframes

AMMRC MS 77-5

CASE STUDIES IN FRACTURE MECHANICS

Rich and Cartwright

DEPARTMENT OF THE ARMY
ARMY MATERIALS AND MECHANICS RESEARCH CENTER
Watertown, Massachusetts 02172

POSTAGE AND FEES PAID
DEPARTMENT OF THE ARMY
DOD 314

OFFICIAL BUSINESS

THIRD CLASS MAIL

DEFENSE DOCUMENTATION CENTER
CAMERON STATION 1 of 12
BUILDING # 5
5010 DUKE ST.
ALEXANDRIA, VA. 22314